UNIVERSITY OF CALIFORNIA
SANTA CRUZ

SOFT LEPTONS, HARD PROBLEMS: SEARCHES FOR THE ELECTROWEAK PRODUCTION OF SUPERSYMMETRIC PARTICLES IN COMPRESSED MASS SPECTRA WITH THE ATLAS DETECTOR

A dissertation submitted in partial satisfaction of the
requirements for the degree of

DOCTOR OF PHILOSOPHY

in

PHYSICS

by

Jeffrey D. Shahinian

March 2020

The Dissertation of Jeffrey D. Shahinian
is approved:

Professor Jason Nielsen, Chair

Professor Michael Hance

Professor Bruce Schumm

Quentin Williams
Acting Vice Provost and Dean of Graduate Studies

Table of Contents

List of Figures

List of Tables

Abstract

Soft Leptons, Hard Problems: Searches for the Electroweak Production of Supersymmetric Particles in Compressed Mass Spectra with the ATLAS Detector

by

Jeffrey D. Shahinian

Supersymmetry is an attractive extension of the Standard Model of particle physics that posits an additional spacetime symmetry relating fermions and bosons. Phenomenologically, supersymmetry predicts the existence of bosonic superpartners for each of the Standard Model fermions and vice versa. In doing so, many outstanding issues in particle physics can be solved, including the nature of dark matter, the hierarchy problem, and gauge coupling unification.

This dissertation presents searches for the direct electroweak production of supersymmetric states within compressed mass spectra, which generically lead to soft particles in the final state. These searches use 139 fb^{-1} of $\sqrt{s} = 13$ TeV proton–proton collision data collected by the ATLAS experiment at the Large Hadron Collider between 2015 and 2018. Selected events contain two oppositely-charged, same-flavor leptons with low transverse momenta, missing transverse energy, and additional hadronic activity from initial-state radiation.

No statistically significant deviations from the Standard Model predictions are observed in the data. The results are used to set limits on the masses of the supersymmetric states in the context of R-parity-conserving simplified models in which the lightest supersymmetric particle is a neutralino arising from nearly mass-degenerate decays of the lightest chargino, the second-to-lightest neutralino, or a slepton. These limits significantly extend existing constraints on well-motivated dark matter scenarios.

For my parents

Acknowledgments

Thank you Mike Hance for advising me on this journey. I've learned so much in the way of physics and what it takes be an independent researcher from you – despite the fact that we didn't overlap on the same continent for very long. In truth, I'll never fully understand your ability to think so cogently about physics during our weekly chats (5 a.m. for you?). All of this speaks to your dedication, generosity, and support as an advisor. For that, I am forever grateful.

I would also like to extend my gratitude to the remaining members of my dissertation committee, Jason Nielsen and Bruce Schumm. Thank you for providing constructive and crucial feedback on this work, especially given the unreasonably tight time frame I gave you. Furthermore, I want to thank you both for providing such a welcoming and supportive environment both within the classroom and the ATLAS group at SCIPP. It was a joy to learn from you both.

A special debt of gratitude is owed to the compressed electroweak SUSY team: Joana Machado Miguens, Stefano Zambito, Michael Holzbock, Julia Gonski, Shun Akatsuka, Lorenzo Rossini, Joey Reichert, and Andy Aukerman. Over the course of putting together this dissertation, I was yet again reminded of how impressive you all are as researchers. I can't thank you enough for welcoming me into the group and putting up with me at the beginning when I was still figuring out how all of this SUSY business works. Your dedication and ingenuity is an inspiration. I've learned a tremendous amount from you all over the past few years and I am genuinely proud to call you colleagues.

Over the course of graduate school, I've been fortunate to make incredible friends both in Santa Cruz and Geneva. Thank you to my fellow UCSC graduate students Christian Johnson, Adam Reyes, Natasha Woods, and Jake Pasner for your friendship and the countless hours spent bouncing (mostly crazy) ideas back

and forth. Thank you as well to the many amazing people who enriched my life in Geneva. There's quite a bit of turnaround at CERN so this list could never be exhaustive, but I want to especially thank Doug Davis, Kelvin Mei, Ian Dyckes, Lucas Flores, Sophia Bennett, Elodie Resseguie, Andrés Delannoy, and Cameron Bravo for making my life abroad a joyous one. I better see you all at la Perle du Lac down the road.

Finally, I would like to thank my parents, whose love and support never ceases. Thank you for being a beacon of hard work and decency throughout my life. You've given me everything. I should call more often.

Part I

Introduction

Abandon all plans, ye who enter here.

Chapter 1

Introduction

Reductionism is the name of the game in particle physics, an area of study that has a rich tradition of shaping our understanding of nature at both the smallest and largest distance scales. By enumerating the fundamental particles and the laws that govern their interactions, the Standard Model (SM) of particle physics has provided both incredible predictive and descriptive power, from the existence of the Higgs boson to the shining of the stars. It has even withstood the test of the TeV scale, which is being probed by the ATLAS and CMS experiments using proton-proton collisions delivered by CERN's Large Hadron Collider (LHC).

Yet the story remains incomplete, as many observed phenomena of nature remain unaccounted for by the SM. Some of these open problems are easy to formulate. For example, what is the nature of the dark matter, which constitutes approximately 25% of the total energy density of the universe based on astrophysical observations? What mechanism in the early universe produced the matter-antimatter asymmetry in the observable universe? Other questions are more slippery and perhaps even aesthetic in nature. What role, if any, does fine-tuning play in the observed Higgs boson mass at the weak scale? If dark energy is simply the cosmological constant, why does it have such a small value and why

is it in the range that can support large scale structure?

Supersymmetry (SUSY) is a well-studied and well-motivated extension of the SM that could provide solutions to some of these problems by positing an additional spacetime symmetry relating bosons to fermions. This symmetry serves to double the particle content of the SM by introducing fermionic superpartners for each of the SM bosons, and vice versa. If these states have masses near the weak scale, then not only can they potentially be produced and discovered at the LHC, but they can also provide a dark matter candidate particle and account for the observed Higgs boson mass in a natural way. This has led to a huge effort on the part of the ATLAS and CMS experiments to search for a multitude of signatures that SUSY could produce. Yet so far, no direct evidence exists in favor of SUSY. Since the LHC collides colored particles, the strongest constraints on SUSY are on strongly-coupled SUSY particles such as the superpartners of the top quark and gluon fields, which are expected to have relatively large production cross-sections for a given (LHC-accessible) mass. Comparatively, searches for the superpartners of the electroweak gauge and Higgs bosons, for example, are significantly weaker. With the current and future LHC datasets, though, the ATLAS and CMS experiments are able to probe the electroweak sector of SUSY more extensively.

This dissertation presents searches for the direct electroweak production of SUSY states within "compressed" mass spectra using 139 fb^{-1} of $\sqrt{s} = 13$ TeV proton–proton collision data collected by the ATLAS experiment at the LHC between 2015 and 2018. In these compressed scenarios, the masses of the targeted SUSY particles have very similar invariant masses. Such models can easily be accounted for in SUSY while simultaneously solving the issues related to dark matter, the weak-scale Higgs mass, and gauge coupling unification at high energy.

They also present significant experimental challenges, as the nearly-degenerate decays of the SUSY particles lead to final states containing low-energy particles that are difficult to faithfully reconstruct in the detector. The searches presented here target events containing two low-momentum leptons of the same flavor (electrons or muons) and opposite electric charge, missing energy in plane transverse to the LHC beam line, and additional hadronic activity from initial-state radiation. The results of the searches are subsequently interpreted in the context of R-parity-conserving SUSY models in which the lightest SUSY particle is a neutralino that is produced from the nearly-mass degenerate decays of the lightest chargino, the second-to-lightest neutralino, or the superpartners of the SM electron and muon.

The overall structure of this dissertation is as follows. The simplified SUSY models used for designing the searches and interpreting the results are presented in Part II. An overview of the LHC and the ATLAS detector is given in Part III. The search design, including optimization and background modeling, is given in Part IV. Finally, the results of the statistical analysis are presented in Part V.

Part II

Theoretical Motivation

For sale: Supersymmetry, possibly worn.

Chapter 2

The Standard Model of Particle Physics

The SM is an internally-consistent and extremely predictive theory of fundamental particles and interactions. In particular, it describes the dynamics of all of the known forces and particles, with the exception of gravity. Its development in the second half of the 20^{th} century was driven by both theoretical and experimental discoveries and remains the state of the art in describing nature at the smallest distance scales and highest energies that can currently be probed in the laboratory. It is a triumph of the human intellect and a testament to the creativity and ingenuity of countless physicists around the world. But it is also known to be an inadequate description of nature on the whole.

This chapter is not meant to provide a complete pedagogical overview of this rich and stubbornly robust theory of fundamental particles and interactions. Instead, Section 2.1 provides a brief description of the important concepts that motivate the construction of the SM Lagrangian density. Section 2.2, meanwhile, describes the particle content of the SM. Finally, a brief survey of the shortcomings of the SM is given in Section 2.3, with emphasis placed on the issues that are

relevant to the searches for new physics presented in this dissertation.

2.1 Theoretical Underpinnings

In broad terms, the SM is a theoretical framework that describes the strong, weak, and electromagnetic forces between the elementary particles that comprise the known universe. It is based on Quantum Field Theory, which describes particles as local excitations in their corresponding relativistic quantized fields. In the SM, these fields are described by a renormalizable Lagrangian density, $\mathcal{L}$, that is invariant under local, continuous transformations of the symmetry group

$$SU(3)_C \otimes SU(2)_L \otimes U(1)_Y \tag{2.1}$$

where the subscripts C, L, and Y indicate the color, weak isospin, and hypercharge quantum numbers, respectively. $SU(3)_C$ is the gauge group that governs the strong interaction that is responsible for nuclear stability, while the group $SU(2)_L \otimes U(1)_Y$ constitutes the weak and electromagnetic forces, which are responsible for nuclear decay and electromagnetism, respectively.

Enforcing the above symmetries leads to terms in $\mathcal{L}$ that include additional spin-1 gauge fields that mediate the strong, weak, and electromagnetic interactions. There are eight generators of $SU(3)_C$, which correspond to the massless gluons that mediate the strong force (and are themselves charged under the group). The $SU(2)_L$ group has three generators, which correspond to the massive $W^{\pm}$ and Z bosons that mediate the weak force. Finally, the $U(1)_Y$ group that produces the electromagnetic interaction has just one generator, corresponding to the massless photon.

The simplest Lagrangian density that satisfies the above criteria has a short-

coming in that it only describes massless fields, which obviously does not correspond to nature. In order to provide masses to the fermions and the massive gauge bosons in a gauge-invariant way, a scalar field is added to the theory that spontaneously breaks the $SU(2)_L \otimes U(1)_Y$ gauge symmetry at low energies. This is known as the Higgs mechanism, which was not experimentally verified until the discovery of the Higgs boson by the ATLAS and CMS collaborations in 2012 [1, 2].

2.2 Particle Content

The SM describes the interactions of quantum fields that can be categorized according to their spin, where fermions constitute the matter that makes up the universe and the gauge bosons mediate interactions between them. The Higgs boson is the only scalar field in the theory and provides a mechanism for generating particle masses in a gauge-invariant way through spontaneous symmetry breaking. A schematic of the particle content of the SM is shown in Figure 2.1, which groups the particles according to the text below.

Fermions are fields that carry spin-1/2 and collectively comprise the known matter content of the universe, whereas bosons have integer spin values and mediate the forces governed by the SM. The fermions can further be divided into quarks and leptons, where both groups are charged under $SU(2)_L \otimes U(1)_Y$ but only the quarks are charged under $SU(3)_C$ and therefore have an associated color. Both the quarks and leptons are organized into three generations of isospin doublets, with each generation corresponding to larger masses. The reason for the existence of three such generations is an open question in theoretical particle physics. The quarks carry fractional electric charge, where the up-type quark within a given generation has a charge of $+\frac{2}{3}e$ and the down-type quark carries charge of $-\frac{1}{3}e$.

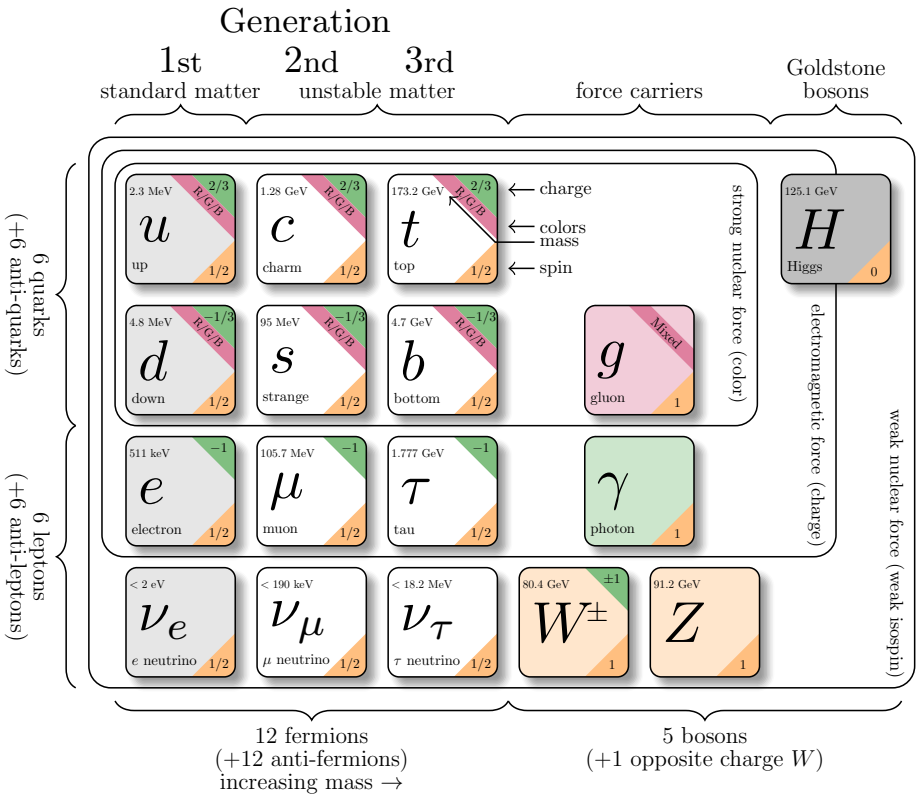

Figure 2.1: A schematic of the particle content of the SM in which the particles are grouped according to the forces they experience/mediate, their spin, and their generation (in the case of fermions), modified from [3].

Leptons, on the other hand, carry integer values of the electric charge. Within a lepton generation, the up-type lepton has electric charge $+1e$, while the down-type lepton, called a neutrino, is uncharged and therefore only participates in the weak interaction. All of these fermions have corresponding anti-particles that carry the opposite charge.

The gauge bosons carry spin-1 and are introduced after demanding $\mathcal{L}$ to be invariant under the respective SM gauge group, as described above. In total, eight massless gluons mediate the strong force, each of which carries both color and anti-color charge. An important consequence of the gluons being charged is that they can interact with themselves, effectively leading to an anti-screening scenario in which the strong force increases in strength at long distances but weakens at short distances. Phenomenologically, this means that quarks can never be observed in isolation. Instead, as the distance between quarks grows, there reaches a point when it becomes energetically favorable to create a quark-antiquark pair from the vacuum, and this process repeats itself until the quarks and gluons are eventually confined into colorless states called hadrons. The time scale over which this "hadronization" process occurs is roughly determined by the QCD scale parameter $\Lambda_{\mathrm{QCD}}^{-1} \approx 250\,\mathrm{MeV}^{-1}$. From the point of view of current particle physics experiments, this time scale can be thought of as being instantaneous. The only exception to this is the top-quark, which decays via the weak force before undergoing hadronization due its large mass.

The electroweak sector consists of a massless photon that mediates the electromagnetic interaction and three massive gauge bosons, $W^{\pm}$ and Z, that mediate the weak force. The $W^{\pm}$ bosons represent charged currents that change lepton and quark flavors, while the neutral Z boson conserves flavor. Finally, a massive scalar Higgs boson, discovered in 2012 by the ATLAS and CMS collaborations,

provides gauge-invariant mass terms in the Lagrangian density for the massive fermions and gauge bosons.

2.3 Shortcomings

It remains difficult to overstate the incredible success of the SM as a predictive framework over a wide range of energy scales. For example, Figure 2.2 shows the excellent agreement between the measured and predicted production cross-sections for a wide variety of SM processes. But the program of particle physics is far from over, as many unresolved experimental observations and theoretical difficulties suggest the need for physical theories that extend beyond the Standard Model (BSM). Of particular relevance for the searches presented here is the existence of dark matter, the stability of the Higgs boson mass at the weak scale, and the anomalous magnetic moment of the muon, as described below. Other tensions that are beyond the scope of this dissertation include (but are certainly not limited to) the observed matter-antimatter asymmetry in the universe, the lack of a quantum description of the gravitational force, the generation of non-zero neutrino masses, and the apparent suppression of CP violation in the strong interaction. Those relevant to the searches presented in this dissertation are briefly discussed below.

Dark matter A host of astrophysical observations indicate the existence of a new form of matter that potentially only interacts gravitationally with SM particles. The lack of any electromagnetic interaction motivates the term "dark matter" (DM) to describe this unexplained particle sector. Evidence for DM has been observed based on its gravitational interaction with ordinary matter, manifested in different ways and across vastly different distance scales. Galactic rotation curves, for example, have been observed to not follow the $v \sim 1/\sqrt{r}$

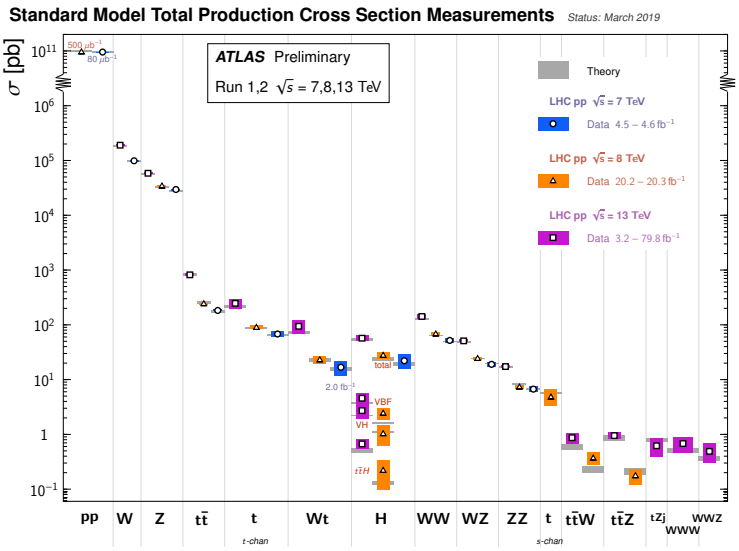

Figure 2.2: A summary of the predicted and ATLAS-measured production cross-sections for a variety of SM processes [4].

prediction from simple Newtonian gravity, where v is the velocity of some massive object in the galaxy (e.g. a star) and r is the radial distance from the center of the galaxy [5]. Galaxy cluster motion [6] and gravitational lensing observations [7] also support the notion of particle DM, in addition to recent surveys of the cosmic microwave background, which indicate that DM contributes approximately 25% of the total energy density of the universe, compared to the $\sim$ 5% contribution from matter explained by the SM [8, 9]. With the above evidence considered, a preferred paradigm has emerged in which the DM candidate is a weakly-interacting massive particle (WIMP) that is cold (i.e. does not travel at relativistic velocities), neutral, stable on cosmological time scales, and has a mass and interaction rate that satisfies the observed relic density. Elucidating the nature of the DM remains one of the most highly-active research programs in particle physics.

Higgs boson mass and fine-tuning Within the SM, the mass of the Higgs boson at tree level, $m_{H,\text{tree}}$ is a free parameter. Crucially, though, it is expected to

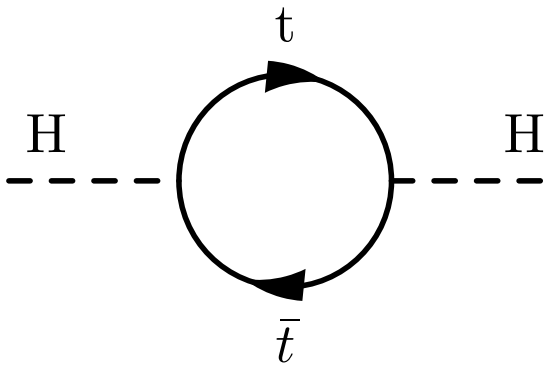

Figure 2.3: A one-loop diagram involving the Higgs propagator and top-quarks, which gives the largest contribution to the Higgs mass radiative correction in the SM.

receive radiative contributions from loop diagrams, where the size of the correction partially depends on the coupling between Higgs and the particle running in the loop. Schematically, the Higgs boson mass can be parameterized according to

$$m_H^2 = m_{H,\text{tree}}^2 + \Delta m_H^2, \tag{2.2}$$

where $m_{H,\text{tree}}$ is a free parameter in the theory that sets the tree level Higgs mass and Δm_H^2 represents the contributions from radiative corrections. The largest coupling in the SM is the Yukawa coupling between the Higgs and the top-quark, y_t, so loops involving top-quarks, an example of which is shown in Figure 2.3, provide the leading contributions to the radiative corrections. Unlike the fermions and gauge bosons, though, no symmetry exists to regulate these radiative corrections and protect the the Higgs mass from running up to some large energy scale.

Taking the top-quark contribution as an example, the radiative correction to

the Higgs mass is given by

$$\Delta m_H^2 = -\frac{|y_t|^2}{16\pi^2}\left[2\Lambda_{\mathrm{UV}}^2 + \mathcal{O}\left(m_t^2 \ln\left(\frac{\Lambda_{\mathrm{UV}}}{m_t}\right)\right)\right], \tag{2.3}$$

where m_t is the mass of the top-quark and Λ_{UV} is the loop-regulating cutoff scale and indicates the energy scale at which the SM is expected to become invalid [10, 11]. The importance takeaway from Equation 2.3 is that the radiative correction to the Higgs mass diverges quadratically with Λ_{UV}. If the cutoff is at the Plank scale such that $\Lambda_{\mathrm{UV}} = 2.4 \times 10^{18}$ GeV, then it becomes difficult to reconcile the observed weak-scale Higgs mass with these corrections. In order for this to happen without extending the particle content of the SM, extremely fine-tuned cancellations would need to occur over many orders of magnitude in order to give the observed Higgs mass of approximately 125 GeV. Fine-tuning to such a degree is generally not deemed to be an attractive solution, and this argument is often used to invoke the need for new physics that provides a dynamical solution. If one instead demands that the radiative corrections represent a small contribution to the observed Higgs mass (i.e. $\Delta m_H^2 < m_H^2$), then $\frac{|y_t|^2}{8\pi^2}\Lambda_{\mathrm{UV}}^2 < m_H^2$. Plugging in $y_t \approx 1$ and $m_H = 125\,\mathrm{GeV}$, one finds that $\Lambda_{\mathrm{UV}} \lesssim 1\,\mathrm{TeV}$. This is an exciting prospect for experimental particle physicists, as this argument suggest that new particles should show up near the TeV scale, which is currently within experimental reach.

Anomalous magnetic moment of the muon The magnetic moment, $\vec{\mu}$, of a point-like spin-1/2 particle is proportional to its spin, $\vec{S}$, according to

$$\vec{\mu} = g\frac{q}{2m}\vec{S}, \tag{2.4}$$

where q is the particle's electric charge, m is its mass, and g is a dimensionless proportionality constant called the gyromagnetic ratio. Tree level calculations in this context predict $g = 2$, while loop diagrams can provide small radiative corrections that contribute to the anomalous magnetic moment:

$$a = \frac{g-2}{2}. \tag{2.5}$$

In the SM, radiative corrections to the muon anomalous magnetic moment, a_μ, arise from QED loops involving leptons and photons, electroweak loops involving the massive gauge and Higgs bosons, and QCD loops involving hadrons. On the other hand, BSM theories such as Supersymmetry introduce new particles that couple to the muon and therefore lead to significant modifications to a_μ. For some lepton ℓ, the BSM contributions to a_ℓ generally scale with m_ℓ^2, which is why a_μ is expected to be more sensitive to new physics than the anomalous magnetic moment of the electron, despite current measurements on the latter being more precise by several orders of magnitude. Since a_μ can be determined by experiment and calculated within the SM with excellent precision, it presents a significant test of the theory. Currently, the most precise measurement of anomalous magnetic moment of the muon, a_μ^{exp}, has been performed by E821 experiment [12] and differs from the SM prediction, a_μ^{SM}, by

$$\Delta a_\mu = a_\mu^{\text{exp}} - a_\mu^{\text{SM}} = 268(63)(43) \times 10^{-11}, \tag{2.6}$$

where the numbers in parentheses represent the experimental and theoretical uncertainties, respectively. Overall, this difference amounts to a 3.5σ discrepancy that remains one of the most significant indications of BSM physics. Interestingly, the Muon $g-2$ experiment [13, 14], stationed at Fermilab, should soon present

an even more precise measurement of a_μ^{exp} that may help elucidate the current tension.

Chapter 3

Supersymmetry

Supersymmetry (SUSY) [15, 16, 17, 18, 19, 20] is a well-motivated extension of the SM that posits an additional spacetime symmetry that relates fermions and bosons through an operator Q that transforms one into the other:

$$Q|\text{ Fermion }\rangle = |\text{ Boson }\rangle, \quad Q|\text{ Boson }\rangle = |\text{ Fermion }\rangle. \tag{3.1}$$

In this way, SUSY predicts the existence of a "superpartner" particle for each SM particle that differs by a half-integer unit of spin. The SM fermions, therefore, are expected to have corresponding spin-0 superpartners, collectively referred to as "sfermions." This naming convention is extended to all superpartners of the individual SM fermions (e.g. slepton, squark, smuon, etc.). Similarly, the SM bosons acquire superpartners with spin-1/2 in the SUSY framework and their names are appended with "ino" to distinguish them from their SM equivalents. The superpartners of the gauge and Higgs bosons are therefore called "gauginos" and "higgsinos," respectively. Over the years, SUSY has been found to potentially provide elegant solutions to the SM shortcomings described in the previous chapter, and has therefore drawn much attention from theorists and experimentalists

alike.

If SUSY were a perfect symmetry of nature, then every superpartner would be mass-degenerate with its SM counterpart. This notion is particularly attractive since it provides an elegant explanation for why the Higgs mass is at the weak scale. To match the example used in the previous section, one can consider the scalar superpartner of the top-quark, $\tilde{t}$, which will couple to the Higgs via a term in the Lagrangian density of the form $-y_{\tilde{t}}|H|^2|\tilde{t}|^2$. In this case, the radiative correction to the Higgs mass due to its coupling to $\tilde{t}$, will be

$$\Delta m_H^2 = +\frac{y_{\tilde{t}}}{16\pi^2}\left[2\Lambda_{\mathrm{UV}}^2 + \mathcal{O}\left(m_{\tilde{t}}^2 \ln\left(\frac{\Lambda_{\mathrm{UV}}}{m_{\tilde{t}}}\right)\right)\right], \tag{3.2}$$

which takes the exact same form as Equation 2.3, but comes with the opposite sign. Note that this argument holds for all pairs of SM fermions f and scalar SUSY partners $\tilde{f}$, not just t and $\tilde{t}$. Thus if $y_{\tilde{f}} = |y_f|^2$, such that the superpartners are mass-degenerate, then the radiative corrections to the Higgs mass exactly cancel at all orders of perturbation theory. This idea is depicted in Figure 3.1, for the example of the Higgs coupling to t and $\tilde{t}$, which would otherwise give the largest contributions to the quadratic divergence if their contributions weren't cancelled by equal and opposite terms in the expansion.

But it is easy to experimentally rule out the existence of a 511 keV selectron, for example, so this symmetry must be broken in such a way that the superpartners acquire larger masses. It is assumed here that SUSY is spontaneously broken in a way that leaves the Lagrangian density invariant under SUSY transformations but the vacuum state breaks the symmetry as low energies. This is completely analogous to the spontaneous breaking of the electroweak symmetry in the SM in which the Higgs mechanism leaves $\mathcal{L}$ invariant under local gauge transformation of the type $SU(2)_L \otimes U(1)_Y$, while the particular vacuum state

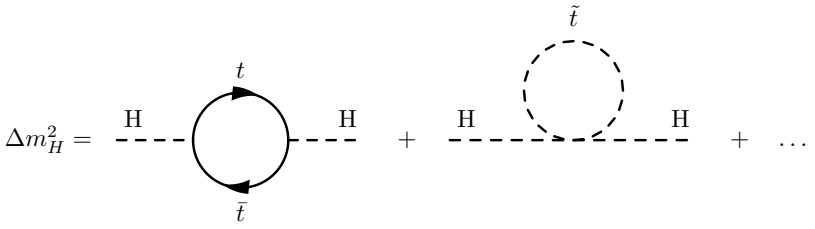

Figure 3.1: A sketch of SUSY's solution to the hierarchy problem, shown for the case of the top-quark and its scalar superpartner. In this framework, the quadratic divergence of the radiative corrections to the Higgs mass is eliminated by introducing particles that only differ by their spin and produce terms in the expansion that have the same magnitude but carry the opposite sign.

breaks the symmetry. While there are many ideas about how SUSY could be broken at high energies, a survey of the possible mechanisms is beyond the scope of this dissertation. Nonetheless, it is assumed here that SUSY is broken softly, such that the superpartners are not too much heavier than their SM counterparts. This choice is made in order to retain the ability to solve the Higgs mass problem in a minimally finely-tuned way. When SUSY is broken, the contributions to the Higgs mass from SM fermions are not exactly canceled by the terms due to their scalar superpartners. At leading order, the correction to the squared Higgs goes like

$$\Delta m_H^2 = \frac{\Lambda_{\text{UV}}^2}{8\pi}\left(y_{\widetilde{S}} - |y_f|^2\right) + \ldots, \tag{3.3}$$

where $\widetilde{S}$ is the SUSY scalar and f is its fermionic SM superpartner. Thus, if the masses are sufficiently different, then the quadratic divergence returns. Similar to the discussion in Section 2.3, if the size of acceptable corrections to the Higgs mass are to be no more than at the level of the weak scale, then the soft SUSY breaking should produce mass-differences between the superpartners that are $\lesssim 1\,\text{TeV}$.

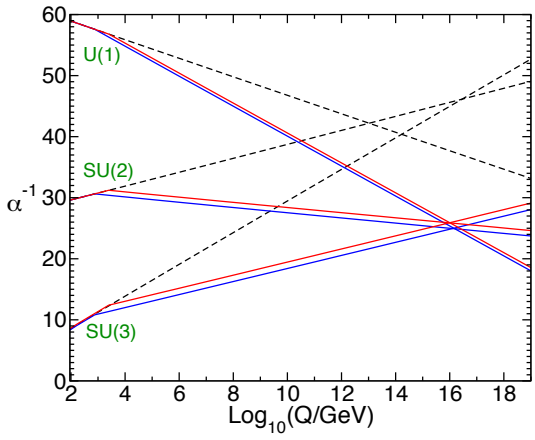

Figure 3.2: The running of the inverse gauge couplings in the SM (dashed lines) and the MSSM (solid lines). The red and blue lines indicate the effect of varying the MSSM particle masses in the range of 750 GeV to 2.5 TeV, as well as varying $\alpha_3(m_Z)$ between 0.117 and 0.120 [11].

3.1 Minimal Supersymmetric Standard Model

Given the complexity introduced by a full theory of SUSY, it is advantageous to instead consider a version that introduces the minimum number of new particles and interactions while remaining internally and phenomenologically consistent. This is the goal of the Minimal Supersymmetric Standard Model (MSSM), which is assumed in the searches for SUSY presented in this dissertation.

Within the MSSM, it has been shown that the introduction of the new SUSY states can approximately unify the separate gauge couplings of $SU(3)_C$, $SU(2)_L$, and $U(1)_Y$ at an energy of $\sim 10^{16}$ GeV [21]. The running of the couplings are shown in Figure 3.2 for the SM with and without a weak-scale MSSM extension. The unification of the couplings within the MSSM is seen as a hint that SUSY could be a good signpost on the way to a Grand Unified Theory of particle physics.

In general, there are perfectly renormalizable and gauge-invariant terms that can be added to the SUSY Lagrangian density that lead to baryon and lepton number violation. Yet such processes are heavily constrained by experiments.

For example, baryon number violation implies proton decay, which is currently constrained by lower limits on the proton lifetime corresponding to 1.6×10^{34} years [22]. Since the MSSM aims to be phenomenologically consistent with observation, these terms are removed from the theory by introducing a symmetry called "R-parity", which is constructed to conserve the quantity

$$P_R = (-1)^{3(B-L)+2s}, \tag{3.4}$$

where B is baryon number, L is lepton number, and s is spin. This symmetry should be understood as being multiplicative, such that the the overall R-parity of a system of particles is given by multiplying the individual particles' values of P_R together. Under this construction, the SM particles have $P_R = +1$, while SUSY particles have $P_R = -1$. This proposed symmetry guarantees that SM and SUSY states do not mix and has important consequences for SUSY phenomenology. In particular, R-parity implies that the lightest Supersymmetric particle (LSP) must be stable since there are no lighter SUSY particles to decay into and decays into SM particles would break the symmetry. Importantly, if the LSP is electrically neutral, then it is a prime candidate for dark matter. Additionally, R-parity conservation implies that SUSY states are produced in pairs at colliders (since the initial state only involves SM particles) and that a non-LSP SUSY state must ultimately decay into an odd number of LSPs.

Within the MSSM, two Higgs doublets are needed in order to maintain the cancellation of gauge anomalies as well as to provide masses for the up-type quarks, down-type quarks, and charged leptons [11]. These doublets are denoted by H_u and H_d, which carry weak hypercharge quantum numbers of $+\frac{1}{2}$ and $-\frac{1}{2}$, respectively. Each of these doublets consists of one electrically charged and one electrically neutral complex scalar field. For H_u, these fields are arranged as (H_u^+, H_u^0),

while the H_d doublet is given by (H_d^0, H_d^-). In this way, H_u gives masses to the up-type quarks and H_d gives masses to the down-type quarks and charged leptons. The spin-1/2 superpartners of these doublets are the Higgsinos, denoted by $\widetilde{H}_u = (\widetilde{H}_u^+, \widetilde{H}_u^0)$ and $\widetilde{H}_d = (\widetilde{H}_d^0, \widetilde{H}_d^-)$. The phenomenology of the MSSM is partially dependent on the ratio of the acquired vacuum expectation values of H_u^0 and H_d^0, which are denoted v_u and v_d, respectively. The ratio $\frac{v_u}{v_d}$ is typically parameterized in terms of an angle β according to $\tan\beta \equiv \frac{v_u}{v_d}$.

While the MSSM is the simplest SUSY extension to the SM, it still boasts a rich phenomenology that is largely outside the scope of this dissertation. Instead, the following will discuss the electroweak sector of the MSSM that is relevant for the searches presented here.

Electroweakinos Due to electroweak symmetry breaking, the higgsinos and electroweak gauginos mix to form what are collectively referred to as "electroweakinos." In particular, a collection of four neutral mass eigenstates called "neutralinos" are formed by the mixing of the neutral higgsinos, $\widetilde{H}_u^0$ and $\widetilde{H}_d^0$, and the neutral electroweak gauginos, $\widetilde{B}$ and $\widetilde{W}^0$. The neutralinos are denoted by $\tilde{\chi}_1^0$, $\tilde{\chi}_2^0$, $\tilde{\chi}_3^0$, and $\tilde{\chi}_4^0$, where the increasing subscript indicates increasing mass. In the models considered in this dissertation the lightest neutralino $\tilde{\chi}_1^0$ is also the LSP. Since the MSSM assumes R-parity conservation and $\tilde{\chi}_1^0$ is electrically neutral, it represents an excellent dark matter candidate that is sufficiently massive to account for the observed relic density, has an indefinite lifetime, and interacts only weakly with matter. The charged mass eigenstates, called "charginos," are similarly formed by the mixing of the charged Higgsinos, $\widetilde{H}_u^+$ and $\widetilde{H}_d^-$, and the winos, $\widetilde{W}^+$ and $\widetilde{W}^-$. These chargino states are denoted by $\tilde{\chi}_1^\pm$ and $\tilde{\chi}_2^\pm$, using the same convention for indicating the relative masses.

The term in the Lagrangian density of the MSSM that gives the neutralino

masses contains the neutralino mixing matrix $\boldsymbol{M}_{\tilde{\chi}^0}$, which can be parameterized as

$$\boldsymbol{M}_{\tilde{\chi}^0} = \begin{pmatrix} M_1 & 0 & -c_\beta s_W m_Z & s_\beta s_W m_Z \\ 0 & M_2 & c_\beta c_W m_Z & -s_\beta c_W m_Z \\ -c_\beta s_W m_Z & c_\beta c_W m_Z & 0 & -\mu \\ s_\beta s_W m_Z & -s_\beta c_W m_Z & -\mu & 0 \end{pmatrix}, \tag{3.5}$$

where $c_\beta = \cos\beta$, $s_\beta = \sin\beta$, $c_W = \cos\theta_W$, and $s_W = \sin\theta_W$. The latter angle, θ_W, is the well-known weak mixing angle of the SM that describes the mixing of the SM W^0 and B fields to form the Z and γ. The analogous chargino mixing matrix $\boldsymbol{M}_{\tilde{\chi}^\pm}$ can be written as block form as

$$\boldsymbol{M}_{\tilde{\chi}^\pm} = \begin{pmatrix} 0 & \boldsymbol{X}^T \\ \boldsymbol{X} & 0 \end{pmatrix}, \text{ where } \boldsymbol{X} = \begin{pmatrix} M_2 & \sqrt{2} s_\beta m_W \\ \sqrt{2} c_\beta m_W & \mu \end{pmatrix}. \tag{3.6}$$

It turns out not be a particularly fruitful exercise to write out the eigenvalues of these matrices in their general form. Instead, taking various limits involving the mass parameters μ, M_1, and M_2 provides simple expressions that are simultaneously relevant to well-motivated models of SUSY involving compressed mass spectra, as discussed in Section 4.1.

Sfermions In the MSSM, the sfermions are superpartners of the left-handed and right-handed SM fermions. Even though these SUSY states are scalars and therefore cannot be assigned a helicity, the superpartners of the left-handed (right-handed) fermions will be referred to as the left-handed (right-handed) sfermions, and can be generically denoted with $\tilde{f}_L$ ($\tilde{f}_R$). Generally speaking, scalars in the MSSM can mix with each other if they have the same quantum numbers for electric charge, R-parity, and color. This leads to quite a messy situation in which mass eigenstates of the squark and sleptons must be obtained by diagonalizing three

6×6 mass matrices: one for the up-type squarks $(\tilde{u}_L, \tilde{c}_L, \tilde{t}_L, \tilde{u}_R, \tilde{c}_R, \tilde{t}_R)$, one for the down-type squarks $(\tilde{d}_L, \tilde{s}_L, \tilde{b}_L, \tilde{d}_R, \tilde{s}_R, \tilde{b}_R)$ and one for the charged sleptons $(\tilde{e}_L, \tilde{\mu}_L, \tilde{\tau}_L, \tilde{e}_R, \tilde{\mu}_R, \tilde{\tau}_R)$. A 3×3 mass matrix for the sneutrinos $(\tilde{\nu}_e, \tilde{\nu}_\mu, \tilde{\nu}_\tau)$ would need to be diagonalized as well.

Fortunately, constraints on flavor-changing neutral currents in the SM suggest that soft SUSY breaking is universal and flavor-agnostic in such a way that most of these mixing angles become very small and depend on the size of the Yukawa coupling [11]. In the case of the first two sfermion generations, the Yukawa couplings are small and the $L - R$ mixing is expected to be negligible, resulting in nearly mass-degenerate states organized according to

$$(\tilde{e}_R, \tilde{\mu}_R), (\tilde{\nu}_e, \tilde{\nu}_\mu), (\tilde{e}_L, \tilde{\mu}_L), (\tilde{u}_R, \tilde{c}_R), \left(\tilde{d}_R, \tilde{s}_R\right), (\tilde{u}_L, \tilde{c}_L) \text{ and } \left(\tilde{d}_L, \tilde{s}_L\right).$$

On the other hand, the mixing in the third sfermion generation can be large, such that the mass eigenstates $(\tilde{f}_1, \tilde{f}_2)$ are a mixture of the gauge eigenstates $(\tilde{f}_L, \tilde{f}_R)$, related by a unitary mixing matrix that partially depends on $\tan\beta$. In the searches presented in this dissertation, only the smuons and selectrons are sought, and so this non-trivial $L - R$ mixing can be neglected.

Chapter 4

Simplified Models and Phenomenology

The searches presented in this dissertation target the direct production of electroweakino and slepton pairs within compressed mass spectra ($\sim 1\,\text{GeV} - 60\,\text{GeV}$). Such models are relatively under-constrained by the LHC experiments due to the difficulty of reconstructing soft (low-momentum) objects in the detector but provide solutions to some of the most important outstanding problems in particle physics. Motivated by naturalness, the searches in this dissertation include a scenario in which the $\widetilde{\chi}_2^0$, $\widetilde{\chi}_1^0$, and $\widetilde{\chi}_1^\pm$ states are pure higgsinos. Additionally, models in which the higgsino component is decoupled are considered, where the $\widetilde{\chi}_1^0$ is a pure bino state, while the $\widetilde{\chi}_2^0$ and $\widetilde{\chi}_1^\pm$ states are wino-like. These models are motivated by dark matter considerations, along with the slepton model in which the directly-produced sleptons decay to wino-like $\widetilde{\chi}_1^0$ states. In all of the SUSY models considered here, R-parity is assumed so that the $\widetilde{\chi}_1^0$ state is stable and represents the dark matter candidate. Details about the simplified SUSY models are given in Section 4.1, while Section 4.2 gives an overview of the phenomenology of compressed electroweak SUSY.

4.1 Simplified Models: Compressed Mass Spectra

Three different simplified electroweakino models are considered. In the first model, called the "higgsino" model, the compressed mass spectra is motivated by naturalness arguments [23, 24], which suggest that $|\mu|$ should be near the weak scale, while the wino and bino mass parameters are much larger: $|\mu| \ll M_1, M_2$. In this case, the lightest triplet of electroweakinos ($\widetilde{\chi}_2^0$, $\widetilde{\chi}_1^0$, $\widetilde{\chi}_1^\pm$) is dominated by the higgsino component. Using the electroweakino mixing matrices from Equation 3.5 and Equation 3.6, the mass-splittings between these higgsino states can be approximated by assuming either the wino or bino states are decoupled. In the case that $|\mu| < M_2 \ll M_1$, the mass-splittings are approximately

$$\left|m_{\tilde{\chi}_1^\pm}\right| - \left|m_{\tilde{\chi}_1^0}\right| \approx \frac{m_W^2\,(1 \mp s_{2\beta})}{2\,(M_2 + |\mu|)}, \tag{4.1}$$

$$\left|m_{\tilde{\chi}_2^0}\right| - \left|m_{\tilde{\chi}_1^\pm}\right| \approx \frac{m_W^2\,(1 \pm s_{2\beta})}{2\,(M_2 - |\mu|)}, \tag{4.2}$$

$$\left|m_{\tilde{\chi}_2^0}\right| - \left|m_{\tilde{\chi}_1^0}\right| \approx \frac{m_W^2\,(\pm|\mu| s_{2\beta} + M_2)}{(M_2^2 - |\mu|^2)}, \tag{4.3}$$

where the $\pm$ sign corresponds to the sign of μ, and the same notation for the trigonometric functions is used (e.g $s_{2\beta} = \sin 2\beta$). If $|\mu| < M_1 \ll M_2$, then these higgsino mass-splittings can be approximated by

$$\left|m_{\tilde{\chi}_1^\pm}\right| - \left|m_{\tilde{\chi}_1^0}\right| \approx \frac{m_W^2 t_{\theta W}^2\,(1 \pm s_{2\beta})}{2\,(M_1 - |\mu|)}, \tag{4.4}$$

$$\left|m_{\tilde{\chi}_2^0}\right| - \left|m_{\tilde{\chi}_1^\pm}\right| \approx \frac{m_W^2 t_{\theta W}^2\,(1 \mp s_{2\beta})}{2\,(M_1 + |\mu|)}, \tag{4.5}$$

$$\left|m_{\tilde{\chi}_2^0}\right| - \left|m_{\tilde{\chi}_1^0}\right| \approx \frac{m_W^2 t_{\theta W}^2 \left(\pm|\mu| s_{2\beta} + M_1\right)}{\left(M_1^2 - |\mu|^2\right)}. \tag{4.6}$$

In this model, the mass-splittings are driven by the decoupling of the winos and binos. In the case that they are completely decoupled, then the higgsino states are essentially mass degenerate, as splittings of only $\mathcal{O}(100\,\text{MeV})$ are generated by radiative corrections. When the wino and bino masses are set to large but finite values, the lightest electroweakino triplet can be dominated by the higgsino component with mass-splittings on the order of one to tens of GeV, as targeted in this search.

The remaining models are motivated by dark matter models in which the LSP is a pure bino state and the next-to-lightest SUSY state is one to tens of GeV heavier. Such models have been shown to satisfy the dark matter relic density constraints through coannihilation processes in the early universe [25, 26]. While these models do not provide a mechanism for explaining the compressed mass-splittings like the higgsino model, the dark matter angle makes them an attractive signature to search for. In the electroweakino case, the higgsino mass parameter $|\mu|$ is decoupled such that $|M_1| < |M_2| \ll |\mu|$. The $\widetilde{\chi}_1^0$, therefore, is a pure bino state, while the slightly heavier $\widetilde{\chi}_2^0$ and $\widetilde{\chi}_1^\pm$ states are wino-like. In the remainder of this dissertation, the models that satisfy this mass and composition spectra are called the "wino/bino" model, of which two are considered. The only difference between the two wino/bino models is the relative signs of the $\widetilde{\chi}_2^0$ and $\widetilde{\chi}_1^0$ mass eigenvalues, the product of which, $m(\widetilde{\chi}_2^0) \times m(\widetilde{\chi}_1^0)$, can be either positive or negative [27, 28]. As shown in Section 8.2.1, this only impacts the shape of the dilepton invariant mass distribution that is used as the final discriminant in the search for electroweakinos.

Finally, these searches consider the direct production of selectrons and smuons that are nearly degenerate with the $\widetilde{\chi}_1^0$ LSP. In this case, $\Delta m(\widetilde{\ell}, \widetilde{\chi}_1^0) \sim 1 - 60$ GeV

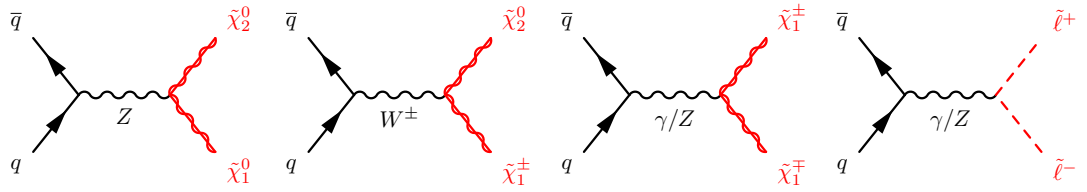

Figure 4.1: Dominant leading-order Feynman diagrams for the direct pair-production production of electroweakinos and sleptons at a proton-proton collider.

is considered. In the rest of this dissertation, "sleptons" will refer to selectrons and smuons, as stau sleptons are not considered. In addition to being able to satisfy the dark matter relic density constraints, the addition of smuons into the theory with masses at the weak scale has also been shown to offer a promising explanation of the muon's anomalous magnetic moment [29], described in Section 2.3.

Production The production of the electroweakino and slepton states is assumed to proceed via s-channel diagrams in which a quark-antiquark pair annihilates to form a gauge boson mediator, which in turn decays to the SUSY states. While it is possible that these particles could be produced in the decays of heavier, colored SUSY states that have much larger production cross-sections, considering such production modes would introduce many additional free parameters into the model (e.g. squark masses and branching ratios). This would greatly complicate the interpretation of the results and it is unclear what a good choice of these parameters would be. Instead, only direct production is considered in order to remain independent of the broader SUSY spectrum, at the cost of lower cross-sections. The dominant tree-level processes considered in these searches are shown in Figure 4.1, while t-channel diagrams involving squark-exchange are ignored since they are expected to have only a small contribution and would also require the precise specification of the squark masses. Details of the production cross-section calculations are given in Section 8.2.

Decays While the SUSY states are assumed to have compressed mass spectra, the range of mass-splitting targeted by these searches still lead to prompt decays in the experiment. Nonetheless, these mass-splittings are smaller than the W and Z boson masses, such that the electroweakino decays must proceed via off-shell gauge bosons according to $\widetilde{\chi}_2^0 \to Z^* \widetilde{\chi}_1^0$ and $\widetilde{\chi}_1^\pm \to W^{\pm *} \widetilde{\chi}_1^0$. In the simplified models, these branching ratios are assumed to be 100%. The sensitivity to electroweakinos in these searches is driven by $Z^* \to \ell\ell$ decays, where these branching ratios depend on the invariant mass of the off-shell Z^*. In the slepton simplified model, the decays are assumed to proceed via $\widetilde{\ell} \to \ell \widetilde{\chi}_1^0$ with a 100% branching ratio. The final state particles from these decays are soft due to the small mass-splittings, making reconstruction and triggering difficult.

4.2 Phenomenology

SUSY within compressed mass spectra is difficult to probe due to the soft objects in the final state, especially at a TeV-scale hadron collider, where these objects can be buried by soft backgrounds. Additionally, if the mass splitting is small enough, the objects may be too soft to pass reconstruction thresholds set by the experiments. In extremely compressed scenarios, the SUSY particles can be long-lived (i.e. $c\tau$ is large enough such that the SUSY particles can fly an appreciable distance into the detector before decaying). These long-lived scenarios are not considered in these searches, however.

Instead, the simplified SUSY models discussed above exhibit prompt decays and lead to events that contain soft leptons. In the case of electroweakino pair-production, the dominant contribution stems from the $\widetilde{\chi}_2^0 \to Z^*(\to \ell\ell)\widetilde{\chi}_1^0$ decay chain. In the simplified slepton models, the leptons arise directly from the decay of the slepton via $\widetilde{\ell} \to \ell \widetilde{\chi}_1^0$. In both cases, there are two soft leptons that are

of the same flavor but have opposite electric charges. The kinematics of these leptons is crucial for disentangling signal events from background processes. In the electroweakinos case, the leptons arise from one leg of the decay chain (for the production of $\widetilde{\chi}_2^0\widetilde{\chi}_1^\pm$, at least) so that their invariant mass will reconstruct the mass-splitting between the $\widetilde{\chi}_2^0$ and $\widetilde{\chi}_1^0$ states. Slepton events are trickier since the final-state leptons originate from different decay legs in the event. Since the other particle in the slepton decays is a $\widetilde{\chi}_1^0$, which is invisible from the point of view of the detector, one cannot calculate an invariant mass that will reconstruct either $m(\widetilde{\ell})$ or $\Delta m(\widetilde{\ell}, \widetilde{\chi}_1^0)$. Fortunately, a variable called m_{T2} can be constructed that provides sensitivity to $\Delta m(\widetilde{\ell}, \widetilde{\chi}_1^0)$, though one needs to guess what the LSP mass is. This variable will be described in detail in Section 10.1. An important feature that is exploited in these searches is the correlation between the mass-splitting of a given signal hypothesis and the transverse momenta of the final-state leptons. When the mass-splitting increases, more energy is available to boost leptons in the decays, leading to harder leptons, on average. As described in Chapter 10, this correlation proves useful for discriminating signal events from backgrounds due to mis-identified leptons.

In addition to the soft leptons, which are below the available trigger thresholds in the signal scenarios considered here, the only other important handle on signal events is the energy in the transverse plane that is carried away by the LSPs. While it is possible to trigger on events in which this missing transverse energy is large, it is not possible for tree-level signal events since the SUSY particles are produced back-to-back in the transverse plane. The missing transverse energy carried away by one of the decay legs, therefore, cancels out the contribution from the other. Overall, then, very little missing transverse energy is reconstructed in events corresponding to the leading-order processes depicted in Figure 4.1.

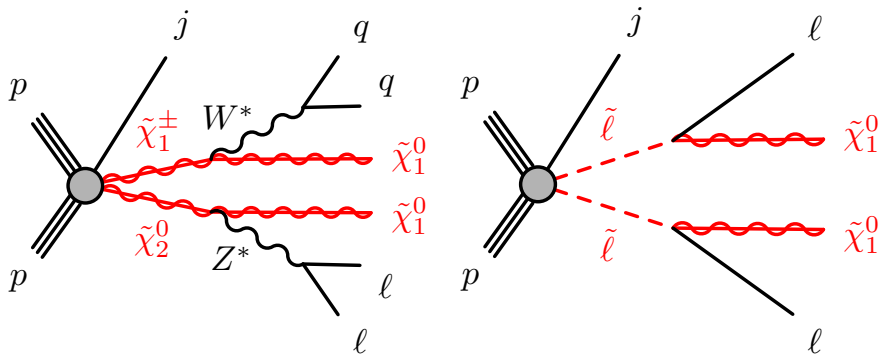

Figure 4.2: Feynman diagrams representing the direct electroweak production of electroweakinos (left) and sleptons (right). As described in the text, an additional hard jet is required to boost the SUSY system.

Taken together, it may seem hopeless to expect a TeV-scale hadron collider to have sensitivity to these scenarios. Fortunately, a workaround exists by instead focusing on next-to-leading order processes in which one of the incoming quarks radiates a gluon, though this of course comes at the cost of lower production cross-sections. Such diagrams for electroweakino and slepton signal processes are shown in Figure 4.2 and represent the targeted processes in these searches. The key insight is that the radiated hadronic activity, which is manifested as a jet in the detector due to the color confinement of QCD, will provide a boost to the SUSY system in the transverse plane. This boost will serve to align the the $\tilde{\chi}_1^0$ states, increasing the reconstructed missing transverse energy in the event. Thus, if the boost is hard enough, missing transverse energy triggers can be used to collect the events. This is the strategy used by the searches presented in this dissertation. But even with the events collected, the hard work of disentangling signal events from various background processes still remains.

Part III

LHC and the ATLAS Detector

Tools of the trade

Chapter 5

The Large Hadron Collider

The Large Hadron Collider (LHC), stationed approximately 100 m underground at the European Organization for Nuclear Research (CERN) outside Geneva, Switzerland, is currently the world's largest and most powerful particle accelerator [30]. The LHC is a circular accelerator with a circumference of 27 km and is designed to collide two counter-propagating proton beams at four different interaction points corresponding to four different experiments: ALICE [31], ATLAS [32], CMS [33], and LHCb [34]. The LHCb experiment was primarily designed to study CP violation in b-hadron interactions. For part of the year, the LHC also produces lead ion collisions, which the ALICE experiment uses to study QCD effects in high energy density environments, such the quark-gluon plasma. ATLAS and CMS are two general purpose particle physics detectors that each have a broad physics program including searches for BSM physics at the high-energy frontier. In this way, ATLAS and CMS are able to provide independent cross-checks of the other experiment's physics results.

Before the protons enter the LHC, they are first accelerated through a series of smaller injection accelerators that each increase the proton energy by an order of magnitude. A diagram of the entire LHC accelerator complex is shown in

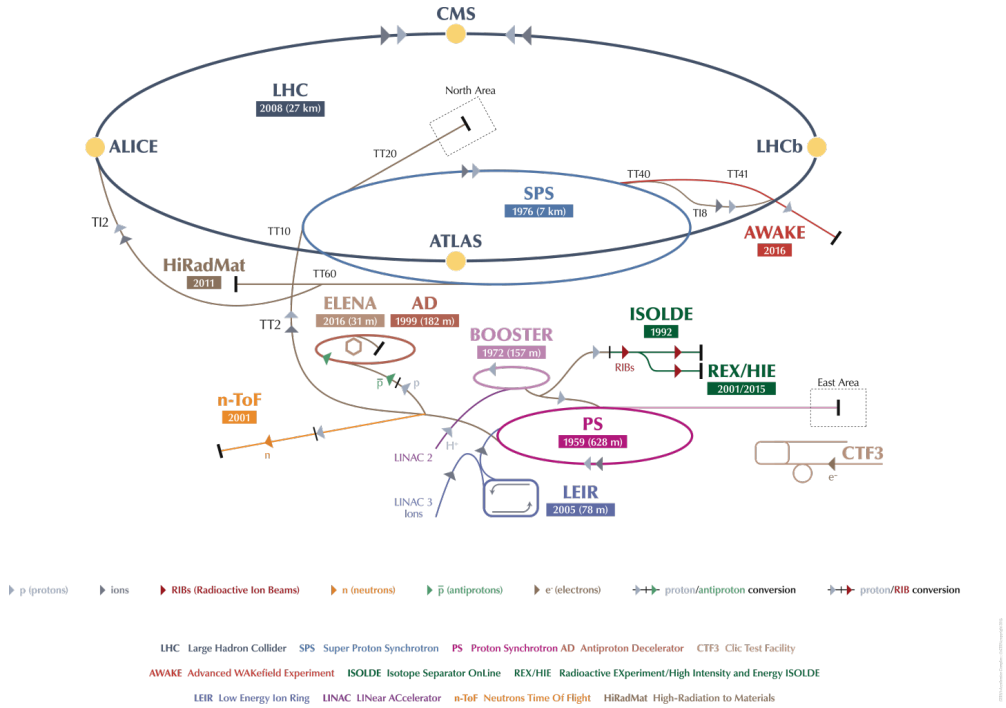

Figure 5.1: Diagram of the CERN accelerator complex with the LHC shown in dark blue [35]. The four main LHC experiments, including ATLAS, are shown as yellow circles.

Figure 5.1. The protons, which are produced by ionizing hydrogen atoms, are first accelerated up to 50 MeV through a linear accelerator called Linac2, though this accelerator will be replaced by another linear accelerator called Linac4 around 2020. Linac4 will actually accelerate H^- ions up to 160 MeV before stripping them of their electrons and handing the protons off to the next step in the accelerator chain. After passing through Linac2, the protons are injected into the remaining circular accelerators. The first of these is the Proton Synchrotron Booster (PSB), which further accelerates them up 1.4 GeV. From there, the protons are injected into the Proton Synchrotron (PS) and then the Super Proton Synchrotron (SPS), which accelerate the protons up to 25 GeV and 450 GeV, respectively.

Finally, the protons enter the LHC at this 450 GeV injection energy, whereupon they are accelerated up to 6.5 TeV using 16 radio frequency cavities that are housed

in four cylindrical refrigerators (two per beam) called called cryomodules. Under normal conditions, the proton beams can circulate in the LHC for ten hours or more before being dumped. While the LHC was designed to accelerate each proton beam to energies as high as 7 TeV, the current center-of-mass energy for the pp collisions is $\sqrt{s} = 13$ TeV. Superconducting magnets are used to control the beam trajectories [30]. A total of 1232 superconducting dipole magnets, each 15 m in length and producing an 8.33 T field, are used to steer the protons around the ring. The beams of protons are also focused by an additional 392 superconducting quadrupole magnets. In order to reach the superconducting state of the NbTi material, liquid helium is used to cool the magnets down to 1.9 K.

Beyond the beam energy, another crucial figure of merit for a hadron collider is the number of inelastic collisions it can produce per unit of time. The physics processes of interest at the LHC, such as Higgs boson and electroweak SUSY production, typically have production cross-sections that are many orders of magnitude below the total pp inelastic cross-section. These processes are therefore incredibly rare, and so the LHC aims to maximize the number of inelastic collisions that it (and the LHC experiments) can safely handle. For this reason, the protons in the LHC are organized into bunches, which are brought into collision with one another. The LHC can hold a maximum of 2808 bunches, each consisting of approximately 10^{11} protons during stable operation [30]. These bunches are circulated at a rate of 40 MHz, corresponding to a 25 ns temporal spacing (or approximately 7.5 m) between each bunch.

Two important quantities characterize the LHC's ability to produce a high number of inelastic pp collisions: instantaneous and integrated luminosity. The first of these is the instantaneous luminosity, L, which measures the number of potential pp interactions produced per second. L is only a function of the beam

parameters, which can be tuned to deliver the desired interaction rates. Assuming that the beams have Gaussian profiles and an equal number of particles in their bunches, the instantaneous luminosity is given by

$$L = \frac{N_b^2 n_b f_{\text{rev}} \gamma}{4\pi \varepsilon_n \beta^*} F, \tag{5.1}$$

where N_b is the number of particles per bunch, n_b is the number of bunches per beam, f_{rev} is the beam's revolution frequency, γ is the relativistic Lorentz factor, ϵ_n is the normalized transverse beam emittance, β^* is the beta function evaluated at the interaction point that characterizes the transverse size of the beam, and F is a geometric factor that can reduce the luminosity by accounting for any crossing angle between the beams. At the LHC, a crossing angle on the order of a few hundred microradians is used to avoid unwanted pp interactions on either side of the interaction point, while avoiding a dramatic reduction in the instantaneous luminosity. The instantaneous luminosity is typically quoted in units of $\text{cm}^{-2}\text{s}^{-1}$, and the peak instantaneous luminosity achieved by the by LHC as a function of time in 2018 is shown in Figure 5.2. To date, the LHC has reached instantaneous luminosities as high as 2.1×10^{34} $\text{cm}^{-2}\text{s}^{-1}$.

The second figure of merit related to the statistical power of particle collider's dataset is the integrated luminosity, $\mathcal{L}$, which is simply the time integral of the instantaneous luminosity:

$$\mathcal{L} = \int L dt. \tag{5.2}$$

The integrated luminosity, is therefore a measure of the total number of pp collisions delivered by over some period of time and is measured in units of inverse area (e.g. cm^{-2} or fb^{-1}). With this definition, the expected total number of events

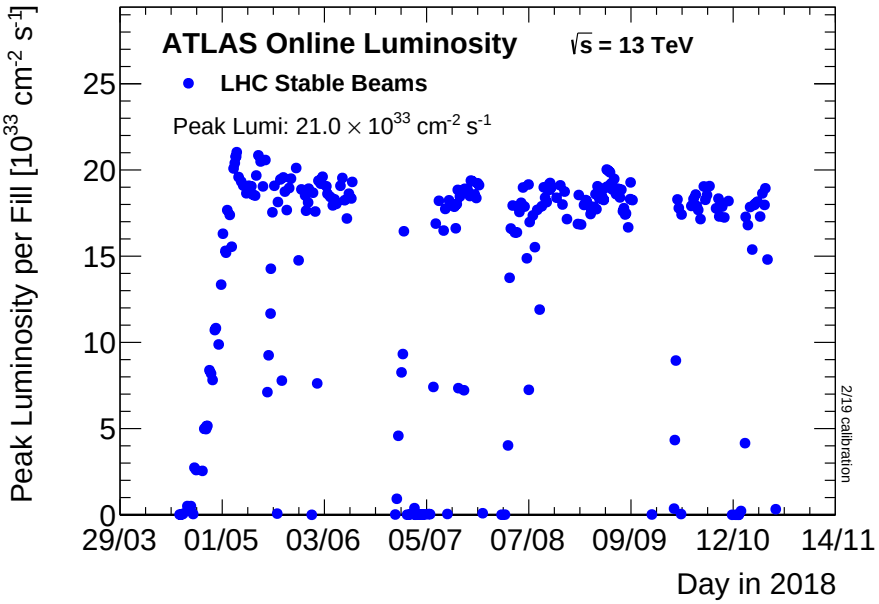

Figure 5.2: The peak instantaneous luminosity delivered to ATLAS as a function of time in 2018 for $\sqrt{s} = 13$ TeV pp collisions with stable beam conditions [36].

produced, N_{event}, for some process with a cross-section σ is just

$$N_{event} = \sigma \mathcal{L}. \tag{5.3}$$

The dataset considered in this work was recorded by the ATLAS detector between 2015 and 2018 and corresponds to an integrated luminosity of 139 fb^{-1}. This dataset could correspond to as many as 75,000 slepton events, assuming a slepton mass of 110 GeV. Crucially, though, this figure does not account for significant reductions due to inefficiencies from the trigger, object reconstruction and identification, as well as event selection and the detector acceptance. After accounting for these effects, that number can easily drop down to tens of events on top of the SM background.

Clearly, then, obtaining large instantaneous luminosities remains crucial for searches for rare processes. By colliding bunches of protons, the LHC does ex-

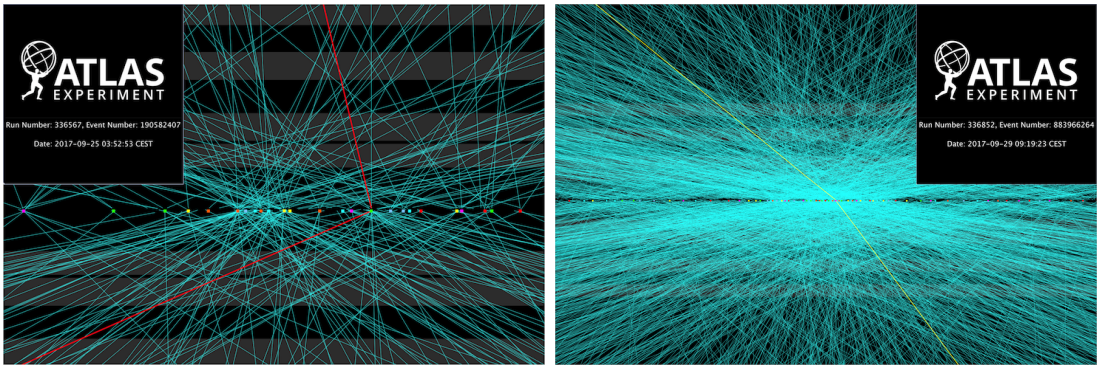

Figure 5.3: ATLAS event displays showing two $Z \to \mu^+\mu^-$ candidate events recorded in 2017. The event on left has a total of 25 reconstructed vertices, while the event on the right has 66. Each reconstructed vertex is indicated by a colored square. The red of yellow lines are associated to the same vertex and indicate the two muons from the potential decay of a Z boson. All other tracks with $p_{\mathrm{T}} > 500\,\mathrm{MeV}$ are shown in light blue [37].

actly this, as many pp interactions take place on average for every bunch-crossing, a phenomenon known as pileup. Often, pileup is given the symbol μ, while its time average is denoted $\langle\mu\rangle$. For data taken between 2015 and 2018, the average number of pp interactions per bunch-crossing was 33.7, while the maximum number reached over 60. While increasing the instantaneous luminosity, multiple interactions per bunch-crossing present a challenge for experiments, as the reconstruction algorithms need to distinguish signatures left in the detector due to one particular interaction from all of the others. Examples of this challenge are presented in Figure 5.3, which shows $Z \to \mu\mu$ candidate events with different numbers of pp interactions. Additionally, since the bunch-spacing at the LHC is only 25 ns, interactions occurring in adjacent bunch-crossings can leave signatures in the event of interest if the electronics integration is longer than this. A detailed description of the ATLAS detector is given in the following chapter.

Chapter 6

The ATLAS Detector

The ATLAS (A Toroidal LHC ApparatuS) detector [32] is a multi-purpose particle detector the surrounds one of the interaction points (IP) at the LHC with nearly 4π solid angle coverage. ATLAS was designed to measure the particles emerging from the proton-proton collisions with excellent precision in order to support a wide-ranging and robust particle physics program, including searches for physics beyond the SM.

The detector has cylindrical symmetry and is 46 m long, 25 m in diameter, and weighs approximately 7000 tons. Many specialized sub-detectors exist within ATLAS in order to detect the wide variety of particles that are produces in the collisions delivered by the LHC. They are arranged in a concentric manner with the innermost system, called the Inner Detector, immersed in a 2 T magnetic field and dedicated to measuring the curved trajectories of charged particles as the emerge from the IP. The Inner Detector is surrounded by a calorimeter system that consists of an Electromagnetic Calorimeter and a Hadronic Calorimeter that measure the energies and directions of electrons/photons and hadrons, respectively. Finally, the Muon Spectrometer is designed to identify and measure the trajectories of muons, which are able to penetrate the all of the previous

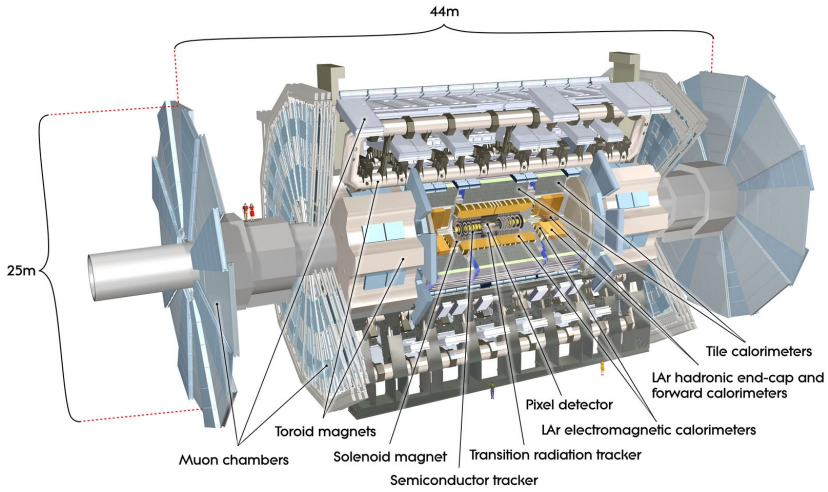

Figure 6.1: A general overview of the ATLAS detector with a cutaway that allows for various sub-detectors to be highlighted [32].

sub-detectors. The Muon Spectrometer is immersed in a toroidal magnetic field in order so that the curved trajectories can be used to make momentum and charge measurements. A rendering of the ATLAS detector, including all of its sub-detectors, is shown in Figure 6.1. In order to select collision events for later analysis, a two-level trigger system is implemented that makes fast decisions about whether or not the event is of interest to ATLAS physics program.

ATLAS uses a right-handed coordinate system centered at the nominal proton-proton IP. The x-axis points towards the center of the LHC ring and the y-axis point vertically upward. Together, these axes define the transverse plane. Using the right-handed convention, the z-axis points along the beam line. Owing to the geometry of the detector, cylindrical coordinates are used. Thus, the (r, ϕ) coordinates are used in the transverse plane, making ϕ the azimuthal angle around the z-axis and $r = \sqrt{x^2 + y^2}$. The polar angle from the z-axis is given by θ. Unfortunately, θ is not a Lorentz-invariant quantity under boosts in the $\hat{z}$ direction.

One could instead use the Lorentz-invariant quantity called rapidity, y, defined as

$$y \equiv \frac{1}{2} \ln \left(\frac{E + p_z}{E - p_z} \right), \tag{6.1}$$

where E is the particle's energy and p_z is the momentum in the $\hat{z}$ direction. But in a coordinate system, it is preferred to use purely geometric quantities and so ATLAS ultimately uses a related quantity called pseudorapidity, denoted by η, which is just the high-energy limit of rapidity. The pseudorapidity is therefore defined as

$$\eta \equiv -\ln \left[\tan \left(\frac{\theta}{2} \right) \right]. \tag{6.2}$$

With this definition, pseudorapidity provides a quantity that is related to θ that is almost perfectly Lorentz-invariant under boosts along the $\hat{z}$ direction and purely geometric. Particles traveling along the y-axis correspond to $\eta = 0$, while particles traveling parallel to the beam line in the positive (negative) $\hat{z}$ direction correspond to $\eta = +\infty$ ($\eta = -\infty$). Additionally, the pseudorapidity equivalents of $\theta = 30°$ and $\theta = 60°$ are $\eta = 1.32$ and $\eta = 0.55$, respectively.

6.1 Inner Detector

The Inner Detector (ID) system is composed of three sub-detectors that are used to measure the momentum of charged particles and reconstruct vertices corresponding to proton-proton interactions and decays of particles with non-negligible lifetimes such as b-hadrons. The ID is immersed in a 2 T solenoidal magnetic field that bends the trajectories of charged particles. After the trajectories have been reconstructed, the charged particles' momenta and electric charge can be measured based on this curvature and a precise mapping of the magnetic field. The transverse momentum resolution of tracks reconstructed by the ID was designed

to follow $\sigma_{p_{\mathrm{T}}}/p_{\mathrm{T}} = 0.05\% p_{\mathrm{T}} \oplus 1\%$, where p_{T} is measured in GeV and the $\oplus$ symbol indicates addition in quadrature [32].

The ID has cylindrical symmetry and provides coverage for $|\eta| < 2.5$. The two innermost sub-detectors – the Pixel Detector, followed by the Semiconductor Tracker (SCT) – both use silicon sensors to record the locations of charged particles as emerge from collisions. Charged particles passing through the silicon produce ionization currents that are collected and ultimately translated into "hits" that are used by track reconstruction algorithms. The outermost sub-detector is a gaseous detector called the Transition Radiation Tracker (TRT). A diagram of the barrel region of the ID is presented in Figure 6.2 and a more detailed schematic of the entire ID layout is shown in Figure 6.3. Precision tracking and vertexing requires excellent spatial resolution for the detectors that are closest to the interaction point. The Pixel Detector, therefore, has the best spatial resolution of these sub-detectors, with the SCT having the second best resolution and the TRT third. This is due to a tradeoff between performance and the cost/complexity of instrumenting expensive silicon pixel technology at larger radii.

6.1.1 Pixel Detector

The Pixel Detector [40] consists of approximately 92 million independent readout channels split between four cylindrical layers of silicon pixel sensors in the barrel and three disk-shaped layers in each of the end-caps to provide coverage out to $|\eta| < 2.5$. The innermost barrel layer, called the Insertable B-Layer (IBL) [41], is at a radius of 33.5 mm with respect to the beam line, while the outermost layer is at a distance of 122.5 mm. In the $\phi \times z$ directions, the IBL pixels have dimensions of 50 µm × 250 µm, while the remaining sensors have larger pixels that are 50 µm × 400 µm. The smaller pixel size in the IBL leads to a spatial resolution

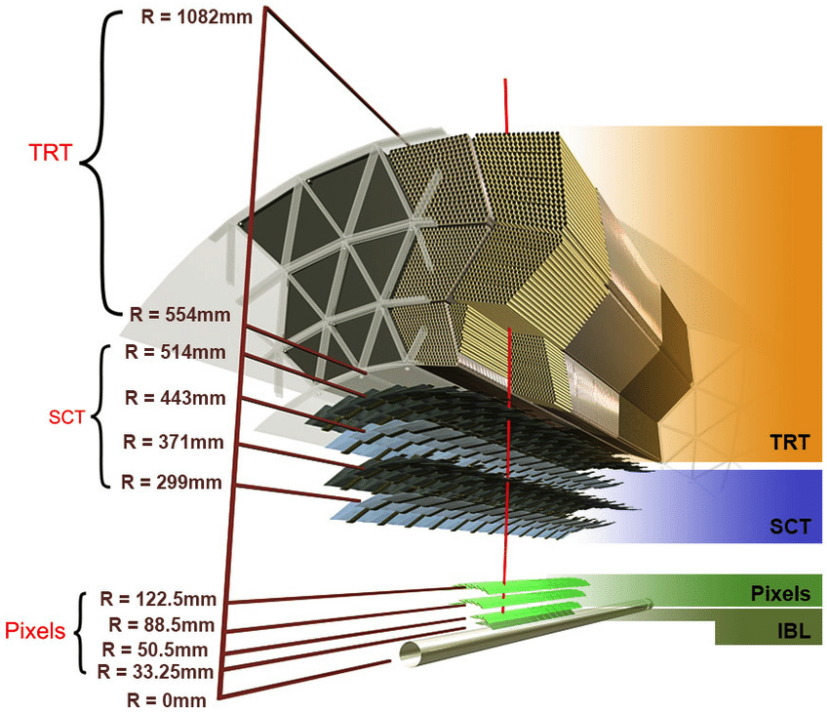

Figure 6.2: A schematic of the barrel region of the Inner Detector [38].

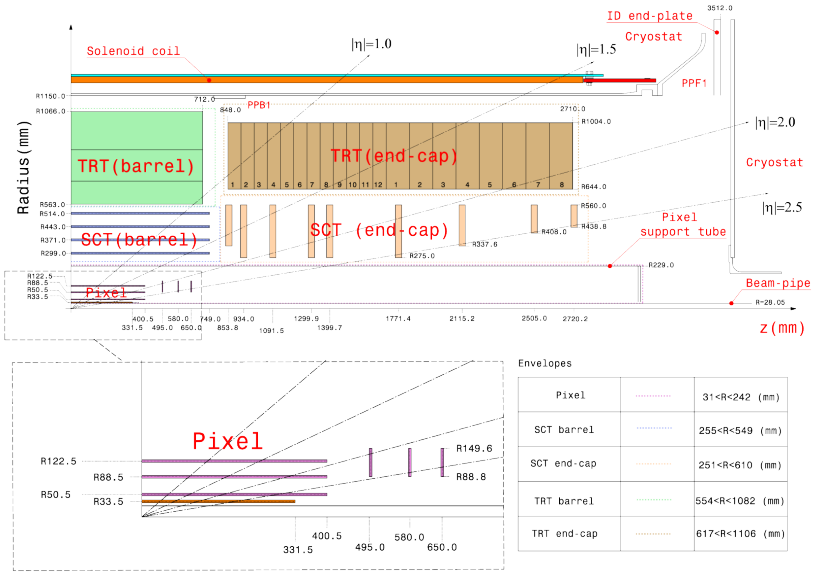

Figure 6.3: A quadrant of the ID layout shown in the $r-z$ plane. The top panel shows the entire quadrant of the ID, while the bottom panel shows just the Pixel Detector [39].

of 9 µm in the $r-\phi$ direction and 65 µm in the z direction. The larger pixels have resolutions of 10 µm and 115 µm in the $r-\phi$ and z directions, respectively. The excellent resolution of the Pixel Detector allows for vertex reconstruction that is used to identify proton-proton interactions. Additionally, the secondary vertices that result from the decay of particles with non-negligible lifetimes (such as b-hadrons) can be reconstructed. Identifying these secondary vertices is thereore crucial for identifying jets containing b-hadrons.

6.1.2 Semiconductor Tracker

The SCT [42] is a silicon micro-strip detector that surrounds the Pixel Detector and has a similar geometry. The strips are 12.6 cm long with an inter-strip pitch 80 µm. The barrel region consists of four cylindrical layers, ranging from $r = 299$ mm to $r = 514$ mm, while the end-caps each contain nine disks that extend the coverage out to $|\eta| < 2.5$. The strips in the barrel are arranged in the axial direction in the barrel, while those in the end-caps are arranged radially. In total, the SCT has 4088 double-sided modules with approximately 6 million independent readout channels [32]. A stereo angle of 40 mrad is maintained between the strip layers on each module in order to provide a two-dimensional space point measurement with an intrinsic resolution of 17 µm in the $r-\phi$ direction and 580 µm in the z direction in the barrel.

6.1.3 Transition Radiation Tracker

The TRT is the outermost layer of the ID that provides both tracking and particle identification information for particles with $|\eta| < 2.0$. It consists of 300,000 drift tubes, each with a 4 mm diameter. In the barrel, the tubes run along the z direction at radial distances between 563 mm and 1066 mm, while the tubes in the

end-caps are oriented radially. Each drift tube is filled with a mixture of Xenon (70%), CO_2 (27%), and O_2 (3%) gases and contain a thin gold-plated tungsten anode wire at the center. An approximately 15 kV potential is applied between the anode wire and the drift tube's shell, which promotes an avalanche of electrons (collected at the anode) after charged particles pass through the tube and ionize the gas.

Each barrel drift tube spans the entire length of the barrel, while the anode wire is segmented into two equal-length pieces at $\eta \approx 0$ that provide separate readout on either side of the detector. Therefore, the drift tubes in the barrel are only able to provide spatial measurements in the $r - \phi$ plane with a spatial resolution of approximately 120 µm. This resolution is based on the drift time for the electron avalanche to arrive at the anode wire, which depends on the distance between the wire and charged particle trajectory. Despite the larger resolution per hit, a charged particle will produce approximately 36 hits in the TRT [32], which can be combined to give a resolution that is comparable to the silicon-based tracking detectors [43].

In addition to tracking, the TRT provides additional discrimination power between electrons and charged hadrons. Polyethylene fibers are interleaved between each of the drift tubes in the barrel, while polypropylene foils are used in the end-caps. This geometry ensures that charged particles will pass through materials of different dielectric constants many times as they traverse the TRT and therefore emit photons, a phenomenon known as transition radiation. The probability that a particle with energy E and mass m will produce transition radiation is proportional to the Lorentz factor $\gamma = E/m$. For a fixed energy, then, electrons will have a much higher probability of emitting transition radiation than charged pions, for example, due to their lower mass. These photons are typically in the range of

$6 - 15$ keV. Xenon is a highly efficient absorber of photons in this energy range (which is why it is chosen for the drift tubes), and so the transition radiation leads to large signals in the detector. In order to take advantage of this, the TRT has two readout thresholds, one at 300 eV used for tracking and another at 6 keV is used to detect transition radiation. The number of high-threshold hits along a particle track can therefore be used to discriminate between electrons and charged hadrons, as electrons are expected to produce a higher number.

6.2 Calorimeters

The calorimetry system within ATLAS consists of an electromagnetic calorimeter and a hadronic calorimeter, which measure the energy of particles that interact via the electromagnetic and strong forces, respectively. The electromagnetic calorimeter is called the Liquid Argon (LAr) Calorimeter and the hadronic calorimeter consists of the Tile Calorimeter, End-cap Calorimeter (HEC), and LAr Forward Calorimeter (FCal). Each system provides coverage for $|\eta| < 4.9$. A diagram of the ATLAS calorimeter system is presented in Figure 6.4.

Both of the calorimeters rely on the "sampling" methodology in which a passive absorber material induces particle showers, the energies of which are subsequently measured by an active material. These absorber and active materials are interleaved with one another in order to sample the particle showers at several points during their development. A large fraction of the energy that is absorbed by the dense, passive material is not ultimately transferred into a form that can be measured directly, necessitating dedicated calibrations based on the calorimeter response.

Sampling calorimeters have energy resolutions resolutions, σ_E, that are typi-

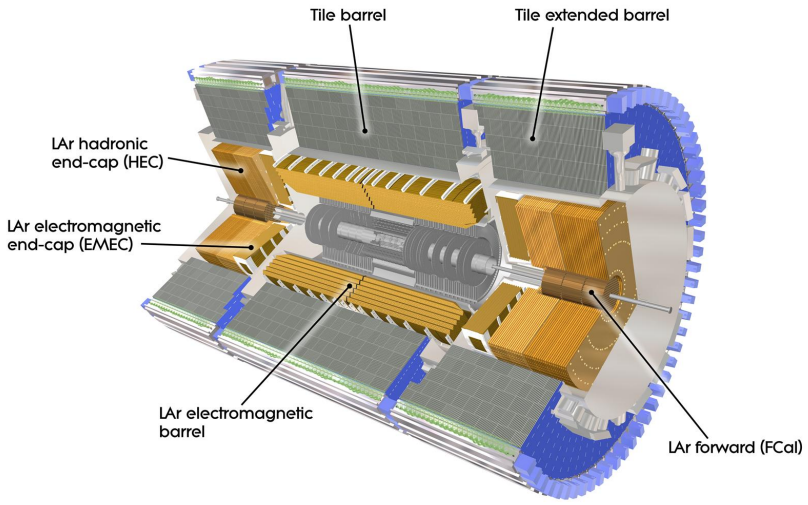

Figure 6.4: A cutaway diagram of the ATLAS calorimeter system [32].

cally parameterized as a function of the energy, E, according to

$$\frac{\sigma_E}{E} = \frac{a}{\sqrt{E}} \oplus \frac{b}{E} \oplus c \tag{6.3}$$

where a, b, and c are constants that characterize the various components of the overall resolution. Again, the $\oplus$ symbol is used to indicate addition in quadrature. The first term accounts for stochastic fluctuations that are intrinsic to the showering, including, for example, the number of photoelectrons produced in the underlying quantum mechanical processes. The second term accounts for noise in the electronics and the effects of additional pileup activity. Finally, the constant term accounts for effects that do not depend on the incident particle energy such as dead material in the calorimeter and nonuniform geometry. At very high energies, this constant term dominates the resolution, which puts strong requirements on the design and construction of the calorimeters.

Another important aspect of calorimeters is the ability to contain as much of the shower as possible in order to fully measure the energy of the incident particle.

For electromagnetic calorimetry, it is useful to define a "radiation length", denoted X_0, which represents the average distance over which an electron (photon) will lose all but $1/e$ of its energy due to bremsstrahlung (pair-production) and is a function of the calorimeter material. For hadronic calorimetry, the metric used is the nuclear interaction length, λ, which is the average distance a hadron will travel before undergoing a nuclear interaction with the absorber material. For pions traversing steel, the nuclear interaction length corresponds to approximately 17 cm, which drives the designed depth of the Tile Calorimeter.

6.2.1 Electromagnetic Calorimeter

The LAr Calorimeter [44] resides just outside of the TRT and is used to measure the energies and directions of electromagnetically-interacting particles including electrons and photons. It consists of lead absorbers and liquid Argon for the active material, which are layered together in an accordion-like geometry, as shown in Figure 6.5. Electromagnetic showers are induced when the incident particle interacts with the lead absorber and loses energy through bremsstrahlung and pair-production processes. The charged particles in the showers subsequently ionize the Argon and these ionization electrons are collected at electrodes via an applied electric field. The energy resolution of the calorimeter is characterized by $\frac{\sigma_E}{E} = \frac{10\%}{\sqrt{E}} \oplus \frac{0.3\%}{E} \oplus 0.4\%$, where E should be given in units of GeV.

A barrel portion of the calorimeter covers the $|\eta| < 1.475$ region, while two endcaps provide additional coverage in the forward regions from $1.375 < |\eta| < 3.2$. The calorimeter is segmented into three layers at different depth and with increasing cell sizes (defined by $\Delta\phi \times \Delta\eta$). The first layer has the finest resolution with a cell size corresponding to $\Delta\eta \times \Delta\phi = 0.025/8 \times 0.1$ in order to provide excellent discrimination between prompt photons and those coming from $\pi^0 \to \gamma\gamma$ decays.

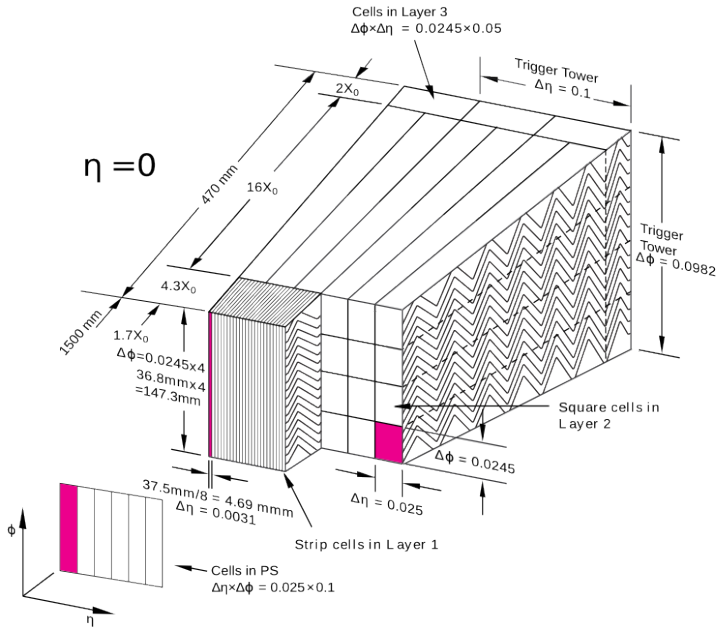

Figure 6.5: A schematic of the LAr geometry showing the accordion geometry and the various layers [32].

The second layer is the thickest and contains the majority of the electromagnetic showers. Finally, the third and outermost layer has the coarsest cell size and is in place to measure any shower components that are not contained in the previous layers. In the central region ($|\eta| < 1.8$), an additional pre-sampling layer containing LAr provides corrections for energy losses occurring prior to the arrival at the calorimeter. In total, the barrel calorimeters have a thickness corresponding to at least $22X_0$, while the end-cap calorimeters have a thickness of at least $24X_0$ in order to contain the electromagnetic showers [32].

6.2.2 Hadronic Calorimeter

The hadronic calorimeter system sits just outside of the electromagnetic calorimeter. The Tile Calorimeter [45] provides coverage for $|\eta| < 1.7$, while the HEC and FCal are instrumented for the regions covering $1.5 < |\eta| < 3.2$ and $3.1 < |\eta| < 4.9$,

respectively. Together, these calorimeters are used to measure the energy of hadrons.

The Tile Calorimeter consists of layers of radially-oriented steel absorbers and plastic scintillating tiles that act as the active material. The particle showers induced by interactions with the absorbers pass through the scintillators, which emit photons that are collected by wavelength-shifting fibers. These fibers direct the photons to photomultiplier tubes that are used to convert the photon energy into electronic signals for the readout system. In total, the Tile Calorimeter consists of 256 wedge-shaped modules, a schematic of which is presented in Figure 6.6. Each module has a radial depth corresponding to approximately 7.4λ split between three sampling layers that are 1.5λ, 4.1λ, and 1.8λ in depth [32]. The first two layers consist of cells of size $\eta \times \phi = 0.1 \times 0.1$, while the outermost layer has coarser cell sizes of 0.2×0.1.

The HEC and FCal both use LAr as the active material and provide additional calorimetry in the forward region. The FCal is to measure both electromagnetic and hadronic showers. The electromagnetic component is measured in the first layer using a copper absorber, while the remaining two layers measure hadronic showers induced by a dense tungsten absorber in order to provide shower containment. The Tile Calorimeter has an energy resolution that is characterized as a function of the energy (in units of GeV) by $\frac{\sigma_E}{E} = \frac{50\%}{\sqrt{E}} \oplus \frac{1.8\%}{E} \oplus 3\%$. The resolution for the FCal is $\frac{\sigma_E}{E} = \frac{100\%}{\sqrt{E}} \oplus 10\%$ [32]. Despite the worse energy resolution in the FCal, it plays an important role in the determination of the missing transverse energy.

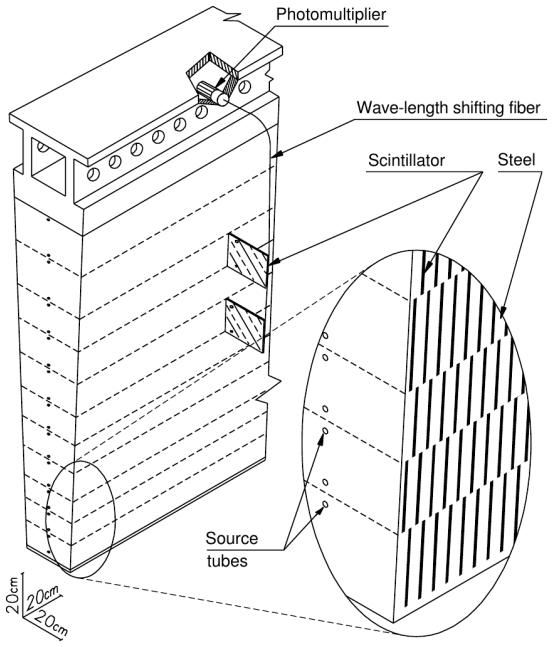

Figure 6.6: A diagram of a Tile Calorimeter module showing the steel absorbers and plastic scintillating tiles. The photons emitted by the scintillators are collected by embedded fibers and delivered to photomultiplier tubes [32].

6.3 Muon Spectrometer

The Muon Spectrometer (MS) [46] is the outermost layer of the ATLAS detector and is designed to measure the trajectories of muons, which are able to penetrate the entire detector. Bending of the muon tracks in the $r - \eta$ plane is provided by a system of superconducting magnets that produce toroidal magnetic fields. A barrel toroid magnet system provides a 1 T field that dominates for $|\eta| < 1.4$, while end-cap toroid magnets are used to bend muon trajectories in the $1.6 < |\eta| < 2.7$ region with 0.5 T fields. A combination of barrel and end-cap magnetic fields are used for the bending in the transition region between $1.4 < |\eta| < 1.6$.

The MS was designed to have excellent transverse momentum resolution, even at high-p_{T} where the muon tracks become straighter, making the momentum

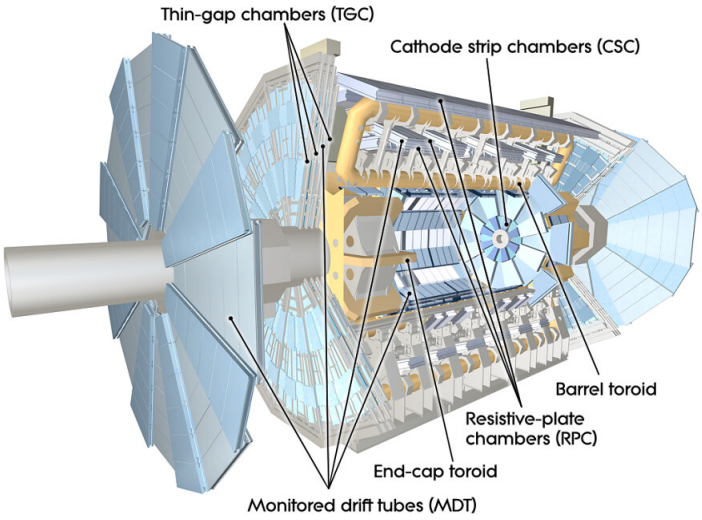

Figure 6.7: A cut-away view of the Muon Spectrometer with the various chamber types highlighted [32].

determination more difficult. The specific design goal is to have a 10% resolution on the muon transverse momentum for muons with $p_{\mathrm{T}} = 1\,\mathrm{TeV}$ [32]. For lower-p_{T} muons, the increased track curvature allows for more precise determinations of the transverse momentum ($\sim 3\%$) [47].

Four different varieties of gaseous detectors are used to provide both excellent spatial and timing resolution for tracking and triggering purposes. The precision tracking is performed by Monitored Drift Tubes (MDTs) and Cathode Strip Chambers (CSCs). Triggering capability is provided by Resistive Plate Chambers (RPCs) and Thin Gap Chambers (TGCs), which have timing resolutions of 1.5 ns and 4 ns, respectively. The layout of the MS, including the locations of each detector technology, is shown in Figure 6.7.

Together, the MDTs and CSCs provide precision tracking in the region with $|\eta| < 2.7$. The MDTs are pressurized drift tube detectors filled with an Ar and CO_2 gas mixture that provide coverage for $|\eta| < 2.7$. Cylindrical symmetry is used in the barrel, while the MDTs are arranged into disks in the end-caps. The

azimuthally-oriented tubes are made of Al and have a diameter of approximately 30 mm. Upon ionization, electrons are collected on a central anode wire made of tungsten and rhenium that is held at a ~ 3 kV potential. Long drift times (up to 700 ns) preclude the MDTs from providing triggering information, but excellent intrinsic resolution (~ 35 µm) is achieved in the muon bending plane η [32]. Due to the length and orientation of the drift tubes, no measurement of ϕ can be made by the MDTs. Instead, the ϕ measurement is provided by the RPCs and TGCs by matching hits in each of the systems.

Due to occupancy limitations of the MDTs, the CSCs are used for tracking purposes in the first layer of the end-cap chambers and cover $2.0 < |\eta| < 2.7$. The CSCs are multi-wire proportional chambers consisting of radially-oriented anode wires running between cathode plates. The ionization medium is also a gas mixture of Ar and CO_2 and the induced charge is readout using two perpendicular sets of cathode strips that provide high-resolution measurements in both η and ϕ. The spatial resolution in the muon bending plane is approximately 60 µm and approximately 5 mm in the non-bending plane [32].

Triggering capability is provided by the RPCs and TGCs, which cover $|\eta| < 1.05$ and $1.05 < |\eta| < 2.4$, respectively. The RPCs are arranged in three concentric layers in the barrel region of the detector. Unlike all of the other technologies used in the MS, the RPCs do not use a wire for charge collection. Instead, a 2 mm gap between highly resistive plastic laminate plates is filled a mixture of $C_2H_2F_4$, Iso-C_4H_{10}, and SF_6 [32]. The readout is performed using capacitive coupling to two orthogonal sets of metallic strips located on the outside of the plates, which provide both η and ϕ measurements.

Muon triggering in the forward region and additional ϕ measurements are provided by the TGCs, which are multi-wire proportional chambers filled with

a highly-quenching mixture of CO_2 and n-C_5H_{12}. The TGCs are arranged in disks that run perpendicular to the beam line. The anode wires are separated by 1.8 mm and the anode-to-cathode distance is just 1.4 mm, which provides the short response time in conjunction with a large electric field. Azimuthal measurements are provided by radially arranged copper strips on the outside of the plates, while the wire groups measure the η coordinate.

6.4 Trigger System

The raw data corresponding to a single collision event recorded by the ATLAS detector is approximately 1.6 MB in size. Since the LHC provides proton-proton collisions at a rate of 40 MHz, the total data rate is therefore upwards of 60 TB/s. Bandwidth and storage limitations, though, prevent ATLAS from recording every collision event to disk. Importantly, the ATLAS physics program focuses on rare processes with cross-sections far below the total proton-proton cross-section. The vast majority of the proton-proton collision events can therefore be discarded as long as events of potential interest are selectively saved to disk for later analysis. This is the job of the ATLAS trigger system, which is tasked with discriminating between interesting and uninteresting events in real time in order to reduce the overall data rate.

The trigger system [48] consists of two levels. The first level is a hardware-based trigger called Level-1 (L1), which uses coarse detector information to reduce the event rate from 40 MHz to a maximum of 100 kHz, all within a 2.5 µs window. In particular, the L1 trigger uses calorimeter information and hits in the muon trigger chambers (RPCs and TGCs) to select events containing high-p_{T} leptons, photons, jets, and/or $E_{\mathrm{T}}^{\mathrm{miss}}$. This coarse information is used to seed regions of interest within the detector to the second trigger level called the High-Level Trigger

(HLT). The HLT is a software-based trigger that runs sophisticated reconstruction algorithms using the full detector readout within the regions of interest. These HLT triggers are required to have processing times with approximately 200 ms and are designed to ultimately reduce the event rate to approximately 1 kHz.

ATLAS uses a so-called "trigger menu," [49, 50, 51, 52] which consists of chains of different triggers that are designed to select specific physics objects (or combination of objects) that pass various p_{T} and quality cuts. An example of the HLT rate is shown as a function of time in Figure 6.8 for triggers targeting various physics objects. The majority of these triggers select every event that passes their particular criteria. These include the $E_{\mathrm{T}}^{\mathrm{miss}}$-triggers that are used to collect the data used in this search and described in Section 8.1. About 15% of the total HLT rate, though, is dedicated to triggers that only select a fraction of the events that pass their criteria. These triggers would otherwise have rates that would saturate the HLT and so a "prescale," N, is applied such that only $1/N$ of the total number of events fulfilling the trigger requirements are actually saved to disk. More specifically, these prescales allow for triggers with low p_{T} thresholds (e.g. a 5 GeV single-electron trigger) to collect events without taking up too much of the trigger bandwidth. Typically, these "prescaled" triggers are used for detector performance studies but they are also used to derive the data-driven background estimate for this search, as described in Section 11.2.2.

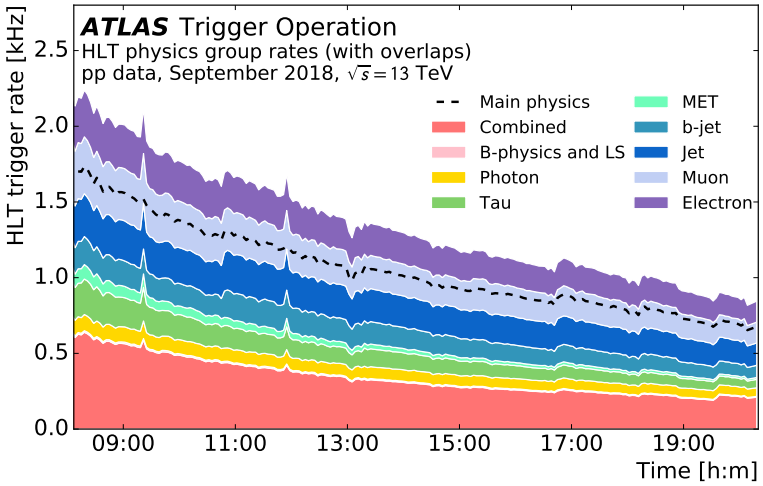

Figure 6.8: Trigger rates at the HLT as a function of time during a fill taken in September 2018 that had a peak instantaneous luminosity of luminosity of $L = 2.0 \times 10^{34}$ cm^{-2}s^{-1}. The peak average number of interactions per bunch-crossing was $\langle\mu\rangle = 56$. Each histogram in the stack corresponds to triggers targeting specific physics objects, as listed in the legend. The "Combined" trigger group consists of triggers that require multiple physics objects of different types. Since a single event can fire multiple triggers, the trigger rate after accounting for this overlap is denoted by the "Main physics" dashed line. The falling trigger rates are a reflection of the instantaneous luminosity delivered by the LHC, which decreases with time over the course of a fill [53].

Part IV

Designing the Search

or: How I Learned to Stop Worrying and Love Soft Leptons

Chapter 7

Search Strategy

The searches presented in this dissertation target models of electroweak SUSY in which the lightest neutralino is produced from nearly mass-degenerate decays of the lightest chargino, the second-to-lightest neutralino, or a slepton. The mass splittings considered are on the order of one to tens of GeV, which leads to soft, same-flavor leptons with low transverse momenta in the final state. Additionally, at tree level, the SUSY states are produces back-to-back such that the overall missing energy in the transverse plane, $E_{\mathrm{T}}^{\mathrm{miss}}$, is small. This poses a significant challenge from a triggering standpoint, as the available lepton and $E_{\mathrm{T}}^{\mathrm{miss}}$ triggers have thresholds that are much higher than the expected lepton p_{T} and $E_{\mathrm{T}}^{\mathrm{miss}}$ in signal events, especially in the most compressed scenarios. Without the ability to trigger on signal-like events with reasonable efficiency, there is no way to have sensitivity to these models.

In order to avoid this constraint, these searches target events in which additional hadronic activity from initial state radiation (ISR) boosts the SUSY system in the transverse plane and in doing so, approximately aligns the invisible SUSY particles such that the overall $E_{\mathrm{T}}^{\mathrm{miss}}$ in the event is significantly increased. Feynman diagrams for these boosted processes are shown in Figure 7.1 and schematics

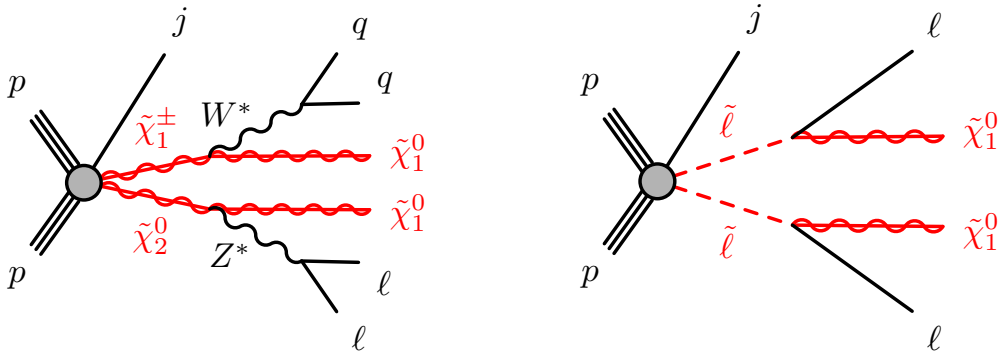

Figure 7.1: Diagrams representing the two-lepton final state following the production of electroweakinos $\widetilde{\chi}_2^0\widetilde{\chi}_1^{\pm}$ (left) and slepton pairs (right) with initial-state radiation (j), The higgsino simplified model also considers $\widetilde{\chi}_2^0\widetilde{\chi}_1^0$ and $\widetilde{\chi}_1^+\widetilde{\chi}_1^-$ production.

of the signal event topologies with and without the ISR boost are presented in Figure 7.2. While this requirement reduces the overall signal cross-sections, the boost allows for efficient $E_{\mathrm{T}}^{\mathrm{miss}}$-based triggering. It also serves to increase the overall reconstruction and identification efficiencies for the signal leptons by increasing their energy in the lab frame, though they still remain relatively soft.

With these boosted topologies in mind, the searches select events containing two soft leptons of the same flavor and opposite electric charge, significant $E_{\mathrm{T}}^{\mathrm{miss}}$, and additional hadronic activity from ISR. Here, and in the remainder of this dissertation, "leptons" refers exclusively to the the charged light-flavor leptons (electrons and muons) unless explicitly stated otherwise. Similarly, "sleptons" will be used to refer to the superpartners of the SM electrons and muons. Separate regions in the data, called signal regions (SRs), are derived for the searches targeting electroweakinos and sleptons. They are designed to be enriched in potential signal events with respect to the total background expectation. A schematic of the SRs exploited by these searches is shown in Figure 7.3, and they are described in detail in Chapter 10. For signals with very small mass-splittings, the leptons can be soft enough that they are not reconstructed within ATLAS. To make up

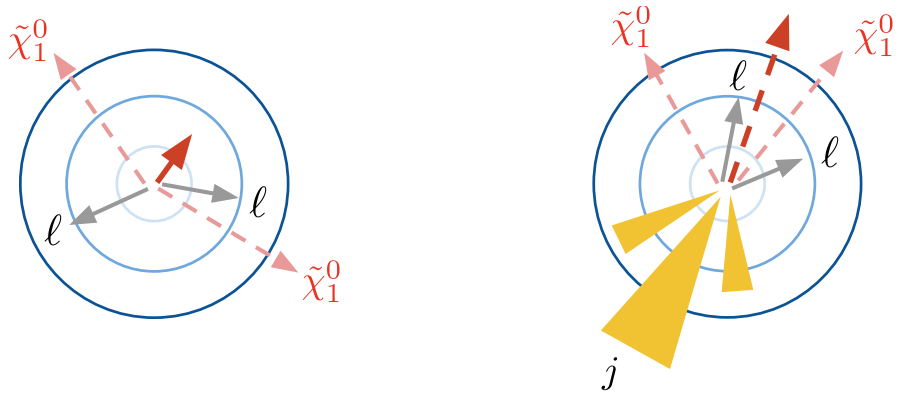

Figure 7.2: Cartoons taken from [54] illustrating the signal event topologies before (left) and after (right) requiring hadronic activity from ISR. The direction of the dark red arrow indicates the reconstructed missing transverse momentum vector and its relative length indicates the magnitude of the this vector (i.e. the reconstructed $E_{\mathrm{T}}^{\mathrm{miss}}$).

for this, the electroweakino searches include a SR called SR–E–1ℓ1T that selects events containing one lepton and an isolated track, which is used as a proxy for an unreconstructed lepton from a SUSY decay. A detailed description of this channel is outside the scope of this dissertation, though.

In each of these searches, the final discriminating variable exhibits a kinematic cutoff in signal events that corresponds to the mass-splitting. Therefore, the SRs are binned in these variables (with each bin representing an "exclusive SR") in order to exploit the shape differences between signal and background events. In the search for electroweakinos, the discriminating variable is the invariant mass of the dilepton system, $m_{\ell\ell}$, from the off-shell $Z^* \to \ell\ell$ decay. For sleptons, the final-state leptons originate from different legs of the decay chain and so the invariant mass does not provide a good handle on the masses of the SUSY states. Instead, the "stransverse mass" variable, m_{T2}, is used, which assumes a value for the $\tilde{\chi}_1^0$ mass and attempts to place an upper bound on the slepton mass. This variable is defined explicitly in Section 10.1. In order to perform a model-independent search for new physics, a series of single-bin "inclusive SRs"

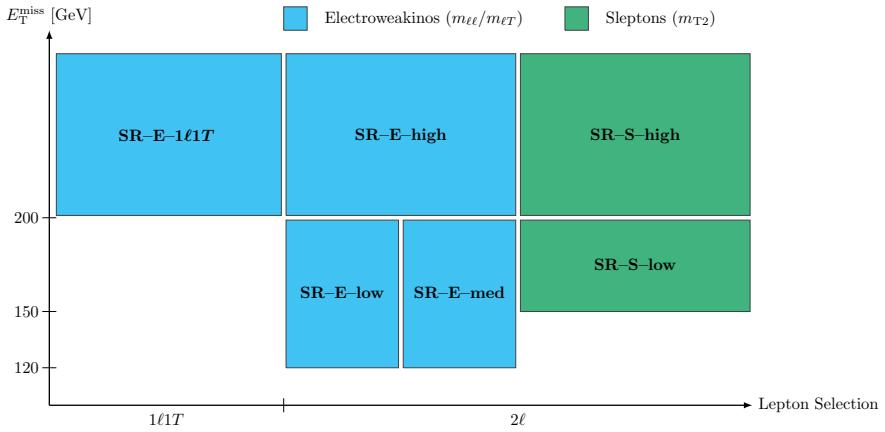

Figure 7.3: A schematic of the analysis strategy. Signal regions targeting electroweakino production are shown in blue, while those targeting slepton production are shown in green. Signal regions targeting the same SUSY states are kept orthogonal to each other so that they may be statistically combined for optimal sensitivity. The electroweakino signal regions are based on $m_{\ell\ell}$ and select events containing either two leptons or one lepton and one isolated track that serves as a proxy for the second lepton. The slepton signal regions only select events with two leptons and are based on m_{T2}. The definition of these signal regions are presented in Chapter 10.

are defined in Section 10.5, which remove any assumptions about the shapes of signal kinematic distributions by merging separately merging the exclusive $m_{\ell\ell}$ and m_{T2} bins.

The backgrounds in these searches can be divided into two categories: irreducible and reducible backgrounds. Irreducible backgrounds are due to SM processes that produce the same final state as the targeted signal processes. The major sources of irreducible background in these searches are due to $t\bar{t}/tW$, $Z^{(*)}/\gamma^{*}(\rightarrow \tau\tau)$ + jets, and WW/WZ production. The kinematic distributions of these backgrounds are taken directly from simulated events that utilize Monte Carlo (MC) techniques, but their normalizations in the SRs are constrained using dedicated control regions (CRs). These CRs are designed to be orthogonal to the SRs, enriched in a given background process, and have minimal signal contamination. Fitting the event yields in MC to the data in the CRs provides normalization

factors that are used to scale the data in the SRs. Reducible backgrounds are due to events from SM processes in which at least one of the final-state particles is misidentified or incorrectly attributed to a prompt decay. In the context of the searches here, the primary source of the reducible background stems from $W+$jets events in which a jet is misidentified as a lepton, though other sources, including semi-leptonic b-hadron decays, are also considered. This fake/non-prompt lepton background tends to dominate at low-p_{T}. Since simulation is not expected to model these processes well, the background is estimated using a data-driven technique. The background estimation is validated in a series of validation regions (VRs) that are orthogonal to the SRs before they are unblinded and assessed for any evidence of new physics.

The details of the analysis design are given in the following chapters. Chapter 8 gives an overview of the dataset used by these searches, as well as details about the simulation of both signal and background event samples. Chapter 9 details the reconstruction and selection criteria of the various physics objects relevant to the searches. Chapter 10 motivates the event selections that define the electroweakino and slepton signal regions. The details of the background estimation strategy are presented in Chapter 11. Finally, the various sources of both experimental and theoretical systematic uncertainties are discussed in Chapter 12.

Chapter 8

Collision Data and Simulated Event Samples

The searches here rely on a combination of proton-proton (pp) collision data recorded by the ATLAS detector and simulated event samples for various background and signal processes. A detailed description of the dataset is provided in Section 8.1. Simulated data is generated using Monte Carlo (MC) methods and reconstructed with the same ATLAS algorithms used for genuine data. The simulated signal and background samples are detailed in Section 8.2 and Section 8.3, respectively.

8.1 Data Sample

The dataset used in these searches is composed of $\sqrt{s} = 13$ TeV pp collisions recorded by the ATLAS detector from 2015 through 2018. This corresponds to a total integrated luminosity of 139 fb^{-1} with an uncertainty of 1.7% [55], as determined primarily by the LUCID-2 detector [56] using van der Meer scans. The total integrated luminosity as a function of time is shown in Figure 8.1.

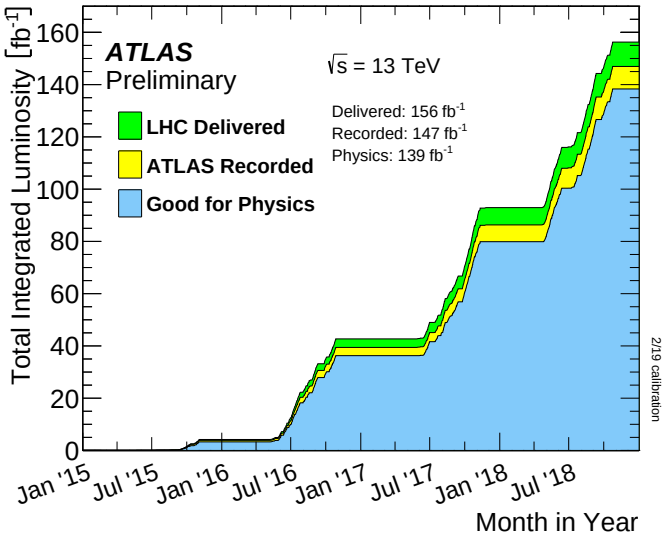

Figure 8.1: The total integrated luminosity as a function of time between 2015 and 2018 that was delivered to ATLAS by the LHC (green), recorded by ATLAS (yellow), and declared to be of sufficient quality for physics analysis (blue) [36].

Over this period, 94% of the luminosity delivered by the LHC was recorded by ATLAS. Of the recorded data, 95% was determined to be of sufficient quality for use in physics analysis. Data is only used when taken during the stable operation of all ATLAS sub-detectors and must satisfy quality criteria that help mitigate non-collision backgrounds. The distribution of the instantaneous mean number of interactions per bunch-crossing corresponding to this dataset is also shown in Figure 8.2. During this period, the average number of interactions per bunch-crossing $\langle\mu\rangle$ was 33.7.

The data used in this search were selected using unprescaled, inclusive $E_{\mathrm{T}}^{\mathrm{miss}}$-based triggers with the lowest threshold available for a given period of data-taking. Unlike searches targeting similar signal processes but with larger mass-splittings, this search cannot use lepton-based triggers since the typical lepton p_{T} within these compressed scenarios are below the available trigger thresholds. The specific triggers used in each year of data-taking are shown in Table 8.1. The reason for

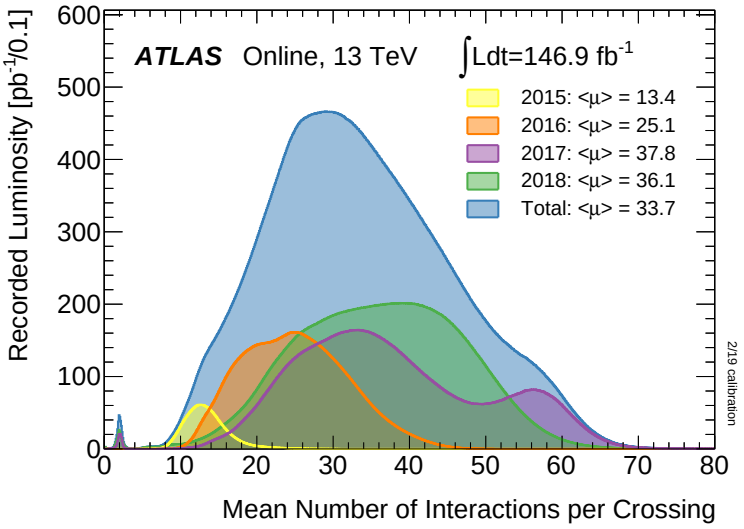

Figure 8.2: The distribution of the mean number of interactions per bunch-crossing during stable beams for each year between 2015 and 2018 [36].

the changing $E_{\mathrm{T}}^{\mathrm{miss}}$ thresholds is that the trigger rates can depend heavily on the changing pileup conditions. Increasing pileup tends to increase the $E_{\mathrm{T}}^{\mathrm{miss}}$ trigger rates and so the thresholds are increased in order to maintain the desired rates, which are limited by the ATLAS data acquisition system.

The triggers used in this search employ one of two different algorithms for calculating $E_{\mathrm{T}}^{\mathrm{miss}}$ at the HLT-level. The `mht` algorithm calculates $E_{\mathrm{T}}^{\mathrm{miss}}$ as the the negative transverse momentum vector sum of all jets with a minimum threshold of 7 GeV before calibration. These jets are reconstructed from calorimeter topological clusters using the anti-k_t jet clustering algorithm with a radius parameter of $R = 0.4$, as implemented in the `FastJet` package [57]. Starting in 2017, the `pufit` algorithm was implemented in order to combat the effects of increased pileup and retain low $E_{\mathrm{T}}^{\mathrm{miss}}$ trigger thresholds. This algorithm calculates $E_{\mathrm{T}}^{\mathrm{miss}}$ as the negative transverse momentum vector sum of all calorimeter topological clusters (grouped into $\eta - \phi$ patches that resemble $R = 0.4$ anti-k_t jets) corrected for pileup [58]. In 2017 and 2018, `pufit` was used in conjunction with the `cell` algorithm, which

Table 8.1: The lowest unprescaled $E_{\mathrm{T}}^{\mathrm{miss}}$ trigger chains in $\sqrt{s} = 13$ TeV pp running for each year from 2015 to 2018. The L1 and HLT thresholds on $E_{\mathrm{T}}^{\mathrm{miss}}$ are given, as well as the specific algorithms used for the $E_{\mathrm{T}}^{\mathrm{miss}}$ calculation at the HLT.

Year	Trigger Name	L1 Threshold [GeV]	HLT Algorithm	HLT Threshold [GeV]
2015	HLT_xe70_mht_L1XE50	50	mht	70
2016	HLT_xe90_mht_L1XE50	50	mht	90
	HLT_xe100_mht_L1XE50	50	mht	100
	HLT_xe110_mht_L1XE50	50	mht	110
2017	HLT_xe110_pufit_L1XE50	50	pufit, cell	110, 50
	HLT_xe110_pufit_L1XE55	55	pufit, cell	110, 50
2018	HLT_xe110_pufit_xe65_L1XE50	50	pufit, cell	110, 65
	HLT_xe110_pufit_xe70_L1XE50	50	pufit, cell	110, 70

calculates $E_{\mathrm{T}}^{\mathrm{miss}}$ as the negative transverse momentum vector sum of all calorimeter cells passing a two-sided noise cut. In general, the triggers have an offline efficiency of at least 95% for events with $E_{\mathrm{T}}^{\mathrm{miss}} > 200$ GeV.

8.2 Simulated Signal Samples

In order to interpret the results of the search in the context of simplified SUSY models, signal events are simulated for electroweakino and slepton production. These samples are used to estimate signal yields and kinematic distributions, which are used for optimizing the signal regions (SRs) and eventually setting model-dependent limits. The configurations used for the simulation of signal events, described in more detail below, are summarized in Table 8.2. The effect of pileup interactions occurring in the same and/or neighboring bunch-crossings is added by by overlaying simulated soft QCD events onto the signal events. These QCD events are generated using Pythia 8.186 with the A3 tune [59] and the MSTW2008LO parton distribution function (PDF) set [60]. Once overlaid, the simulated events are reweighted to match the distribution of the mean number of interactions per bunch-crossing that is observed in data and shown in Figure 8.2.

Table 8.2: Configurations for the simulation of signal processes. The PDF set refers to that used for the matrix element. The cross-sections are calculated using Resummino 2.0.1.

Process	Matrix element	Parton shower	PDF set	Cross-section
Slepton pair production	MG5_aMC@NLO 2.6.1	Pythia 8.230	NNPDF 2.3 LO	NLO+NLL
Electroweakino pair production	MG5_aMC@NLO 2.6.1	Pythia 8.212	NNPDF 2.3 LO	NLO+NLL

EvtGen 1.6.0 and 1.2.0 are used to model the decays of bottom and charm quarks for all signal events. Unlike the simulated background samples, all signal events are processed using a fast simulation called AtlFast2 [61], which parameterizes the calorimeter responses to particles passing through them.

In total, three different electroweakino signal models are considered and each receive separate model-dependent interpretations. The higgsino model assumes that the lightest SUSY particles consists of a triplet of higgsino-like states. In the wino/bino models, the higgsinos are decoupled. In this case, $\widetilde{\chi}_1^0$ is assumed to be bino-like, while the $\widetilde{\chi}_1^0$ and $\widetilde{\chi}_1^\pm$ states are wino-like and degenerate in mass. The only difference between the two wino/bino models is the assumption on the relative sign of the $\widetilde{\chi}_1^0$ and $\widetilde{\chi}_2^0$ mass parameters, which affects the $m_{\ell\ell}$ lineshape as discussed below. Finally, in the slepton model, the sleptons decay directly to a bino-like $\widetilde{\chi}_1^0$ via $\widetilde{\ell} \to \ell\widetilde{\chi}_1^0$. Figure 8.3 shows a schematic of the mass spectra and electroweakino compositions in each of the models considered.

8.2.1 Electroweakino Models

Much of the signal sample generation is common between the simplified electroweakino signals. The commonalities are discussed first before proceeding to the differences. All electroweakino signal processes were generated with MG5_aMC@NLO 2.6.1 using the NNPDF2.3LO parton distribution function set with the A14 tune and interfaced with Pythia 8.212 for the parton shower. Mass splittings in the

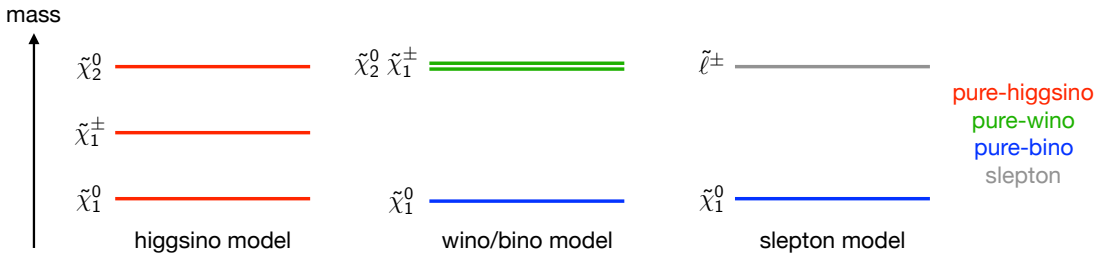

Figure 8.3: Cartoon of the assumed mass spectra in the simplified SUSY models considered by this search. The line color for each SUSY state indicates whether it is purely higgsino, purely wino, purely bino, or a slepton. In the higgsino model, the chargino mass is set to $m(\tilde{\chi}_1^\pm) = \frac{1}{2}\left[m(\tilde{\chi}_1^0) + m(\tilde{\chi}_2^0)\right]$. In the wino/bino model, the $\tilde{\chi}_1^\pm$ and $\tilde{\chi}_2^0$ wino states are assumed to be mass-degenerate.

range of 1 GeV to 60 GeV are considered. The jet-parton matching was performed according to the CKKW-L prescription [62] with the merging scale set to 15 GeV.

In each case, production cross-sections for each process, shown in Figure 8.4, are calculated using Resummino 2.0.1 at NLO+NLL precision. In general, wino production has a larger cross-section compared to higgsino production. Note that the $\tilde{\chi}_1^0\tilde{\chi}_1^\pm$ processes are not generated since these searches target final states involving two leptons. The cross-section uncertainties are determined according to Ref. [63] by taking the envelope of the resulting cross-sections after varying the PDF sets, as well as the factorization and renormalization scales. In all models, the branching ratios for the $\tilde{\chi}_2^0 \to Z^*\tilde{\chi}_1^0$ and $\tilde{\chi}_1^\pm \to W^*\tilde{\chi}_1^0$ processes are set to 100% and the decays are handled by MadSpin [64] to accurately model the decay kinematics due to spin correlations.

Due to the compressed mass spectra that are targeted by the search, the decays to stable SM particles proceed via off-shell vector bosons, and so special care is needed to determine the ratios for the $Z^* \to \ell\ell$ and $W^{\pm *} \to \ell\nu$ decays. These branching ratios, which depend on the invariant mass of the off-shell vector boson (and therefore the mass splitting), are calculated with SUSY-HIT 1.5a [68]. The finite b-quark and τ-lepton masses are accounted for in these calculations so that

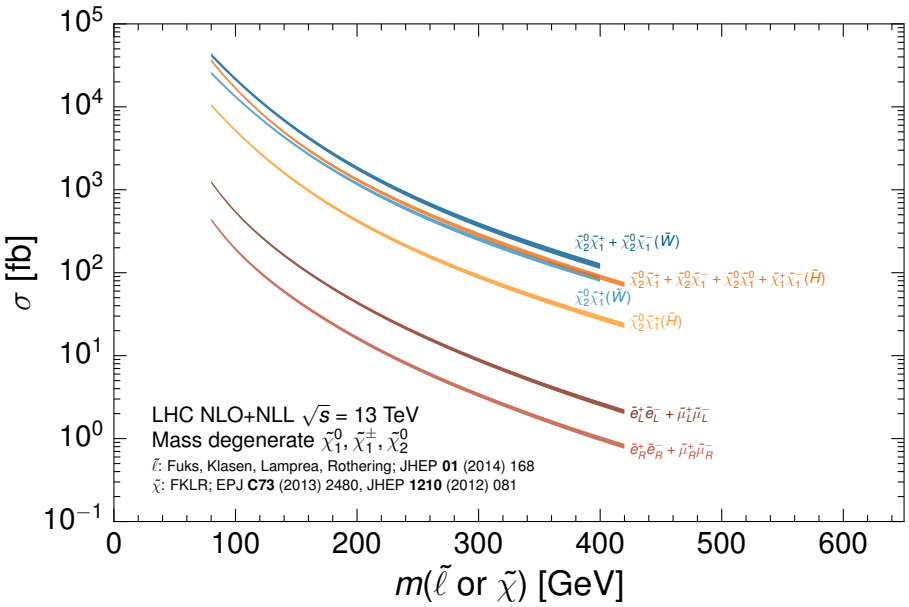

Figure 8.4: Cross-sections for electroweakino and slepton pair-production for pp collisions at $\sqrt{s} = 13$ TeV, taken from the public LHC SUSY Cross-sections Working Group and Refs. [65, 66, 67]. The cross-sections for higgsino-like (wino-like) electroweakinos are denoted by $\tilde{H}$ ($\tilde{W}$). The cross-sections for left-handed and right-handed sleptons are distinguished using L and R subscripts, respectively.

decays involving these particles are turned off when the invariant mass of the off-shell vector boson is below threshold. For example, at $\Delta m\,(\widetilde{\chi}_2^0, \widetilde{\chi}_1^0) = 40$ GeV, the invariant masses of the vector bosons are well above threshold for b-quark and τ-lepton production and the $Z^* \to \ell\ell$ branching ratio is 3.5% for both electrons and muons. If instead, $\Delta m\,(\widetilde{\chi}_2^0, \widetilde{\chi}_1^0) = 1$ GeV, decays involving b/c-quarks and τ-leptons are forbidden by kinematics, and so the $Z^* \to \ell\ell$ branching ratios increase to 5.3% and 5.0% for electrons and muons, respectively. The same features occur for the $W^* \to \ell\nu$ decays, where the branching ratios to electrons and muons grow from 11% when $\Delta m\,(\widetilde{\chi}_2^0, \widetilde{\chi}_1^0) = 40$ GeV to 20% and 17%, respectively, when $\Delta m\,(\widetilde{\chi}_2^0, \widetilde{\chi}_1^0) = 1$ GeV.

Higgsino model For the higgsino simplified model, events are generated based on the production of $\widetilde{\chi}_1^+\widetilde{\chi}_1^-$, $\widetilde{\chi}_2^0\widetilde{\chi}_1^\pm$, and $\widetilde{\chi}_2^0\widetilde{\chi}_1^0$. It assumed in this model that

$|\mu| \ll |M_1|, |M_2|$ such that the wino and bino states are decoupled and the lightest electroweakino triplet is higgsino-dominated, as motivated by naturalness arguments. In all cases, the chargino mass is set to $m(\widetilde{\chi}_1^{\pm}) = \frac{1}{2}[m(\widetilde{\chi}_1^0) + m(\widetilde{\chi}_2^0)]$. Since this search exploits the kinematic endpoint in the dilepton invariant mass distribution from leptonic Z^* decays, the sensitivity to higgsinos is dominated by the processes involving $\widetilde{\chi}_2^0$ production.

Wino/bino models For the wino/bino simplified model, only $\widetilde{\chi}_2^0\widetilde{\chi}_1^{\pm}$ production is generated, as $\widetilde{\chi}_2^0\widetilde{\chi}_1^0$ production is suppressed and there is negligible acceptance for $\widetilde{\chi}_1^+\widetilde{\chi}_1^-$ production in this search. The higgsino states in this model are decoupled by assuming that $|M_1| < |M_2| \ll |\mu|$, such that $\widetilde{\chi}_2^0$ and $\widetilde{\chi}_1^{\pm}$ are mass-degenerate, pure wino states, while $\widetilde{\chi}_1^0$ is a bino-like LSP. Unlike the higgsino model, which only allows negative values, the product of the signed neutralino mass eigenvalues $m(\widetilde{\chi}_2^0) \times m(\widetilde{\chi}_1^0)$ can be positive or negative in the wino/bino model. As shown below, this leads to two distinct $m_{\ell\ell}$ lineshapes and motivates two different interpretations of the results: one in which $m(\widetilde{\chi}_2^0) \times m(\widetilde{\chi}_1^0)$ is positive, and one in which it is negative.

As discussed in Section 7, the discriminating variable in the search for electroweakinos is $m_{\ell\ell}$, which has a kinematic cutoff in signal events that corresponds to the mass-splitting. This exact shape of this distribution, though, is sensitive to the relative signs of the $\widetilde{\chi}_1^0$ and $\widetilde{\chi}_2^0$ mass parameters, as shown in [69]. When generating the wino/bino signals, the product of these signed values is chosen to be positive, and the analogous signal sample with $m(\widetilde{\chi}_1^0) \times m(\widetilde{\chi}_2^0) < 0$ is obtained by reweighting the generated $m_{\ell\ell}$ distribution according to an analytical description of the expected lineshape derived in [69]. The $m_{\ell\ell}$ distributions for each of the simplified electroweakino models are shown in for the generated samples in Figure 8.5, where it can be seen that the reweighted wino/bino dis-

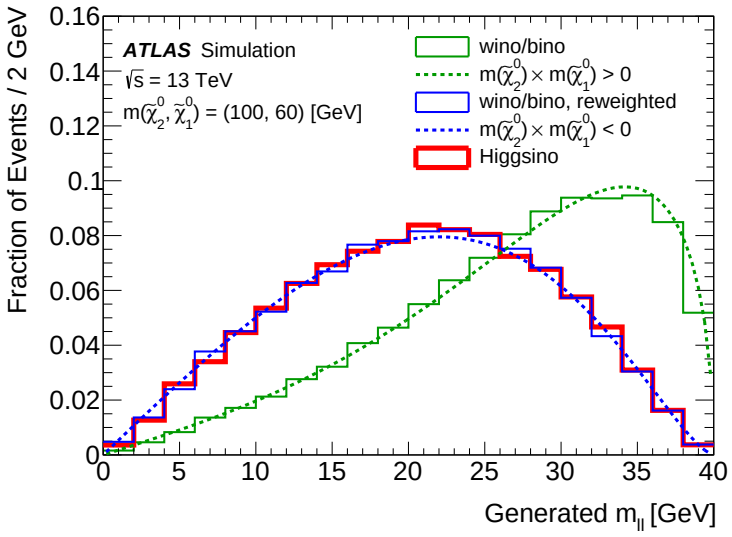

Figure 8.5: The normalized dilepton invariant mass distributions for each of the higgsino and wino/bino simplified models, assuming $m(\widetilde{\chi}_2^0) = 100$ GeV and $m(\widetilde{\chi}_1^0) = 60$ GeV. In the wino/bino simplified model, the shape of the distribution depends on the product of the signed mass eigenvalues ($m\,(\widetilde{\chi}_2^0) \times m\,(\widetilde{\chi}_1^0)$), which can be positive or negative. In the higgsino model, this product can only take negative values. In each case, the distributions are characterized by a kinematic endpoint that corresponds to the mass-splitting between the $\widetilde{\chi}_2^0$ and $\widetilde{\chi}_1^0$. The results from Monte Carlo simulation are shown as histograms, to be compared with the dashed lines that represent expected lineshapes, which were determined analytically in Ref. [69].

tribution shows good agreement with the expected lineshape. The lineshapes are essentially the same between the higgsino model and the wino/bino model with $m(\widetilde{\chi}_1^0) \times m(\widetilde{\chi}_2^0) < 0$, so that any differences in the results between these models is due their respective cross-sections. The final point worth noting is that the lineshape for the wino/bino model with $m(\widetilde{\chi}_1^0) \times m(\widetilde{\chi}_2^0) > 0$ is much more asymmetric than the others so that the results will be more sensitive to fluctuations in a single (or a few adjacent) $m_{\ell\ell}$ bins.

8.2.2 Slepton Model

The slepton simplified model assumes that sleptons of a given flavor and chirality are produced in pairs. Only selectrons ($\widetilde{e}_{L,R}$) and smuons ($\widetilde{\mu}_{L,R}$) are considered in this search and are hereafter collectively referred to as "sleptons" ($\widetilde{\ell}_{L,R}$). Of course, sleptons are scalar particles and so their "chirality" actually refers to the chirality of their SM counterparts that carry spin. In this notation, the L and R subscripts denote the left- and right-handed chiral states of the corresponding SM lepton partners, respectively. The slepton samples were generated with MG5_aMC@NLO 2.6.1 and interfaced with Pythia 8.230 for the parton shower. As with the electroweakino signals, the NNPDF2.3LO PDF set was used with the A14 tune and the jet-parton matching was performed according to the CKKW-L prescription with the merging scale set to one quarter of the slepton mass. When generating these events, all slepton flavors and chiral states are assumed to be degenerate in mass. Additionally, the sleptons are assumed to decay to their SM partner lepton and a purely bino-like neutralino, $\widetilde{\chi}_1^0$, with a 100% branching ratio.

The cross-sections, shown in Figure 8.4, are calculated at NLO+NLL precision using Resummino 2.0.1. As with electroweakino signals, the cross-section uncertainties are determined according to Ref. [63] by taking the envelope of the resulting cross-sections after varying the PDF sets, as well as the factorization and renormalization scales. The discriminating variable for the slepton search is the stransverse mass, which is constructed by assuming a $\widetilde{\chi}_1^0$ mass of 100 GeV. This variable, denoted by m_{T2}^{100}, is shown for some generated slepton samples with different masses in Figure 8.6, where the kinematic endpoint agrees well with the signal mass-splitting. Samples are generated with slepton masses, $m(\widetilde{\ell}_{L,R})$, between 50 GeV and 300 GeV and mass splittings, $\Delta m(\widetilde{\ell}_{L,R}, \widetilde{\chi}_1^0)$, between 300 MeV and 40 GeV.

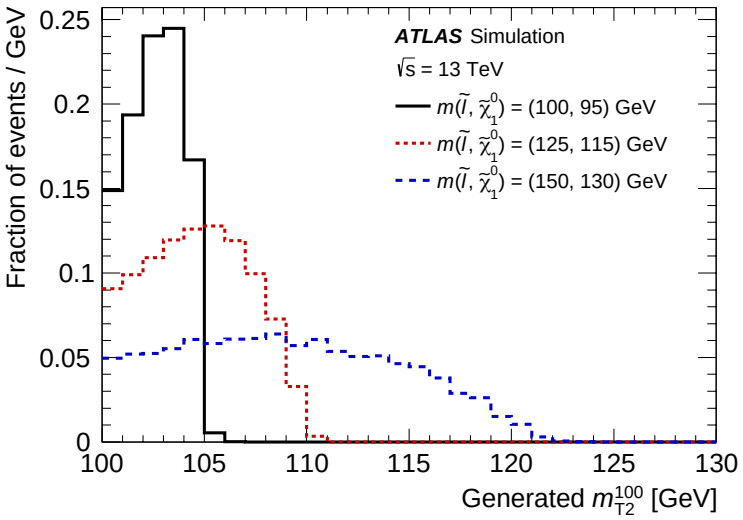

Figure 8.6: The normalized stransverse mass distribution assuming an LSP mass of 100 GeV (m_{T2}^{100}) for slepton events from different signal samples. The endpoint of the distribution (minus 100 GeV, the assumed LSP mass) is determined by the mass-splitting between the slepton and LSP.

8.3 Simulated Background Samples

Aside from processes involving fake/non-prompt leptons, described in Section 11.2, the SM background processes are estimated using MC simulation. The generator configurations used for the relevant SM background processes are summarized in Table 8.3, including information about the cross-section used for normalization. All of these background events are processed using the ATLAS simulation framework [70] in GEANT4 [71]. Unlike the signal samples, the SM background samples employ the full simulation of the ATLAS detector as implemented in GEANT4.

SHERPA 2.2.1 and 2.2.2 are used to generate and shower the V+jets ($V = W, Z, \gamma^*$), VV ($V = W, Z$), and triboson processes using the NNPDF 3.0 NNLO PDF set. The matrix element calculations use up to four partons at leading-order and are merged with the SHERPA parton shower according to the ME+PS@NLO

Table 8.3: Configurations for the simulation of SM background processes. The PDF set refers to that used for the matrix element.

Process	Matrix element	Parton shower	PDF set	Cross-section
V+jets	Sherpa 2.2.1		NNPDF 3.0 NNLO [72]	NNLO [73]
VV	Sherpa 2.2.1/2.2.2		NNPDF 3.0 NNLO	Generator NLO
Triboson	Sherpa 2.2.1		NNPDF 3.0 NNLO	Generator LO, NLO
h (ggF)	Powheg-Box	Pythia 8.212	NLO CTEQ6L1 [74]	N^{3}LO [75]
h (VBF)	Powheg-Box	Pythia 8.186	NLO CTEQ6L1 [74]	NNLO + NLO [75]
$h + W/Z$	Pythia 8.186		NNPDF 2.3 LO [76]	NNLO + NLO [75]
$h + t\bar{t}$	MG5_aMC@NLO 2.2.3	Pythia 8.210	NNPDF 2.3 LO	NLO [75]
$t\bar{t}$	Powheg-Box	Pythia 8.230	NNPDF 2.3 LO	NNLO+NNLL [77, 78, 79, 80, 81]
t (s-channel)	Powheg-Box	Pythia 8.230	NNPDF 2.3 LO	NNLO+NNLL [82]
t (t-channel)	Powheg-Box	Pythia 8.230	NNPDF 2.3 LO	NNLO+NNLL [83, 84]
$t + W$	Powheg-Box	Pythia 8.230	NNPDF 2.3 LO	NNLO+NNLL [85]
$t + Z$	MG5_aMC@NLO 2.3.3	Pythia 8.212	NNPDF 2.3 LO	NLO [86]
$t\bar{t}WW$	MG5_aMC@NLO 2.2.2	Pythia 8.186	NNPDF 2.3 LO	NLO [86]
$t\bar{t} + Z/W/\gamma^*$	MG5_aMC@NLO 2.3.3	Pythia 8.210/8.212	NNPDF 2.3 LO	NLO [75]
$t + WZ$	MG5_aMC@NLO 2.3.3	Pythia 8.212	NNPDF 2.3 LO	NLO [86]
$t + t\bar{t}$	MG5_aMC@NLO 2.2.2	Pythia 8.186	NNPDF 2.3 LO	LO [86]
$tt\bar{t}\bar{t}$	MG5_aMC@NLO 2.2.2	Pythia 8.186	NNPDF 2.3 LO	NLO [86]

prescription [87]. Both of these background samples include coverage down to dilepton invariant masses of 0.5 GeV for $Z^{(*)}/\gamma^* \to ee/\mu\mu$ and 3.8 GeV for $Z^{(*)}/\gamma^* \to \tau\tau$. While Sherpa is used for the $Z(\to \mu\mu)$+jets background modeling, this process is also generated using MG5_aMC@NLO with the same configuration as the signal samples in order to assess the initial- and final-state radiation modeling in signal events, as described in Section 12.3.2.

Though small, single-Higgs boson production also presents a background for this search. The following production modes are considered for this process: gluon-gluon fusion (ggF), vector boson fusion (VBF), associated production with a massive vector boson ($h + W/Z$), and associated production with a top quark pair ($h + t\bar{t}$). The ggF and VBF processes are generated using Powheg-Box and the NLO CTEQ6L1 PDF set. The generated ggF and VBF events are interfaced with Pythia 8.212 and 8.186, respectively, for parton showering. For $h + W/Z$, Pythia 8.186 is used for both the matrix element and parton showering, while $h + t\bar{t}$ events are generated using MG5_aMC@NLO 2.2.3 interfaced with Pythia 8.210. Both the $h + W/Z$ and $h + t\bar{t}$ event generation use the NNPDF 2.3 LO

PDF set for the matrix element.

POWHEG-BOX interfaced with PYTHIA 8.230 is used to model the $t\bar{t}$ [88, 89, 90, 91], single-top (t- and s-channels) [84], and $t + W$ [92] processes. Rarer top quark processes include $t + Z$, $t\bar{t}WW$, $t\bar{t} + Z/W/\gamma^*$, $t + WZ$, $t + t\bar{t}$, and $tt\bar{t}\bar{t}$. The matrix elements for these backgrounds are all generated with MG5_aMC@NLO and showered with PYTHIA 8 (see Table 8.3 for the specific versions). All of the top quark processes use the NNPDF 2.3 LO PDF set for the matrix element.

Out of the box, the simulated events do not account for the effect of additional pp interactions than can occur in the same and/or neighboring bunch-crossings as the hard-scatter process. In order to simulate these effects, additional events from soft QCD processes are generated using PYTHIA 8.186 with the A3 tune [59] and the MSTW2008LO PDF set [60]. These QCD events are then overlaid onto the simulated hard-scatter events for both signal and background processes. Finally, these MC events, which are typically generated before the pileup conditions in data are known, are reweighted in order to match the observed distribution of the average number of interactions per bunch-crossing, as shown in Figure 8.2. The modeling of bottom and charm quark decays is performed by EVTGEN 1.6.0 and 1.2.0 for background and signal events, except those generated by SHERPA, which employs its own internal modeling of heavy-flavor decays.

Chapter 9

Physics Objects

The ATLAS detector elements described in Chapter 6 provide information about energy deposits in specific parts of the detector. In order to perform physics analysis, these signatures need to be processed by dedicated reconstruction algorithms that are optimized to efficiently identify various particle types in addition to determining their energies and momenta with excellent resolution. Figure 9.1 gives an overview of the characteristic signatures that are left in the ATLAS detector by different particles and exploited by these reconstruction algorithms.

Once the particles are reconstructed and identified, additional quality criteria can be placed on them in such a way that maintains a high level of signal efficiency and low misidentification rates. In the searches presented here, the electrons, muons and jets are first selected according to relatively loose "baseline" requirements. All signal, control, and validation regions additionally require these objects to pass tighter "signal" criteria. The exceptions to this are with the the regions used to derive and validate the data-driven fake/non-prompt lepton background, described in Section 11.2, which makes use of leptons that pass the baseline selection but fail to satisfy the signal lepton requirements. A summary of the signal and baseline object requirements is given in Table 9.1. These selec-

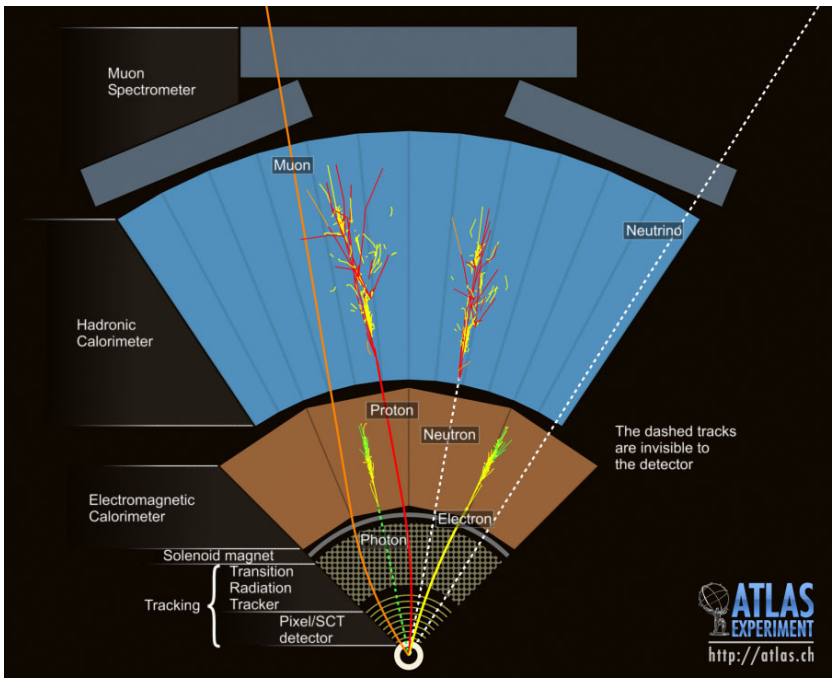

Figure 9.1: A cartoon showing a transverse slice of the ATLAS detector showing how various particles traverse the the detector and what type of signatures they produce. The curved trajectories of electrically charged particles are reconstructed using hits in the Inner Detector, while neutral particles are not (indicated by dashed white lines). Electrons and photons produce particle showers in the Electromagnetic Calorimeter, while hadrons produce showers in the Hadronic Calorimeter. Muons penetrate the detector, and their curved trajectories are reconstructed using hits in both the Inner Detector and the Muon Spectrometer. Finally, electrically neutral neutrinos penetrate the detector without interacting with it at all [93].

Table 9.1: Summary of the signal and baseline object definitions.

Property	Signal	Baseline
Electrons		
Kinematic	$p_{\mathrm{T}} > 4.5$ GeV, $\lvert\eta\rvert < 2.47$	$p_{\mathrm{T}} > 4.5$ GeV, $\lvert\eta\rvert < 2.47$
Identification	`Medium`	`VeryLoose`
Isolation	`Gradient`	–
Impact parameter	$\lvert d_0/\sigma(d_0)\rvert < 5$, $\lvert z_0 \sin\theta\rvert < 0.5$ mm	$\lvert z_0 \sin\theta\rvert < 0.5$ mm
Muons		
Kinematic	$p_{\mathrm{T}} > 3$ GeV, $\lvert\eta\rvert < 2.5$	$p_{\mathrm{T}} > 3$ GeV, $\lvert\eta\rvert < 2.5$
Identification	`LowPt`	`LowPt`
Isolation	`FCTightTrackOnly`	–
Impact parameter	$\lvert d_0/\sigma(d_0)\rvert < 3$, $\lvert z_0 \sin\theta\rvert < 0.5$ mm	$\lvert z_0 \sin\theta\rvert < 0.5$ mm
Jets (Anti-k_t, $R = 0.4$)		
Kinematic	$p_{\mathrm{T}} > 30$ GeV, $\lvert\eta\rvert < 2.8$	$p_{\mathrm{T}} > 20$ GeV, $\lvert\eta\rvert < 4.5$
Pileup mitigation	JVT `Medium` for $p_{\mathrm{T}} < 120$ GeV, $\lvert\eta\rvert < 2.5$	–
b-Jets (Anti-k_t, $R = 0.4$)		
Kinematic	$p_{\mathrm{T}} > 20$ GeV, $\lvert\eta\rvert < 2.5$	$p_{\mathrm{T}} > 20$ GeV, $\lvert\eta\rvert < 4.5$
Pileup mitigation	JVT `Medium` for $p_{\mathrm{T}} < 120$ GeV, $\lvert\eta\rvert < 2.5$	–
b-tagging	`MV2c10` (85% efficiency)	–

tions, as well as the reconstruction methods, are described in more detail in the following sections.

9.1 Tracks and Vertices

Tracks that correspond to the trajectories of charged particles in the ID are constructed by first clustering hits in the Pixel Detector and SCT to ultimately form three-dimensional space-points. These space-points indicate the locations where the particles interact with the silicon sensors in the ID and the track seeds consist of three space-points. A combinatorial Kalman filter [94] is employed to build track candidates from the track seeds by adding additional space-points from other layers in the ID that are consistent with the seed trajectory. This process

can lead to multiple track candidates per seed and this ambiguity is solved by assigning track scores to the candidates that reflect the track quality. The track scores incorporate information including the χ^2 of the track fit, the p_{T} of the track, and the number of "holes" along the track trajectory, which are defined as intersections between the track trajectory and active ID material where no matching cluster is found. After the ambiguity solving, the surviving tracks are extrapolated to the TRT to look for consistent tracks that can be incorporated into the final high-resolution fit that uses all three ID subsystems. Though the individual hit resolution is lower in the TRT than in the silicon sensors, the long lever arm can improve the track momentum resolution when such extrapolations are possible.

In ATLAS, tracks are defined using the five parameters that form the perigee basis, where each parameter is evaluated at the point of closest approach to the z-axis. These parameters are chosen to be the azimuthal angle ϕ_0, the polar angle θ_0, the charge-to-momentum ratio q/p, the longitudinal impact parameter z_0, and the transverse impact parameter d_0. Since the reconstruction of racks relies on hits in the ID, all reconstructed tracks are limited to the region defined by $|\eta| < 2.5$. The lower bound on the transverse momentum of reconstructed tracks is 500 MeV.

Vertices are formed via an iterative fit procedure using tracks that satisfy a quality criteria based on the number of hits in the Pixel Detector and SCT [95, 96]. The minimum number of tracks needed to form a vertex is two. Of particular importance is the construction of the Primary Vertex (PV), which is taken to be the location in space of the hard-scatter process in the event. In the fitting procedure, the seed location of the PV in the transverse direction is taken to be the center of the nominal beam spot, and the longitudinal coordinate is the mode of the z-coordinates of all tracks at their points of closest approach to the

center of the beam spot. Tracks are then fit along with the PV seed in an iterative process that down-weights tracks that are less compatible with PV (based on the χ^2) at each step. This process is repeated until tracks with small enough weights are deemed incompatible with the PV and removed. In order to reconstruct other candidate vertices, this process is then repeated using these removed tracks until no more vertices can be reconstructed. The PV in the event is chosen to be the one with the highest $\sum p_{\mathrm{T}}^2$ of associated tracks.

9.2 Charged Light-Flavor Leptons

The searches presented here do not consider τ-leptons; instead they only focus on the charged light-flavor leptons: electrons and muons. The following sections outline the electron and muon reconstruction techniques and kinematic requirements applied in these searches, including a summary of dedicated isolation corrections used to boost signal efficiency and improve the fake/non-prompt background modeling in events with highly-collimated leptons. The combined reconstruction, identification, isolation, and vertex association efficiencies for signal leptons (within the detector acceptance) from various slepton and higgsino signal samples are shown in Figure 9.2. This efficiency for electrons ranges from $\sim 20\%$ at $p_{\mathrm{T}} = 4.5\,\mathrm{GeV}$ to over 75% for $p_{\mathrm{T}} > 30\,\mathrm{GeV}$. For muons, the efficiencies vary from $\sim 50\%$ at $p_{\mathrm{T}} = 3\,\mathrm{GeV}$ to $\sim 90\%$ for $p_{\mathrm{T}} > 30\,\mathrm{GeV}$. Brief accounts of the electron and muon reconstruction procedures are given below, as well as details about their requirements for consideration in these searches.

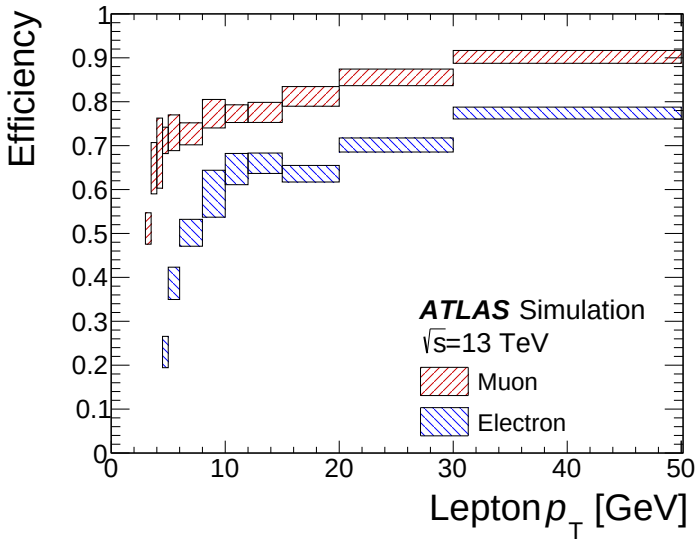

Figure 9.2: Signal lepton efficiencies for electrons and muons in a mix of slepton and higgsino samples. Combined reconstruction, identification, isolation and vertex association efficiencies are shown for leptons within the detector acceptance, and with lepton p_{T} within a factor of 3 of $\Delta m(\widetilde{\ell}, \widetilde{\chi}_1^0)$ for sleptons or of $\Delta m(\widetilde{\chi}_2^0, \widetilde{\chi}_1^0)/2$ for higgsinos. The average number of interactions per crossing in the MC samples is $\langle\mu\rangle = 33.7$. Uncertainty bands represent the range of efficiencies observed across all signal samples used for the given p_{T} bin.

9.2.1 Electrons

Electrons traversing the detector leave a distinct signature that consists of tracks in the ID followed by a shower in EM calorimeter. The goal of electron reconstruction is to reconstruct these signatures separately and then match the tracks to the energy depositions to form electron candidates. A detailed account of the reconstruction is given in [97]. Multiple tracks can be assigned to electron candidates due to the bremsstrahlung process in which the radiated photon converts to an electron-positron pair that leave additional tracks near the original electron. The first step in the reconstruction is to identify candidate clusters of energy deposits in the EM calorimeter layers. The algorithm divides the layers of the EM calorimeter into projective "towers" of size $\Delta\eta \times \Delta\phi = 0.025 \times 0.025$, which matches the granularity of the second layer. The energy in each tower is the sum of the energies in each layer of the calorimeter. From there, a sliding window algorithm is employed to identify groups of towers in windows of size 3×5 (in $\eta \times \phi$) that have total transverse energies of at least 2.5 GeV. Tracks in the ID are extrapolated to the first layer of the EM calorimeter and matched to these seed-clusters based on their consistency in η and ϕ while accounting for energy losses such as bremsstrahlung.

The efficiencies for seed-clustering, track reconstruction, and track-cluster matching are shown in Figure 9.3 for simulated electrons as a function of their generator-level E_{T}. The loss of efficiency at low E_{T} is mostly due to the $\sum E_{\mathrm{T}} > 2.5\,\mathrm{GeV}$ requirement on the electron clusters. The reconstruction efficiency is measured in data using $Z \to ee$ events, and differences in the efficiencies between data and simulation are used to derive scale factors that are applied to the simulated samples to match the data. The electron energies are calibrated using a combination of $Z \to ee$ and $J/\psi \to ee$ events in data and simulation [98].

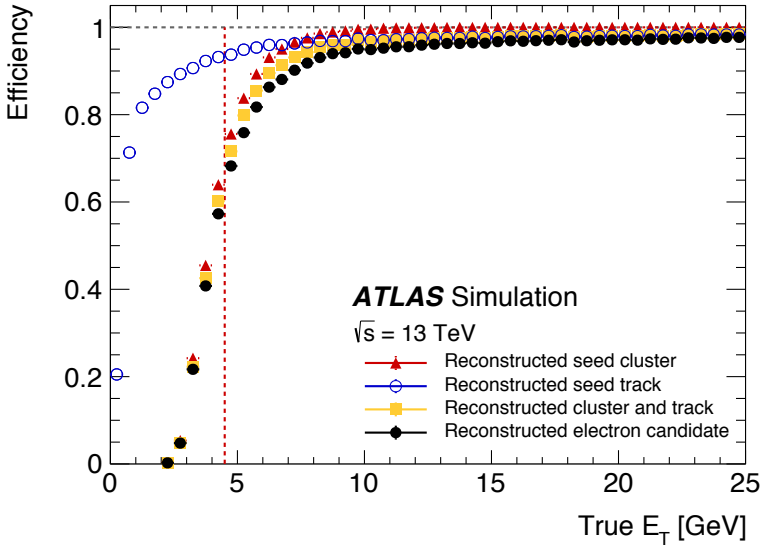

Figure 9.3: The electron reconstruction efficiency in simulation at several steps in the overall reconstruction procedure as a function of the true electron E_{T}. The vertical dashed line indicates the current 4.5 GeV threshold for electron use in ATLAS physics analysis [97].

In order to improve the purity of the reconstructed electrons, which have backgrounds including misidentified jets (described Section 9.3) and photon conversions, the electrons used for physics analysis in ATLAS must satisfy some quality criteria. These identification criteria are based on multi-dimensional electron and background likelihoods that are built from a variety of sensitive observables that include tracking and EM shower shape information, as well as consistency between the ID and calorimeter measurements [97]. Different cuts on the likelihood function, called "working points," produce different electron efficiencies and background rejection factors.

Baseline and signal electrons are required to have $p_{\mathrm{T}} > 4.5\,\mathrm{GeV}$, $|\eta| < 2.47$, and $z_0 \sin\theta < 0.5\,\mathrm{mm}$. Baseline electrons must satisfy the `VeryLoose` identification working point [99], while signal electrons must satisfy the tighter `Medium` working point [99], which has an efficiency of $\sim 79\%$ at $p_{\mathrm{T}} = 4.5\,\mathrm{GeV}$ that increases to $\sim 93\%$ for $p_{\mathrm{T}} \gtrsim 80\,\mathrm{GeV}$. Finally, signal electrons must satisfy the `Gradient`

isolation working point [99], described in more detail below, and have $\left|\frac{d_0}{\sigma(d_0)}\right| < 5$, where $\sigma(d_0)$ is the uncertainty on the transverse impact parameter d_0.

9.2.2 Muons

Muons are reconstructed by combining separate tracking information in the ID and the MS. As a first step, hit patterns in the bending plane of the MS layers are used to establish track segments that are the result of straight-line fits. MS track candidates are then formed by fitting the track segments from different layers together, where segments in the middle layers are used as seeds and segments in the other layers are selected based on hit multiplicity and fit quality criteria using the χ^2 method. Once the track candidates are formed, a global χ^2 fit is performed using the associated MS hits, where hits can be removed from the fit if they have a large impact on the χ^2. Track candidates are accepted if the χ^2 satisfies a cut on the fit quality. Once the tracks are defined, a combined fit is performed using these MS track hits and hits from ID tracks, which are reconstructed independently. Again, hits can be removed from the fit if the removal improves the overall χ^2 of the global fit. This reconstruction method defines "combined" (CB) muons, though other flavors of muons exist within ATLAS reconstruction [100]. In most cases, the CB muons are reconstructed using an "outside-in" method in which MS tracks are reconstructed first and extrapolated inward to the ID for track-matching. An "inside-out" method in which the ID tracks are extrapolated outward to the MS for track-matching can be used as a complementary approach.

In these searches, both baseline and signal muons are required to have $p_{\mathrm{T}} > 3\,\mathrm{GeV}$, $|\eta| < 2.5$, and $z_0 \sin\theta < 0.5\,\mathrm{mm}$. Additionally, they are required to satisfy the `LowPt` identification working point, which provides calibrations for muons with $3\,\mathrm{GeV} < p_{\mathrm{T}} < 4\,\mathrm{GeV}$ for the first time in ATLAS [101]. A tighter selection is placed

on signal muons by additionally requiring them to pass the `FCTightTrackOnly` isolation working point [100] and have a small transverse impact parameter significance, $\left|\frac{d_0}{\sigma(d_0)}\right| < 3$.

The `LowPt` working point was designed to provide improved efficiencies for real muons as well as lower misidentification rates for muon candidates with $p_{\mathrm{T}} < 10\,\mathrm{GeV}$. This working point uses only CB tracks, though the hit requirements in the MS are loosened in order to retain efficiency for low-p_{T} muons. Since these muons can deposit a significant fraction of their energy in the calorimeters, `LowPt` only requires hits in at least one MS station in the central region defined by $|\eta| < 1.3$. For $1.3 < |\eta| < 1.55$, hits in at least two MS stations are required. In the forward region, $|\eta| > 1.55$, the hit requirements from the `Medium` [100] muon identification working point are used.

`LowPt` provides discrimination between real and misidentified muons from hadron decays by exploiting variables that are sensitive to imbalances in the track momentum as measured in the ID and the MS and compared to the energy lost in the calorimeters, as well as significant changes in the track trajectory, which are indicative of a charged hadron decaying to a muon. Compared to the `Medium` working point, `LowPt` maintains a similar fake muon rate in the $|\eta| < 1.2$ region for $3\,\mathrm{GeV} < p_{\mathrm{T}} < 6\,\mathrm{GeV}$ while improving the efficiency by approximately 20%, as shown in Figure 9.4. The efficiencies are measured in data using a tag-and-probe method in $J/\psi \to \mu\mu$ events, and differences in the efficiencies between data and MC are used to derive efficiency scale factors that are applied to the background and signal samples in these searches.

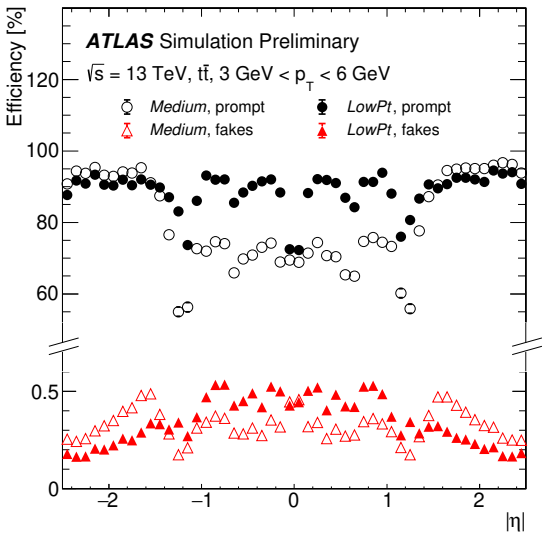

Figure 9.4: The expected efficiencies of the `LowPt` (filled markers) and `Medium` (empty markers) muon identification working points in simulated $t\bar{t}$ events as a function of η [101].

9.2.3 Isolation Corrections

One way to help distinguish between promptly-produced leptons (e.g. from $W \to \ell\nu$) and those from non-prompt processes (e.g. semi-leptonic decays of b-hadrons) is to determine how isolated they are inside the detector. Prompt leptons tend to be produced in isolation, while non-prompt and fake leptons are often close to other reconstructed objects. Isolation variables for leptons are constructed by summing the p_{T} or E_{T} of unassociated tracks and topologically-connected calorimeter clusters (topoclusters), respectively, within a cone of some size around the lepton. A selection criteria is applied to the objects entering the calculation to mitigate biases from pileup contributions. Various working points targeting different lepton efficiencies are constructed by placing cuts on these isolation variables.

For signal muons, the chosen isolation working point is `FCTightTrackOnly`, which performs the sum over track p_{T} within a cone that has a maximum size of

$\Delta R = 0.3$ and shrinks with increasing muon p_{T} according to $\Delta R = \min(\frac{10\,\mathrm{GeV}}{p_{\mathrm{T}}}, 0.3)$. The sum, called $p_{\mathrm{T}}^{\mathrm{varcone30}}$, is only performed using tracks that are consistent with the PV and have $p_{\mathrm{T}} > 1\,\mathrm{GeV}$. The final isolation cut is based on the scalar sum of the transverse momentum contained within this cone in relation to the muon p_{T}, such that signal muons must satisfy $\frac{p_{\mathrm{T}}^{\mathrm{varcone30}}}{p_{\mathrm{T}}} < 0.06$.

Signal electrons, meanwhile, must satisfy the `Gradient` isolation working point, which uses a combination of tracking and calorimeter topocluster information. For the cone defined by the sum over track p_{T}, the variable used is $p_{\mathrm{T}}^{\mathrm{varcone20}}$, which is defined in the same way as $p_{\mathrm{T}}^{\mathrm{varcone30}}$ except it has a maximum size of $\Delta R = 0.2$. The cone that sums over the E_{T} of topoclusters is called $E_{\mathrm{T}}^{\mathrm{cone20}}$, which has a fixed radius of $\Delta R = 0.2$. In order not to count the energy deposits from the electrons themselves, all topoclusters within a rectangle of size $\Delta\eta \times \Delta\phi = 0.125 \times 0.175$ around the center of the electrons are removed from the sum. Additional corrections to the $E_{\mathrm{T}}^{\mathrm{cone20}}$ variable are applied to account for potential leakage of the electron energy outside of this rectangle, as well as pileup effects. A schematic of this procedure is shown in Figure 9.5. Ultimately, the cuts on these $p_{\mathrm{T}}^{\mathrm{varcone30}}$ and $E_{\mathrm{T}}^{\mathrm{cone20}}$ are designed to provide electron isolation efficiencies of 90% at $p_{\mathrm{T}} = 25\,\mathrm{GeV}$ and 99% at $p_{\mathrm{T}} = 60\,\mathrm{GeV}$, uniform in η [99]. At $p_{\mathrm{T}} = 4.5\,\mathrm{GeV}$, this efficiency is approximately 84%.

The above description outlines the general way in which lepton isolation variables are calculated by ATLAS. Nonetheless, the specific topologies targeted by these searches necessitates two corrections to the isolation calculation procedures. In these boosted topologies, the soft leptons from signal events are highly collimated. This is especially true for electroweakino production, where the leptons are produced from a boosted $Z^* \to \ell\ell$ decay. In such cases, the leptons often fall within each other's isolation cones, which leads to a loss in efficiency for the

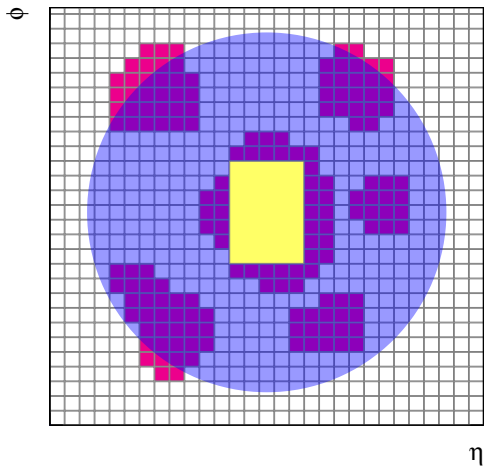

Figure 9.5: A schematic of the calorimeter-based isolation calculation for electrons. The grid represents the cells of the second layer of the EM calorimeter in the $\eta - \phi$ plane. The purple circle represents the isolation cone, with the electron candidate at the center. Topoclusters are shown in red, and those with barycenters inside of the cone are included in the isolation calculation. The yellow rectangle indicates the expected core of the electron shower and all topoclusters within this area are excluded from the calculation [97].

most compressed signal scenarios. To combat this, the isolation variables for both muons and electrons are calculated in a way that omits the contribution from the nearby lepton. Specifically, each event looks for baseline leptons that fail the signal isolation requirement. If another baseline lepton is found within its isolation cones, the tracks and/or topoclusters associated to this nearby lepton are removed from the isolation sums and the isolation requirements are reevaluated, ultimately leading to a significant increase in signal efficiencies for events at low-$m_{\ell\ell}$.

Despite the improved handling of the isolation variables in events with nearby leptons, it was found that the fake/non-prompt lepton estimate, detailed in Section 11.2, became negative for small angular separations between the leptons where the isolation cones overlap. Schematically, there is a term in the expression for the fake/non-prompt lepton estimate that subtracts events containing two baseline leptons that fail the isolation criteria, and if this terms gets too

large, then the estimate can become negative. Such poor modeling would severely limit the sensitivity to the most compressed electroweakino signals that produce these collimated di-lepton events. As described in Section 11.2.1, this feature was traced back to an underlying assumption in the method for deriving the data-driven fake/non-prompt background. Specifically, the method assumes that the probabilities for the baseline leptons in an event to fail the isolation criteria can be thought of as being uncorrelated. This is manifestly not true when there is significant overlap between the isolation cones, in which case if one lepton fails the isolation requirement, then the second lepton has a higher probability of also failing it. The correlation obviously grows with the amount of overlap between the cones.

To combat this effect, an additional correction has been developed and implemented to address tracks and topoclusters that fall within both leptons' isolation cones and yet cannot be associated to either lepton (otherwise they would have been corrected for by the method described above). Such objects are called "stray" tracks and topoclusters and the goal of the algorithm is to assign all of the stray tracks and topoclusters entering into the overlapping region to only one of the leptons' isolation cones.

After the previous correction takes place, additional loops are initiated over stray tracks and topoclusters, and those that fall into both leptons' isolation cones have their four-vectors summed to form new four-vectors. The four-vector sum of these stray tracks is called $\mathbf{v}_{\text{trk}}$ and the equivalent four-vector sum for topoclusters is called $\mathbf{v}_{\text{topo}}$. Once these four-vectors are formed, their angular distances from each lepton are calculated based on ΔR. Finally, the contributions from the stray tracks (topoclusters) that went into building $\mathbf{v}_{\text{trk}}$ ($\mathbf{v}_{\text{topo}}$) are subtracted from the isolation cone of the lepton that is farther away based on this distance measure. A

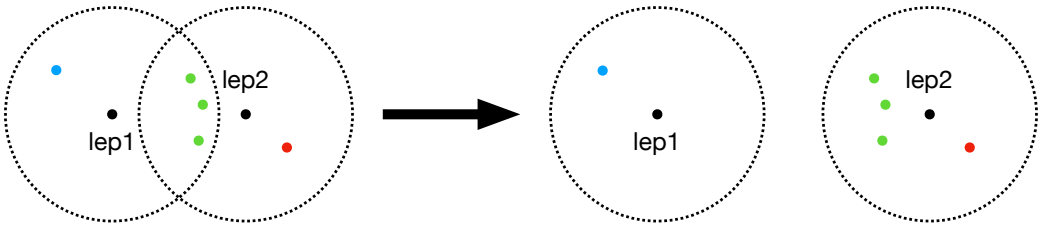

Figure 9.6: An illustration of the additional isolation correction for tracks/topoclusters that lie within the overlapping isolation cones of nearby leptons but are not associated to either lepton. Here, the green points generically represent these stray tracks or topoclusters. Before the correction, they contribute equally to both leptons' isolation cones. After the correction, they only contribute to the isolation cone of the lepton that is closest in ΔR to the sum of their four-vectors – in this case, the lepton on the right.

generic cartoon describing this additional correction is shown in Figure 9.6. After this additional correction, significant improvements are observed in the modeling of fake/non-prompt leptons in highly collimated events, though some residual mismodeling is observed in ee and $e\mu$ events, which is reflected in the cuts detailed in Section 10.2.

9.3 Jets

Due to the confinement phenomenon of QCD, the bare quarks and gluons that are produced in the pp collisions are not observed in the final state. Instead, these particles undergo hadronization, which results in a jet of colorless hadrons along the original particle direction that leave energy deposits in the electromagnetic and hadronic calorimeters, where the electromagnetic component comes from e.g. $\pi^0 \to \gamma\gamma$ decays. From there, a series of clustering algorithms are used to ultimately reconstruct objects called jets that can be thought of as representing the underlying parton.

The jet clustering algorithms in ATLAS are performed using three-dimensional

topoclusters, which consist of adjacent calorimeter cells with signals that are at least four times the expected noise level. Several sequential jet clustering algorithms exist [102, 103, 104], but they are all based on the distance measures d_{ij} between different topoclusters and d_{iB}, which is a distance in momentum space between the topocluster and the beam line. These are generally defined as

$$\begin{aligned} d_{ij} &= \min\left(k_{ti}^{2p}, k_{tj}^{2p}\right) \frac{\Delta_{ij}^2}{R^2}, \\ d_{iB} &= k_{ti}^{2p}, \end{aligned} \tag{9.1}$$

where $\Delta_{ij}^2 = (y_i - y_j)^2 + (\phi_i - \phi_j)^2$, and k_{ti}, y_i, and ϕ_i are the transverse momentum, rapidity, and azimuthal angle of the i^{th} topocluster, respectively. R is a radius parameter that sets the overall size of the jet and p is a parameter that controls the relative power of the energy scale in relation to the geometrical scale used for the clustering. These sequential jet clustering algorithms proceed by first computing all values of d_{ij} and d_{iB}. If the smallest such value is a d_{ij}, then the objects i and j are combined by summing their four-momenta and they are removed from the list. If the smallest value is d_{iB}, then object i is considered a jet and removed from the list. This process is repeated until there are no more remaining objects i. Different choices of p correspond to different sequential jet clustering algorithms. In ATLAS, the anti-k_t algorithm [104, 57] is used, which sets $p = -1$, such that hard objects are clustered first and the resulting jets are cone-shaped (for sufficiently hard jets). In the jets considered in these search, the radius parameter that controls the size of the jet cones is $R = 0.4$.

Reconstructed jets are calibrated according to the procedure defined in [105]. The goal of the calibration is to establish the Jet Energy Scale (JES) that corrects the measured jet energy to that of the underlying parton. The JES calibration starts with correcting the jet direction (without changing its energy) so that it

points back to the PV in order to obtain better resolution on η. A series of corrections are then applied to reduce the contamination in the jet from pileup interaction. These corrections are based on the jet area as well as the number of reconstructed primary vertex candidates and μ, where the latter two corrections are based on MC studies. The next step is to derive a global JES calibration that aims to correct the jet four-momentum to the particle-level energy scale by using comparisons of the reconstructed and truth-level jets in a PYTHIA MC sample. A global sequential calibration is then applied to reduce the impact on the jet energy due to flavor-dependence. In particular, jets initiated by quarks and gluons tend to produce showers with different particle multiplicities and energy spectra. For example, gluon splitting tends to produce showers containing more particles with lower energies on average compared to quark jets. Finally, an *in situ* calibration is performed to account for residual discrepancies between jets in data and MC by using p_{T}-balance in dijet events, which are also used to measure the Jet Energy Resolution (JER). After applying all of these calibrations, baseline jets in these searches must have $p_{\mathrm{T}} > 20\,\mathrm{GeV}$ and $|\eta| < 4.5$, while the signal jets that are used to calculate analysis-level variables are required to satisfy $p_{\mathrm{T}} > 30\,\mathrm{GeV}$ and $|\eta| < 2.8$.

In order to discriminate between jets produced from the hard scatter vertex and those from pileup interactions, a multivariate algorithm call the Jet Vertex Tagger (JVT) is used [106]. This consists of a two-dimensional likelihood using variables called the corrected Jet Vertex Fraction (corrJVF) and R_{pT}. The corrJVF variable is defined to be the scalar transverse momentum sum of tracks assigned to the jet and associated to the PV divided by the scalar transverse momentum sum off all of the tracks assigned to the jet. An additional correction is applied to this variable to account for a bias in the scalar transverse momentum sum due to the

number of interaction vertices in the event. Jets with larger values of corrJVF are more likely to have originated from the hard-scatter. The R_{pT} variable is defined as the scalar sum of the transverse momenta of the tracks assigned to the jet as well as the PV divided by the fully calibrated jet p_{T}. Again, larger values of this variable indicate a higher probability that the jet originated from the hard-scatter. In the searches presented here, signal jets with $p_{\mathrm{T}} < 120\,\mathrm{GeV}$ and $|\eta| < 2.5$ are required to pass the `Medium` JVT working point [106].

9.3.1 *b*-Tagging

Identifying *b*-hadrons inside of jets, a process called *b*-tagging, can act as a powerful discriminant across many analyses at the LHC due to the large cross-sections for top-quark production, coupled with the $\sim 100\%$ branching ratio of $t \to bW$. In these searches, this discrimination power allows for a reduction of the SM background involving top-quarks by vetoing events containing *b*-tagged jets. Inverting this veto also allows for control regions to be constructed and used for estimating the normalization of these backgrounds.

Tagging jets as containing a *b*-hadron is made possible by the relatively long lifetime of *b*-hadrons, which is approximately 1.5 ps. At relativistic speeds, this corresponds to a decay distance of around 450 µm, which is long enough for secondary vertices to be reconstructed due to the excellent resolution of the ID. It is also possible to reconstruct tertiary vertices from the decays of hadrons containing *c*-quarks that can be produced from the *b*-hadron decay. Aside from these vertices, the other hallmark of *b*-hadron decays is the presence of tracks with large impact parameters when evaluated with respect to the PV. Several algorithms are used by ATLAS to exploit these features, with each algorithm focusing on either secondary vertex reconstruction or using the impact parameters and their

uncertainties to tag jets via a likelihood ratio. To further increase the b-tagging performance, the output of these low-level algorithms are passed to a multivariate algorithm called `MV2` [107] that is based on boosted decision trees and trained on a SM $t\bar{t}$ and a high-p_{T} $Z' \to t\bar{t}$ sample. The particular version of the algorithm used in these searches is called `MV2c10`, which uses a mixture of 93% light-flavor jets and 7% c-jets as the background sample for the training.

In these searches, b-tagging is applied to baseline jets with $p_{\mathrm{T}} > 20\,\mathrm{GeV}$ and $|\eta| < 4.5$. A working point for the `MV2c10` algorithm is chosen such that the b-tagging efficiency in a simulated $t\bar{t}$ sample is 85% with rejection factors of 2.7 and 25 for c-jets and light-flavor jets, respectively [107]. As summarized in Table 9.1, signal b-tagged jets are further required to have $|\eta| < 2.5$ and pass the same JVT requirements as signal jets.

9.4 Overlap Removal

After running the identification algorithms for the objects defined above, it is possible that some combination of energy deposits in the ATLAS detector will be reconstructed as two distinct physics objects. For example, a jet can deposit a significant fraction of its energy in the LAr calorimeter due to $\pi^0 \to \gamma\gamma$ decays, which may result in the additional reconstruction of an electron. In order to mitigate such double-counting, a procedure known as "overlap removal" is implemented in order to solve the ambiguities and guarantee object exclusivity. The overlap removal procedure is based on a distance between two reconstructed objects defined as $\Delta R_y = \sqrt{(\Delta y)^2 + (\Delta\phi)^2}$, where y is the rapidity. Rapidity is used for this procedure (in place of pseudorapidity) to better account for the jet mass.

This procedure is performed sequentially, with the surviving object being fed into the next step of the removal. The first takes place between reconstructed

electrons and muons. In order to account for muon bremsstrahlung followed by photon conversion, electrons sharing an ID track with a muon are removed. After this, non-b-tagged jets are removed if they are within $\Delta R_y < 0.2$ of an electron. Electrons are then removed from the event if they are within $\Delta R_y < 0.4$ of a jet. These last two steps are in place to remove electrons that are likely due to semi-leptonic b- or c-hadron decays, while also removing jets that were likely reconstructed from an electron shower. Next, non-b-tagged jets are removed if they are within $\Delta R_y < 0.2$ of a muon and have less than three associated tracks with $p_{\mathrm{T}} > 500\,\mathrm{MeV}$ in order to account for muon bremsstrahlung. Finally, muons within $\Delta R_y < 0.4$ of a surviving jet are removed. Again, this combination of criteria is in place to remove muons that are likely due to semi-leptonic b- or c-hadron decays while rejecting fake jets.

9.5 Missing Transverse Energy

At the LHC, the pp collisions are at sufficiently high enough energies to resolve the internal structure of the protons, so the collisions are best described by interactions among individual partons. Unfortunately, the longitudinal component of the parton momenta cannot be known, which precludes the overall conservation of momentum from being exploited by reconstruction and analysis techniques. What is known, however, is that the initial-state partons do not carry momentum in the transverse plane. Consequently, the transverse momentum of all particles emerging from a single parton-parton interaction should sum to zero to conserve momentum. In cases where particles that do not interact with the detector are produced (e.g. neutrinos and various SUSY states), their transverse momenta is not measured, which leads to an overall imbalance in the transverse momentum in the event. This imbalance can therefore be used to infer the production of such

particles.

This missing transverse momentum vector, $\mathbf{p}_{\mathrm{T}}^{\mathrm{miss}}$, is calculated as the negative vectorial sum of the transverse momenta of all reconstructed objects that pass an overlap removal procedure similar to the one described in Section 9.4, including a "soft" term that accounts for tracks from the PV that are not associated to any object. More explicitly,

$$-\mathbf{p}_{\mathrm{T}}^{\mathrm{miss}} = \sum_{e} \mathbf{p}_{\mathrm{T}} + \sum_{\mu} \mathbf{p}_{\mathrm{T}} + \sum_{\tau} \mathbf{p}_{\mathrm{T}} + \sum_{\gamma} \mathbf{p}_{\mathrm{T}} + \sum_{\mathrm{jet}} \mathbf{p}_{\mathrm{T}} + \sum_{\mathrm{soft}} \mathbf{p}_{\mathrm{T}}, \tag{9.2}$$

where each term represents the contribution from electrons, muons, taus, photons, jets, and unassociated tracks, respectively. The missing transverse momentum, $E_{\mathrm{T}}^{\mathrm{miss}}$, is a scalar that is defined to be the magnitude of the missing transverse momentum vector. All baseline objects described in the above sections are used in the calculation of $\mathbf{p}_{\mathrm{T}}^{\mathrm{miss}}$, though jets with $20\,\mathrm{GeV} < p_{\mathrm{T}} < 30\,\mathrm{GeV}$ and $|\eta| > 2.4$ are omitted to reduce pileup dependency. Since $E_{\mathrm{T}}^{\mathrm{miss}}$ is an event-level variable, its resolution is highly-dependent on the object content of the event. Fake sources of $E_{\mathrm{T}}^{\mathrm{miss}}$ include mis-measurements of jets, contributions from pileup jets, and particles traversing regions of the detector that are not sufficiently instrumented.

Chapter 10

Event Selection

This chapter is dedicated to motivating the set of event-level criteria that are used to define the SRs. For both the electroweakino and slepton searches, dedicated high-$E_{\mathrm{T}}^{\mathrm{miss}}$ and low-$E_{\mathrm{T}}^{\mathrm{miss}}$ SRs are constructed in order to maximize sensitivity to a wide range of SUSY mass-splittings. Most of the sensitivity in each search stems from the high-$E_{\mathrm{T}}^{\mathrm{miss}}$ SRs, while the low-$E_{\mathrm{T}}^{\mathrm{miss}}$ versions provide complementary sensitivity for moderate and large mass-splittings since less boost is required from the ISR activity to put the leptons over the reconstruction thresholds.

First, a series of variables that are used as discriminants between the background and signal processes are described in Section 10.1. Next, a set of criteria called the "preselection" is applied to all SRs in order to target common topologies and is described in Section 10.2. The remaining requirements on the electroweakino and slepton SRs are motivated in Section 10.3 and Section 10.4, respectively. Finally, the strategy of forming inclusive SRs to be used for model-independent searches for new physics is provided in Section 10.5.

The optimization procedures make use of the significance metric Z_n [108],

defined as

$$Z_n = \left[2\left((s+b)\ln\left[\frac{(s+b)\,(b+\sigma_b^2)}{b^2+(s+b)\sigma_b^2}\right] - \frac{b^2}{\sigma_b^2}\ln\left[1+\frac{\sigma_b^2 s}{b\,(b+\sigma_b^2)}\right]\right)\right]^{1/2}, \qquad (10.1)$$

where s and b are the expected signal and background event yields, respectively, and σ_b is the expected uncertainty on the background yield. This metric provides an estimate of the discovery significance and performs similarly to the profile likelihood ratio method described in Section 13.3. When optimizing a cut on a variable, the $N-1$ method is used. In this method, all cuts are applied except on the variable in question. Then, the Z_n metric is calculated as a function of different cuts on this variable and the cut that produces the largest value of Z_n is considered optimal. Since this analysis ultimately exploits the shape of the discriminating variables $m_{\ell\ell}$ and m_{T2}^{100}, the $N-1$ procedure is performed separately for each bin of these variables to arrive at cuts that provide good discrimination across the entire SR.

10.1 Discriminating Variables

Analysis variables are built using the physics objects defined in Chapter 9, and selections are placed on them in order to define the signal, control, and validation regions. In this section, the variables that are used to build these regions and discriminate between signal and background are defined. In the following, ℓ_1 refers to the lepton with the highest p_{T} (leading lepton) and ℓ_2 refers to the lepton lepton with the lower p_{T} (subleading lepton). Similarly j_1 denotes the jet in the event with the highest p_{T}, which is also referred to as the leading jet.

$\boldsymbol{\Delta R_{\ell\ell}}$ The angular distance between the leptons ℓ_1 and ℓ_2 defined by $\Delta R_{\ell\ell} = \sqrt{(\eta_{\ell_1} - \eta_{\ell_2})^2 + (\phi_{\ell_1} - \phi_{\ell_2})^2}$. Leptons from electroweakino production tend to be collimated, especially for low mass-splittings, since they originate from off-shell Z boson decays. Comparatively, the leptons from the pair-production of sleptons tend to be further apart since they originate from different decay legs. A lower bound on $\Delta R_{\ell\ell}$ is useful for rejecting photon conversions.

$\boldsymbol{\Delta\phi(j_1, p_{\mathrm{T}}^{\mathrm{miss}})}$ The angular separation in ϕ between the highest-p_{T} jet in the event and the missing transverse momentum vector. A lower bound on this variable ensures the boosted topology, as expected in signal events, in which the invisible particles recoil from additional hadronic activity.

$\boldsymbol{\min(\Delta\phi(\text{any jet}, p_{\mathrm{T}}^{\mathrm{miss}}))}$ The minimum angle in ϕ between any jet and the missing transverse momentum vector. This variable is sensitive to mis-measurements of the jet energies, which often result in $\mathbf{p}_{\mathrm{T}}^{\mathrm{miss}}$ being aligned with one of the jets. Placing a lower bound on this variable helps to reduce contributions from QCD multi-jet and Z + jets events.

$\boldsymbol{m_{\mathrm{T}}^{\ell_1}}$ This is the transverse mass associated with the highest-p_{T} lepton in the event, which is defined using the missing transverse momentum to be

$$m_{\mathrm{T}}^{\ell_1} = \sqrt{2\left(E_{\mathrm{T}}^{\ell_1} E_{\mathrm{T}}^{\mathrm{miss}} - \mathbf{p}_{\mathrm{T}}^{\ell_1} \cdot \mathbf{p}_{\mathrm{T}}^{\mathrm{miss}}\right)} \tag{10.2}$$

The transverse mass is a variable with a kinematic endpoint corresponding to the mass of a parent particle if it decays to one visible and one invisible particle in the detector (and no other invisible particles are produced in the event). It is therefore useful for rejecting $W(\to \ell\nu)$ + jets events (which can enter the SRs when the jet is misidentified as a lepton) as it attempts to reconstruct the W

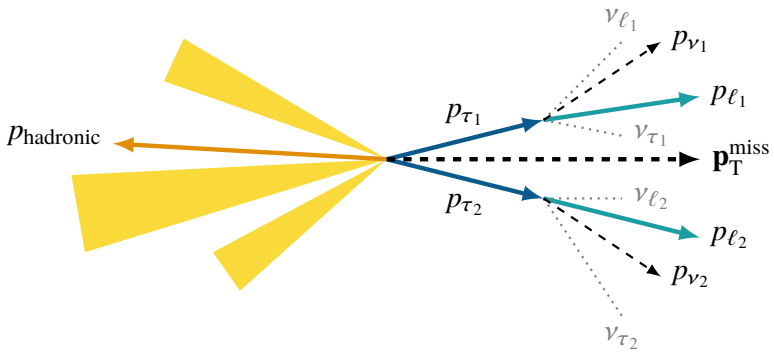

Figure 10.1: A schematic of the boosted $Z \to \tau\tau$ topology targeted by the $m_{\tau\tau}$ variable. The tau leptons decays are both fully leptonic and the boost provided by the hadronic activity approximately aligns the neutrino momentum with the visible lepton momentum.

mass in such events.

$\boldsymbol{E_{\text{T}}^{\text{miss}}/H_{\text{T}}^{\text{lep}}}$ In this ratio, $H_{\text{T}}^{\text{lep}}$ is defined to be the scalar sum of the lepton p_{T}. This variable is useful for distinguishing between signal and background, as events from $t\bar{t}$ and $WW \to \ell\nu\ell\nu$, for example, tend to have harder leptons than signal for a given value of $E_{\text{T}}^{\text{miss}}$.

$\boldsymbol{m_{\tau\tau}}$ In order to reject events coming from fully leptonic $Z \to \tau\tau$ decays, a variable called $m_{\tau\tau}$ [109, 110, 111] is constructed. In these fully leptonic decays, the tau leptons decay according to $\tau \to \nu_\tau \ell \nu_\ell$. The $m_{\tau\tau}$ variable attempts to reconstruct the invariant mass of the tau lepton pair in events where this system is boosted so that the tau leptons are not produced back-to-back in the detector. In sufficiently boosted cases, the neutrinos from the tau decays are approximately collinear with the visible leptons. A schematic of this boosted topology is shown in Figure 10.1.

The four-momentum of the neutrino system in a given decay leg is $p_{\nu_i} = p_{\nu_{\tau_i}} + p_{\nu_{\ell_i}}$, where the subscript i refers to the specific decay leg. In the collinear regime, this can be approximated as a rescaling of the visible lepton momentum such that

$p_{\nu_i} \simeq \xi_i p_{\ell_i}$, where ξ_i is the rescaling factor. Since the tau four-momentum, p_{τ_i}, is the sum of the visible lepton's four-momentum and the neutrino system's four-momentum, it can be written as $p_{\tau_i} = (1+\xi_i)p_{\ell_i}$. In this case, the di-tau invariant mass is given by

$$m_{\tau\tau}^2 = (p_{\tau_1} + p_{\tau_2})^2 \simeq 2p_{\ell_1} \cdot p_{\ell_2}(1+\xi_1)(1+\xi_2), \tag{10.3}$$

where the masses of the tau leptons have been neglected in the second step since the boosted topology ensures that the tau leptons are ultra-relativistic in the laboratory frame. All that is needed now is to solve for the scaling factors ξ_1 and ξ_2, which are constrained by the missing transverse momentum according to

$$\mathbf{p}_{\mathrm{T}}^{\mathrm{miss}} = \xi_1 \mathbf{p}_{\mathrm{T}}^{\ell_1} + \xi_2 \mathbf{p}_{\mathrm{T}}^{\ell_2}. \tag{10.4}$$

This is just a system of two equations with two unknown variables, which can easily be solved. Notably, as defined in Equation 10.3, $m_{\tau\tau}^2$ can obtain negative values if exactly one of the decay legs has $\xi_i < -1$ and $E_{\mathrm{T}}^{\mathrm{miss}} > |\mathbf{p}_{\mathrm{T}}^{\ell_i}|$. It is also asymmetric about $m_{\tau\tau} = 0$. Negative $m_{\tau\tau}$ situation corresponds to events in which one of the leptons is in the opposite hemisphere of the detector as the the missing transverse momentum and has a p_{T} that is smaller in magnitude. This is a rare occurrence for boosted $Z \to \tau\tau$ events but is more likely for less-boosted processes like WW and $t\bar{t}$ where the leptons are produced back-to-back. To account for the asymmetric nature of $m_{\tau\tau}^2$, the $m_{\tau\tau}$ discriminating variable is finally defined to be

$$m_{\tau\tau} = \begin{cases} \sqrt{m_{\tau\tau}^2}, & \text{for } m_{\tau\tau}^2 \geq 0 \\ -\sqrt{|m_{\tau\tau}^2|}, & \text{for } m_{\tau\tau}^2 < 0 \end{cases}. \tag{10.5}$$

With this definition, the region defined by $0\,\mathrm{GeV} < m_{\tau\tau} < 160\,\mathrm{GeV}$ is expected

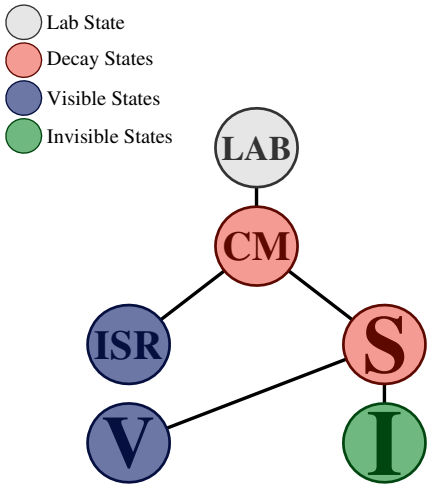

Figure 10.2: The RJR decay tree imposed on the events [113]. This tree targets topologies consistent with ISR activity boosting a SUSY system that decays to visible and invisible particles.

to be dominated by fully leptonic $Z \to \tau\tau$ events, with a peak at the Z mass.

R_{ISR}* and *M_T^S Both of these variables are derived from the recursive jigsaw reconstruction technique [112], which attempts to resolve issues associated with events containing indistinguishable or invisible particles by imposing a set of decay trees and reference frames consistent with the targeted event topology. In these searches, the jets associated with the hadronic ISR activity are assigned to a frame called "ISR," while the remaining visible and invisible particles in the events that originate from the sparticle decays are assigned to the "S" frame. The S frame itself can be further divided in the decay tree according an invisible frame "I" that contains the missing transverse momentum associated to the final-state $\tilde{\chi}_1^0$ particles, and a visible frame "V" which consists of the visible final-state particles from the sparticle decays. Together, the ISR and S frames form the center-of-mass frame "CM," which moves with respect to the lab frame "Lab." A schematic of this decay tree is shown in Figure 10.2.

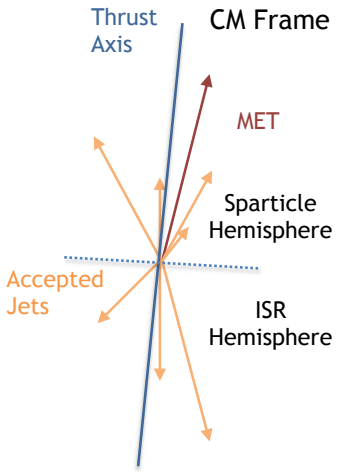

Figure 10.3: A schematic of an event that is divided into the plane transverse to the thrust axis as determined by the applied jigsaw rule in the RJR procedure. All objects in the event are placed into either the sparticle or ISR hemisphere.

The ISR, V, and I frames consist of the four-vectors of the objects that are assigned to them. In the case of the I frame, which consists of the missing transverse momentum vector, both the z component of the four-vector and mass of the invisible particles are unknown. Following the procedure laid out in [113], the longitudinal component of the momentum and the mass are both set to zero. For the V and ISR frames, there is an assignment ambiguity. While the leptons are obviously assigned to the V frame, a choice must be made when assigning other final-state particles to either V or ISR. This is accomplished via a "jigsaw" rule, which in this case, is designed to maximize the back-to-back p_{T} of the ISR and S frames. This essentially defines the thrust axis that divides the event into two hemispheres in the CM frame, as shown schematically in Figure 10.3. One hemisphere is expected to contain the ISR system and the other is expected to contain the sparticle system.

From here, the RJR variables are constructed. R_{ISR} is designed to be an estimator of the quantity $E_{\mathrm{T}}^{\mathrm{miss}}/p_{\mathrm{T}}^{\mathrm{ISR}}$, where $p_{\mathrm{T}}^{\mathrm{ISR}}$ is the transverse momentum of

the ISR system. The explicit definition takes the form

$$R_{\mathrm{ISR}} \equiv \frac{\left|\vec{p}_{\mathbf{I},T}^{\,\mathbf{CM}} \cdot \hat{p}_{\mathbf{ISR},T}^{\,\mathbf{CM}}\right|}{\left|\vec{p}_{\mathbf{ISR},T}^{\,\mathbf{CM}}\right|}. \tag{10.6}$$

Signal events, therefore, exhibit a peak at $R_{\mathrm{ISR}} \approx 1$. An additional feature is that R_{ISR} scales approximately with $\frac{m(\widetilde{\chi}_1^0)}{m(\tilde{s})}$, where $\tilde{s}$ is a placeholder for a generic parent sparticle that decays to $\widetilde{\chi}_1^0$. Therefore, R_{ISR} is sensitive to the mass-splitting, which is exploited in the SR definitions. Finally, the $M_{\mathrm{T}}^{\mathrm{S}}$ variable is defined to be transverse mass of the S system, which tends to peak at lower values compared to the backgrounds.

$\boldsymbol{m_{\ell\ell}}$ The invariant mass of the dilepton system. This variable is kinematically bound by $m(\widetilde{\chi}_2^0) - m(\widetilde{\chi}_1^0)$ in simplified electroweakino models considered and its shape is used as the final discriminant in those searches. An upper bound on $m_{\ell\ell}$ is also useful for rejecting backgrounds involving on-shell $Z \to \ell\ell$ decays, such as those from $Z + \text{jets}$ and $ZZ \to \ell\ell\nu\nu$.

$\boldsymbol{m_{\mathbf{T2}}^{m_{\tilde{\chi}}}}$ The "stransverse mass" [114, 115], which is the generalization of the transverse mass for events in which a particle is pair-produced and each of these particles subsequently decays into one visible and one invisible particle. Such is the case for the slepton signatures considered in this dissertation, where each slepton decays according to $\widetilde{\ell} \to \ell\widetilde{\chi}_1^0$. The complication in these events arises from the ambiguity induced by the presence of two invisible particles in the final state. The transverse momenta of these particles cannot be inferred separately, since they both contribute to $\mathbf{p}_{\mathrm{T}}^{\mathrm{miss}}$. If it were possible to reconstruct each invisible particle's transverse momenta, then one could simply derive a bound on slepton

mass according to

$$m_{\tilde{\ell}} \geq \max\left\{m_{\mathrm{T}}\left(\mathbf{p}_{\mathrm{T}}^{\ell_1}, \mathbf{p}_{\mathrm{T}}^{\tilde{\chi}_1}\right), m_{\mathrm{T}}\left(\mathbf{p}_{\mathrm{T}}^{\ell_2}, \mathbf{p}_{\mathrm{T}}^{\tilde{\chi}_2}\right)\right\} \tag{10.7}$$

Since this is not possible, the stransverse mass attempts to recover the useful features of the transverse mass by considering all possible partitions of $\mathbf{p}_{\mathrm{T}}^{\mathrm{miss}}$ among the two invisible particles and performing a minimization over these partitions. Defining $\mathbf{q}_{\mathrm{T}}$ to be sum of the invisible transverse momenta vectors $\mathbf{p}_{\mathrm{T}}^{\tilde{\chi}_1}$ and $\mathbf{p}_{\mathrm{T}}^{\tilde{\chi}_2}$, the stransverse mass is expressed as

$$m_{\mathrm{T2}}^{m_{\tilde{\chi}}}\left(\mathbf{p}_{\mathrm{T}}^{\ell_1}, \mathbf{p}_{\mathrm{T}}^{\ell_2}, \mathbf{p}_{\mathrm{T}}^{\mathrm{miss}}\right) = \min_{\mathbf{q}_{\mathrm{T}}}\left(\max\left[m_{\mathrm{T}}\left(\mathbf{p}_{\mathrm{T}}^{\ell_1}, \mathbf{q}_{\mathrm{T}}, m_{\tilde{\chi}}\right), m_{\mathrm{T}}\left(\mathbf{p}_{\mathrm{T}}^{\ell_2}, \mathbf{p}_{\mathrm{T}}^{\mathrm{miss}} - \mathbf{q}_{\mathrm{T}}, m_{\tilde{\chi}}\right)\right]\right), \tag{10.8}$$

which retains the feature that $m_{\mathrm{T2}}^{m_{\tilde{\chi}}} \leq m_{\tilde{\ell}}$ when the mass of the invisible particles, $m_{\tilde{\chi}}$, is correctly chosen. In the searches presented here, it is assumed in the calculation of $m_{\mathrm{T2}}^{m_{\tilde{\chi}}}$ that $m_{\tilde{\chi}} = 100\,\mathrm{GeV}$, which is denoted by the variable m_{T2}^{100}. This distribution exhibits a kinematic endpoint that corresponds to the mass-splitting between the slepton and the lightest neutralino. This feature provides an excellent handle on signal and background discrimination, and is therefore used as the final discriminant in slepton search. Importantly, in the slepton mass ranges and mass-splittings considered by this search, it is found that the m_{T2}^{100} distribution does not change significantly for the generated signals with $m_{\tilde{\chi}} \neq 100\,\mathrm{GeV}$.

10.2 Preselection

All events entering the SRs are required to pass a common set of cuts called the preselection. The purpose of the preselection is to provide a starting point for dedicated SR optimization studies by first establishing a loose selection that tar-

Table 10.1: Preselection requirements applied to all events entering into electroweakino and slepton SRs.

Variable	Preselection Requirements
Number of leptons	$= 2$ leptons
Lepton p_{T} [GeV]	$p_{\mathrm{T}}^{\ell_1} > 5$
$\Delta R_{\ell\ell}$	$\Delta R_{ee} > 0.30$, $\Delta R_{\mu\mu} > 0.05$, $\Delta R_{e\mu} > 0.2$
Lepton charge and flavor	$e^{\pm}e^{\mp}$ or $\mu^{\pm}\mu^{\mp}$
Lepton invariant mass [GeV]	$3 < m_{ee} < 60$, $1 < m_{\mu\mu} < 60$
J/ψ invariant mass [GeV]	veto $3 < m_{\ell\ell} < 3.2$
$m_{\tau\tau}$ [GeV]	< 0 or > 160
$E_{\mathrm{T}}^{\mathrm{miss}}$ [GeV]	> 120
Number of jets	≥ 1
Number of b-tagged jets	$= 0$
Leading jet p_{T} [GeV]	≥ 100
$\min(\Delta\phi(\text{any jet}, \mathbf{p}_{\mathrm{T}}^{\mathrm{miss}}))$	> 0.4
$\Delta\phi(j_1, \mathbf{p}_{\mathrm{T}}^{\mathrm{miss}})$	≥ 2.0

gets signal-like topologies and suppresses common backgrounds. Control regions can also be built by inverting one or more of these preselection requirements so that they remain orthogonal to the SRs but close in kinematic phase space. A summary of the preselection is presented in Table 10.1 and the variables therein are defined below.

Exactly two signal leptons of the same flavor (ee or $\mu\mu$) and opposite electric charge are required since the sleptons are assumed to be pair-produced and the electroweakino searches target leptons from $Z^* \to \ell\ell$ decays. In this dissertation, the lepton with the largest p_{T} in the event is referred to as the "leading" lepton (ℓ_1) and the softer lepton in the event is denoted as the "subleading" lepton (ℓ_2). This convention is carried over to the jets as well, such that the leading jet in the event is the jet with highest p_{T} and is indicated by j_1. In order to reduce the fake/non-prompt lepton background in the SRs, the leading lepton in the event

is required to have $p_{\mathrm{T}}^{\ell_1} > 5\,\mathrm{GeV}$.

To promote the boosted topology in which the SUSY particles recoil against hadronic ISR activity, the leading jet in the event must have $p_{\mathrm{T}} > 100\,\mathrm{GeV}$ and the missing transverse energy must satisfy $E_{\mathrm{T}}^{\mathrm{miss}} > 120\,\mathrm{GeV}$. It is possible, though, to reconstruct significant $E_{\mathrm{T}}^{\mathrm{miss}}$ in events where there is also a significant mis-measurement of the jet energy. In such events, the missing transverse momentum vector, $\mathbf{p}_{\mathrm{T}}^{\mathrm{miss}}$, tends to be aligned with one the jets. To suppress these events, the minimum angular separation in ϕ between any of the jets and $\mathbf{p}_{\mathrm{T}}^{\mathrm{miss}}$ is required to be greater than 0.4 radians. The leading jet and $\mathbf{p}_{\mathrm{T}}^{\mathrm{miss}}$ are also required to have an angular separation in ϕ of at least 2.0 radians in order to further enforce the boosted topology. Due to the large $t \to Wb$ branching ratio, events are rejected if they contain any b-tagged jets in order to suppress the backgrounds containing top-quarks.

Various selections are applied based on the invariant mass of objects decaying to leptons in order to suppress these resonant backgrounds. The invariant mass of the di-lepton system, $m_{\ell\ell}$, is required to be less than 60 GeV in order to veto on-shell $Z \to ee/\mu\mu$ decays. On the other end of the spectrum, requiring $m_{\ell\ell} > 1\,\mathrm{GeV}$ reduces the contribution from collinear leptons due to energetic photon conversions. The requirement that $\Delta R_{\ell\ell} > 0.05$ also helps to reject events with photon conversions. In order to veto events with lepton pairs originating from J/ψ decays, the invariant di-lepton invariant mass must not satisfy $3.0\,\mathrm{GeV} < m_{\ell\ell} < 3.2\,\mathrm{GeV}$. No equivalent vetoes exist for other low-mass resonances such as the Υ states since their contributions to the SRs are expected to be negligible. As good background modeling could not be achieved in ee events with $m_{\ell\ell} < 3\,\mathrm{GeV}$, these events are excluded from the SRs. Finally, events entering the SRs are required have $m_{\tau\tau} < 0\,\mathrm{GeV}$ or $m_{\tau\tau} > 160\,\mathrm{GeV}$ in order to suppress fully leptonic $Z \to \tau\tau$

events.

The remaining cuts at preselection-level are on the angular distances between the leptons in order to ensure good modeling of the fake/non-prompt lepton background. As noted in Section 11.2.1, the data-driven estimate of the fake/non-prompt lepton background becomes difficult in highly collimated di-lepton events due to correlations between their isolation cones and shower shapes (in the case of electrons). Events containing two electrons are therefore required to have $\Delta R_{ee} > 0.30$ in order to avoid overlapping electron showers, while events containing an electron and a muon must satisfy $\Delta R_{e\mu} > 0.2$ to avoid the muon overlapping with the electron showers. Note that these $e\mu$ events do not enter any of the SRs but are instead only used in CRs and VRs, as described in Section 11.1.

10.3 Electroweakino Signal Regions

In total, four orthogonal SRs are constructed for the electroweakino search in order to establish sensitivity to a wide range possible mass-splittings. In each case, the final discriminant is $m_{\ell\ell}$, which is divided into exclusive bins in order to exploit the kinematic endpoint that is expected in signal events. The final event selections that result from the optimizations described below are given in Table 10.2, where the preselection cuts from Table 10.1 are implied.

A region called SR–E–high provides the majority of the overall electroweakino sensitivity and is kept orthogonal from other SRs called SR–E–low and SR–E–med by requiring $E_{\mathrm{T}}^{\mathrm{miss}} > 200\,\mathrm{GeV}$. Both SR–E–low and SR–E–med, meanwhile, require $120\,\mathrm{GeV} < E_{\mathrm{T}}^{\mathrm{miss}} < 200\,\mathrm{GeV}$. SR–E–low is constructed to be sensitive to electroweakinos with $\Delta m \gtrsim 10\,\mathrm{GeV}$, while SR–E–med is sensitive to low mass-splitting. As indicated in Table 10.1, SR–E–low and SR–E–med are constructed to be orthogonal based on $E_{\mathrm{T}}^{\mathrm{miss}}/H_{\mathrm{T}}^{\mathrm{lep}}$. Finally, a region called SR–E–1ℓ1T, briefly

Table 10.2: Requirements applied to events entering into the four signal regions used for electroweakino searches. The $1\ell 1T$ preselection requirements from Table 10.1 are implied for SR–E–$1\ell 1T$, while the 2ℓ ones are implied for the other SRs.

	Electroweakino SR Requirements			
Variable	SR–E–low	SR–E–med	SR–E–high	SR–E–$1\ell 1T$
$E_{\mathrm{T}}^{\mathrm{miss}}$ [GeV]	$[120, 200]$	$[120, 200]$	> 200	> 200
$E_{\mathrm{T}}^{\mathrm{miss}}/H_{\mathrm{T}}^{\mathrm{lep}}$	< 10	> 10	–	> 30
$\Delta\phi(\mathrm{lep}, \mathbf{p}_{\mathrm{T}}^{\mathrm{miss}})$	–	–	–	< 1.0
Lepton or track p_{T} [GeV]	$p_{\mathrm{T}}^{\ell_2} > 5 + m_{\ell\ell}/4$	–	$p_{\mathrm{T}}^{\ell_2} > \min(10, 2 + m_{\ell\ell}/3)$	$p_{\mathrm{T}}^{\mathrm{track}} < 5$
$M_{\mathrm{T}}^{\mathrm{S}}$ [GeV]	–	< 50	–	–
$m_{\mathrm{T}}^{\ell_1}$ [GeV]	$[10, 60]$	–	< 60	–
R_{ISR}	$[0.8, 1.0]$	–	$[\max(0.85, 0.98 - 0.02 \times m_{\ell\ell}),\ 1.0]$	–

described below, also requires $E_{\mathrm{T}}^{\mathrm{miss}} > 200\,\mathrm{GeV}$ but is kept orthogonal from SR–E–high by selecting events containing one signal lepton and one isolated track that is not associated to a signal lepton. This SR targets events from signals with very small mass splittings where one of the leptons is too soft to be reconstructed.

SR–E–high In order to be on the plateau of the inclusive $E_{\mathrm{T}}^{\mathrm{miss}}$-trigger efficiency curve, where the efficiency is $> 95\%$, SR–E–high requires $E_{\mathrm{T}}^{\mathrm{miss}} > 200\,\mathrm{GeV}$. The $m_{\ell\ell}$ binning corresponding to the exclusive SR–E–high regions is chosen to be

$m_{\ell\ell}$ [GeV]: [1,2], [2,3], [3.2,5], [5,10], [10,20], [20,30], [30,40], [40,60],

which provides good discrimination for a large range of mass-splittings.

An important feature of the signal processes is that R_{ISR} and the transverse momenta of the leptons are correlated with the mass-splitting. In order to exploit these features, sliding cuts are placed on R_{ISR} and $p_{\mathrm{T}}^{\ell_2}$ that scale with $m_{\ell\ell}$. The latter cut is particularly powerful in discriminating signal from the fake/non-prompt lepton background. The scaling retains good lepton efficiency for signals with low Δm, while rejecting fake/non-prompt leptons in the larger $m_{\ell\ell}$ bins. The $m_{\ell\ell}$-dependence of both R_{ISR} and $p_{\mathrm{T}}^{\ell_2}$ is roughly linear, which is reflected by the linear optimized cuts.

In each case, $N-1$ scans are performed separately in the exclusive $m_{\ell\ell}$ bins using the Z_n metric, and the evolution of the optimal cuts with $m_{\ell\ell}$ is used to derive final cut values. Examples of the $N-1$ scans for $p_{\mathrm{T}}^{\ell_2}$ are shown in Figure 10.4, where the optimal cuts are seen to increase when moving to a higher $m_{\ell\ell}$ bin. The optimized cut that provides good discrimination for a variety of signal mass-splittings is given by $p_{\mathrm{T}}^{\ell_2} > \min(10\,\mathrm{GeV}, 2\,\mathrm{GeV} + m_{\ell\ell}/3)$. The correlations between R_{ISR} and $m_{\ell\ell}$ for both the background and higgsino signals of different mass-splittings are shown in Figure 10.5, where the red line indicates the analogous optimized sliding cut on R_{ISR}: $R_{\mathrm{ISR}} > [\max(0.85, 0.8 - 0.02 \times m_{\ell\ell}, 1.0)]$.

Finally, the $m_{\mathrm{T}}^{\ell_1}$ variable is found to provide good separation between signal and background events containing W bosons, which peak near the W mass, while signal events reside at lower values. Since the fake/non-prompt lepton background originates mostly from $W+$jets events in which a jet is reconstructed as a lepton, this variable also provides good rejection power against these events. During the optimization, the $N-1$ procedure for $m_{\mathrm{T}}^{\ell_1}$ is performed in separate $m_{\ell\ell}$ bins, but no strong dependence is found on the optimal cut. Instead, a simple cut of $m_{\mathrm{T}}^{\ell_1} < 60\,\mathrm{GeV}$ is found to perform well for a wide variety of higgsino signals, as shown in the $m_{\ell\ell}$-inclusive distribution in Figure 10.6.

Figure 10.7 shows the final blinded SRs ee and $\mu\mu$ events using the exclusive $m_{\ell\ell}$ binning defined above, prior to any normalization of the major backgrounds. Despite the cut on $p_{\mathrm{T}}^{\ell_2}$ designed to reject fake/non-prompt leptons, these processes still represent the largest expected background in these SRs.

SR–E–low/SR–E–med The $E_{\mathrm{T}}^{\mathrm{miss}}/H_{\mathrm{T}}^{\mathrm{lep}}$ variable has been shown to be a good discriminant in compressed SUSY topologies and was used in a previous ATLAS search for these signal scenarios [116]. Its distribution is sensitive to the electroweakino mass splitting, where larger mass splittings correspond to harder

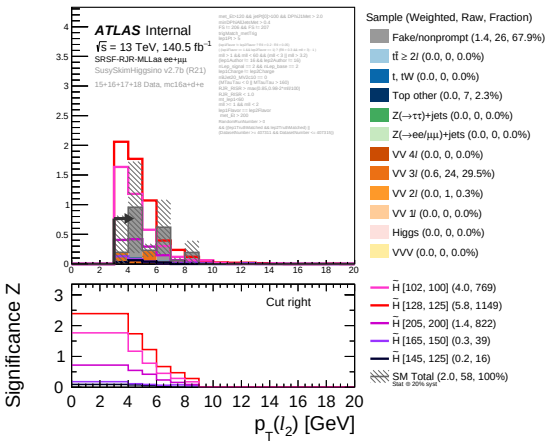

(a) $1 \leq m_{ll} < 2$ GeV.

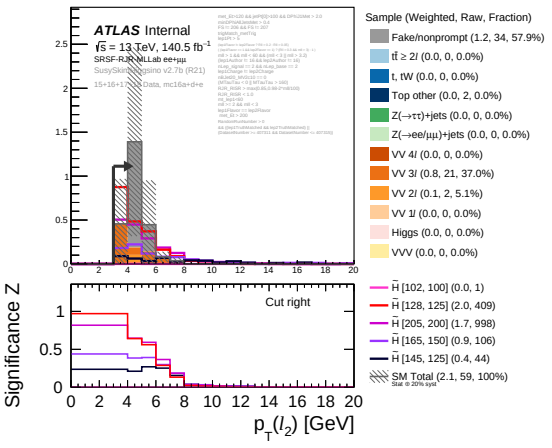

(b) $2 \leq m_{ll} < 3$ GeV.

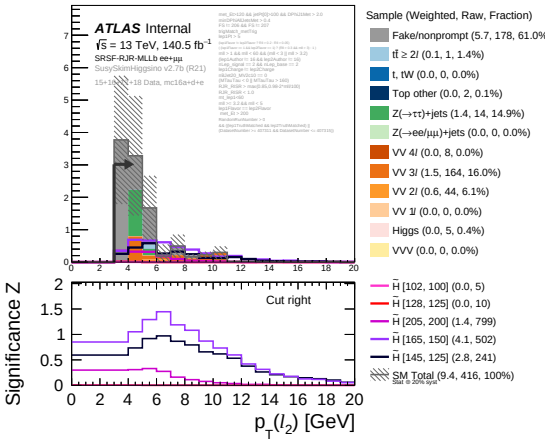

(c) $3.2 \leq m_{ll} < 5$ GeV.

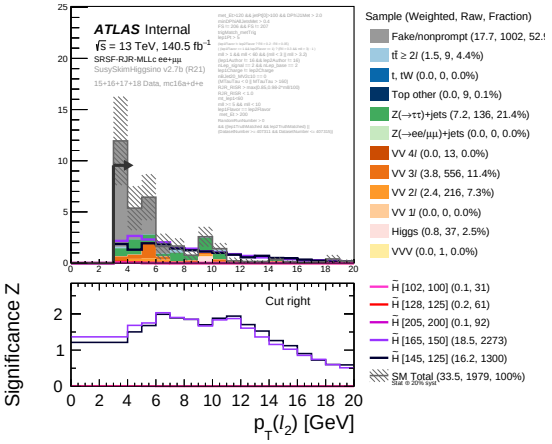

(d) $5 \leq m_{ll} < 10$ GeV.

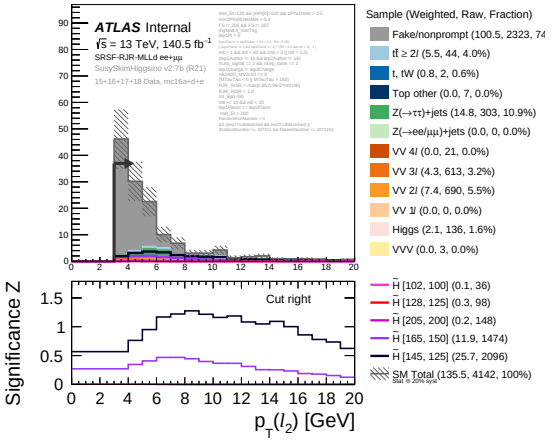

(e) $10 \leq m_{ll} < 15$ GeV.

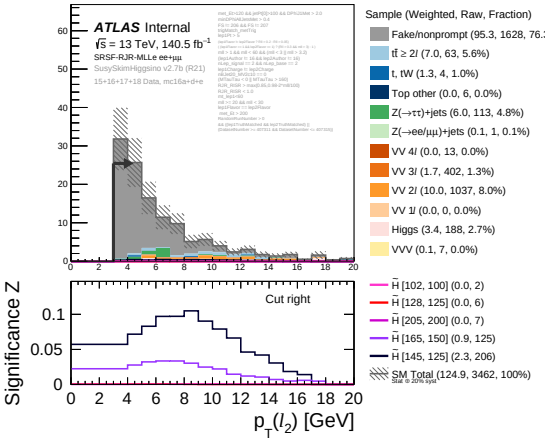

(f) $15 \leq m_{ll} < 20$ GeV.

Figure 10.4: Example $N-1$ plots for $p_{\mathrm{T}}^{\ell_2}$ in SR–E–high. The bottom panel shows the Z_n values for different higgsino signals and different cuts. In this case, the black arrow indicates the lower bound on $p_{\mathrm{T}}^{\ell_2}$.

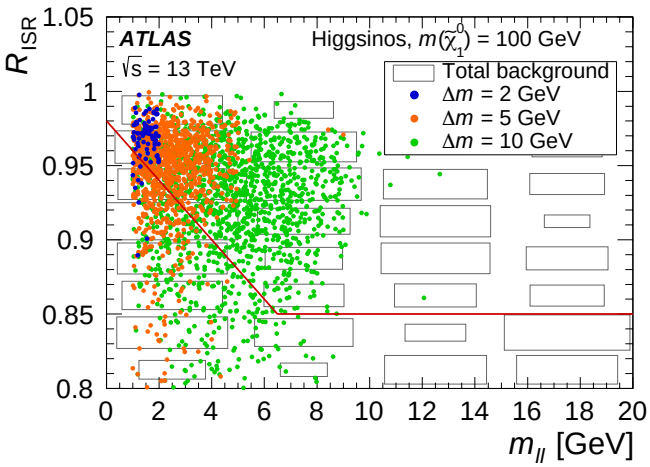

Figure 10.5: Distribution of R_{ISR} for the SR–E–high region, after applying all signal selection criteria except that on R_{ISR}. The solid red line indicates the requirement applied in the signal region such that events in the region below the red line are rejected. Representative benchmark signals for the higgsino simplified model are shown as circles. The gray rectangular boxes show the distribution of the total background expectations.

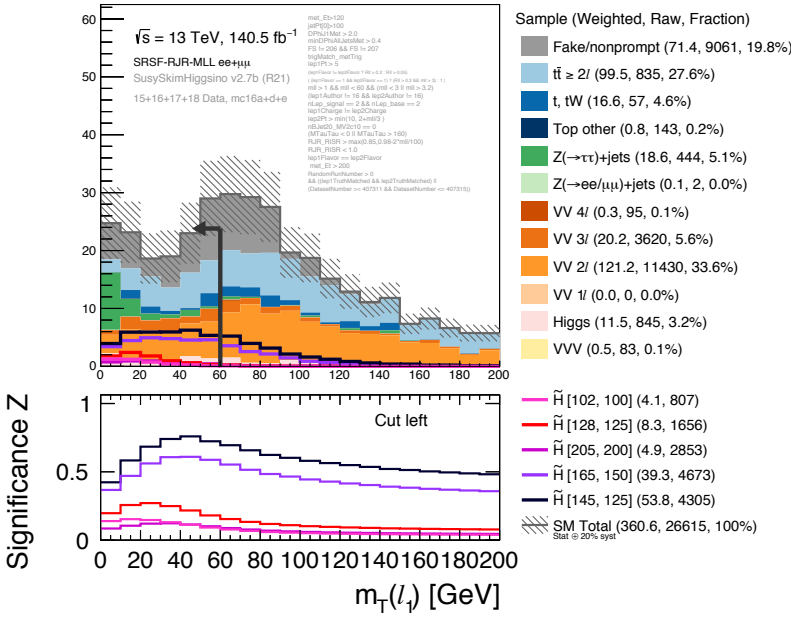

Figure 10.6: $N-1$ plot for the $m_{\mathrm{T}}^{\ell_1}$ variable in the $m_{\ell\ell}$-inclusive SR–E–high. The bottom panel shows the Z_n values for different higgsino signals and different cuts. The black arrow indicates the final cut used in the definition of the SR.

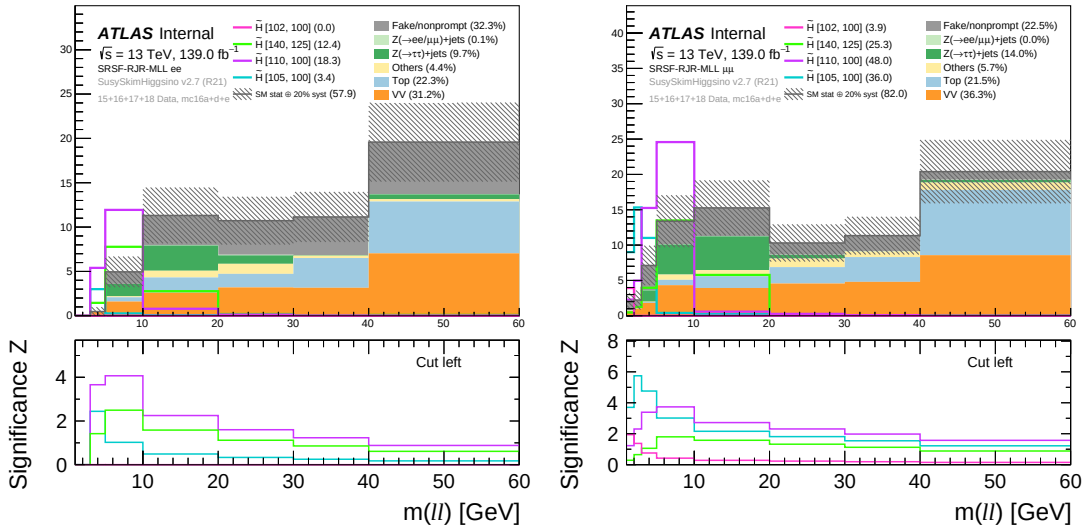

Figure 10.7: The blinded $m_{\ell\ell}$ distributions in SR–E–high for the ee channel (left) and the $\mu\mu$ channel (right) before normalizing the backgrounds with the CRs. The uncertainty bands account for both statistical uncertainties on the backgrounds and a flat 20% systematic uncertainty.

leptons and thus smaller values of $E_{\mathrm{T}}^{\mathrm{miss}}/H_{\mathrm{T}}^{\mathrm{lep}}$. In order to exploit this, the low-$E_{\mathrm{T}}^{\mathrm{miss}}$ SRs are kept orthogonal by a cut on this variable, with SR–E–low requiring $E_{\mathrm{T}}^{\mathrm{miss}}/H_{\mathrm{T}}^{\mathrm{lep}} < 10$ and SR–E–med requiring $E_{\mathrm{T}}^{\mathrm{miss}}/H_{\mathrm{T}}^{\mathrm{lep}} > 10$. In this way, SR–E–low has sensitivity to signals with larger mass-splitting, while SR–E–med targets lower mass splittings. Figure 10.9 shows both the $E_{\mathrm{T}}^{\mathrm{miss}}$ and $E_{\mathrm{T}}^{\mathrm{miss}}/H_{\mathrm{T}}^{\mathrm{lep}}$ distributions for higgsino signals with a variety of mass-splittings after applying the preselection (except the $E_{\mathrm{T}}^{\mathrm{miss}} > 200\,\mathrm{GeV}$ requirement). The $m_{\ell\ell}$ binning within SR–E–low and SR–E–med is the same as that used for SR–E–high. The only difference is that the bins with $m_{\ell\ell} > 30\,\mathrm{GeV}$ are excluded from SR–E–med, since these bins are not expected to be populated by the low-Δm signals that this SR is sensitive to.

The combination of the $E_{\mathrm{T}}^{\mathrm{miss}} < 200\,\mathrm{GeV}$ and $E_{\mathrm{T}}^{\mathrm{miss}}/H_{\mathrm{T}}^{\mathrm{lep}} > 10$ cuts that partly define SR–E–med restricts the value of $H_{\mathrm{T}}^{\mathrm{lep}}$to a narrow range of $12\,\mathrm{GeV} < H_{\mathrm{T}}^{\mathrm{lep}} < 20\,\mathrm{GeV}$. Given the available statistics, cuts on $R_{\mathrm{ISR}}$and $p_{\mathrm{T}}^{\ell_2}$ while retaining some

signal acceptance are not feasible. The M_{T}^{S} variable, though, was observed to provide additional discrimination for the targeted low mass-splitting signals and an $N-1$ scan in the various $m_{\ell\ell}$ bins suggests an optimal cut of $M_{\mathrm{T}}^{\mathrm{S}} < 50\,\mathrm{GeV}$, as shown in Figure 10.8. This variable performs well since SR–E–med is dominated by the fake/non-prompt lepton background, which primarily originates from misidentified $W+\mathrm{jets}$ events. In such events, $M_{\mathrm{T}}^{\mathrm{S}}$ has a peak around the W boson mass, which is effectively cut away by the $M_{\mathrm{T}}^{\mathrm{S}} < 50\,\mathrm{GeV}$ requirement.

On the other hand, the $E_{\mathrm{T}}^{\mathrm{miss}}/H_{\mathrm{T}}^{\mathrm{lep}} < 10$ requirement applied to SR–E–low does not limit the phase space as severely, leaving enough room for further optimization. It is found that in these less-boosted, low-$E_{\mathrm{T}}^{\mathrm{miss}}$ regions, the correlation between R_{ISR} and $m_{\ell\ell}$ is diminished, thought the signals still peak near one. Ultimately, a window cut of $0.8 < R_{\mathrm{ISR}} < 1.0$ is chosen for SR–E–low, which provides a good balance of background rejection and signal acceptance for the larger mass-splitting signals. The $m_{\ell\ell}$-dependent cut is still viable for this SR, though, since fake/non-prompt leptons are typically soft, while high-Δm signals tend to produce harder leptons. The strategy used for the optimization of this cut in SR–E–high was applied to SR–E–low, and the resulting cut is $p_{\mathrm{T}}^{\ell_2} > 5\,\mathrm{GeV} + \frac{m_{\ell\ell}\ [\mathrm{GeV}]}{4}$. Finally, another window cut is placed on $m_{\mathrm{T}}^{\ell_1}$ according to $10\,\mathrm{GeV} < m_{\mathrm{T}}^{\ell_1} < 60\,\mathrm{GeV}$. While the large-$\Delta m$ signals are roughly flat in this variable, the $Z^{(*)}/\gamma^{*}(\to \tau\tau) + \mathrm{jets}$ background tends to peak around $m_{\mathrm{T}}^{\ell_1} < 10\,\mathrm{GeV}$, and the remaining backgrounds peak around $m_{\mathrm{T}}^{\ell_1} \gtrsim 80\,\mathrm{GeV}$, motivating this cut.

The blinded SRs with this binning scheme are shown in Figure 10.10 and Figure 10.11 for SR–E–low and SR–E–med, respectively, before any background normalization. Since fake/non-prompt leptons tend to be soft, the fake/non-prompt background mostly falls into SR–E–med.

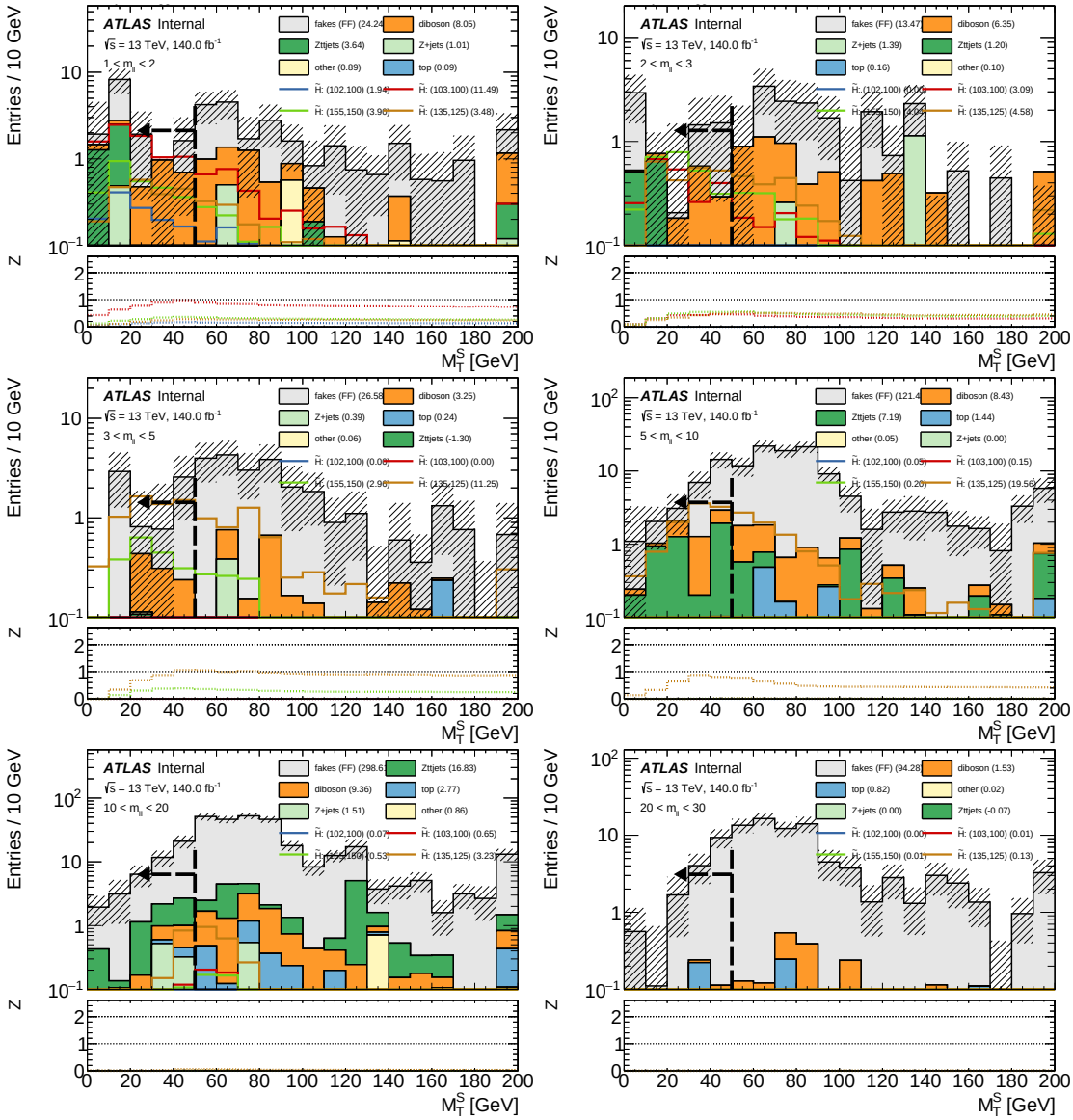

Figure 10.8: $N-1$ plots for the $M_{\mathrm{T}}^{\mathrm{S}}$ variable in each exclusive $m_{\ell\ell}$ bin of SR–E–med. The black arrow indicates the final cut in the SR definition.

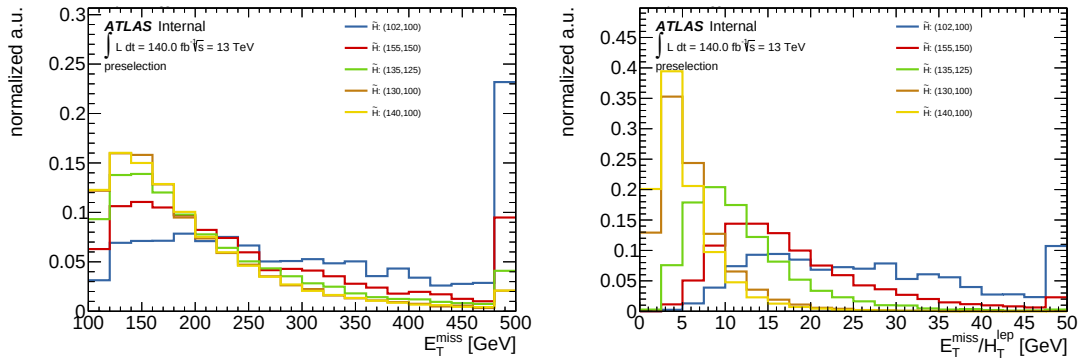

Figure 10.9: The $E_{\mathrm{T}}^{\mathrm{miss}}$ (left) and $E_{\mathrm{T}}^{\mathrm{miss}}/H_{\mathrm{T}}^{\mathrm{lep}}$(right) distributions for a variety of higgsino signal samples after applying the event preselection.

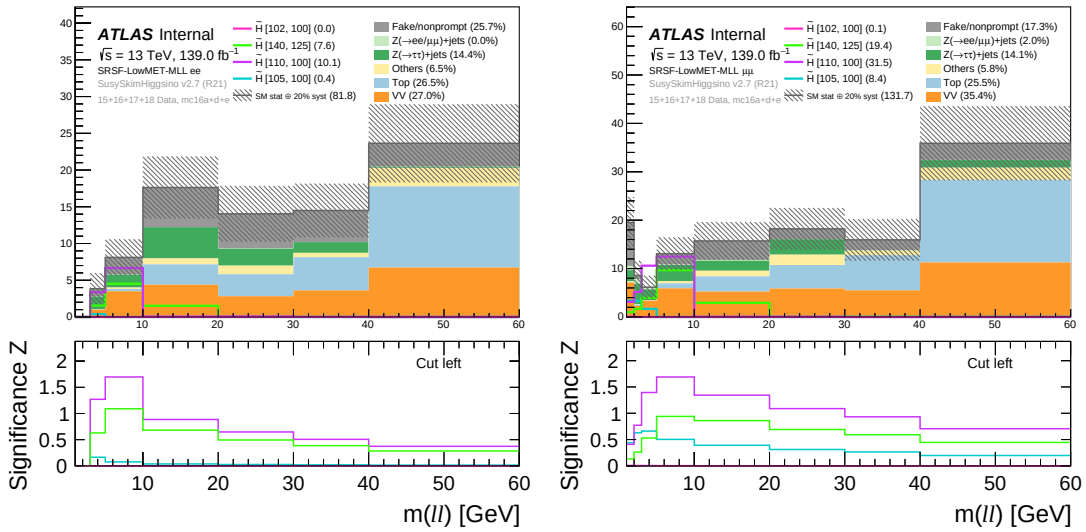

Figure 10.10: The blinded $m_{\ell\ell}$ distributions in SR–E–low for the ee channel (left) and the $\mu\mu$ channel (right) before normalizing the backgrounds with the CRs. The uncertainty bands account for both statistical uncertainties on the backgrounds and a flat 20% systematic uncertainty.

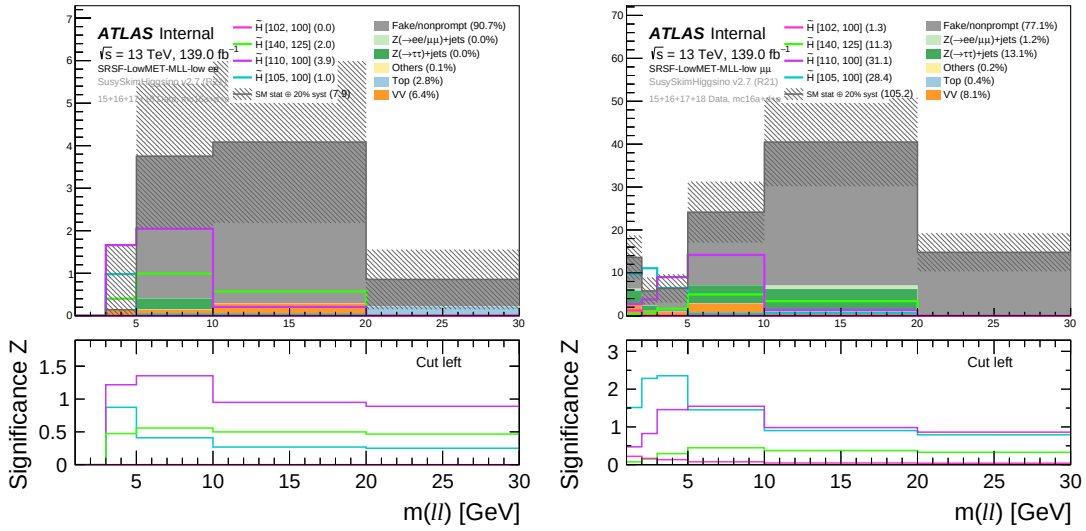

Figure 10.11: The blinded $m_{\ell\ell}$ distributions in SR–E–med for the ee channel (left) and the $\mu\mu$ channel (right) before normalizing the backgrounds with the CRs. The uncertainty bands account for both statistical uncertainties on the backgrounds and a flat 20% systematic uncertainty.

SR–E–1ℓ1T A signal region called SR–E–1ℓ1T was designed to target electroweakinos with very small mass-splittings. In these scenarios, one of the leptons may be too soft to be reconstructed as such, leading to a significant loss in signal efficiency. In most cases, though, these soft leptons will still lead to reconstructed tracks, which have a minimum p_{T} threshold of 500 MeV. The approach taken by SR–E–1ℓ1T is therefore to select events with exactly one reconstructed signal lepton and one isolated signal track (of the opposite electric charge), which is used as a proxy for the second lepton. In this case, the final discriminating variable is the invariant mass of the selected lepton and track, $m_{\ell\mathrm{track}}$. In order to reduce the large combinatorial background of tracks in a given event, the signal tracks must be matched to an electron or muon candidate that have transverse momentum reconstruction thresholds of 3 GeV and 2 GeV, respectively. To remain orthogonal to the two-lepton electroweakino SRs, these electron and muon candidates must fail the signal lepton requirements. A similar preselection as that listed in

Table 10.1 is employed in order to select boosted topologies, including a cut on the angular distance between the lepton and track of $0.05 < \Delta R_{\ell\text{track}} < 1.5$ to enforce that they be near each other. The remaining SR requirements are listed in Table 10.2, which are in place to maximize the signal event yields with respect to the background from selecting random tracks in the event.

Since MC is not expected to provide good modeling of this combinatorial background, the background estimation is completely data-driven using events in which the lepton and track have the same electric charge. This method assumes that same-sign and opposite-sign events are produced with equal rates such that the same-sign events can directly used as the background estimate in the opposite-sign SR. Uncertainties on this assumption are derived by comparing same-sign and opposite-sign event yields in kinematic phase spaces that are close to the SR. Since SR–E–1ℓ1T is in place to target very compressed signals, the lepton-track invariant mass is required to satisfy $0.5\,\text{GeV} < m_{\ell\text{track}} < 5\,\text{GeV}$ with bins boundaries at $m_{\ell\text{track}} = 0.5, 1, 1.5, 2, 3, 4$, and $5\,\text{GeV}$. A detailed description of this SR and its associated background estimation is beyond the scope of this dissertation, but its results are included in the model-independent search for new physics detailed in Section 14.3 as well as the model-dependent limits within the wino/bino models that are derived in Section 15.2.1.

10.4 Slepton Signal Regions

Two separate SRs called SR–S–high and SR–S–low are optimized to provide sensitivity to slepton production over a wide range of mass splittings. The optimized SR requirements are given in Table 10.3, where the preselection requirements in Table 10.1 are implied. Similar to the electroweakino SRs, they are kept orthogonal by cuts on $E_{\text{T}}^{\text{miss}}$, with SR–S–low requiring $150\,\text{GeV} < E_{\text{T}}^{\text{miss}} <$

Table 10.3: Requirements applied to all events entering into signal regions used for slepton searches. The preselection requirements from Table 10.1 are implied.

	Slepton SR Requirements	
Variable	SR–S–low	SR–S–high
$E_{\mathrm{T}}^{\mathrm{miss}}$ [GeV]	$[150, 200]$	> 200
m_{T2}^{100} [GeV]	< 140	< 140
$p_{\mathrm{T}}^{\ell_2}$ [GeV]	$> \min(15, 7.5 + 0.75 \times (m_{\mathrm{T2}}^{100} - 100))$	$> \min(20, 2.5 + 2.5 \times (m_{\mathrm{T2}}^{100} - 100))$
R_{ISR}	$[0.8,\ 1.0]$	$[\max(0.85, 0.98 - 0.02 \times (m_{\mathrm{T2}}^{100} - 100)),\ 1.0]$

200 GeV and SR–S–high requiring $E_{\mathrm{T}}^{\mathrm{miss}} > 200\,\mathrm{GeV}$. SR–S–high is designed to have good sensitivity over the bulk of the $m(\widetilde{\ell})$ vs. $\Delta m(\widetilde{\ell}, \widetilde{\chi}_1^0)$ mass plane, while SR–S–low provides additional sensitivity to signals with larger mass splittings ($\Delta m \gtrsim 10\,\mathrm{GeV}$). For $m(\widetilde{\ell}) = 100\,\mathrm{GeV}$, the inclusion of SR–S–low extends the expected sensitivity by $\sim 10\,\mathrm{GeV}$ in Δm. The exclusive SRs within SR–S–high and SR–S–low, which consist of non-overlapping regions in m_{T2}^{100}, are binned according to:

m_{T2}^{100} [GeV]: [100, 100.5], [100.5,101],[100,102],[102,105],
[105, 110], [110, 120], [120, 130], [130, 140].

The optimization strategy for the slepton SRs is similar to that used for the electroweakino SRs. Cuts on $p_{\mathrm{T}}^{\ell_2}$ scale with m_{T2}^{100} in order to exploit the dependence of the lepton kinematics on the signal mass splitting. These sliding cuts manage to retain good soft lepton efficiency for the most compressed signals, while significantly reducing the background due to fake/non-prompt leptons in the higher m_{T2}^{100} bins that provide sensitivity to signals with larger mass splittings. For a fixed mass-splitting, the leptons from the slepton decays will tend to be harder than those from the electroweakino decays due to the two-body nature of the former process. This allows for tighter sliding cuts on $p_{\mathrm{T}}^{\ell_2}$ in SR–S–high and SR–S–low compared to those in the electroweakino SRs, thereby giving slightly better at rejection of fake/non-prompt leptons, which tend to be very soft.

SR–S–high Since the lepton p_{T} in signal events should scale roughly linearly with Δm, the m_{T2}^{100}-dependent cut on $p_{\mathrm{T}}^{\ell_2}$ was optimized by considering a linear cut of the form $p_{\mathrm{T}}^{\ell_2} > \alpha(m_{\mathrm{T2}}^{100} - 100\,\mathrm{GeV}) + \beta$. Subsequently, a two-dimensional optimization was performed over the variables α and β according to the following procedure.

For each cut corresponding to particular values of α and β, the significance metric $Z_n(i)$ is calculated for each m_{T2}^{100} bin i, assuming a 30% background uncertainty. In order to better emulate the results of a likelihood test that exploits the shape of the m_{T2}^{100} distribution, each $Z_n(i)$ is added in quadrature according to

$$Z_n = \sum_i \sqrt{Z_n(i)^2} \tag{10.9}$$

to derive a single value of the expected significance Z_n. Since the m_{T2}^{100}distribution in signal is bounded by the mass-splitting, only m_{T2}^{100} bins with $m_{\mathrm{T2}}^{100} < 100\,\mathrm{GeV} + \Delta m$ are included in the sum. The optimized cut for a given signal hypothesis corresponds to values of α and β that maximize Z_n. Examples of the optimized cuts for different signal hypotheses are shown in Figure 10.12.

Since the goal is to have a single m_{T2}^{100}-dependent cut on $p_{\mathrm{T}}^{\ell_2}$ that provides sensitivity to the widest range of signal hypotheses, the final metric is chosen to be the number of signal samples with with $Z_n > 1.0$ after applying a given cut. In this way, the cut that maximizes this metric should lead to the broadest sensitivity to compressed sleptons. The results of the scan over α and β are shown in Figure 10.13, where an island around $\alpha = 2.5$ and $\beta = 2.5$ indicates the cuts that lead to the best overall sensitivity across the $m(\widetilde{\ell})$ vs. $\Delta m(\widetilde{\ell}, \widetilde{\chi}_1^0)$ plane. Other hotspots can be seen in this distribution, but they are not expected to be robust against statistical fluctuations. Ultimately, the sliding cut on $p_{\mathrm{T}}^{\ell_2}$ is chosen according to use $\alpha = 2.5$ and $\beta = 2.5$, as indicated in Table 10.3.

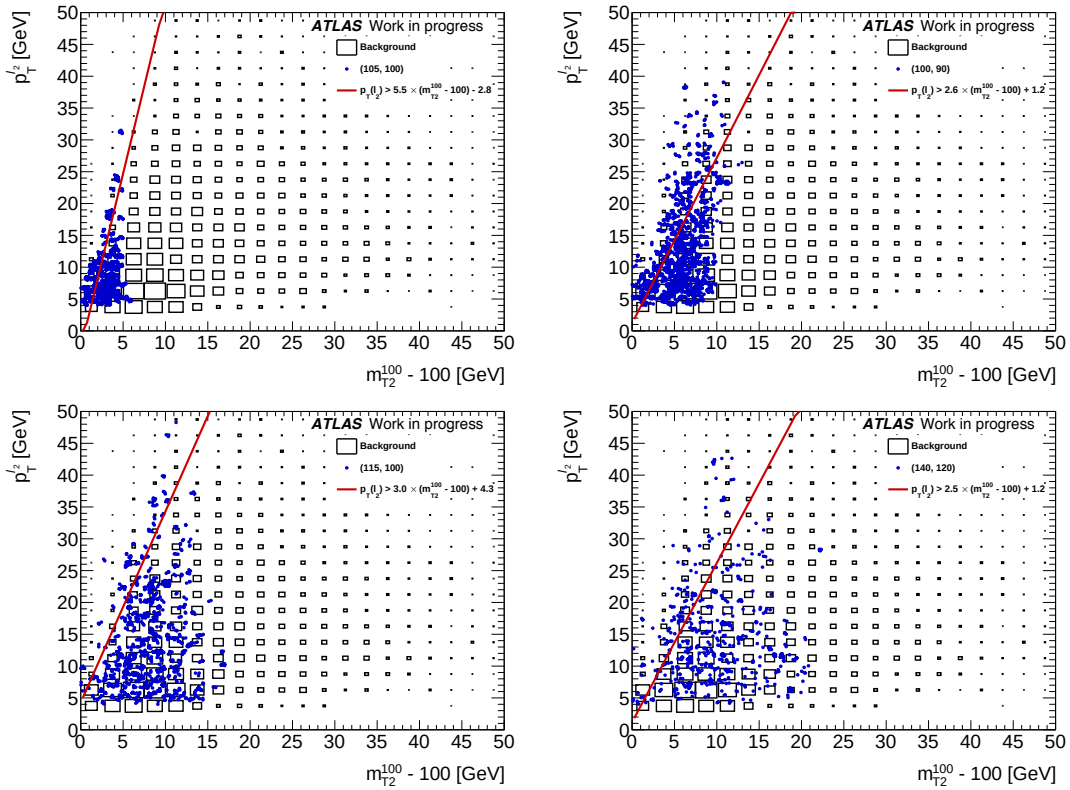

Figure 10.12: Results of the optimized cuts on $p_{\mathrm{T}}^{\ell_2}$ for examples slepton signal samples with $\Delta m = 5, 10, 15,$ and 20 GeV. The signal distributions are shown in blue, while the total expected background is indicated by the boxes. The optimized cuts are shown using a red line.

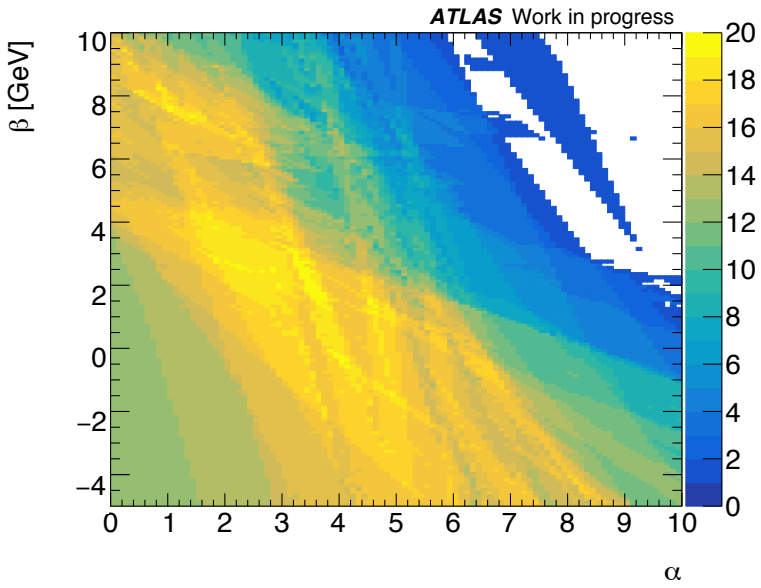

Figure 10.13: The results of the optimization of the m_{T2}^{100}-dependent cut on $p_{\mathrm{T}}^{\ell_2}$, where α indicates the slope of the linear cut and β indicates the offset. The colors indicate the number of the slepton signal samples that have a significance of $Z_n > 1.0$ after applying the cut. Empty bins indicate extreme cuts that do not lead to meaningful values of Z_n due to low statistics.

Similar to SR–E–high, the R_{ISR} distribution in SR–S–high signal events is highly correlated with m_{T2}^{100}, while background events show no strong dependence. This motivates the m_{T2}^{100}-dependent cut on R_{ISR}, which is optimized using the $N-1$ method within each of the m_{T2}^{100} bins. The result of the optimization is given by $R_{\mathrm{ISR}} > [\max(0.85, 0.98 - 0.02 \times (m_{\mathrm{T2}}^{100} - 100)), 1.0]$ and depicted in Figure 10.14. After applying all of the optimized cuts, the blinded SRs are shown in Figure 10.15 before any background normalization factors are applied.

SR–S–low A similar methodology is used to optimize this SR with respect to slepton signals in less compressed mass spectra. In order to remain orthogonal to SR–S–high, an upper bound of 200 GeV is placed on $E_{\mathrm{T}}^{\mathrm{miss}}$. The lower bound of $E_{\mathrm{T}}^{\mathrm{miss}} > 150\,\mathrm{GeV}$ is determined using the $N-1$ method separately for each exclusive m_{T2}^{100} bin and a variety of signal samples. The significance metric for the

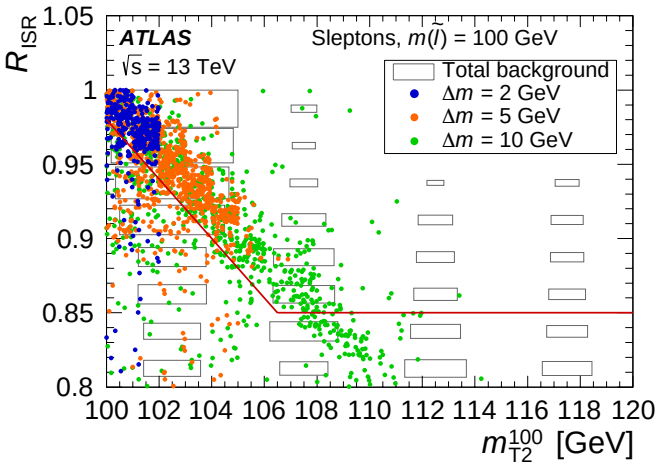

Figure 10.14: Distribution of R_{ISR} for the SR–S–high region, after applying all signal selection criteria except that on R_{ISR}. The solid red line indicates the requirement applied in the signal region such that events in the region below the red line are rejected. Representative benchmark signals for the slepton simplified model are shown as circles. The gray rectangular boxes show the distribution of the total background expectations.

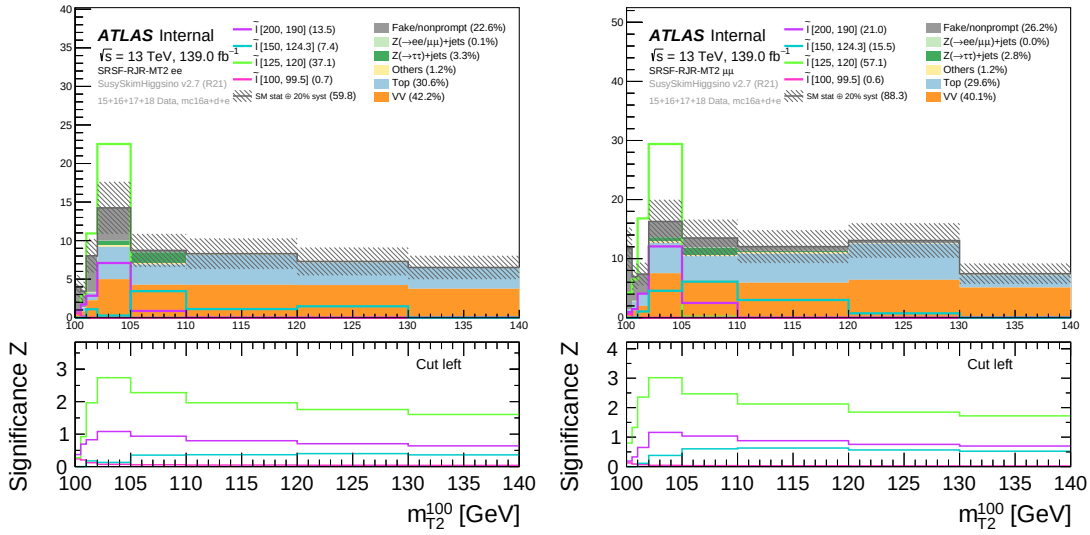

Figure 10.15: The blinded m_{T2}^{100} distributions in SR–S–high for the ee channel (left) and the $\mu\mu$ channel (right) before normalizing the backgrounds with the CRs. The uncertainty bands account for both statistical uncertainties on the backgrounds and a flat 20% systematic uncertainty.

high-m_{T2}^{100} bins is rather flat across $E_{\mathrm{T}}^{\mathrm{miss}}$ in the $120\,\mathrm{GeV} < E_{\mathrm{T}}^{\mathrm{miss}} < 200\,\mathrm{GeV}$, but peaks around 150 GeV for the bins with $m_{\mathrm{T2}}^{100} \lesssim 105\,\mathrm{GeV}$, motivating this tighter cut compared to the low-$E_{\mathrm{T}}^{\mathrm{miss}}$ electroweakino SRs. This method is repeated for the R_{ISR} variable and, like SR–E–low, the study shows that no improvements to the sensitivity are expected by scaling a cut on R_{ISR} according to the reconstructed m_{T2}^{100} of the event. Instead, the significance metric indicates that a simple window cut of $0.8 < R_{\mathrm{ISR}} < 1.0$ around the signal peaks is sufficient. On the other hand, a strong correlation between m_{T2}^{100} and $p_{\mathrm{T}}^{\ell_2}$ is again found for signal events, which motivates an m_{T2}^{100}-dependent cut on the p_{T} of the subleading lepton p_{T}. The $N-1$ scans on $p_{\mathrm{T}}^{\ell_2}$ for each m_{T2}^{100} bin are shown in Figure 10.16 and are used to motivate the final cut of $p_{\mathrm{T}}^{\ell_2} > \min(15\,\mathrm{GeV}, 7.5\,\mathrm{GeV} + 0.75 \times (m_{\mathrm{T2}}^{100} - 100\,\mathrm{GeV}))$. The blinded m_{T2}^{100} distributions in SR–S–high are shown separately for the ee and $\mu\mu$ channels in Figure 10.17 before applying any background normalization factors.

10.5 Inclusive Signal Regions

In addition to the exclusive SRs defined in the previous sections, which consist of non-overlapping regions in m_{T2}^{100} or $m_{\ell\ell}/m_{\ell\mathrm{track}}$, a series of inclusive SRs are provided in order to search for new physics with minimal model assumptions. These inclusive SRs are built by simply merging the exclusive SRs below some m_{T2}^{100} or $m_{\ell\ell}/m_{\ell\mathrm{track}}$ boundary so that each inclusive SR consists of a single bin, thereby removing any shape information. In the case of the slepton SRs, a total of eight inclusive SRs are defined by merging m_{T2}^{100} bins in both SR–S–high and SR–S–low according to $m_{\mathrm{T2}}^{100} < 100.5, 101, 102, 105, 110, 120, 130$, and 140 GeV. For the electroweakino version, a total of nine inclusive SRs are defined by performing the merging of SR–E–high, SR–E–med, SR–E–low, and SR–E–$1\ell 1T$ according to $m_{\ell\ell}/m_{\ell\mathrm{track}} < 1, 2, 3, 5, 10, 20, 30, 40$, and 60 GeV. These inclusive SRs are there-

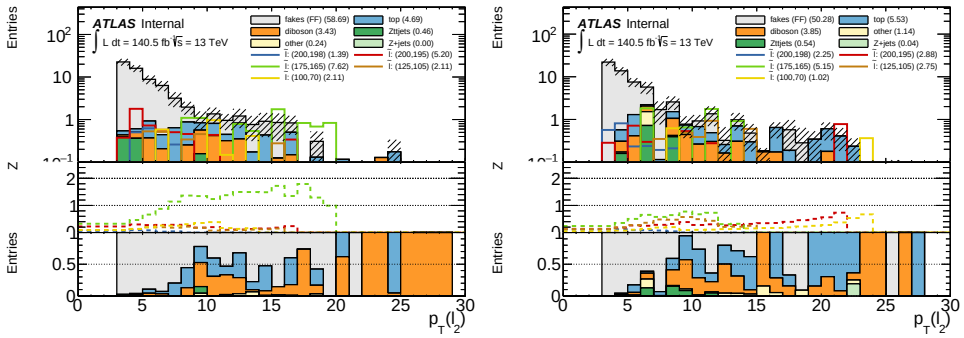

(a) $m_{\mathrm{T2}}^{100} \in [100, 100.5]$ **(b)** $m_{\mathrm{T2}}^{100} \in [100.5, 101]$

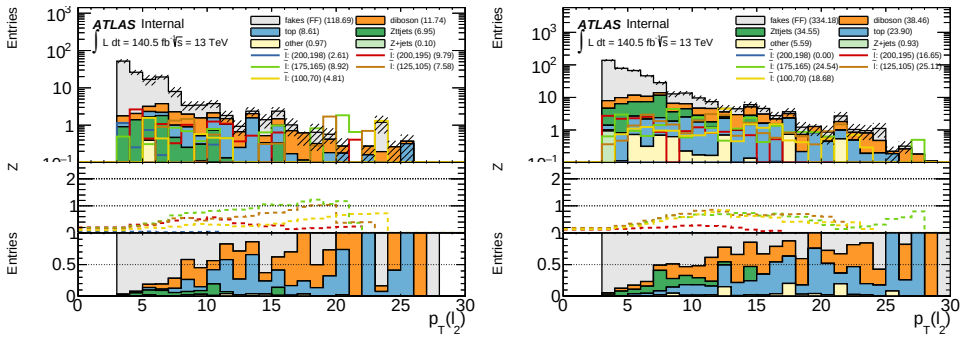

(c) $m_{\mathrm{T2}}^{100} \in [101, 102]$ **(d)** $m_{\mathrm{T2}}^{100} \in [102, 105]$

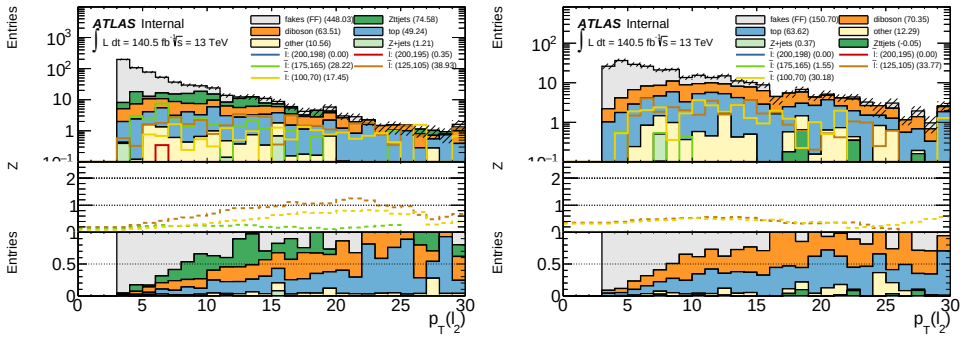

(e) $m_{\mathrm{T2}}^{100} \in [105, 110]$ **(f)** $m_{\mathrm{T2}}^{100} \in [110, 120]$

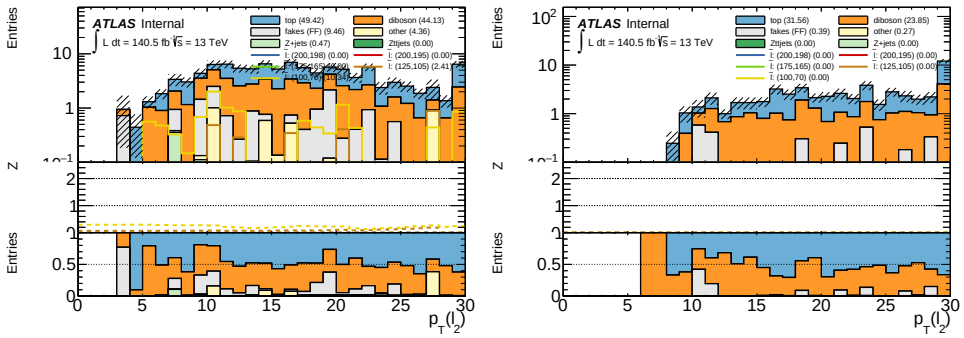

(g) $m_{\mathrm{T2}}^{100} \in [120, 130]$ **(h)** $m_{\mathrm{T2}}^{100} \in [130, 140]$

Figure 10.16: N-1 plots of $p_{\mathrm{T}}^{\ell_2}$ in SR–S–low for all exclusive m_{T2}^{100} bins. The middle panel shows the value of the significance metric where the cut is applied to the right. The bottom panel shows the relative contributions from each background.

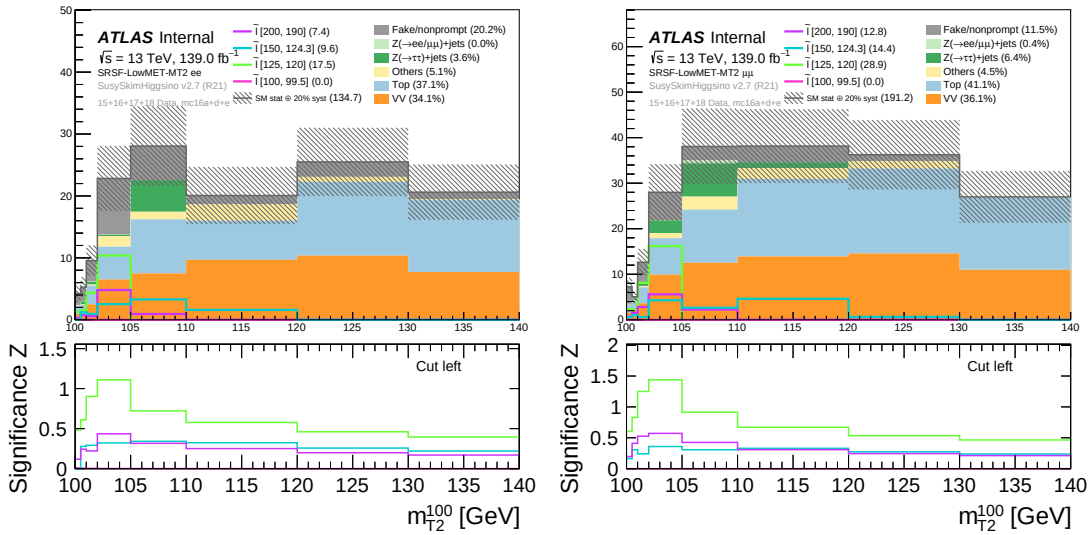

Figure 10.17: The blinded m_{T2}^{100} distributions in SR–S–low for the ee channel (left) and the $\mu\mu$ channel (right) before normalizing the backgrounds with the CRs. The uncertainty bands account for both statistical uncertainties on the backgrounds and a flat 20% systematic uncertainty.

fore not orthogonal, as the SR defined by some boundary contains all of the events in the inclusive SRs with lower boundaries. By merging the ee and $\mu\mu$ events together, these definitions of the inclusive SRs implicitly assume that the new physics does not violate lepton flavor conservation.

Chapter 11

Background Estimation

The searches presented here target signal processes that produce events containing hadronic activity, significant $E_{\mathrm{T}}^{\mathrm{miss}}$, and two soft leptons of the same flavor and opposite electric charge. While the SRs are optimized to be enriched in these signal-like events, contributions from SM background processes must be estimated and well-understood. The major sources of irreducible backgrounds containing two leptons arise from $t\bar{t}/tW$, $Z^{(*)}/\gamma^{*}(\rightarrow \tau\tau)$ + jets, and events containing two vector bosons (VV). These backgrounds are normalized using dedicated control regions and their estimation is detailed in Section 11.1. The reducible background arises from events containing at least one fake or non-prompt lepton. This background is derived using a data-driven technique called the fake factor method and is discussed in Section 11.2.

11.1 Irreducible Backgrounds

When targeting final states involving jets, significant $E_{\mathrm{T}}^{\mathrm{miss}}$, and two same-flavor, opposite-sign leptons with low-p_{T}, the dominant sources of irreducible background arise from the $t\bar{t}/tW$, WW/WZ, and $Z^{(*)}/\gamma^{*}(\rightarrow \tau\tau)$ + jets processes.

Smaller contributions arise from the Drell-Yan production of electron or muon pairs, as well as triboson, Higgs boson, and other single-top processes in association with vector bosons. For all of these backgrounds, the shapes of all kinematic distributions are taken directly from the simulated samples described in Section 8.3. Those backgrounds that only lead to small contributions in the SRs are normalized according to simulation as well.

For the dominant irreducible backgrounds, though, a data-driven approach is used in order to constrain their normalizations in the SRs. In particular, dedicated single-bin control regions (CRs) are constructed for the $t\bar{t}/tW$, WW/WZ, and $Z^{(*)}/\gamma^*(\rightarrow \tau\tau)+$jets processes, each of which are designed to be orthogonal to the SRs and enriched in the targeted background process, all while remaining close to the kinematic phase space defined by the SRs. The methodology employed is to perform a simultaneous likelihood fit to these CRs in order to extract normalization factors that separately scale the $t\bar{t}/tW$, WW/WZ, and $Z^{(*)}/\gamma^*(\rightarrow \tau\tau)+$jets processes to match the data yields in these regions. A more detailed description of this this fit is given in Section 14.1. Once the normalization factors are extracted from the fit, they are applied to MC background estimates in validation regions (VRs), designed to be closer to the SRs, in order to assess the background modeling. Eventually, these normalization factors are applied to the background estimates in the SRs when searching for evidence of new physics in the SRs.

Summaries of the CR and VR definitions, including their orthogonality with respect to the SRs, are given in Table 11.1 and Table 11.2 for the searches targeting electroweakinos and sleptons, respectively. Those regions denoted by "CRtop" are designed to constrain the normalization of the $t\bar{t}/tW$ processes. The $Z^{(*)}/\gamma^*(\rightarrow \tau\tau)+$ jets background normalization is targeted by those regions denoted by "CRtau." Finally, the "CRVV" control regions are in place

Table 11.1: Definition of control ("CR" prefix) and validation ("VR" prefix) regions used for background estimation in the electroweakino search, presented relative to the definitions of the corresponding signal regions SR–E–high, SR–E–med and SR–E–low. The 2ℓ preselection criteria from Table 10.1 and selection criteria from Table 10.2 are implied, unless specified otherwise.

Region	SR orthogonality	Lepton Flavor	Additional requirements
CRtop–E–high CRtop–E–low	$N^{20}_{b-\text{jet}} \geq 1$	$ee + \mu\mu + e\mu + \mu e$	$R_{\text{ISR}} \in [0.7, 1.0]$, $m_{\text{T}}^{\ell_1}$ removed $E_{\text{T}}^{\text{miss}}/H_{\text{T}}^{\text{lep}}$ and $m_{\text{T}}^{\ell_1}$ removed
CRtau–E–high CRtau–E–low VRtau–E–med	$m_{\tau\tau} \in [60, 120]$ GeV	$ee + \mu\mu + e\mu + \mu e$	$R_{\text{ISR}} \in [0.7, 1.0]$, $m_{\text{T}}^{\ell_1}$ removed $R_{\text{ISR}} \in [0.6, 1.0]$, $m_{\text{T}}^{\ell_1}$ removed –
CRVV–E–high CRVV–E–low	$R_{\text{ISR}} \in [0.7, 0.85]$ $R_{\text{ISR}} \in [0.6, 0.8]$	$ee + \mu\mu + e\mu + \mu e$	$m_{\text{T}}^{\ell_1}$ removed $m_{\text{T}}^{\ell_1} > 30$ GeV, $N_{\text{jets}} \in [1, 2]$, $E_{\text{T}}^{\text{miss}}/H_{\text{T}}^{\text{lep}}$ removed
VRSS–E–high VRSS–E–low VRSS–E–med	Same sign $\ell^{\pm}\ell^{\pm}$	$ee + \mu e,\ \mu\mu + e\mu$	$R_{\text{ISR}} \in [0.7, 1.0]$, $m_{\text{T}}^{\ell_1}$ and $p_{\text{T}}^{\ell_2}$ removed $E_{\text{T}}^{\text{miss}}/H_{\text{T}}^{\text{lep}}$, $m_{\text{T}}^{\ell_1}$ and $p_{\text{T}}^{\ell_2}$ removed –
VRDF–E–high VRDF–E–low VRDF–E–med	$e\mu + \mu e$	$e\mu + \mu e$	– – –

to constrain the diboson contributions. Notably, the $t\bar{t}/tW$, WW/WZ, and $Z^{(*)}/\gamma^*(\rightarrow \tau\tau)$ + jets processes produce same-flavor and different-flavor lepton pairs at the same rate. All of the CRs, therefore, accept all lepton flavor combinations (ee, $\mu\mu$, $e\mu$, and μe, where the first lepton is the leading lepton) in order to increase their statistical power when constraining the normalization factors. Cuts on kinematic variables such as R_{ISR} and $m_{\text{T}}^{\ell_1}$ are also loosened with respect to the SR definitions in order increase the statistics and purity in the CRs. Each of the CRs are described in more detail in the following sections.

For assessing the background modeling, three types of VRs are defined in Table 11.1 and Table 11.2. The first set is denoted by "VRDF," which is a shorthand for "different-flavor validation region." For each SR, a corresponding VRDF region is defined that only differs from the SR definition by requiring two different-flavor leptons ($e\mu$ or μe, where the first lepton is the leading lepton). In this way, the backgrounds can be checked in regions that have the exact same

Table 11.2: Definition of control ("CR" prefix) and validation ("VR" prefix) regions used for background estimation in the slepton search, presented relative to the definitions of the corresponding signal regions SR–S–high and SR–S–low. The 2ℓ preselection criteria from Table 10.1 and selection criteria from Table 10.3 are implied, unless specified otherwise.

Region	SR orthogonality	Lepton Flavor	Additional requirements
CRtop–S–high	$N^{20}_{b-\text{jet}} \geq 1$	$ee + \mu\mu + e\mu + \mu e$	$R_{\text{ISR}} \in [0.7, 1.0]$
CRtop–S–low			–
CRtau–S–high	$m_{\tau\tau} \in [60, 120]$ GeV	$ee + \mu\mu + e\mu + \mu e$	$R_{\text{ISR}} \in [0.7, 1.0]$
CRtau–S–low			$R_{\text{ISR}} \in [0.6, 1.0]$
CRVV–S–high	$R_{\text{ISR}} \in [0.7, 0.85]$	$ee + \mu\mu + e\mu + \mu e$	–
CRVV–S–low	$R_{\text{ISR}} \in [0.6, 0.8]$		$m^{\ell_1}_{\text{T}} > 30$, $N_{\text{jets}} \in [1, 2]$
VRSS–S–high	Same sign $\ell^{\pm}\ell^{\pm}$	$ee + \mu e,\ \mu\mu + e\mu$	$R_{\text{ISR}} \in [0.7, 1.0]$, $p^{\ell_2}_{\text{T}}$ removed
VRSS–S–low			$p^{\ell_2}_{\text{T}}$ removed
VRDF–S–high	$e\mu + \mu e$	$e\mu + \mu e$	–
VRDF–S–low			–

kinematic requirements as the SRs and similar background compositions. The second set of VRs is denoted by "VRSS," which is meant to convey "same-sign validation region." These regions are kept orthogonal to the SRs by requiring two leptons with the same electric charge and are designed to be enriched in events containing fake/non-prompt leptons. Scrutiny of these regions is given in Section 11.2.5. Unfortunately, it is difficult to construct a dedicated CR targeting the $Z^{(*)}/\gamma^*(\to \tau\tau)+$jets normalization in the SR–E–med due to limited statistics. Instead, this background is normalized using CRtau–E–low, and the extrapolation is checked in VRtau–E–med, which requires $m_{\tau\tau} \in [60, 120]$ GeV but is otherwise identical to SR–E–med.

11.1.1 Top-quark Control Regions

In total, four CRs are defined in order to constrain the $t\bar{t}/tW$ normalization in the various SRs. CRtop–E–high and CR–top–E–low are are used to derive normalization factors for the electroweakino SRs with $E_{\mathrm{T}}^{\mathrm{miss}} > 200\,\mathrm{GeV}$ and $E_{\mathrm{T}}^{\mathrm{miss}} < 200\,\mathrm{GeV}$, respectively. CRtop–S–high and CRtop–S–low are the analogous CRs for the slepton SRs. In each case, these CRs take advantage of the large $t \to Wb$ branching ratio by requiring at least one b-tagged jet in the event, thereby enforcing orthogonality with the SRs. Based on simulation, these regions are between 83% and 94% pure in the $t\bar{t}/tW$ processes. Relevant kinematic distributions for CRtop–E–high and CRtop–E–low are presented in Figure 11.1 and Figure 11.2, respectively. Distributions in CR–S–high and CR–S–low are presented in Figure 11.3 and Figure 11.4. In each case, the regions are shown prior to any fits and therefore do not include any normalization factors for the dominant irreducible backgrounds. Nonetheless, good agreement is observed between the data and the background estimates, though some mis-modeling is apparent in the number of b-tagged jets.

11.1.2 Ditau Control Regions

Similarly, CRtau–E–high, CRtau–E–low, CRtau–S–high, and CRtau–S–low are constructed in order to extract normalization factors for the $Z^{(*)}/\gamma^{*}(\to \tau\tau) +$ jets irreducible background for the electroweakinos and slepton SRs with $E_{\mathrm{T}}^{\mathrm{miss}} > 200\,\mathrm{GeV}$ and $E_{\mathrm{T}}^{\mathrm{miss}} < 200\,\mathrm{GeV}$. In order to enrich these regions in $Z^{(*)}/\gamma^{*}(\to \tau\tau) + \mathrm{jets}$ events, the $m_{\tau\tau}$ variable is required to be consistent with the Z boson mass. In particular, the $m_{\tau\tau}$window that defines the SRs is inverted so that the CRtau regions remain orthogonal by selecting events with $m_{\tau\tau} \in [60, 120]$ GeV. In this case, the CRtau regions are at least 75% pure in $Z^{(*)}/\gamma^{*}(\to \tau\tau) + \mathrm{jets}$

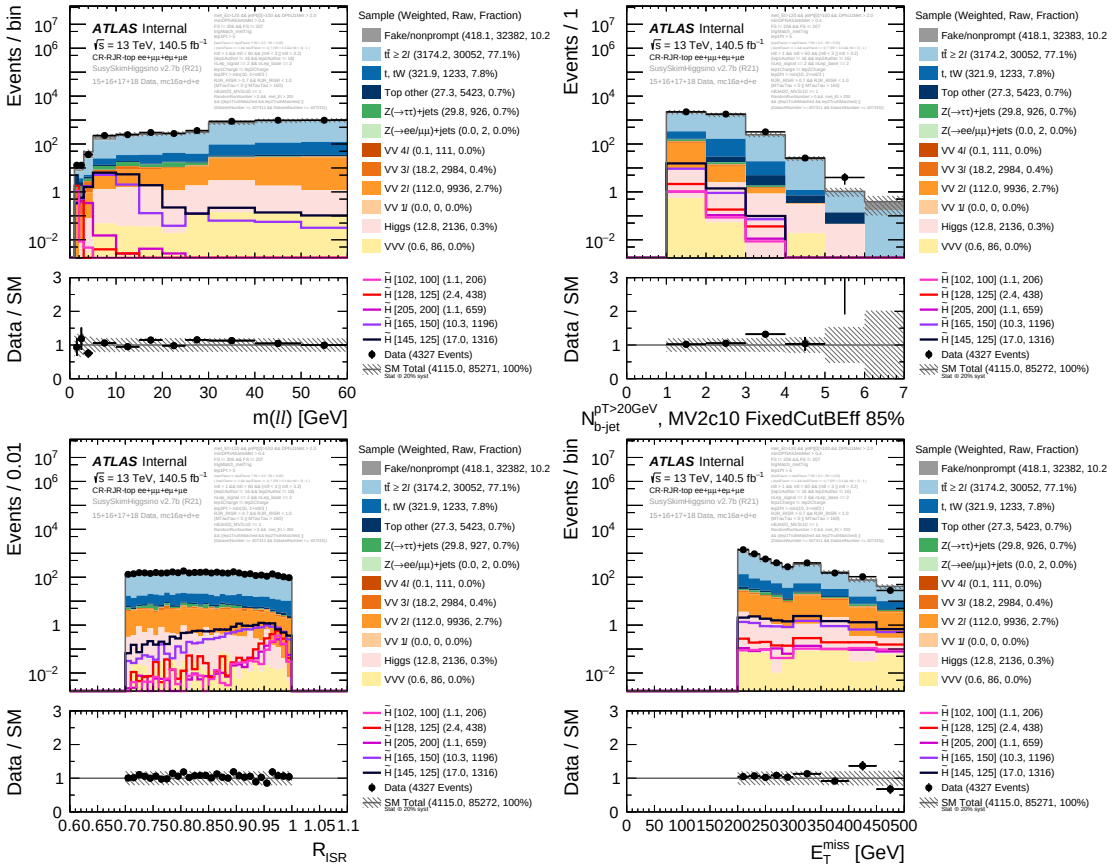

Figure 11.1: Kinematic distributions in CRtop–E–high prior to the application of any normalization factors. The uncertainty band shows the statistical uncertainty added in quadrature with a flat 20% systematic uncertainty.

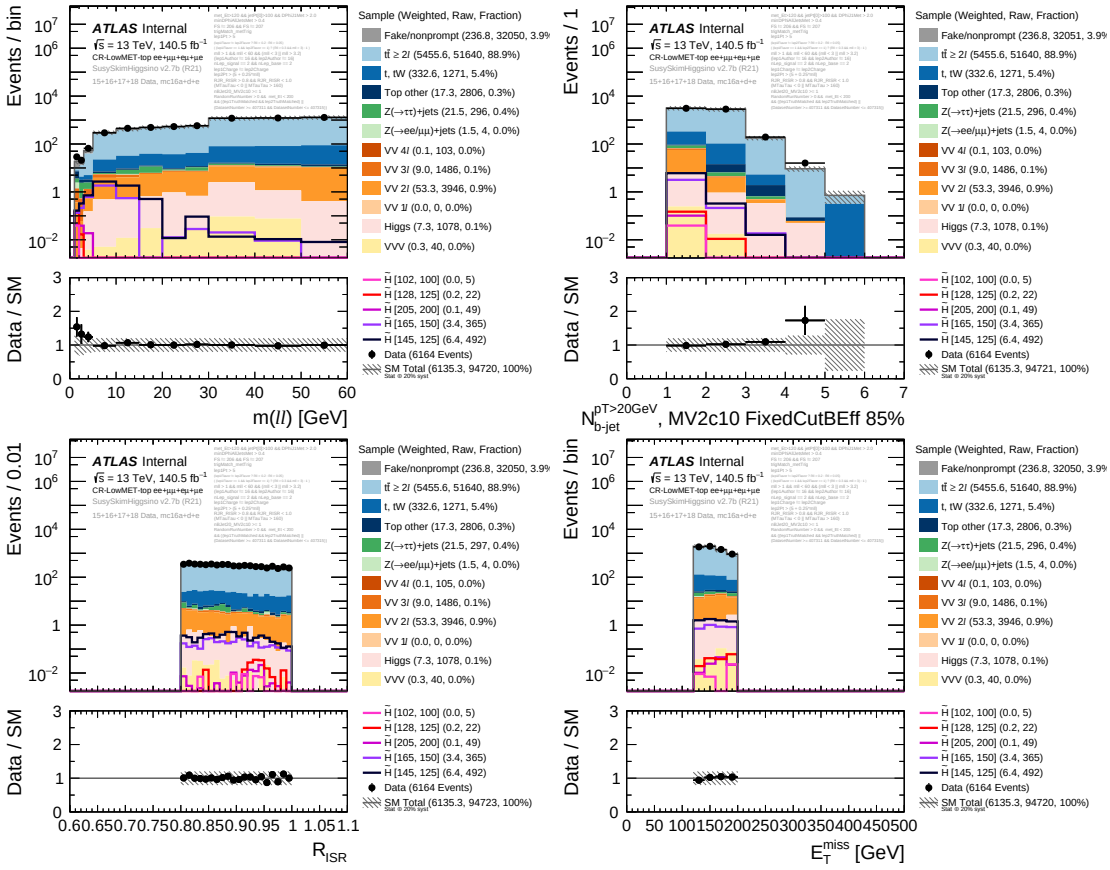

Figure 11.2: Kinematic distributions in CRtop–E–low prior to the application of any normalization factors. The uncertainty band shows the statistical uncertainty added in quadrature with a flat 20% systematic uncertainty.

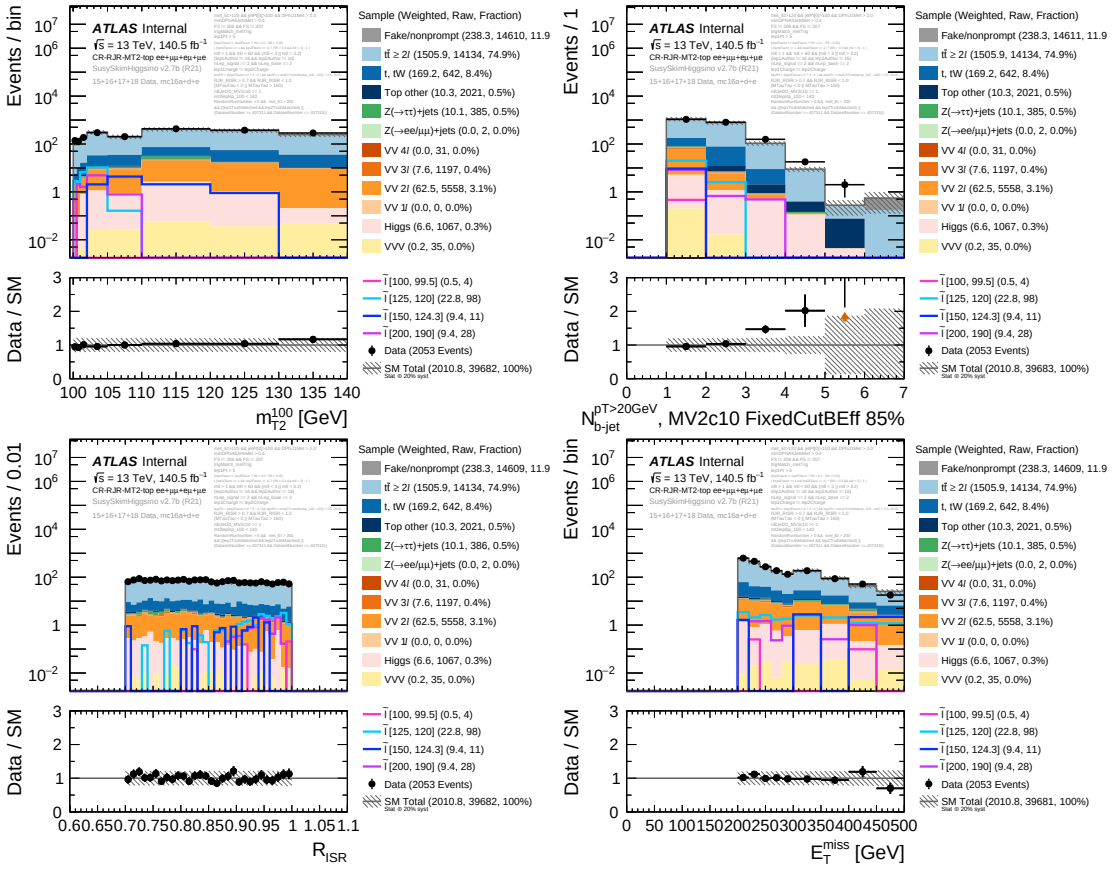

Figure 11.3: Kinematic distributions in CRtop–S–high prior to the application of any normalization factors. The uncertainty band shows the statistical uncertainty added in quadrature with a flat 20% systematic uncertainty.

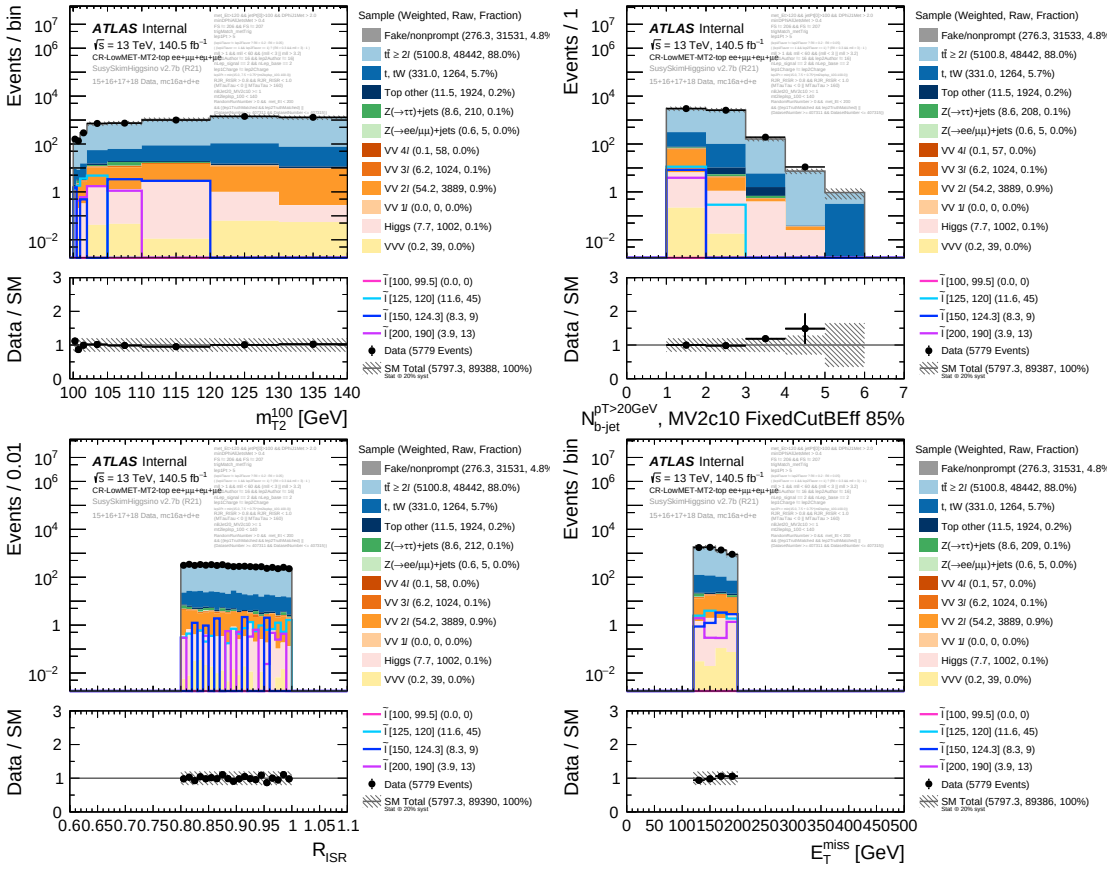

Figure 11.4: Kinematic distributions in CRtop–S–low prior to the application of any normalization factors. The uncertainty band shows the statistical uncertainty added in quadrature with a flat 20% systematic uncertainty.

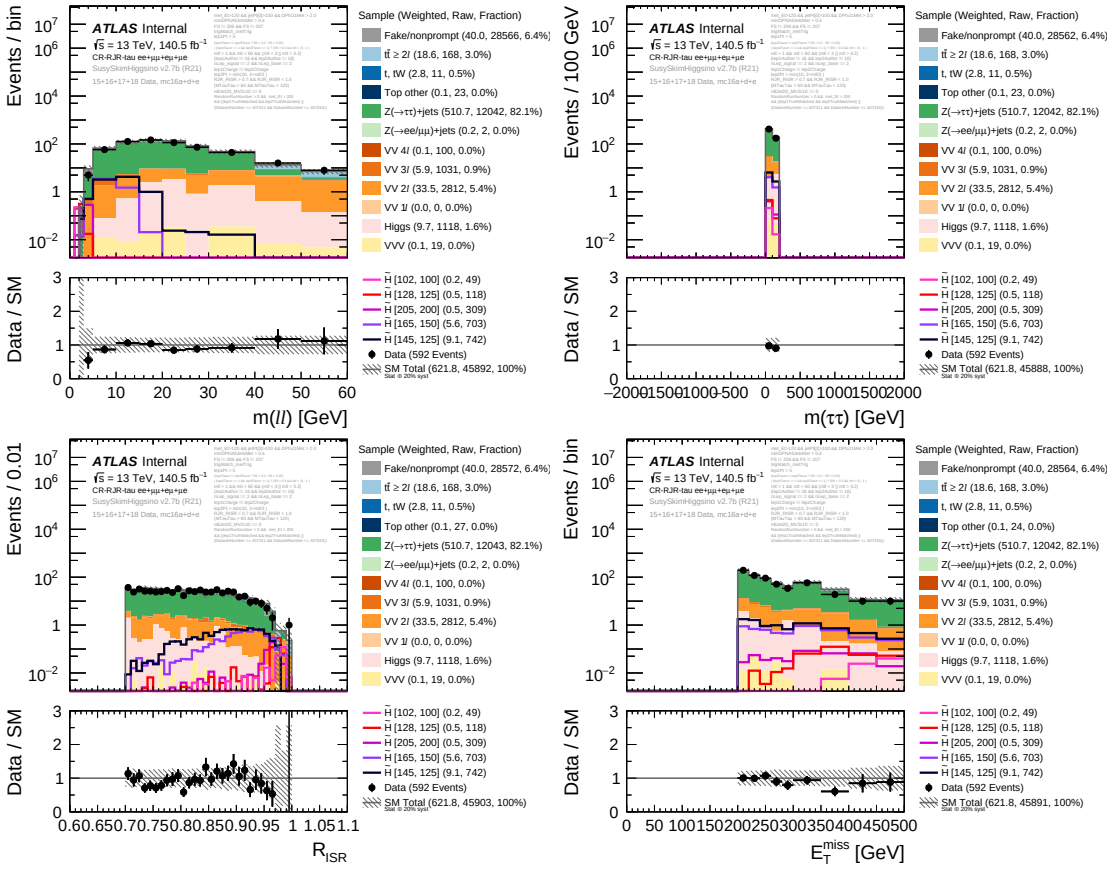

Figure 11.5: Kinematic distributions in CRtau–E–high prior to the application of any normalization factors. The uncertainty band shows the statistical uncertainty added in quadrature with a flat 20% systematic uncertainty.

events according to simulation. Pre-fit kinematic distributions in CRtau–E–high and CRtau–E–low are shown in Figures 11.5–11.6, while those for CRtau–S–high and CRtau–S–low are presented in Figures 11.7–11.8. Again, good agreement is observed between the data and the pre-fit background expectation.

11.1.3 Diboson Control Regions

Finally, the CRVV regions are in place to derive normalization factors for the diboson processes that contribute to the SRs. These control regions are kept orthogonal from their corresponding SRs by selecting events in the R_{ISR} side-

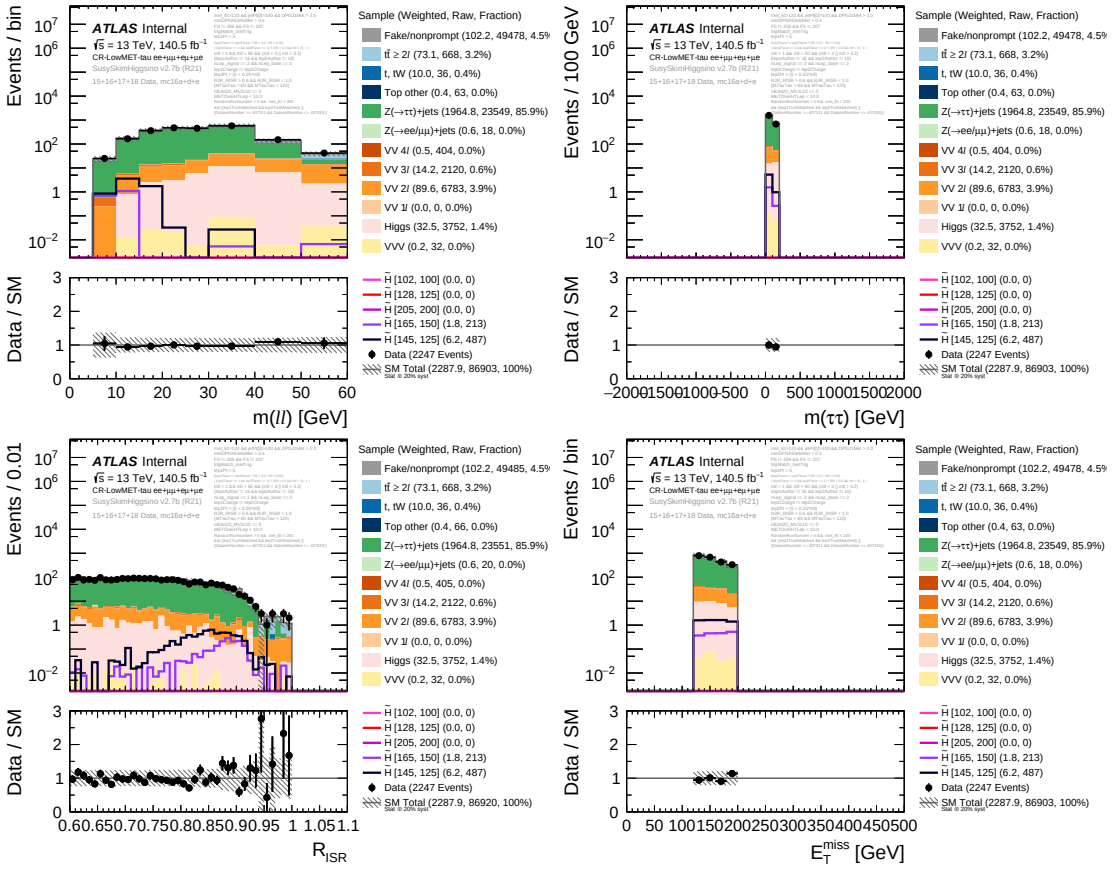

Figure 11.6: Kinematic distributions in CRtau–E–low prior to the application of any normalization factors. The uncertainty band shows the statistical uncertainty added in quadrature with a flat 20% systematic uncertainty.

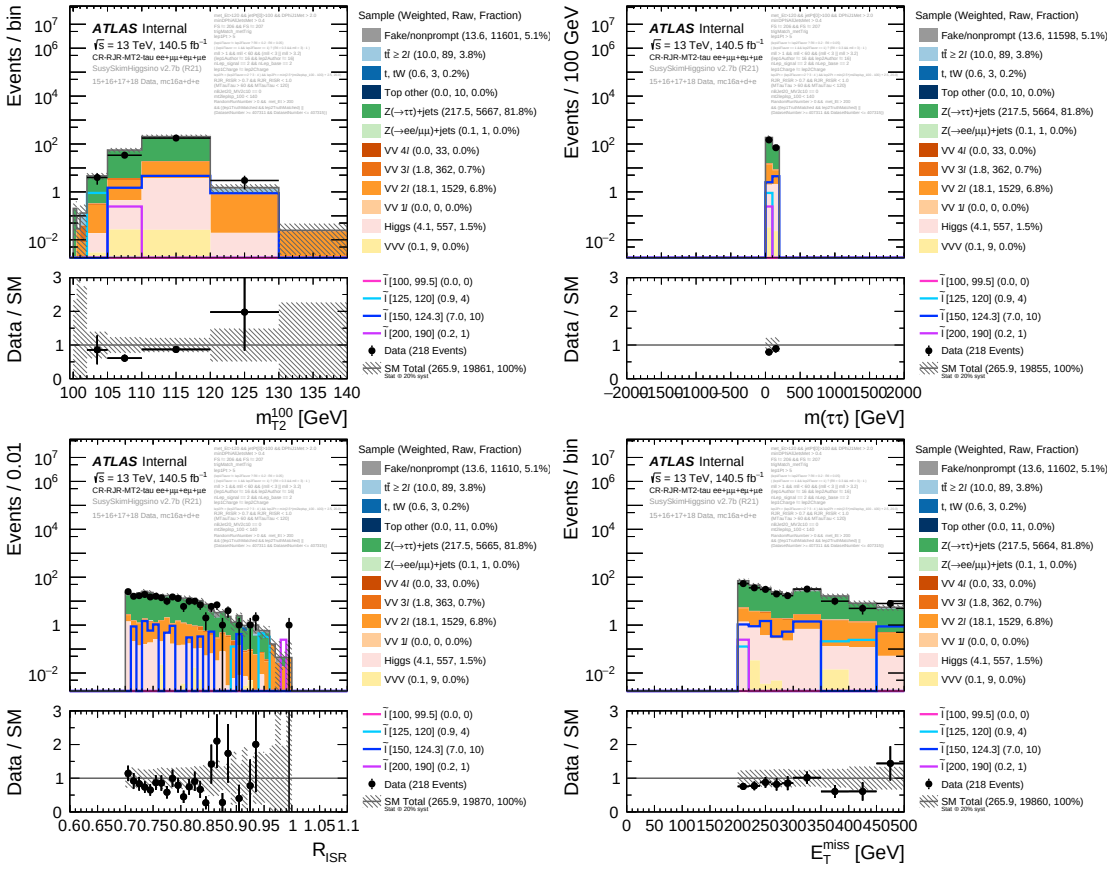

Figure 11.7: Kinematic distributions in CRtau–S–high prior to the application of any normalization factors. The uncertainty band shows the statistical uncertainty added in quadrature with a flat 20% systematic uncertainty.

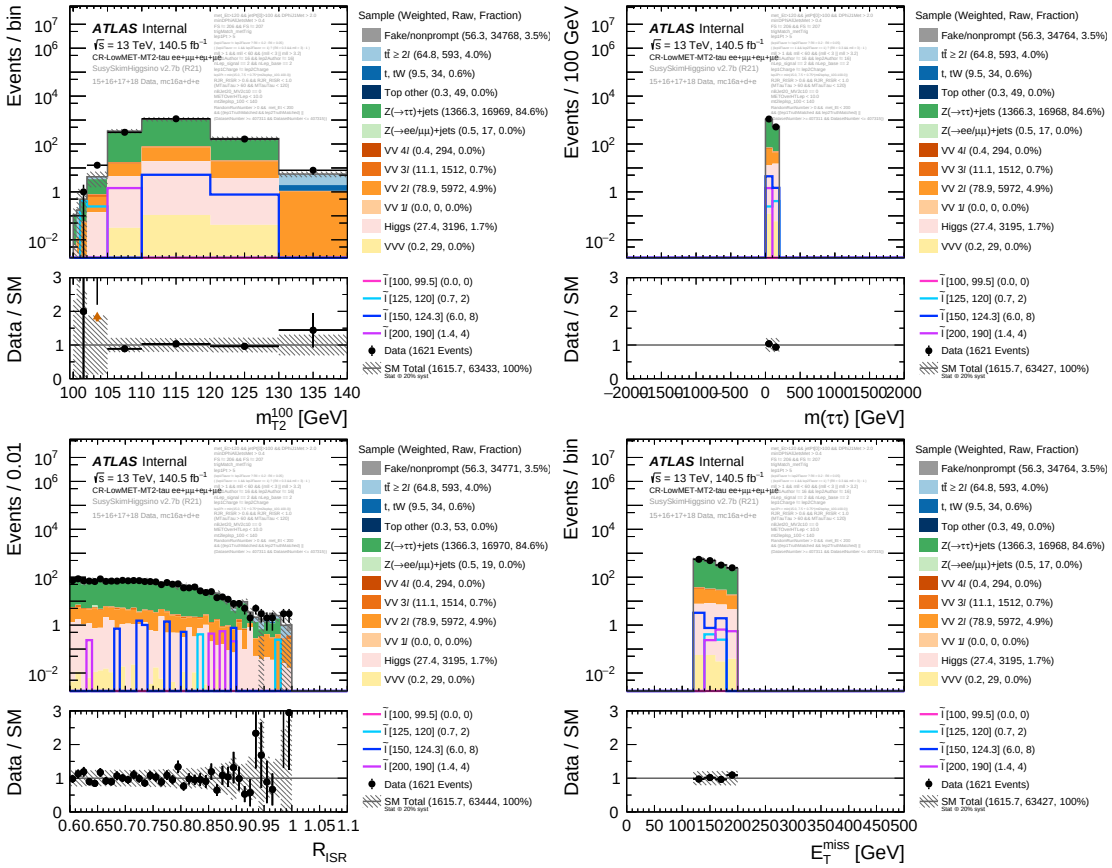

Figure 11.8: Kinematic distributions in CRtau–S–low prior to the application of any normalization factors. The uncertainty band shows the statistical uncertainty added in quadrature with a flat 20% systematic uncertainty.

bands, with CRVV–E–high and CRVV–S–high requiring $R_{\text{ISR}} \in [0.7, 0.85]$ GeV and CRVV-E–low and CRVV requiring $R_{\text{ISR}} \in [0.6, 0.8]$ GeV. Pre-fit kinematic distributions in the CRs that are used to normalize the diboson background in the electroweakino SRs are shown in Figures 11.9–11.10. Similar distributions for CRVV–S–high and CRVV–S–low are shown in Figures 11.11–11.12, again before any normalization factors are applied. According to simulation, these CRs are only 41%–45% pure in VV events. Of the remaining irreducible backgrounds in these regions, the largest contributions come from $t\bar{t}/tW$ and $Z^{(*)}/\gamma^*(\rightarrow \tau\tau)$+jets, respectively. Since these processes are constrained by their own dedicated CRs in the combined background-only fits to CRs, normalization factors for the diboson processes can still be obtained with reasonable uncertainties. While the shapes of the distributions in these CRs show good agreement between the data and background expectation, the latter consistently over-predicts, indicating some mis-modeling of the diboson production rates in these phase spaces. This offset is eventually accounted for in the SRs by the diboson normalization factors that are extracted from the fits to the CRs.

11.1.4 Validation Regions

Since the shapes of all background processes producing real leptons are taken directly from simulation, it is instructive to inspect the various VRs even before the application of any normalization factors in order to check for signs of systematic mis-modeling. The VRSS regions are used to assess the data-driven modeling of the fake/non-prompt lepton background and so those regions are shown in Section 11.2.5. Instead, the VRDF regions are shown here in order to inspect the background modeling in regions that occupy the same kinematic phase space as the SRs and have similar background compositions. Additionally, the agreement

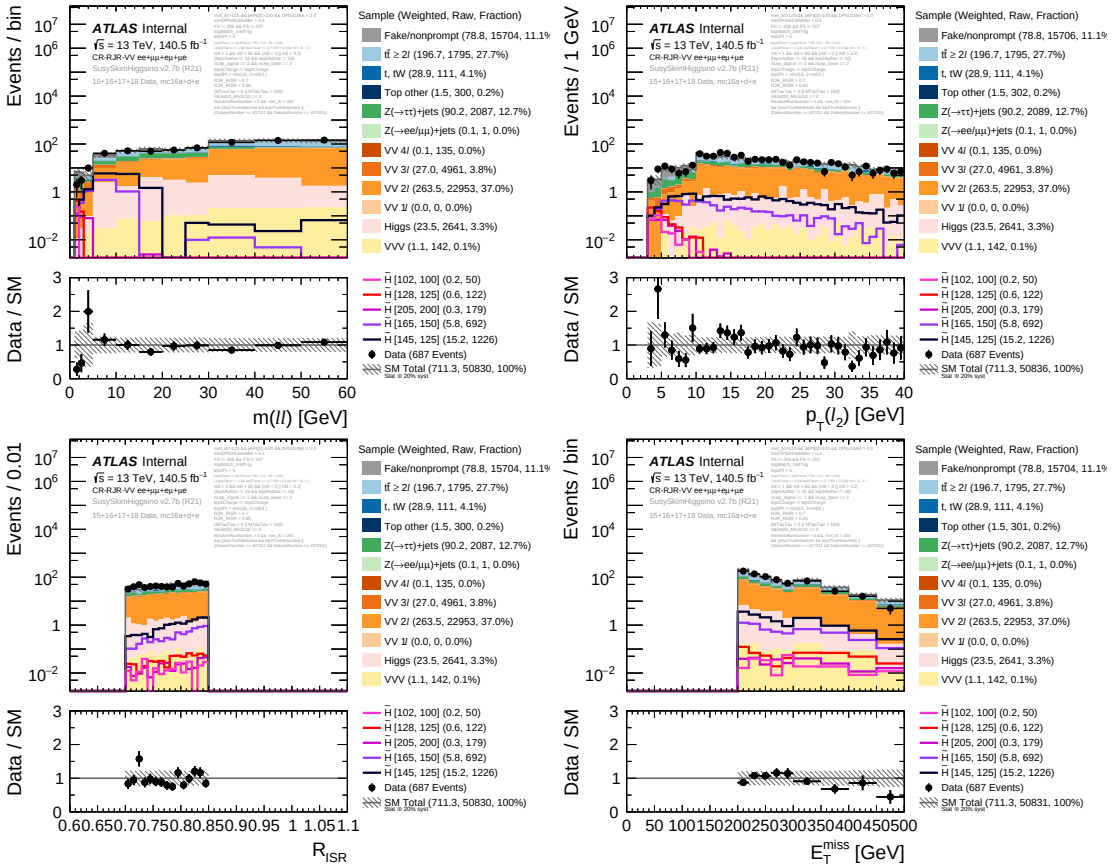

Figure 11.9: Kinematic distributions in CRVV–E–high prior to the application of any normalization factors. The uncertainty band shows the statistical uncertainty added in quadrature with a flat 20% systematic uncertainty.

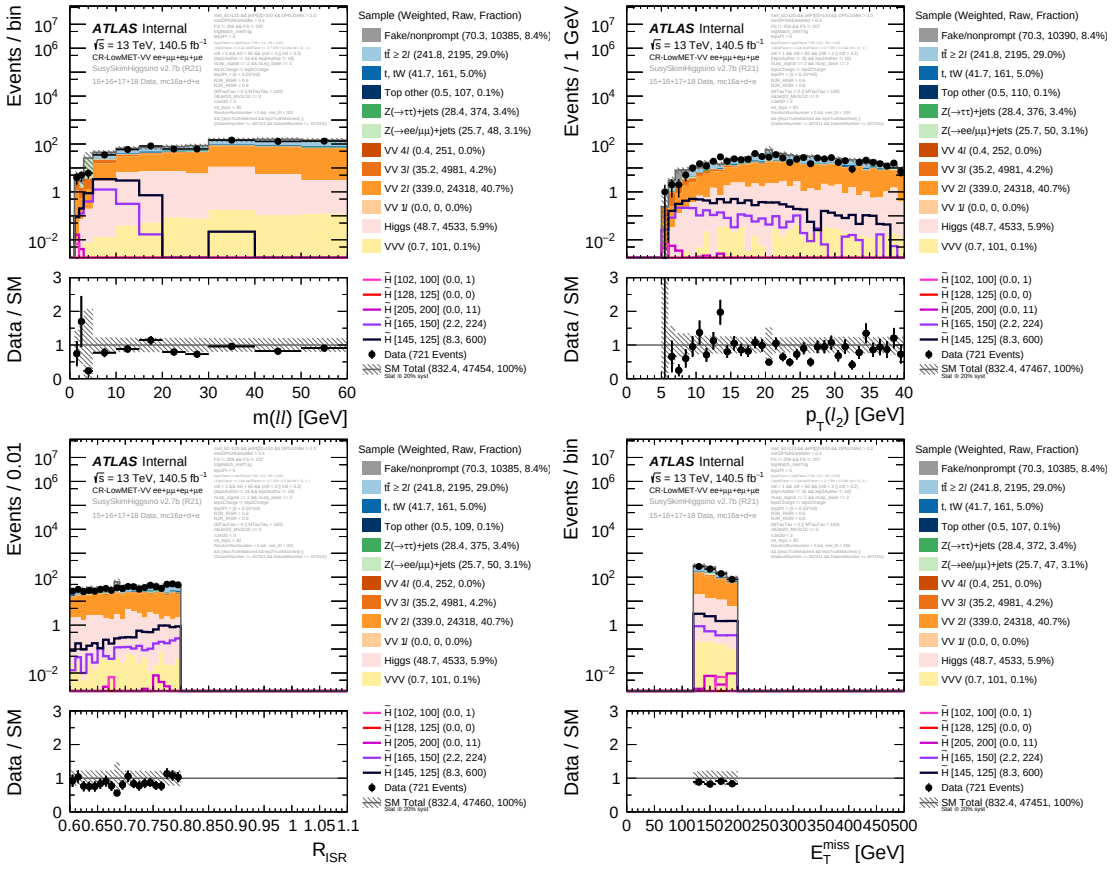

Figure 11.10: Kinematic distributions in CRVV–E–low prior to the application of any normalization factors. The uncertainty band shows the statistical uncertainty added in quadrature with a flat 20% systematic uncertainty.

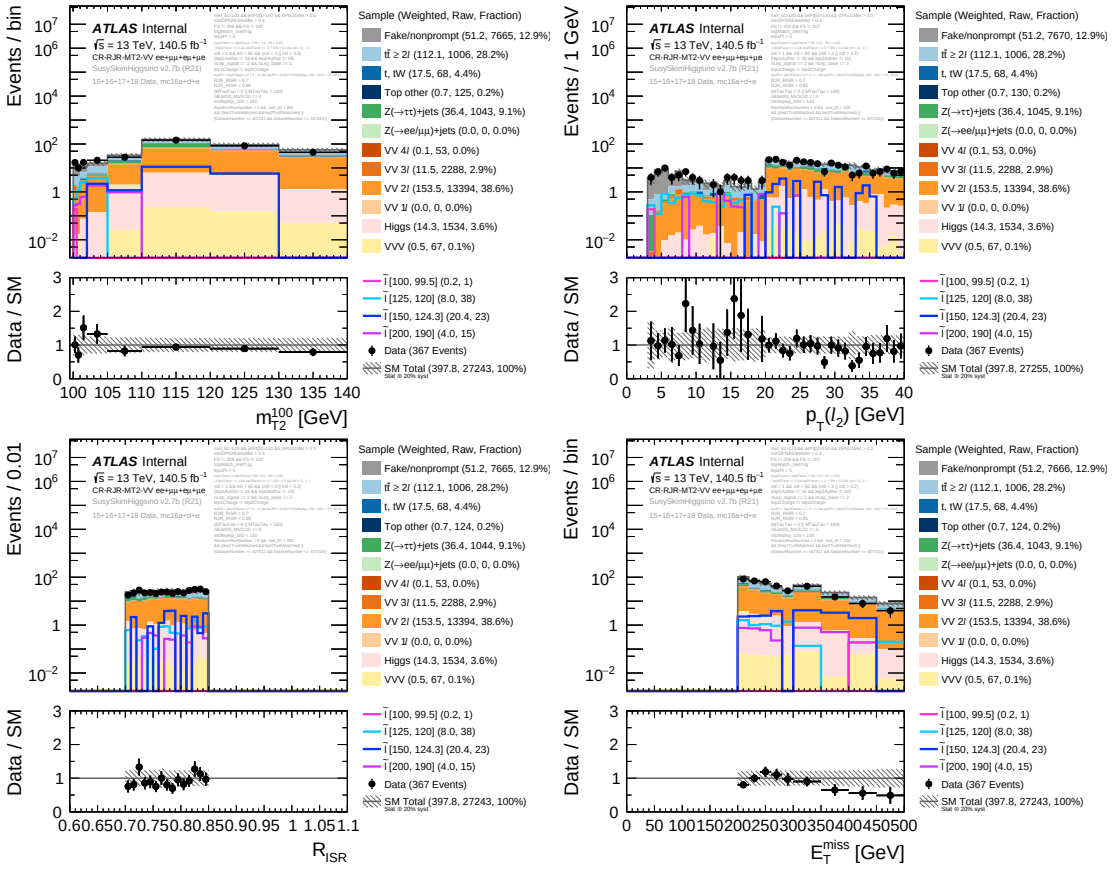

Figure 11.11: Kinematic distributions in CRVV–S–high prior to the application of any normalization factors. The uncertainty band shows the statistical uncertainty added in quadrature with a flat 20% systematic uncertainty.

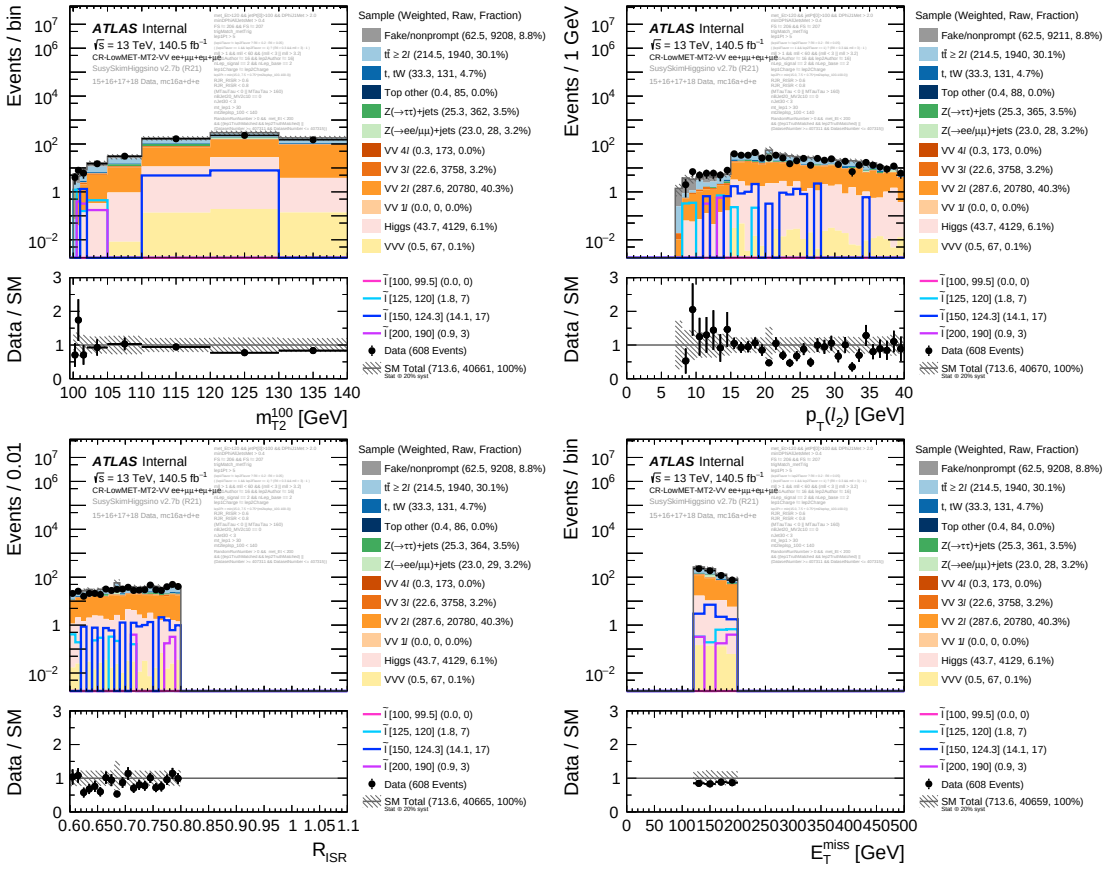

Figure 11.12: Kinematic distributions in CRVV–S–low prior to the application of any normalization factors. The uncertainty band shows the statistical uncertainty added in quadrature with a flat 20% systematic uncertainty.

in VRtau–E–med is checked in order to verify that CRtau–E–low can be used to normalize the $Z^{(*)}/\gamma^*(\rightarrow \tau\tau) + \text{jets}$ background in SR–E–med.

Pre-fit kinematic distributions for important observables are shown in Figures 11.13–11.15 for VRDF–E–high, VRDF–E–med, and VR–DF–low. In VRDF–E–high and VRDF–E–low, events due to real leptons represent approximately 70% and 76% of the total background expectation, respectively. On the other hand, VRDF–E–med is dominated by the fake/non-prompt lepton background (as is its corresponding SR), with approximately 26% of the expected background coming from events producing real leptons. In general, there is good agreement between the data and the pre-fit backgrounds in the VRs.

The different-flavor VRs that mirror the slepton SRs are also inspected. Figure 11.16 shows important kinematic distributions in VRDF–S–high, while Figure 11.17 shows the same distributions in VRDF–S–low. In the case of VRDF–S–high, approximately 70% of the total pre-fit background estimate is expected to be due to processes producing real leptons. This figure increases to approximately 83% for VRDF–S–low. Excellent agreement is observed in these validation regions even before any normalization factors are applied.

Finally an inspection is made of VRtau–E–med in Figure 11.18. Despite the limited statistics, good agreement is observed between the data and the pre-fit background estimate, giving confidence to the chosen method for constraining the $Z^{(*)}/\gamma^*(\rightarrow \tau\tau) + \text{jets}$ process in SR–E–med.

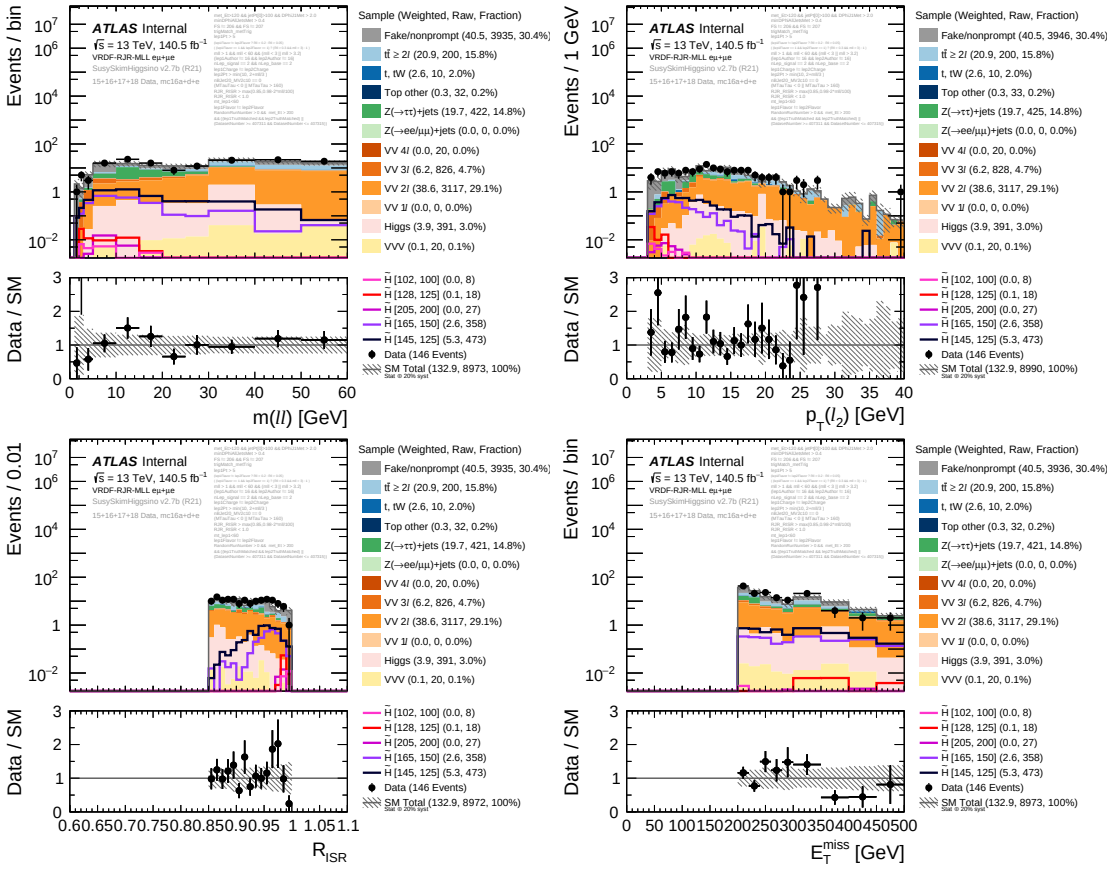

Figure 11.13: Kinematic distributions in VRDF–E–high prior to the application of any normalization factors. The uncertainty band shows the statistical uncertainty added in quadrature with a flat 20% systematic uncertainty.

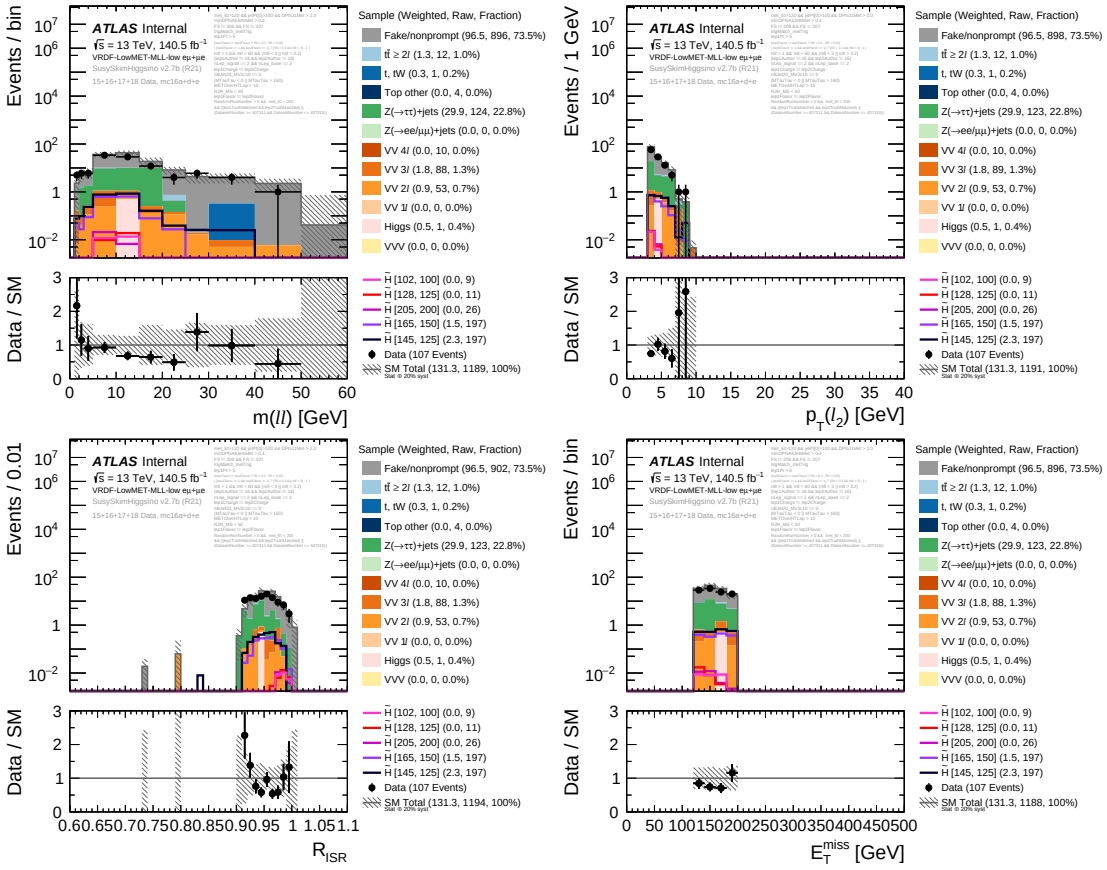

Figure 11.14: Kinematic distributions in VRDF–E–med prior to the application of any normalization factors. The uncertainty band shows the statistical uncertainty added in quadrature with a flat 20% systematic uncertainty.

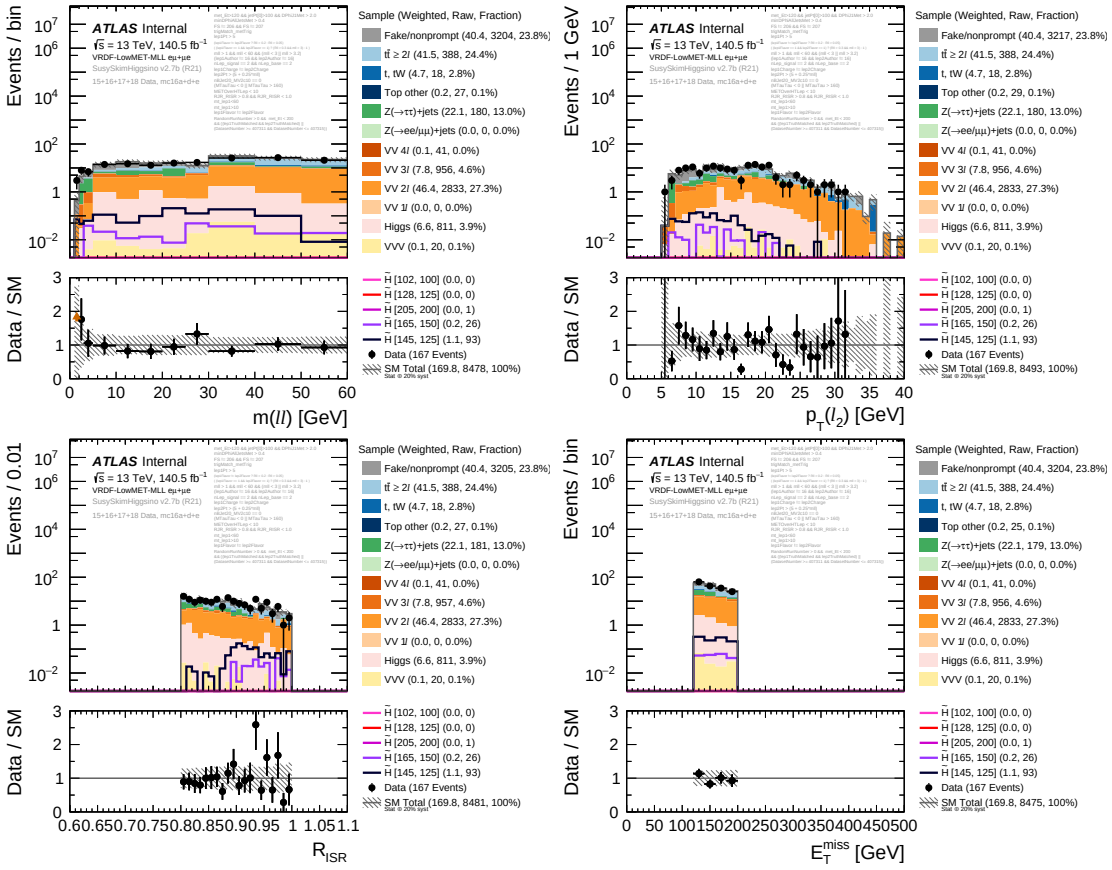

Figure 11.15: Kinematic distributions in VRDF–E–low prior to the application of any normalization factors. The uncertainty band shows the statistical uncertainty added in quadrature with a flat 20% systematic uncertainty.

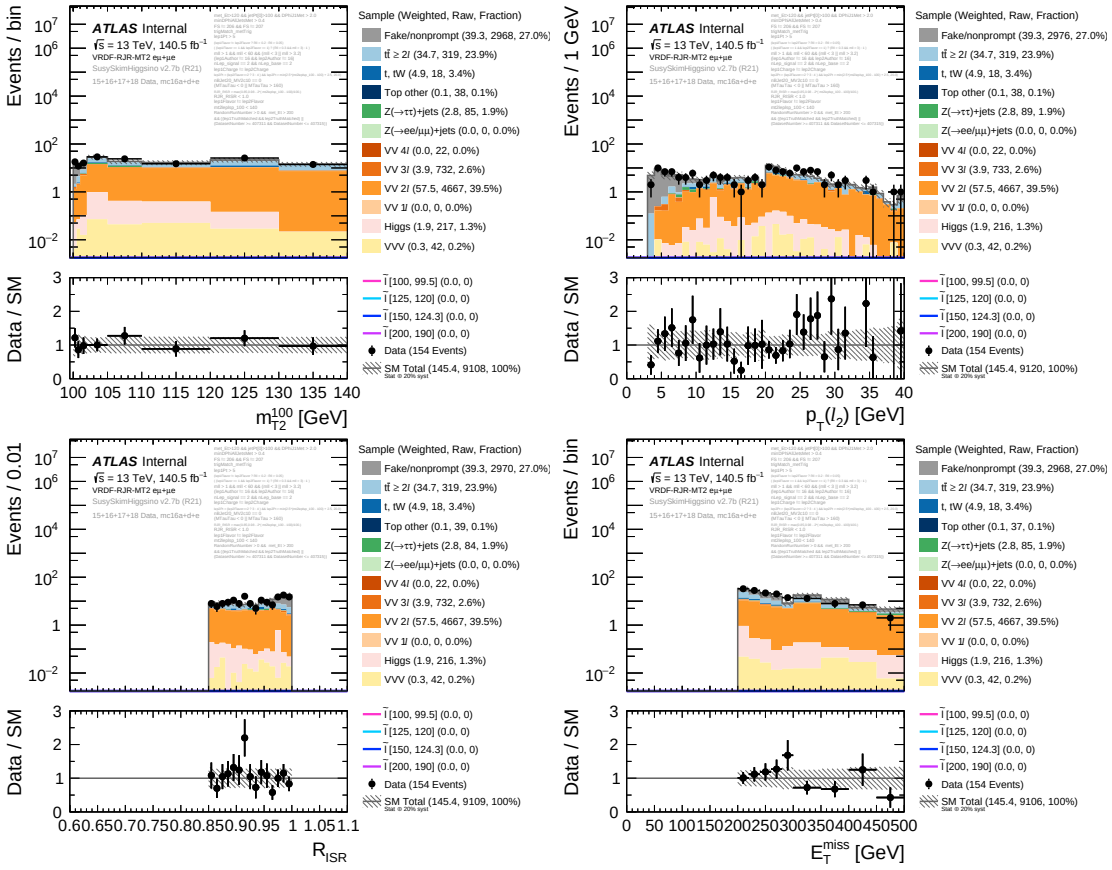

Figure 11.16: Kinematic distributions in VRDF–S–high prior to the application of any normalization factors. The uncertainty band shows the statistical uncertainty added in quadrature with a flat 20% systematic uncertainty.

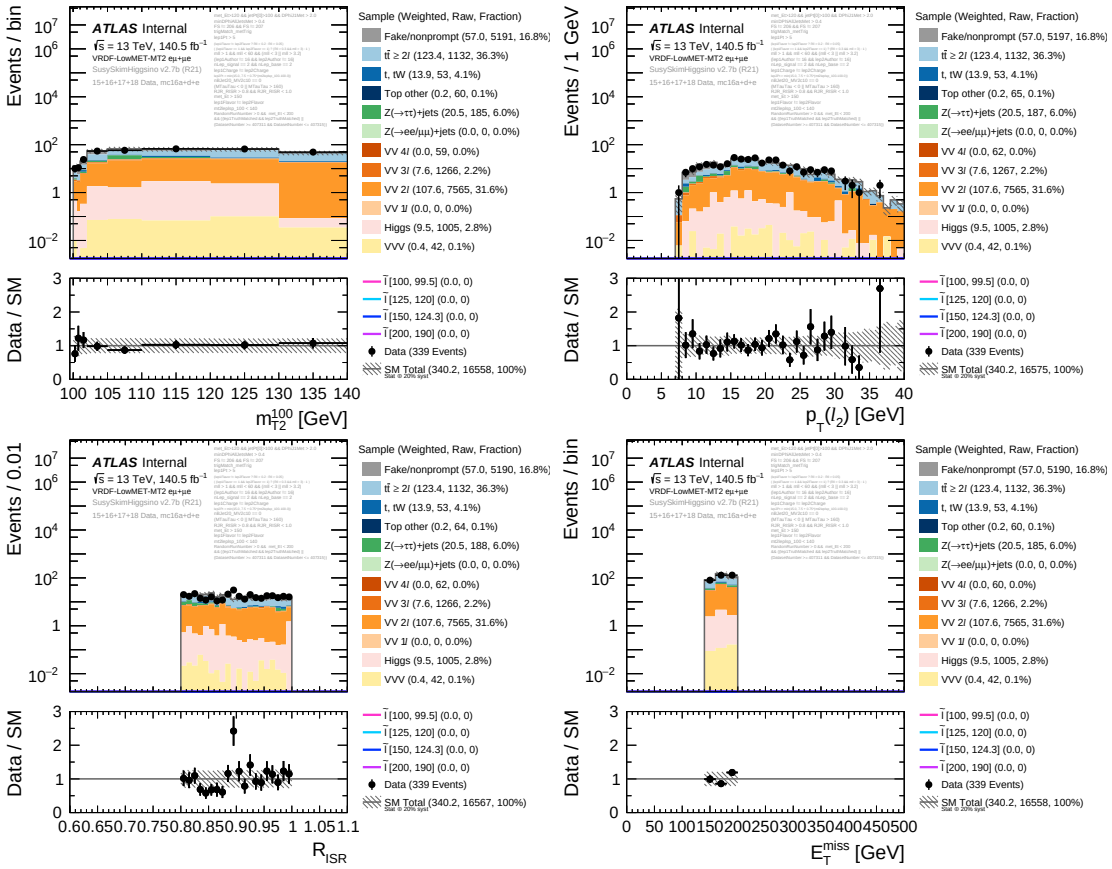

Figure 11.17: Kinematic distributions in VRDF–S–low prior to the application of any normalization factors. The uncertainty band shows the statistical uncertainty added in quadrature with a flat 20% systematic uncertainty.

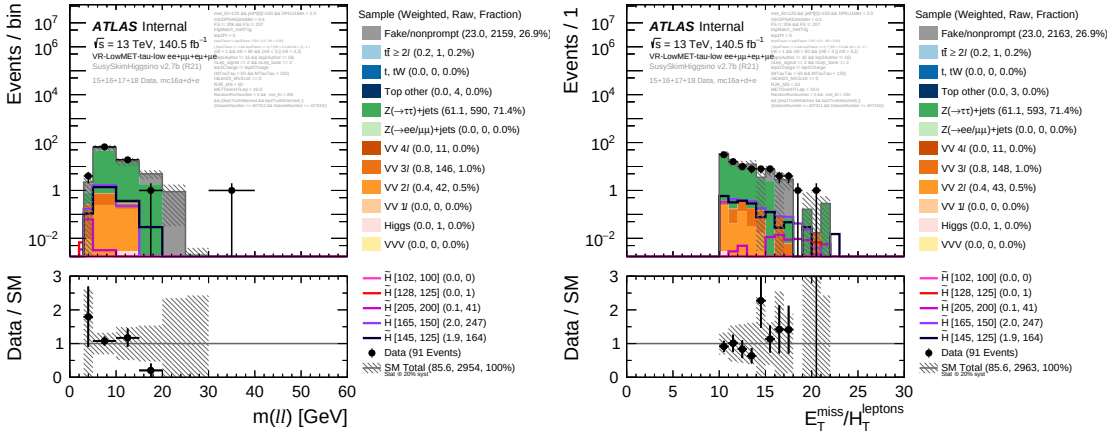

Figure 11.18: Kinematic distributions in VRtau–E–med prior to the application of any normalization factors. The uncertainty band shows the statistical uncertainty added in quadrature with a flat 20% systematic uncertainty.

11.2 Reducible Background: Fake/Non-prompt Leptons

The primary source of reducible background in the searches presented here arises from fake and non-prompt leptons that primarily originate from $W(\rightarrow \ell\nu) + \text{jets}$ events. In this vernacular, fake leptons refer to charged hadrons whose energy deposits in the calorimeters cause them to be misidentified at leptons. Non-prompt leptons, instead, refer to real leptons that are produced in the event but do not originate from the primary interaction (e.g. from prompt W or Z decays). This category includes real leptons originating from semi-leptonic decays of heavy-flavor hadrons, in-flight meson decays, and photon conversions. Since muon reconstruction requires hits in both the ID and MS, the majority of the reducible muon background comes from non-prompt muons produced in these heavy-flavor and meson decays. Electron reconstruction, meanwhile, requires energy deposits in the calorimeters; therefore jets, photon conversions, and semi-leptonic heavy flavor decays all contribute to the overall fake/non-prompt electron background. For both electrons and muons, the fake/non-prompt backgrounds increase sharply at low-p_{T}, exactly where these searches are focused.

In general, though, the identification, isolation, and impact parameter cuts that are applied to signal leptons provide excellent discrimination against these fake/non-prompt backgrounds, with jet suppression at the level of 10^{-5}. On the other hand, the production cross-section for the $W + \text{jets}$ process is many orders of magnitude larger than the signal cross-sections targeted here so that even these otherwise relatively rare backgrounds are expected to make significant contributions to the SRs.

Unfortunately, these backgrounds are not expected to be well-modeled in sim-

ulation, as this would require an excellent understanding of the misidentification rates for each of the fake/non-prompt sources mentioned above. These rates are primarily determined by the non-Gaussian tails of the detector response to jets, the modeling of which is beyond the current level of detail included in simulation of particle reconstruction. Instead, the fake/non-prompt lepton backgrounds are determined using data-driven techniques. The particular data-driven approach chosen for the searches presented here is called the fake factor method. A generic description of this method is given in the next section, followed by a detailed description of the fake/non-prompt background estimation performed for the searches presented here.

11.2.1 The Fake Factor Method

The fake factor method is well-established technique for deriving the fake/non-prompt lepton background in a data-driven way, though it can be generalized to other objects as well (e.g. fake photons). In the context of the searches presented here, the basic principle of the fake factor method is to select a CR enriched in fake/non-prompt leptons and apply extrapolation factors (called fake factors) to estimate this background in the corresponding SR. The kinematic requirements on this CR should be as close as possible to the SR so that the extrapolation only takes place in particle identification space.

To measure the fake factors, two sets of lepton selection criteria called "ID" and "anti-ID" are defined. ID leptons are reconstructed leptons that pass the signal lepton criteria presented in Chapter 9, while "anti-ID" leptons satisfy the baseline lepton requirements but fail at least one of the signal requirements. The anti-ID definition should be chosen in such a way that the anti-ID sample is dominated by fake/non-prompt leptons. Typically, this is done by requiring the anti-ID leptons

to fail some combination of the identification, isolation, and impact parameter requirements that partly define the ID leptons. Using these lepton categories, the fake factor, F, is defined as

$$F(i) = \frac{N_{\text{ID}}(i)}{N_{\text{anti-ID}}(i)}, \tag{11.1}$$

where N_{ID} and $N_{\text{anti-ID}}$ are the number of the ID and anti-ID leptons, respectively. The fake factors are usually measured in different bins of some correlated kinematic variable and so the i in this definition refers to the i^{th} bin of that distribution.

The fake factors should be measured in kinematic regions that are enriched in fake/non-prompt leptons, with a composition similar to what is expected in the SR. While these regions can reach very high levels of purity, some contamination is expected from processes producing prompt leptons. The ID lepton definition is efficient at selecting these prompt leptons by design. The anti-ID selection criteria will also have some non-zero efficiency for selecting prompt leptons, and so the contribution from prompt processes must be subtracted during the fake factor measurement in order to better isolate the contributions to the numerator and denominator of the fake factor from fake/non-prompt leptons. This subtraction is performed using MC estimates of the prompt lepton processes that contaminate the measurement region. Accounting for this subtraction modifies the fake factor definition to be

$$F(i) = \frac{N_{\text{ID}}(i) - N_{\text{ID}}^{\text{MC}}(i)}{N_{\text{anti-ID}}(i) - N_{\text{anti-ID}}^{\text{MC}}(i)}, \tag{11.2}$$

where $N_{\text{ID}}^{\text{MC}}$ and $N_{\text{anti-ID}}^{\text{MC}}$ are the number of ID and anti-ID leptons from prompt lepton processes, respectively, as estimated using MC.

Once the fake factors are measured, they are used to estimate the background

in the SR by scaling events in a CR that is enriched in fake/non-prompt leptons but otherwise kinematically the same as the SR. Since the anti-ID selection criteria is designed to be efficient for fake/non-prompt leptons, this CR is orthogonal to the SR only by requiring at least one anti-ID lepton. This fake/non-prompt enriched CR is therefore called the anti-ID CR. As in the case of the fake factor measurement region, the anti-ID CR is expected to have a small contribution from prompt lepton processes that need to be subtracted using MC estimates. In the simplest case of a SR that requires exactly one signal lepton, the fake/non-prompt lepton contribution to the SR, $N^{\text{SR}}_{\text{reducible}}$, is given by

$$N^{\text{SR}}_{\text{reducible}} = \sum_i \left(N_{\text{anti-ID CR}}(i) - N^{\text{MC}}_{\text{anti-ID CR}}(i) \right) \cdot F(i), \tag{11.3}$$

where $N_{\text{anti-ID CR}}(i)$ is the number of events in the i^{th} bin of the anti-ID CR and $N^{\text{MC}}_{\text{anti-ID CR}}(i)$ is the number of events in the same bin due to prompt lepton processes. Again, the sum runs over the bins in the kinematic distribution in which the fake factors are measured.

In the searches presented here, though, the SRs target di-lepton final states. This complicates the estimate since it is possible for events containing two fake/non-prompt leptons to enter the SRs, which needs to be accounted for in the background estimation. It can be shown (see [117], for example) that a proper treatment of the fake factor method in di-lepton events results in a fake/non-prompt lepton estimate given by

$$N^{\text{SR}}_{\text{reducible}} = F_1 \left(N_{\text{AI}} - N^{\text{MC}}_{\text{AI}} \right) + F_2 \left(N_{\text{IA}} - N^{\text{MC}}_{\text{IA}} \right) - F_1 F_2 \left(N_{\text{AA}} - N^{\text{MC}}_{\text{AA}} \right), \tag{11.4}$$

where N indicates the number of events in the anti-ID control region and its subscripts indicate whether the leptons pass the ID (I) or anti-ID (A) criteria.

These subscripts are also ordered such that the first subscript corresponds to the lepton with the largest p_{T}. For example, N_{AI} is the number of events in the anti-ID CR where the highest-p_{T} lepton is an anti-ID lepton and the softer lepton is an ID lepton. Terms with an "MC" superscript indicate the contributions from prompt lepton processes that are estimated using MC and subtracted in order to better isolate the fake/non-prompt lepton contribution. Finally, F_1 and F_2 correspond to the fake factors of the harder and softer lepton in the event, respectively. Note that the minus sign in the last term serves to correct for the double-counting of events with two fake/non-prompt leptons, since these can contribute to both the N_{IA} and N_{AI} terms.

An important assumption of the fake factor method in di-lepton events is that the leptons can be thought of as uncorrelated objects. Specifically, it does not account for situations in which the leptons are so collimated that their isolation cones (or even their showers, in the case of electrons) overlap and become highly correlated. Since the signal isolation requirement is often inverted in the anti-ID lepton definition, if one of the leptons in these highly-collimated events is an anti-ID lepton, then the other lepton has a higher probability of being one as well. This leads to a larger fraction of events containing two anti-ID leptons when the angular separation is small, resulting in over-subtraction according to Equation 11.4. Left unchecked, the fake factor method will therefore systematically underestimate the fake/non-prompt lepton background at low values of $\Delta R_{\ell\ell}$ (and equivalently, low-$m_{\ell\ell}$), which would severely limit the ability to search for the most compressed electroweakino signals considered targeted in this dissertation. One solution could be to drop the inverted isolation requirement from the anti-ID lepton definition, but this results in a large drop in anti-ID CR statistics that make the fake/non-prompt estimation unreliable. Instead, a new isolation algorithm was developed,

as described in Section 9.2.3, in order to break the correlation between overlapping isolation cones and avoid over-subtraction.

11.2.2 Fake Factor Measurement Regions

Since the fake/non-prompt lepton background in this analysis is primarily due to $W(\to \ell\nu) + \text{jets}$ events, the fake factors would ideally be measured in a region of the data dominated by this process. Unfortunately, $W(\to \ell\nu) + \text{jets}$ events have very similar topologies to other processes with large cross-sections (including $t\bar{t}$, for example) that make it difficult to construct a measurement region with sufficient purity. Instead, the fake factors are measured in dijet events firing low-p_{T}, prescaled single-lepton triggers. At the cost of being less topologically similar to the SRs, such events provide a rather pure sample of fake/non-prompt leptons, with small contributions from both $t\bar{t}$ and $W + \text{jets}$ that are eventually subtracted off using MC. The prescaled single-lepton triggers used for measuring the electron and muon fake factors are listed according to the year of data-taking in Table 11.3, with p_{T} thresholds ranging from 5–20 GeV for electrons and 4–18 GeV for muons. In each case, the trigger-level requirements on the lepton identification quality are kept looser than those used to define the anti-ID leptons in order to avoid a bias in the fake factors. When measuring the fake factors, the trigger prescales are used to unfold the kinematic distributions of the ID and anti-ID leptons. which are defined in the following sections.

Events entering the fake factor measurement regions are required to contain a single ID or anti-ID lepton, a jet with $p_{\mathrm{T}} > 100\,\mathrm{GeV}$, and $m_{\mathrm{T}}^{\ell_1} < 40\,\mathrm{GeV}$. The ID or anti-ID lepton must have a p_{T} that is consistent with the single-lepton trigger that fired and events firing multiple triggers are vetoed to avoid significant complications that would arise when applying the prescales. The hard jet requirement

Table 11.3: Prescaled single-lepton triggers used to compute the fake factors, broken down by year of data-taking. Trigger names starting with "`HLT_eX`" are single-electron triggers and those starting with "`HLT_muX`" are single-muon triggers, where the "`X`" refers to the specific lepton p_{T} threshold. The "`lhvloose`" in the electron trigger names indicates that the `VeryLoose` identification requirement is applied at trigger-level.

2015 and 2016	2017	2018
HLT_e5_lhvloose	HLT_e5_lhvloose_nod0	HLT_e5_lhvloose_nod0
HLT_e10_lhvloose_L1EM7	HLT_e12_lhvloose_nod0_L1EM10VH	HLT_e10_lhvloose_nod0_L1EM7
HLT_e15_lhvloose_L1EM13VH	HLT_e17_lhvloose_nod0	HLT_e15_lhvloose_nod0_L1EM7
HLT_e20_lhvloose	HLT_e20_lhvloose_nod0	HLT_e20_lhvloose_nod0
HLT_mu4	HLT_mu4	HLT_mu4
HLT_mu10	HLT_mu10_idperf	HLT_mu10_idperf
HLT_mu14	HLT_mu14	HLT_mu14
HLT_mu18		

is in place in order to make the measurement region more kinematically similar to the SRs, while the $m_{\mathrm{T}}^{\ell_1}$ requirement serves to suppress contributions from the $t\bar{t}$ and $W+\text{jets}$ processes. These processes are normalized to the data in a region with $m_{\mathrm{T}}^{\ell_1} > 100\,\mathrm{GeV}$ that is dominated by prompt lepton processes before any subtraction is performed. In contrast to the electron fake factor measurement region, requirements on the muon-jet overlap removal are relaxed in order to have sufficient statistics when measuring the muon fake factors. Finally, separate measurement regions for both the electron and muon fake factors are constructed based on the number of b-tagged jets in the event in order to account for any jet flavor-dependence. Specifically, events are categorized as containing exactly zero or at least one b-tagged jet and dedicated fake factors are measured in each of these bins. Practically speaking, the fake factors that are measured in events with $N_{b-\mathrm{jet}}^{20} > 0$ are only used to estimate the fake/non-prompt lepton background in the CRtop regions.

11.2.3 Electron Fake Factors

When measuring the electron fake factors, ID electrons are defined to be identical to the signal electrons described in Section 9.2.1. The ID electrons, therefore, are required to be baseline electrons that also pass the `MediumLLH` identification working point, the `Gradient` isolation working point, and have $|d_0/\sigma(d_0)| < 5.0$. Anti-ID electrons, on the other hand, are required to pass an identification working point called `LooseAndBLayer`, which is tighter than the baseline lepton requirement but looser than the requirement for signal leptons. Additionally, anti-ID electrons must fail some combination of the signal identification, isolation, and impact parameter requirements, but are not allowed to fail identification and isolation requirements simultaneously. While reducing the available statistics in the anti-ID electron CR, the decision to not allow all failure modes was made in order to reduce the extrapolation from anti-ID to ID electrons. This definition was also seen to give better closure in the VRSS regions and has little impact on the fake factor statistical uncertainties since they are dominated by the available ID lepton statistics in the measurement region. A summary of the anti-ID electron definition is given in Table 11.4. Additionally, the composition of electrons in the measurement region failing at least one of the identification, isolation, and $|d_0/\sigma(d_0)|$ requirements is shown as a function of several observables in Figure 11.19 and Figure 11.20.

Events from $t\bar{t}$ and $W+$jets processes that enter the fake factor measurement regions are taken from directly from MC and are normalized to the data in a region with $m_{\mathrm{T}}^{\ell_1} > 100\,\mathrm{GeV}$. This rescaling of the prompt lepton background processes is performed separately for ID and anti-ID electrons, as well as for the $N_{b-\mathrm{jet}}^{20} = 0$ and $N_{b-\mathrm{jet}}^{20} > 0$ regions. For events with $N_{b-\mathrm{jet}}^{20} = 0$, the normalization factor for ID electrons is 1.42 ± 0.04 and 6.14 ± 0.44 for anti-ID electrons. For events with

Table 11.4: Summary of the anti-ID electron definition. Anti-ID electrons must fail at least one of the identification, isolation, or $|d_0/\sigma(d_0)|$ requirements applied to signal electrons, but are not allowed to fail the isolation and identification requirements simultaneously.

Anti-ID Electrons
$p_{\mathrm{T}} > 4.5\,\mathrm{GeV}$
$\lvert\eta\rvert < 2.47$
$\lvert z_0 \sin\theta\rvert < 0.5$ mm
Pass `LooseAndBLayer` identification
(Fail `Medium` identification OR fail `Gradient` isolation OR $\lvert d_0/\sigma(d_0)\rvert > 5.0$) AND (pass `Medium` identification OR pass `Gradient` isolation)

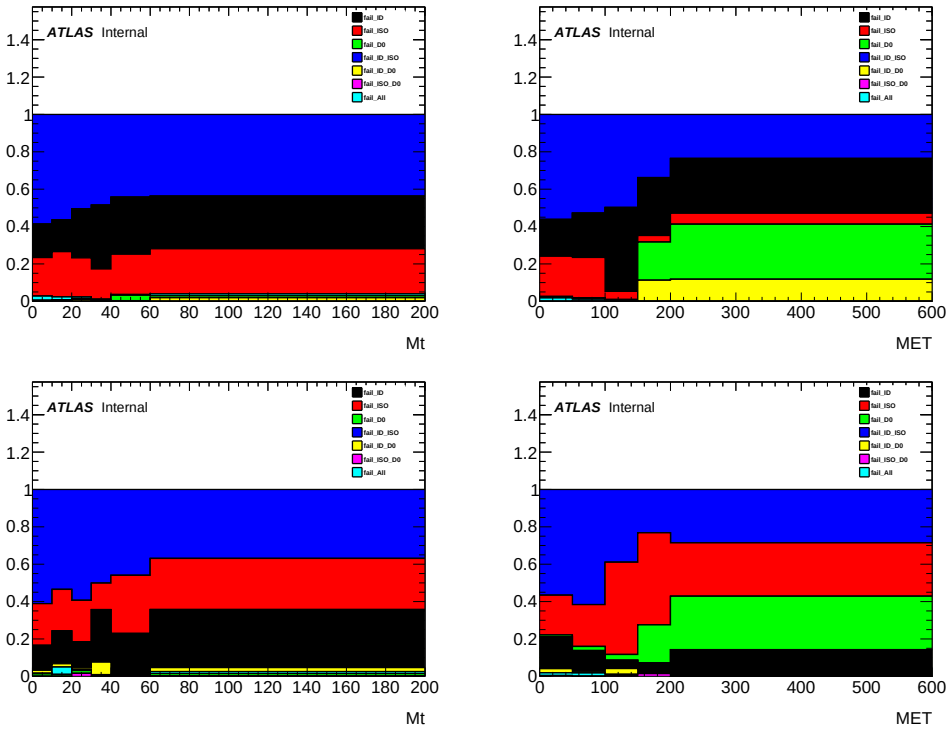

Figure 11.19: Anti-ID electron composition in events with exactly zero b-tagged jets (top) and one or more b-tagged jets (bottom) as a function of $m_{\mathrm{T}}^{\ell_1}$ (left) and as a function of $E_{\mathrm{T}}^{\mathrm{miss}}$ (right). The $E_{\mathrm{T}}^{\mathrm{miss}}$ distribution corresponds to events with $m_{\mathrm{T}}^{\ell_1} < 40$ GeV. Note that electrons failing both the isolation and identification working points are not considered anti-ID electrons.

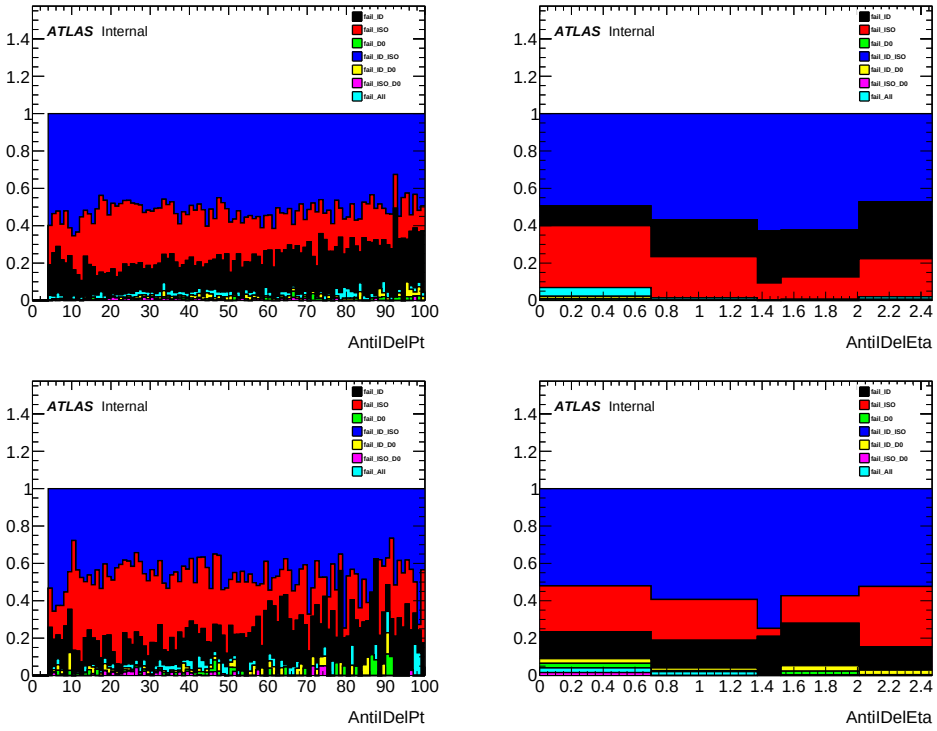

Figure 11.20: Anti-ID electron composition in events with exactly zero b-tagged jets (top) and one or more b-tagged jets (bottom) as a function of p_{T} (left) and as a function of η (right). Only events with $m_{\mathrm{T}}^{\ell_1} < 40$ GeV are shown. Note that electrons failing both the isolation and identification working points are not considered anti-ID electrons.

$N^{20}_{b-\text{jet}} > 0$, the extracted normalization factors are 1.13 ± 0.04 and 2.54 ± 0.22 for ID and anti-ID electrons, respectively. If the MC is instead rescaled to the data in a region with $E_{\text{T}}^{\text{miss}} > 200\,\text{GeV}$, also thought to be dominated by processes involving prompt lepton production, these normalization factors become 2.30 ± 0.19 and 1.38 ± 0.30 for ID and anti-ID electrons in events with $N^{20}_{b-\text{jet}} = 0$. For events containing at least one b-tagged jet, the new ID and anti-ID electron normalization factors obtained are 0.91 ± 0.09 and 0.85 ± 0.31. While the normalization factors themselves appear to show a large dependence on the chosen normalization region, the impact on the fake factors themselves is small since these prompt processes contribute relatively little to the fake factor measurement regions. The $m_{\text{T}}^{\ell_1}$ distributions for ID and anti-ID electrons are shown in Figure 11.21, where the MC has been scaled to match the data in the $m_{\text{T}}^{\ell_1} > 100\,\text{GeV}$ regions and the fake factor measurement regions reside in the $m_{\text{T}}^{\ell_1} < 40\,\text{GeV}$ part of the distributions.

Ultimately, the fake factors are measured and applied as a function of the lepton p_{T} such that the fake factor, F, corresponding to a some p_{T} bin is given by

$$F = \frac{N_{\text{data}}^{\text{ID}} - N_{\text{MC}}^{\text{ID}}}{N_{\text{data}}^{\text{anti-ID}} - N_{\text{MC}}^{\text{anti-ID}}} \tag{11.5}$$

where $N_{\text{data}}^{\text{ID}}$ and $N_{\text{data}}^{\text{anti-ID}}$ are the number of ID and anti-ID electrons in data, respectively, and $N_{\text{MC}}^{\text{ID}}$ and $N_{\text{MC}}^{\text{anti-ID}}$ are the number of ID and anti-ID electrons from prompt lepton processes modeled by MC. These distributions are shown in Figure 11.22 and Figure 11.23 for events with $N^{20}_{b-\text{jet}} = 0$ and $N^{20}_{b-\text{jet}} > 0$, respectively, before the final binning in lepton p_{T} is applied.

Unfortunately, no single-electron triggers exist in ATLAS with p_{T} thresholds lower than 5 GeV, eliminating the possibility of using the above methodology to measure fake factors for electrons with $p_{\text{T}} < 5\,\text{GeV}$. Instead, the ID and anti-ID p_{T} distributions are extrapolated below 5 GeV and the ratios of the ID

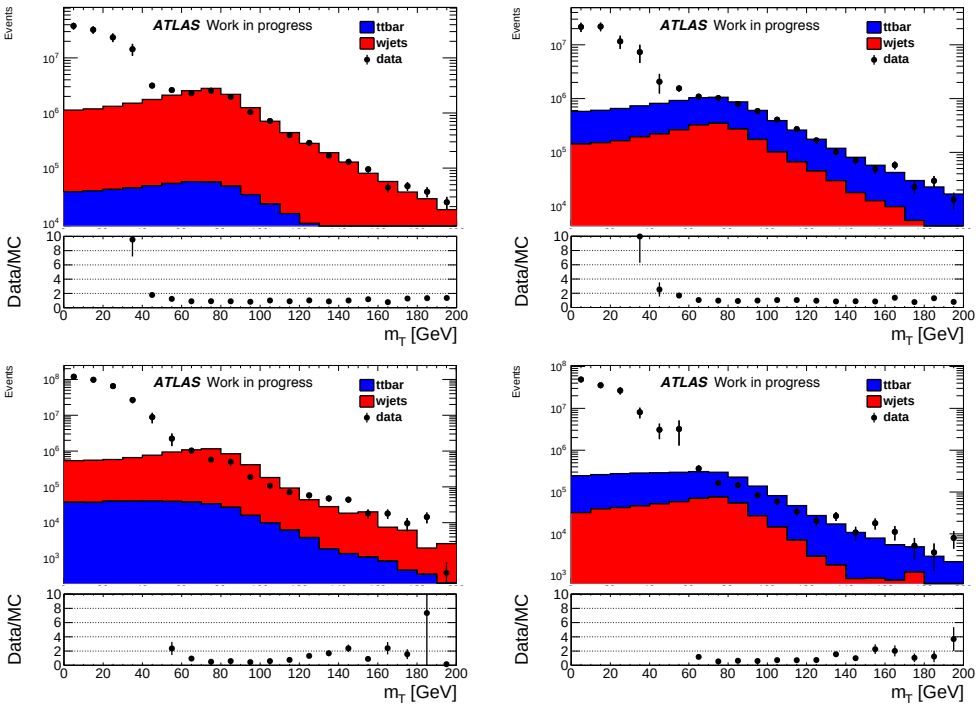

Figure 11.21: The $m_{\mathrm{T}}^{\ell_1}$ distributions for ID (top) and anti-ID (bottom) electrons in the fake factor measurement region for events with exactly zero b-tagged jets (left) and at least one b-tagged jet (right). The MC contributions have been scaled to the data in the $m_{\mathrm{T}}^{\ell_1} > 100$ GeV region.

and anti-ID extrapolations are used to derive fake factors for the electrons with $4.5\,\mathrm{GeV} < p_{\mathrm{T}} < 5\,\mathrm{GeV}$. These extrapolations are derived from exponential fits to the p_{T} distributions with fit ranges that are chosen to mitigate biases from trigger turn-on effects. Specifically, the fits, as shown in Figure 11.24, are performed from 6 GeV to 10 GeV in order to avoid the turn-on effect from the 5 GeV triggers and any discontinuity from the transition to the 10 GeV triggers. In order to be conservative, the uncertainty on the extrapolated fake factor is chosen to be the statistical uncertainty of the lowest directly-measured fake factor (i.e. from 5-6 GeV) added in quadrature with the uncertainty from the fit.

The electron fake factors used in this search, which include the extrapolation below 5 GeV are shown in Figure 11.25. Due to the large prescales applied to

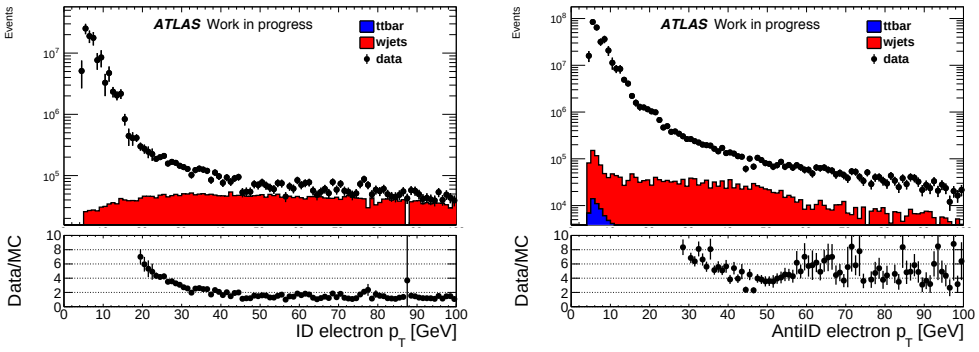

Figure 11.22: The p_{T} distributions for ID (left) and anti-ID (right) electrons in the fake factor measurement region with $N^{20}_{b-\mathrm{jet}} = 0$. Contributions from processes involving prompt leptons are modeled by MC and are rescaled to the data in the $m^{\ell_1}_{\mathrm{T}} > 100$ GeV region.

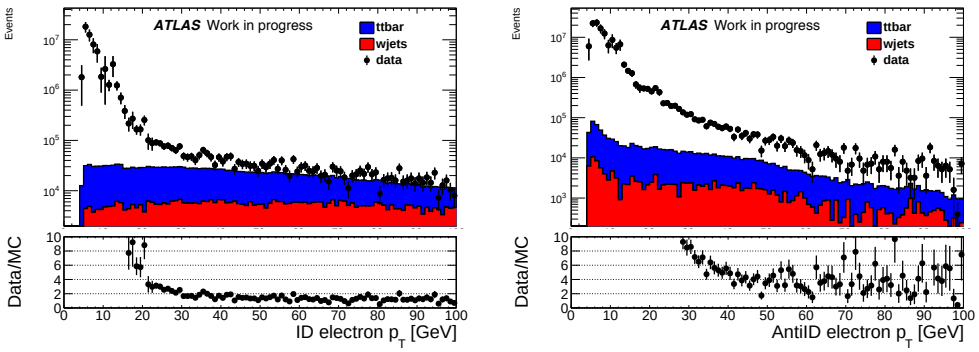

Figure 11.23: The p_{T} distributions for ID (left) and anti-ID (right) electrons in the fake factor measurement region with $N^{20}_{b-\mathrm{jet}} > 0$. Contributions from processes involving prompt leptons are modeled by MC and are rescaled to the data in the $m^{\ell_1}_{\mathrm{T}} > 100$ GeV region.

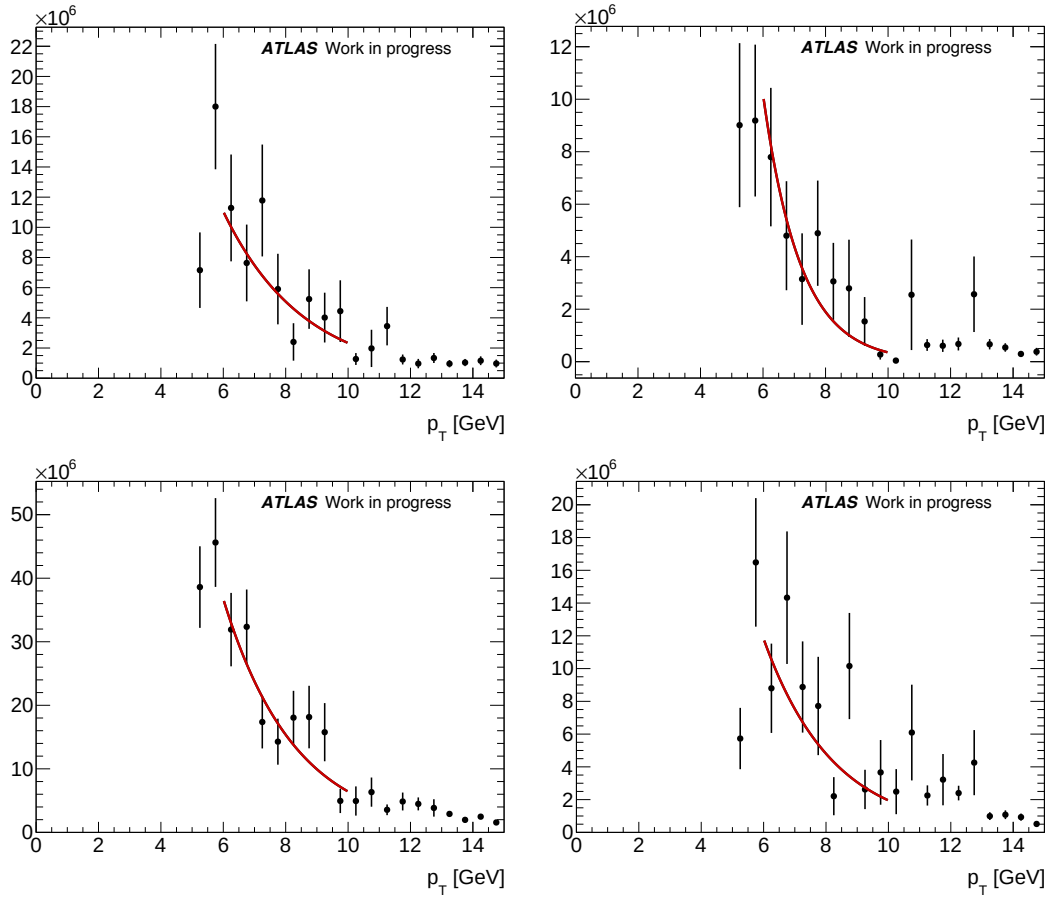

Figure 11.24: Exponential fits to the ID (top) and anti-ID (bottom) electron p_{T} distributions used for the fake factor extrapolation. Events with exactly zero b-tagged jets are shown on the left, while events with at least one b-tagged jet are shown on the right.

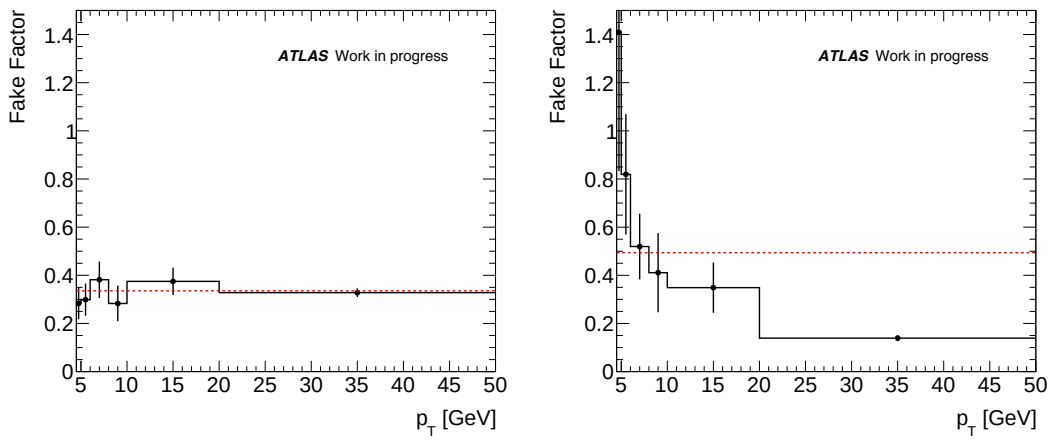

Figure 11.25: Electron fake factors as a function of electron p_{T} for events with zero b-tagged jets (left) and at least one b-tagged jet (right). A red line denotes the average electron fake factor over all electron p_{T} values.

the low-p_{T} single-lepton triggers, the data sample in the fake factor measurement region is too small to allow for the fake factors to be binned in several observables without acquiring very large statistical uncertainties. Nonetheless, the fake factors are measured as a function of other kinematic variables to check for additional dependencies that can be used to derive systematic uncertainties based on the choice of parameterization. This issue is discussed in more detail in Section 12.2. Figures 11.26–11.28 show the fake factors as a function of other observables in order to check for strong dependencies.

11.2.4 Muon Fake Factors

The strategy for computing the muon fake factors is completely analogous to the electron case. ID muons are defined to be identical to the signal muons described in Section 9.2.2. Specifically, ID muons are baseline muons that also pass the `FCTightTrackOnly` isolation working point and have $|d_0/\sigma(d_0)| < 3.0$. Anti-ID muons, as summarized in Table 11.5, are instead defined to be baseline muons that fail exactly one of these additional requirements. Again, this choice

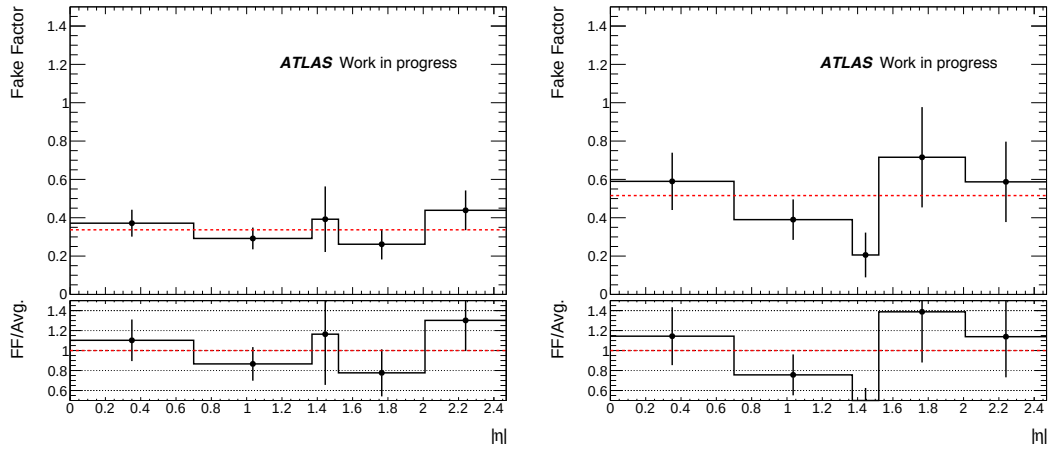

Figure 11.26: Electron fake factors as a function of electron $|\eta|$ for events with zero b-tagged jets (left) and at least one b-tagged jet (right). A red line denotes the average electron fake factor.

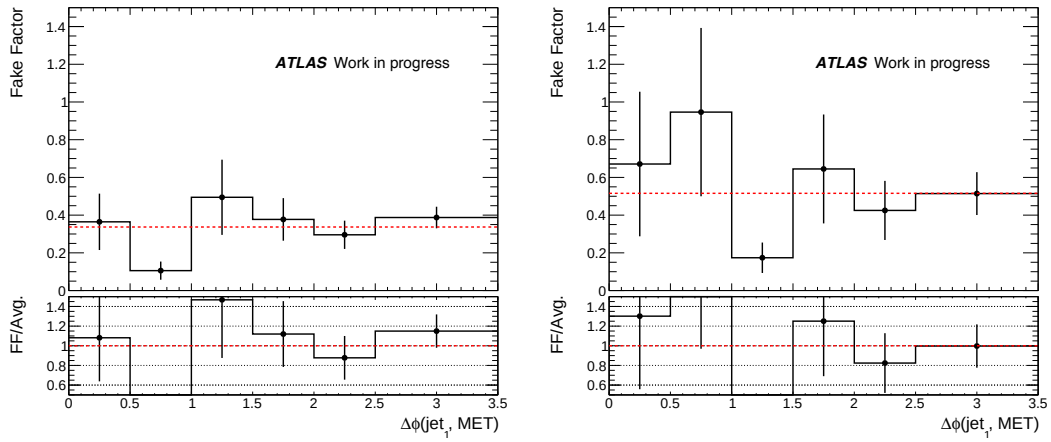

Figure 11.27: Electron fake factors as a function of $\Delta\phi(j_1, \mathbf{p}_{\mathrm{T}}^{\mathrm{miss}})$ for events with zero b-tagged jets (left) and at least one b-tagged jet (right). A red line denotes the average electron fake factor.

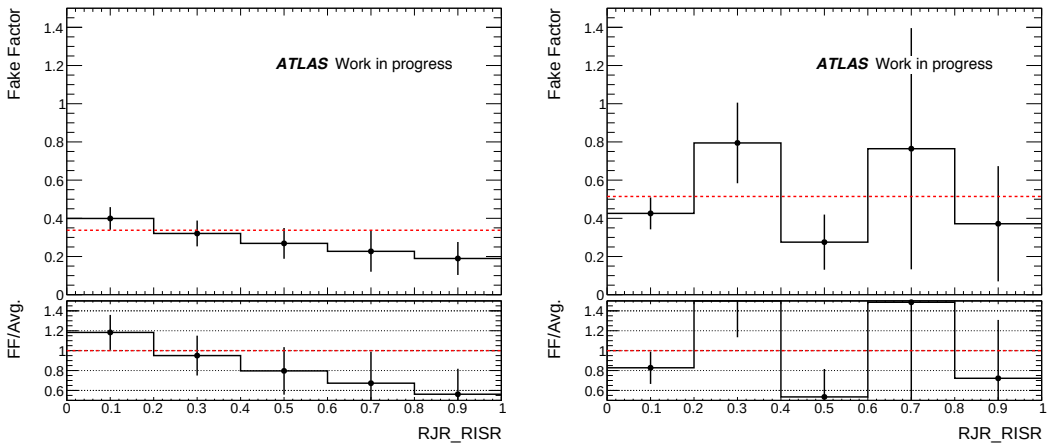

Figure 11.28: Electron fake factors as a function of R_{ISR} for events with zero b-tagged jets (left) and at least one b-tagged jet (right). A red line denotes the average electron fake factor.

Table 11.5: Summary of the anti-ID muon definition. Anti-ID muons must fail exactly one of the isolation and $|d_0/\sigma(d_0)|$ requirements applied to signal muons.

Anti-ID Muons
$p_{\mathrm{T}} > 3\,\mathrm{GeV}$
$\lvert\eta\rvert < 2.5$
$\lvert z_0 \sin\theta\rvert < 0.5$ mm
Pass `LowPt` identification
(Fail `FCTightTrackOnly` isolation OR $\lvert d_0/\sigma(d_0)\rvert > 3.0$)
AND (pass `FCTightTrackOnly` isolation OR $\lvert d_0/\sigma(d_0)\rvert < 3.0$)

reduces the anti-ID CR statistics but also reduces the extrapolation from anti-ID to ID muons and has little impact on the fake factor statistical uncertainties. The composition of muons in the measurement region failing at least one of the isolation or $|d_0/\sigma(d_0)|$ requirements is shown as a function of several observables in Figure 11.29 and Figure 11.30.

The $t\bar{t}$ and $W+\mathrm{jets}$ processes that produce real leptons contaminate can also contaminate the muon fake factor measurement regions and need to be subtracted using MC during the fake factor calculation. Before the subtraction, these simulated events are rescaled to match the data in the $m_{\mathrm{T}}^{\ell_1} > 100\,\mathrm{GeV}$ region where the

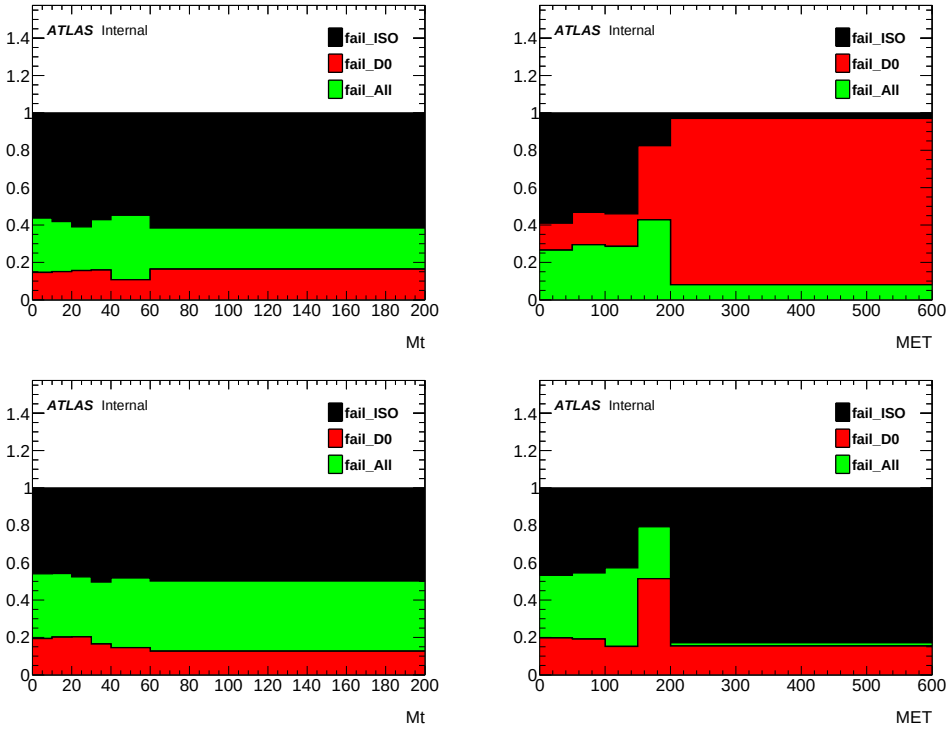

Figure 11.29: Anti-ID muon composition in events with exactly zero b-tagged jets (top) and one or more b-tagged jets (bottom) as a function of $m_{\mathrm{T}}^{\ell_1}$ (left) and as a function of $E_{\mathrm{T}}^{\mathrm{miss}}$ (right). The $E_{\mathrm{T}}^{\mathrm{miss}}$ distribution corresponds to events with $m_{\mathrm{T}}^{\ell_1} < 40$ GeV. Note that muons failing both isolation and d_0 significance are not considered anti-ID muons.

fake/non-prompt lepton contribution is expected to be small. The extracted normalization factors in events with zero b-tagged jets are 1.32 ± 0.05 and 3.62 ± 0.7 for ID and anti-ID muons, respectively. When requiring at least one b-tagged jet, the ID muon normalization factor is 1.10 ± 0.05 and the anti-ID muon normalization factor is 2.90 ± 0.46. Again, the effect of the choice of normalization region is tested by re-deriving these factors using a region requiring $E_{\mathrm{T}}^{\mathrm{miss}} > 200\,\mathrm{GeV}$. In doing so, the normalization factor for ID muons becomes 3.74 ± 0.76 in events with zero b-tagged jets and 1.42 ± 0.19 in events with at least one. The anti-ID muon normalization factors extracted from this high-$E_{\mathrm{T}}^{\mathrm{miss}}$ region are 6.09 ± 3.91 and 1.58 ± 1.76 for events with zero and at least one b-tagged jet, respectively.

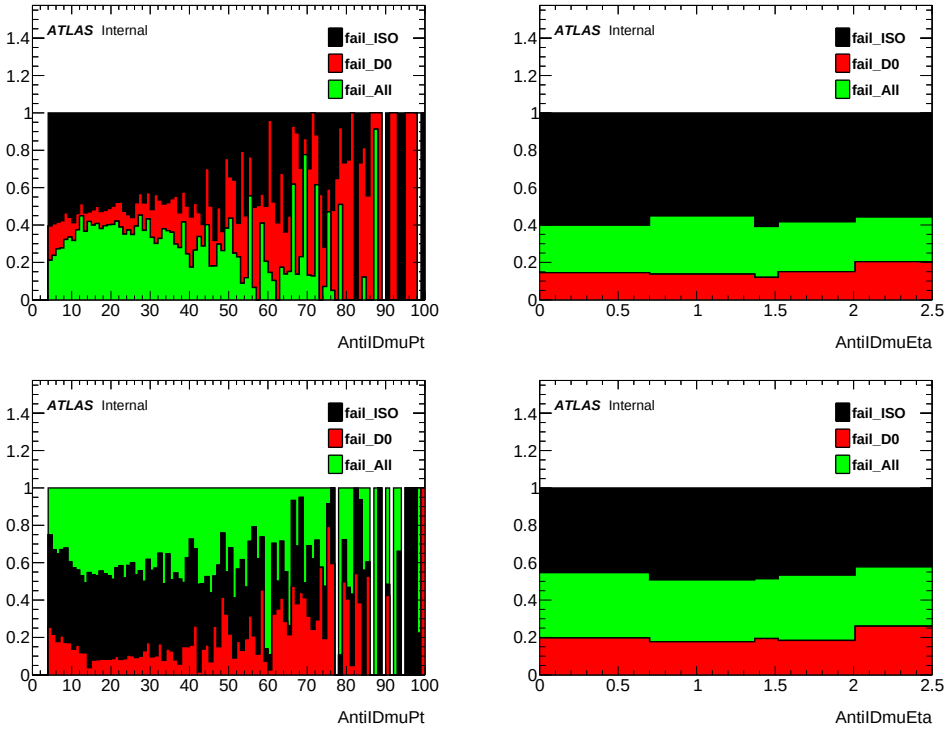

Figure 11.30: Anti-ID muon composition in events with exactly zero b-tagged jets (top) and one or more b-tagged jets (bottom) as a function of p_{T} (left) and as a function of η (right). Only events with $m_{\mathrm{T}}^{\ell_1} < 40$ GeV are shown. Note that muons failing both isolation and d_0 significance are not considered anti-ID muons.

Since the $t\bar{t}$ and W + jets processes provide only a small fraction of the overall contribution to the fake factor measurement regions, the change in the muon fake factors due to choice of normalization region is small compared to the statistical uncertainties themselves. After the normalizing the $t\bar{t}$ and W + jets contributions, the p_{T} distributions for ID and anti-ID muons are shown in Figure 11.32 for events with $N_{b-\mathrm{jet}}^{20} = 0$ and in Figure 11.33 for events with $N_{b-\mathrm{jet}}^{20} > 0$.

Similar to the electron case, the use of single-muon triggers prohibits the direct measurement of fake factors for muons with $p_{\mathrm{T}} < 4\,\mathrm{GeV}$ since no such triggers exist with p_{T} thresholds below 4 GeV. Since this search utilizes with muons transverse momenta as low as 3 GeV, the ID and anti-ID muon p_{T} distributions are extrapolated down to 3 GeV in order to derive these fake factors. Again, these

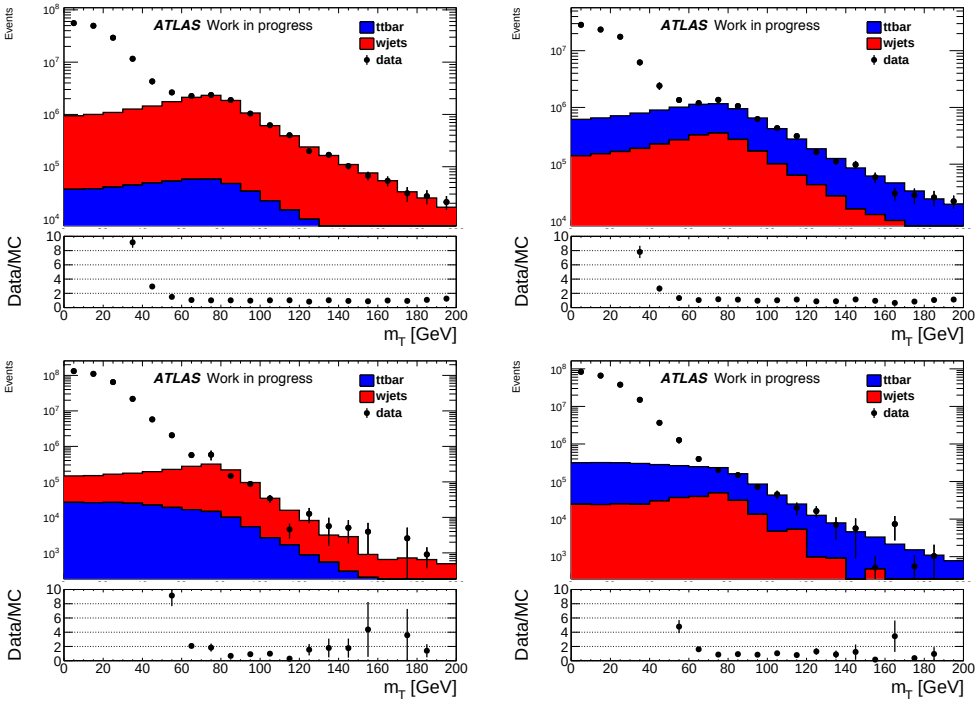

Figure 11.31: The $m_{\mathrm{T}}^{\ell_1}$ distributions for ID (top) and anti-ID (bottom) muons in the fake factor measurement region for events with exactly zero b-tagged jets (left) and at least one b-tagged jet (right). The MC contributions have been scaled to match the data in the $m_{\mathrm{T}}^{\ell_1} > 100$ GeV region.

distributions are fit using a simple exponential function, where the fit range now runs from 4.5 GeV to 10 GeV in order to avoid the trigger turn-on at 4 GeV and the transition to a different trigger at 10 GeV, which can bias the fits. These fit results are shown in Figure 11.34 for both b-tagged jet multiplicity bins. The statistical uncertainty on the extrapolated fake factor for muons with $3\,\mathrm{GeV} < p_{\mathrm{T}} < 4\,\mathrm{GeV}$ is conservatively set to be the uncertainty from the fit added in quadrature with the statistical uncertainty on the nearest directly-measurable fake factor (in this case corresponding to $4\,\mathrm{GeV} < p_{\mathrm{T}} < 5\,\mathrm{GeV}$.

In this search, the muon fake factors are applied as a function of the muon p_{T}. These fake factors, including the extrapolation, are presented in Figure 11.35. The fake factors are also checked as a function of other observables for other significant

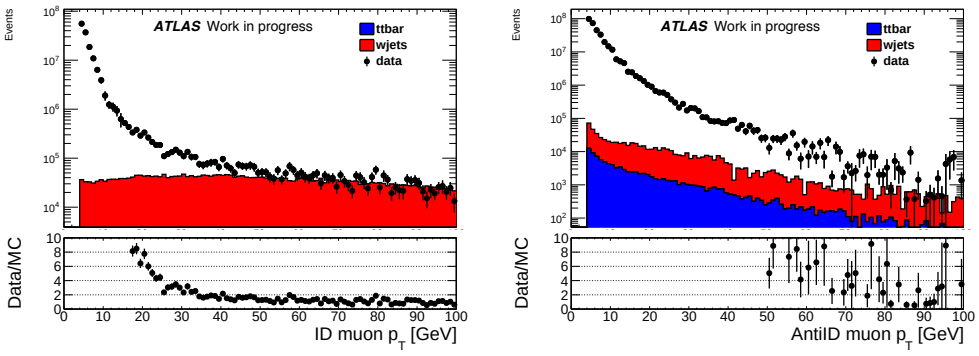

Figure 11.32: The p_{T} distributions for ID (left) and anti-ID (right) muons in the fake factor measurement region with $N^{20}_{b-\mathrm{jet}} = 0$. Contributions from processes involving prompt leptons are modeled by MC and are rescaled to the data in the $m^{\ell_1}_{\mathrm{T}} > 100$ GeV region.

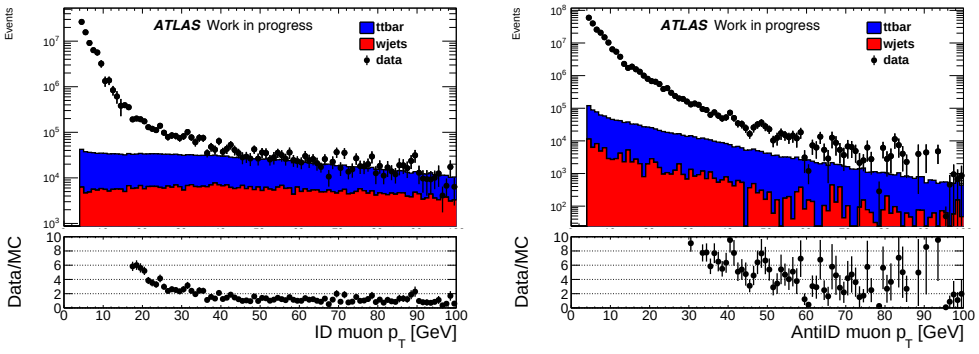

Figure 11.33: The p_{T} distributions for ID (left) and anti-ID (right) muons in the fake factor measurement region with $N^{20}_{b-\mathrm{jet}} > 0$. Contributions from processes involving prompt leptons are modeled by MC and are rescaled to the data in the $m^{\ell_1}_{\mathrm{T}} > 100$ GeV region.

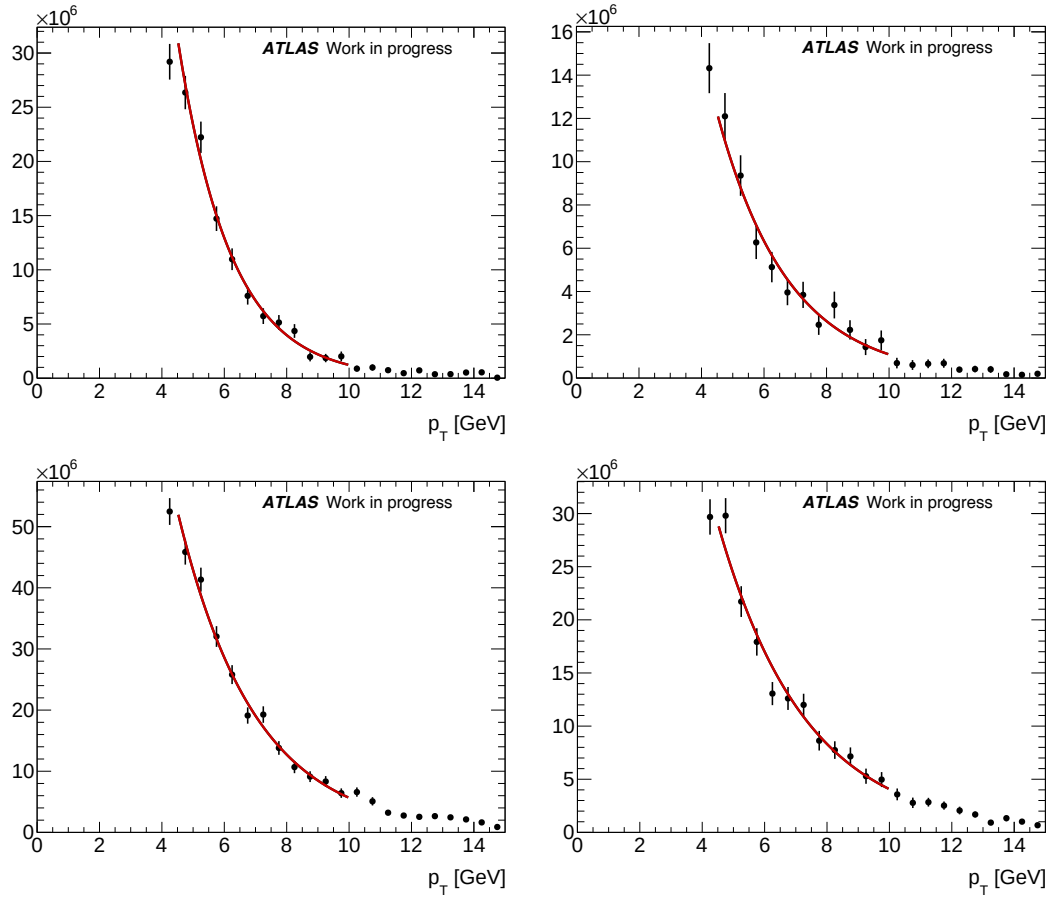

Figure 11.34: Exponential fits to the ID (top) and anti-ID (bottom) muon p_{T} distributions used for the fake factor extrapolation. Events with exactly zero b-tagged jets are shown on the left, while events with at least one b-tagged jet are shown on the right.

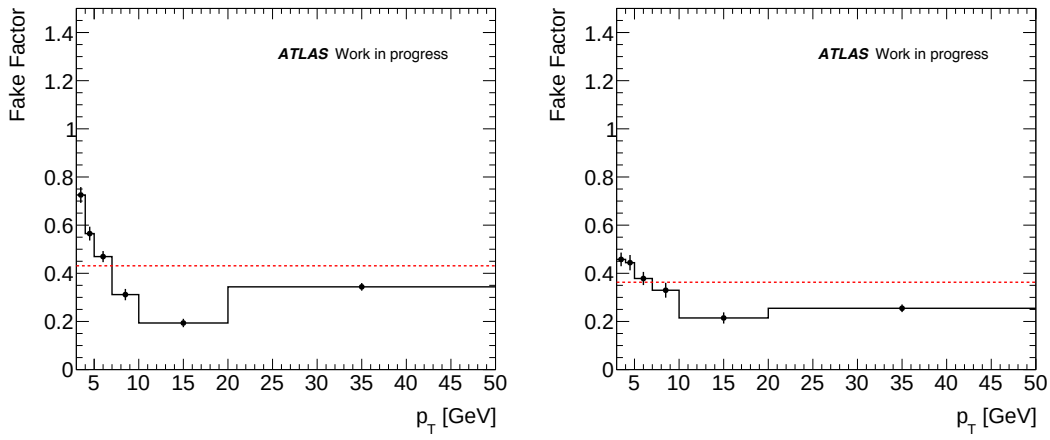

Figure 11.35: Muon fake factors as a function of muon p_{T} for events with zero b-tagged jets (left) and at least one b-tagged jet (right). A red line denotes the average muon fake factor over all muon p_{T}.

dependencies that are later used to derive a flat systematic uncertainty on the fake factors themselves. Figures 11.36–11.38 show such distributions.

11.2.5 Fake/Non-Prompt Lepton Background Validation

The VRSS regions defined in Table 11.1 and Table 11.2 are used to validate the modeling of the fake/non-prompt lepton background. Within these same-sign regions, the subleading lepton is treated as a proxy for the fake/non-prompt lepton. Therefore, events in which the subleading lepton is an electron (denoted $ee + \mu e$) are used to assess the modeling of the fake/non-prompt electron background. Similarly, events in which a muon is the subleading lepton ($\mu\mu + e\mu$) are used to validate the fake/non-prompt muon background. With respect to the SRs, the VRSS regions also relax some of the kinematic requirements in order to increase the available statistics. Most notably, the cuts on the subleading lepton p_{T} are removed since these are designed to suppress the fake/non-prompt lepton background. The pre-fit distributions of $m_{\ell\ell}$ and $p_{\mathrm{T}}^{\ell_2}$ are presented in Figures 11.39–11.41 for VRSS–E–high, VRSS–E–med, and VRSS–E–low, with each

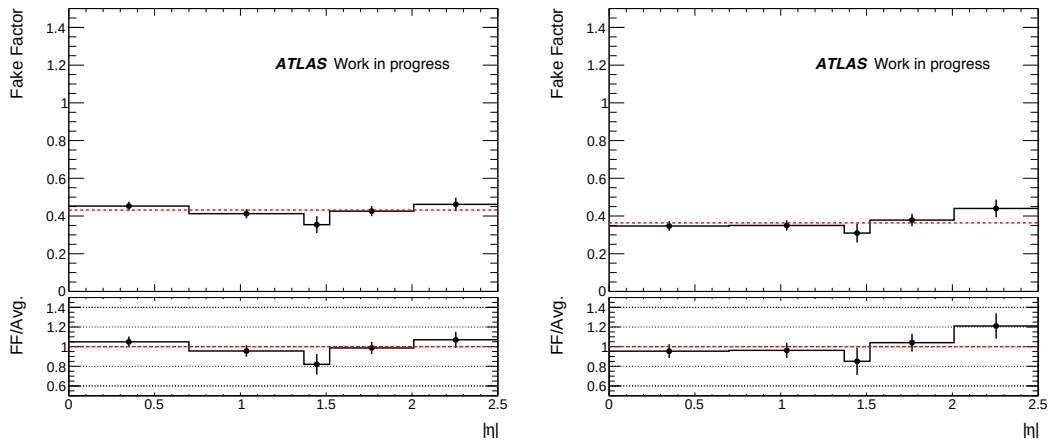

Figure 11.36: Muon fake factors as a function of muon $|\eta|$ for events with zero b-tagged jets (left) and at least one b-tagged jet (right). A red line denotes the average muon fake factor.

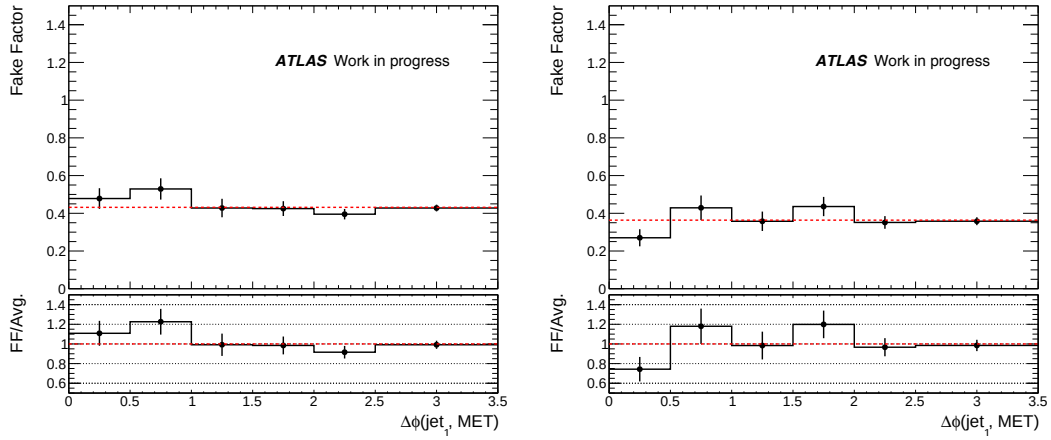

Figure 11.37: Muon fake factors as a function of $\Delta\phi(j_1, \mathbf{p}_{\mathrm{T}}^{\mathrm{miss}})$ for events with zero b-tagged jets (left) and at least one b-tagged jet (right). A red line denotes the average muon fake factor.

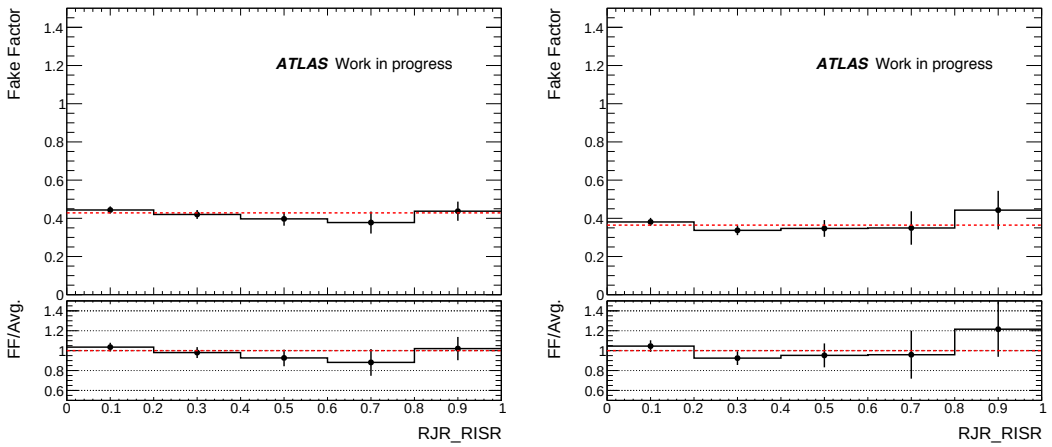

Figure 11.38: Muon fake factors as a function of R_{ISR} for events with zero b-tagged jets (left) and at least one b-tagged jet (right). A red line denotes the average electron fake factor.

separated into $ee + \mu e$ and $\mu\mu + e\mu$ events. For the slepton search, the m_{T2}^{100} and $p_{\mathrm{T}}^{\ell_2}$ distributions in VRSS–S–high and VRSS–S–low are presented in Figure 11.42 and Figure 11.43, respectively, again separated into $ee + \mu e$ and $\mu\mu + e\mu$ events.

In each case, good agreement is seen between the total background prediction and the data in both the $p_{\mathrm{T}}^{\ell_2}$ distributions and the distributions corresponding to the final discriminating variables. In each of the $p_{\mathrm{T}}^{\ell_2}$ distributions shown, the lowest bin includes the events that have the extrapolated fake factors applied and the excellent agreement validates the methodology. Importantly, the $p_{\mathrm{T}}^{\ell_2}$ distributions in these regions are used to derive dedicated non-closure uncertainties to account for any differences between the data and predicted background that are not already covered by other systematic uncertainties related to the fake/non-prompt background. A detailed description of these uncertainties is given in Section 12.2.

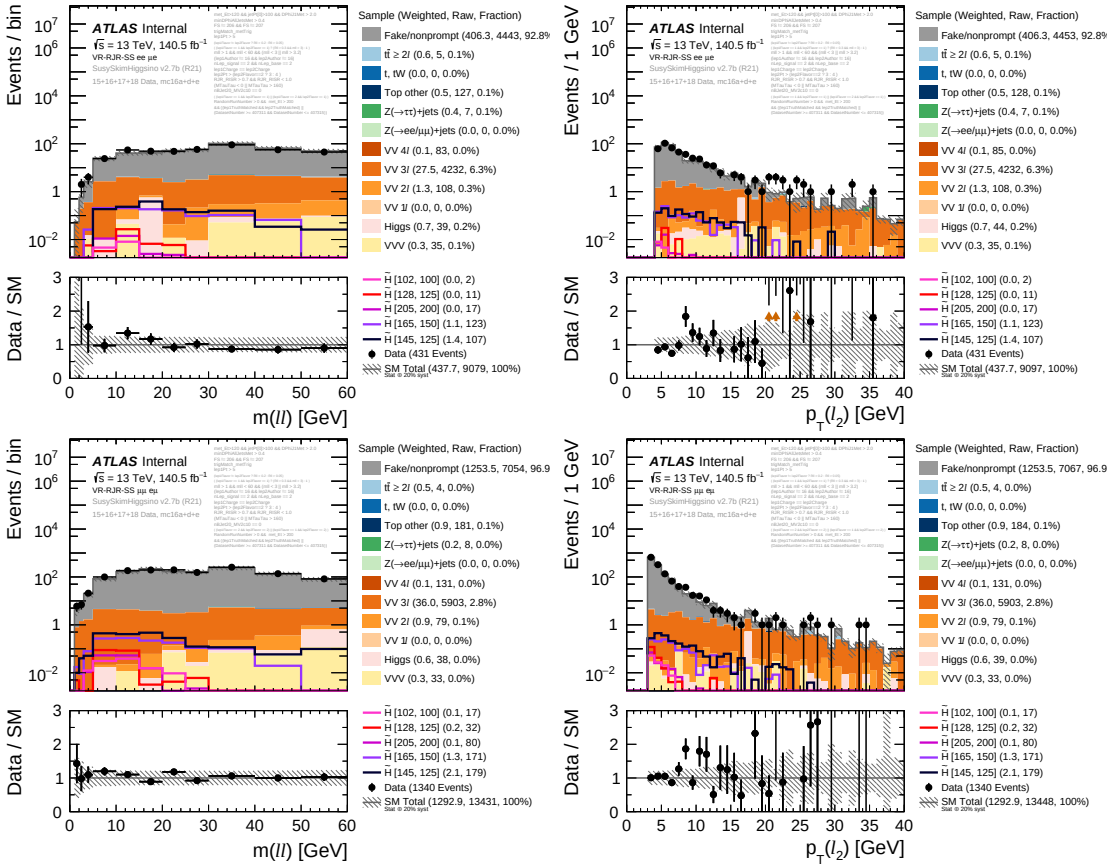

Figure 11.39: Kinematic distributions in VRSS–E–high prior to the application of any normalization factors. The ee+μe channel is shown in the top row, while the bottom row shows the $\mu\mu$+$e\mu$ channel. The uncertainty band shows the statistical uncertainty added in quadrature with a flat 20% systematic uncertainty.

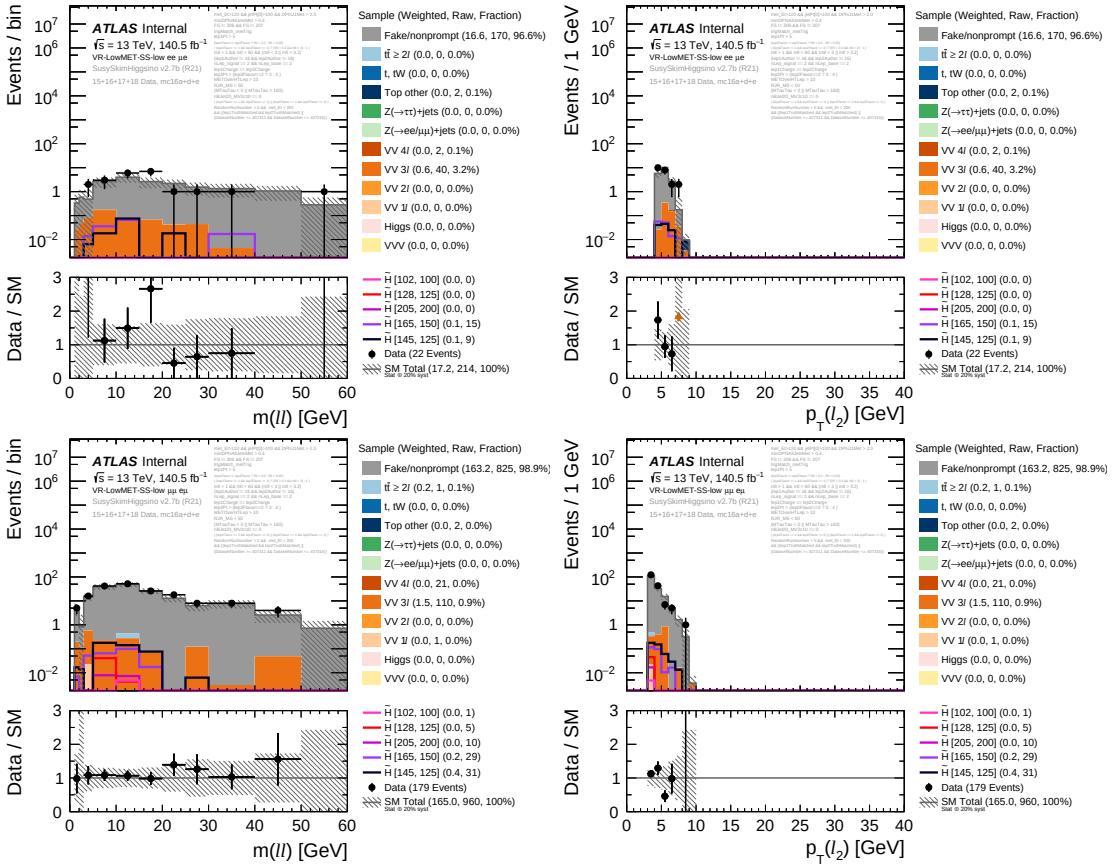

Figure 11.40: Kinematic distributions in VRSS–E–med prior to the application of any normalization factors. The ee+μe channel is shown in the top row, while the bottom row shows the $\mu\mu$+$e\mu$ channel. The uncertainty band shows the statistical uncertainty added in quadrature with a flat 20% systematic uncertainty.

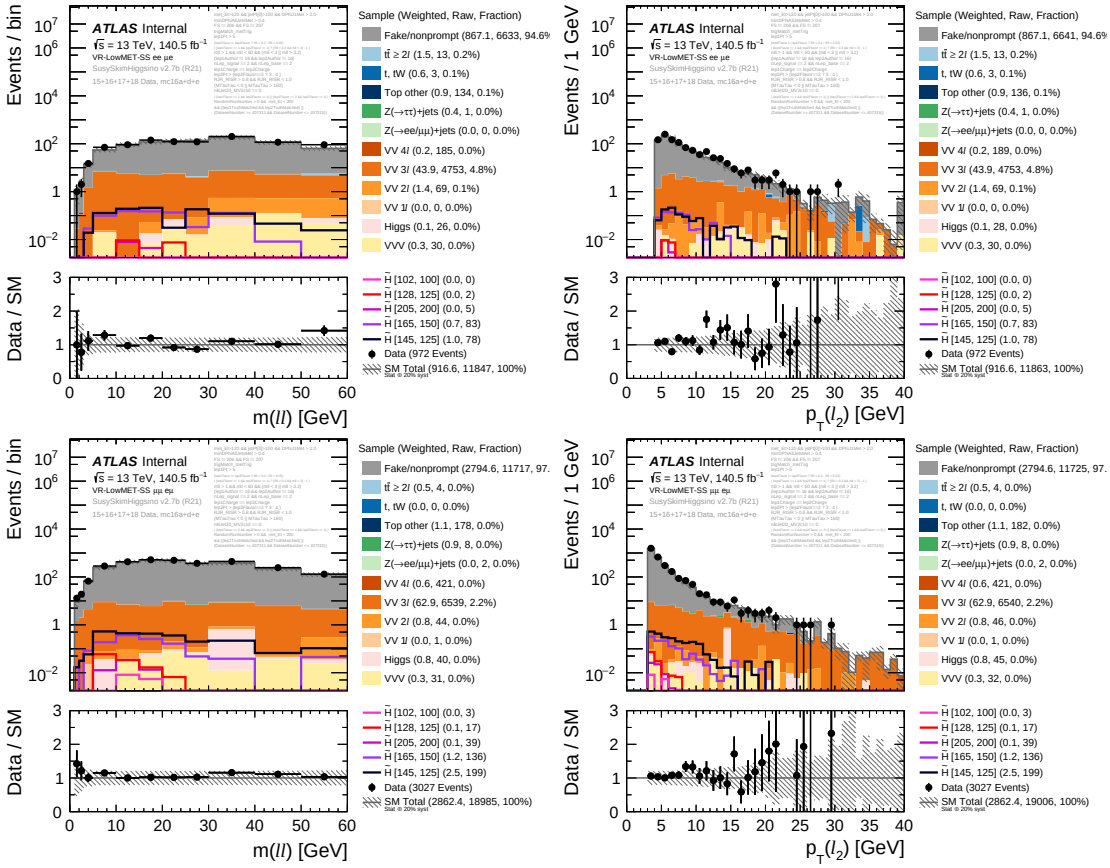

Figure 11.41: Kinematic distributions in VRSS–E–low prior to the application of any normalization factors. The $ee + \mu e$ channel is shown in the top row, while the bottom row shows the $\mu\mu + e\mu$ channel. The uncertainty band shows the statistical uncertainty added in quadrature with a flat 20% systematic uncertainty.

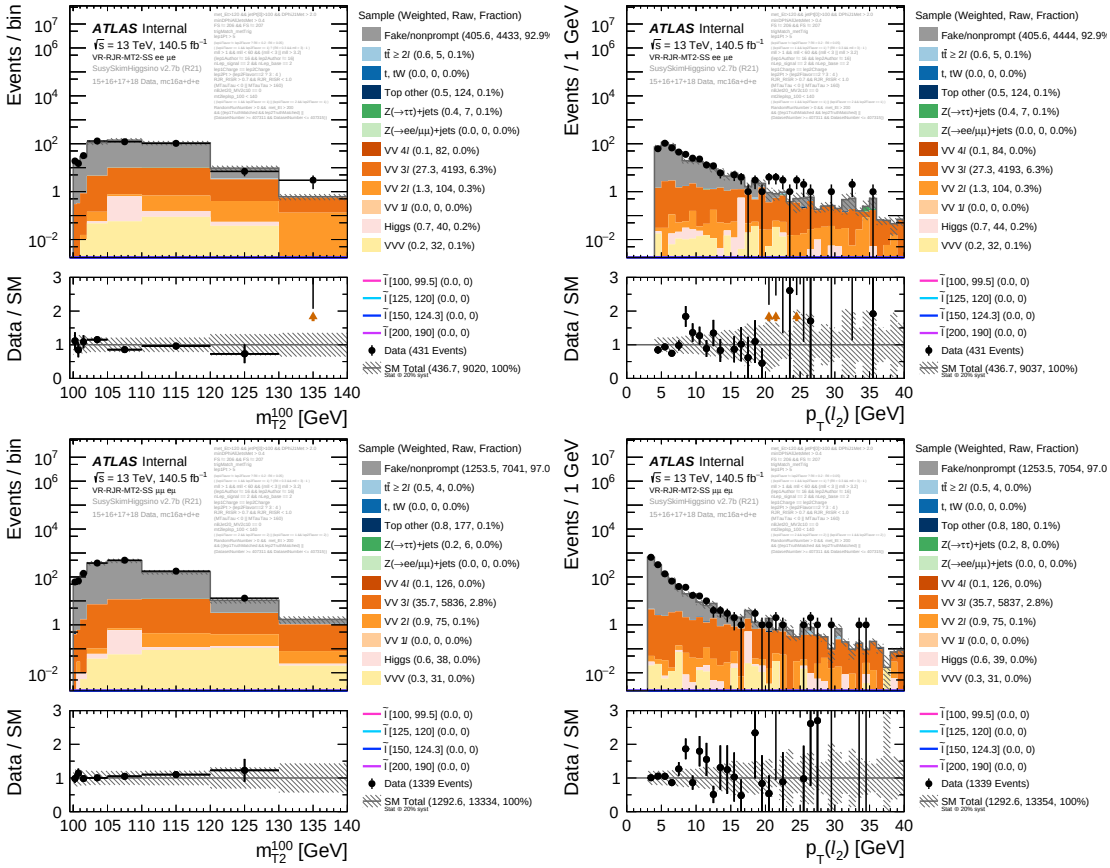

Figure 11.42: Kinematic distributions in VRSS–S–high prior to the application of any normalization factors. The ee+μe channel is shown in the top row, while the bottom row shows the $\mu\mu$+$e\mu$ channel. The uncertainty band shows the statistical uncertainty added in quadrature with a flat 20% systematic uncertainty.

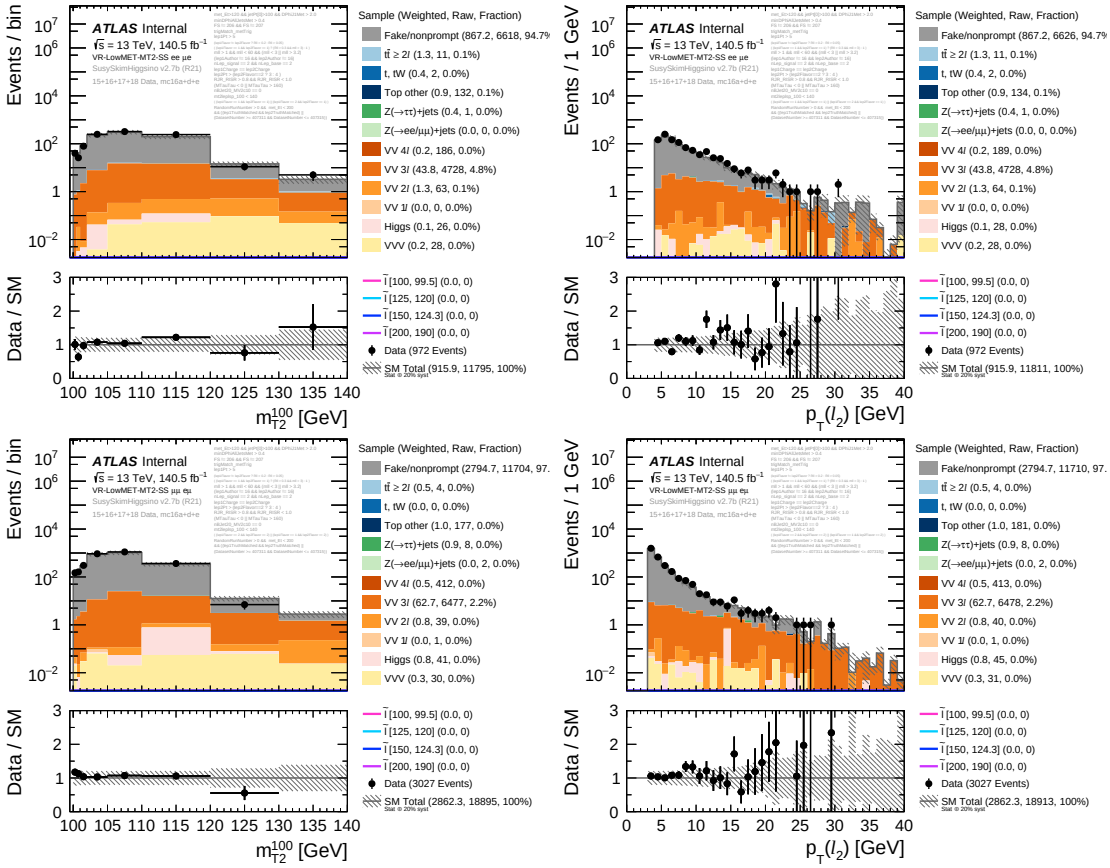

Figure 11.43: Kinematic distributions in VRSS–S–low prior to the application of any normalization factors. The $ee + \mu e$ channel is shown in the top row, while the bottom row shows the $\mu\mu + e\mu$ channel. The uncertainty band shows the statistical uncertainty added in quadrature with a flat 20% systematic uncertainty.

Chapter 12

Systematic Uncertainties

Systematic uncertainties are categorized according to experimental and theoretical sources. Experimental uncertainties stem from the modeling of particle identification, pileup, and the luminosity measurement and are discussed in Section 12.1. Additionally, dedicated experimental uncertainties are derived on the modeling of the fake/non-prompt lepton background, as described in Section 12.2. Theoretical uncertainties, outlined in Section 12.3, are due to the choice of generator and PDF configurations, as well the modeling of the ISR process in signal events. Each uncertainty is incorporated as a nuisance parameter in the likelihood function described in Section 13.2

The impact of these uncertainties on the event yields in the SRs is shown in Section 15.1, where the dominant contributions are from the modeling fake/non-prompt lepton background, especially in the low-$m_{\ell\ell}$ and low-m_{T2}^{100} bins, as well those associated to the jet energy scale and resolution.

12.1 Experimental Uncertainties

Within the ATLAS collaboration, systematic uncertainties related to physics object reconstruction, luminosity measurements, and pileup conditions are provided by dedicated working groups. As these uncertainties can affect both the background and signal yields, they need to be accounted for when searching for new physics. The experimental systematic uncertainties that end up having sizable impacts on the results depends on the physics objects that are used in the analysis. In this search, the targeted final states include jets, $E_{\mathrm{T}}^{\mathrm{miss}}$, and electrons or muons. In addition to luminosity and pileup uncertainties, systematic uncertainties related to these objects are therefore considered. Additionally, since this search includes cuts on the number of b-tagged jets in the event, systematic uncertainties related to flavor-tagging performance are included. The relevant experimental uncertainties for this search are described in more detail below, grouped by their source.

- *Luminosity*: The uncertainty on the luminosity corresponding to this dataset is 1.7%, which affects the background and signal yields in a correlated way. The absolute luminosity scale and uncertainty was determined using dedicated van der Meer scans with the primary measurements coming from the LUCID-2 detector.

- *Pileup conditions*: As a matter of practicality, MC samples for both signal and background processes are simulated before the end of the data-taking period. Therefore, when overlaying soft QCD events to simulate the effects of pileup, an assumption is made about what the pileup profile will be in the final dataset. Since reconstruction performance depends on these pileup conditions, differences in the observed and assumed profiles could result in

poor modeling of many physics processes. In order to account for deficiencies in the pileup assumption used for MC generation, the simulated samples are reweighted in order to match the $\langle\mu\rangle$ distribution observed in data. The uncertainty on this procedure is determined by varying this reweighting factor by an amount that reflects uncertainties related to vertex reconstruction efficiencies.

- *Electrons and muons*: The tag-and-probe method is used to derive uncertainties on the reconstruction, identification, and isolation efficiency scale factors that are applied to simulated events in order to match the overall muon [100] and electron [99] efficiencies observed in data. For muons, the method uses $Z \to \mu\mu$ events, while a combination of $Z \to ee$, $W \to e\nu$, and $J/\psi \to ee$ events are used for electrons. Additional uncertainties are placed on the momentum scale and resolution. For the muon momentum resolution, dedicated uncertainties are derived for ID and MS tracks. Finally, the muon systematic effects include an uncertainty on the track-to-vertex association efficiency scale factor. Overall, the experimental uncertainties related to muons and electrons are found to be small.

- *Jets*: Uncertainties on the jet energy scale and resolution are derived as a function of the jet p_{T} and η, as well as the pileup conditions and jet flavor composition in the jet sample under study. These *in situ* calibrations are performed using dijet, $\gamma + \text{jets}$, and $Z + \text{jets}$ events in simulation and data, taking advantage of the p_{T} balance in the events [105]. These studies result in many JES and JER uncertainties, the number of which can be reduced using the method of eigenvector decomposition while still maintaining a good model for the experimental uncertainty. In this search, the reduced set of JES and JER uncertainties amount to 8 and 12 nuisance parameters, respec-

tively. Additionally, dedicated systematic uncertainties are implemented to account for differences in the JVT and b-tagging efficiencies observed in data and simulation.

- *Missing transverse energy*: As defined in Section 9.5, $E_{\mathrm{T}}^{\mathrm{miss}}$ is calculated using all identified physics objects in the event, as well as an additional soft term to account for tracks from the primary vertex that are not associated to any of these objects. As such, the uncertainty on $E_{\mathrm{T}}^{\mathrm{miss}}$ is partially determined by propagating the uncertainties on the momenta of these physics objects to $E_{\mathrm{T}}^{\mathrm{miss}}$ calculation. The largest such contribution comes from the jet uncertainties. Dedicated uncertainties related to the scale and resolution of the soft term entering the $E_{\mathrm{T}}^{\mathrm{miss}}$ calculation are also considered [118].

- *Trigger scale factors*: For events with $E_{\mathrm{T}}^{\mathrm{miss}} < 200\,\mathrm{GeV}$, where the $E_{\mathrm{T}}^{\mathrm{miss}}$-triggers are not fully efficient, scale factors are derived to account for differences in the trigger efficiencies between the data and simulation. Statistical uncertainties on these scale factors stem from the size of the dataset in the measurement region. Systematic uncertainties are also derived to account for any potential dependence of the scale factors on $m_{\ell\ell}$, m_{T2}^{100}, and R_{ISR} and amount to 5%. Finally, the trigger efficiencies are checked for dependence on the underlying physics process and uncertainties on the scale factors are derived in accordance with these differences. Overall, these uncertainties have small impact on the results. A more detailed description of the $E_{\mathrm{T}}^{\mathrm{miss}}$-trigger scale factor uncertainties is given in Appendix A.4. Uncertainties on the trigger efficiencies for events with $E_{\mathrm{T}}^{\mathrm{miss}} > 200\,\mathrm{GeV}$ are negligible.

Of the systematic uncertainties described above, the largest contribution to the overall experimental uncertainty comes from uncertainties on the jet energy

scale (JES) and jet energy resolution (JER). The impact that these uncertainties have on the expected yields in the SRs is shown in more detail in Section 15.1.

12.2 Fake Factor Method Uncertainties

The background from events containing fake/non-prompt leptons is derived in a data-driven way such that the experimental uncertainties enumerated in the previous section do not apply. Instead, several sources of uncertainty are identified in the fake factor method that in turn affect the uncertainty on the fake/non-prompt lepton background, which tends to dominate the overall background uncertainty in the SRs, especially those targeting electroweakino production. More details about the relative size of the fake/non-prompt lepton background uncertainty are given in Section 15.1 and Section 15.2.2. The systematic uncertainties considered for the fake factor method are due to statistical uncertainties on the fake factors, the fake factor extrapolation at low-p_{T}, subtraction of MC events containing prompt leptons, kinematic dependencies of the fake factors, and non-closure in the same-sign validation regions.

Statistical uncertainties on the fake factors themselves are due to the available statistics in the fake factor measurement region. These events are collected using heavily prescaled single-lepton triggers that only accept a small fraction of the total number of dijet events containing a fake/non-prompt lepton. Additionally, the size of the data sample in the fake factor measurement region impacts the exponential fits that are used to derive the extrapolated fake factors in the lowest p_{T} bins. In order to be conservative, the statistical uncertainty on the extrapolated fake factors is set equal to the statistical uncertainty on the lowest directly-measurable fake factor summed in quadrature with the fit uncertainty. These relative statistical uncertainties on the fake factors are shown in Figure 12.1 and Figure 12.2

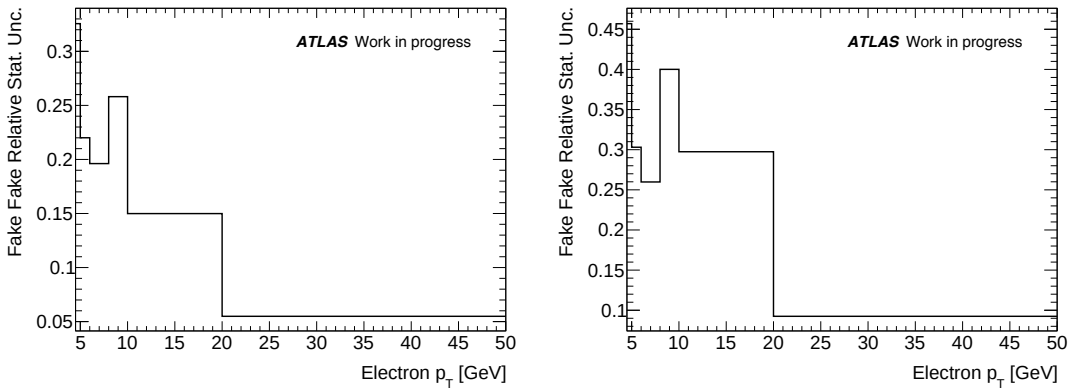

Figure 12.1: The relative statistical uncertainties on the electron fake factors for events with $N^{20}_{b-\text{jet}} = 0$ (left) and $N^{20}_{b-\text{jet}} > 0$ (right) The relative uncertainties in the lowest p_{T} bins are the sum in quadrature of the statistical uncertainty from the neighboring bin and the uncertainty from the extrapolation procedure.

for electrons and muons, respectively.

While the fake factor measurement region is dominated by dijet events containing fake/non-prompt leptons, there is still a small prompt lepton contribution from the $t\bar{t}$ and W + jets processes, which grows with the lepton p_{T}. In order to isolate the fake/non-prompt lepton contribution, these prompt processes are first normalized in a high-m_{T} control region and then subtracted using MC before the fake factors are measured. In order to assess the impact of this subtraction, this normalization factor is varied up and down by a factor of two before recalculating the fake factors. An additional check on this subtraction is performed by instead normalizing the prompt processes in a region with $E_{\text{T}}^{\text{miss}} > 200\,\text{GeV}$. In each case, the changes in the fake factors are small compared to the other uncertainties considered. The other place where prompt subtraction comes into play is in the anti-ID control region (where the fake factors are applied), since this region also has a small amount of prompt lepton contamination. In this case, the amount of prompt subtraction is varied up and down by 10%. The impact on the expected yields in the SRs is then checked and the yields are observed to change by a few

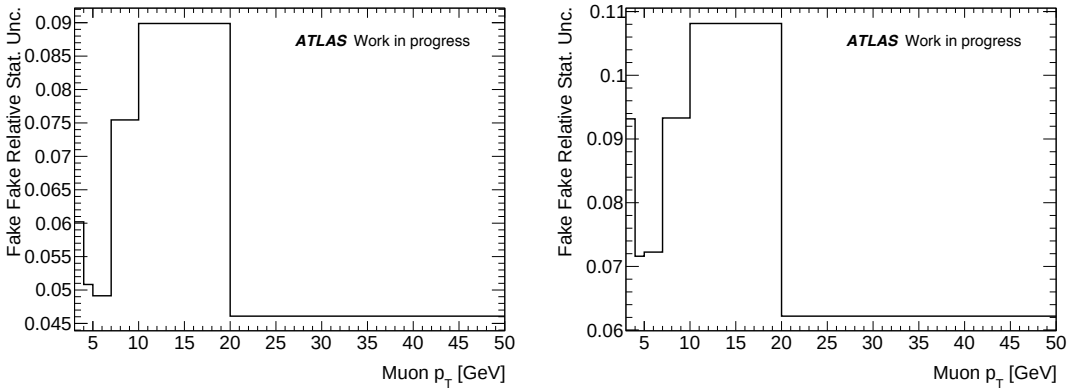

Figure 12.2: The relative statistical uncertainties on the muon fake factors for events with $N^{20}_{b-\text{jet}} = 0$ (left) and $N^{20}_{b-\text{jet}} > 0$ (right) The relative uncertainties in the lowest p_{T} bins are the sum in quadrature of the statistical uncertainty from the neighboring bin and the uncertainty from the extrapolation procedure.

percent at most, as shown in Figure 12.3 and Figure 12.4 for SR–E–high and SR–S–high, respectively.

The fake factors are ultimately parameterized and applied as a function of the lepton p_{T} and the number of b-tagged jets in the event, although other important kinematic dependencies are possible. Given the limited statistics in the fake factor measurement region, though, it is not feasible to bin the fake factors in more observables in order to capture these correlations. Instead, these kinematic dependencies are checked and flat systematic uncertainties are applied to the fake factors in order to cover any statistically significant differences in these distributions with respect to the average fake factors. For electrons, the fake factors are shown as a function of important kinematic variables in Figures 11.26–11.28, while those for muons are shown in Figures 11.36–11.38. The observables with the strongest kinematic dependencies are R_{ISR} and the lepton $|\eta|$. For the electron fake factors, this uncertainty amounts to 40%, while the muon fake factors acquire a 20% uncertainty. These parameterization uncertainties represent the dominant source of uncertainty on the fake/non-prompt lepton background.

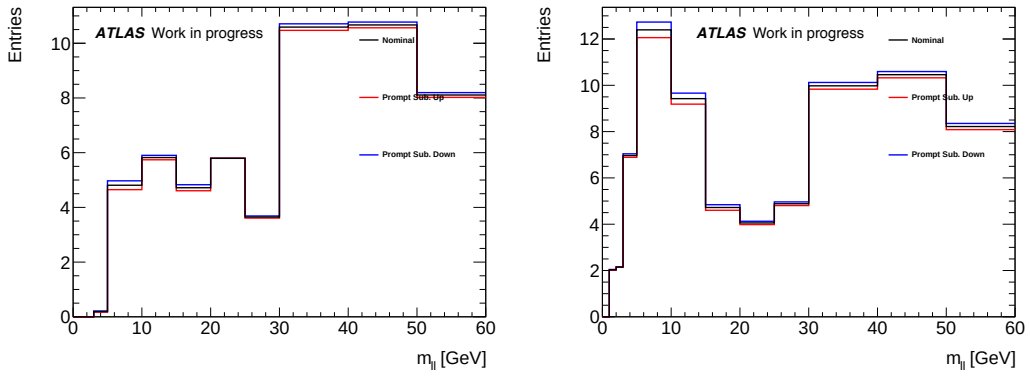

(a) ee channel **(b)** $\mu\mu$ channel

Figure 12.3: The $m_{\ell\ell}$ distributions in SR–E–high after varying the amount of prompt subtraction in the anti-ID CR by 10%.

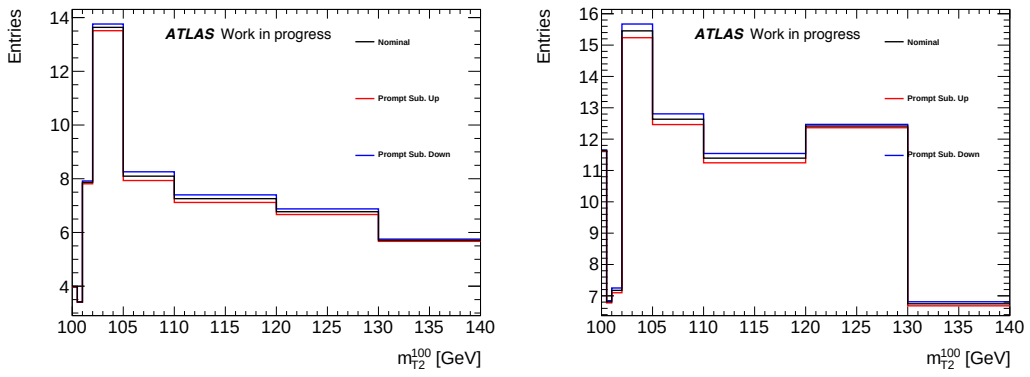

(a) ee channel **(b)** $\mu\mu$ channel

Figure 12.4: The m_{T2}^{100} distributions in SR–S–high after varying the amount of prompt subtraction in the anti-ID CR by 10%.

Finally, the modeling of this background is checked in same-sign validation regions, which are dominated by events containing fake/non-prompt leptons. Here, the fake/non-prompt lepton is assumed to be the subleading lepton in the event. Those events where the subleading lepton is an electron are used to assess the need for an additional non-closure uncertainty on the electron fake factors, while those where the subleading lepton is a muon are used to do the same for the muon fake factors. Since the fake factors are parameterized as a function of the lepton p_{T}, the subleading lepton p_{T} distribution is used for the comparison. This distribution is binned to match the fake factor binning, and any discrepancies between the data and the background prediction that are not already covered by the uncertainties described above are used to derive an additional non-closure uncertainty.

In particular, the uncertainty on the fake/non-prompt lepton background in a given $p_{\mathrm{T}}^{\ell_2}$ bin is taken as the RMS of the variations due to the above uncertainties, and any uncovered discrepancy is measured in quadrature and taken to be the non-closure uncertainty. If the difference between the data and the prediction is already covered by the variation, then no additional uncertainty is assigned. Since VV processes represent the subleading contribution to the same-sign validation regions, a normalization factor obtained with a background-only fit to the CRs (described in Section 14.1) is applied to better isolate the fake/non-prompt background in the comparison. The data and fake/non-prompt background comparisons for the high-$E_{\mathrm{T}}^{\mathrm{miss}}$ and low-$E_{\mathrm{T}}^{\mathrm{miss}}$ same-sign validation regions are shown in Figure 12.5 and Figure 12.6, respectively. The largest non-closure uncertainty by far is assigned to the electron fake factor for $p_{\mathrm{T}} > 20\,\mathrm{GeV}$. Ultimately, though, this uncertainty has little effect on the yields in the SRs, as the fake/non-prompt lepton contribution resides at lower values of p_{T}.

Nominally, the same-sign validation regions just discussed require $N_{b-\mathrm{jet}}^{20} = 0$,

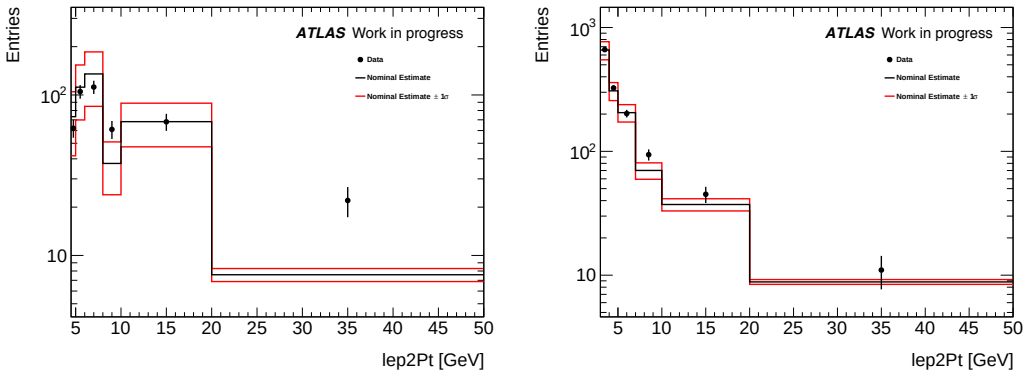

(a) $ee + \mu e$ channel **(b)** $\mu\mu + e\mu$ channel

Figure 12.5: Data compared with the fake/non-prompt lepton estimate in high-$E_{\mathrm{T}}^{\mathrm{miss}}$ VRSS region for the $ee + \mu e$ channel (left) and the $\mu\mu + e\mu$ channel (right). Differences beyond the $\pm 1\sigma$ band are used to derive non-closure systematic uncertainties.

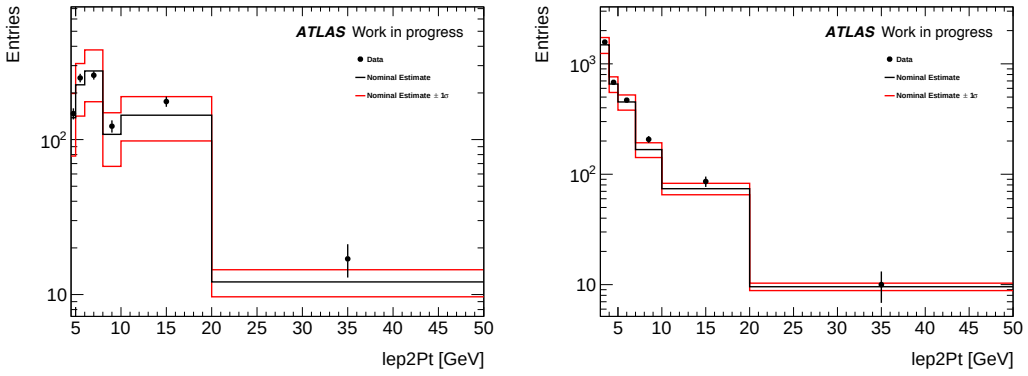

(a) $ee + \mu e$ channel **(b)** $\mu\mu + e\mu$ channel

Figure 12.6: Data compared with the fake lepton estimate in low-MET `VR-SS` for the $ee + \mu e$ channel (left) and the $\mu\mu + e\mu$ channel (right). Differences beyond the $\pm 1\sigma$ band are used to derive non-closure systematic uncertainties.

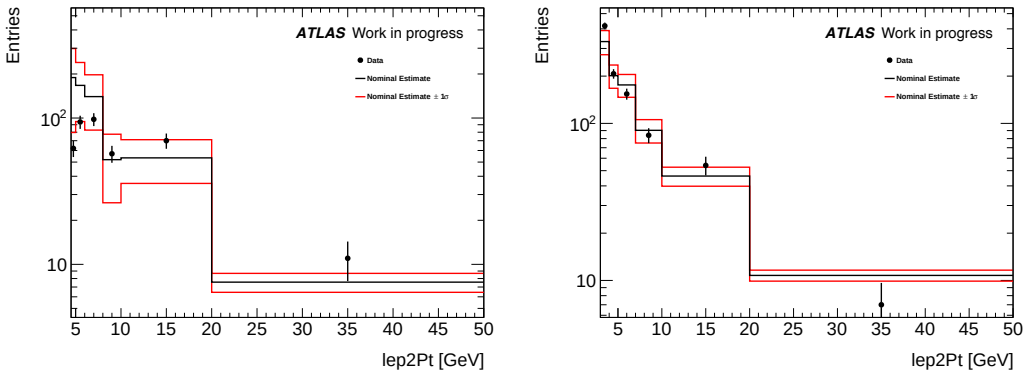

(a) $ee + \mu e$ channel **(b)** $\mu\mu + e\mu$ channel

Figure 12.7: Data compared with the fake/non-prompt lepton estimate in the same-sign high-$E_{\mathrm{T}}^{\mathrm{miss}}$ CRtop region for the $ee + \mu e$ channel (left) and the $\mu\mu + e\mu$ channel (right). Differences beyond the $\pm 1\sigma$ band are used to derive non-closure systematics uncertainties.

which does not allow for a non-closure uncertainty to be assigned on the fake factors that are measured in events with $N_{b-\mathrm{jet}}^{20} > 0$. Therefore, this procedure is also performed in same-sign versions of the CRtop regions, which differ from their definition given in Section 11.1 only by requiring two signal leptons with the same electric charge. The comparisons between the background estimate and the data, including the $\pm 1\sigma$ band from all other fake factor uncertainties, are shown in Figure 12.7 and Figure 12.8.

12.3 Theoretical Uncertainties

Theoretical uncertainties on the signal and background event yields arise from the choice of various parameters used for the event generation, as described in the following sections. Additionally, a dedicated uncertainty on the modeling of the ISR process in the signal samples is derived by comparing data and simulated events in $Z \to \mu\mu + \mathrm{jets}$ events, where the MC samples are generated using the same generator configuration as that used for the signals.

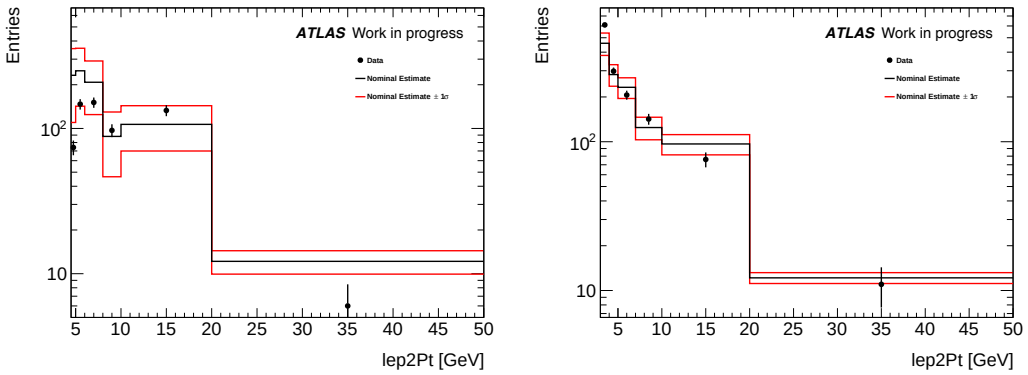

(a) $ee + \mu e$ channel **(b)** $\mu\mu + e\mu$ channel

Figure 12.8: Data compared with the fake/non-prompt lepton estimate in the same-sign low-$E_{\mathrm{T}}^{\mathrm{miss}}$ CRtop region for the $ee + \mu e$ channel (left) and the $\mu\mu + e\mu$ channel (right). Differences beyond the $\pm 1\sigma$ band are used to derive non-closure systematics.

12.3.1 Background Processes

The dominant sources of background taken from MC simulation are $t\bar{t}/Wt$, $Z^{(*)}/\gamma^{*}(\rightarrow \tau\tau) + \text{jets}$, and VV. While their normalizations are determined using dedicated CRs, the shapes of their $m_{\ell\ell}$ and m_{T2}^{100} distributions remain sensitive to theoretical uncertainties related to the parameters of the MC generators. The theoretical uncertainties are determined by evaluating the changes in the background yields in the $m_{\ell\ell}$ and m_{T2}^{100} bins that define the exclusive electroweakino and slepton SRs.

In order to assess the effect of the choice of QCD renormalization scale (μ_R) and factorization scale (μ_F), the corresponding MC generator parameters are varied up and down by a factor of two around their nominal values. The envelope of the six possible variation combinations is taken as the uncertainty. Additionally, an uncertainty is derived by varying the strong coupling constant, α_{s}, up and down within its uncertainty. Finally, the uncertainty due to the choice of the PDF set is assessed by reweighting the nominal samples to the central values of the `MMHT2014`

and CT14 PDF sets. The uncertainty is determined by symmetrizing the changes in the signal yields and taking the envelope.

Figures 12.9–12.11 show the changes in the event yields in SR–E–high and SR–S–high after applying the variations on α_s, μ_R and μ_F, and the PDF sets for the $t\bar{t}$, VV, and $Z^{(*)}/\gamma^*(\rightarrow \tau\tau)$ + jets, respectively. The equivalent results for SR–E–low and SR–S–low are presented in Figures 12.12–12.14. Finally, the results for SR–E–med are shown in Figures 12.15–12.16. All lepton flavor combinations are considered in these results since the theoretical uncertainties involved are not expected to be flavor-dependent. Integrating over the full $m_{\ell\ell}$ and m_{T2}^{100} distributions, uncertainties on the background estimation in the SRs due to α_s and PDF variations are both $\lesssim 3\%$. The uncertainties from variations of μ_R and μ_F are larger but typically $\lesssim 25\%$.

12.3.2 Signal Processes

Since the targeted signal processes rely on hadronic ISR to boost the SUSY system, the generator modeling of this ISR process represents an important source systematic uncertainty. This uncertainty is assessed in a data-driven way by comparing data to the simulated background in $Z(\rightarrow \mu\mu)$+jets events and treating the dimuon system as a proxy for the SUSY system. Since the dominant production modes for $Z(\rightarrow \mu\mu)$+jets, electroweakinos, and sleptons involve quarks in the initial state, the ISR process is assumed to be similar for each of these processes. In order to ensure that the ISR modeling is the same between the simulated events, the $Z(\rightarrow \mu\mu)$ + jets MC sample is generated using the same MG5_aMC@NLO configuration as the signal samples.

Events containing exactly two muons with opposite electric charge are collected using unprescaled single-muon triggers, which must be matched to one of

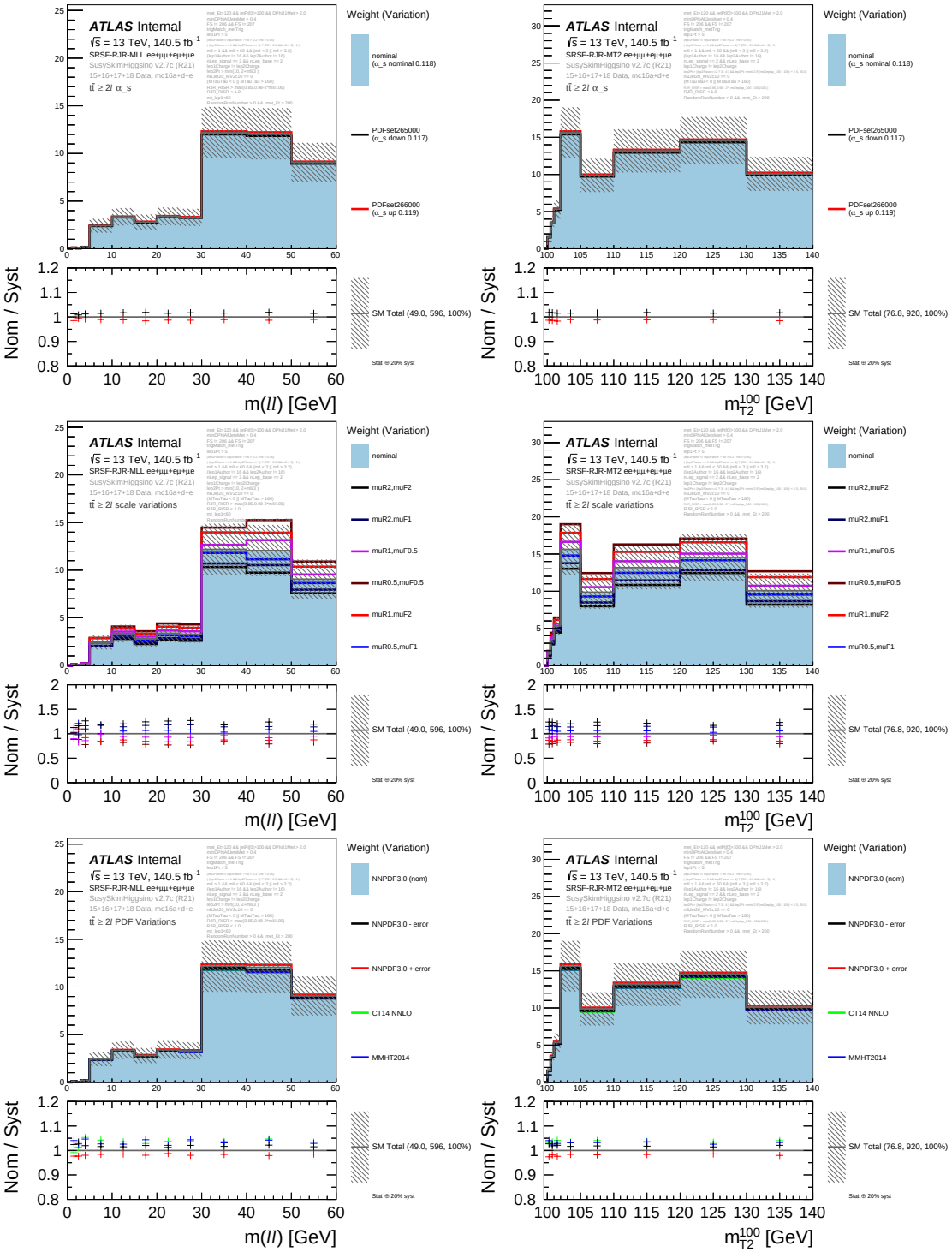

Figure 12.9: Uncertainties on α_s (top), QCD renormalization/factorization (middle), and PDF (bottom) as a function of m_{ll} in SR–E–high (left) and m_{T2}^{100} in SR–S–high (right) for the $t\bar{t}$ background.

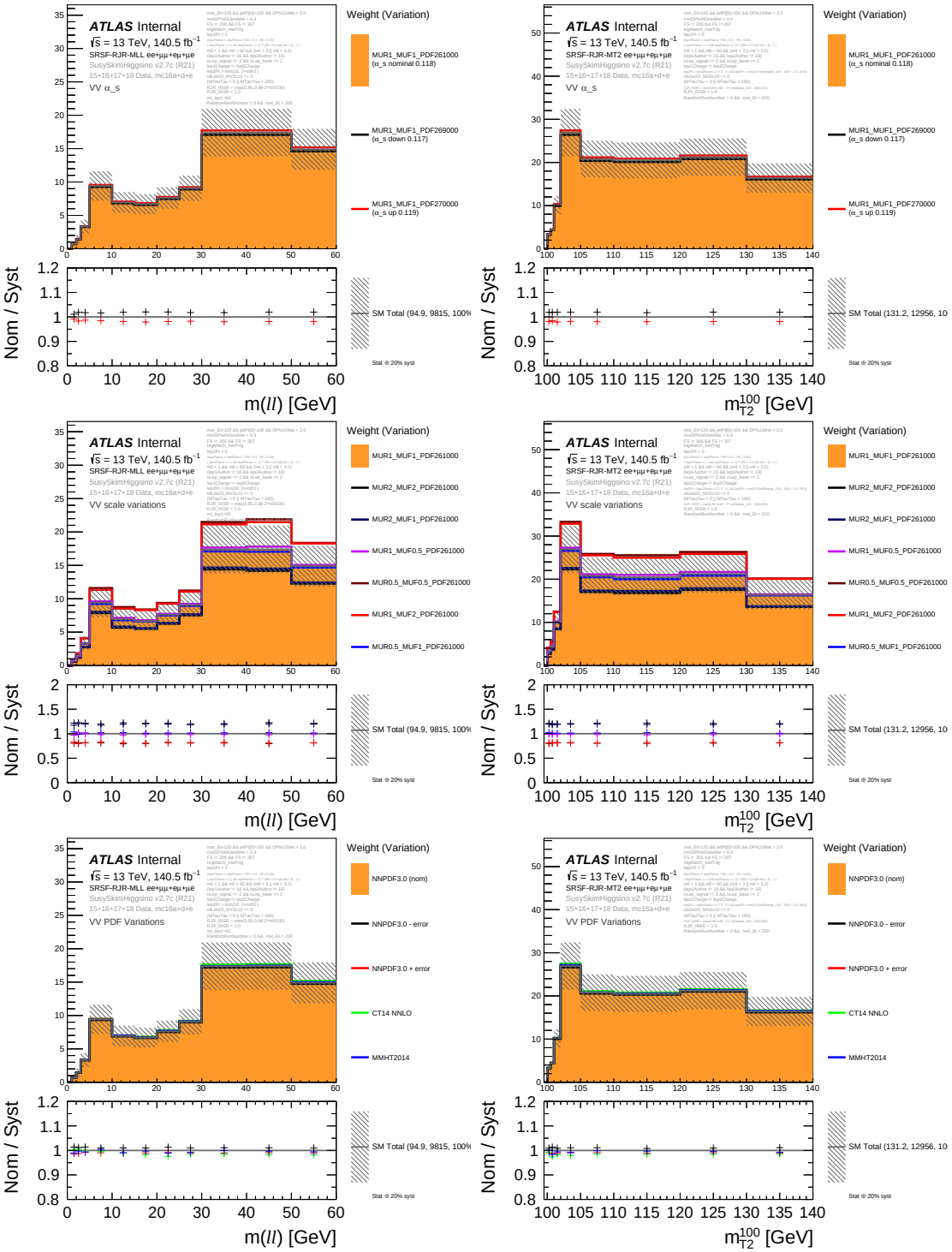

Figure 12.10: Uncertainties on α_s (top), QCD renormalization/factorization (middle), and PDF (bottom) as a function of m_{ll} in SR–E–high (left) and m_{T2}^{100} in SR–S–high (right) for the VV background.

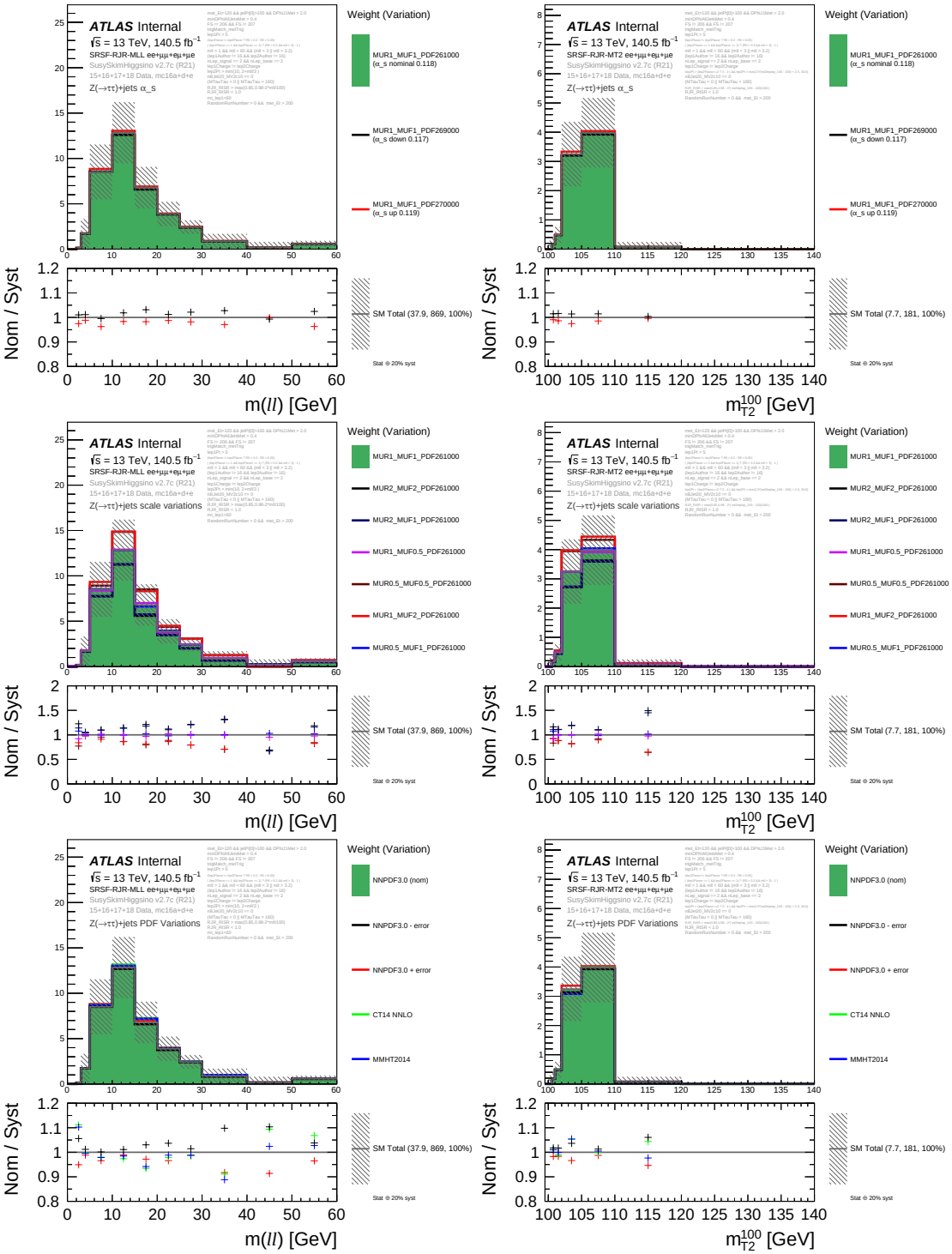

Figure 12.11: Uncertainties on α_s (top), QCD renormalization/factorization (middle), and PDF (bottom) as a function of m_{ll} in SR–E–high (left) and m_{T2}^{100} in SR–S–high (right) for the $Z^{(*)}/\gamma^{*}(\rightarrow \tau\tau) + \mathrm{jets}$ background.

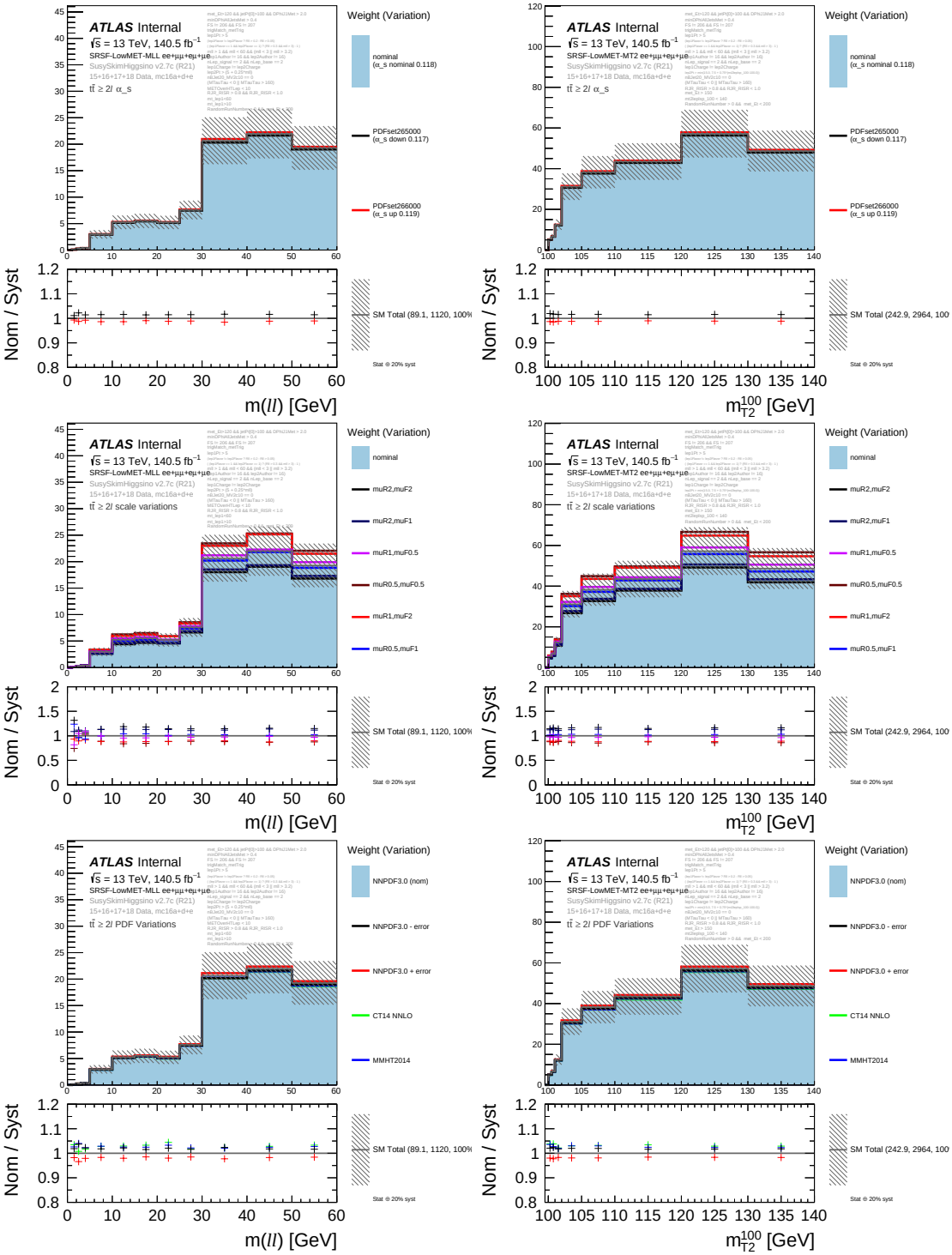

Figure 12.12: Uncertainties on α_s (top), QCD renormalization/factorization (middle), and PDF (bottom) as a function of m_{ll} in SR–E–low (left) and m_{T2}^{100} in SR–S–low (right) for the $t\bar{t}$ background.

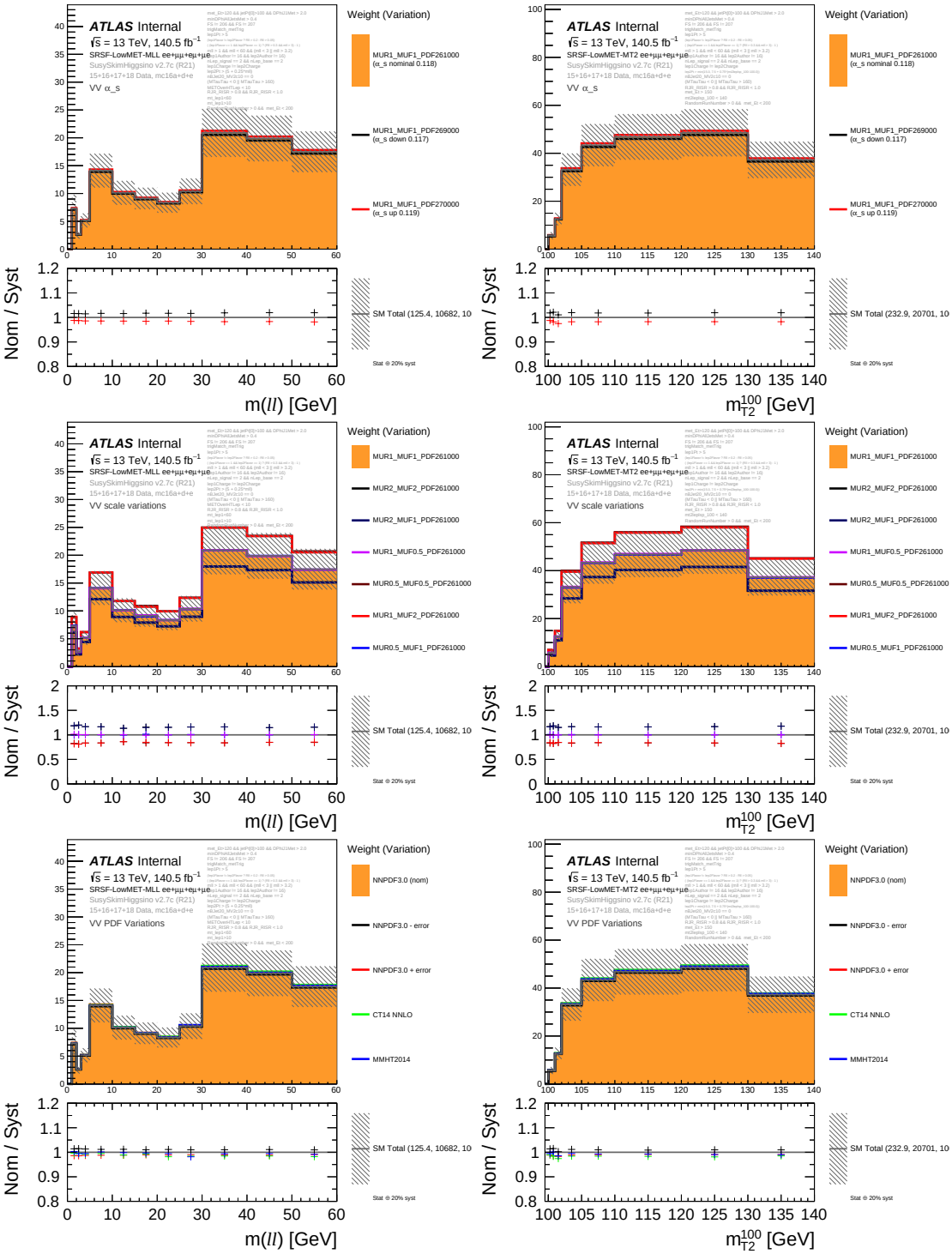

Figure 12.13: Uncertainties on α_s (top), QCD renormalization/factorization (middle), and PDF (bottom) as a function of m_{ll} in SR–E–low (left) and m_{T2}^{100} in SR–S–low (right) for the VV background.

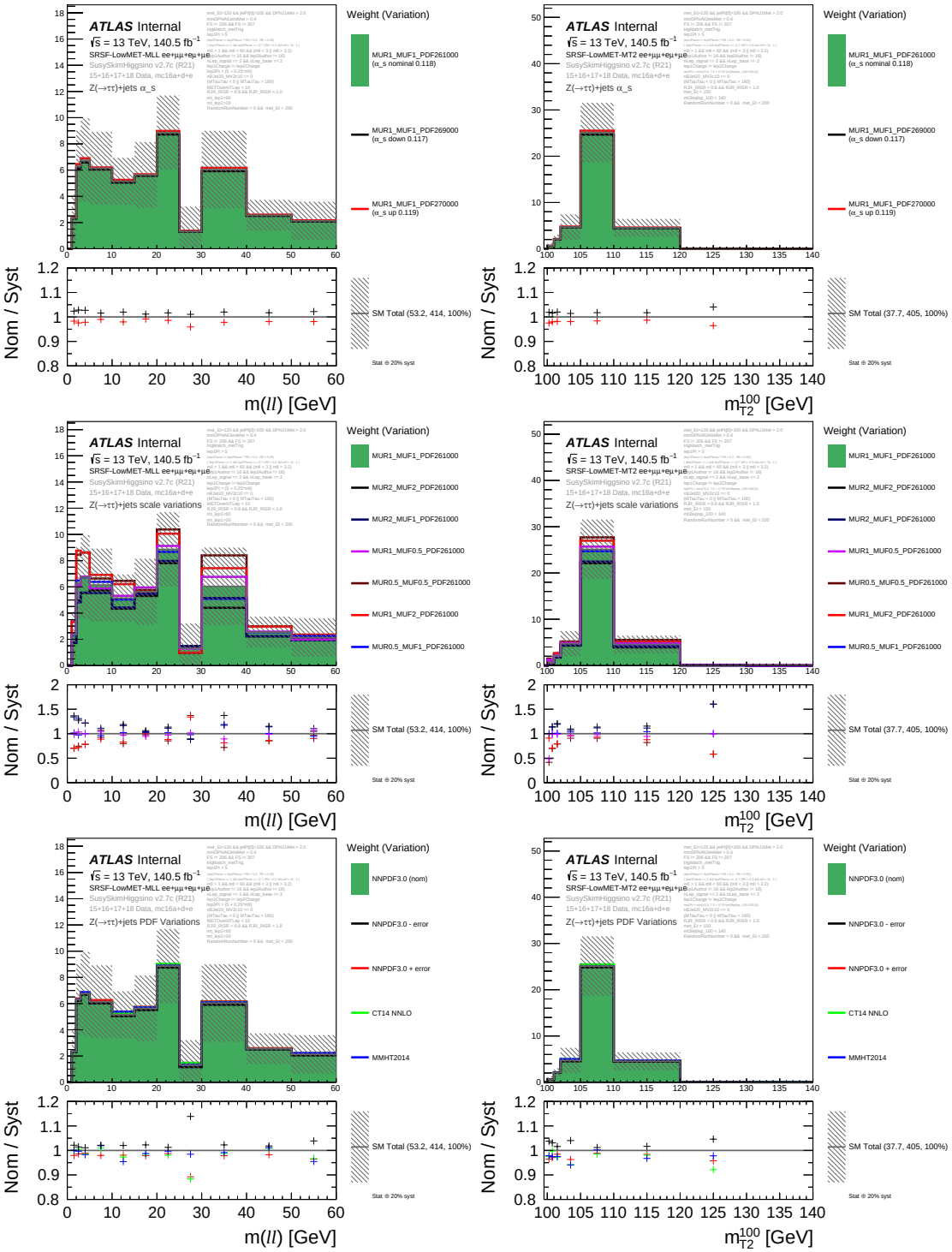

Figure 12.14: Uncertainties on α_s (top), QCD renormalization/factorization (middle), and PDF (bottom) as a function of m_{ll} in SR–E–low (left) and m_{T2}^{100} in SR–S–low (right) for the $Z^{(*)}/\gamma^{*}(\rightarrow \tau\tau) + \mathrm{jets}$ background.

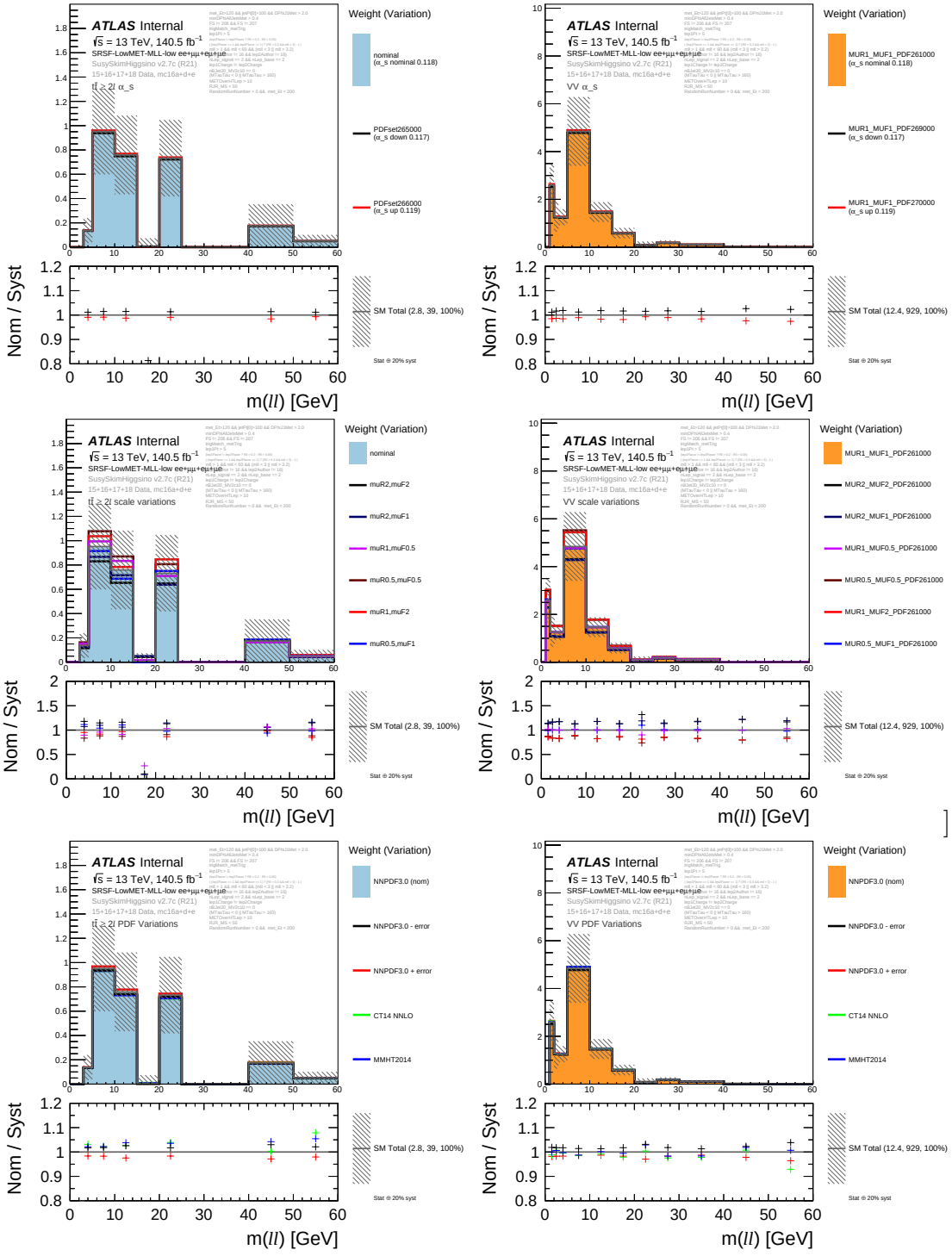

Figure 12.15: Uncertainties on $t\bar{t}$ (left) and VV (right) backgrounds from α_s (top), QCD renormalization/factorization (middle), and PDF (bottom) as a function of m_{ll} in SR–E–med.

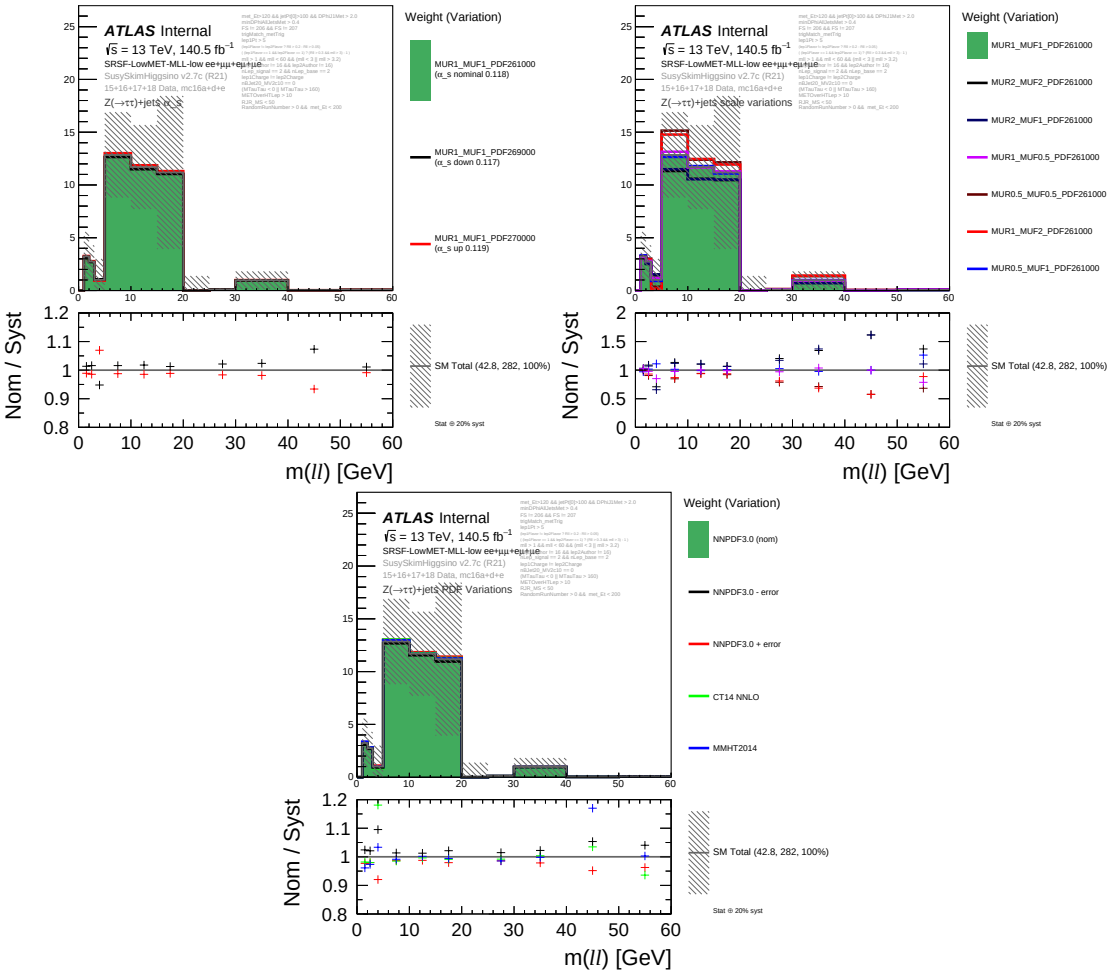

Figure 12.16: Uncertainties on the $Z^{(*)}/\gamma^*(\rightarrow \tau\tau) + \text{jets}$ background from α_s (top left), QCD renormalization/factorization (top right), and PDF (bottom) as a function of m_{ll} in SR–E–low.

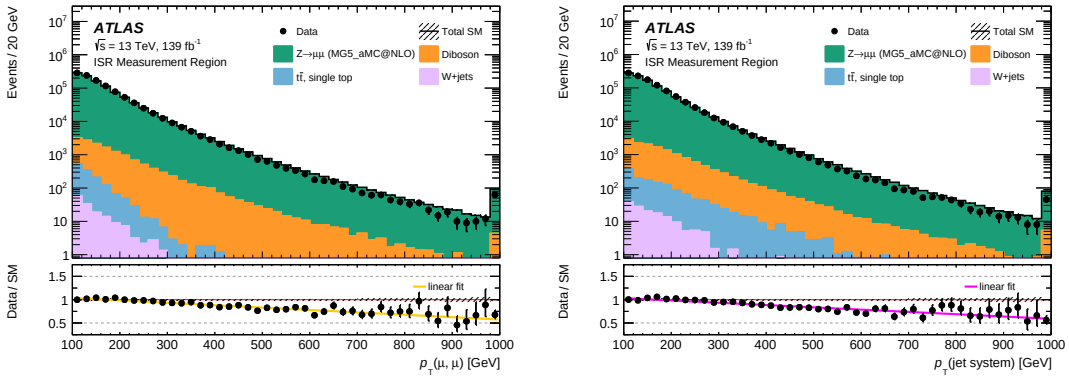

Figure 12.17: Comparison of $Z \to \mu\mu$ events in data with $Z \to \mu\mu$+jets events generated using the same MG5_aMC@NLO configuration as the higgsino and wino/bino signal samples. Only statistical uncertainties are shown. The p_{T} of the dimuon (jet) system is shown on the left (right). In each case, a linear fit to the data/MC ratio is performed in the bottom panel.

the muons in the event. The invariant mass of the dimuon system must satisfy 70 GeV $< m_{\mu\mu} <$ 110 GeV in order to select events around the Z resonance. In order to enforce the boosted topology targeted by the electroweakino and slepton SRs, the leading jet in the event is required to have $p_{\mathrm{T}} > 100$ GeV and the recoiling Z system must satisfy $p_{\mathrm{T}}(\mu,\mu) > 100$ GeV. Finally, events are vetoed if they contain at least one b-tagged jet in order to suppress contributions from events containing top-quarks, such as $t\bar{t}$. In simulation, this selection is around 98% pure in the $Z(\to \mu\mu)$ + jets process. Since the uncertainty is derived using only the shape of the $p_{\mathrm{T}}(\mu,\mu)$ distribution, the simulated background is normalized to the data in this region.

The distributions of $p_{\mathrm{T}}(\mu,\mu)$ in data and simulation are shown for this measurement region in Figure 12.17. As a cross-check, this figure also shows the p_{T} of the jet system, which is calculated using the sum of all jet four-vectors in the event, since this should also be sensitive to the ISR modeling. In each case, a discrepancy between the data and background prediction is observed, which grows with $p_{\mathrm{T}}(\mu,\mu)$ and p_{T}(jet system). In order to assess the mismodeling, a linear fit

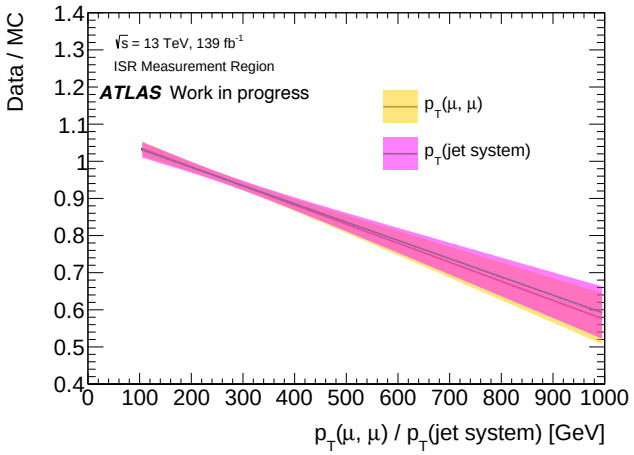

Figure 12.18: Linear fits to the data/MC distributions for $p_{\mathrm{T}}(\mu,\mu)$ (yellow) and the p_{T} of the jet system (purple). The bands represent the fit uncertainties using the 95% CL interval for the fit parameters.

is performed to the data/MC ratio as a function of both of these variables between 100 GeV and 1 TeV. The results of these fits are compared in Figure 12.18, which shows consistent results for each ISR proxy system.

In order to derive a systematic uncertainty on the ISR modeling, the fit to data/MC as a function of $p_{\mathrm{T}}(\mu,\mu)$ is used to reweight signal events on an event-by-event basis. In particular, each signal event is assigned a weight that corresponds to the value of the fit function as evaluated at the truth-level p_{T} of the SUSY system. As the impact on the $m_{\ell\ell}$ and m_{T2}^{100} distributions from this reweighting is small, the ISR uncertainties for each signal point are only given by the relative changes in the SR yields after applying these weights. In mathematical terms, the relative uncertainty due to the ISR modeling in a given SR, $\Delta\sigma_{\mathrm{ISR}}/\sigma_{\mathrm{ISR}}$ is given by

$$\frac{\Delta\sigma_{\mathrm{ISR}}}{\sigma_{\mathrm{ISR}}} = \frac{|N_{\mathrm{nom}}(\mathrm{SR}) - N_{\mathrm{syst}}(\mathrm{SR})|}{N_{\mathrm{nom}}(\mathrm{SR})}, \tag{12.1}$$

where $N_{\mathrm{nom}}(SR)$ is the nominal signal yield in the SR and $N_{\mathrm{syst}}(SR)$ is the yield

after applying the event-by-event ISR weights. The electroweakino uncertainties due to ISR modeling are shown in the $\Delta m(\widetilde{\chi}_2^0, \widetilde{\chi}_1^0)$ vs $m(\widetilde{\chi}_2^0)$ plane for each of the electroweakino SRs in Figure 12.19. The analogous uncertainties for the slepton signals are shown in the $\Delta m(\widetilde{\ell}, \widetilde{\chi}_1^0)$ vs $m(\widetilde{\ell})$ plane in Figure 12.20. In the case of SR–S–high, the SR definition was slightly loosened in order to have sufficient signal statistics for a reliable uncertainty calculation. Specifically, the m_{T2}^{100}-dependent cut on $p_{\mathrm{T}}^{\ell_2}$is removed and the cut on R_{ISR} is loosened to $R_{\mathrm{ISR}} > 0.85$. Since the modeling of the p_{T} of the SUSY system gets worse at larger values, the ISR uncertainties are larger in the SRs requiring $E_{\mathrm{T}}^{\mathrm{miss}} > 200$ GeV. Additionally, the p_{T} distribution of the SUSY system tends to be harder for signal points with smaller mass-splittings, making these uncertainties similarly larger. In general, the SRs requiring $E_{\mathrm{T}}^{\mathrm{miss}} < 200$ GeV have ISR modeling uncertainties on the order of 2–3%. In the SRs requiring $E_{\mathrm{T}}^{\mathrm{miss}} > 200$ GeV, these uncertainties range from 7–20%, with the largest uncertainties corresponding to the most compressed signals. In a previous version of this analysis [116], these uncertainties were assessed by varying the renormalization, factorization, and jet-parton matching scales in addition to the shower tune parameters. This method resulted in ISR modeling uncertainties as large as 40% for compressed sleptons, showing the advantage of the data-driven approach presented here.

Uncertainties related to the underlying proton PDF are evaluated for the signal samples according to PDF4LHC15 recommendations [119] and the impact on the shape of the $m_{\ell\ell}$ and m_{T2}^{100} distributions is found to be negligible. The uncertainty on the signal yields in the SRs is 15% at most, with the largest uncertainties corresponding to the signal points with the largest values of $m(\widetilde{\chi}_2^0)$ and $m(\widetilde{\ell})$ – indicative of the larger PDF uncertainties at high values of the momentum fraction. Finally, uncertainties on the signal cross-sections, as described in Section 8.2, are

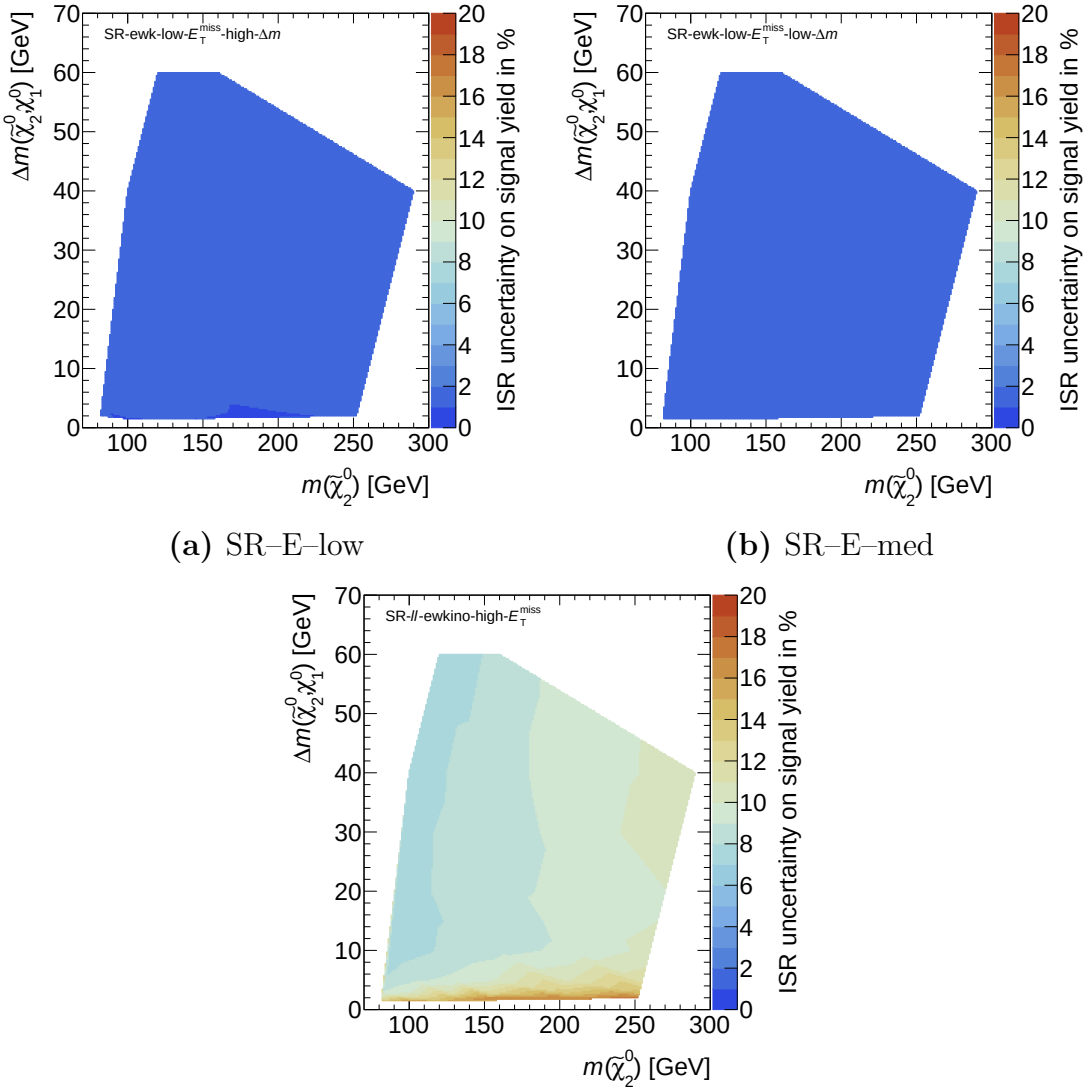

(a) SR–E–low

(b) SR–E–med

(c) SR–E–high

Figure 12.19: Data-driven ISR uncertainty estimates for the electroweakino SRs.

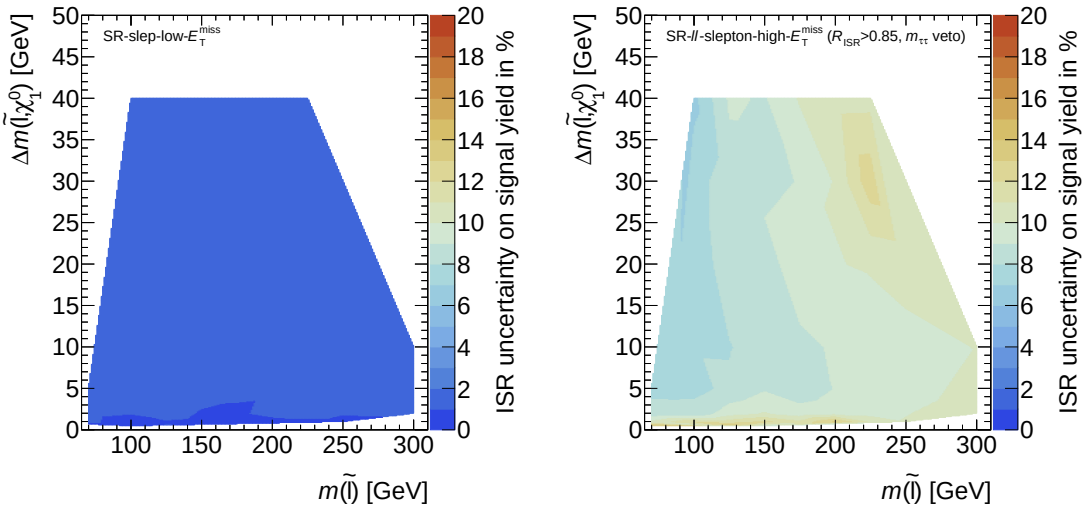

(a) SR–S–low **(b)** SR–S–high

Figure 12.20: Data-driven ISR uncertainty estimates for the slepton SRs. The SR–E–high definition is loosened for these calculations, as described in the text.

typically less than 5%.

Part V

Statistical Analysis and Results

Is SUSY the best fit?

Chapter 13

Statistical Methods in the Search for New Physics

A statistical analysis based on the profile likelihood ratio is used to assess the compatibility of the data observed in the SRs with various hypotheses. When searching for evidence of new physics, the data are compared to the background-only hypothesis in which only contributions form SM processes are considered. If the observed data are determined to be sufficiently improbable under this hypothesis, then a discovery of new physics can be claimed. In almost all cases, BSM physics processes produce an excess of events over the SM background, thus a deficit in the data compared to the background-only hypothesis is not taken to be evidence of new physics.

If no evidence of new physics is found based on the background-only hypothesis test, then limits on the production of new physics can be derived. This is done by comparing the data to the signal-plus-background hypothesis that includes a signal component that is scaled by a signal strength parameter μ. This parameter is extracted by fitting the data to the signal-plus-background hypothesis and is

defined by

$$\mu = \frac{\sigma_{\text{obs}}}{\sigma_{\text{exp}}}, \tag{13.1}$$

where σ_{obs} is the fitted value of the signal cross-section and σ_{exp} is the expected cross-section from the signal model. Thus, $\mu = 0$ corresponds to the background-only hypothesis and $\mu = 1$ corresponds to the signal-plus-background hypothesis. Additionally, the best-fit value of μ can be transformed into an upper limit on the production cross-section of some new physics process.

All of the likelihood construction, fitting machinery, and statistical tests are incorporated into the HistFitter package [120], which is utilized by these searches. This chapter proceeds by first reviewing the concept of hypothesis testing in Section 13.1 before describing the likelihood function in Section 13.2. Finally, an outline of the profile likelihood ratio method in the context of searching for new physics and setting limits is given in Section 13.3.

13.1 Hypothesis Testing

Central to the search for new phenomena at the LHC is the notion of hypothesis testing. The goal of such a test is to construct a test statistic that maps the outcome of an experiment to a single real number (called a p-value) that quantifies the probability of obtaining data of equal or greater incompatibility with some hypothesis. This p-value can then be used to claim the discovery or exclusion of some physics process at a chosen confidence level (CL). When conducting a hypothesis test in the context of a particle physics experiment, one needs to construct two hypotheses: the background-only hypothesis (H_0) and the signal-plus-background hypothesis (H_1), each of which are represented by probability density functions called likelihoods. In these experiments, which essentially count the number of

events satisfying some kinematic properties, the presence of signal almost always implies the presence of additional events when compared to the background-only hypothesis. In some cases, quantum mechanical interference effects from the introduction of a new physics process can lead to event yields that are not strictly additive, but this scenario is outside the scope of this dissertation.

Often, the p-value is translated into a significance Z, which is the corresponding quantile of a unit Gaussian distribution, expressed as a multiple of the standard deviation σ. When comparing the data to the background-only hypothesis, the threshold adopted by the particle physics community for claiming a discovery is $Z = 5\sigma$, which has a corresponding p-value of $p = 2.9 \times 10^{-7}$. Similarly, the conventional threshold for rejecting the signal-plus-background hypothesis is $p = 0.05$, which corresponds to $Z = 1.64\sigma$.

13.2 Likelihood Function

The likelihood function consists of all of the event yields in the relevant SRs and CRs as well additional nuisance parameter terms that account for both statistical and systematic uncertainties. The set of nuisance parameters is denoted by $\boldsymbol{\theta}$, whose values can impact the expected signal and background contributions. Therefore, the expected total number of events in a given bin i of region r is given by $\mu s_{ri}(\boldsymbol{\theta}) + b_{ri}(\boldsymbol{\theta})$, where $s_{ri}(\boldsymbol{\theta})$ and $b_{ri}(\boldsymbol{\theta})$ are the expected number of signal and background events, respectively. In the likelihood function, these event rates are modeled using Poisson terms. In the case of systematic uncertainties, the nuisance parameter terms are described by Gaussian probability distribution functions that are constrained by auxiliary measurements. Poisson probabilities are used for nuisance parameter terms related to statistical uncertainties. The likelihood function L, which is a function of the parameter of interest μ and the

nuisance parameters $\boldsymbol{\theta}$, is constructed as the product of these terms according to

$$L(\mu, \boldsymbol{\theta}) = \prod_{r \in \text{regions}} \prod_{i \in \text{bins}} \frac{\left(\mu s_{ri}(\boldsymbol{\theta}) + b_{ri}(\boldsymbol{\theta})\right)^{n_{ri}}}{n_{ri}!} e^{-(\mu s_{ri}(\boldsymbol{\theta}) + b_{ri}(\boldsymbol{\theta}))} \prod_{k \in \boldsymbol{\theta}} f_k\left(\theta'_k | \theta_k\right), \quad (13.2)$$

where n_{ri} is the observed number of events in bin i of region r and f_k is the probability distribution function used to model the nuisance parameter θ_k.

When setting limits on direct slepton production, the SRs included in the likelihood are all of the exclusive SRs bins within SR–S–high and SR–S–low. Similarly, the likelihood for electroweakino exclusion fits includes the exclusive SR bins in SR–E–high, SR–E–med, SR–E–low. Only the wino/bino interpretations include SR–E–1ℓ1T, since this SR is not expected to be sensitive to direct higgsino production due to the lower cross-sections.

13.3 Test Statistics, Discovery, and Limit Setting

The Neyman–Pearson lemma states that the optimal test statistic for discerning between H_1 and H_0 is the likelihood ratio $\frac{L_{s+b}}{L_b}$, where L_{s+b} and L_b are the likelihood functions of H_1 and H_0, respectively. But the simple likelihood ratio has an important drawback in that it is a function of both the signal strength parameter and nuisance parameters, whereas searches for new physics are only interested in the former. The experiments at the LHC have therefore adopted the profile likelihood ratio method, which eliminates the explicit dependence of the likelihood ratio on the nuisance parameters by making them functions of the signal strength itself in a process called "profiling." Explicitly, the profile likelihood

ratio test statistic $\lambda(\mu)$ is given by

$$\lambda(\mu) = \frac{L(\mu, \hat{\hat{\boldsymbol{\theta}}}(\mu))}{L(\hat{\mu}, \hat{\boldsymbol{\theta}})} \ , \tag{13.3}$$

where $\hat{\mu}$ and $\hat{\boldsymbol{\theta}}$ are maximum likelihood estimators and $\hat{\hat{\boldsymbol{\theta}}}$ is a conditional maximum likelihood estimator. That is, $\hat{\mu}$ and $\hat{\boldsymbol{\theta}}$ are the values that maximize $L(\mu, \boldsymbol{\theta})$ globally, while $\hat{\hat{\boldsymbol{\theta}}}(\mu)$ is the value of $\boldsymbol{\theta}$ that maximizes $L(\mu, \boldsymbol{\theta})$ for some fixed value of μ. Thus, by profiling over $\boldsymbol{\theta}$, the profile likelihood ratio is manifestly independent of the values of the nuisance parameters. In practice, the profiling over the nuisance parameters is achieved by interpolating between histograms that represent the yield variations due to a given uncertainty. One should understand $\lambda(\mu)$ as having the property that $0 \leq \lambda(\mu) \leq 1$, with larger values indicating better agreement between the data and the model for a given value of μ.

Unfortunately, the profile likelihood ratio as defined in Equation 13.3 does not satisfy our physical intuition in at least one special case: what happens if we observe fewer events than is predicted by the $\mu = 0$ (i.e. background-only) hypothesis? In this case, the maximum likelihood estimator $\hat{\mu}$ will be negative, when in fact, the presence of signal should not reduce the number of expected events compared to background-only hypothesis [1]. Another way to state this is that physicists work in a theoretical framework where signal processes can only have positive or vanishing rates (i.e. $\mu \geq 0$). Simply using Equation 13.3 as the test statistic would also have the undesirable feature of counting a downward fluctuation in the data as evidence against the background-only hypothesis.

Nevertheless, allowing for $\hat{\mu} < 0$ means that $\hat{\mu}$ can be approximated as be-

[1] Again, we are ignoring the rare case where quantum mechanical interference effects between the background and signal processes can lead to a signal-plus-background model that is not strictly additive in the number of events.

ing Gaussian-distributed, which in turn allows one to determine the asymptotic behavior of the final test statistics used in searches for new physics at the LHC [121]. Instead, the profile likelihood ratio can be redefined in such a way that when $\hat{\mu} < 0$, the best agreement with the data is taken to be at $\hat{\mu} = 0$:

$$\tilde{\lambda}(\mu) = \begin{cases} \frac{L(\mu, \hat{\hat{\boldsymbol{\theta}}}(\mu))}{L(\hat{\mu}, \hat{\boldsymbol{\theta}})} & \hat{\mu} \geq 0, \\ \frac{L(\mu, \hat{\hat{\boldsymbol{\theta}}}(\mu))}{L(0, \hat{\hat{\boldsymbol{\theta}}}(0))} & \hat{\mu} < 0. \end{cases} \tag{13.4}$$

By convention (and to reduce computational cost), a new test statistic $\tilde{t}_\mu$ is defined based on Equation 13.4:

$$\tilde{t}_\mu = -2 \ln \tilde{\lambda}(\mu) = \begin{cases} -2 \ln \frac{L(\mu, \hat{\hat{\boldsymbol{\theta}}}(\mu))}{L(0, \hat{\hat{\boldsymbol{\theta}}}(0))} & \hat{\mu} < 0, \\ -2 \ln \frac{L(\mu, \hat{\hat{\boldsymbol{\theta}}}(\mu))}{L(\hat{\mu}, \hat{\boldsymbol{\theta}})} & \hat{\mu} \geq 0. \end{cases} \tag{13.5}$$

Thus, the problem of maximizing the likelihood becomes a problem of minimizing its negative logarithm. With this definition of the test statistic, larger values correspond to worse agreement between the data and the model at a given value of μ. In order to determine p-values, one must know the distribution of the test statistic. This can be achieved by generating pseudo-experiments with MC techniques, but this procedure can be extremely computationally expensive. An important feature of this test statistic is that its distribution asymptotically approaches a χ^2 distribution [121]. Thus, the asymptotic formulation of $\tilde{t}_\mu$ can be used when the data sample is sufficiently large, which is the approach taken in the exclusion fits presented in this dissertation.

During the discovery phase of the search, the compatibility of the observed data is tested against the background-only hypothesis (i.e. $\mu = 0$). In this case,

the test statistic is denoted by q_0 and takes the form

$$q_0 = \begin{cases} -2\ln\lambda(0) & \hat{\mu} \geq 0 \\ 0 & \hat{\mu} < 0 \end{cases}. \tag{13.6}$$

In this definition, larger values of q_0 indicate greater disagreement between the data and the background-only hypothesis. The discovery p-value, p_0, can then be calculated according to

$$p_0 = \int_{q_{0,\text{obs}}}^{\infty} f\left(q_0|\mu = 0\right) dq_0, \tag{13.7}$$

where $q_{0,\text{obs}}$ is the observed value of the test statistic and $f\left(q_0|\mu = 0\right)$ is the distribution of the test statistic q_0 under the background-only hypothesis, estimated either with MC methods or asymptotic approximations.

For limit setting, the data are checked for consistency with the signal-plus-background hypothesis. With the constraint that $\mu \geq 0$, the test statistic, $\tilde{q}_\mu$, is given by

$$\tilde{q}_\mu = \begin{cases} -2\ln\tilde{\lambda}(\mu) & \hat{\mu} \leq \mu \\ 0 & \hat{\mu} > \mu \end{cases}. \tag{13.8}$$

Similar to the discovery case, the p-value for a given value of μ is obtained using the observed value of $\tilde{q}_\mu$ and the expected distribution of the test statistic for some signal-plus-background hypothesis, $f(\tilde{q}_\mu|\mu)$, according to

$$p_\mu = \int_{q_{\mu,\text{obs}}}^{\infty} f\left(q_\mu|\mu\right) dq_\mu. \tag{13.9}$$

Instead of using p_μ to set limits, ATLAS has adopted the CL_s method [122], which prescribes the use of

$$\text{CL}_\text{s} = \frac{p_\mu}{1 - p_b}, \tag{13.10}$$

where p_b is the p-value corresponding to the background-only hypothesis using the same test statistic:

$$p_b = \int_{q_{\mu,\mathrm{obs}}}^{\infty} f\left(q_\mu | \mu = 0\right) dq_\mu. \tag{13.11}$$

Since $1 - p_b < 1$, this construction is a conservative method that aims to mitigate cases in which downward fluctuations of the data can lead to exclusions for arbitrarily small signals. In order to set upper limits on a particular signal hypothesis, a scan is performed over μ to find the particular value, μ_{95}, corresponding to $\mathrm{CL_s} = 0.05$. One can therefore claim that all values of μ greater than μ_{95} are excluded at the 95% CL. All signal hypotheses with $\mu_{95} < 1.0$ are therefore considered to be excluded, also at the 95% CL.

Chapter 14

Model-Independent Search for New Physics

With the SRs, background estimation strategy, and fit models defined, the discovery phase of the searches begins. First, background-only fits to the CRs are performed using the statistical methods described in the previous chapter. These fits result in normalization factors that are propagated to the VRs in order to inspect the overall background modeling. After this validation, the SRs can be unblinded to check for significant excesses over the background expectation. All of this is presented in Section 14.1.

During the search for generic new physics, the agreement between the data and the SM expectation is quantified by extracting p-values under the background-only hypothesis from simultaneous fits to the CRs and one of the single-bin inclusive SRs. The results of the fit can also be used to set 95% CL upper limits on the number of signal events in the inclusive SRs and the visible cross-section, which accounts for the efficiencies of the reconstruction and event selections. Motivation for providing these limits is discussed in Section 14.2 and the results themselves are given in Section 14.3.

14.1 Background-Only Fits to the CRs and Unblinded Results

Before the SRs can be unblinded, the quality of the background modeling needs to be assessed. The shapes of all kinematic distributions for all background processes are taken directly from MC simulation, aside from the component due to fake/non-prompt leptons. Of the simulated backgrounds, the largest contributions to the SRs come from the $t\bar{t}/Wt$, $Z^{(*)}/\gamma^*(\rightarrow \tau\tau)+\text{jets}$, and VV processes. Dedicated CRs are constructed in order to extract normalization factors for these backgrounds, which are then propagated to the VRs when assessing the background modeling.

The normalization factors and uncertainties are obtained from a background-only fit of the CRs. These fits are performed simultaneously to all of the CRs targeting sleptons or electroweakinos, with floating parameters of interest that correspond to the normalization factors for the $t\bar{t}/Wt$, $Z^{(*)}/\gamma^*(\rightarrow \tau\tau)+\text{jets}$, and VV backgrounds. While the CRs constructed for the VV background are not very pure, the fact that these fits are performed simultaneously still allows for a reasonable normalization factor uncertainty to be obtained since the contributions from $t\bar{t}/Wt$ and $Z^{(*)}/\gamma^*(\rightarrow \tau\tau)+\text{jets}$ are constrained by their own dedicated CRs. In order to match the SR definitions, separate normalization factors are derived for the high-$E_{\text{T}}^{\text{miss}}$ and low-$E_{\text{T}}^{\text{miss}}$ regions. The results of the background-only fit of the CRs are shown in Table 14.1. The normalization factors obtained for the low-$E_{\text{T}}^{\text{miss}}$ CRs targeting the VV background differ from unity by slightly more than their uncertainties, indicating some mis-modeling in this phase space. Examples of various kinematic distributions in the electroweakino CRs after the background-only fit of the CRs are shown in Figure 14.1, while those for the slepton CRs are

presented in Figure 14.2.

Table 14.1: Normalization factors obtained from a background-only fit of the CRs defined for electroweakino and slepton searches. The uncertainties account for both statistical and systematic contributions.

Backgrounds	$E_{\mathrm{T}}^{\mathrm{miss}}$ region	Normalization Parameters electroweakino	slepton
$t\bar{t}/Wt$	high	1.08 ± 0.20	1.05 ± 0.20
	low	1.08 ± 0.18	1.09 ± 0.19
$Z^{(*)}/\gamma^*(\rightarrow \tau\tau) + \text{jets}$	high	0.96 ± 0.14	0.80 ± 0.17
	low	1.02 ± 0.15	1.08 ± 0.17
VV	high	0.89 ± 0.27	0.85 ± 0.28
	low	0.69 ± 0.22	0.71 ± 0.23

Applying the fitted normalization factors, the backgrounds are extrapolated to the VRs to check the level of agreement between the data and the background estimates. Figure 14.3 shows the results in the VRDF regions, which are designed to have similar background compositions to the SRs. Additionally, they consist of exclusive bins in either $m_{\ell\ell}$ or m_{T2}^{100} that match the bin intervals used by the SRs. Overall, good agreement is observed between the data and the extrapolated backgrounds, as no deviations exceed the 2σ level. Additional kinematic distributions in the VRDF and VRtau–E–med regions are shown in Figure 14.4, where both the shape and normalization of the background predictions are in good agreement with the data. Due to the limited number of events, it is difficult to derive a dedicated CR for the $Z^{(*)}/\gamma^*(\rightarrow \tau\tau) + \text{jets}$ contribution to SR–E–med. Instead, CRtau–E–low is used to normalize this background in SR–E–med and this method is subsequently checked in VRtau–E–med, which is only orthogonal to SR–E–med by requiring $m_{\tau\tau} \in [60, 120]$ GeV. The good background modeling seen in VRtau–E–med gives confidence in the extrapolation from CRtau–E–low

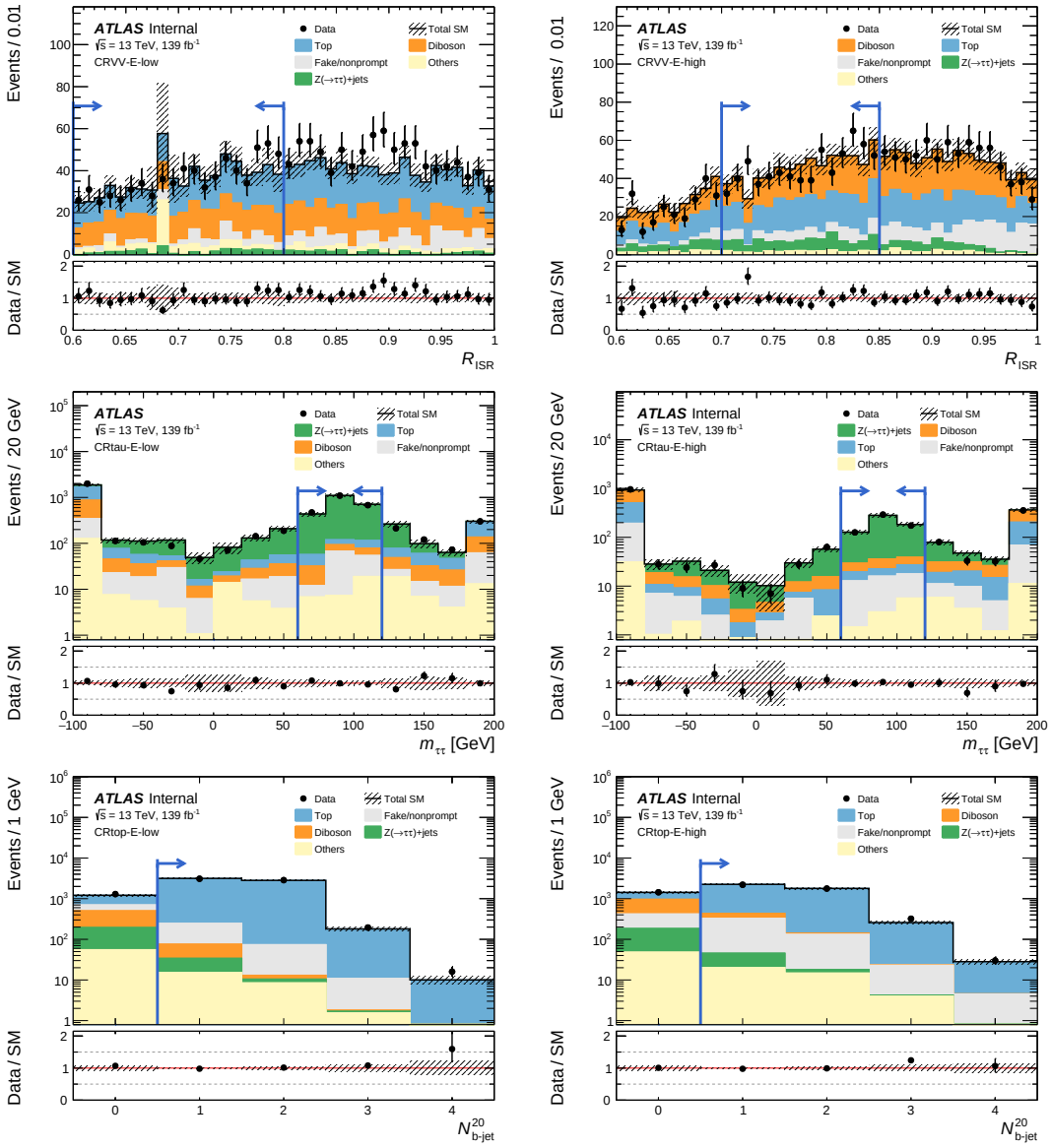

Figure 14.1: Examples of kinematic distributions after the background-only fit of the electroweakino CRs showing the data as well as the expected background in the control regions. The full event selection of the corresponding regions is applied, except for distributions showing blue arrows, where the requirement on the variable being plotted is removed and indicated by the arrows in the distributions instead. The first (last) bin includes underflow (overflow). The uncertainty bands plotted include all statistical and systematic uncertainties.

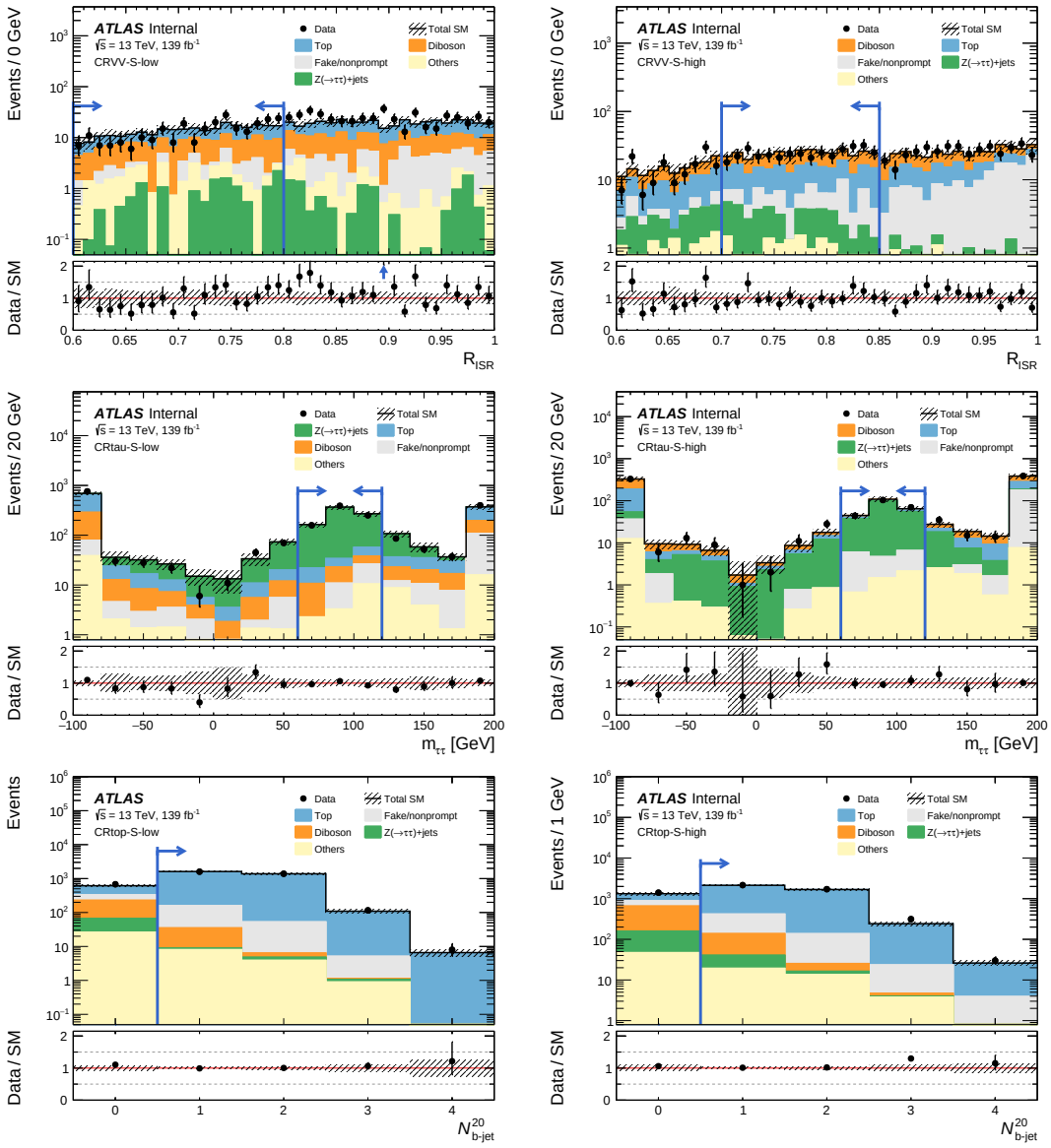

Figure 14.2: Examples of kinematic distributions after the background-only fit of the slepton CRs showing the data as well as the expected background in the control regions. The full event selection of the corresponding regions is applied, except for distributions showing blue arrows, where the requirement on the variable being plotted is removed and indicated by the arrows in the distributions instead. The first (last) bin includes underflow (overflow). The uncertainty bands plotted include all statistical and systematic uncertainties.

to SR–E–med, which requires $E_{\mathrm{T}}^{\mathrm{miss}}/H_{\mathrm{T}}^{\mathrm{lep}} < 10$ and $E_{\mathrm{T}}^{\mathrm{miss}}/H_{\mathrm{T}}^{\mathrm{lep}} > 10$, respectively.

Additionally, the VRSS regions are checked after background-only fit of the CRs. By requiring two leptons of the same electric charge, these VRs are enriched with events containing fake/non-prompt leptons that allow the modeling of this background to be assessed. The $m_{\ell\ell}$- and m_{T2}^{100}-dependent cuts on $p_{\mathrm{T}}^{\ell_2}$ are not applied in the VRSS regions in order to increase the statistics of this background. Figure 14.5 and Figure 14.6 show several kinematic distributions in the electroweakino and slepton VRSS regions, respectively, where good agreement between the data and prediction can be seen, indicating sufficient modeling of the fake/non-prompt background via the fake factor method.

Once the background modeling in the VRs is deemed sufficient, the SRs can be unblinded and checked for excesses over the background prediction that could indicate the existence of some BSM process. Examples of ee and $\mu\mu$ events that fall into SR–E–high and SR–S–high are shown in Figure 14.7 and 14.8, respectively. When forming the background prediction in the SRs, the normalization factors obtained from the simultaneous fits to the CRs under the background-only hypothesis are applied to the $t\bar{t}/Wt$, $Z^{(*)}/\gamma^{*}(\rightarrow \tau\tau)$+jets, and VV processes. The data and extrapolated background yields in the exclusive electroweakino and slepton SRs are shown in Table 14.2 and Table 14.3, respectively. Various kinematic distributions in the electroweakino SRs are presented in Figure 14.9 after performing the background-only fit of the CRs. Distributions in the slepton SRs are shown in Figure 14.10 and Figure 14.11. While the data yields are consistently higher than the fitted background yields in SR–E–med, none of the other SRs show signs of obvious excesses above the background prediction. In order to test for the production of some generic BSM physics process that could be populating the SRs, these fits are extended to include one of the single-bin inclusive SRs. The

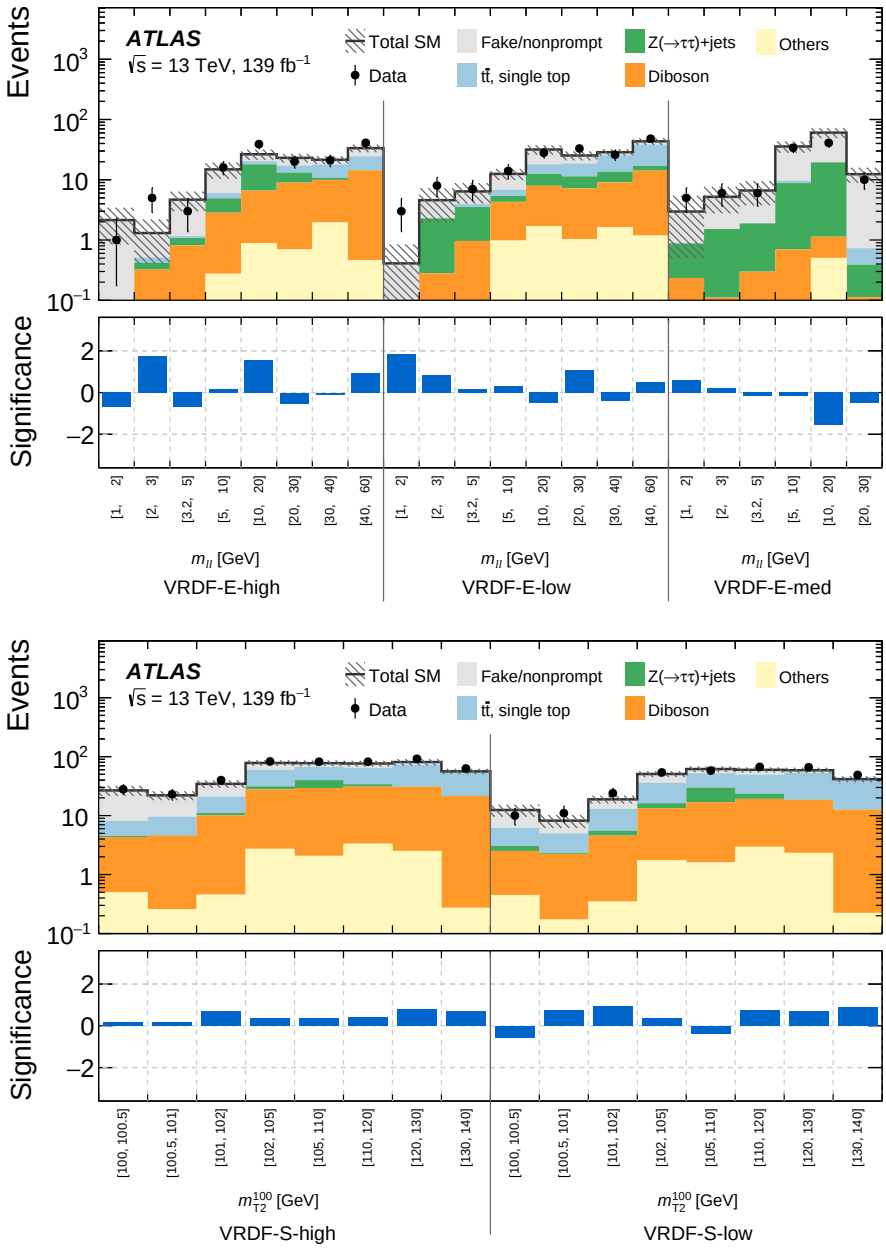

Figure 14.3: Comparison of observed and expected event yields in the VRDF regions after a background-only fit of the CRs. The three VRDF–E regions are shown at the top, while the the two VRDF–S regions are shown at the bottom. In each case, the VRs are binned in the relevant discriminating variable according to the corresponding SR. The background uncertainties shown include those from both statistical and systematic sources. The bottom panel in both plots shows the significance of the difference between the expected and observed yields.

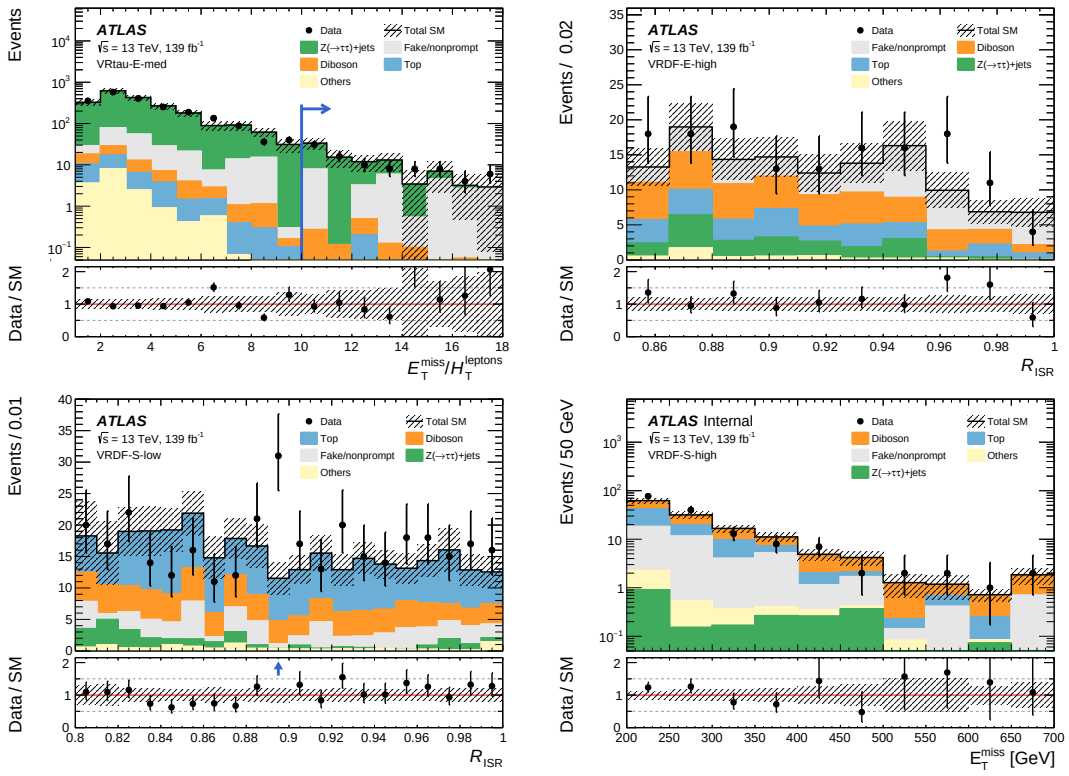

Figure 14.4: Examples of kinematic distributions after the background-only fit of the CRs showing the data as well as the expected background in the validation regions VRtau–E–med (top left), VRDF–E–high (top right), VRDF–S–low (bottom left), and VRDF–S–high (bottom right). The full event selection of the corresponding regions is applied, except for distributions showing blue arrows, where the requirement on the variable being plotted is removed and indicated by the arrows in the distributions instead. The first (last) bin includes underflow (overflow). The uncertainty bands plotted include all statistical and systematic uncertainties.

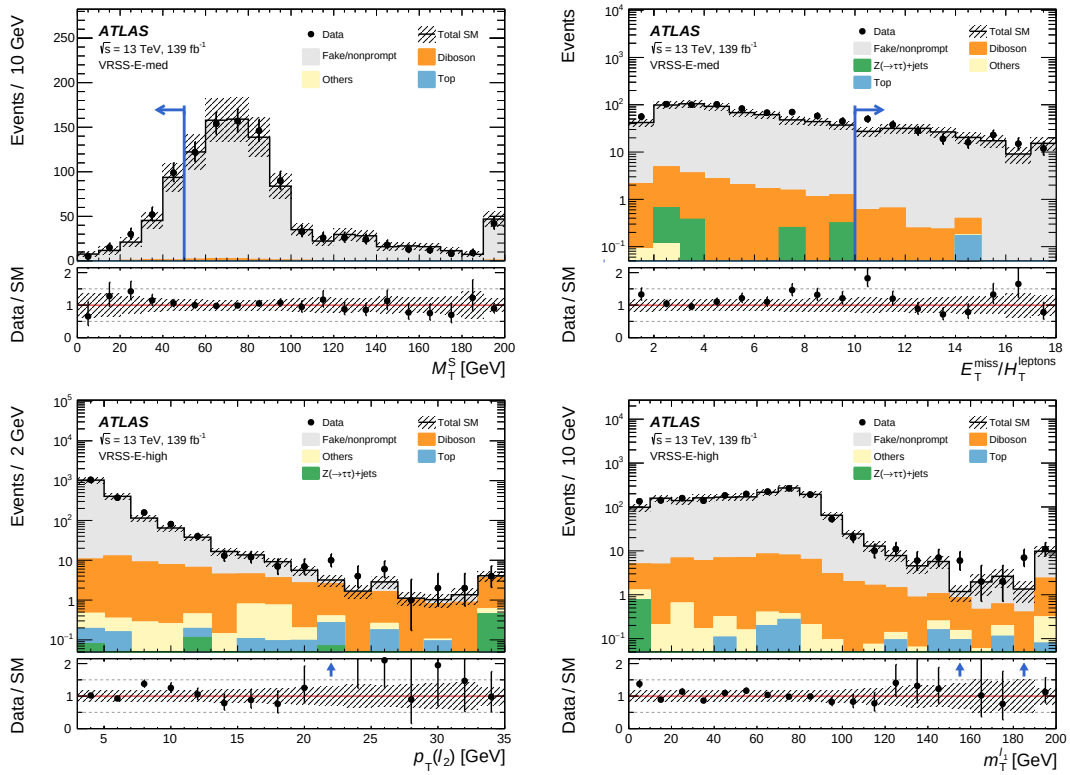

Figure 14.5: Examples of kinematic distributions after the background-only fit of the CRs showing the data as well as the expected background in the validation regions VRSS–E–med (top) and VRSS–E–high (bottom). The full event selection of the corresponding regions is applied, except for distributions showing blue arrows, where the requirement on the variable being plotted is removed and indicated by the arrows in the distributions instead. The first (last) bin includes underflow (overflow). The uncertainty bands plotted include all statistical and systematic uncertainties.

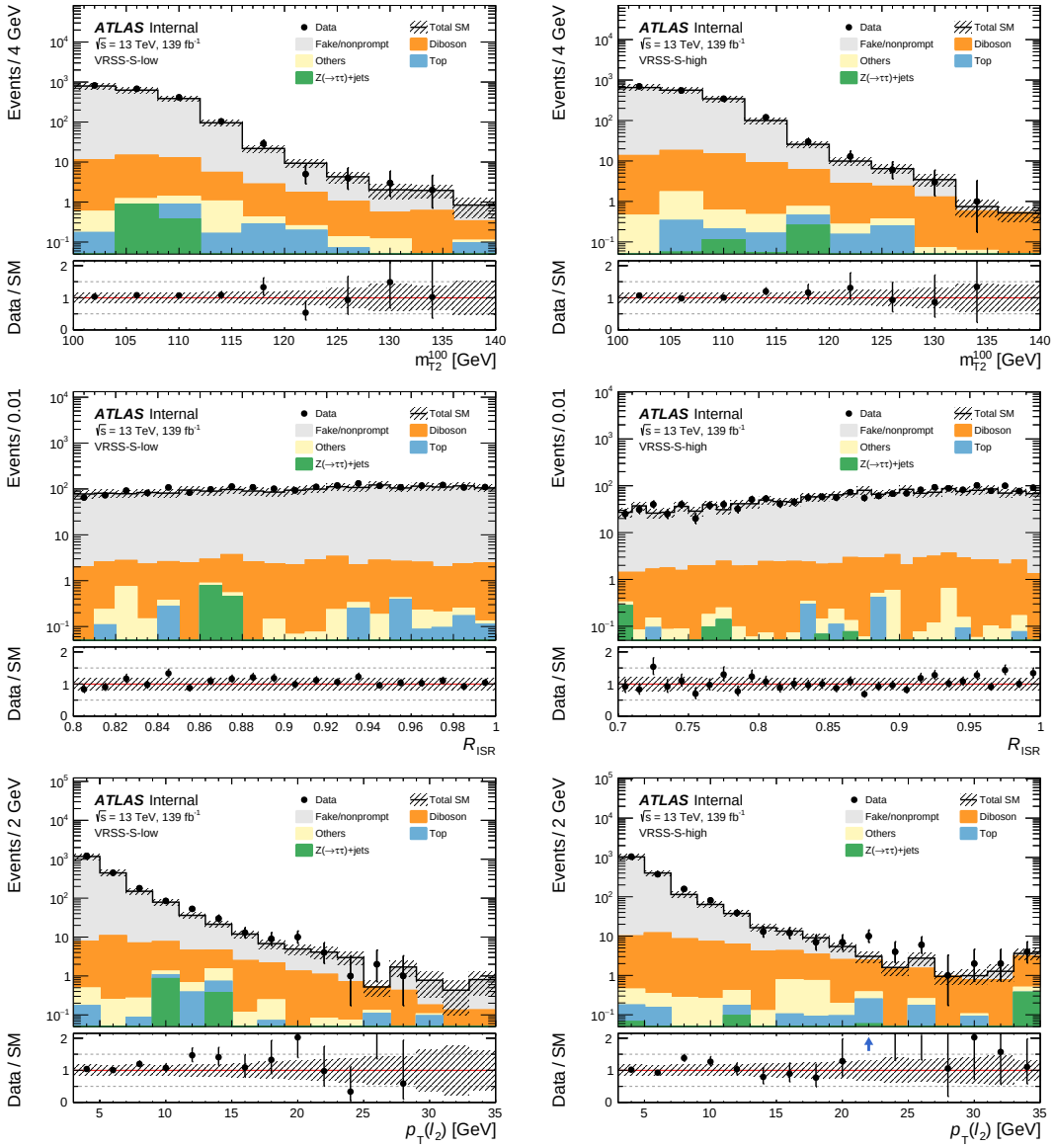

Figure 14.6: Examples of kinematic distributions after the background-only fit of the CRs showing the data as well as the expected background in the validation regions VRSS–S–low (left) and VRSS–S–high (right). The first (last) bin includes underflow (overflow). The uncertainty bands plotted include all statistical and systematic uncertainties.

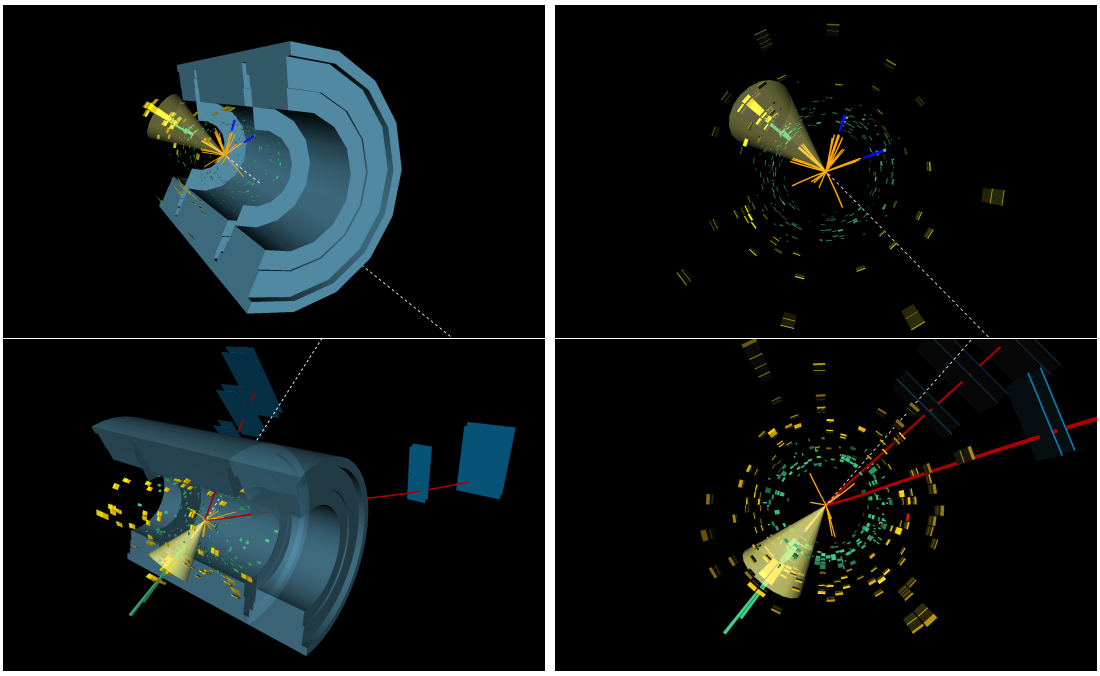

Figure 14.7: Event displays of two events from 2018 data that fall into SR–E–high. The top (bottom) row shows two different views of the same event containing two electrons (muons) with $m_{\ell\ell} = 7.8\,\text{GeV}$ (13.2 GeV). The missing momentum in the event is displayed as a dashed white line. Muon trajectories are shown in red and energy deposits corresponding to electrons are shown in blue. Finally, reconstructed jets are pictured as yellow cones. Various p_{T} thresholds are applied to each object type in order to make the event displays cleaner.

background predictions in these inclusive SRs are determined by the background-only fit of the CRs and are compared to the data yields via hypothesis tests. The result of the hypothesis tests are p-values that represent the probability under the background-only hypothesis to produce event yields greater than or equal to the observed data in a given inclusive SR. These model-independent limits on the production of new physics phenomena are presented in Section 14.3.

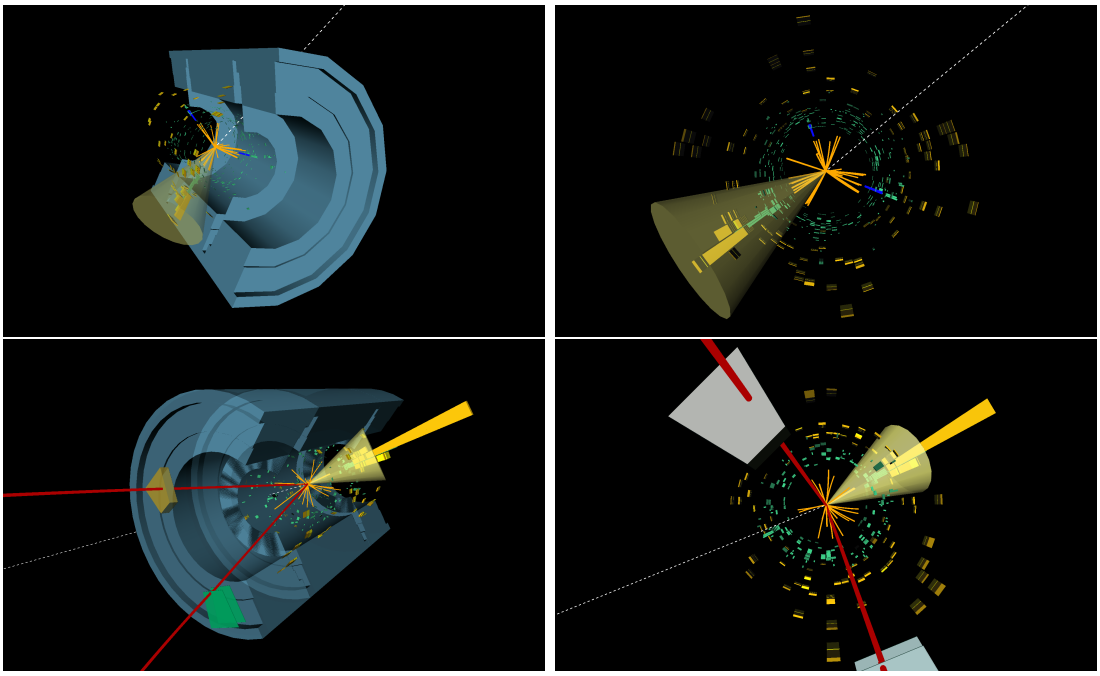

Figure 14.8: Event displays of two events from 2018 data that fall into SR–S–high. The top (bottom) row shows two different views of the same event containing two electrons (muons) with $m_{\mathrm{T2}}^{100} = 103.2\,\mathrm{GeV}$ (101.2 GeV). The missing momentum in the event is displayed as a dashed white line. Muon trajectories are shown in red and energy deposits corresponding to electrons are shown in blue. Finally, reconstructed jets are pictured as yellow cones. Various p_{T} thresholds are applied to each object type in order to make the event displays cleaner.

Table 14.2: Observed event yields and fit results using a background-only fit of the CRs for the exclusive electroweakino SRs. Background processes containing fewer than two prompt leptons are categorized as "Fake/nonprompt." The category "Others" contains rare backgrounds from triboson, Higgs boson, and the remaining top-quark production processes listed in Table 8.3. Uncertainties in the fitted background estimates combine statistical and systematic uncertainties.

	SR bin [GeV]	[1,2]	[2,3]	[3.2,5]	[5,10]	[10,20]	[20,30]	[30,40]	[40,60]
SR-E-high ee	Observed			1	16	13	8	8	18
	Fitted SM events			0.7 ± 0.4	4.8 ± 1.6	11.3 ± 3.0	10.5 ± 2.5	11.1 ± 2.6	19.2 ± 3.5
	Fake/nonprompt			$0.00^{+0.16}_{-0.00}$	1.4 ± 1.3	3.4 ± 2.0	3.8 ± 2.1	4.3 ± 2.3	5.9 ± 3.0
	$t\bar{t}$, single top			$0.00^{+0.05}_{-0.00}$	0.51 ± 0.24	1.8 ± 0.5	1.6 ± 0.4	3.6 ± 0.7	6.3 ± 1.1
	Diboson			0.68 ± 0.29	1.4 ± 0.5	2.5 ± 0.8	2.8 ± 0.9	2.8 ± 0.7	6.3 ± 1.4
	$Z(\rightarrow \tau\tau)$+jets			$0.00^{+0.24}_{-0.00}$	1.3 ± 0.6	2.7 ± 1.5	0.92 ± 0.31	0.06 ± 0.06	0.52 ± 0.16
	Others			$0.000^{+0.006}_{-0.000}$	0.11 ± 0.06	0.76 ± 0.19	1.20 ± 0.20	0.27 ± 0.07	0.26 ± 0.18
SR-E-high $\mu\mu$	Observed	5	5	0	9	23	3	5	20
	Fitted SM events	2.5 ± 1.2	2.1 ± 1.3	6.9 ± 2.4	12.1 ± 2.6	14.6 ± 3.0	10.0 ± 2.0	11.1 ± 2.0	20.1 ± 2.8
	Fake/nonprompt	1.3 ± 1.1	1.2 ± 1.2	3.5 ± 1.9	3.3 ± 2.1	4.0 ± 2.1	1.7 ± 1.1	2.3 ± 1.2	$1.1^{+1.2}_{-1.1}$
	$t\bar{t}$, single top	$0.00^{+0.05}_{-0.00}$	$0.00^{+0.05}_{-0.00}$	0.13 ± 0.12	0.81 ± 0.34	1.8 ± 0.6	2.5 ± 0.7	3.8 ± 1.2	10.0 ± 1.9
	Diboson	1.1 ± 0.4	0.9 ± 0.4	1.7 ± 0.8	3.1 ± 0.8	3.4 ± 0.8	4.1 ± 1.1	4.3 ± 1.0	7.6 ± 1.7
	$Z(\rightarrow \tau\tau)$+jets	$0.00^{+0.24}_{-0.00}$	$0.00^{+0.24}_{-0.00}$	1.5 ± 0.7	4.1 ± 1.1	4.6 ± 1.4	0.5 ± 0.4	$0.00^{+0.24}_{-0.00}$	0.4 ± 0.4
	Others	$0.04^{+0.07}_{-0.04}$	0.0 ± 0.0	0.04 ± 0.04	0.7 ± 0.5	0.86 ± 0.16	1.21 ± 0.22	0.78 ± 0.24	1.06 ± 0.10
SR-E-med ee	Observed			0	4	11	4		
	Fitted SM events			$0.13^{+0.31}_{-0.13}$	4.5 ± 2.3	4.1 ± 1.9	0.9 ± 0.8		
	Fake/nonprompt			$0.00^{+0.16}_{-0.00}$	3.3 ± 1.7	3.8 ± 1.9	$0.6^{+0.7}_{-0.6}$		
	$t\bar{t}$, single top			$0.00^{+0.05}_{-0.00}$	$0.00^{+0.05}_{-0.00}$	$0.00^{+0.05}_{-0.00}$	$0.23^{+0.27}_{-0.23}$		
	Diboson			0.09 ± 0.05	0.14 ± 0.14	0.25 ± 0.24	$0.00^{+0.09}_{-0.00}$		
	$Z(\rightarrow \tau\tau)$+jets			$0.00^{+0.25}_{-0.00}$	$1.0^{+1.5}_{-1.0}$	$0.00^{+0.25}_{-0.00}$	$0.00^{+0.25}_{-0.00}$		
	Others			$0.000^{+0.019}_{-0.000}$	0.0 ± 0.0	0.0 ± 0.0	0.0 ± 0.0		
SR-E-med $\mu\mu$	Observed	16	8	6	41	59	21		
	Fitted SM events	13 ± 5	5.5 ± 2.9	6.3 ± 3.1	23 ± 5	40 ± 8	15 ± 4		
	Fake/nonprompt	7 ± 4	3.5 ± 2.8	5.4 ± 3.0	17 ± 5	33 ± 7	14 ± 4		
	$t\bar{t}$, single top	$0.00^{+0.05}_{-0.00}$	$0.00^{+0.05}_{-0.00}$	$0.00^{+0.05}_{-0.00}$	$0.09^{+0.10}_{-0.09}$	0.21 ± 0.08	$0.10^{+0.13}_{-0.10}$		
	Diboson	2.3 ± 0.9	0.9 ± 0.4	0.75 ± 0.27	1.9 ± 0.7	0.84 ± 0.26	0.14 ± 0.07		
	$Z(\rightarrow \tau\tau)$+jets	3.2 ± 1.9	1.2 ± 0.5	$0.1^{+0.4}_{-0.1}$	4.1 ± 1.5	5.2 ± 2.1	$0.00^{+0.25}_{-0.00}$		
	Others	0.5 ± 0.4	$0.01^{+0.04}_{-0.01}$	0.036 ± 0.022	$0.016^{+0.018}_{-0.016}$	0.8 ± 0.7	0.0 ± 0.0		
SR-E-low ee	Observed			7	11	16	16	10	9
	Fitted SM events			3.9 ± 1.8	6.9 ± 2.2	16 ± 4	13 ± 4	13.6 ± 3.2	21.9 ± 3.5
	Fake/nonprompt			1.1 ± 0.9	2.3 ± 1.5	5.4 ± 2.8	4.7 ± 2.6	4.3 ± 2.6	3.2 ± 2.1
	$t\bar{t}$, single top			$0.000^{+0.006}_{-0.000}$	$0.31^{+0.33}_{-0.31}$	2.9 ± 0.8	3.1 ± 1.2	4.7 ± 1.3	11.5 ± 2.1
	Diboson			1.0 ± 0.6	2.3 ± 0.8	3.2 ± 0.8	2.2 ± 0.8	2.5 ± 0.8	4.6 ± 1.2
	$Z(\rightarrow \tau\tau)$+jets			1.8 ± 1.1	1.8 ± 0.9	4.3 ± 1.8	2.3 ± 1.1	1.5 ± 0.9	$0.2^{+0.7}_{-0.2}$
	Others			$0.01^{+0.04}_{-0.01}$	0.19 ± 0.06	0.79 ± 0.26	1.1 ± 0.8	0.58 ± 0.11	2.5 ± 0.6
SR-E-low $\mu\mu$	Observed	9	7	7	12	17	18	16	44
	Fitted SM events	18 ± 4	9.2 ± 2.8	6.0 ± 2.4	11.0 ± 2.4	14.8 ± 3.0	16.4 ± 3.0	14.6 ± 2.5	33 ± 4
	Fake/nonprompt	9.0 ± 2.5	$0.7^{+1.2}_{-0.7}$	$0.00^{+0.21}_{-0.00}$	2.3 ± 1.2	3.9 ± 1.8	2.1 ± 1.4	2.2 ± 1.5	3.4 ± 1.7
	$t\bar{t}$, single top	$0.00^{+0.05}_{-0.00}$	0.28 ± 0.08	$0.00^{+0.05}_{-0.00}$	1.1 ± 0.7	3.3 ± 0.9	5.1 ± 1.8	7.7 ± 1.6	18.1 ± 3.3
	Diboson	6.1 ± 1.9	2.9 ± 0.9	3.1 ± 1.1	3.8 ± 1.1	4.1 ± 1.0	3.8 ± 0.9	3.7 ± 0.9	7.7 ± 1.7
	$Z(\rightarrow \tau\tau)$+jets	2.4 ± 0.9	4.3 ± 1.6	2.3 ± 1.9	3.4 ± 1.5	2.1 ± 1.8	3.2 ± 1.1	$0.00^{+0.25}_{-0.00}$	1.6 ± 0.6
	Others	1.1 ± 1.1	1.0 ± 1.0	0.51 ± 0.29	0.53 ± 0.17	1.32 ± 0.19	2.1 ± 0.4	0.92 ± 0.13	2.50 ± 0.20

Table 14.3: Observed event yields and exclusion fit results using a background-only fit of the CRs for the exclusive slepton SRs. Background processes containing fewer than two prompt leptons are categorized as "Fake/nonprompt." The category "Others" contains rare backgrounds from triboson, Higgs boson, and the remaining top-quark production processes listed in Table 8.3. Uncertainties in the fitted background estimates combine statistical and systematic uncertainties.

	SR bin [GeV]	[100,100.5]	[100.5,101]	[101,102]	[102,105]	[105,110]	[110,120]	[120,130]	[130,140]
SR-S-high ee	Observed	3	3	9	13	9	6	8	6
	Fitted SM events	4.0 ± 1.6	3.3 ± 1.3	7.8 ± 2.7	13.6 ± 2.9	7.9 ± 1.6	7.8 ± 1.6	6.8 ± 1.4	6.1 ± 1.2
	Fake/nonprompt	3.0 ± 1.5	2.1 ± 1.2	4.7 ± 2.5	4.3 ± 2.4	$0.2^{+0.7}_{-0.2}$	$0.00^{+0.16}_{-0.00}$	$0.00^{+0.16}_{-0.00}$	$0.00^{+0.16}_{-0.00}$
	$t\bar{t}$, single top	0.50 ± 0.24	0.49 ± 0.31	1.0 ± 0.5	4.4 ± 1.0	2.7 ± 0.8	4.1 ± 1.0	3.1 ± 0.8	2.9 ± 0.7
	Diboson	0.51 ± 0.21	0.69 ± 0.25	2.0 ± 0.7	4.3 ± 1.3	3.6 ± 1.1	3.6 ± 1.1	3.6 ± 1.0	3.2 ± 0.9
	$Z(\to \tau\tau)$+jets	$0.00^{+0.20}_{-0.00}$	$0.00^{+0.20}_{-0.00}$	0.052 ± 0.020	0.44 ± 0.18	1.12 ± 0.27	$0.00^{+0.04}_{-0.00}$	$0.00^{+0.20}_{-0.00}$	$0.00^{+0.20}_{-0.00}$
	Others	0.0 ± 0.0	$0.016^{+0.029}_{-0.016}$	0.08 ± 0.05	0.24 ± 0.17	0.21 ± 0.11	$0.14^{+0.32}_{-0.14}$	$0.14^{+0.16}_{-0.14}$	$0.029^{+0.032}_{-0.029}$
SR-S-high $\mu\mu$	Observed	10	3	11	12	9	11	10	8
	Fitted SM events	11.6 ± 3.2	6.9 ± 1.9	7.1 ± 1.7	15.4 ± 2.5	12.5 ± 2.2	11.3 ± 1.9	12.4 ± 2.0	6.8 ± 1.4
	Fake/nonprompt	10.2 ± 3.2	4.0 ± 1.7	3.3 ± 1.5	2.7 ± 1.5	1.6 ± 1.2	$0.7^{+0.9}_{-0.7}$	$0.5^{+0.6}_{-0.5}$	$0.19^{+0.35}_{-0.19}$
	$t\bar{t}$, single top	0.5 ± 0.4	1.6 ± 0.6	1.9 ± 0.5	5.4 ± 1.0	4.3 ± 0.9	5.1 ± 0.9	6.4 ± 1.0	2.2 ± 0.8
	Diboson	0.90 ± 0.33	1.1 ± 0.4	1.7 ± 0.8	6.5 ± 1.9	5.3 ± 1.5	5.0 ± 1.4	5.5 ± 1.6	4.3 ± 1.2
	$Z(\to \tau\tau)$+jets	$0.00^{+0.20}_{-0.00}$	0.14 ± 0.04	0.15 ± 0.12	0.5 ± 0.5	1.0 ± 0.4	0.16 ± 0.12	$0.00^{+0.20}_{-0.00}$	$0.00^{+0.20}_{-0.00}$
	Others	$0.000^{+0.009}_{-0.000}$	0.029 ± 0.018	0.09 ± 0.05	0.28 ± 0.15	0.22 ± 0.15	0.28 ± 0.21	0.07 ± 0.06	0.07 ± 0.05
SR-S-low ee	Observed	8	5	15	19	30	24	32	11
	Fitted SM events	4.0 ± 1.4	5.3 ± 2.4	9.1 ± 2.4	21 ± 5	27 ± 5	17.8 ± 3.1	23 ± 4	19.2 ± 2.7
	Fake/nonprompt	1.9 ± 1.2	2.4 ± 1.4	3.4 ± 1.9	9 ± 4	5.5 ± 3.3	$1.4^{+1.6}_{-1.4}$	2.4 ± 1.9	1.2 ± 1.2
	$t\bar{t}$, single top	1.4 ± 0.5	1.9 ± 0.7	3.2 ± 1.0	5.7 ± 1.5	9.4 ± 1.7	6.8 ± 1.8	12.7 ± 2.7	12.5 ± 1.9
	Diboson	0.7 ± 0.4	0.52 ± 0.22	1.8 ± 0.6	4.6 ± 1.4	5.4 ± 1.7	7.0 ± 2.0	7.3 ± 2.1	5.5 ± 1.5
	$Z(\to \tau\tau)$+jets	$0.00^{+0.26}_{-0.00}$	$0.4^{+1.7}_{-0.4}$	0.5 ± 0.5	$0.3^{+0.8}_{-0.3}$	5.4 ± 2.1	$0.00^{+0.26}_{-0.00}$	$0.00^{+0.26}_{-0.00}$	$0.00^{+0.26}_{-0.00}$
	Others	0.09 ± 0.06	0.09 ± 0.07	0.22 ± 0.14	1.7 ± 0.9	$1.2^{+1.6}_{-1.2}$	2.6 ± 2.2	0.8 ± 0.7	0.11 ± 0.07
SR-S-low $\mu\mu$	Observed	3	6	15	23	37	44	41	28
	Fitted SM events	7.0 ± 1.6	4.4 ± 1.2	11.8 ± 2.1	25.9 ± 3.4	36 ± 5	35 ± 4	34 ± 4	24.8 ± 2.9
	Fake/nonprompt	3.8 ± 1.4	0.8 ± 0.7	4.6 ± 1.6	6.2 ± 2.2	3.0 ± 1.9	3.5 ± 1.9	1.4 ± 1.1	$0.00^{+0.10}_{-0.00}$
	$t\bar{t}$, single top	1.8 ± 0.5	2.2 ± 0.7	3.8 ± 0.9	8.6 ± 1.4	12.6 ± 2.4	18.4 ± 2.7	20.0 ± 2.7	16.9 ± 2.6
	Diboson	1.1 ± 0.4	1.1 ± 0.4	2.5 ± 0.8	6.9 ± 2.0	9.2 ± 2.5	9.5 ± 2.5	10.5 ± 3.0	7.7 ± 2.1
	$Z(\to \tau\tau)$+jets	$0.19^{+0.27}_{-0.19}$	$0.1^{+0.4}_{-0.1}$	0.65 ± 0.26	3.0 ± 1.7	7.8 ± 3.1	1.4 ± 0.9	$0.00^{+0.26}_{-0.00}$	$0.00^{+0.26}_{-0.00}$
	Others	0.12 ± 0.09	0.18 ± 0.10	0.28 ± 0.15	1.1 ± 0.6	3.5 ± 2.1	2.3 ± 1.2	1.6 ± 1.2	0.14 ± 0.09

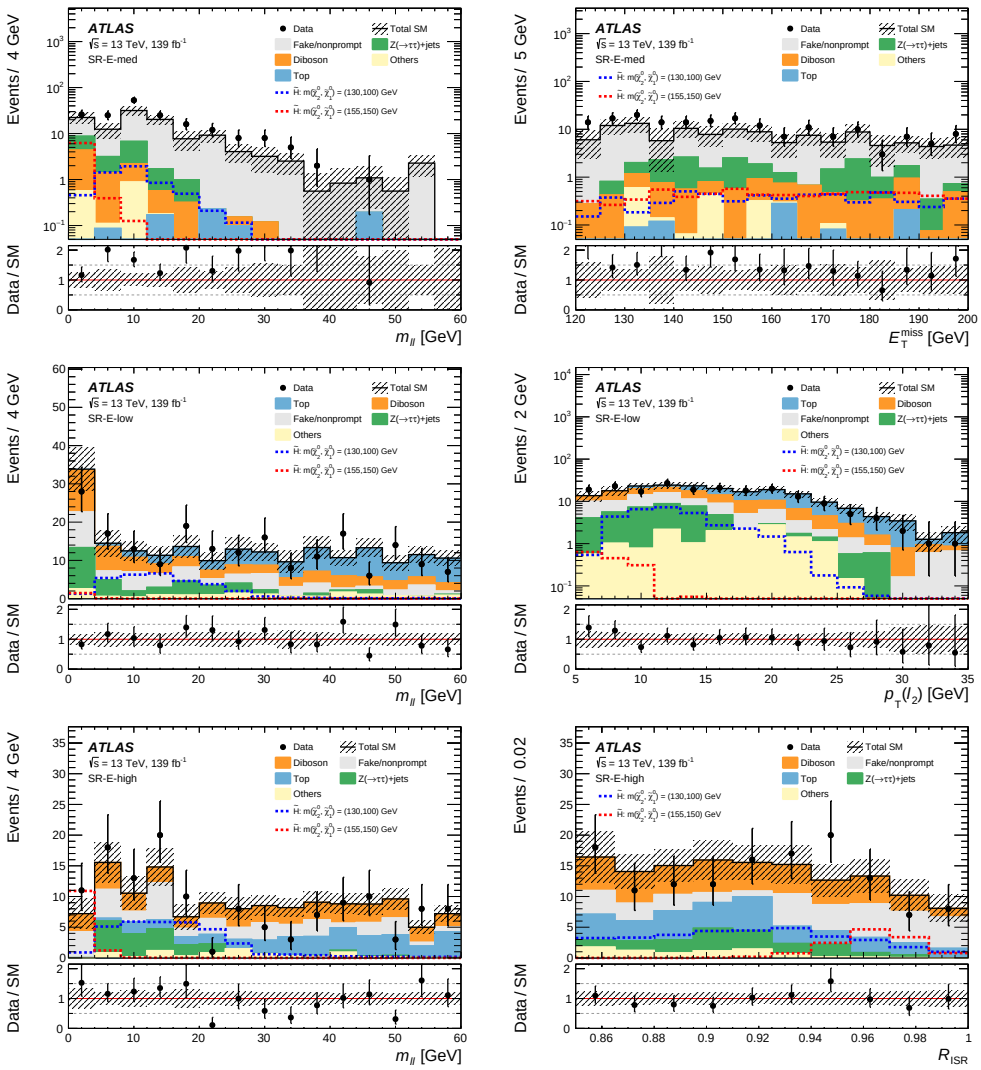

Figure 14.9: Examples of kinematic distributions after the background-only fit of the CRs showing the data as well as the expected background in the signal regions sensitive to electroweakinos. The first (last) bin includes underflow (overflow). The uncertainty bands plotted include all statistical and systematic uncertainties.

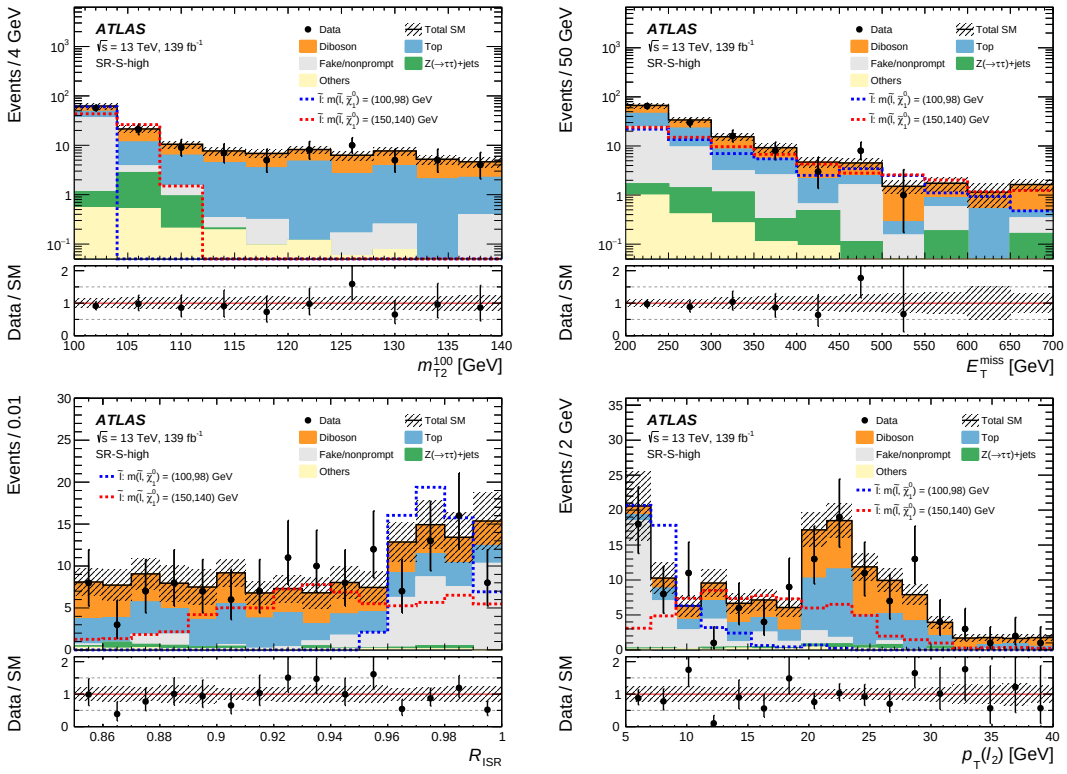

Figure 14.10: Examples of kinematic distributions after the background-only fit of the CRs showing the data as well as the expected background in SR–S–high. The first (last) bin includes underflow (overflow). The uncertainty bands plotted include all statistical and systematic uncertainties.

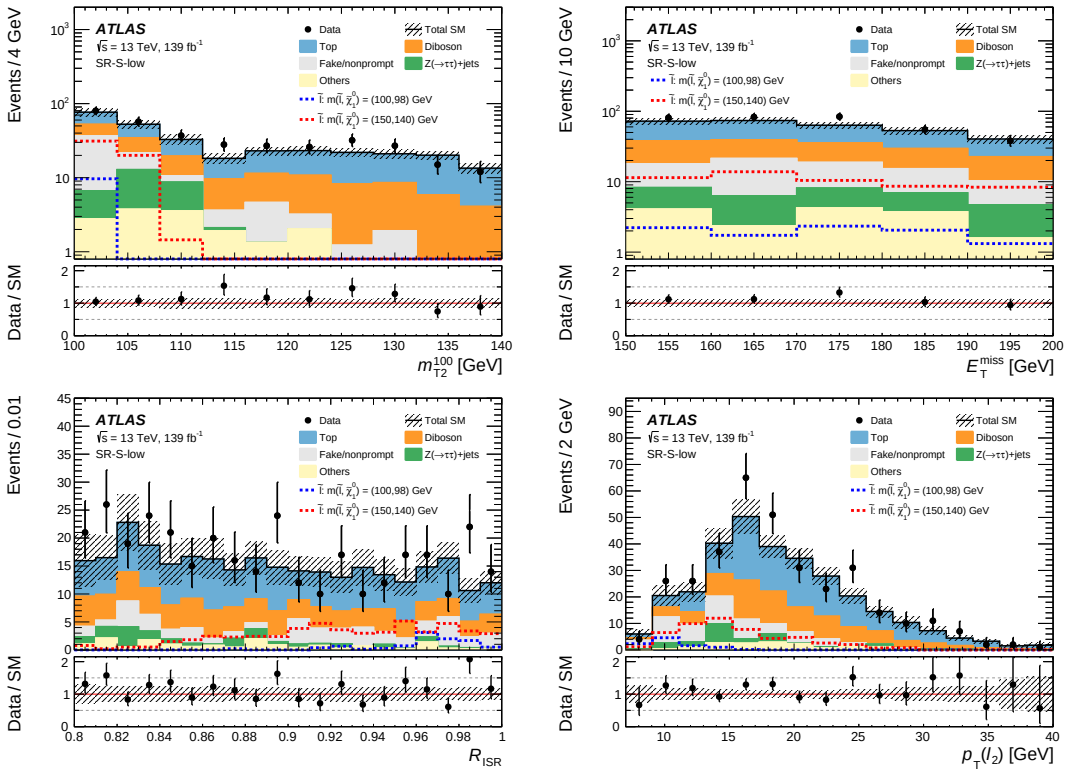

Figure 14.11: Examples of kinematic distributions after the background-only fit of the CRs showing the data as well as the expected background in SR–S–low. The first (last) bin includes underflow (overflow). The uncertainty bands plotted include all statistical and systematic uncertainties.

14.2 Motivation

Despite the attractiveness of the simplified SUSY models targeted in this analysis, it is crucial to remain agnostic about potential sources of new physics that could populate the various signal regions. Even if SUSY is realized in nature, there is certainly no guarantee that it adheres to the simplifying assumptions made in Section 4.1. Instead, these simplified models often serve as tractable benchmark scenarios for which analyses can be optimized. When a well-motivated model for BSM physics has many free parameters, its phenomenology can be very complicated and it is often unfeasible to address the model in the most general way. Instead, physicists have recently focused their attention on the simplest parameter configurations as a practical way of probing these models. Such has been the case for SUSY searches at the LHC ever since the start of Run 2, at least, whereas the Run 1 searches tended to interpret results in the context of the MSSM. Regardless of this strategic choice, to limit the results of a search for new physics to statements about a particular model would be to reduce its value to the broader program of particle physics.

Instead, given the complexity of its phenomenology, any search for a particular flavor of SUSY should provide an interpretation of the results that is as independent of the model assumptions as possible. In doing so, the results can be used by others to check the validity of any other model for BSM physics that would produce the same final states considered by the analysis. Of particular interest for these reinterpretations are the number of expected and observed events in the signal regions, obtained using a background-only fit to the CRs and a single SR bin. From these, one can derive model-independent upper limits on the visible cross section for generic BSM processes, to which models can be compared. Here, the visible cross-section represents the production cross-section for a BSM physics

process multiplied by the detector's reconstruction efficiency and the acceptance of the inclusive SR. Since this limit includes the effects of the detector's reconstruction efficiency and the SR acceptance, this is often done by employing a fast, parametric simulation of the detector response like DELPHES [123]. The model-independent limits on new physics obtained by this analysis are presented in the following section.

14.3 Search Results and Model-Independent Limits

Inclusive SRs, as defined in Section 10.5, are used to search for physics processes that can lead to final states containing jets, $E_{\mathrm{T}}^{\mathrm{miss}}$, and soft leptons. This is done by calculating p-values that quantify the probability of producing event yields greater than or equal to those observed in the SRs, assuming the background-only hypothesis. Additionally, hypothesis tests are performed using the $\mathrm{CL_s}$ prescription [122] to set 95% CL upper limits on the number of events from some generic new physics process that could be populating the SRs. Since no information about the shapes of the $m_{\ell\ell}$ or m_{T2}^{100} distributions is assumed for a potential signal process, these SRs consists of a single bin in either $m_{\ell\ell}$ or m_{T2}^{100}. They are constructed and correlated in such a way that the more inclusive SRs contain all of the events in the less inclusive SRs. This is done by increasing the upper limit on either $m_{\ell\ell}$ or m_{T2}^{100}. The SR–E inclusive SRs are constructed by merging all of the SR–E–high, SR–E–med, SR–E–low, and SR–E–$1\ell 1T$ bins below some $m_{\ell\ell}$ value that corresponds to a bin edge. Similarly, the SR–S inclusive SRs are constructed by merging all of the SR–S–high and SR–S–low bins below some m_{T2}^{100} value that corresponds to a bin edge.

Each fit used to derive the model-independent results consists of the CRs and one single-bin inclusive SR. The CRs are assumed to contain no signal events. A single unconstrained normalization factor is included in the fit to account for any potential contribution to the SR in question from processes not described by the SM. A hypothesis test is performed using the CL_s prescription to extract limits on the number of observed (expected) signal events $S^{95}_{\text{obs (exp)}}$ in a given inclusive SR at 95% CL. Upper limits on the observed (expected) visible cross-section for new physics $\langle \epsilon\sigma \rangle^{95}_{\text{obs (exp)}}$ are obtained by dividing $S^{95}_{\text{obs (exp)}}$ by the integrated luminosity. Additionally, p-values under the background-only hypothesis are calculated for each inclusive SR using 200,000 pseudo-experiments. A summary of the model-independent results is shown in Table 14.4. The smallest observed p-value is associated with the SR–E bin defined by $m_{\ell\ell} < 20$ GeV, and corresponds to a local significance of 2.7σ. Examples of the scans over the 95% CL upper limits on the observed (S^{95}_{obs}) and expected $\left(S^{95}_{\text{exp}}\right)$ number of events from some generic BSM signal process are shown in Figure 14.12, including those corresponding to the $m_{\ell\ell}$- and m^{100}_{T2}-defined SRs with the smallest p-values. As all excesses fall well short of the conventional threshold for claiming a discovery, the data is subsequently used to place model-dependent limits on the production of electroweak SUSY within simplified models.

Table 14.4: Left to right: The first column denotes the inclusive signal regions according to their upper bound on the discriminating variables. These SRs are defined in Section 10.5. The regions defined by $m_{\ell\ell}$ include events from both the 2ℓ and $1\ell 1T$ channels, while those defined by m_{T2}^{100} only include 2ℓ events. The next two columns show the observed (N_{obs}) and expected (N_{exp}) number of events in the SRs, respectively. N_{exp} is obtained from the background-only fit of the CRs. The next column shows the observed 95% CL upper limits on the visible cross-section ($\langle\epsilon\sigma\rangle_{\mathrm{obs}}^{95}$) for some potentially new physics process. The next two columns show the 95% CL upper limits on the observed (S_{obs}^{95}) and expected $\left(S_{\mathrm{exp}}^{95}\right)$ number of signal events. The latter is obtained by assuming the expected number of background events from the background-only fit of the CRs. The last column shows the discovery p-value ($p(s=0)$) obtained from the background-only hypothesis test.

	Signal Region	N_{obs}	N_{exp}	$\langle\epsilon\sigma\rangle_{\mathrm{obs}}^{95}$ [fb]	S_{obs}^{95}	S_{exp}^{95}	$p(s=0)$
SR–E	$m_{\ell\ell} < 1$	0	1.0 ± 1.0	0.022	3.0	$3.0^{+1.3}_{-0.0}$	0.50
	$m_{\ell\ell} < 2$	46	44 ± 6.8	0.15	21	19^{+7}_{-5}	0.38
	$m_{\ell\ell} < 3$	90	77 ± 12	0.29	41	31^{+11}_{-9}	0.18
	$m_{\ell\ell} < 5$	151	138 ± 18	0.38	52	43^{+16}_{-11}	0.24
	$m_{\ell\ell} < 10$	244	200 ± 19	0.62	86	49^{+26}_{-13}	0.034
	$m_{\ell\ell} < 20$	383	301 ± 23	0.95	132	61^{+22}_{-16}	0.0034
	$m_{\ell\ell} < 30$	453	366 ± 27	1.04	144	70^{+26}_{-20}	0.0065
	$m_{\ell\ell} < 40$	492	420 ± 30	0.96	134	74^{+29}_{-20}	0.027
	$m_{\ell\ell} < 60$	583	520 ± 35	0.97	135	84^{+32}_{-23}	0.063
SR–S	$m_{\mathrm{T2}}^{100} < 100.5$	24	27 ± 4.8	0.09	13	14^{+5}_{-4}	0.50
	$m_{\mathrm{T2}}^{100} < 101$	41	46 ± 6.5	0.11	16	18^{+7}_{-5}	0.50
	$m_{\mathrm{T2}}^{100} < 102$	91	82 ± 10	0.25	35	28^{+10}_{-8}	0.25
	$m_{\mathrm{T2}}^{100} < 105$	158	158 ± 17	0.30	41	41^{+16}_{-11}	0.50
	$m_{\mathrm{T2}}^{100} < 110$	243	242 ± 21	0.38	52	52^{+19}_{-14}	0.36
	$m_{\mathrm{T2}}^{100} < 120$	328	312 ± 24	0.51	71	60^{+22}_{-17}	0.26
	$m_{\mathrm{T2}}^{100} < 130$	419	388 ± 28	0.66	92	68^{+27}_{-18}	0.17
	$m_{\mathrm{T2}}^{100} < 140$	472	443 ± 31	0.69	95	74^{+28}_{-21}	0.19

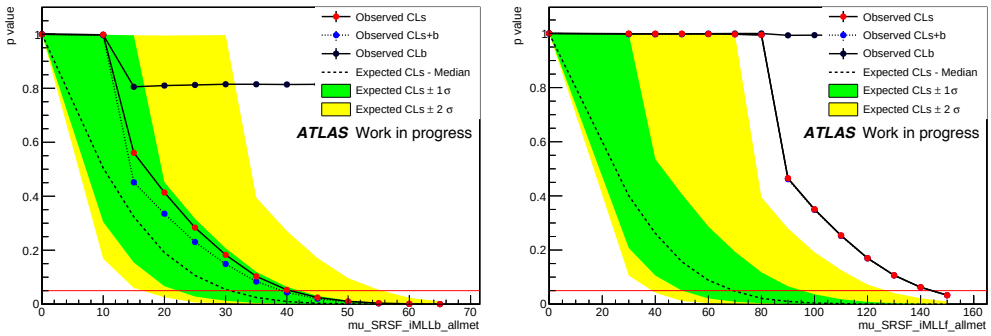

(a) 0.5 GeV $\leq m_{ll} <$ 3 GeV **(b)** 0.5 GeV $\leq m_{ll} <$ 20 GeV

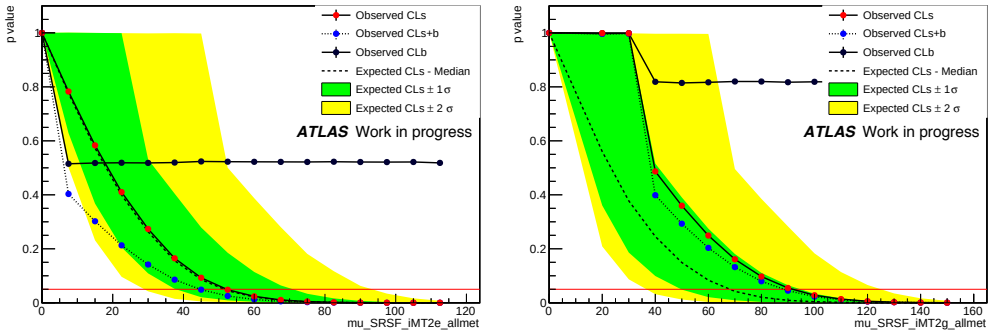

(c) 100 GeV $\leq m_{\mathrm{T2}}^{100} <$ 110 GeV **(d)** 100 GeV $\leq m_{\mathrm{T2}}^{100} <$ 130 GeV

Figure 14.12: Example scans of the 95% CL upper limits on the observed (S_{obs}^{95}) and expected $\left(S_{\mathrm{exp}}^{95}\right)$ number of events from some generic BSM signal process using the inclusive signal regions defined by $m_{\ell\ell}$ (top) and m_{T2}^{100}(bottom).

Chapter 15

Model-Dependent Limits on Compressed Electroweak SUSY

In the absence of any statistically significant excesses over the SM background, results are interpreted in the context of specific signal models with well-defined kinematics and cross-sections. These additional handles allow for the construction of dedicated, non-overlapping SRs that can be combined in a statistical manner in order to gain additional sensitivity via bin-by-bin correlations exhibited by the signal process. Ultimately, the results are used to set limits on the masses of the SUSY particles.

For electroweakinos (sleptons), the relevant kinematic distribution is $m_{\ell\ell}$ (m_{T2}^{100}), which has a characteristic cutoff that corresponds to the mass-splitting between the $\widetilde{\chi}_2^0$ ($\widetilde{\ell}$) and $\widetilde{\chi}_1^0$. Binning these distributions therefore allows one to exploit the different kinematic shapes of the signal and background processes to improve sensitivity to this mass-splitting. The parameter of interest in these exclusion fits is the signal strength μ_{sig}, which is defined as the ratio of the observed cross-section limit, σ_{obs}, to the theoretical cross-section, σ_{theory}:

$$\mu_{\text{sig}} = \frac{\sigma_{\text{obs}}}{\sigma_{\text{theory}}} \tag{15.1}$$

In this way, $\mu_{\text{sig}} = 1$ corresponds to the signal hypothesis in question, while $\mu_{\text{sig}} = 0$ corresponds to the background-only hypothesis. This parameter, which coherently scales the signal yield across all regions, is allowed to float in the exclusion fit. Following the CL_s prescription, one can calculate a CL_s value for $\mu_{\text{sig}} = 1$ and therefore reject the signal hypothesis at some CL. By convention, the LHC experiments typically use the 95% CL threshold (i.e. $\text{CL}_\text{s}(\mu_{\text{sig}} = 1) < 0.05$) for excluding signals. When setting mass limits in a two-dimensional plane, $\text{CL}_\text{s}(\mu_{\text{sig}} = 1)$ is first calculated for a grid of signal points in the plane. Exclusion contours are then constructed by interpolating $\log\Big(\text{CL}_\text{s}(\mu_{\text{sig}} = 1)\Big)$ and drawing the contour corresponding to $\text{CL}_\text{s}(\mu_{\text{sig}} = 1) = 0.05$.

The addition of many SR bins greatly increases the overall fit complexity and so validating the fit model and overall stability is an important check to perform before proceeding to limit setting. This can be done by performing background-only fits that are constrained by both the CRs and exclusive SRs, which gives an idea of how the various background contributions will behave in the eventual exclusion fits with a floating signal strength parameter. This assessment is detailed in Section 15.1, while the model-dependent limits on direct electroweakino and slepton production are provided in Section 15.2.1 and Section 15.2.2, respectively.

15.1 Background-Only Fits to the CRs and Exclusive SRs

In order to assess the stability of the exclusion fits that exploit the $m_{\ell\ell}$ or m_{T2}^{100} shapes, diagnostic fits are performed simultaneously to the CRs and exclusive

SRs, assuming the background-only hypothesis. Even with assumption, these fits act as a good proxy for how the background prediction will be constrained in the fits that include a signal component when setting model-dependent limits on electroweakino and slepton production. As with the background-only fits to the CRs, the only floating parameters in these CR+SR background-only fits are the normalization factors for the $t\bar{t}/Wt$, $Z^{(*)}/\gamma^*(\rightarrow \tau\tau)+\text{jets}$, and VV processes, but now each exclusive SR also acts to constrain the backgrounds. A comparison of the data and the post-fit backgrounds in the $m_{\ell\ell}$ and m_{T2}^{100} bins that define the exclusive SRs are shown in Figure 15.1. The event yields and uncertainties after the CR+SR background-only fits are also shown in Table 15.1 and Table 15.2 for the electroweakino and slepton exclusive SRs, respectively. All excesses in the data over the predicted backgrounds are within the 2σ level.

Since the SRs consist of several non-overlapping bins, the CR+SR background-only fits will attempt to accommodate any deviations from the nominal background estimate by pulling the nuisance parameters away from their original estimates during the likelihood maximization. Once typically defines the pull of a nuisance parameter to be $(\theta - \theta_0)/\sigma(\theta_0)$, where θ and θ_0 are the post-fit and pre-fit values of the nuisance parameters, respectively, and $\sigma(\theta_0)$ is the pre-fit uncertainty on the nuisance parameter. The nuisance parameters pulls resulting from the CR+SR background-only fits are shown in Figure 15.2 and Figure 15.3 using the electroweakino and slepton regions, respectively. In each case, the nuisance parameters are never pulled outside of their pre-fit uncertainties, which are generally consistent with the post-fit uncertainties, lending credence to the validity of these complex fits. Despite the large number of jet-related nuisance parameters included in the likelihood, they appear to be over-constrained by the electroweakino fit, as the post-fit uncertainties are consistently smaller than their

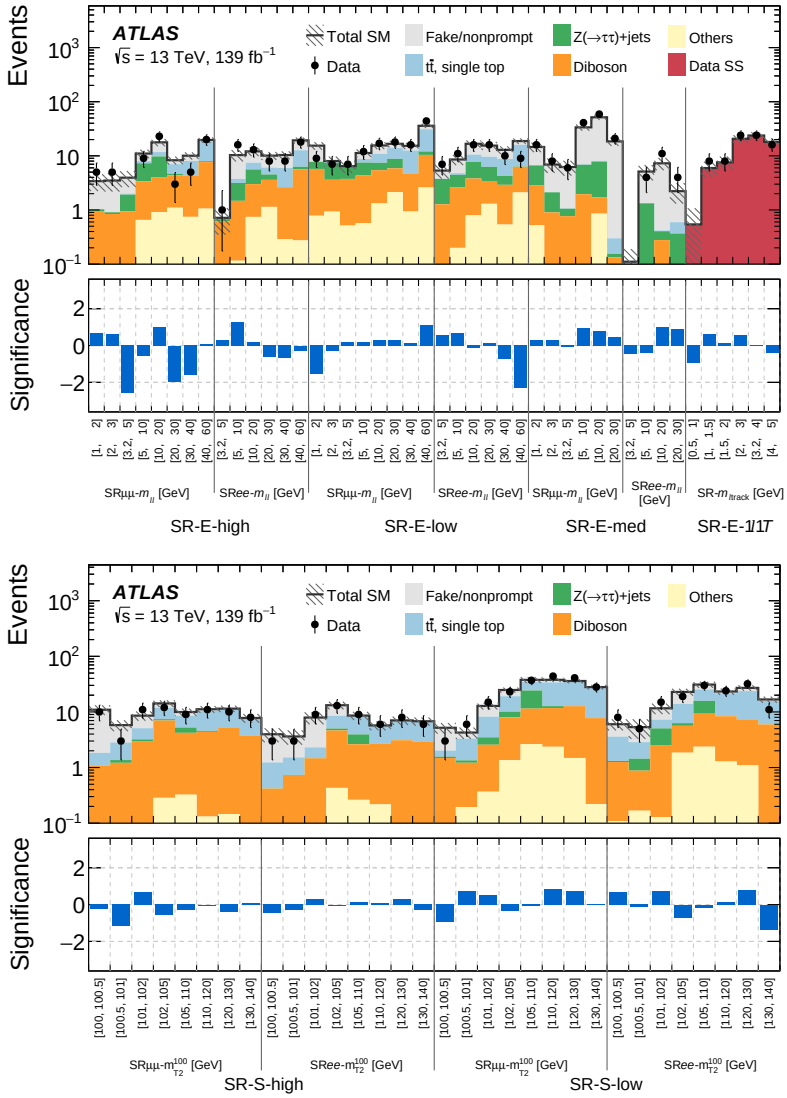

Figure 15.1: Comparison of observed and expected event yields in the SRs after the CR+SR background-only fits. The SRs used in searches for electroweakinos recoiling against ISR are shown at the top, binned in $m_{\ell\ell}$. The SRs used in searches for sleptons recoiling against ISR are shown at the bottom, binned in m_{T2}^{100}. Uncertainties in the background estimates include both the statistical and systematic uncertainties.

Table 15.1: Observed event yields and fit results using a CR+SR background-only fit for the exclusive electroweakino SRs. Background processes containing fewer than two prompt leptons are categorized as "Fake/nonprompt." The category "Others" contains rare backgrounds from triboson, Higgs boson, and the remaining top-quark production processes listed in Table 8.3. Uncertainties in the fitted background estimates combine statistical and systematic uncertainties.

	SR bin [GeV]	[1,2]	[2,3]	[3.2,5]	[5,10]	[10,20]	[20,30]	[30,40]	[40,60]
SR–E–high ee	Observed			1	16	13	8	8	18
	Fitted SM events			0.7 ± 0.4	10.3 ± 2.5	12.1 ± 2.2	10.1 ± 1.7	10.4 ± 1.7	19.3 ± 2.5
	Fake/nonprompt			$0.03^{+0.19}_{-0.03}$	6.6 ± 2.7	4.6 ± 2.0	4.0 ± 1.5	4.4 ± 1.6	6.7 ± 2.3
	$t\bar{t}$, single top			$0.01^{+0.06}_{-0.01}$	0.59 ± 0.27	1.9 ± 0.5	1.6 ± 0.4	3.3 ± 0.6	6.4 ± 0.9
	Diboson			0.62 ± 0.23	1.4 ± 0.5	2.3 ± 0.7	2.5 ± 0.7	2.3 ± 0.6	5.4 ± 1.3
	$Z(\to \tau\tau)$+jets			$0.06^{+0.29}_{-0.06}$	1.7 ± 0.7	2.6 ± 1.2	0.93 ± 0.24	0.04 ± 0.04	0.62 ± 0.23
	Others			$0.000^{+0.004}_{-0.000}$	0.12 ± 0.05	0.74 ± 0.18	1.14 ± 0.19	0.29 ± 0.07	0.27 ± 0.14
SR–E–high $\mu\mu$	Observed	5	5	0	9	23	3	5	20
	Fitted SM events	3.4 ± 1.2	3.5 ± 1.3	3.9 ± 1.3	11.0 ± 2.0	17.8 ± 2.7	8.3 ± 1.4	10.1 ± 1.5	19.6 ± 2.3
	Fake/nonprompt	2.4 ± 1.2	2.6 ± 1.4	1.9 ± 1.0	3.1 ± 1.7	6.0 ± 2.8	1.3 ± 0.8	2.0 ± 0.9	1.4 ± 1.3
	$t\bar{t}$, single top	$0.01^{+0.06}_{-0.01}$	$0.01^{+0.06}_{-0.01}$	0.09 ± 0.07	0.67 ± 0.25	2.0 ± 0.5	2.4 ± 0.5	3.7 ± 0.9	10.2 ± 1.7
	Diboson	0.92 ± 0.32	0.84 ± 0.32	0.9 ± 0.4	2.7 ± 0.7	3.1 ± 0.8	3.3 ± 0.8	3.6 ± 0.8	6.6 ± 1.5
	$Z(\to \tau\tau)$+jets	$0.07^{+0.34}_{-0.07}$	$0.06^{+0.34}_{-0.06}$	1.0 ± 0.4	3.9 ± 0.9	5.7 ± 1.6	0.31 ± 0.25	$0.00^{+0.04}_{-0.00}$	0.31 ± 0.16
	Others	$0.032^{+0.035}_{-0.032}$	–	0.025 ± 0.018	0.66 ± 0.33	0.91 ± 0.14	1.10 ± 0.18	0.75 ± 0.16	1.06 ± 0.09
SR–E–med ee	Observed			0	4	11	4		
	Fitted SM events			0.11 ± 0.08	5.1 ± 1.6	7.3 ± 1.9	2.2 ± 0.9		
	Fake/nonprompt			$0.000^{+0.016}_{-0.000}$	3.8 ± 1.3	6.9 ± 2.0	1.6 ± 1.1		
	$t\bar{t}$, single top			$0.00^{+0.05}_{-0.00}$	$0.00^{+0.04}_{-0.00}$	$0.01^{+0.06}_{-0.01}$	$0.23^{+0.25}_{-0.23}$		
	Diboson			0.10 ± 0.05	0.10 ± 0.09	0.28 ± 0.26	$0.02^{+0.13}_{-0.02}$		
	$Z(\to \tau\tau)$+jets			$0.000^{+0.028}_{-0.000}$	1.2 ± 1.2	$0.1^{+0.5}_{-0.1}$	$0.3^{+0.6}_{-0.3}$		
	Others			$0.000^{+0.012}_{-0.000}$	–	–	–		
SR–E–med $\mu\mu$	Observed	16	8	6	41	59	21		
	Fitted SM events	14.6 ± 2.9	6.9 ± 2.1	6.2 ± 1.9	34 ± 4	52 ± 6	18.5 ± 3.2		
	Fake/nonprompt	7.9 ± 3.2	4.8 ± 2.1	5.1 ± 2.0	27 ± 5	44 ± 6	18.2 ± 3.2		
	$t\bar{t}$, single top	$0.01^{+0.06}_{-0.01}$	$0.01^{+0.06}_{-0.01}$	$0.00^{+0.05}_{-0.00}$	$0.12^{+0.13}_{-0.12}$	0.24 ± 0.08	$0.14^{+0.19}_{-0.14}$		
	Diboson	2.3 ± 0.8	0.9 ± 0.4	0.73 ± 0.24	1.9 ± 0.7	0.87 ± 0.26	0.13 ± 0.07		
	$Z(\to \tau\tau)$+jets	3.8 ± 1.8	1.2 ± 0.5	$0.3^{+0.6}_{-0.3}$	4.9 ± 1.6	6.1 ± 2.1	$0.02^{+0.29}_{-0.02}$		
	Others	0.5 ± 0.4	$0.000^{+0.026}_{-0.000}$	0.036 ± 0.015	0.019 ± 0.017	0.9 ± 0.6	–		
SR–E–low ee	Observed			7	11	16	16	10	9
	Fitted SM events			5.3 ± 1.5	8.6 ± 1.8	16.7 ± 2.5	15.5 ± 2.6	12.9 ± 2.1	18.8 ± 2.2
	Fake/nonprompt			1.6 ± 1.1	3.8 ± 1.8	6.2 ± 2.2	5.8 ± 2.3	4.2 ± 1.8	2.8 ± 1.4
	$t\bar{t}$, single top			0.015 ± 0.006	0.32 ± 0.30	2.8 ± 0.6	3.4 ± 1.1	4.5 ± 0.9	9.7 ± 1.5
	Diboson			1.3 ± 0.6	2.4 ± 0.8	3.0 ± 0.7	2.1 ± 0.7	2.4 ± 0.7	4.2 ± 1.0
	$Z(\to \tau\tau)$+jets			2.5 ± 1.1	1.8 ± 0.7	3.9 ± 1.3	2.8 ± 1.0	1.4 ± 0.7	$0.07^{+0.20}_{-0.07}$
	Others			$0.01^{+0.05}_{-0.01}$	0.20 ± 0.05	0.79 ± 0.23	1.3 ± 0.8	0.54 ± 0.09	2.10 ± 0.34
SR–E–low $\mu\mu$	Observed	9	7	7	12	17	18	16	44
	Fitted SM events	15.4 ± 2.4	8.0 ± 1.7	6.5 ± 1.6	11.3 ± 1.9	15.6 ± 2.3	16.7 ± 2.3	15.3 ± 2.0	35.9 ± 3.3
	Fake/nonprompt	7.7 ± 1.9	$0.3^{+0.6}_{-0.3}$	$0.01^{+0.22}_{-0.01}$	2.6 ± 1.3	4.7 ± 1.9	2.8 ± 1.6	2.8 ± 1.6	4.9 ± 2.3
	$t\bar{t}$, single top	$0.00^{+0.04}_{-0.00}$	0.26 ± 0.07	$0.01^{+0.06}_{-0.01}$	1.2 ± 0.5	3.4 ± 0.7	5.1 ± 1.5	7.8 ± 1.3	18.9 ± 2.7
	Diboson	4.9 ± 1.3	2.7 ± 0.7	3.2 ± 0.9	3.8 ± 0.9	4.1 ± 1.0	3.7 ± 0.9	3.8 ± 0.8	7.8 ± 1.6
	$Z(\to \tau\tau)$+jets	2.0 ± 0.7	3.8 ± 1.1	2.7 ± 1.2	3.2 ± 1.1	2.0 ± 1.2	2.9 ± 0.8	$0.01^{+0.27}_{-0.01}$	1.6 ± 0.6
	Others	0.8 ± 0.5	0.9 ± 0.8	0.52 ± 0.24	0.57 ± 0.16	1.32 ± 0.18	2.1 ± 0.4	0.94 ± 0.11	2.60 ± 0.20

Table 15.2: Observed event yields and fit results using a CR+SR background-only fit for the exclusive slepton SRs. Background processes containing fewer than two prompt leptons are categorized as "Fake/nonprompt." The category "Others" contains rare backgrounds from triboson, Higgs boson, and the remaining top-quark production processes listed in Table 8.3. Uncertainties in the fitted background estimates combine statistical and systematic uncertainties.

	SR bin [GeV]	[100,100.5]	[100.5,101]	[101,102]	[102,105]	[105,110]	[110,120]	[120,130]	[130,140]
SR-S-high ee	Observed	3	3	9	13	9	6	8	6
	Fitted SM events	4.0 ± 1.1	3.6 ± 1.0	7.9 ± 1.9	13.2 ± 2.1	8.6 ± 1.4	5.7 ± 1.0	7.0 ± 1.2	6.8 ± 1.1
	Fake/nonprompt	2.7 ± 1.1	2.1 ± 1.0	5.6 ± 1.9	4.7 ± 1.9	$0.2^{+0.5}_{-0.2}$	$0.01^{+0.17}_{-0.01}$	$0.01^{+0.17}_{-0.01}$	$0.00^{+0.15}_{-0.00}$
	$t\bar{t}$, single top	0.8 ± 0.4	0.8 ± 0.5	0.8 ± 0.4	3.5 ± 0.7	4.5 ± 1.2	3.0 ± 0.7	3.9 ± 0.9	3.9 ± 0.9
	Diboson	0.42 ± 0.16	0.68 ± 0.23	1.4 ± 0.4	4.2 ± 1.1	2.4 ± 0.7	2.5 ± 0.7	3.0 ± 0.8	2.8 ± 0.7
	$Z(\to \tau\tau)$+jets	$0.00^{+0.08}_{-0.00}$	$0.00^{+0.18}_{-0.00}$	0.027 ± 0.012	0.38 ± 0.16	1.32 ± 0.31	$0.00^{+0.12}_{-0.00}$	$0.02^{+0.22}_{-0.02}$	$0.00^{+0.19}_{-0.00}$
	Others	0.0 ± 0.0	$0.06^{+0.11}_{-0.06}$	0.09 ± 0.05	0.43 ± 0.32	0.26 ± 0.14	$0.2^{+0.5}_{-0.2}$	$0.06^{+0.08}_{-0.06}$	0.05 ± 0.05
SR-S-high $\mu\mu$	Observed	10	3	11	12	9	11	10	8
	Fitted SM events	11.0 ± 2.2	5.8 ± 1.3	8.6 ± 1.6	14.2 ± 1.9	10.0 ± 1.5	11.2 ± 1.6	11.5 ± 1.5	7.8 ± 1.4
	Fake/nonprompt	9.1 ± 2.2	3.0 ± 1.1	3.5 ± 1.4	2.4 ± 1.2	1.5 ± 1.0	$0.7^{+0.8}_{-0.7}$	$0.4^{+0.5}_{-0.4}$	$0.19^{+0.33}_{-0.19}$
	$t\bar{t}$, single top	0.8 ± 0.5	1.5 ± 0.5	1.9 ± 0.5	4.4 ± 0.8	3.3 ± 0.7	5.9 ± 1.1	5.9 ± 0.9	3.9 ± 1.3
	Diboson	1.1 ± 0.4	1.2 ± 0.4	2.9 ± 1.3	6.7 ± 1.7	3.9 ± 1.1	4.2 ± 1.0	5.0 ± 1.3	3.7 ± 0.9
	$Z(\to \tau\tau)$+jets	$0.00^{+0.19}_{-0.00}$	0.15 ± 0.04	0.22 ± 0.19	0.40 ± 0.34	1.03 ± 0.34	0.19 ± 0.12	$0.00^{+0.19}_{-0.00}$	$0.00^{+0.21}_{-0.00}$
	Others	$0.000^{+0.019}_{-0.000}$	0.029 ± 0.017	0.09 ± 0.05	0.29 ± 0.14	0.32 ± 0.22	0.13 ± 0.11	0.15 ± 0.12	0.06 ± 0.05
SR-S-low ee	Observed	8	5	15	19	30	24	32	11
	Fitted SM events	6.0 ± 1.4	5.3 ± 2.1	11.6 ± 2.5	22.9 ± 3.3	31 ± 4	23.3 ± 3.0	27.1 ± 3.1	16.8 ± 2.1
	Fake/nonprompt	2.4 ± 1.2	2.5 ± 1.2	4.4 ± 2.0	9.0 ± 2.8	5.7 ± 2.7	$1.6^{+1.7}_{-1.6}$	3.4 ± 2.3	1.0 ± 0.9
	$t\bar{t}$, single top	2.3 ± 0.9	1.4 ± 0.5	2.2 ± 0.7	7.6 ± 1.7	9.6 ± 1.7	13.3 ± 3.3	16.4 ± 3.0	9.8 ± 1.5
	Diboson	1.1 ± 0.6	0.71 ± 0.30	2.4 ± 0.8	3.8 ± 1.3	6.9 ± 2.1	7.1 ± 2.1	6.2 ± 2.0	5.9 ± 1.6
	$Z(\to \tau\tau)$+jets	$0.1^{+0.4}_{-0.1}$	$0.6^{+2.0}_{-0.6}$	2.5 ± 2.4	$0.7^{+1.5}_{-0.7}$	6.5 ± 2.2	$0.01^{+0.26}_{-0.01}$	$0.03^{+0.30}_{-0.03}$	$0.000^{+0.032}_{-0.000}$
	Others	0.11 ± 0.06	0.17 ± 0.15	0.13 ± 0.09	1.8 ± 0.9	2.4 ± 2.4	1.3 ± 1.2	1.1 ± 1.0	0.042 ± 0.034
SR-S-low $\mu\mu$	Observed	3	6	15	23	37	44	41	28
	Fitted SM events	5.2 ± 1.1	4.3 ± 1.0	12.8 ± 1.8	24.8 ± 2.6	38 ± 5	37.8 ± 3.3	36.0 ± 3.4	28.0 ± 2.7
	Fake/nonprompt	3.2 ± 1.0	0.9 ± 0.7	4.6 ± 1.5	5.6 ± 1.8	2.8 ± 1.7	3.8 ± 2.0	1.5 ± 1.2	$0.00^{+0.10}_{-0.00}$
	$t\bar{t}$, single top	0.45 ± 0.18	2.0 ± 0.5	4.7 ± 1.0	9.1 ± 1.6	10.6 ± 1.9	21.2 ± 2.9	21.8 ± 2.6	20.2 ± 2.7
	Diboson	1.4 ± 0.5	1.02 ± 0.34	2.2 ± 0.8	6.7 ± 1.9	8.8 ± 2.6	9.4 ± 2.6	11.2 ± 3.2	7.5 ± 2.2
	$Z(\to \tau\tau)$+jets	$0.09^{+0.16}_{-0.09}$	$0.1^{+0.5}_{-0.1}$	0.9 ± 0.4	2.1 ± 1.0	13 ± 5	1.0 ± 0.6	$0.02^{+0.29}_{-0.02}$	$0.00^{+0.26}_{-0.00}$
	Others	0.032 ± 0.026	0.19 ± 0.11	0.37 ± 0.19	1.4 ± 0.8	2.6 ± 1.5	2.4 ± 1.2	1.5 ± 0.8	0.22 ± 0.13

pre-fit counterparts. It is difficult to say whether or not this could be due to a lack of flexibility in the likelihood function (which could be improved by including even more nuisance parameters) or a genuine example of being able to measure these jet uncertainties with more precision than the auxiliary measurements due to the specific phase space targeted by this search. In any case, these complicated fits are deemed to be sufficiently healthy for setting model-dependent limits on electroweakinos and sleptons, as presented in Section 15.2.

Another important check of these fits is to determine how the various sources of systematic uncertainties contribute to the overall uncertainty on the background yields. Figure 15.4 shows the breakdown of the systematic uncertainties in each exclusive SR after the CR+SR background-only fits, grouped according to the source of the uncertainty. Here, the bins defined by exclusive ranges of $m_{\ell\ell}$ or m_{T2}^{100} include both dielectron and dimuon events. The uncertainties related to the data-driven fake/non-prompt lepton background estimate tend to dominate at low values of $m_{\ell\ell}$ and m_{T2}^{100}, where these events tend to concentrate. This is not the case for SR–E–med, though, which is consistently dominated by events with fake/non-prompt leptons as it does not include an $m_{\ell\ell}$-dependent cut on $p_{\mathrm{T}}^{\ell_2}$. For the SRs defined by higher values of $m_{\ell\ell}$ and m_{T2}^{100}, the total systematic uncertainties are more evenly split between those related to the normalization of the $t\bar{t}/Wt$, $Z^{(*)}/\gamma^*(\rightarrow \tau\tau)+\text{jets}$, and VV processes, theoretical uncertainties on the shape of the backgrounds, statistical size of the simulated background samples, and various experimental uncertainties (such as that on the jet energy resolution). With the unblinded SRs and confidence in the fit models, hypothesis tests can now be run to quantify the consistency of the background-only hypothesis with the data. Additionally, in the absence of any statistically significant excess, limits can be derived on the production of electroweak SUSY with compressed

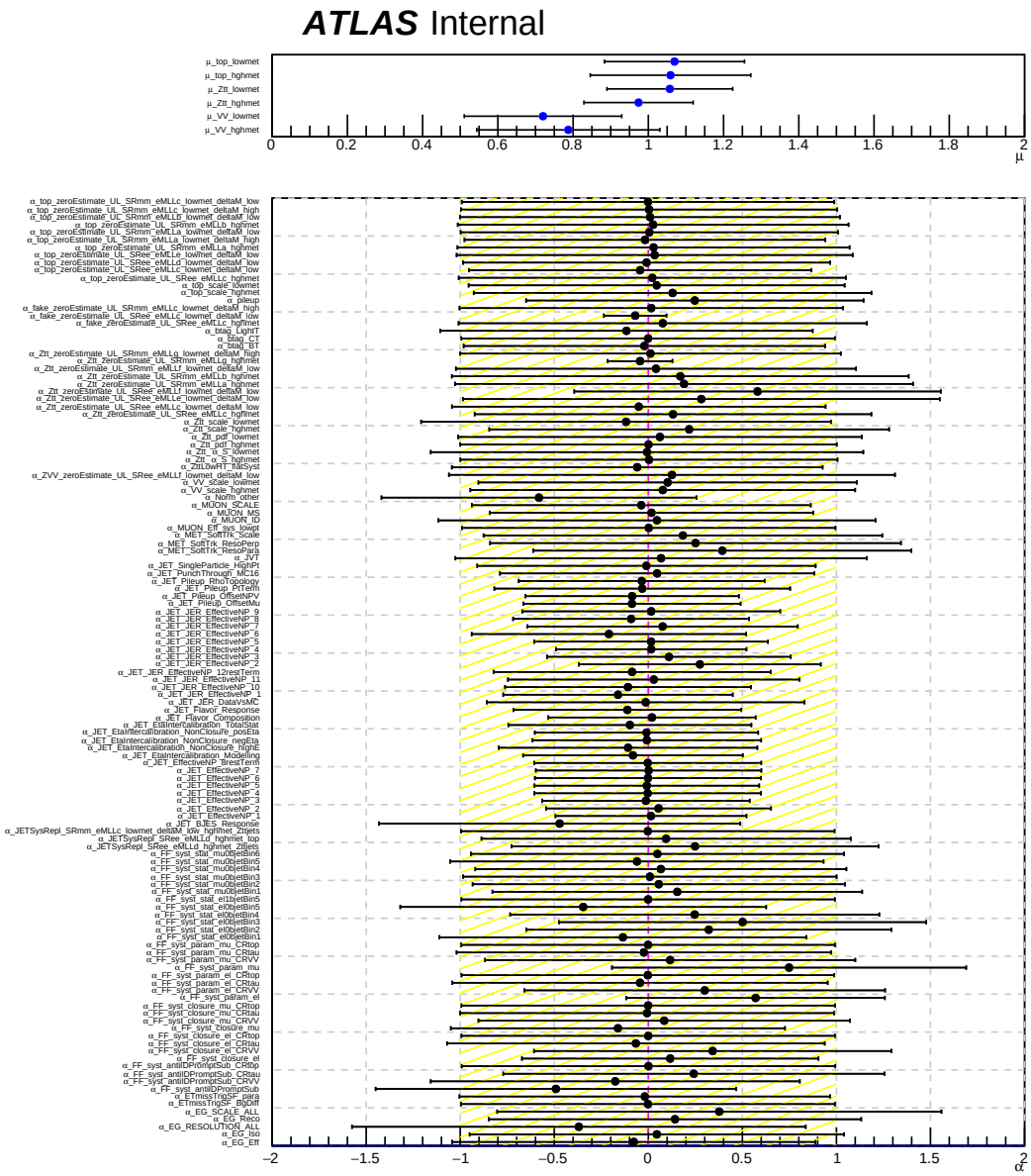

Figure 15.2: Nuisance parameter pull plots from the CR+SR background-only fits to the electroweakino regions. The top panel shows the best-fit values and uncertainties for the normalization factors that scale the $t\bar{t}/Wt$, $Z^{(*)}/\gamma^{*}(\rightarrow \tau\tau)+$ jets, and VV backgrounds. For each nuisance parameter, the markers in the bottom panel show $(\theta - \theta_0)/\sigma(\theta_0)$, where θ is the post-fit value, θ_0 is pre-fit value, and $\sigma(\theta_0)$ is pre-fit uncertainty. The marker errors indicate the post-fit uncertainties on the nuisance parameters.

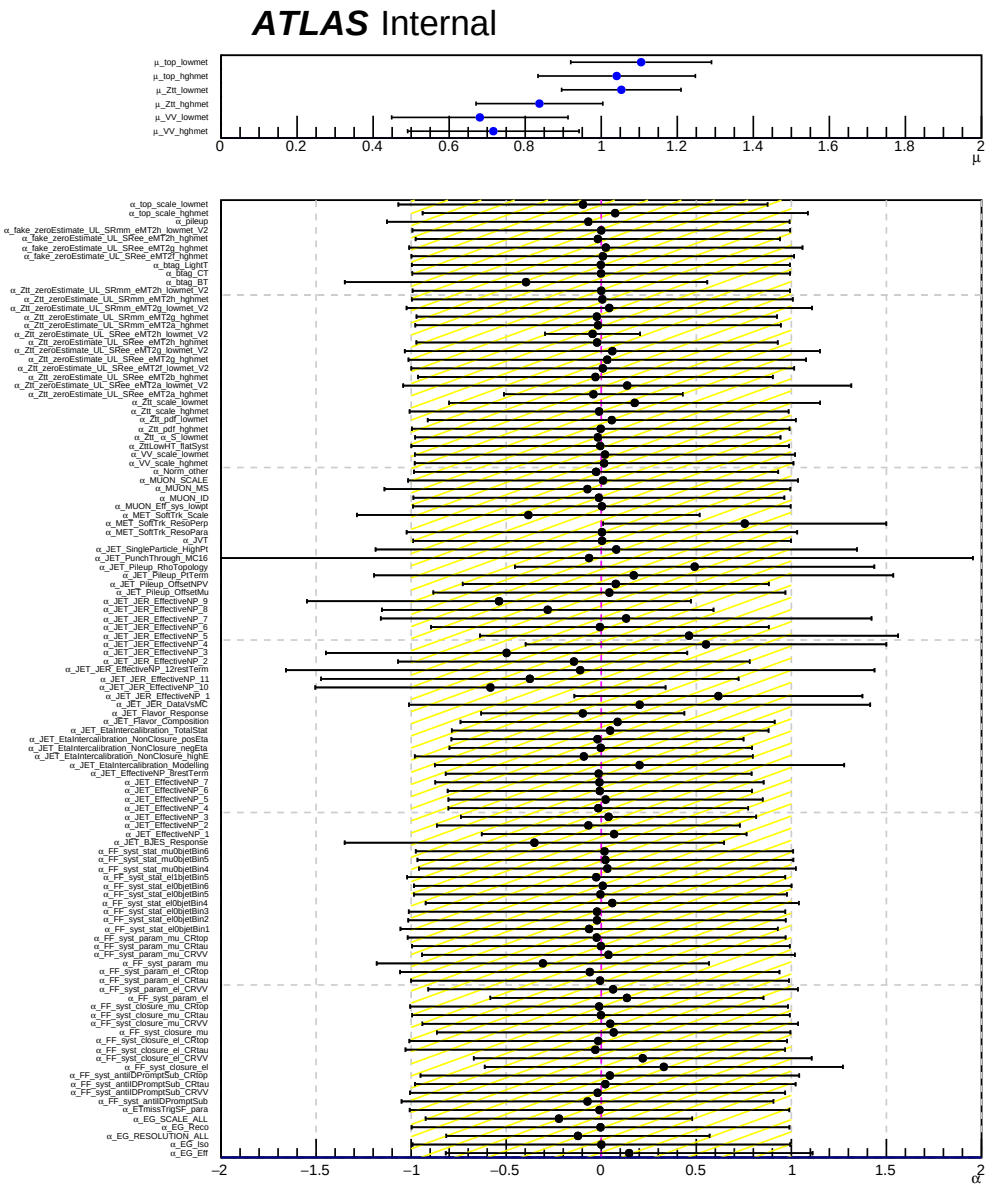

Figure 15.3: Nuisance parameter pull plots from the CR+SR background-only fits to the slepton regions. The top panel shows the best-fit values and uncertainties for the normalization factors that scale the $t\bar{t}/Wt$, $Z^{(*)}/\gamma^{*}(\rightarrow \tau\tau)+\text{jets}$, and VV backgrounds. For each nuisance parameter, the markers in the bottom panel show $(\theta-\theta_0)/\sigma(\theta_0)$, where θ is the post-fit value, θ_0 is pre-fit value, and $\sigma(\theta_0)$ is pre-fit uncertainty. The marker errors indicate the post-fit uncertainties on the nuisance parameters.

mass spectra.

15.2 Model-Dependent Limits

With the fit model validated, the fits to the CRs and exclusive SRs are extended to include signal contributions. These contributions are unconstrained in the fits and the signal strength μ_{sig} represents the parameter of interest. The results for the direct production of electroweakinos are presented in Section 15.2.1 and those for direct slepton production are presented in Section 15.2.2.

15.2.1 Electroweakinos

As no statistically significant excesses over the SM background prediction are found in the inclusive SRs defined by $m_{\ell\ell}$, exclusion fits are performed using the exclusive SRs to set limits on electroweakino production in several simplified models. These limits are then projected onto the $\Delta m(\widetilde{\chi}_2^0, \widetilde{\chi}_1^0)$ vs. $m(\widetilde{\chi}_2^0)$ plane to derive regions of excluded masses at 95% CL. The upper limits on the production cross-sections are shown in Appendix C.1.

Exclusion contours are derived for each of the three simplified electroweakino models. Figure 15.5 shows the exclusion contour for the simplified higgsino model. For direct wino production, the shape of the $m_{\ell\ell}$ distribution for the signal process depends on the relative sign of the $\widetilde{\chi}_2^0$ and $\widetilde{\chi}_1^0$ mass parameters. Therefore, separate exclusion contours are derived for each of these possibilities. Figure 15.6 shows the mass exclusions for direct wino production in the simplified model under the assumption that $m(\widetilde{\chi}_2^0) \times m(\widetilde{\chi}_1^0) > 0$, while Figure 15.7 assumes that $m(\widetilde{\chi}_2^0) \times m(\widetilde{\chi}_1^0) < 0$. In addition to the final exclusion contours that result from the statistical combination of all of the electroweakino SRs, the contributions

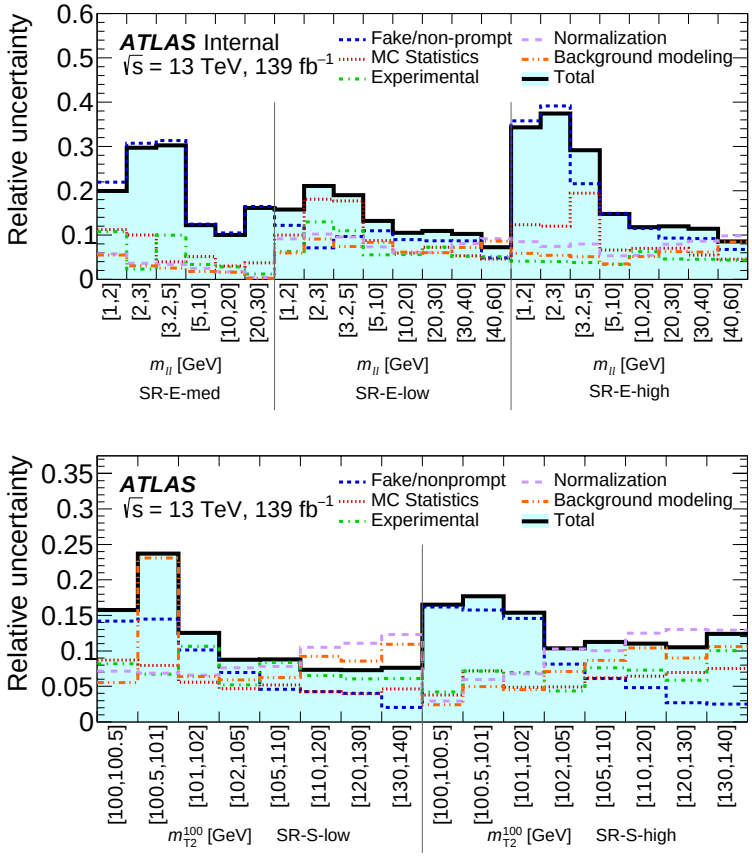

Figure 15.4: The relative systematic uncertainties in the fitted SM background as obtained from CR+SR background-only fits for the electroweakino SRs (top) and slepton SRs (bottom). The *MC Statistics* uncertainty originates from the limited size of the MC samples used to model the irreducible background contributions. The *Normalization* uncertainty arises from the use of CRs to normalize the contributions of $t\bar{t}/tW$, $Z^{(*)}/\gamma^{*}(\rightarrow \tau\tau)$ + jets and WW/WZ backgrounds, while *Background modeling* includes the different sources of theoretical modeling uncertainties in the $m_{\ell\ell}$ or m_{T2}^{100} lineshapes for the irreducible backgrounds. All sources of uncertainty affecting the fake/non-prompt background estimate are included under *Fake/nonprompt*. The uncertainties arising from the reconstruction and selection of signal leptons, jets and $E_{\mathrm{T}}^{\mathrm{miss}}$ are included under the *Experimental* category. The individual uncertainties can be correlated and do not necessarily add up in quadrature to the total uncertainty.

from each individual SR are also shown to highlight their respective sensitivity to different ranges of mass-splitting.

In general, the search is more sensitive to winos than higgsinos, as the former process is expected to have a larger production cross-section for a given $\widetilde{\chi}_2^0$ mass. Additionally, in each interpretation, the vast majority of the overall exclusion power is due to SR–E–high. SR–E–med and SR–E–low provide additional expected exclusion power at moderate and high mass splittings, respectively. Finally, SR–E–$1\ell 1T$ contributes to the sensitivity at very low mass splittings for wino production, while it has no sensitivity to the lower cross-section higgsino process. Some large differences exist between the expected and observed exclusion contours at high-Δm. This can be attributed to an underestimation of the SM background in SR–E–high for 10 GeV $< m_{\mu\mu} <$ 20 GeV and an overestimation from 20 GeV $< m_{\mu\mu} <$ 40 GeV, as shown in Figure 15.1. This effect is especially strong for wino production with $m(\widetilde{\chi}_2^0) \times m(\widetilde{\chi}_1^0) > 0$ due to the asymmetric nature of the signal's $m_{\ell\ell}$ distribution, which peaks at higher values of $m_{\ell\ell}$ for a given mass splitting.

In the case of higgsino production, the maximum excluded $\widetilde{\chi}_2^0$ mass reaches up to 193.4 GeV, corresponding to a mass splitting of 9.3 GeV. The minimum mass splitting excluded by this search for higgsino production is 2.4 GeV. For wino production, the maximum excluded $\widetilde{\chi}_2^0$ mass is 240.5 GeV (240.7 GeV) at a mass splitting of 7 GeV (9 GeV) when the mass eigenvalues $m(\widetilde{\chi}_2^0)$ and $m(\widetilde{\chi}_1^0)$ have the same (opposite) sign. When $m(\widetilde{\chi}_2^0) \times m(\widetilde{\chi}_1^0) > 0$, the minimum excluded mass splitting is 1.5 GeV. For $m(\widetilde{\chi}_2^0) \times m(\widetilde{\chi}_1^0) < 0$, this value corresponds to 1.7 GeV. A summary of these exclusion values is shown in Table 15.3.

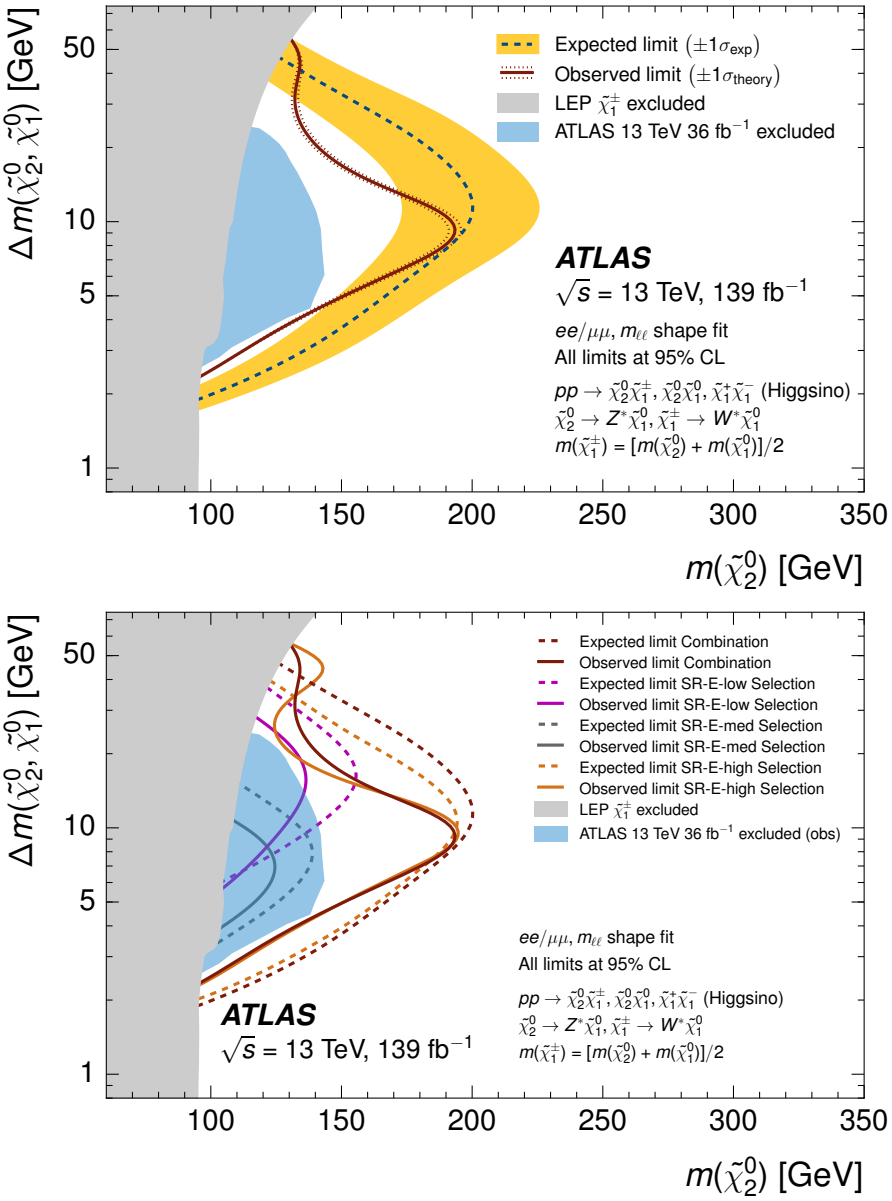

Figure 15.5: Expected (dashed lines) and observed (solid lines) exclusion limits at 95% CL for direct higgsino production within the simplified higgsino model where the chargino $\tilde{\chi}_1^{\pm}$ mass is assumed to be halfway between the $\tilde{\chi}_2^0$ and $\tilde{\chi}_1^0$ masses. The limits are derived using fits to the $m_{\ell\ell}$ spectrum with the signal process included (up to an overall normalization factor). The gray regions show the constraints on the chargino mass from LEP [124]. The blue regions show the constraints from an ATLAS Run 2 search with 36 fb^{-1} [116]. The top plot shows the results of the combined fits to SR–E–high, SR–E–med, SR–E–low, and SR–E–1ℓ1T. The bottom plot shows the limits from each of these SRs separately, as well as their combination. SR–E–1ℓ1T has no sensitivity to higgsino production and is therefore not shown in the plot.

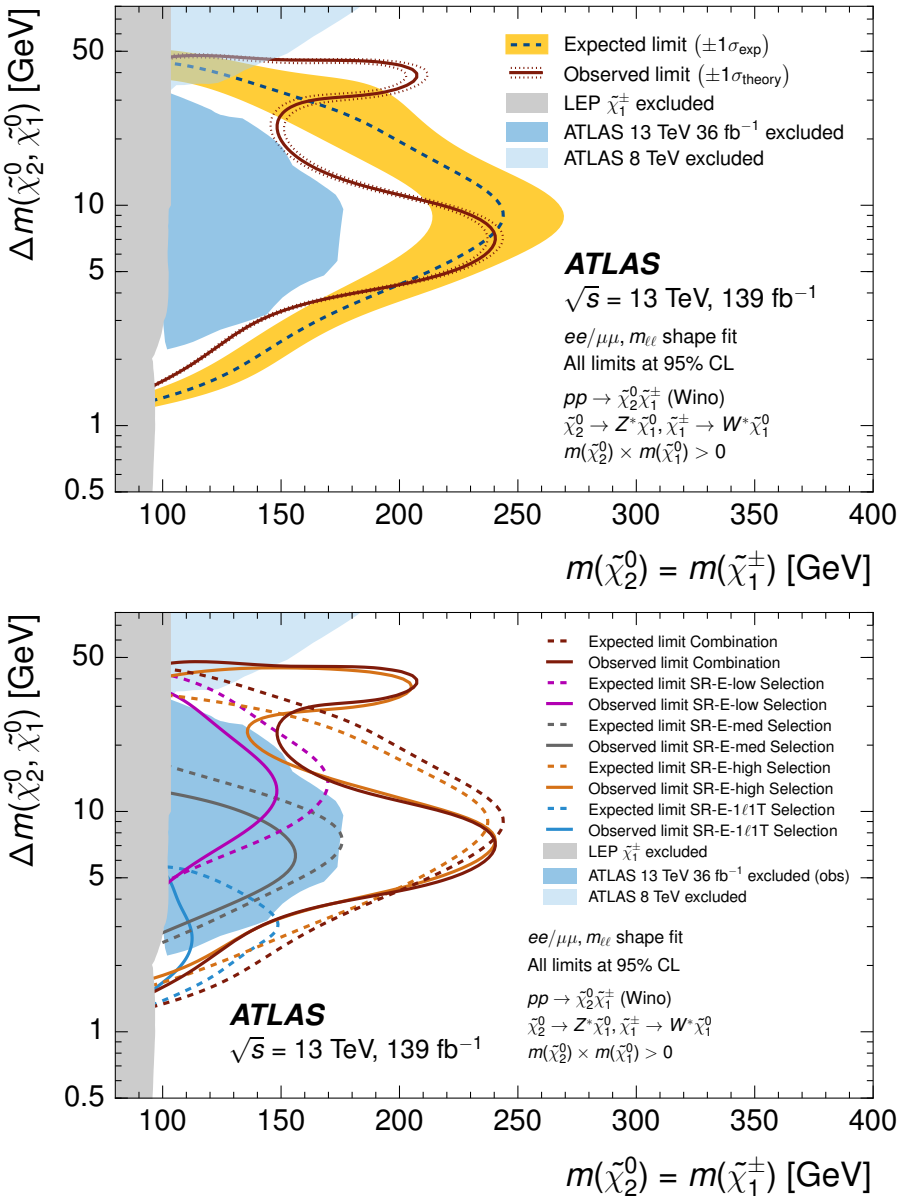

Figure 15.6: Expected (dashed lines) and observed (solid lines) exclusion limits at 95% CL for direct wino production within the simplified wino/bino model where $m(\tilde{\chi}_1^{\pm}) = m(\tilde{\chi}_2^0)$ is assumed. Here, $m(\tilde{\chi}_2^0) \times m(\tilde{\chi}_1^0) > 0$ is also assumed.The limits are derived using fits to the $m_{\ell\ell}$ spectrum with the signal process included (up to an overall normalization factor). The gray regions show the constraints on the chargino mass from LEP [124]. The blue regions show the constraints from ATLAS Run 1 [125, 126] and ATLAS Run 2 [116] searches. The top plot shows the results of the combined fits to SR–E–high, SR–E–med, SR–E–low, and SR–E–1ℓ1T. The bottom plot shows the limits from each of these SRs separately, as well as their combination.

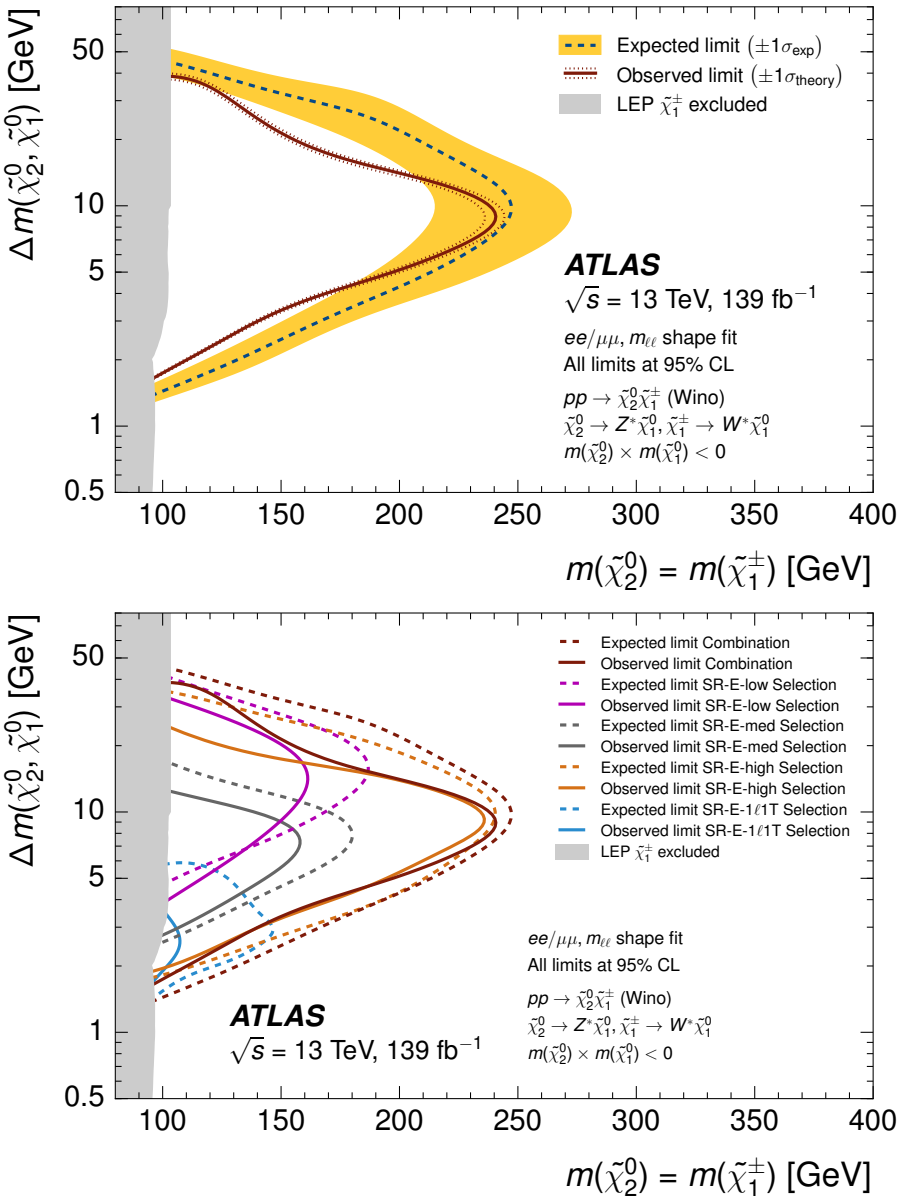

Figure 15.7: Expected (dashed lines) and observed (solid lines) exclusion limits at 95% CL for direct wino production within the simplified wino/bino model where $m(\tilde{\chi}_1^{\pm}) = m(\tilde{\chi}_2^0)$ is assumed. Here, $m(\tilde{\chi}_2^0) \times m(\tilde{\chi}_1^0) < 0$ is also assumed.The limits are derived using fits to the $m_{\ell\ell}$ spectrum with the signal process included (up to an overall normalization factor). The gray regions show the constraints on the chargino mass from LEP [124]. The top plot shows the results of the combined fits to SR–E–high, SR–E–med, SR–E–low, and SR–E–1ℓ1T. The bottom plot shows the limits from each of these SRs separately, as well as their combination.

Table 15.3: Left to right: the first column indicates the specific electroweakino interpretation being considered. For the wino/bino interpretations, "same sign" and "opposite sign" refer to the relative signs of the mass eigenvalues $m(\widetilde{\chi}_2^0)$ and $m(\widetilde{\chi}_1^0)$. The second column shows the maximum excluded $\widetilde{\chi}_2^0$ mass obtained via the exclusion fits. The third column shows the mass-splitting between the $\widetilde{\chi}_2^0$ and the LSP evaluated at the maximum excluded $\widetilde{\chi}_2^0$ mass. The fourth (fifth) column shows the minimum (maximum) excluded mass-splitting between the $\widetilde{\chi}_2^0$ and the LSP.

Interpretation	$m(\widetilde{\chi}_2^0)^{\text{excl}}_{\text{max}}$	$\Delta m(\widetilde{\chi}_2^0, \widetilde{\chi}_1^0)\big\vert_{m(\widetilde{\chi}_2^0)^{\text{excl}}_{\text{max}}}$	$\Delta m(\widetilde{\chi}_2^0, \widetilde{\chi}_1^0)^{\text{excl}}_{\text{min}}$	$\Delta m(\widetilde{\chi}_2^0, \widetilde{\chi}_1^0)^{\text{excl}}_{\text{max}}$
Higgsino	193.4 GeV	9.3 GeV	2.4 GeV	54.7 GeV
Wino/Bino (same sign)	240.5 GeV	7.0 GeV	1.5 GeV	46.5 GeV
Wino/Bino (opposite sign)	240.7 GeV	9.0 GeV	1.7 GeV	38.7 GeV

15.2.2 Sleptons

In the absence of statistically significant excesses over the background estimation in the slepton SRs, exclusion fits are used to set upper limits on the cross-section for slepton pair production in the simplified model. These exclusion fits are performed using all of the slepton CRs and exclusive SRs and exploit the characteristic shape of the m_{T2}^{100} distribution for the signal processes. The parameter of interest in these fits is the signal strength, which is a single factor that coherently scales the signal yields across all regions included in the fit. The resulting limits are projected onto the $\Delta m(\widetilde{\ell}, \widetilde{\chi}_1^0)$ vs. $m(\widetilde{\ell})$ plane to derive the range of excluded masses at 95% CL. The upper limits on the production cross-sections are shown in Appendix C.2.

In general, the simplified model makes no assumptions about potential mass-degeneracies based on either the slepton flavor or the chirality of the slepton's corresponding SM partner. Nevertheless, limits are set using a variety of different mass-degeneracy assumptions since these degeneracies are not strictly forbidden.

For simplicity, whenever the chirality of a slepton is referred to in the text, it is really a statement about the chirality of its SM partner lepton. The following mass-degeneracy scenarios are considered in this analysis:

- Sleptons are both flavor- and chirality-degenerate: $m(\widetilde{\mu}_L) = m(\widetilde{\mu}_R) = m(\widetilde{e}_L) = m(\widetilde{e}_R)$
- Sleptons are flavor-degenerate: $m(\widetilde{\mu}_L) = m(\widetilde{e}_L)$, $m(\widetilde{\mu}_R) = m(\widetilde{e}_R)$
- Sleptons are chirality-degenerate: $m(\widetilde{\mu}_L) = m(\widetilde{\mu}_R)$, $m(\widetilde{e}_L) = m(\widetilde{e}_R)$
- Sleptons are neither flavor- nor chirality-degenerate: $m(\widetilde{\mu}_L) \neq m(\widetilde{\mu}_R) \neq m(\widetilde{e}_L) \neq m(\widetilde{e}_R)$

When setting limits on a specific slepton flavor, the signal region targeting the other flavor is not included in the fit. For example, when setting limits on chirality-degenerate selectrons, the signal regions that require two muons in the event are not considered in the exclusion fit. This choice was made by inspecting the expected exclusion contours with and without the opposite-flavor signal regions included. In principle, these opposite-flavor signal regions can help constrain the background but the impact on the expected sensitivity was found to be negligible. Therefore, in order to simplify the final exclusion fits, they are not included when assuming $m(\widetilde{\mu}) \neq m(\widetilde{e})$.

The available slepton signal samples contain an admixture of left-handed and right-handed sleptons. In these samples, the fraction of events containing sleptons of a given chirality is determined by its relative production cross-section compared to the opposite chirality state. In general, the cross-section for producing left-handed sleptons, σ_L, is larger than that for producing right-handed sleptons, σ_R. The ratio of these two cross-sections depends on the slepton mass, where the relative cross-section for left-handed sleptons increases as the slepton

mass decreases. In the mass range considered by this analysis, the ratio $\frac{\sigma_L}{\sigma_R}$ runs from ~ 2.98 at $m(\widetilde{\ell}) = 50$ GeV to ~ 2.64 at $m(\widetilde{\ell}) = 300$ GeV.

When setting limits on sleptons of a given chirality, the number of events in the signal samples proved to be a limiting factor when only signal events with the corresponding chirality were selected. The efficiencies of the event selections defining the slepton signal regions were checked separately for sleptons of a given flavor but different chirality. An example of the selection efficiencies for each cut in the slepton SRs is shown for the $\left(m(\tilde{\ell}), m(\tilde{\chi}_1^0)\right) = (150\text{ GeV}, 140\text{ GeV})$ signal point in Figure 15.8. Further details on this study are shown in Appendix B. In each case, no systematic difference was observed in the selection efficiency for left-handed and right- handed sleptons, indicating that the relevant event-level kinematics do not depend on the slepton chirality. Thus, in order to increase the statistical power of the available signal samples, both right-handed and left-handed signal events are considered when setting limits on sleptons of a given chirality. When doing so, the signal events are scaled down such that the inclusion of both chirality states does not modify the expected event yield. In particular, when setting limits on right-handed sleptons, signal events are scaled down by a factor of $\frac{1}{1+\sigma_L/\sigma_R}$ in order to maintain the expected signal yield. For the left-handed interpretations, the signal events are correspondingly scaled down by a factor of $\frac{1}{1+\sigma_R/\sigma_L}$. Due to the mass-dependence of $\frac{\sigma_L}{\sigma_R}$, shown in Figure 15.9, these factors are calculated and applied separately for each slepton mass.

Figures 15.10–15.13 show the expected and observed exclusion contours for each mass-degeneracy assumption. Representative examples of the scans over the signal strength parameter μ_{sig} are shown in Figure 15.14, under the assumption that the sleptons are both flavor- and chirality-degenerate. Naturally, the maximum excluded slepton mass is derived under the assumption that the sleptons are

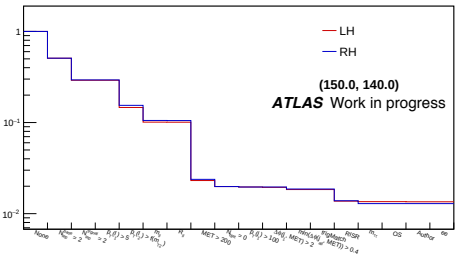

(a) Selectrons: SR–S–high

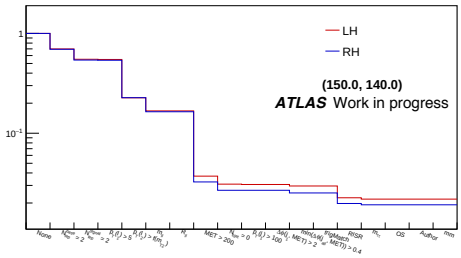

(b) Smuons: SR–S–high

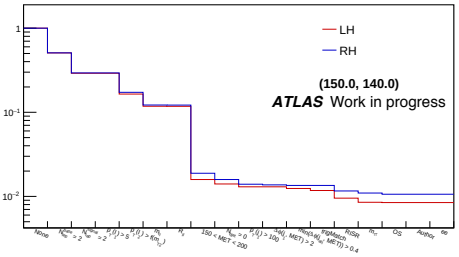

(c) Selectrons: SR–S–low

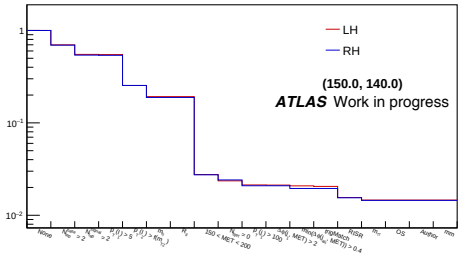

(d) Smuons: SR–S–low

Figure 15.8: Cutflows for the $\left(m(\tilde{\ell}), m(\tilde{\chi}_1^0)\right) = (150\text{ GeV}, 140\text{ GeV})$ slepton signal point. The top (bottom) row shows the efficiencies of the cuts defining SR–S–high (SR–S–low). The left (right) column corresponds to selectrons (smuons).

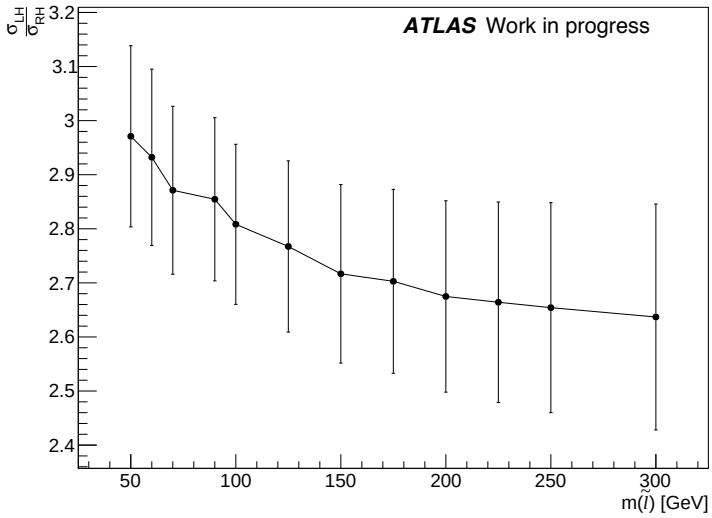

Figure 15.9: The Left-handed slepton cross-section divided by the right-handed slepton cross-section as a function of the slepton mass. The cross-sections and associated uncertainties, which are independent of slepton flavor, are calculated using Resummino 2.0.1 at NLO+NLL precision.

both flavor- and chirality-degenerate (Figure 15.10). In this case, the maximum excluded slepton mass is observed to be 251 GeV, which corresponds to a mass-splitting of 10.0 GeV. The maximum (minimum) mass splitting that is excluded by the observed data under this assumption is 30.4 GeV (0.55 GeV). A summary of these exclusion numbers is shown for each of the mass-degeneracy assumptions in Table 15.4.

Table 15.4: Left to right: the first column indicates the specific slepton interpretation being considered. The second column shows the maximum excluded slepton mass obtained via the exclusion fits. The third column shows the mass-splitting between the slepton and the LSP evaluated at the maximum excluded slepton mass. The fourth (fifth) column shows the minimum (maximum) excluded mass-splitting between the slepton and the LSP.

Interpretation	$m(\widetilde{\ell})^{\text{excl}}_{\text{max}}$	$\Delta m(\widetilde{\ell}, \widetilde{\chi}^0_1)\big\vert_{m(\widetilde{\ell})^{\text{excl}}_{\text{max}}}$	$\Delta m(\widetilde{\ell}, \widetilde{\chi}^0_1)^{\text{excl}}_{\text{min}}$	$\Delta m(\widetilde{\ell}, \widetilde{\chi}^0_1)^{\text{excl}}_{\text{max}}$
$\widetilde{\ell}_{L,R}$	251.0 GeV	10.0 GeV	0.6 GeV	30.4 GeV
$\widetilde{e}_{L,R}$	187.6 GeV	7.5 GeV	1.0 GeV	21.9 GeV
$\widetilde{\mu}_{L,R}$	242.3 GeV	10.5 GeV	0.4 GeV	32.0 GeV
$\widetilde{\ell}_L$	221.0 GeV	9.5 GeV	0.6 GeV	26.4 GeV
$\widetilde{\ell}_R$	157.3 GeV	8.2 GeV	1.3 GeV	16.6 GeV
$\widetilde{\mu}_L$	216.0 GeV	10.0 GeV	0.4 GeV	27.6 GeV
$\widetilde{\mu}_R$	150.2 GeV	8.2 GeV	0.9 GeV	16.0 GeV
$\widetilde{e}_L$	169.4 GeV	7.1 GeV	1.2 GeV	19.0 GeV
$\widetilde{e}_R$	101.4 GeV	7.5 GeV	5.5 GeV	9.3 GeV

Since the slepton chirality does not affect the event kinematics, the exclusion power for left-handed sleptons is greater than that for right-handed sleptons, simply due to their larger cross-sections. Additionally, larger exclusion power is observed for smuons compared to selectrons, which is largely driven by the higher overall efficiency for signal muons compared to signal electrons. Finally, Figure 15.10 shows how SR–S–high and SR–S–low contribute to the combined sensitivity of the analysis. While SR–S–high drives the most of the sensitivity, SR–S–low improves the expected exclusion power at high mass splittings. This

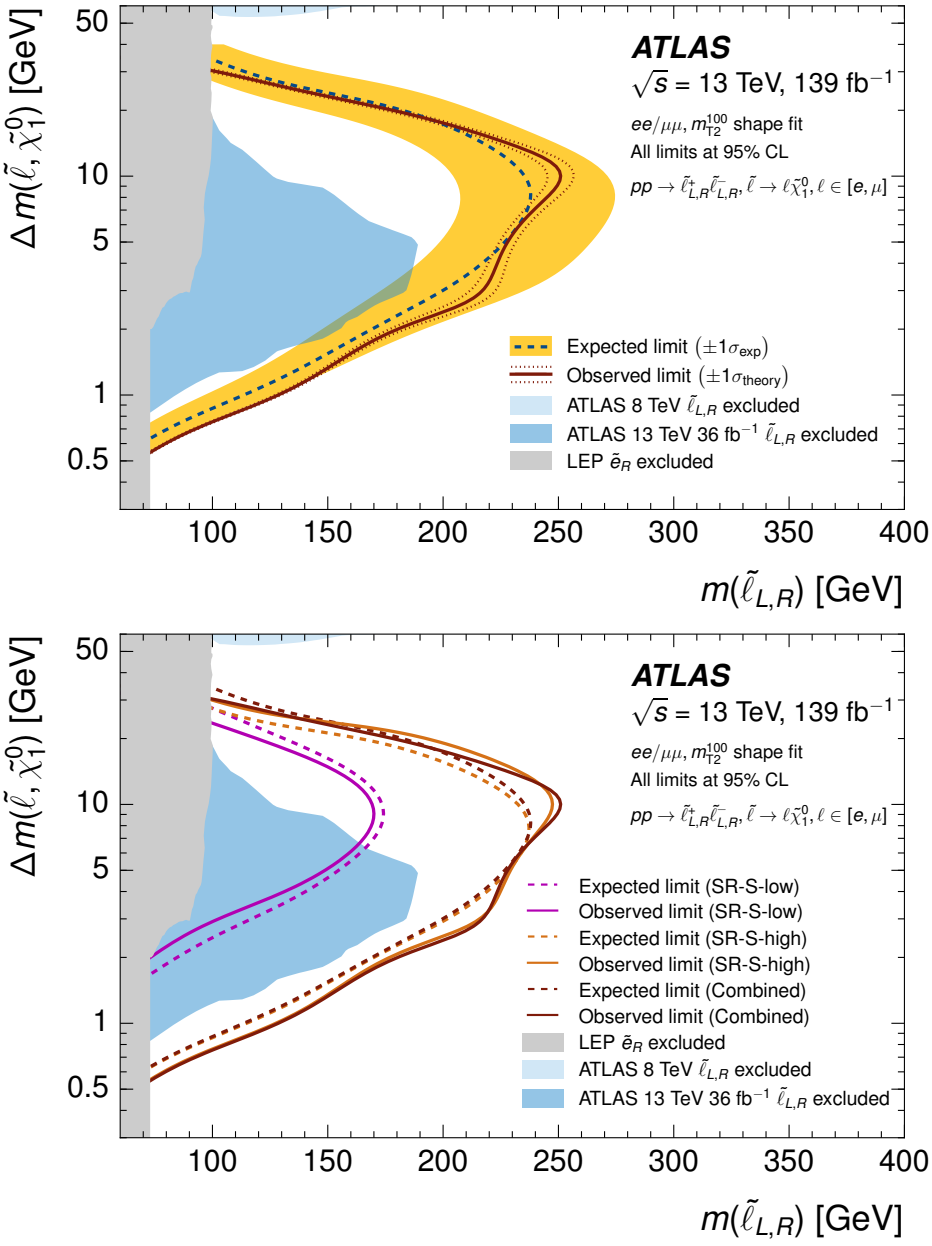

Figure 15.10: Expected (dashed lines) and observed (solid lines) exclusion limits at 95% CL for fully-degenerate sleptons. The limits are derived using fits to the m_{T2}^{100} spectrum with the signal process included (up to an overall normalization factor). The gray region shows the constraints on right-handed selectrons from LEP [127]. The blue regions show the constraints on fully-degenerate sleptons from ATLAS Run 1 [125] and ATLAS Run 2 [116] searches. The top plot shows the results of the combined fits to both SR–S–low and SR–S–high. The bottom plot shows the limits from SR–S–low and SR–S–high separately, as well as their combination.

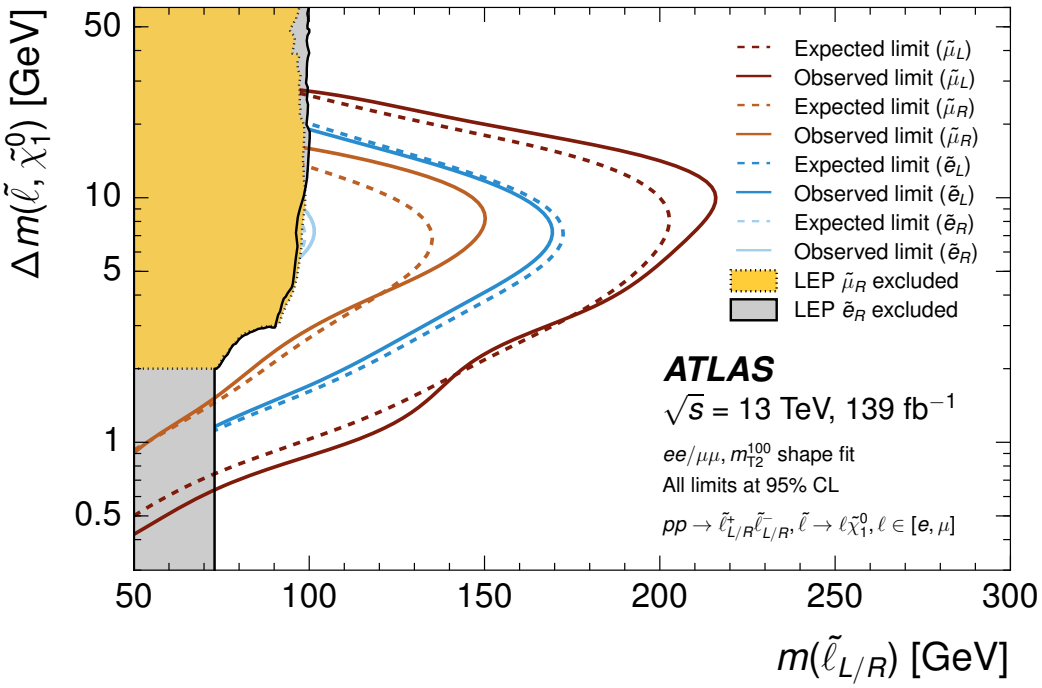

Figure 15.11: Expected (dashed lines) and observed (solid lines) exclusion limits at 95% CL for non-degenerate sleptons. The limits are derived using fits to the m_{T2}^{100} spectrum with the signal process included (up to an overall normalization factor). The gray (yellow) region shows the constraints on right-handed selectrons (smuons) from LEP [127].

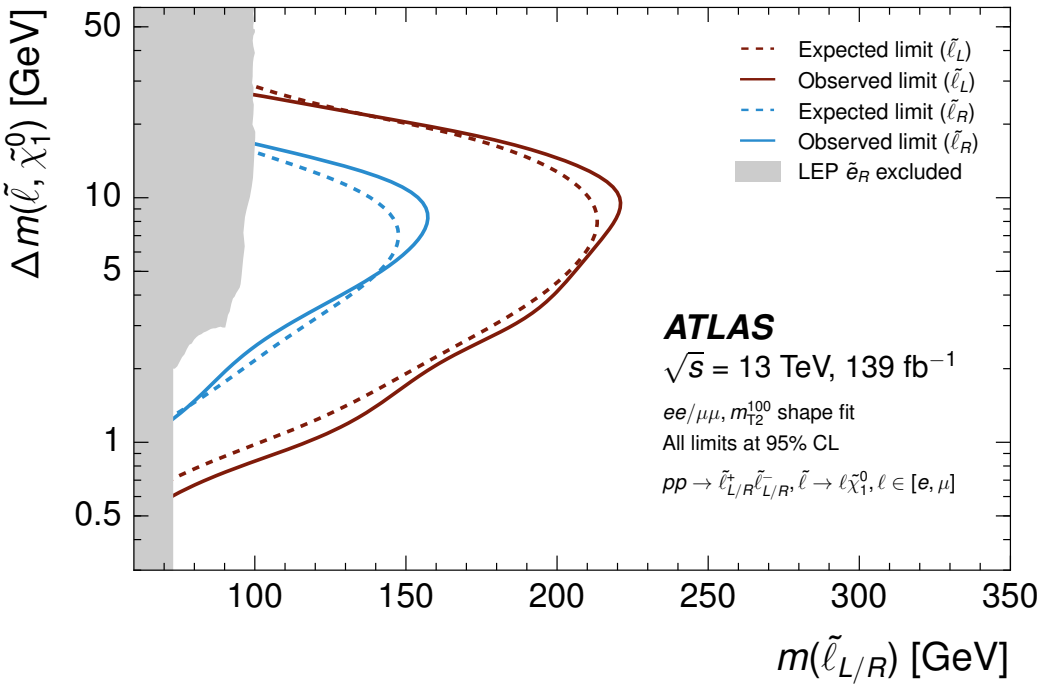

Figure 15.12: Expected (dashed lines) and observed (solid lines) exclusion limits at 95% CL for flavor-degenerate sleptons. The limits are derived using fits to the m_{T2}^{100} spectrum with the signal process included (up to an overall normalization factor). The gray region shows the constraints on right-handed selectrons from LEP [127].

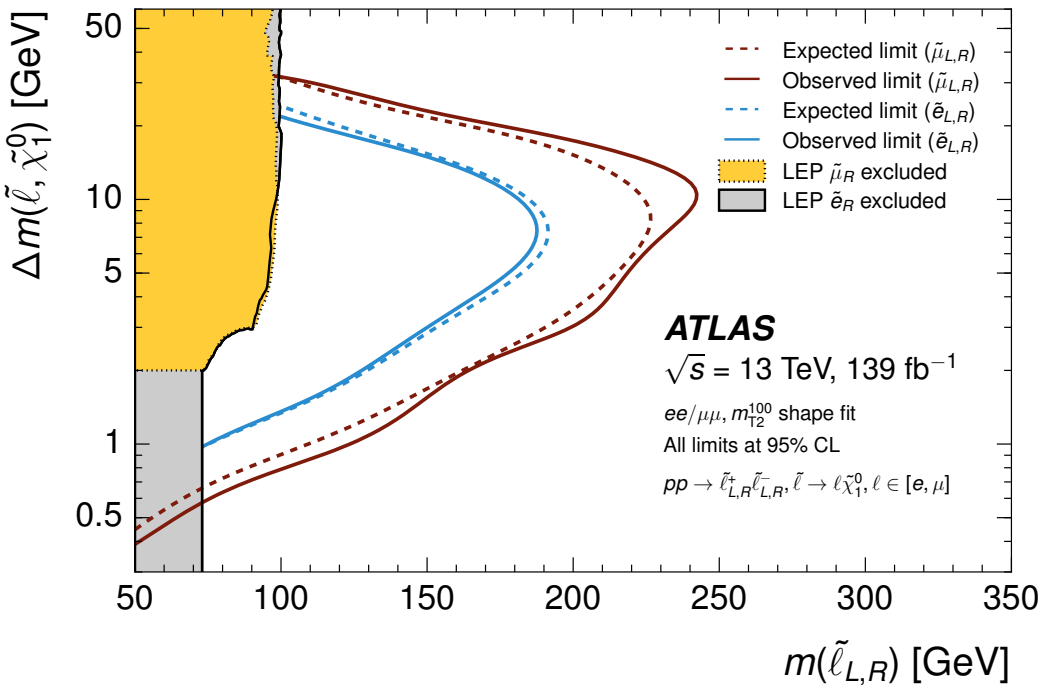

Figure 15.13: Expected (dashed lines) and observed (solid lines) exclusion limits at 95% CL for chirality-degenerate sleptons. The limits are derived using fits to the m_{T2}^{100} spectrum with the signal process included (up to an overall normalization factor). The gray (yellow) region shows the constraints on right-handed selectrons (smuons) from LEP [127].

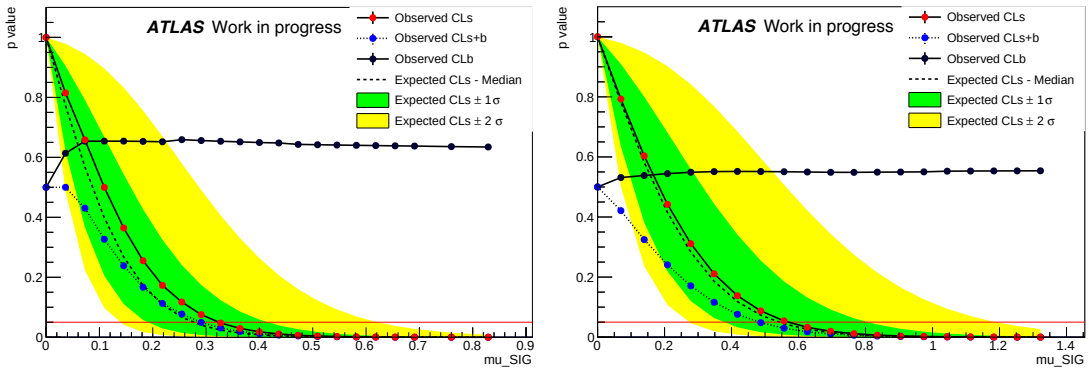

(a) $m(\widetilde{\ell}) = 100$ GeV, $m(\widetilde{\chi}_1^0) = 198$ GeV **(b)** $m(\widetilde{\ell}) = 125$ GeV, $m(\widetilde{\chi}_1^0) = 105$ GeV

Figure 15.14: Results of the hypothesis tests as a function of the signal strength parameter μ_{sig} for two excluded signal points. Here, the sleptons are assumed to have a four-fold mass degeneracy (i.e. $m(\widetilde{\mu}_L) = m(\widetilde{\mu}_R) = m(\widetilde{e}_L) = m(\widetilde{e}_R)$). In each case shown, $\mu_{\mathrm{sig}} = 1$ is excluded at 95% CL using the $\mathrm{CL_s}$ prescription.

slightly counterintuitive feature is due to the fact that, in low-$E_{\mathrm{T}}^{\mathrm{miss}}$ events, larger mass splittings are needing in order to boost the leptons enough to put them over their reconstruction and analysis selection thresholds.

An important aspect understanding the limitations the search is inspecting which uncertainties have the largest impact on the fitted signal strength. This can be done by checking how the results of the exclusion fits change after fixing each nuisance parameter (one at a time) to it's maximum and minimum values, defined by its post-fit uncertainty. In general, fixing these parameters in the fit allows for different best-fit values of μ_{sig} to be obtained. These values are then compared to the best-fit value of μ_{sig} that was obtained using the fit with all nuisance parameters floating, and the deviations are used to rank the nuisance parameters according to their impact on the exclusion power for a given signal hypothesis. Since the background composition changes across the m_{T2}^{100} spectrum and because signals with different mass-splittings populate different ranges of m_{T2}^{100}, it is important to make perform this check for different for a variety of signal hypotheses. In doing so, one can get a sense of which uncertainties have the biggest impact in different parts of the $\Delta m(\widetilde{\ell}, \widetilde{\chi}_1^0)$ vs. $m(\widetilde{\ell})$ plane.

Assuming that the sleptons are both flavor- and chirality-degenerate, Figures 15.15–15.20 show the top 25 nuisance parameters according to this metric for exclusion fits using signals hypothesis with mass-splittings ranging from 1 GeV to 40 GeV. The nuisance parameter pulls and post-fit uncertainties are also presented and show little signs of profiling, indicating a healthy fit model.

Depending on the mass splitting, the nuisance parameters with the largest impact on μ_{sig} are related to either the fake/non-prompt background estimate or the normalization of the VV background. Since the fake/non-prompt lepton background dominates at small values of m_{T2}^{100} in the slepton SRs, these uncertainties

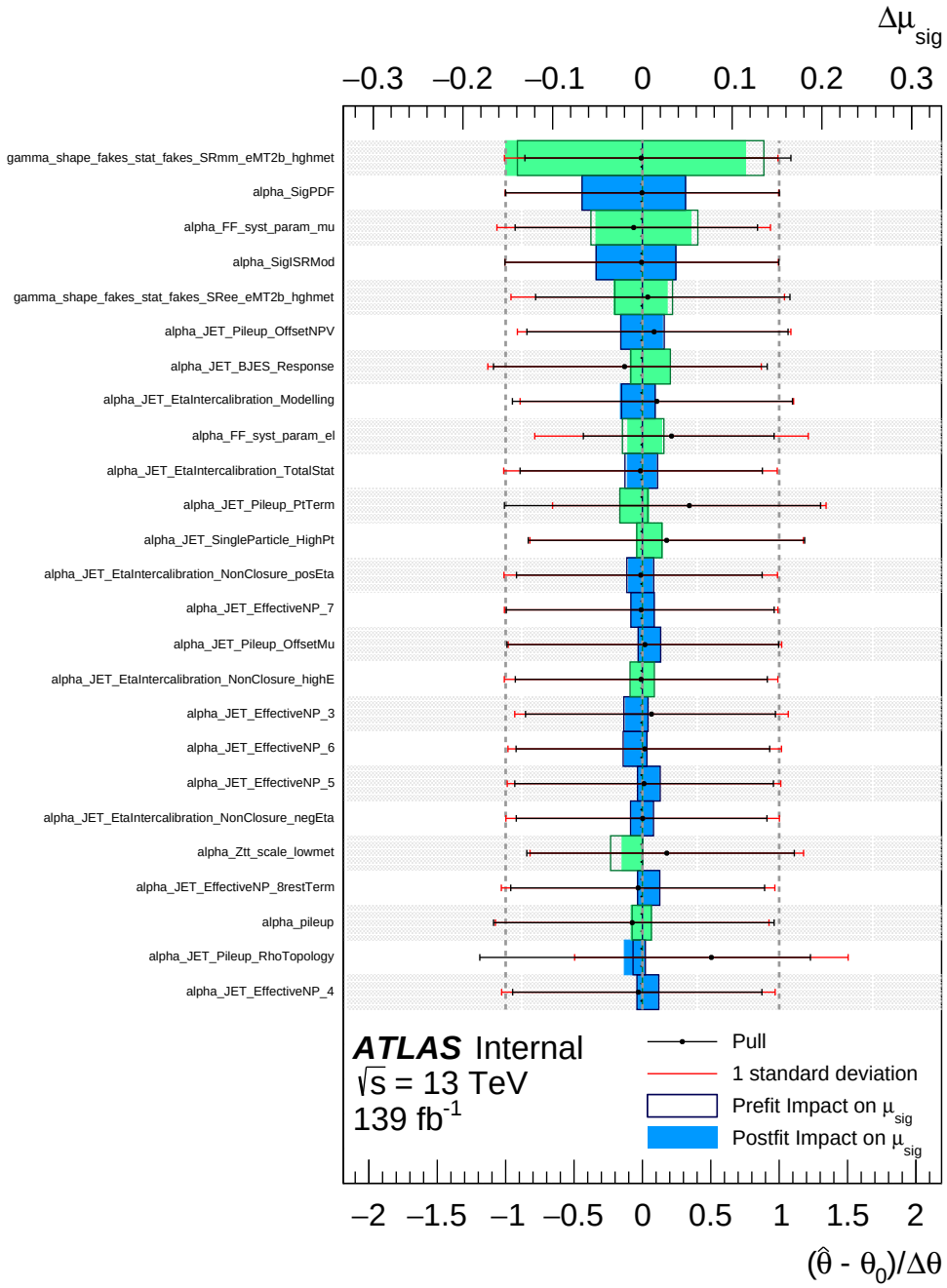

Figure 15.15: The top 25 NPs, ranked according to their impact on the best-fit value of μ_{sig}, assuming $m(\widetilde{\ell}) = 100$ GeV and $m(\widetilde{\chi}_1^0) = 99$ GeV. NPs that are correlated (anticorrelated) with μ_{sig} are shown in blue (green). The NP pulls and post-fit uncertainties are shown using black points and their associated error bars. NP names that start with "alpha" are systematic in nature, while those starting with "gamma" correspond to statistical uncertainties.

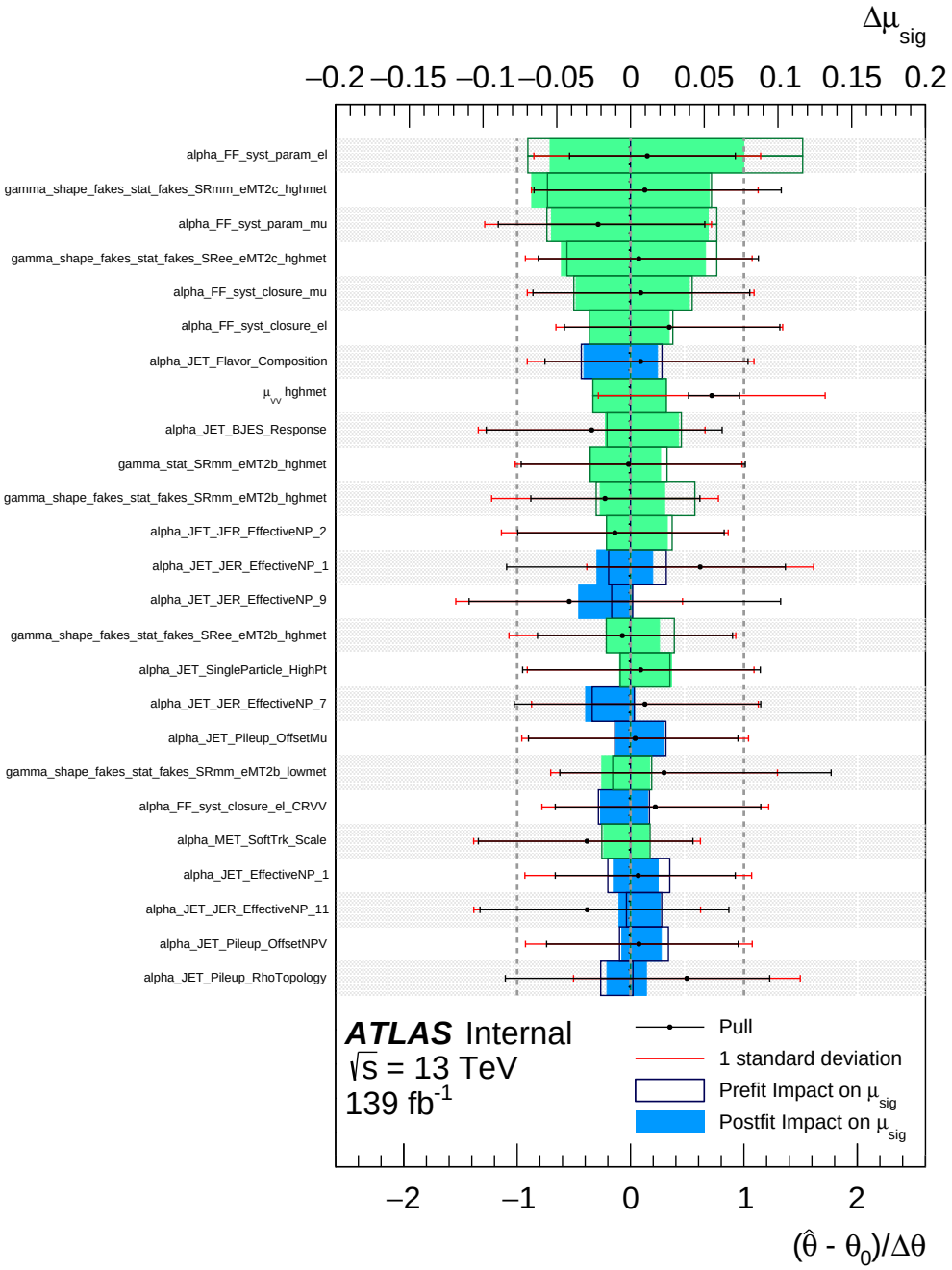

Figure 15.16: The top 25 NPs, ranked according to their impact on the best-fit value of μ_{sig}, assuming $m(\widetilde{\ell}) = 125$ GeV and $m(\widetilde{\chi}_1^0) = 123$ GeV. NPs that are correlated (anticorrelated) with μ_{sig} are shown in blue (green). The NP pulls and post-fit uncertainties are shown using black points and their associated error bars. NP names that start with "alpha" are systematic in nature, while those starting with "gamma" correspond to statistical uncertainties.

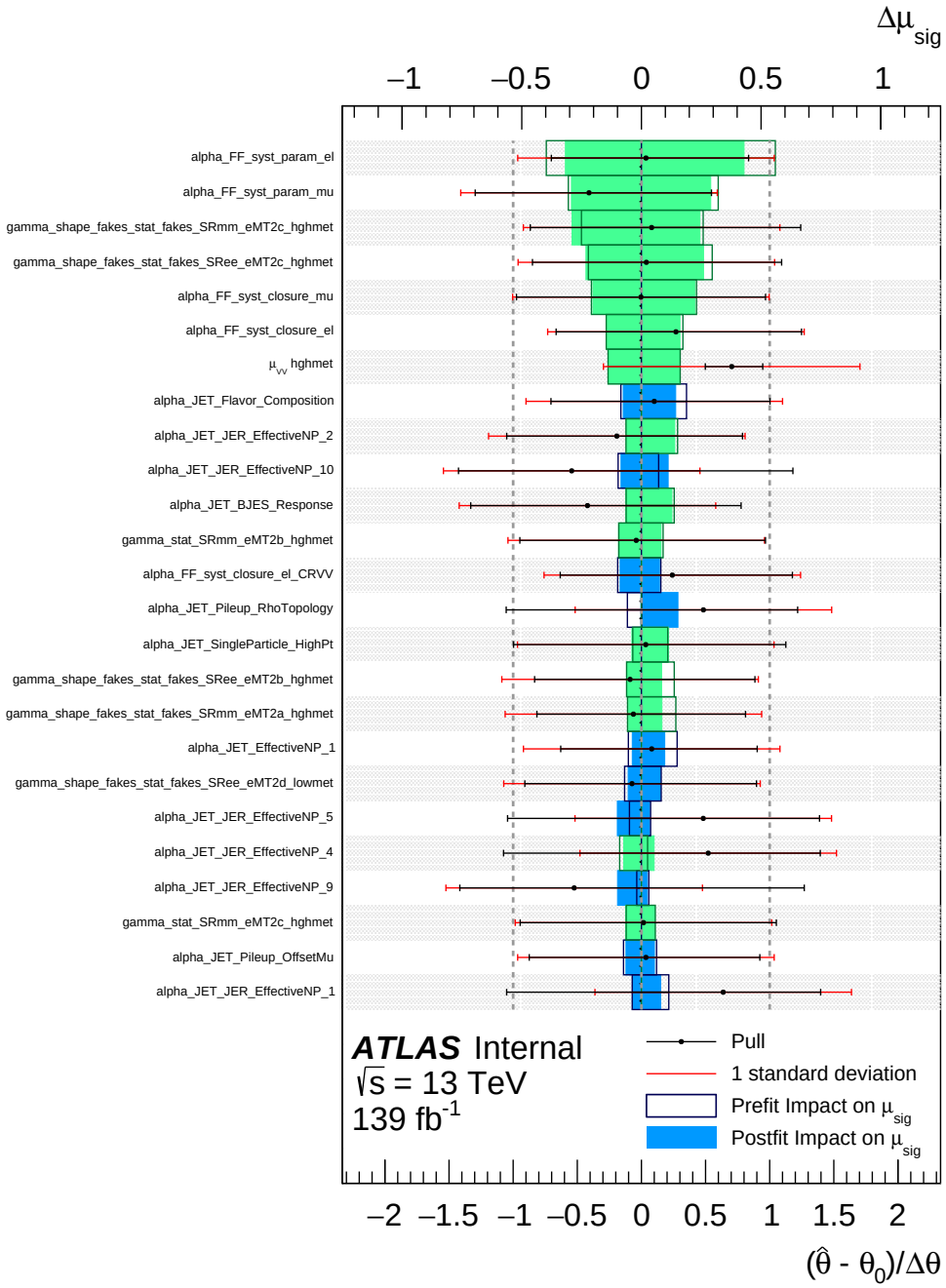

Figure 15.17: The top 25 NPs, ranked according to their impact on the best-fit value of μ_{sig}, assuming $m(\widetilde{\ell}) = 300$ GeV and $m(\widetilde{\chi}_1^0) = 295$ GeV. NPs that are correlated (anticorrelated) with μ_{sig} are shown in blue (green). The NP pulls and post-fit uncertainties are shown using black points and their associated error bars. NP names that start with "alpha" are systematic in nature, while those starting with "gamma" correspond to statistical uncertainties.

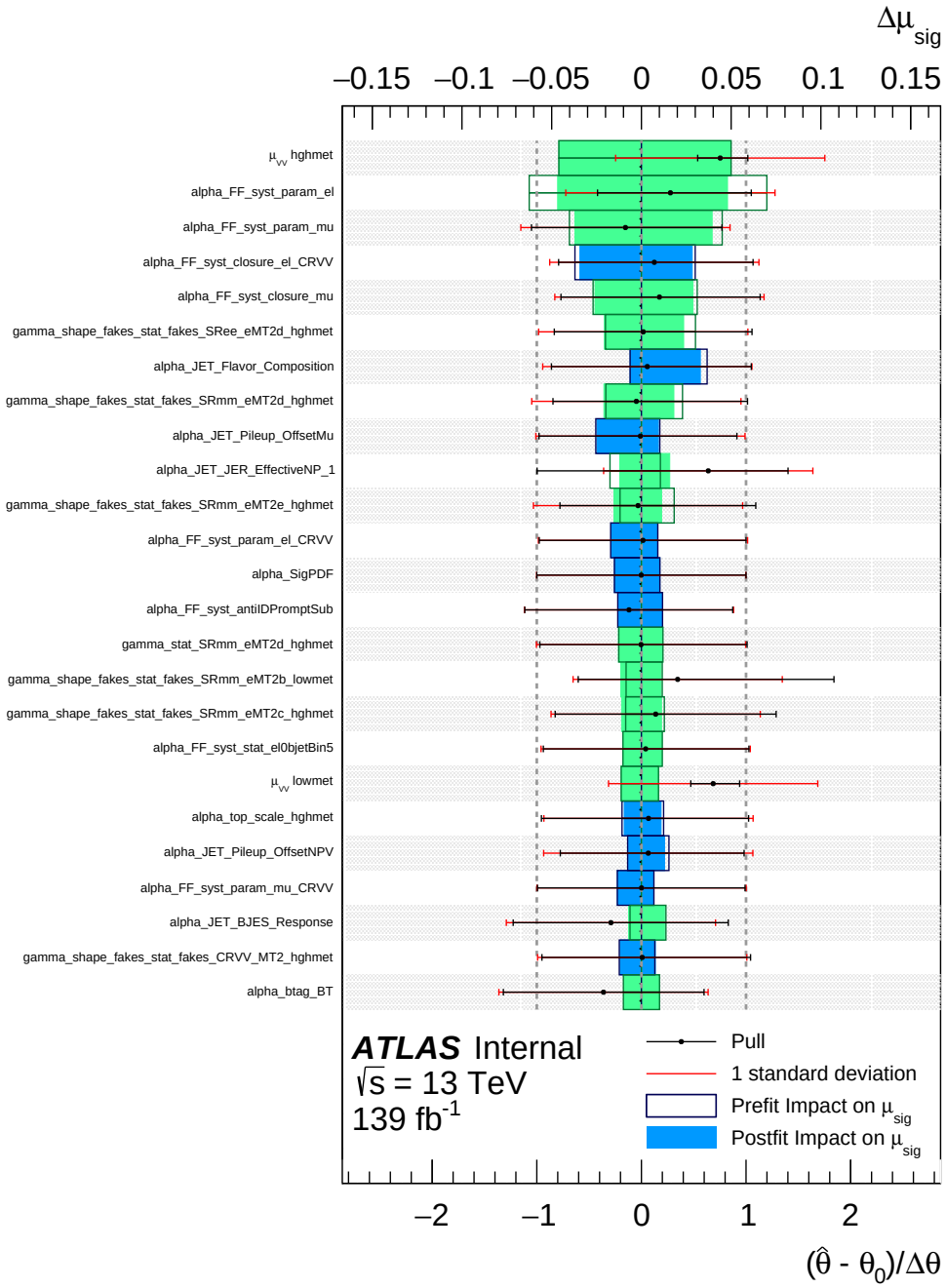

Figure 15.18: The top 25 NPs, ranked according to their impact on the best-fit value of μ_{sig}, assuming $m(\widetilde{\ell}) = 150$ GeV and $m(\widetilde{\chi}_1^0) = 140$ GeV. NPs that are correlated (anticorrelated) with μ_{sig} are shown in blue (green). The NP pulls and post-fit uncertainties are shown using black points and their associated error bars. NP names that start with "alpha" are systematic in nature, while those starting with "gamma" correspond to statistical uncertainties.

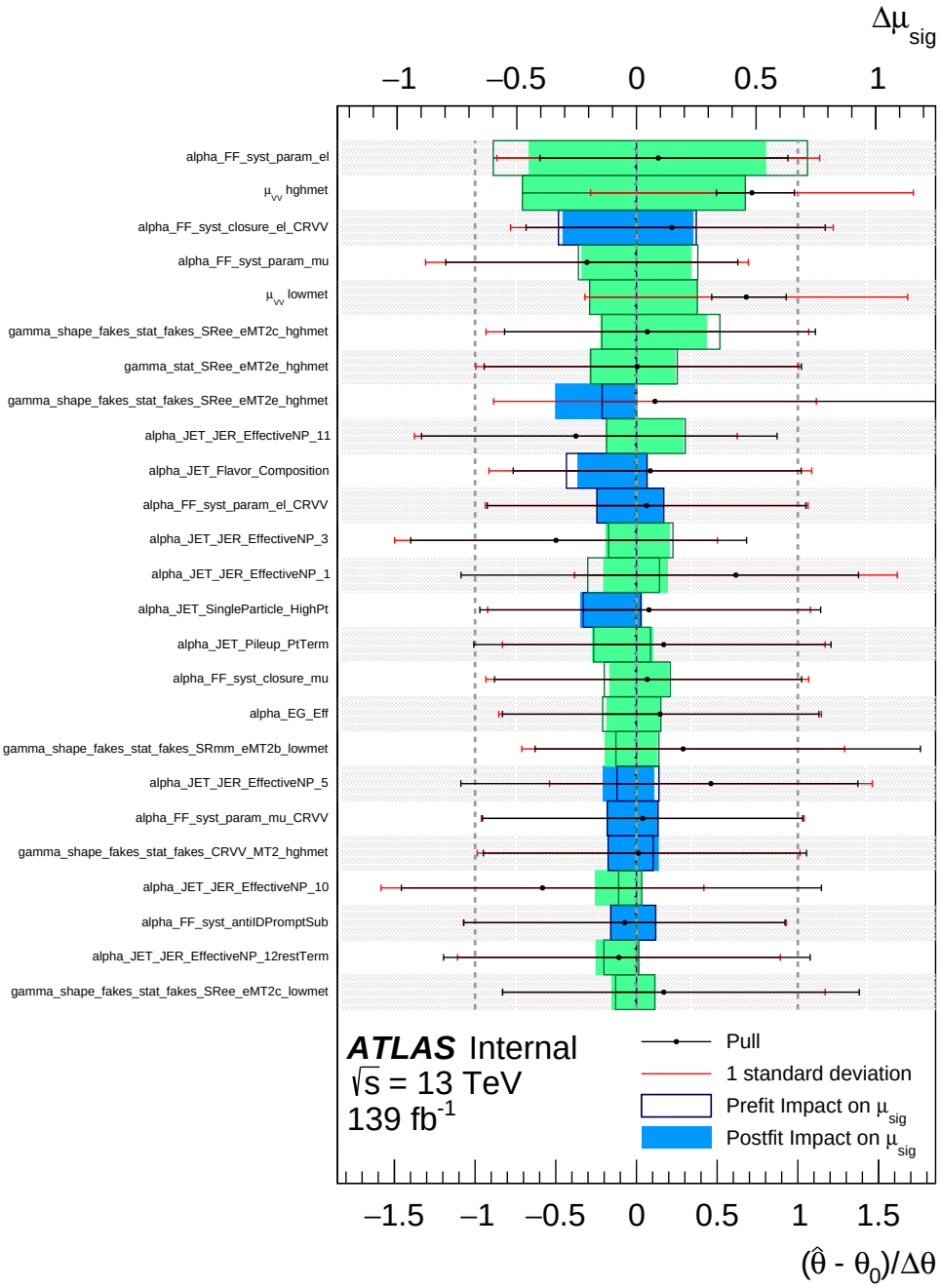

Figure 15.19: The top 25 NPs, ranked according to their impact on the best-fit value of μ_{sig}, assuming $m(\widetilde{\ell}) = 250$ GeV and $m(\widetilde{\chi}_1^0) = 230$ GeV. NPs that are correlated (anticorrelated) with μ_{sig} are shown in blue (green). The NP pulls and post-fit uncertainties are shown using black points and their associated error bars. NP names that start with "alpha" are systematic in nature, while those starting with "gamma" correspond to statistical uncertainties.

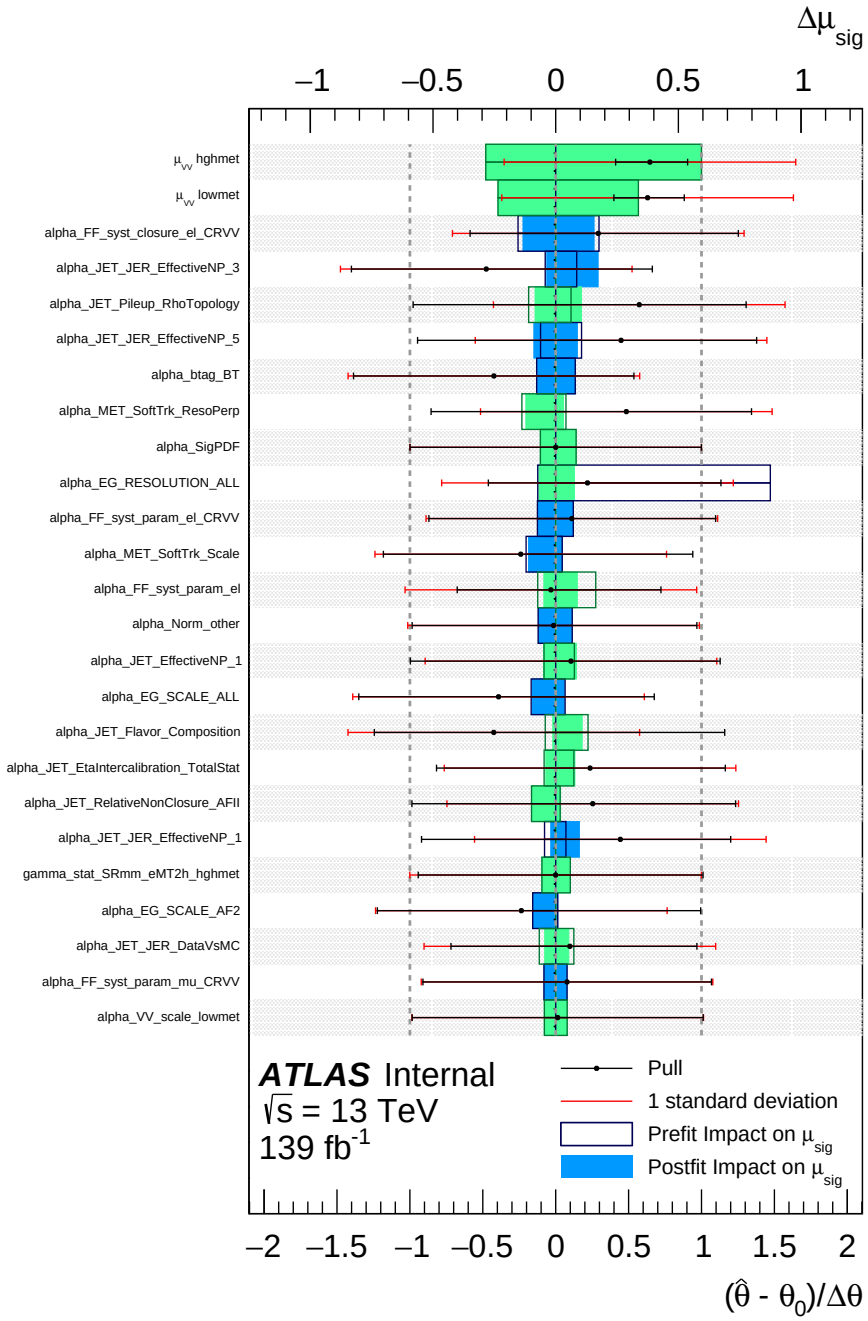

Figure 15.20: The top 25 NPs, ranked according to their impact on the best-fit value of μ_{sig}, assuming $m(\widetilde{\ell}) = 150$ GeV and $m(\widetilde{\chi}_1^0) = 110$ GeV. NPs that are correlated (anticorrelated) with μ_{sig} are shown in blue (green). The NP pulls and post-fit uncertainties are shown using black points and their associated error bars. NP names that start with "alpha" are systematic in nature, while those starting with "gamma" correspond to statistical uncertainties.

tend to dominate as well for signals with small mass-splittings. The fake/non-prompt lepton uncertainties with the largest impact on μ_{sig} in this regime are both statistical and systematic in nature. The former refers to the statistical uncertainty on the fake/non-prompt background simply due to the available data statistics in the anti-ID CRs. The dominant systematic uncertainties related to this background are the "parameterization" systematics that place flat uncertainties on the fake factors themselves in order to account for potential correlations with kinematic variables other than the lepton p_{T}. For the very compressed signal hypothesis with $m(\widetilde{\ell}) = 100$ GeV and $m(\widetilde{\chi}_1^0) = 99$ GeV, the uncertainties on the signal yields due to ISR modeling and the choice of PDF set are also among the top-ranked nuisance parameters.

As the mass splitting increases, a larger fraction of the the signal events populate the SR bins corresponding to larger values of m_{T2}^{100}, where the dominant backgrounds are from the $t\bar{t}/Wt$ and VV processes. Since the CRs targeting the VV background are not particularly pure in these processes, the VV normalization factors obtained from the fit come with larger uncertainties than those controlling the $t\bar{t}/Wt$ normalization. The end result is that the VV normalization parameters tend to be among the top ranked nuisance parameters when performing hypothesis tests using signals with mass-splittings $\gtrsim 10\,\text{GeV}$. In general, nuisance parameters associated with experimental uncertainties are subleading compared to the fake/non-prompt and VV normalization systematics. Within these experimental uncertainties, though, those related to the jet energy resolution and pileup effects tend to have the largest impact on the extracted signal strength. Finding ways of reducing these uncertainties, especially those relate to the fake/non-prompt lepton background will be of clear importance for future searches for electroweak SUSY in compressed scenarios.

Chapter 16

Analysis Preservation for Reinterpretation

In the current state of particle physics, there is no shortage of ideas when it comes to extending the SM.. Despite the huge effort from experimentalists, addressing the large number of viable models of new physics remains a significant challenge at the LHC.

Typically, a search for new physics will target some small set of models, for which constraints are derived in the absence of signal. This is not because experimental physicists want to limit the impact of their results, but rather because performing these interpretations requires significant personpower, time, and expertise. Quite often, though, the sensitivity of these searches still extends beyond the set of models they were originally designed to address. In such cases, it is possible in principle to rerun the analysis code using a new simulated signal sample and ultimately provide constraints on the model. In practice, though, the complexity of these searches and the expertise required to execute them make reinterpretation a rather difficult task. Despite internal documentation, it could be years after a search is completed before an interest in reinterpreting the results

takes hold. By this time, the technical challenges that come with running the full analysis chain often make this impossible.

Instead, the experiments at the LHC have recently made an effort to use modern computing technologies to preserve the analysis software, workflow, and results in such a way that executing the analysis can be done much more easily and reliably. This chapter highlights the effort to preserve this search for electroweak SUSY so that the results can be reinterpreted in the context of other models leading to final states with $E_{\mathrm{T}}^{\mathrm{miss}}$ and soft leptons.

16.1 Overview and Methodology

The execution of analysis code at LHC-based experiments has itself become a complex issue. Reproducing a result requires the use of specific software releases and a complex workflow to be executed correctly. As analyzers come and go, expertise is lost and reproducibility becomes harder and harder to achieve. Yet, as the time it takes to double the size of the ATLAS dataset increases, using the results of previous searches to derive constraints on new physics models will become more and more important. Recently, the LHC experiments have made a push to utilize advances in operating system virtualization in order to preserve the entire software environments that are used to produce physics results, making reproducibility a much more tractable problem. Additionally, the RECAST framework [128] has been introduced to not only preserve analysis software, but also provide infrastructure for reinterpreting the results of searches for new physics in the context of models that were not considered originally. In this way, RECAST aims to broaden the scientific impact of such searches by capturing the necessary software and automating the analysis workflow. The goal of this effort is to establish a framework in which the user only needs to provide a minimal set of inputs

(the signal samples, cross-sections, and theoretical uncertainties) and receives the result of a hypothesis test as the output.

In order to recast the analysis, the entire software environment needs to be preserved. This not only includes the analysis code and its dependencies, but also the compiler and operating system used when originally performing the analysis. While this could be accomplished with virtual machines, ATLAS has chosen to utilize recent developments in Linux container images, which do not require hardware virtualization. Specifically, the software environments used by this analysis are captured using Docker images [129], which can be deployed on a wide variety of computing infrastructures. Two Docker images are used to fully preserve this analysis. The first image captures the software used to process the data, including the specific ATLAS software release that is used to calibrate the various physics objects. A second image preserves the software environment that was used when performing the statistical analysis.

Once the software environment is captured in Docker images, the series of commands needed to execute the analysis from start to finish must also be preserved. These interdependent commands are captured using the workflow description language `yadage` [130], which models workflows using directed acyclic graphs. This allows the workflows to be non-linear and even makes the workflows executable across distributed systems. The workflow design and specific commands are defined in `YAML` files. Where necessary, the commands are parameterized in order to accept different inputs from the user. A detailed description of the workflow used for this search is presented in Section 16.3.

Finally, since the background estimates (including their systematic uncertainties) and data yields are frozen, they are archived in the form of `ROOT` histogram objects that can be used directly in the exclusion fits without the need for any

additional data processing.

16.2 Required Inputs for New Signals

Beyond providing the simulated signal samples themselves, further information related to the signal process must be provided by the user in order to reinterpret the results of any search for new physics. This section briefly describes what is needed in order to ensure that the new signal is handled properly within the analysis workflow.

Firstly, the user must specify the necessary information for correctly normalizing the simulated signal events to the overall expected event yield. Therefore, the inputs to the preserved analysis workflow include a text file that must contain the signal cross-section (along with its uncertainty) and any branching fractions to the desired final states. Additionally, if any generator-level requirements are applied during the event generation, the efficiency of these cuts must be specified. This file is referred to as `signal_xsec` in the workflow described in Section 16.3.

One important complication when trying to reinterpret a preserved analysis is accounting for theoretical uncertainties that depend on the specific signal under test. The user should not assume that the uncertainties derived for the SUSY processes considered by this analysis are also applicable to their signal. Therefore, the user must provide the uncertainties on the signal yields in the SRs that stem from the theoretical modeling of the ISR process, as described in Section 12.3.2. This information must be stored in a `JSON` file, referred to as `ISR_unc_file` in Section 16.3, that pairs each SR name with a number representing the relative uncertainty on the signal event yield within it.

16.3 Analysis Workflow

The goal of the preserved analysis workflow is to take some signal process as the input and output a CL_s value that represents the compatibility of the observed data with this new hypothesis. In broad terms, this is achieved by processing the signal events, applying the event selection to them, and finally performing the exclusion fits using the archived background histograms. These fits are configured in exactly the same way as those described in Section 15.2 and therefore exploit any differences in the shape of the $m_{\ell\ell}$ or m_{T2}^{100} distributions between the background and signal processes. A schematic of the full workflow, which currently does not include the $1\ell 1T$ channel, is shown in Figure 16.1 and the individual steps are described in detail below.

- `dataprocessing_mc16a/d/e`: Convert the centrally-produced signal samples from an ATLAS data format called the "derived Analysis Object Data" (DxAOD) format to standard `ROOT` files. These samples are generated with different pileup profiles to match the data taken in 2015+2016, 2017, and 2018, and therefore there is a dedicated step for processing the events corresponding to each of these periods. The events corresponding to each of these periods are reweighted according that period's relative contribution to the total integrated luminosity. During the processing, important kinematic variables such as $m_{\ell\ell}$ and m_{T2}^{100} are are calculated and the events are reweighted according to the user-defined signal cross-section. This process is repeated for each experimental systematic uncertainty. While functionally the same, these steps remain separate so that they can run in parallel and therefore cut down on computing time.

- `fetchfiles`: Retrieves the `ROOT` files containing the background and data

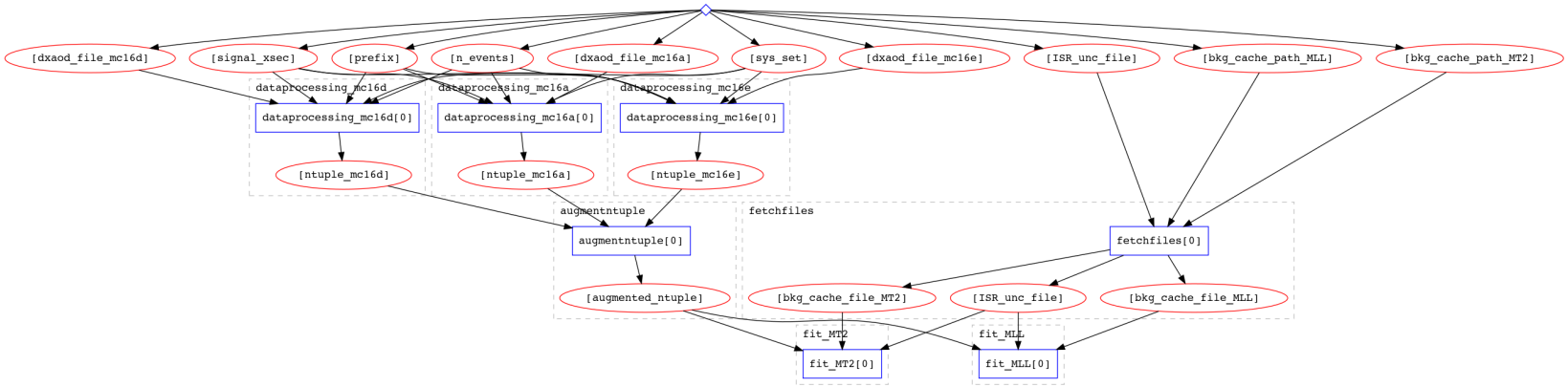

Figure 16.1: A diagram of the preserved workflow used for reinterpretation of the analysis results. The various steps in the workflow are shown in blue. The results of the individual steps as well as the user-defined inputs are shown in red.

histograms as well as the user-defined `JSON` file that stores the ISR modeling uncertainties for the signal being tested. These files are then passed to the `fit_MLL` and `fit_MT2` steps.

- `augmentntuple`: Merges the `ROOT` files from the data processing steps and adds the $E_{\mathrm{T}}^{\mathrm{miss}}$ trigger scale factors that model the trigger efficiencies observed in data.

- `fit_MLL`: Applies the event selection on the signal events and performs the exclusion fit to the two-lepton CRs and exclusive SRs defined by $m_{\ell\ell}$. Additionally, a scan is performed over the signal strength parameter μ_{sig}.

- `fit_MT2`: Applies the event selection and performs the exclusion fit using the CRs and exclusive SRs defined by m_{T2}^{100}. Additionally, a scan is performed over the signal strength parameter μ_{sig}.

16.4 Validation

In order to validate the RECAST workflow, the machinery was run using some of the same signal samples that were used in the search for slepton and wino production. The figure of merit for the validation is the $\mathrm{CL_s}$ from the model-dependent exclusion fits.

To validate the fits to the exclusive SRs defined by ranges of m_{T2}^{100}, the slepton signal sample with $m(\widetilde{\ell}) = 125$ GeV and $m(\widetilde{\chi}_1^0) = 105$ GeV was chosen. For this test, a fourfold mass degeneracy is assumed between left- and right-handed smuons and selectrons. Assuming $\mu_{\mathrm{sig}} = 1$, both the RECAST workflow and nominal analysis results give $\mathrm{CL_s} = 1.80 \times 10^{-3}$ for this hypothesis test. Additionally, scans of the $\mathrm{CL_s}$ values as a function of μ_{sig} are shown in Figure 16.2, where again the RECAST results are identical to what was obtained originally.

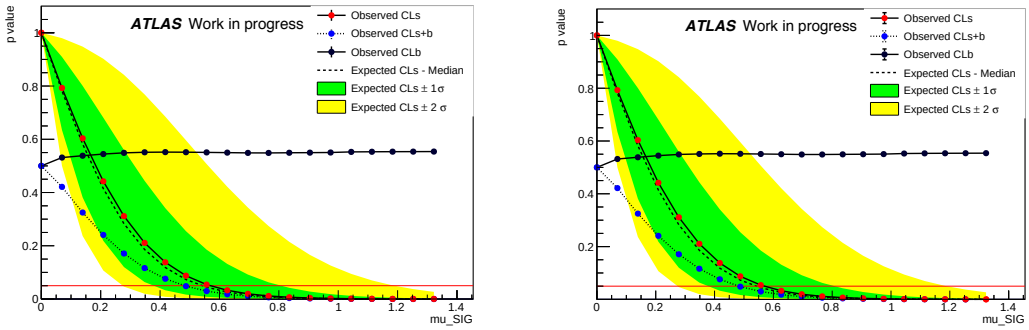

Figure 16.2: Results of the hypothesis tests as a function of the signal strength parameter μ_{sig} for the slepton interpretation assuming both flavor- and chirality-degeneracy with $m(\widetilde{\ell}) = 125$ GeV and $m(\widetilde{\chi}_1^0) = 105$ GeV. The results from the original analysis are shown on the left, while those obtained with the RECAST workflow are shown on the right.

Equivalently, the RECAST workflow is validated against the fits to the exclusive SRs that are defined by ranges of $m_{\ell\ell}$ by running on an electroweakino signal sample that was used in the nominal analysis. The chosen signal sample corresponds to the wino/bino simplified model with $(m(\widetilde{\chi}_2^0), m(\widetilde{\chi}_1^0)) = (150, 140)$ GeV and assuming $m(\widetilde{\chi}_2^0) \times m(\widetilde{\chi}_1^0) > 0$. The choice of mass splitting was made in order to avoid the part of the mass-plane where the $1\ell 1T$ channel has some sensitivity ($\Delta m(\widetilde{\chi}_2^0, \widetilde{\chi}_1^0) \lesssim 5$ GeV), since this part of the analysis is not yet included in the RECAST workflow. This makes a comparison of the CL_s values much more direct. As with the previous check, the RECAST workflow and nominal analysis results agree, this time giving $\text{CL}_\text{s} = 1.97 \times 10^{-6}$ under the $\mu_{\text{sig}} = 1$ assumption. Again, the scans of the CL_s values from each set of hypothesis tests, presented in Figure 16.3, yield identical results. With the full workflow validated and preserved, this results of this analysis can now be reinterpreted in the context of other models that can produce events with E_T^miss and soft leptons.

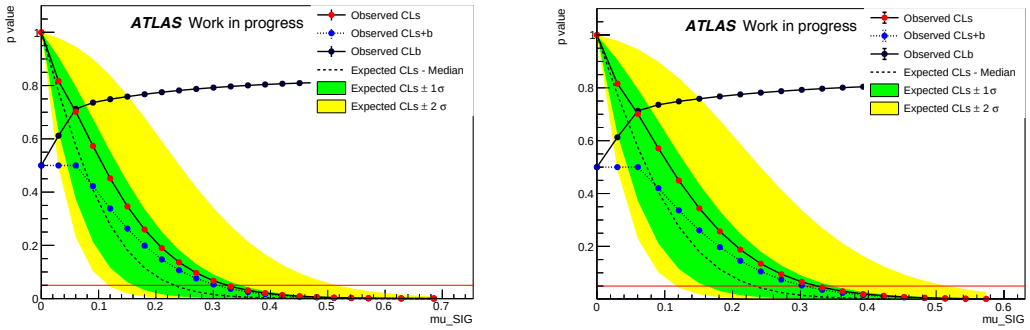

Figure 16.3: Results of the hypothesis tests as a function of the signal strength parameter μ_{sig} for the wino/bino interpretation assuming $m(\widetilde{\chi}_2^0) \times m(\widetilde{\chi}_1^0) > 0$, $m(\widetilde{\chi}_2^0) = 150$ GeV, and $m(\widetilde{\chi}_1^0) = 140$ GeV. The results from the original analysis are shown on the left, while those obtained with the RECAST workflow are shown on the right.

Chapter 17

Conclusions

This dissertation presented searches for the direct production of electroweakinos and sleptons in $\sqrt{s} = 13\,\text{TeV}$ proton-proton collisions provided by the LHC between 2015 and 2018. The collisions were recorded by the ATLAS detector, resulting in a dataset corresponding to an integrated luminosity of $139\,\text{fb}^{-1}$. The SUSY models targeted by these searches involve compressed mass spectra and decay chains that lead to missing transverse energy and soft leptons of the same flavor and opposite electric charge in the final state. At tree level, these scenarios are difficult to probe at the LHC due to trigger bandwidth limitations and lepton reconstruction thresholds. To combat this, additional hadronic activity in the form of ISR is required in order to provide a boost to the SUSY system in the transverse plane, affectively aligning the LSPs so that $E_{\text{T}}^{\text{miss}}$-triggers can be used to collect events with sufficient efficiency. This boost also serves to increase the p_{T} of the final-state leptons, thus increasing the acceptance for the most compressed signals.

The final discriminants used to search for electroweakinos and sleptons were chosen to be $m_{\ell\ell}$ and m_{T2}^{100}, respectively. In each case, signal events have kinematic endpoints in these variables that correspond to the mass splitting, which

is exploited by the model-dependent exclusion fits. Various kinematic cuts were optimized separately for electroweakinos and sleptons to promote boosted topologies and provide signal sensitivity over a wide range of mass-splittings. Notably, SRs that require $E_{\mathrm{T}}^{\mathrm{miss}} < 200\,\mathrm{GeV}$ were developed in order to target signals with moderate-to-large mass splittings, though the high-$E_{\mathrm{T}}^{\mathrm{miss}}$ SRs provide the bulk of the exclusion power in the SUSY mass planes.

Due to the presence of very soft leptons, a large reducible background from fake/non-prompt leptons was estimated using the data-driven Fake Factor method, which required new isolation algorithms for successful modeling in highly collimated dilepton events. Major sources of irreducible background arise from $t\bar{t}/tW$, $Z^{(*)}/\gamma^{*}(\rightarrow \tau\tau) + \mathrm{jets}$, and VV events, whose normalizations were constrained using background-only fits to dedicated high-$E_{\mathrm{T}}^{\mathrm{miss}}$ and low-$E_{\mathrm{T}}^{\mathrm{miss}}$ CRs. Systematic uncertainties stem from both experimental and theoretical sources, with those related to the fake/non-prompt lepton estimation and the normalization of the major irreducible backgrounds having the largest effect on the background uncertainty in the SRs.

Hypothesis tests were performed to quantify the consistency of the data in the inclusive SRs with the background-only hypothesis, but no statistically significant excesses were observed (the largest corresponding to a local significance of 2.7σ). These results were used to set model-independent limits on the production of BSM physics. Additionally, the exclusive SRs defined by $m_{\ell\ell}$ and m_{T2}^{100} were used to perform hypothesis tests on a variety of signals within the context of simplified SUSY models. The results of these hypothesis tests were then transformed into 95% CL exclusion contours in the $\Delta m(\widetilde{\chi}_2^0, \widetilde{\chi}_1^0)$ vs. $m(\widetilde{\chi}_2^0)$ and $\Delta m(\widetilde{\ell}, \widetilde{\chi}_1^0)$ vs. $m(\widetilde{\ell})$ planes.

For direct wino production, lower bounds on $m(\widetilde{\chi}_2^0)$ reach up to 240 GeV at a

mass-splitting of 7 GeV and extend down to $\Delta m(\widetilde{\chi}_2^0, \widetilde{\chi}_1^0) = 1.5\,\text{GeV}$ at the LEP chargino mass limit, regardless of the relative sign of the $\widetilde{\chi}_1^0$ and $\widetilde{\chi}_2^0$ mass eigenvalues. For direct higgsino production, the lower limits on the $\widetilde{\chi}_2^0$ mass reach up to 193 GeV at a mass-splitting of 9.3 GeV and extend down to $\Delta m(\widetilde{\chi}_2^0, \widetilde{\chi}_1^0) = 2.4\,\text{GeV}$ at the LEP chargino mass limit. In the case of direct light-flavor slepton production, several mass-degeneracy scenarios were considered. Assuming a four-fold mass degeneracy among the sleptons, the lower limit on $m(\ell_{L.R})$ reaches up 251 GeV at a mass-splitting of 10 GeV and extends down to $\Delta m(\widetilde{\ell}_{L,R}, \widetilde{\chi}_1^0) = 550\,\text{MeV}$ at the LEP $\widetilde{e}_R$ mass limit. A rather important point to make is that all of these limits were derived within simplified models that make optimistic assumptions on e.g. the branching ratios of the produced SUSY states. With this in mind, the searches presented here have been preserved within the RECAST framework in order to allow for easy reinterpretations using more realistic SUSY models and even non-SUSY models of BSM physics.

The story is far from over, though. Plenty of the parameter space relevant to natural SUSY models remains to be explored, especially in the electroweak sector. The upcoming data from Run 3 of the LHC (and the eventual HL-LHC) will provide an opportunity to extend the sensitivity to higher masses, but significant improvements in the most compressed regime will require new ideas, from improved reconstruction and background-rejection techniques to completely new event topologies. The problems facing particle physics today are deep and it's not clear whether current (or even planned) experiments will be able shed light on them. But there's only one way to find out.

Happy hunting!

Part VI

Appendices

Appendix A

$E_{\mathrm{T}}^{\mathrm{miss}}$-Trigger Scale Factors

The triggers used in this search are based on $E_{\mathrm{T}}^{\mathrm{miss}}$ and are found to be fully efficient only for events with $E_{\mathrm{T}}^{\mathrm{miss}} > 200\,\mathrm{GeV}$. Below this threshold, the efficiency changes quickly with $E_{\mathrm{T}}^{\mathrm{miss}}$ in what is knows as a trigger "turn-on" curve. Since the low-$E_{\mathrm{T}}^{\mathrm{miss}}$ regions used in the search fall into this region, the modeling of the trigger efficiencies in simulation needs to be checked and corrected for. In this section, the trigger efficiencies in both data and MC are measured in an unbiased event sample with kinematic requirements similar to the SRs and CRs. Differences in these efficiencies are measured as a function of $E_{\mathrm{T},\,\mu\ \mathrm{invis}}^{\mathrm{miss}}$ (defined in the following section) and are ultimately used to derive scale factors that are applied to MC events, thereby improving the background modeling in the regions with $E_{\mathrm{T}}^{\mathrm{miss}} < 200\,\mathrm{GeV}$.

A.1 Methodology and Event Selection

The basic strategy for measuring the the $E_{\mathrm{T}}^{\mathrm{miss}}$-trigger scale factors is to select and unbiased sample and compare data and MC efficiencies in a region that has similar kinematic requirements as the SRs. Since the $E_{\mathrm{T}}^{\mathrm{miss}}$ that is calculated

at the trigger-level does not include information from the Muon Spectrometer system, the unbiased sample is therefore selected using single-muon triggers. The efficiencies and scale factors are measured separately for each $E_{\mathrm{T}}^{\mathrm{miss}}$-trigger used in the search, where the efficiencies are defined as the number of events passing both the the muon-triggers and the $E_{\mathrm{T}}^{\mathrm{miss}}$-trigger divided by the number of events that only pass the muon triggers. In order to account for the difference between the trigger-level and offline $E_{\mathrm{T}}^{\mathrm{miss}}$ calculations, the efficiencies and scale factors are measured as a function of $E_{\mathrm{T},\ \mu\ \mathrm{invis}}^{\mathrm{miss}}$, which differs from the offline $E_{\mathrm{T}}^{\mathrm{miss}}$ definition by treating the muons as if they were invisible to the detector.

Since $E_{\mathrm{T}}^{\mathrm{miss}}$ is an event-level variable, it remains sensitive to specific event topologies, and so an event selection is derived to target the boosted topologies that motivate the SRs. Events are required to contain exactly two signal leptons with opposite electric charge and have $\Delta R_{\ell\ell} > 0.05$. One of the signal leptons needs to be a muon that can be matched to the firing muon trigger. In order to avoid contributions from low-mass resonances such as J/ψ and Υ, the dilepton invariant mass is required to be $m_{\ell\ell} > 10\,\mathrm{GeV}$. Finally, boosted-like topologies are selected by requiring the same jet requirements that are used to define the preselection defined in Table 10.2. As with the fake factors, the $E_{\mathrm{T}}^{\mathrm{miss}}$-trigger scale factors are measured separately for events with zero and at least one b-tagged jet. Since the lowest muon-trigger threshold used for this measurement is $p_{\mathrm{T}} > 20\,\mathrm{GeV}$, the contribution from fake/non-prompt leptons is assumed to be small and so this process is taken from the MC simulation.

A.2 Efficiency and Scale Factor Measurements

The efficiencies, as defined in the previous section, measured in data and MC are shown in Figure A.1 for the representative `HLT_xe110_pufit_L1XE55` trigger,

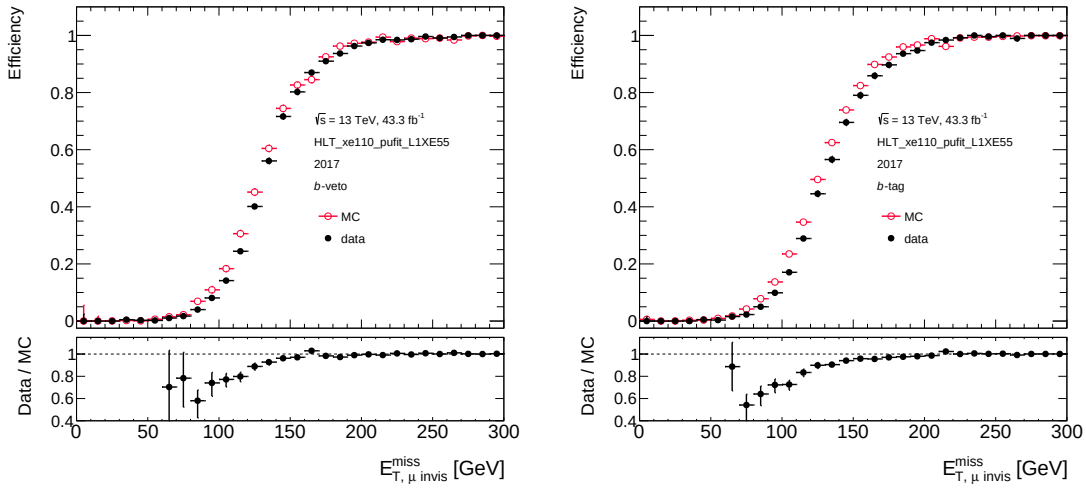

(a) Zero b-tagged jets **(b)** At least one b-tagged jet

Figure A.1: $E_{\mathrm{T}}^{\mathrm{miss}}$-trigger efficiencies in data (black) and MC (red) as a function of $E_{\mathrm{T},\,\mu\ \mathrm{invis}}^{\mathrm{miss}}$ for the `HLT_xe110_pufit_L1XE55` trigger.

where the turn-on effect is clearly visible for events with $E_{\mathrm{T},\,\mu\ \mathrm{invis}}^{\mathrm{miss}} < 200\,\mathrm{GeV}$. The ratio of the efficiencies in data to the efficiencies in MC are used to derive the scale factors.

In order to mitigate the effects of statistical fluctuations, especially at low values of $E_{\mathrm{T},\,\mu\ \mathrm{invis}}^{\mathrm{miss}}$, a fit is performed to this ratio and the scale factors are taken from the fit. The fit function used is

$$F(E_{\mathrm{T},\,\mu\ \mathrm{invis}}^{\mathrm{miss}}) = 0.5 \cdot \left[1 + Erf\left(\frac{E_{\mathrm{T},\,\mu\ \mathrm{invis}}^{\mathrm{miss}} - p_0}{\sqrt{2p_1^2}}\right)\right], \tag{A.1}$$

where Erf is the error function and p_0 and p_1 are free parameters that roughly map onto the location and width of the turn-on. Using the `HLT_xe110_pufit_L1XE55` trigger as a representative example, the fit results, representing the scale factors for this trigger, are shown in Figure A.2. In each case, a χ^2 test is used to validate the fit model against the data.

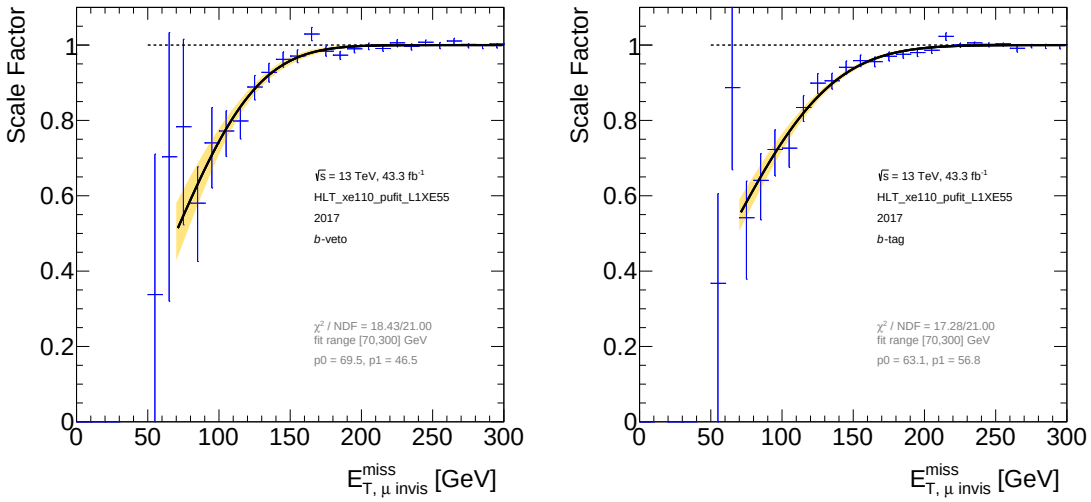

(a) Zero b-tagged jets **(b)** At least one b-tagged jet

Figure A.2: Fits to the data/MC efficiency ratio that provide $E_{\mathrm{T}}^{\mathrm{miss}}$-trigger scale factors for the trigger `HLT_xe110_pufit_L1XE55`. The yellow band indicates the statistical uncertainty of the fit.

A.3 Application

The scale factors described in the previous section are applied to the MC background events with $E_{\mathrm{T},\,\mu\ \mathrm{invis}}^{\mathrm{miss}}$ in order to account for any mismodeling of the $E_{\mathrm{T}}^{\mathrm{miss}}$-trigger efficiencies. Figure A.3 shows improved modeling of the $E_{\mathrm{T}}^{\mathrm{miss}}$ distribution at preselection-level after applying the scale factors. In general, the $E_{\mathrm{T}}^{\mathrm{miss}}$-triggers appear more efficient in MC compared to data and the scale factors act to scale down the MC yields to be in better agreement with the data.

A.4 Uncertainties

Various sources of uncertainties on the $E_{\mathrm{T}}^{\mathrm{miss}}$-trigger scale factors are considered and applied for events with $E_{\mathrm{T}}^{\mathrm{miss}} < 200\,\mathrm{GeV}$. These uncertainties can be both statistical and systematic in nature. The statistical uncertainty on the scale factors arises from the limited size of the dataset used to derive them. When per-

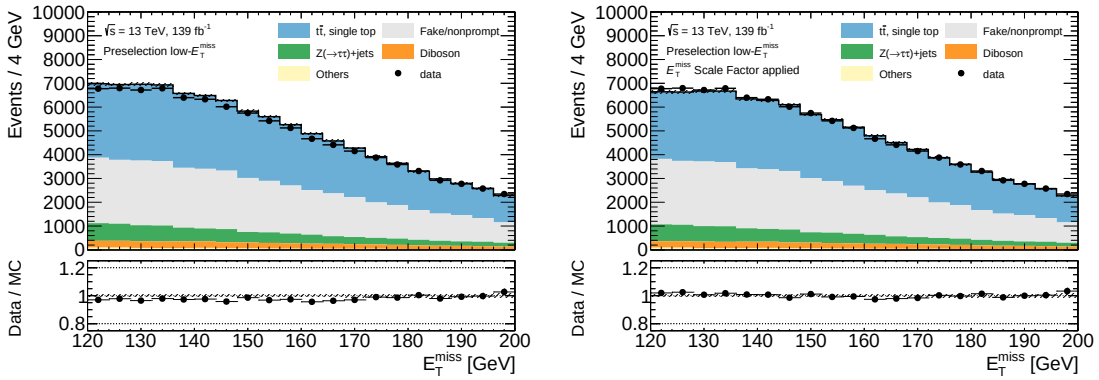

(a) without $E_{\mathrm{T}}^{\mathrm{miss}}$-trigger scale factor **(b)** $E_{\mathrm{T}}^{\mathrm{miss}}$-trigger scale factor applied

Figure A.3: The $E_{\mathrm{T}}^{\mathrm{miss}}$ distributions at preselection level before and after applying the $E_{\mathrm{T}}^{\mathrm{miss}}$-trigger scale factors. The hatched band in the bottom panel shows only the statistical uncertainty.

forming the fit using the function defined in Equation A.1, the floating parameters p_0 and p_1 acquire uncertainties that are reflective of the available statistics. Ultimately, the statistical uncertainty on the scale factors are obtained by propagating the uncertainties on p_0 and p_1 (including their correlation) to the function. This statistical uncertainty is shown as the yellow bands in Figure A.2, for example.

One source of systematic uncertainty on the $E_{\mathrm{T}}^{\mathrm{miss}}$-trigger scale factors arises from potential dependence on important kinematic variables other than $E_{\mathrm{T},\ \mu\ \mathrm{invis}}^{\mathrm{miss}}$. In order to check this, the scale factors are checked for correlations with $m_{\ell\ell}$, m_{T2}, and R_{ISR} at the preselection level, defined in Table 10.1, with $E_{\mathrm{T}}^{\mathrm{miss}} < 200\,\mathrm{GeV}$. These correlations are shown in Figure A.4, where little dependence on these variables is observed. Still, a conservative uncertainty of 5% is applied to the scale factors. Finally, the trigger efficiencies are checked for individual background and signal processes separately and uncertainties on the scale factors are derived in order to cover these differences.

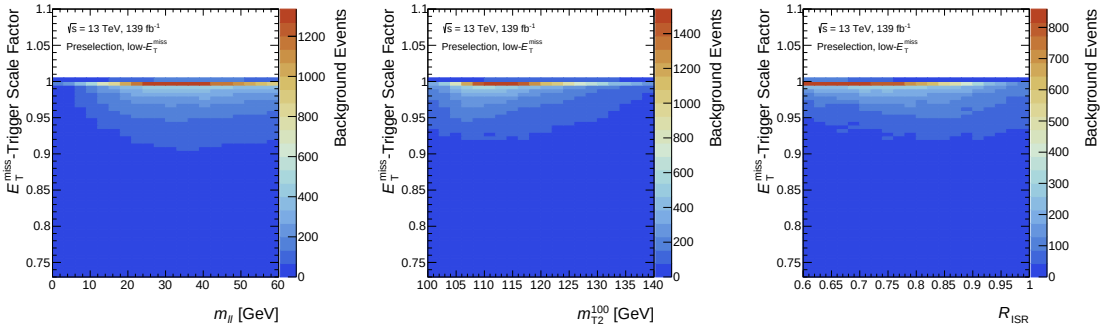

(a) $m_{\ell\ell}$ **(b)** m_{T2} **(c)** R_{ISR}

Figure A.4: Correlation between the $E_{\mathrm{T}}^{\mathrm{miss}}$ trigger scale factors and $m_{\ell\ell}$, m_{T2} and R_{ISR} at preselection level with $E_{\mathrm{T}}^{\mathrm{miss}} < 200\,\mathrm{GeV}$. The z-axis shows the number of weighted background MC events.

Appendix B

Slepton Chirality: Effect on Kinematics

The available slepton signal samples contain an admixture of left-handed and right-handed sleptons, according to their relative cross-sections. For the interpretations that do not assume mass degeneracy between sleptons of different chirality, in principle, one should only consider the sleptons in the signal samples that have the correct chirality. Unfortunately, this leads to a significant reduction in the statistical power of these samples and may lead to results that are sensitive to statistical fluctuations.

In order to retain the original statistical power of the signal samples, one can instead try to include the sleptons of the opposite chirality in such a way that the signal yield is preserved. For example, when searching for $\widetilde{\mu}_{\mathrm{L}}$, one can include the $\widetilde{\mu}_{\mathrm{R}}$ events (rather than throwing them away), provided that the events are reweighted to maintain the expected yield for the $\widetilde{\mu}_{\mathrm{L}}$ process alone. Crucially, though, this procedure is only valid if the acceptance and efficiency of the analysis are the same for both left-handed and right-handed sleptons. If this were not true, then some additional correction factors would need to be derived on an event-by-

event basis using the relevant kinematic variables in order to avoid a bias. To check whether or not the event kinematics are chirality-dependent, important kinematic distributions and cutflows for the slepton SRs are investigated for left-handed and right-handed sleptons separately. No systematic bias based on the slepton chirality is observed and differences in the final SR efficiencies are typically below the percent level, giving confidence to the assumption that the slepton chirality has a negligible effect on the relevant kinematics.

B.1 Kinematics

In this section, we show relevant kinematic distributions for left-handed and right-handed selectrons and smuons to check for a potential bias that could be introduced by the chirality of the particles. For a representative sample of signal points, we show the following normalized distributions, where the only selection applied is to require exactly two baseline leptons:

- $p_{\mathrm{T}}(\ell_1)$ in Figure B.1
- $p_{\mathrm{T}}(\ell_2)$ in Figure B.2
- $\eta(\ell_1)$ in Figure B.3
- $\eta(\ell_2)$ in Figure B.4
- $E_{\mathrm{T}}^{\mathrm{miss}}$ in Figure B.5
- R_{ISR} in Figure B.6
- m_{T2}^{100} in Figure B.7

In general, no evidence of a chirality dependence on the shapes of these distributions is observed.

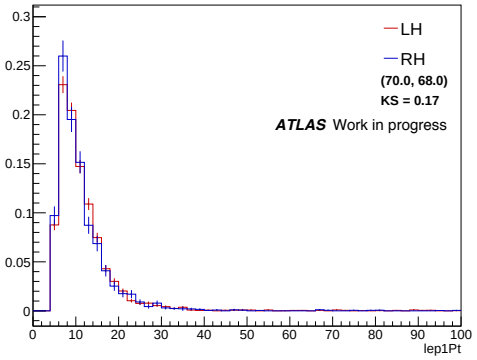

(a) $\left(m(\tilde{\ell}), m(\tilde{\chi}_1^0)\right) = (70, 68)$

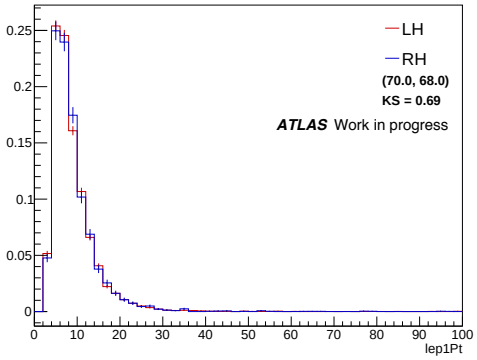

(b) $\left(m(\tilde{\ell}), m(\tilde{\chi}_1^0)\right) = (70, 68)$

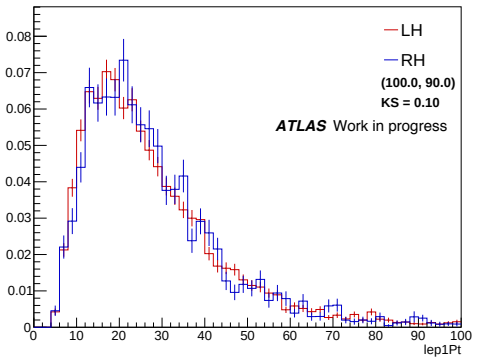

(c) $\left(m(\tilde{\ell}), m(\tilde{\chi}_1^0)\right) = (100, 90)$

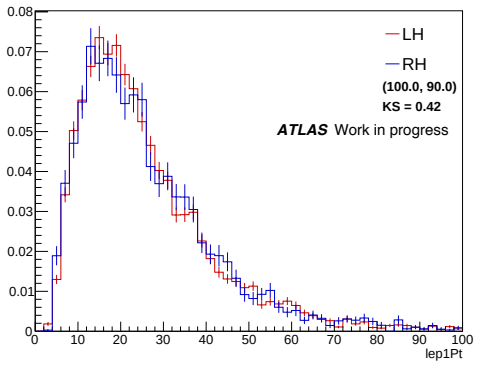

(d) $\left(m(\tilde{\ell}), m(\tilde{\chi}_1^0)\right) = (100, 90)$

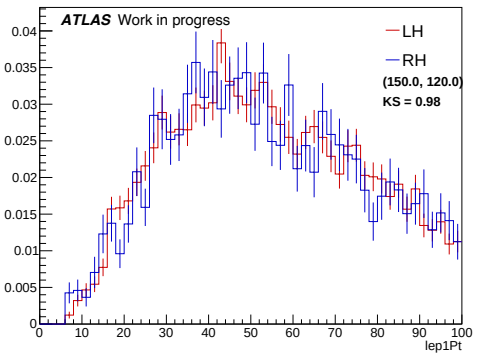

(e) $\left(m(\tilde{\ell}), m(\tilde{\chi}_1^0)\right) = (150, 120)$

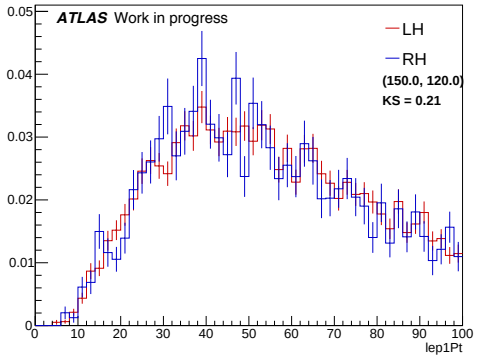

(f) $\left(m(\tilde{\ell}), m(\tilde{\chi}_1^0)\right) = (150, 120)$

Figure B.1: Leading lepton p_{T} distributions for selectrons (left) and smuons (right) split by chirality for various signal points.

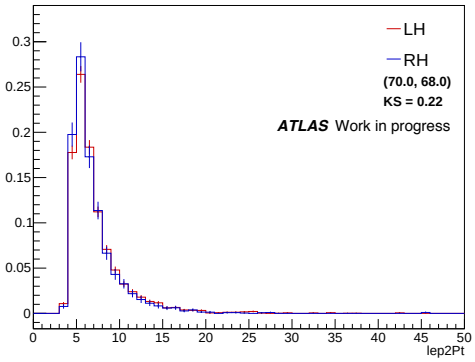

(a) $\left(m(\tilde{\ell}), m(\tilde{\chi}_1^0)\right) = (70, 68)$

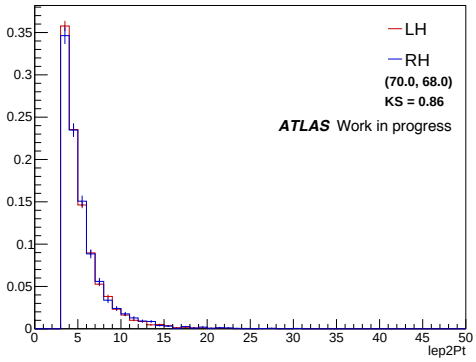

(b) $\left(m(\tilde{\ell}), m(\tilde{\chi}_1^0)\right) = (70, 68)$

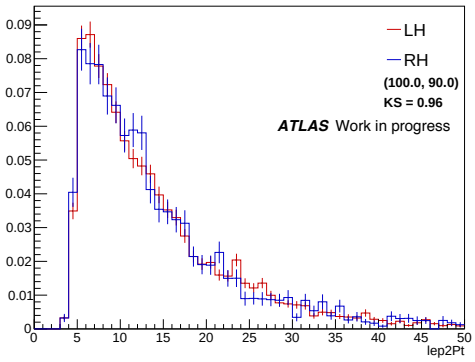

(c) $\left(m(\tilde{\ell}), m(\tilde{\chi}_1^0)\right) = (100, 90)$

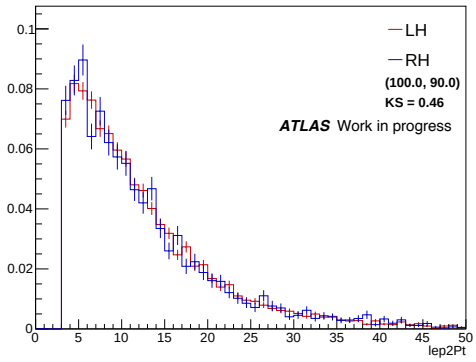

(d) $\left(m(\tilde{\ell}), m(\tilde{\chi}_1^0)\right) = (100, 90)$

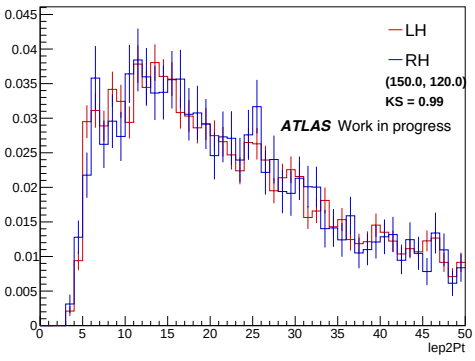

(e) $\left(m(\tilde{\ell}), m(\tilde{\chi}_1^0)\right) = (150, 120)$

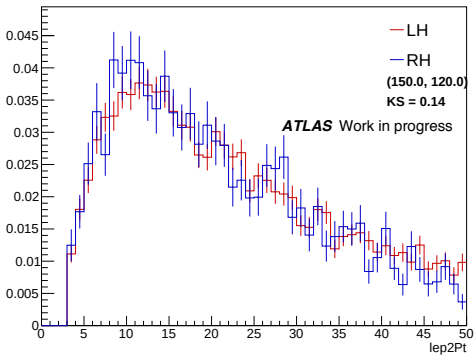

(f) $\left(m(\tilde{\ell}), m(\tilde{\chi}_1^0)\right) = (150, 120)$

Figure B.2: Subleading lepton p_{T} distributions for selectrons (left) and smuons (right) split by chirality for various signal points.

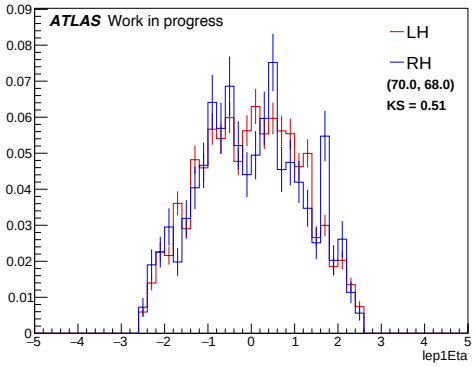

(a) $\left(m(\tilde{\ell}), m(\tilde{\chi}_1^0)\right) = (70, 68)$

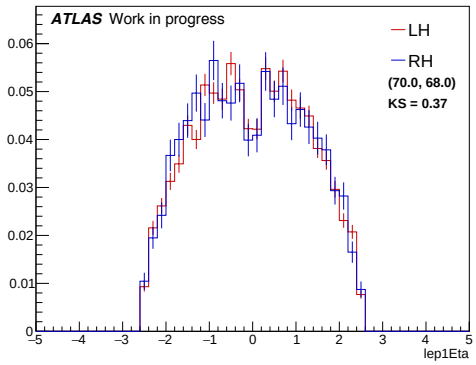

(b) $\left(m(\tilde{\ell}), m(\tilde{\chi}_1^0)\right) = (70, 68)$

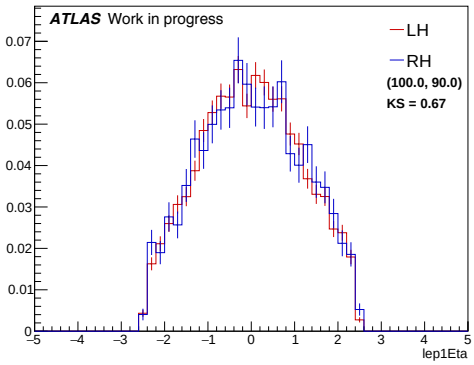

(c) $\left(m(\tilde{\ell}), m(\tilde{\chi}_1^0)\right) = (100, 90)$

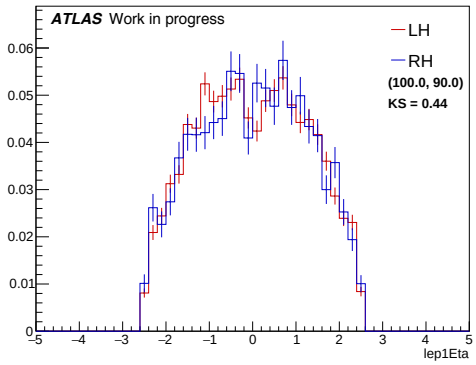

(d) $\left(m(\tilde{\ell}), m(\tilde{\chi}_1^0)\right) = (100, 90)$

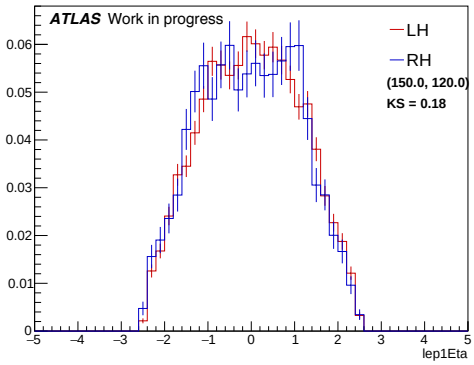

(e) $\left(m(\tilde{\ell}), m(\tilde{\chi}_1^0)\right) = (150, 120)$

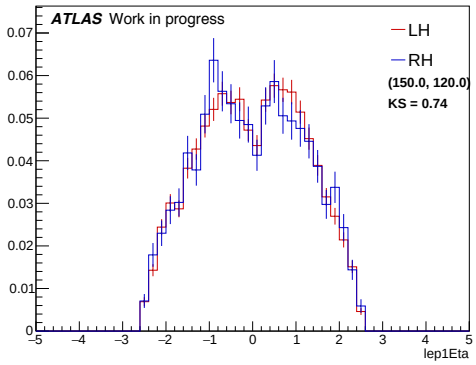

(f) $\left(m(\tilde{\ell}), m(\tilde{\chi}_1^0)\right) = (150, 120)$

Figure B.3: Leading lepton η distributions for selectrons (left) and smuons (right) split by chirality for various signal points.

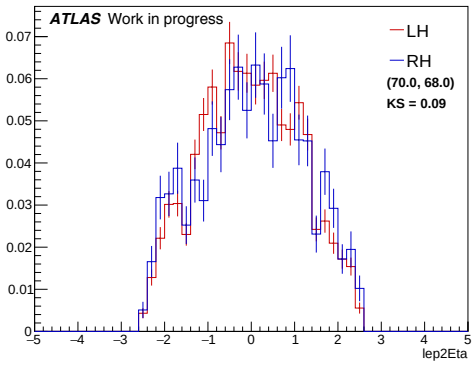

(a) $\left(m(\tilde{\ell}), m(\tilde{\chi}_1^0)\right) = (70, 68)$

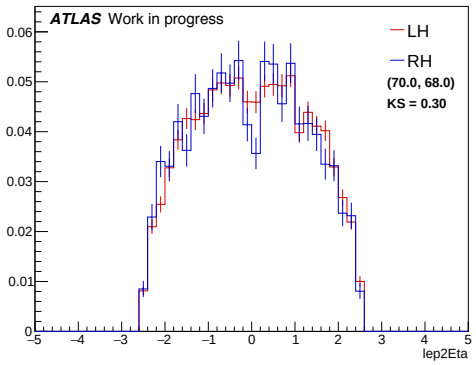

(b) $\left(m(\tilde{\ell}), m(\tilde{\chi}_1^0)\right) = (70, 68)$

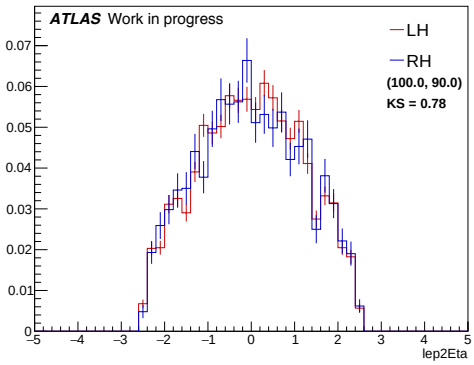

(c) $\left(m(\tilde{\ell}), m(\tilde{\chi}_1^0)\right) = (100, 90)$

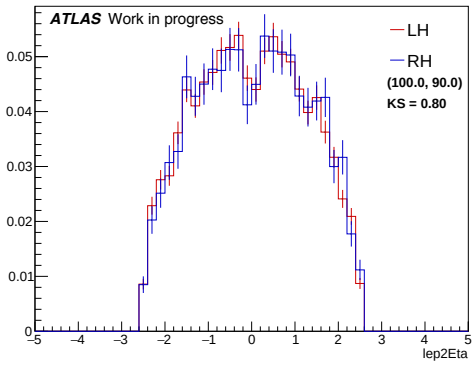

(d) $\left(m(\tilde{\ell}), m(\tilde{\chi}_1^0)\right) = (100, 90)$

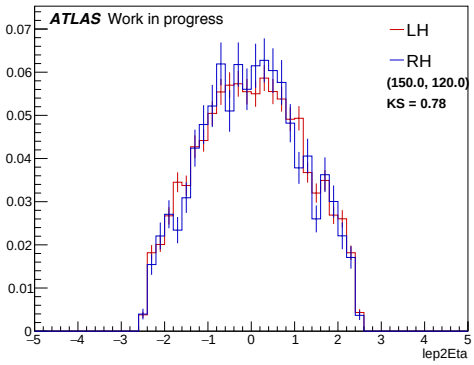

(e) $\left(m(\tilde{\ell}), m(\tilde{\chi}_1^0)\right) = (150, 120)$

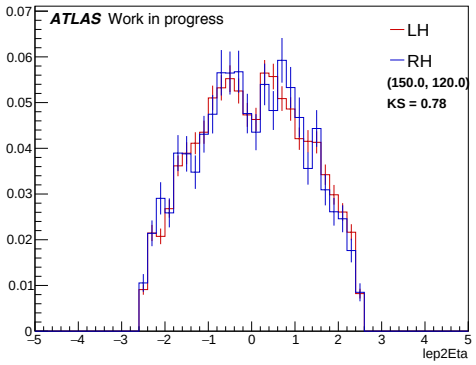

(f) $\left(m(\tilde{\ell}), m(\tilde{\chi}_1^0)\right) = (150, 120)$

Figure B.4: Subleading lepton η distributions for selectrons (left) and smuons (right) split by chirality for various signal points.

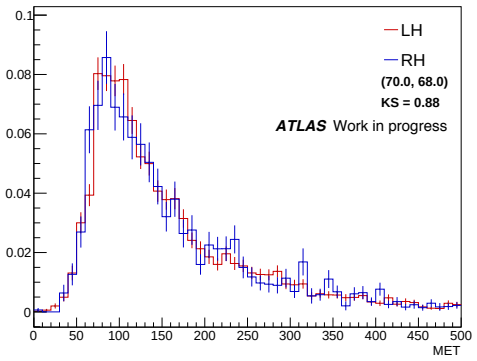

(a) $\left(m(\tilde{\ell}), m(\tilde{\chi}_1^0)\right) = (70, 68)$

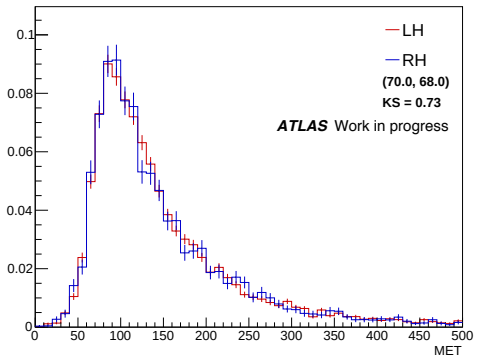

(b) $\left(m(\tilde{\ell}), m(\tilde{\chi}_1^0)\right) = (70, 68)$

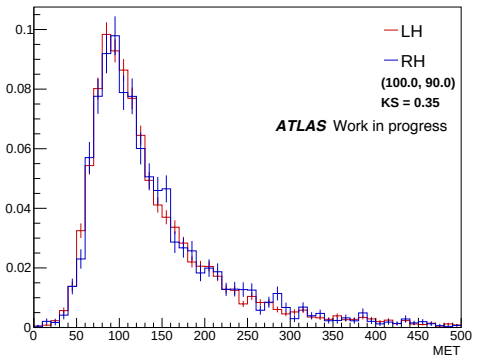

(c) $\left(m(\tilde{\ell}), m(\tilde{\chi}_1^0)\right) = (100, 90)$

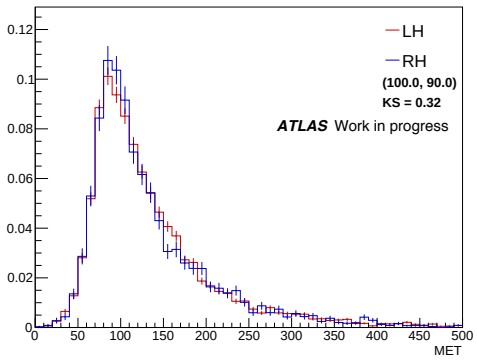

(d) $\left(m(\tilde{\ell}), m(\tilde{\chi}_1^0)\right) = (100, 90)$

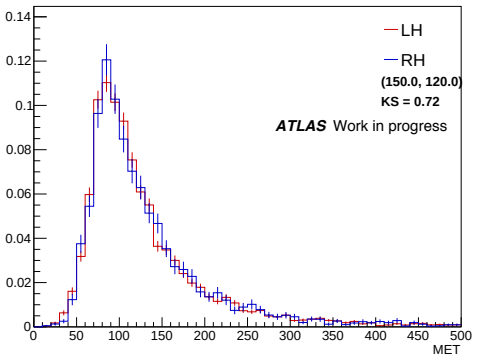

(e) $\left(m(\tilde{\ell}), m(\tilde{\chi}_1^0)\right) = (150, 120)$

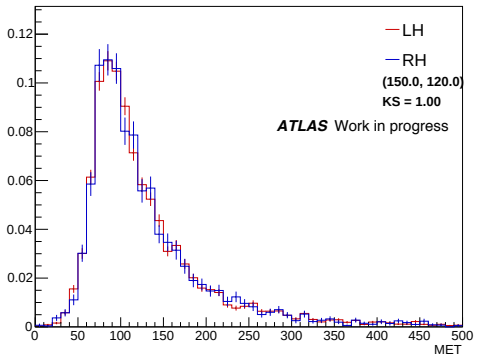

(f) $\left(m(\tilde{\ell}), m(\tilde{\chi}_1^0)\right) = (150, 120)$

Figure B.5: $E_{\mathrm{T}}^{\mathrm{miss}}$ distributions for selectrons (left) and smuons (right) split by chirality for various signal points.

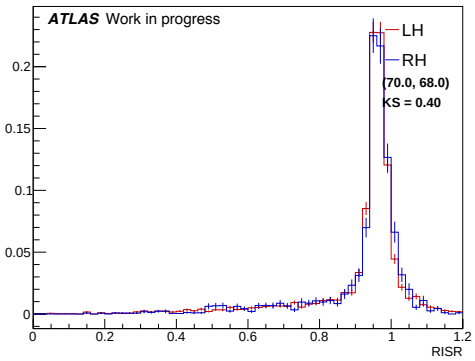

(a) $\left(m(\tilde{\ell}), m(\tilde{\chi}_1^0)\right) = (70, 68)$

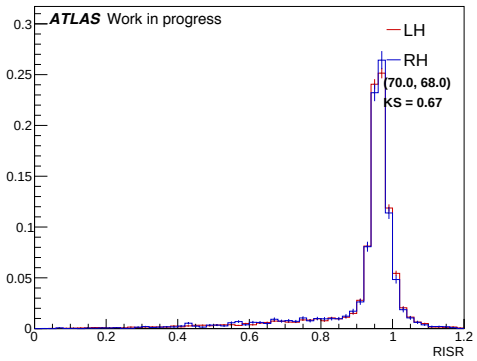

(b) $\left(m(\tilde{\ell}), m(\tilde{\chi}_1^0)\right) = (70, 68)$

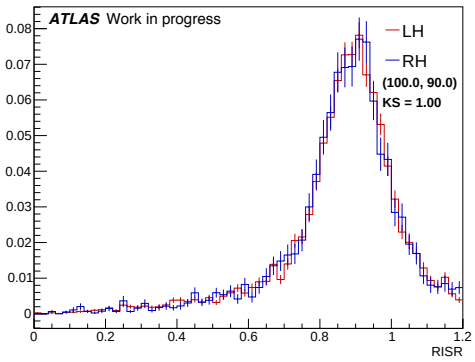

(c) $\left(m(\tilde{\ell}), m(\tilde{\chi}_1^0)\right) = (100, 90)$

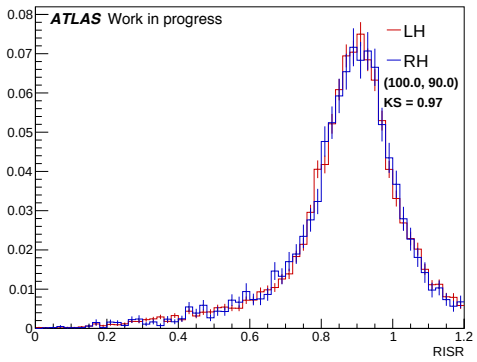

(d) $\left(m(\tilde{\ell}), m(\tilde{\chi}_1^0)\right) = (100, 90)$

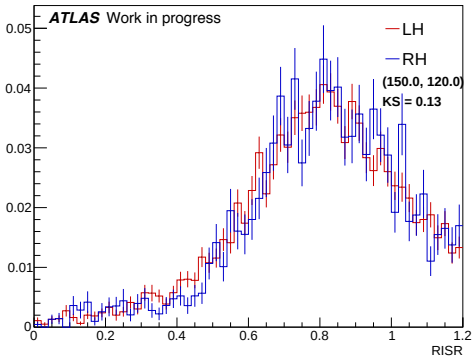

(e) $\left(m(\tilde{\ell}), m(\tilde{\chi}_1^0)\right) = (150, 120)$

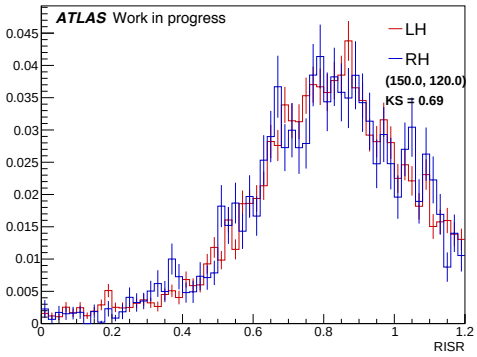

(f) $\left(m(\tilde{\ell}), m(\tilde{\chi}_1^0)\right) = (150, 120)$

Figure B.6: R_{ISR} distributions for selectrons (left) and smuons (right) split by chirality for various signal points.

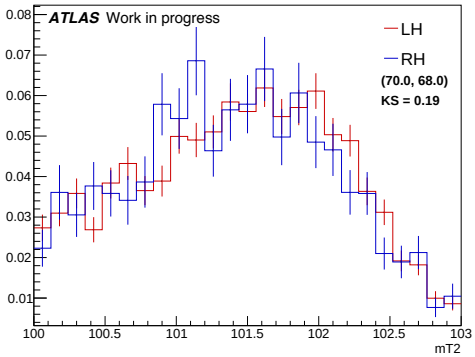

(a) $\left(m(\tilde{\ell}), m(\tilde{\chi}_1^0)\right) = (70, 68)$

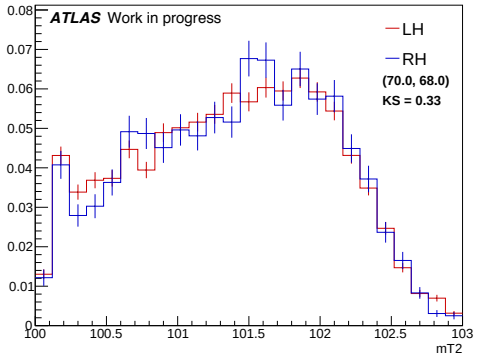

(b) $\left(m(\tilde{\ell}), m(\tilde{\chi}_1^0)\right) = (70, 68)$

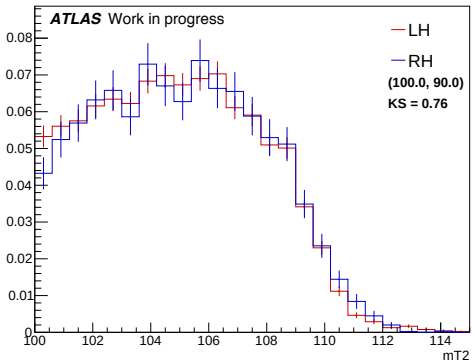

(c) $\left(m(\tilde{\ell}), m(\tilde{\chi}_1^0)\right) = (100, 90)$

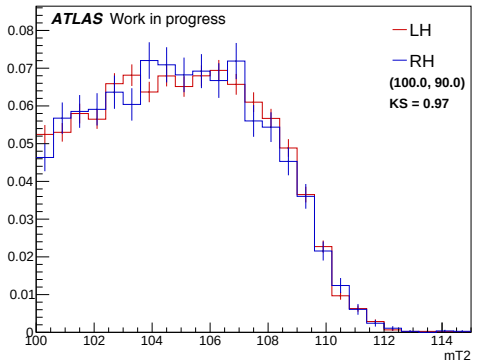

(d) $\left(m(\tilde{\ell}), m(\tilde{\chi}_1^0)\right) = (100, 90)$

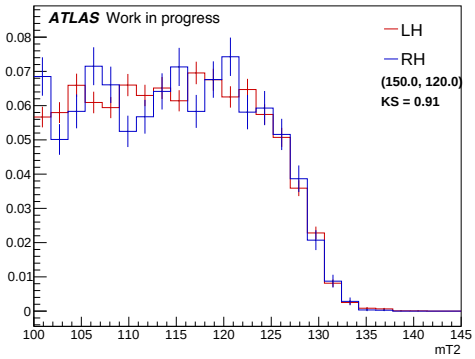

(e) $\left(m(\tilde{\ell}), m(\tilde{\chi}_1^0)\right) = (150, 120)$

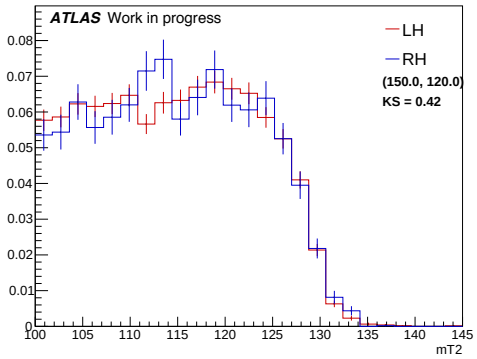

(f) $\left(m(\tilde{\ell}), m(\tilde{\chi}_1^0)\right) = (150, 120)$

Figure B.7: m_{T2}^{100} distributions for selectrons (left) and smuons (right) split by chirality for various signal points.

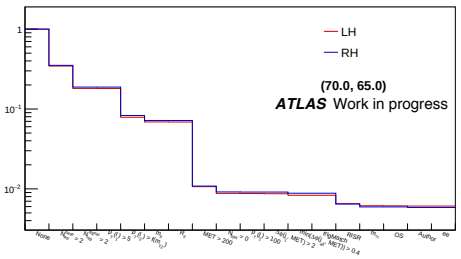

(a) Selectrons: high-$E_{\mathrm{T}}^{\mathrm{miss}}$

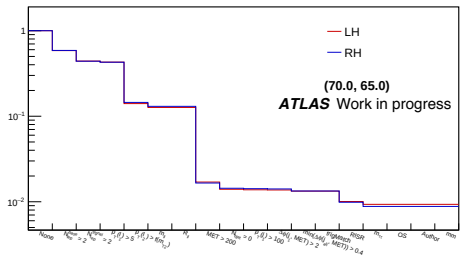

(b) Smuons: high-$E_{\mathrm{T}}^{\mathrm{miss}}$

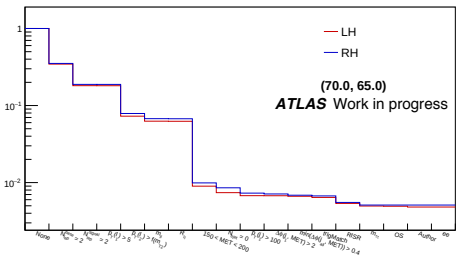

(c) Selectrons: low-$E_{\mathrm{T}}^{\mathrm{miss}}$

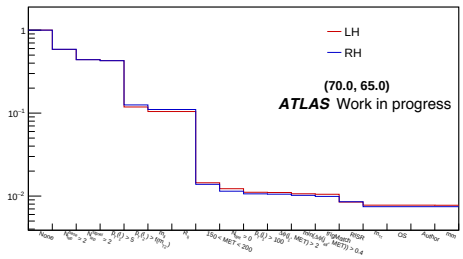

(d) Smuons: low-$E_{\mathrm{T}}^{\mathrm{miss}}$

Figure B.8: Cutflows for the $\left(m(\tilde{\ell}), m(\tilde{\chi}_1^0)\right) = (70, 65)$ signal point.

B.2 Cutflows

Here we check the cut efficiencies separately for left-handed and right-handed smuons and selectrons. Cutflows are produced for both the high-$E_{\mathrm{T}}^{\mathrm{miss}}$ and low-$E_{\mathrm{T}}^{\mathrm{miss}}$ slepton SRs to check for systematic differences in efficiency that would imply significant differences in the event kinematics between left-handed and right-handed sleptons. These are produced using unskimmed signal ntuples and are shown in Figures B.8-B.38, with the selectron SRs on the left and the smuon SRs on the right. Small differences in efficiency are are observed for left-handed and right-handed sleptons, especially for very low mass-splitting points where statistics in the signal samples are limited, but no systematic effect is apparent.

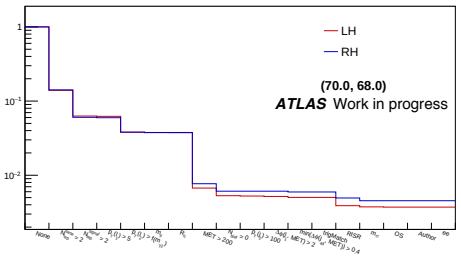

(a) Selectrons: high-$E_{\mathrm{T}}^{\mathrm{miss}}$

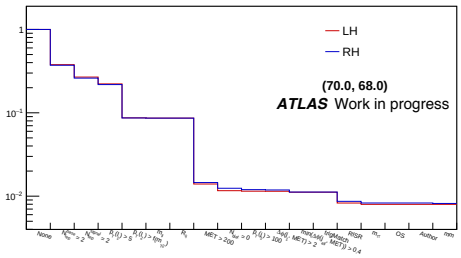

(b) Smuons: high-$E_{\mathrm{T}}^{\mathrm{miss}}$

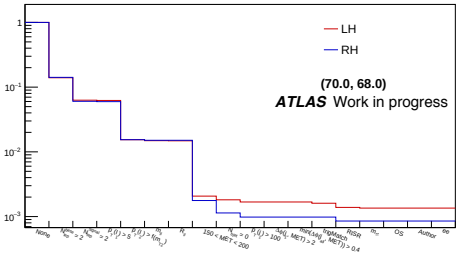

(c) Selectrons: low-$E_{\mathrm{T}}^{\mathrm{miss}}$

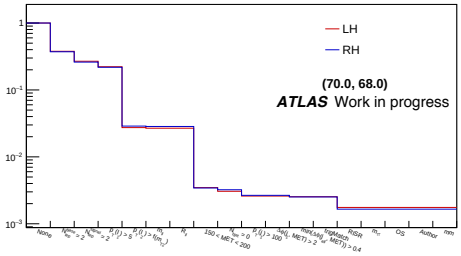

(d) Smuons: low-$E_{\mathrm{T}}^{\mathrm{miss}}$

Figure B.9: Cutflows for the $\left(m(\tilde{\ell}), m(\tilde{\chi}_1^0)\right) = (70, 68)$ signal point.

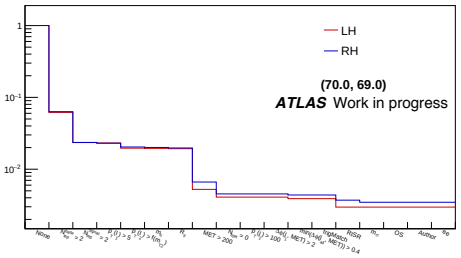

(a) Selectrons: high-$E_{\mathrm{T}}^{\mathrm{miss}}$

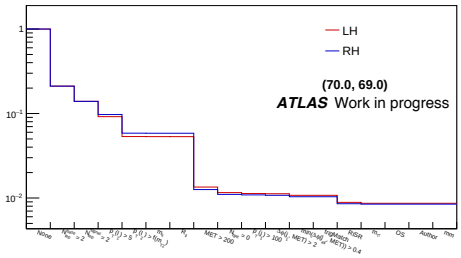

(b) Smuons: high-$E_{\mathrm{T}}^{\mathrm{miss}}$

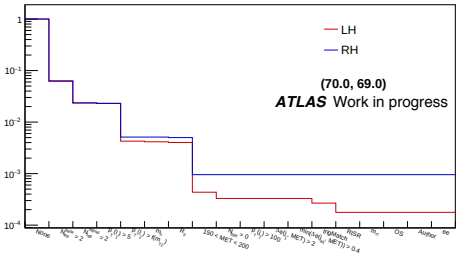

(c) Selectrons: low-$E_{\mathrm{T}}^{\mathrm{miss}}$

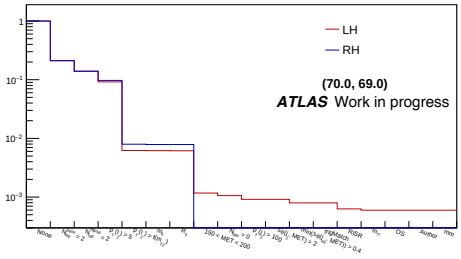

(d) Smuons: low-$E_{\mathrm{T}}^{\mathrm{miss}}$

Figure B.10: Cutflows for the $\left(m(\tilde{\ell}), m(\tilde{\chi}_1^0)\right) = (70, 69)$ signal point.

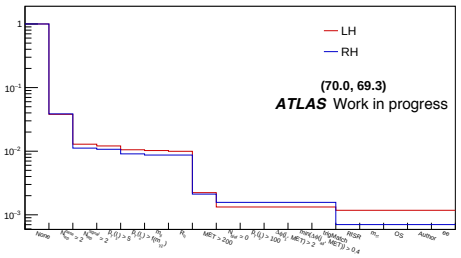

(a) Selectrons: high-$E_{\mathrm{T}}^{\mathrm{miss}}$

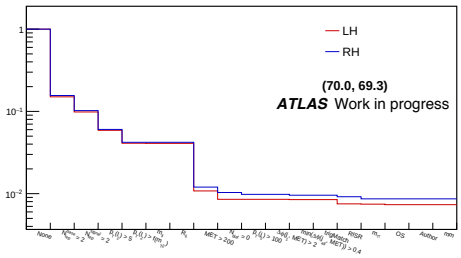

(b) Smuons: high-$E_{\mathrm{T}}^{\mathrm{miss}}$

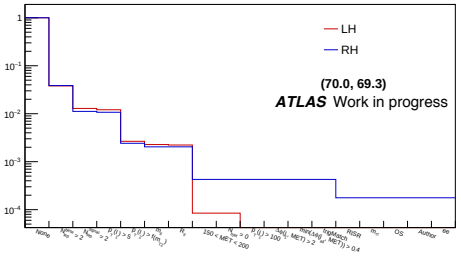

(c) Selectrons: low-$E_{\mathrm{T}}^{\mathrm{miss}}$

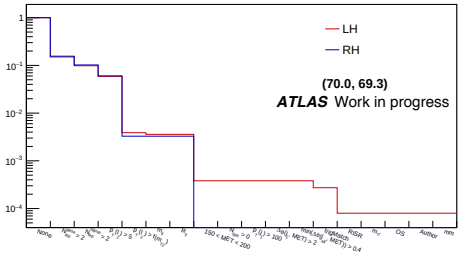

(d) Smuons: low-$E_{\mathrm{T}}^{\mathrm{miss}}$

Figure B.11: Cutflows for the $\left(m(\tilde{\ell}), m(\tilde{\chi}_1^0)\right) = (70, 69.3)$ signal point.

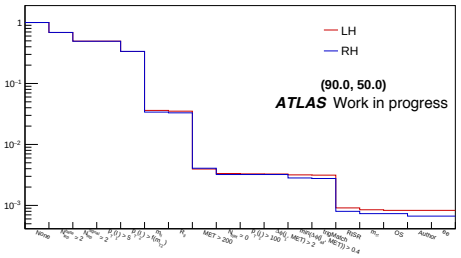

(a) Selectrons: high-$E_{\mathrm{T}}^{\mathrm{miss}}$

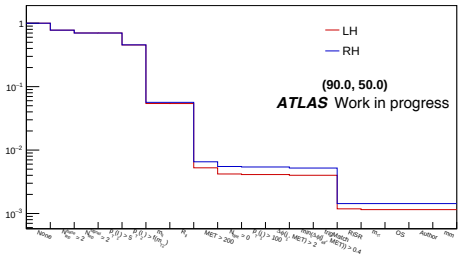

(b) Smuons: high-$E_{\mathrm{T}}^{\mathrm{miss}}$

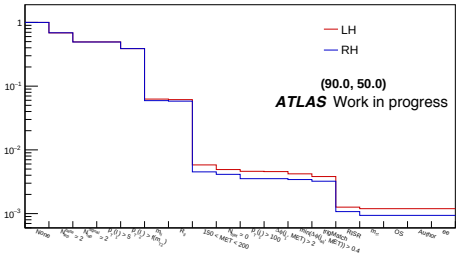

(c) Selectrons: low-$E_{\mathrm{T}}^{\mathrm{miss}}$

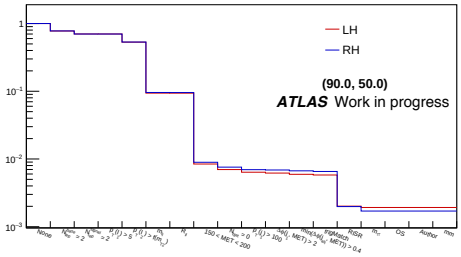

(d) Smuons: low-$E_{\mathrm{T}}^{\mathrm{miss}}$

Figure B.12: Cutflows for the $\left(m(\tilde{\ell}), m(\tilde{\chi}_1^0)\right) = (90, 50)$ signal point.

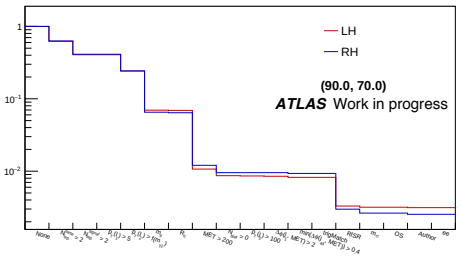

(a) Selectrons: high-$E_{\mathrm{T}}^{\mathrm{miss}}$

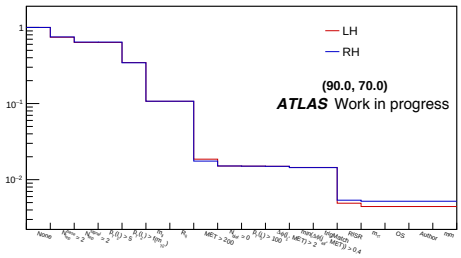

(b) Smuons: high-$E_{\mathrm{T}}^{\mathrm{miss}}$

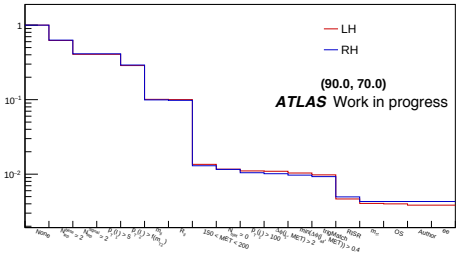

(c) Selectrons: low-$E_{\mathrm{T}}^{\mathrm{miss}}$

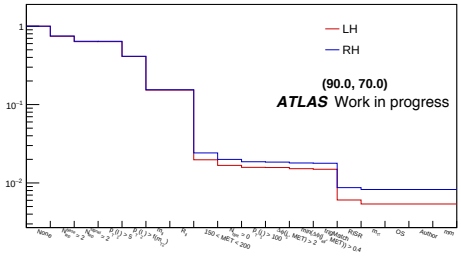

(d) Smuons: low-$E_{\mathrm{T}}^{\mathrm{miss}}$

Figure B.13: Cutflows for the $\left(m(\tilde{\ell}), m(\tilde{\chi}_1^0)\right) = (90, 70)$ signal point.

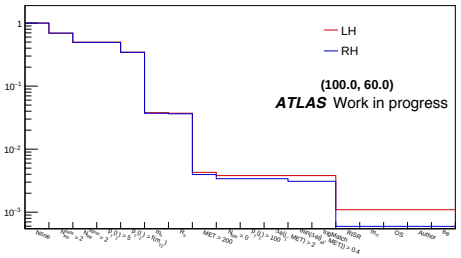

(a) Selectrons: high-$E_{\mathrm{T}}^{\mathrm{miss}}$

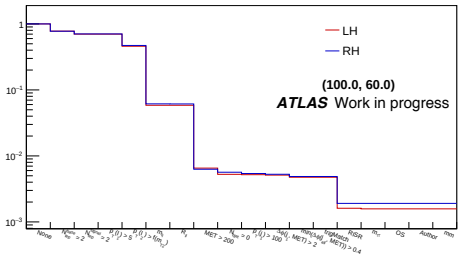

(b) Smuons: high-$E_{\mathrm{T}}^{\mathrm{miss}}$

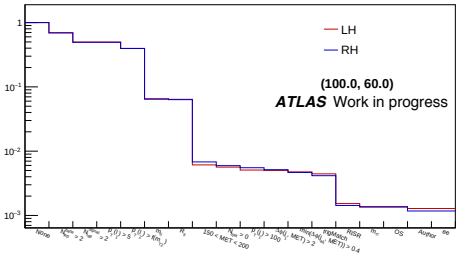

(c) Selectrons: low-$E_{\mathrm{T}}^{\mathrm{miss}}$

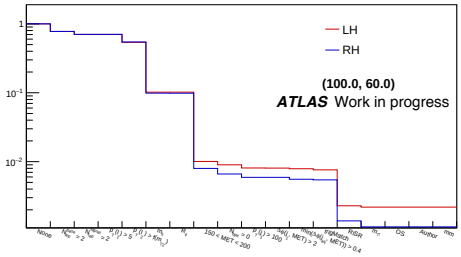

(d) Smuons: low-$E_{\mathrm{T}}^{\mathrm{miss}}$

Figure B.14: Cutflows for the $\left(m(\tilde{\ell}), m(\tilde{\chi}_1^0)\right) = (100, 60)$ signal point.

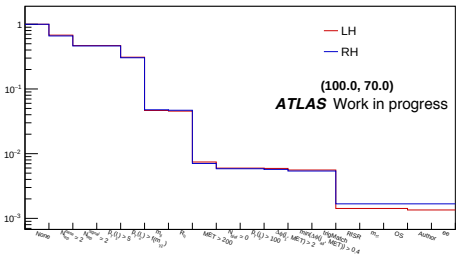

(a) Selectrons: high-$E_{\mathrm{T}}^{\mathrm{miss}}$

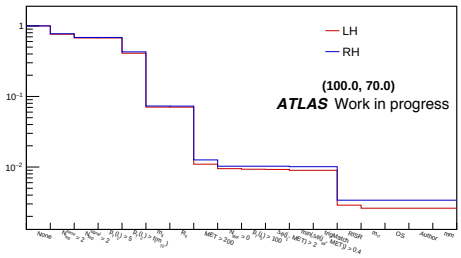

(b) Smuons: high-$E_{\mathrm{T}}^{\mathrm{miss}}$

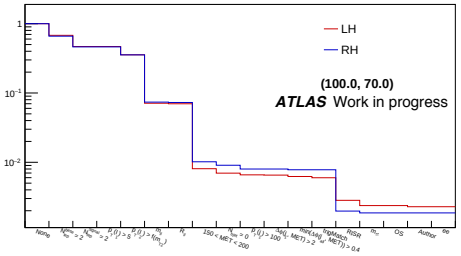

(c) Selectrons: low-$E_{\mathrm{T}}^{\mathrm{miss}}$

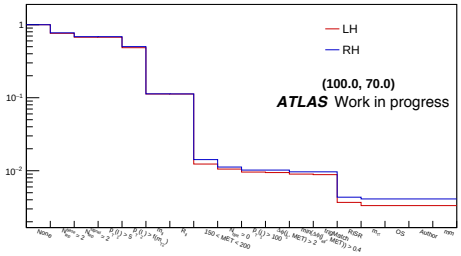

(d) Smuons: low-$E_{\mathrm{T}}^{\mathrm{miss}}$

Figure B.15: Cutflows for the $\left(m(\tilde{\ell}), m(\tilde{\chi}_1^0)\right) = (100, 70)$ signal point.

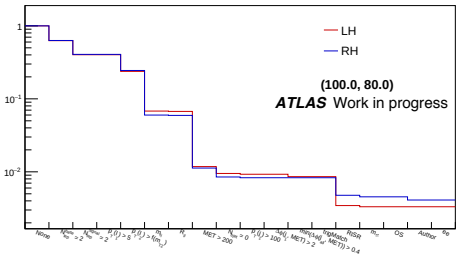

(a) Selectrons: high-$E_{\mathrm{T}}^{\mathrm{miss}}$

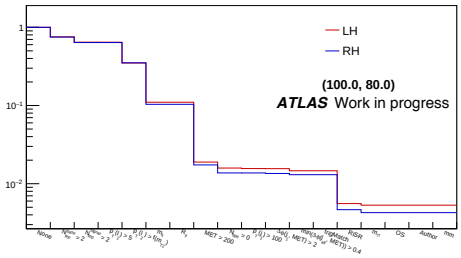

(b) Smuons: high-$E_{\mathrm{T}}^{\mathrm{miss}}$

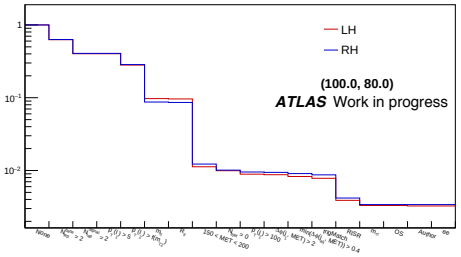

(c) Selectrons: low-$E_{\mathrm{T}}^{\mathrm{miss}}$

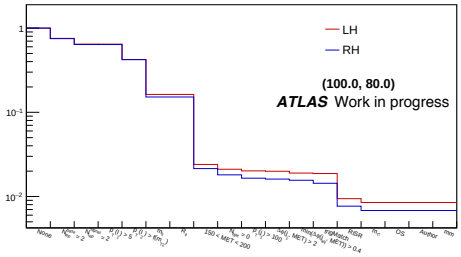

(d) Smuons: low-$E_{\mathrm{T}}^{\mathrm{miss}}$

Figure B.16: Cutflows for the $\left(m(\tilde{\ell}), m(\tilde{\chi}_1^0)\right) = (100, 80)$ signal point.

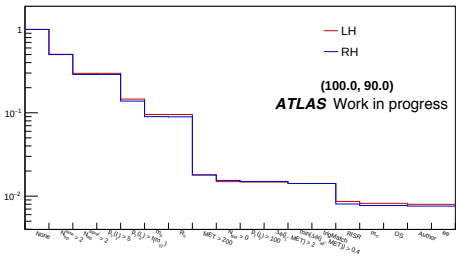

(a) Selectrons: high-$E_{\mathrm{T}}^{\mathrm{miss}}$

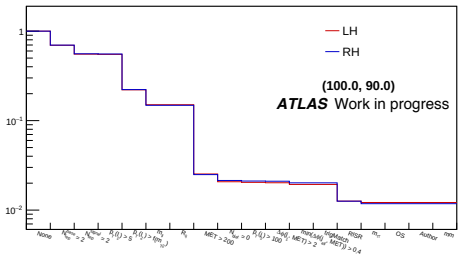

(b) Smuons: high-$E_{\mathrm{T}}^{\mathrm{miss}}$

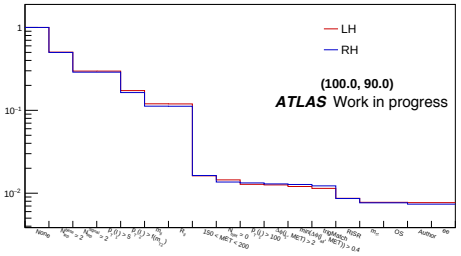

(c) Selectrons: low-$E_{\mathrm{T}}^{\mathrm{miss}}$

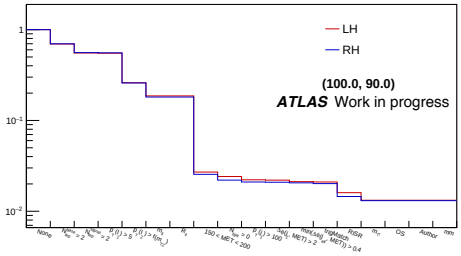

(d) Smuons: low-$E_{\mathrm{T}}^{\mathrm{miss}}$

Figure B.17: Cutflows for the $\left(m(\tilde{\ell}), m(\tilde{\chi}_1^0)\right) = (100, 90)$ signal point.

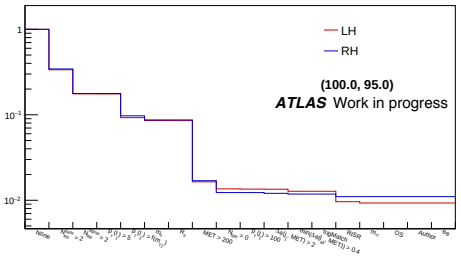

(a) Selectrons: high-$E_{\mathrm{T}}^{\mathrm{miss}}$

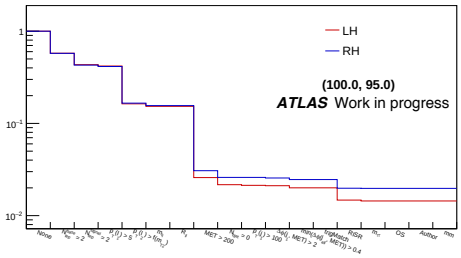

(b) Smuons: high-$E_{\mathrm{T}}^{\mathrm{miss}}$

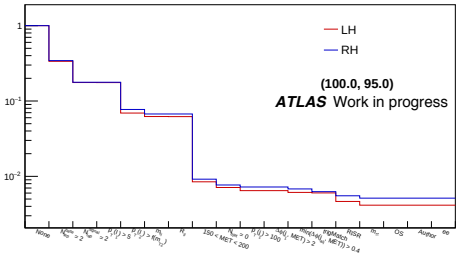

(c) Selectrons: low-$E_{\mathrm{T}}^{\mathrm{miss}}$

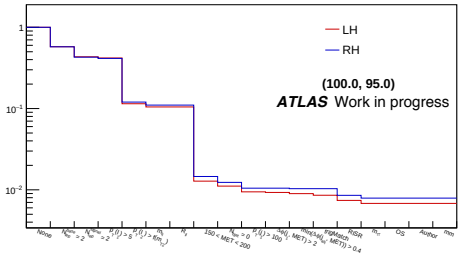

(d) Smuons: low-$E_{\mathrm{T}}^{\mathrm{miss}}$

Figure B.18: Cutflows for the $\left(m(\tilde{\ell}), m(\tilde{\chi}_1^0)\right) = (100, 95)$ signal point.

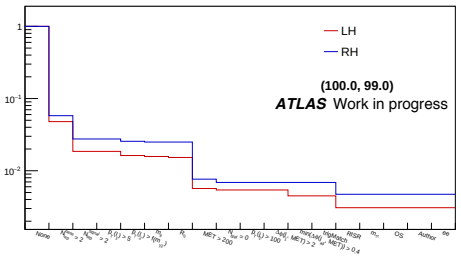

(a) Selectrons: high-$E_{\mathrm{T}}^{\mathrm{miss}}$

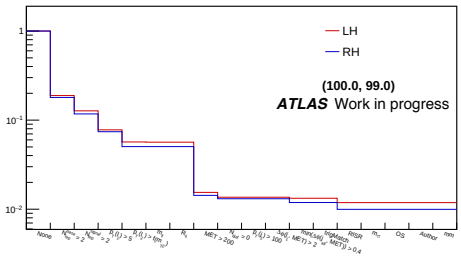

(b) Smuons: high-$E_{\mathrm{T}}^{\mathrm{miss}}$

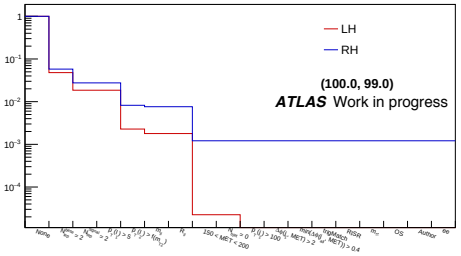

(c) Selectrons: low-$E_{\mathrm{T}}^{\mathrm{miss}}$

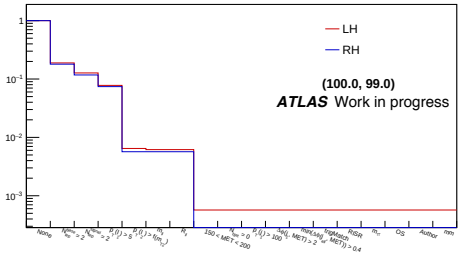

(d) Smuons: low-$E_{\mathrm{T}}^{\mathrm{miss}}$

Figure B.19: Cutflows for the $\left(m(\tilde{\ell}), m(\tilde{\chi}_1^0)\right) = (100, 99)$ signal point.

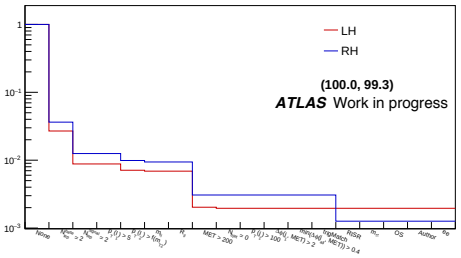

(a) Selectrons: high-$E_{\mathrm{T}}^{\mathrm{miss}}$

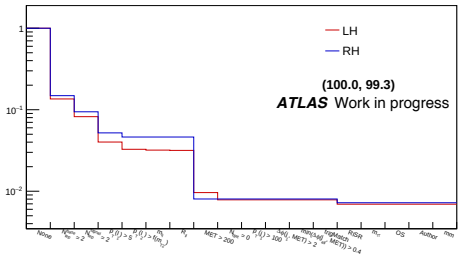

(b) Smuons: high-$E_{\mathrm{T}}^{\mathrm{miss}}$

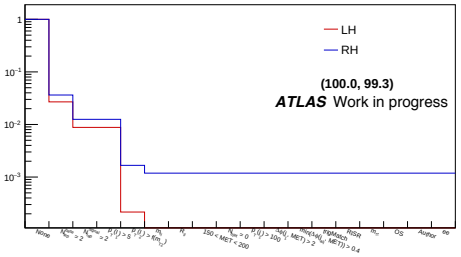

(c) Selectrons: low-$E_{\mathrm{T}}^{\mathrm{miss}}$

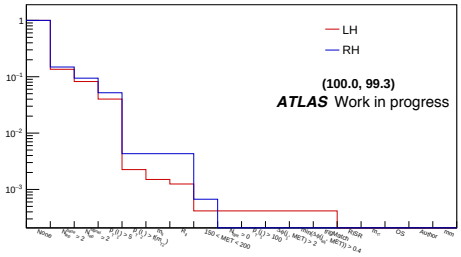

(d) Smuons: low-$E_{\mathrm{T}}^{\mathrm{miss}}$

Figure B.20: Cutflows for the $\left(m(\tilde{\ell}), m(\tilde{\chi}_1^0)\right) = (100, 99.3)$ signal point.

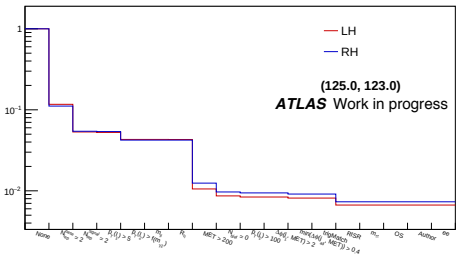

(a) Selectrons: high-$E_{\mathrm{T}}^{\mathrm{miss}}$

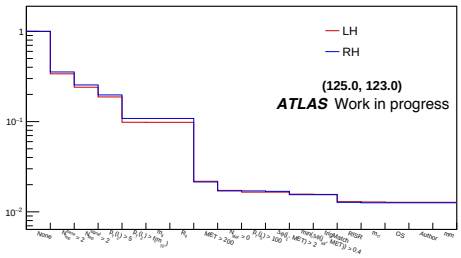

(b) Smuons: high-$E_{\mathrm{T}}^{\mathrm{miss}}$

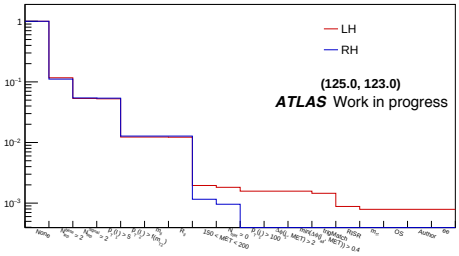

(c) Selectrons: low-$E_{\mathrm{T}}^{\mathrm{miss}}$

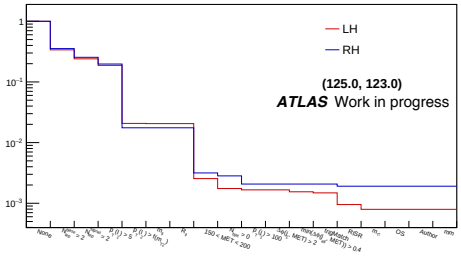

(d) Smuons: low-$E_{\mathrm{T}}^{\mathrm{miss}}$

Figure B.21: Cutflows for the $\left(m(\tilde{\ell}), m(\tilde{\chi}_1^0)\right) = (125, 123)$ signal point.

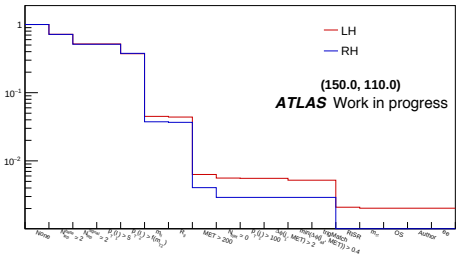

(a) Selectrons: high-$E_{\mathrm{T}}^{\mathrm{miss}}$

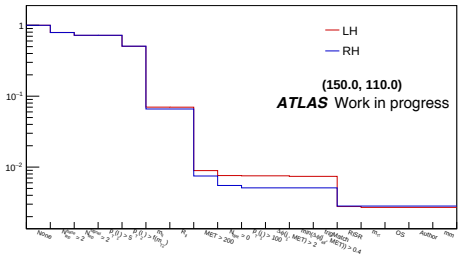

(b) Smuons: high-$E_{\mathrm{T}}^{\mathrm{miss}}$

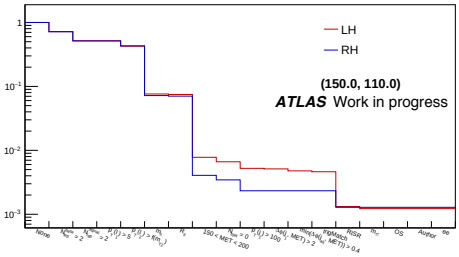

(c) Selectrons: low-$E_{\mathrm{T}}^{\mathrm{miss}}$

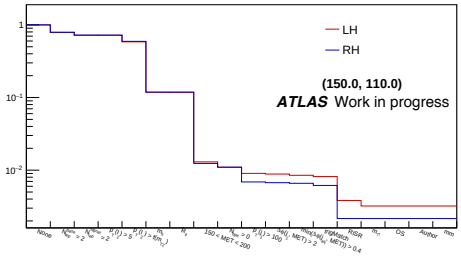

(d) Smuons: low-$E_{\mathrm{T}}^{\mathrm{miss}}$

Figure B.22: Cutflows for the $\left(m(\tilde{\ell}), m(\tilde{\chi}_1^0)\right) = (150, 110)$ signal point.

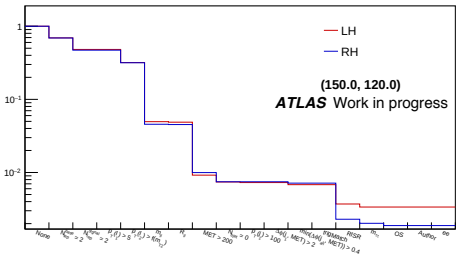

(a) Selectrons: high-$E_{\mathrm{T}}^{\mathrm{miss}}$

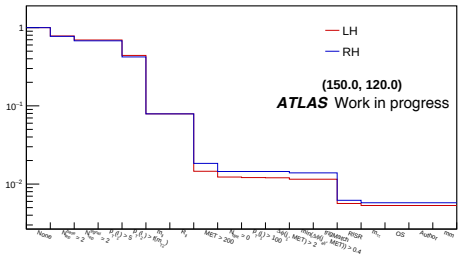

(b) Smuons: high-$E_{\mathrm{T}}^{\mathrm{miss}}$

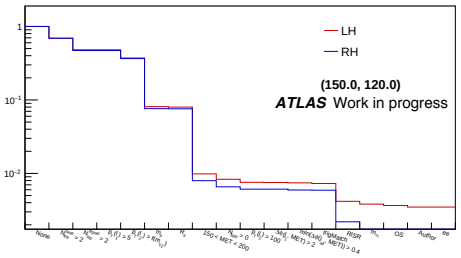

(c) Selectrons: low-$E_{\mathrm{T}}^{\mathrm{miss}}$

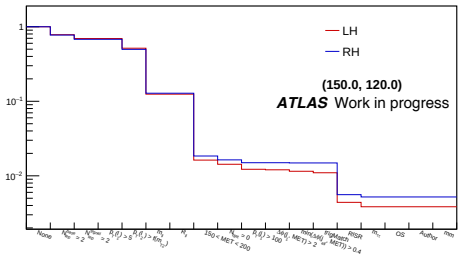

(d) Smuons: low-$E_{\mathrm{T}}^{\mathrm{miss}}$

Figure B.23: Cutflows for the $\left(m(\tilde{\ell}), m(\tilde{\chi}_1^0)\right) = (150, 120)$ signal point.

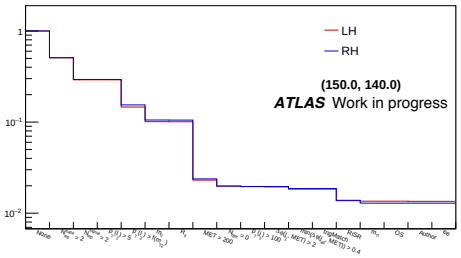

(a) Selectrons: high-$E_{\mathrm{T}}^{\mathrm{miss}}$

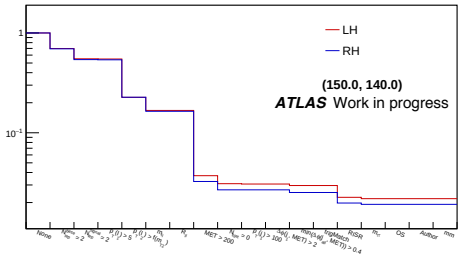

(b) Smuons: high-$E_{\mathrm{T}}^{\mathrm{miss}}$

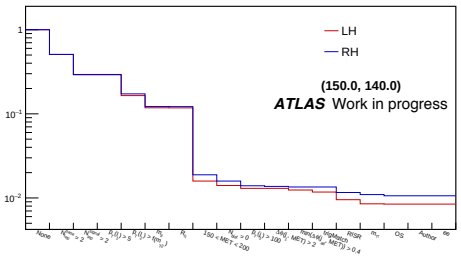

(c) Selectrons: low-$E_{\mathrm{T}}^{\mathrm{miss}}$

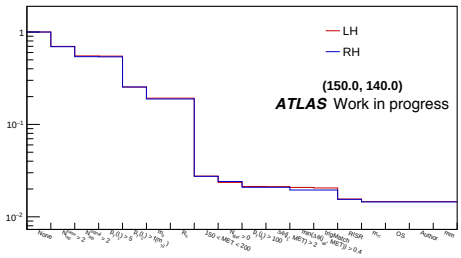

(d) Smuons: low-$E_{\mathrm{T}}^{\mathrm{miss}}$

Figure B.24: Cutflows for the $\left(m(\tilde{\ell}), m(\tilde{\chi}_1^0)\right) = (150, 140)$ signal point.

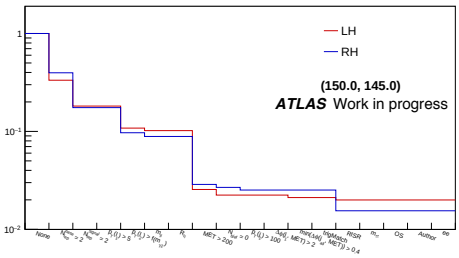

(a) Selectrons: high-$E_{\mathrm{T}}^{\mathrm{miss}}$

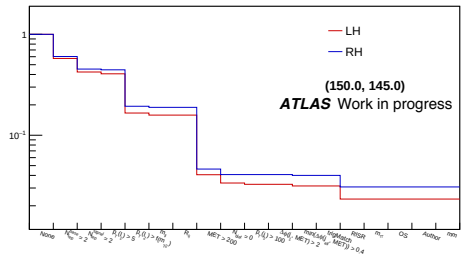

(b) Smuons: high-$E_{\mathrm{T}}^{\mathrm{miss}}$

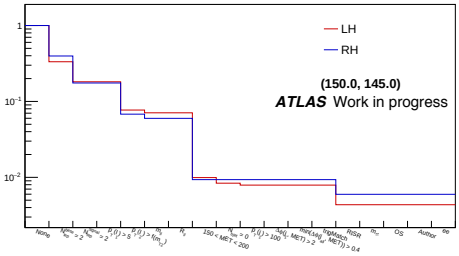

(c) Selectrons: low-$E_{\mathrm{T}}^{\mathrm{miss}}$

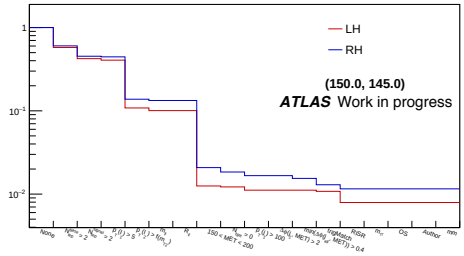

(d) Smuons: low-$E_{\mathrm{T}}^{\mathrm{miss}}$

Figure B.25: Cutflows for the $\left(m(\tilde{\ell}), m(\tilde{\chi}_1^0)\right) = (150, 145)$ signal point.

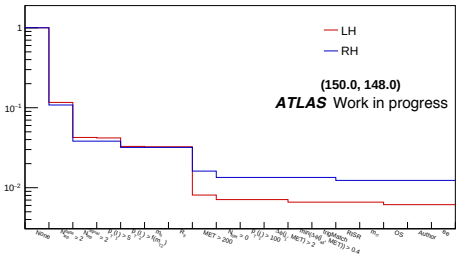

(a) Selectrons: high-$E_{\mathrm{T}}^{\mathrm{miss}}$

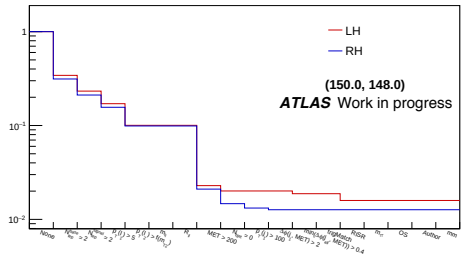

(b) Smuons: high-$E_{\mathrm{T}}^{\mathrm{miss}}$

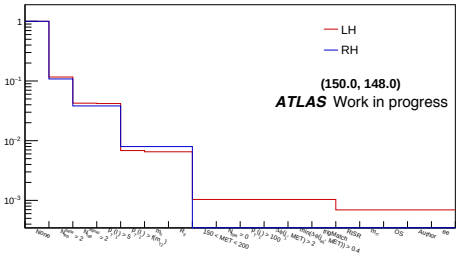

(c) Selectrons: low-$E_{\mathrm{T}}^{\mathrm{miss}}$

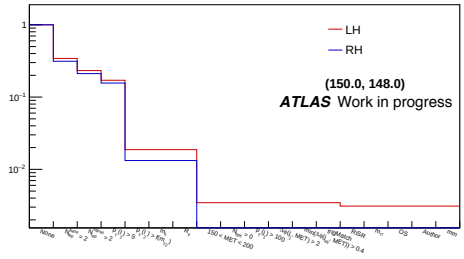

(d) Smuons: low-$E_{\mathrm{T}}^{\mathrm{miss}}$

Figure B.26: Cutflows for the $\left(m(\tilde{\ell}), m(\tilde{\chi}_1^0)\right) = (150, 148)$ signal point.

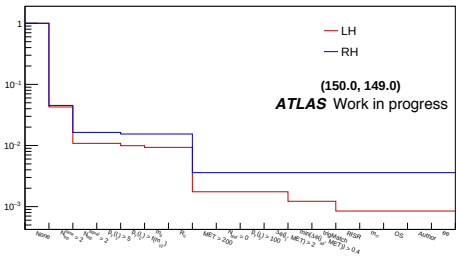

(a) Selectrons: high-$E_{\mathrm{T}}^{\mathrm{miss}}$

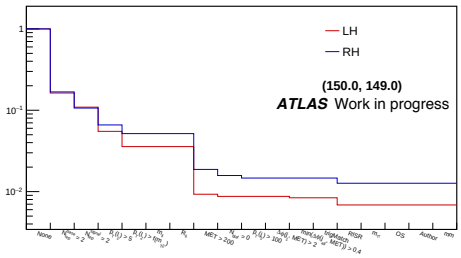

(b) Smuons: high-$E_{\mathrm{T}}^{\mathrm{miss}}$

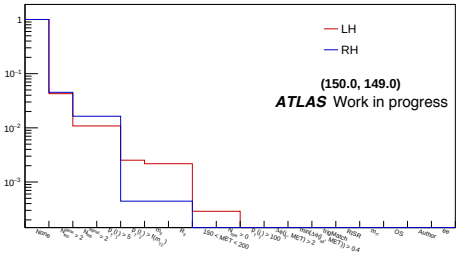

(c) Selectrons: low-$E_{\mathrm{T}}^{\mathrm{miss}}$

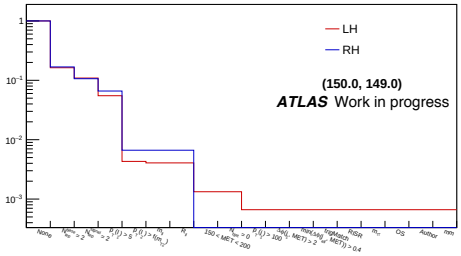

(d) Smuons: low-$E_{\mathrm{T}}^{\mathrm{miss}}$

Figure B.27: Cutflows for the $\left(m(\tilde{\ell}), m(\tilde{\chi}_1^0)\right) = (150, 149)$ signal point.

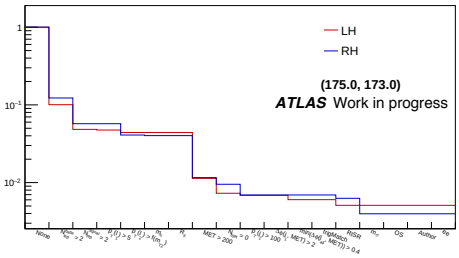

(a) Selectrons: high-$E_{\mathrm{T}}^{\mathrm{miss}}$

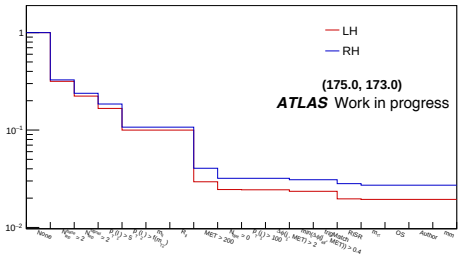

(b) Smuons: high-$E_{\mathrm{T}}^{\mathrm{miss}}$

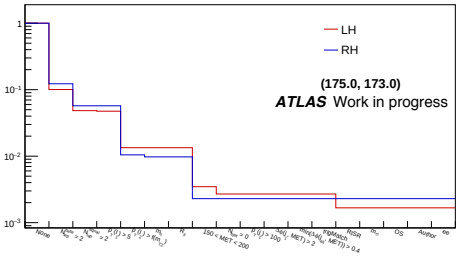

(c) Selectrons: low-$E_{\mathrm{T}}^{\mathrm{miss}}$

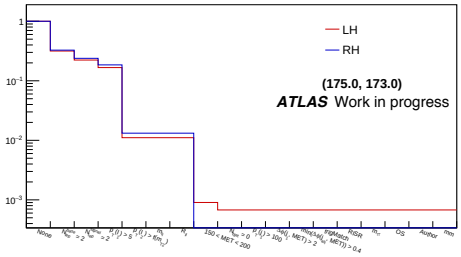

(d) Smuons: low-$E_{\mathrm{T}}^{\mathrm{miss}}$

Figure B.28: Cutflows for the $\left(m(\tilde{\ell}), m(\tilde{\chi}_1^0)\right) = (175, 173)$ signal point.

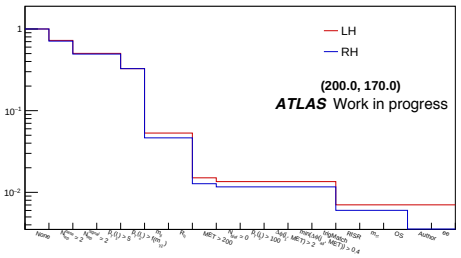

(a) Selectrons: high-$E_{\mathrm{T}}^{\mathrm{miss}}$

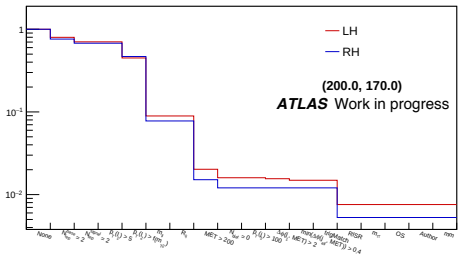

(b) Smuons: high-$E_{\mathrm{T}}^{\mathrm{miss}}$

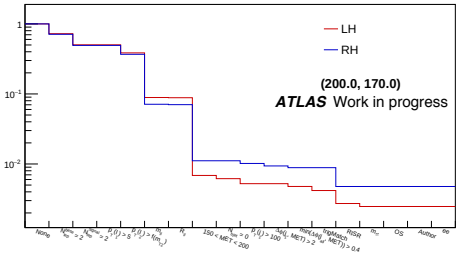

(c) Selectrons: low-$E_{\mathrm{T}}^{\mathrm{miss}}$

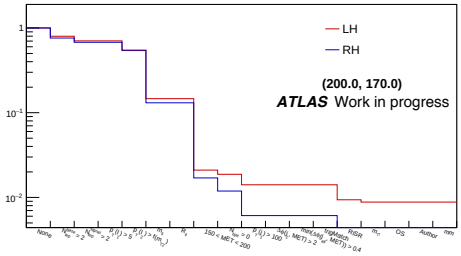

(d) Smuons: low-$E_{\mathrm{T}}^{\mathrm{miss}}$

Figure B.29: Cutflows for the $\left(m(\tilde{\ell}), m(\tilde{\chi}_1^0)\right) = (200, 170)$ signal point.

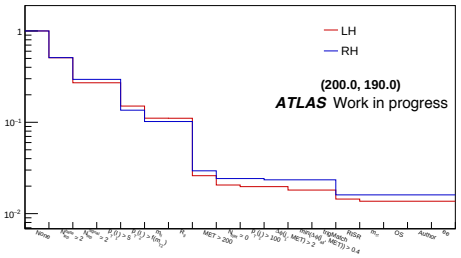

(a) Selectrons: high-$E_{\mathrm{T}}^{\mathrm{miss}}$

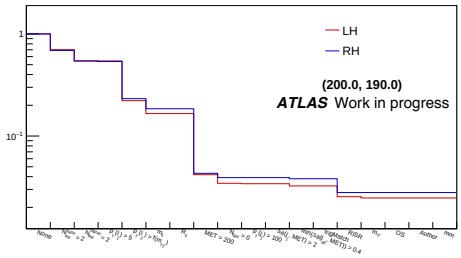

(b) Smuons: high-$E_{\mathrm{T}}^{\mathrm{miss}}$

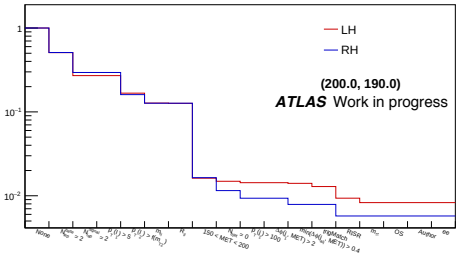

(c) Selectrons: low-$E_{\mathrm{T}}^{\mathrm{miss}}$

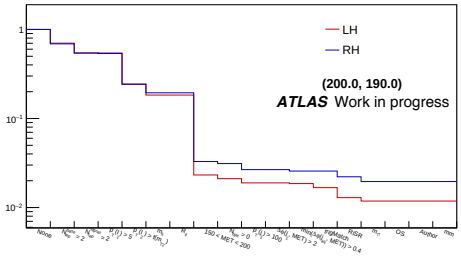

(d) Smuons: low-$E_{\mathrm{T}}^{\mathrm{miss}}$

Figure B.30: Cutflows for the $\left(m(\tilde{\ell}), m(\tilde{\chi}_1^0)\right) = (200, 190)$ signal point.

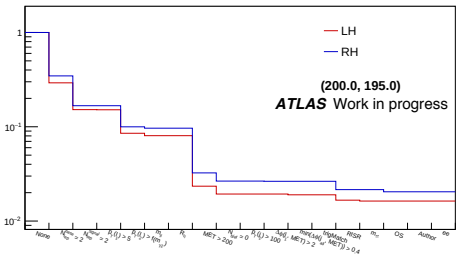

(a) Selectrons: high-$E_{\mathrm{T}}^{\mathrm{miss}}$

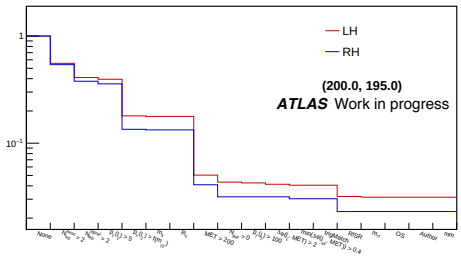

(b) Smuons: high-$E_{\mathrm{T}}^{\mathrm{miss}}$

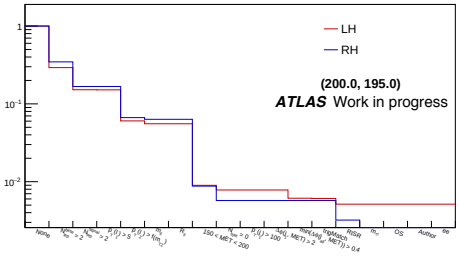

(c) Selectrons: low-$E_{\mathrm{T}}^{\mathrm{miss}}$

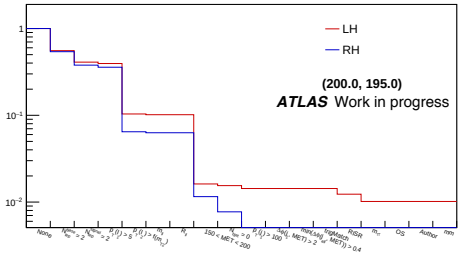

(d) Smuons: low-$E_{\mathrm{T}}^{\mathrm{miss}}$

Figure B.31: Cutflows for the $\left(m(\tilde{\ell}), m(\tilde{\chi}_1^0)\right) = (200, 195)$ signal point.

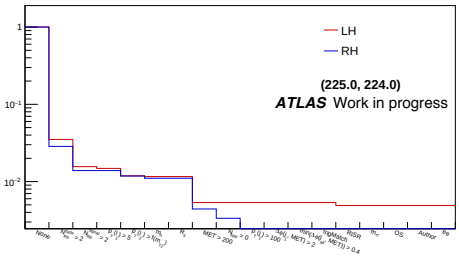

(a) Selectrons: high-$E_{\mathrm{T}}^{\mathrm{miss}}$

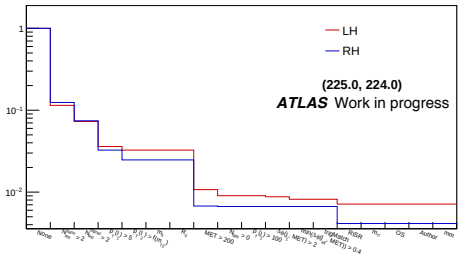

(b) Smuons: high-$E_{\mathrm{T}}^{\mathrm{miss}}$

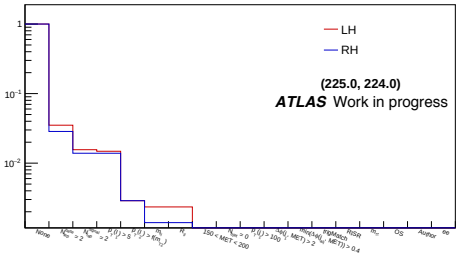

(c) Selectrons: low-$E_{\mathrm{T}}^{\mathrm{miss}}$

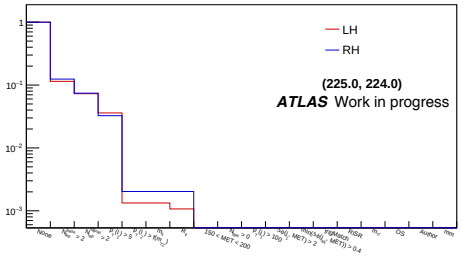

(d) Smuons: low-$E_{\mathrm{T}}^{\mathrm{miss}}$

Figure B.32: Cutflows for the $\left(m(\tilde{\ell}), m(\tilde{\chi}_1^0)\right) = (225, 224)$ signal point.

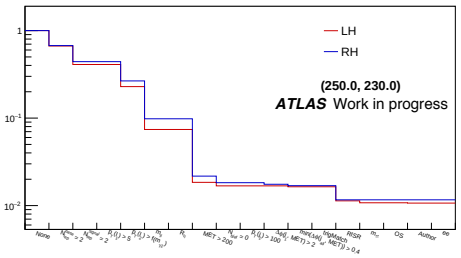

(a) Selectrons: high-$E_{\mathrm{T}}^{\mathrm{miss}}$

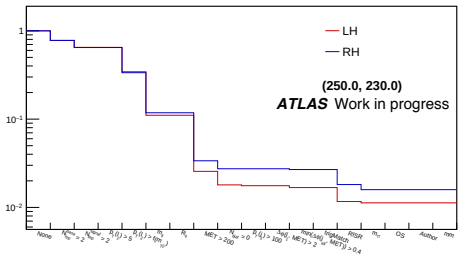

(b) Smuons: high-$E_{\mathrm{T}}^{\mathrm{miss}}$

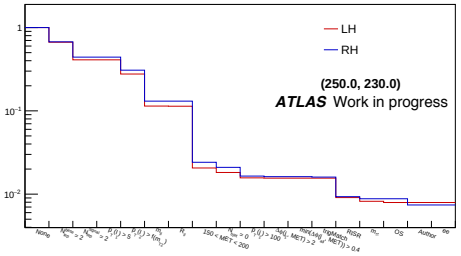

(c) Selectrons: low-$E_{\mathrm{T}}^{\mathrm{miss}}$

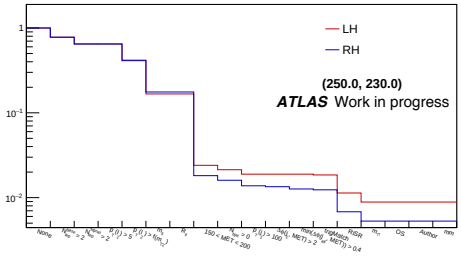

(d) Smuons: low-$E_{\mathrm{T}}^{\mathrm{miss}}$

Figure B.33: Cutflows for the $\left(m(\tilde{\ell}), m(\tilde{\chi}_1^0)\right) = (250, 230)$ signal point.

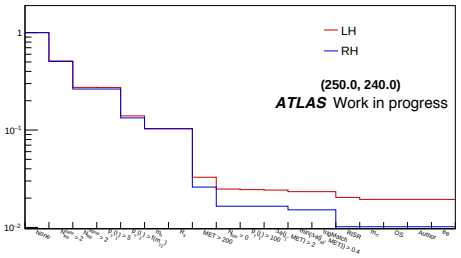

(a) Selectrons: high-$E_{\mathrm{T}}^{\mathrm{miss}}$

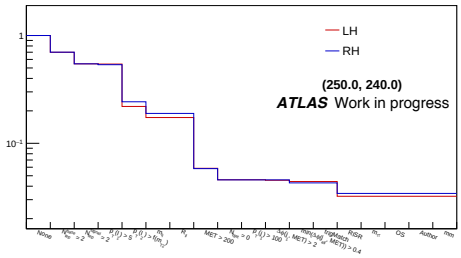

(b) Smuons: high-$E_{\mathrm{T}}^{\mathrm{miss}}$

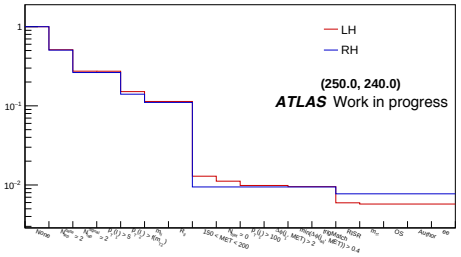

(c) Selectrons: low-$E_{\mathrm{T}}^{\mathrm{miss}}$

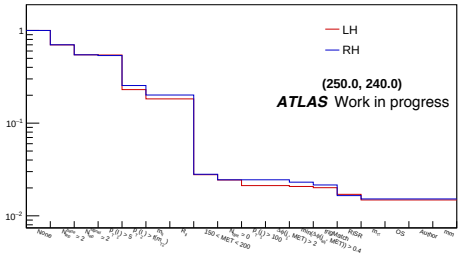

(d) Smuons: low-$E_{\mathrm{T}}^{\mathrm{miss}}$

Figure B.34: Cutflows for the $\left(m(\tilde{\ell}), m(\tilde{\chi}_1^0)\right) = (250, 240)$ signal point.

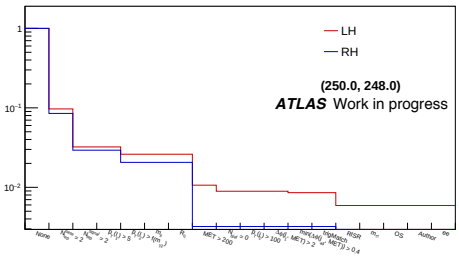

(a) Selectrons: high-$E_{\mathrm{T}}^{\mathrm{miss}}$

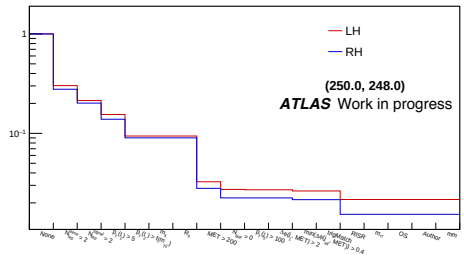

(b) Smuons: high-$E_{\mathrm{T}}^{\mathrm{miss}}$

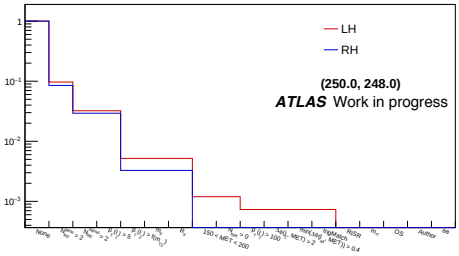

(c) Selectrons: low-$E_{\mathrm{T}}^{\mathrm{miss}}$

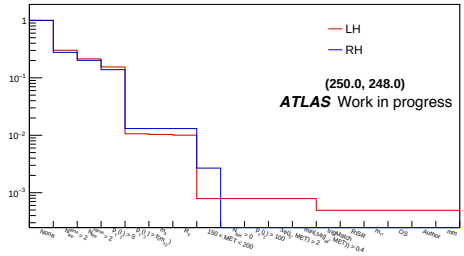

(d) Smuons: low-$E_{\mathrm{T}}^{\mathrm{miss}}$

Figure B.35: Cutflows for the $\left(m(\tilde{\ell}), m(\tilde{\chi}_1^0)\right) = (250, 248)$ signal point.

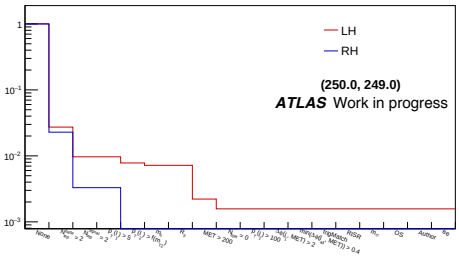

(a) Selectrons: high-$E_{\mathrm{T}}^{\mathrm{miss}}$

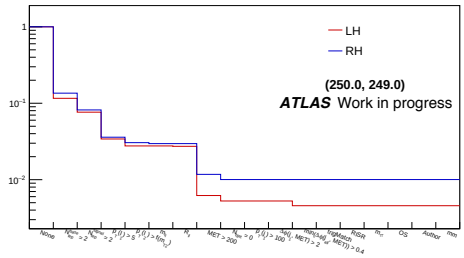

(b) Smuons: high-$E_{\mathrm{T}}^{\mathrm{miss}}$

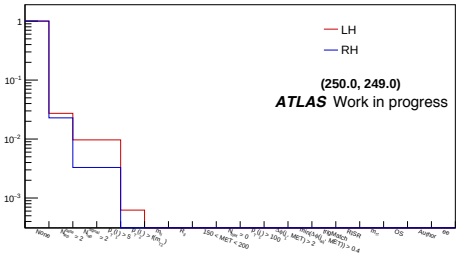

(c) Selectrons: low-$E_{\mathrm{T}}^{\mathrm{miss}}$

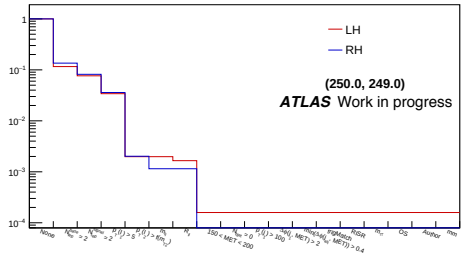

(d) Smuons: low-$E_{\mathrm{T}}^{\mathrm{miss}}$

Figure B.36: Cutflows for the $\left(m(\tilde{\ell}), m(\tilde{\chi}_1^0)\right) = (250, 249)$ signal point.

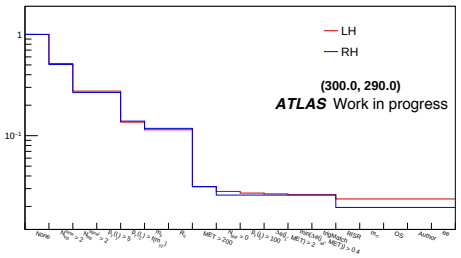

(a) Selectrons: high-$E_{\mathrm{T}}^{\mathrm{miss}}$

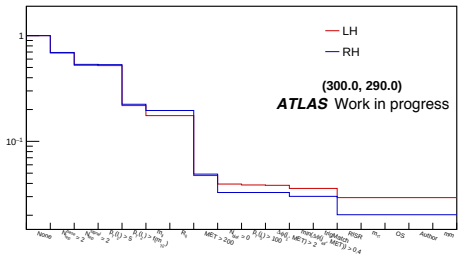

(b) Smuons: high-$E_{\mathrm{T}}^{\mathrm{miss}}$

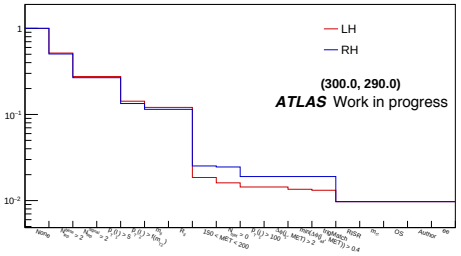

(c) Selectrons: low-$E_{\mathrm{T}}^{\mathrm{miss}}$

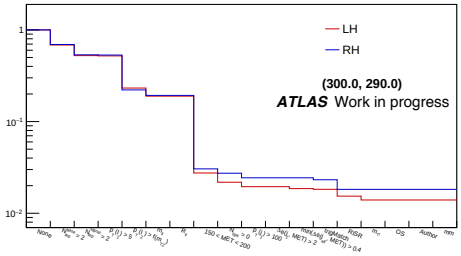

(d) Smuons: low-$E_{\mathrm{T}}^{\mathrm{miss}}$

Figure B.37: Cutflows for the $\left(m(\tilde{\ell}), m(\tilde{\chi}_1^0)\right) = (300, 290)$ signal point.

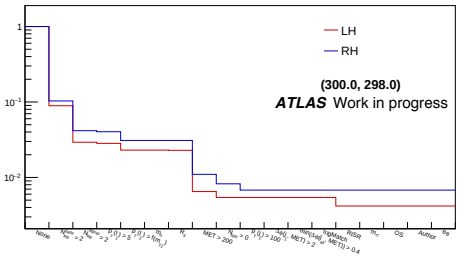

(a) Selectrons: high-$E_{\mathrm{T}}^{\mathrm{miss}}$

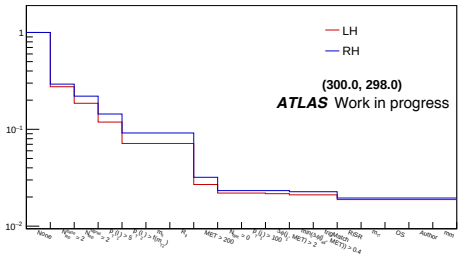

(b) Smuons: high-$E_{\mathrm{T}}^{\mathrm{miss}}$

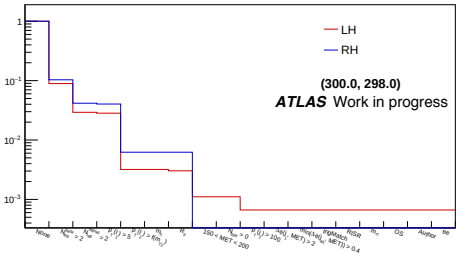

(c) Selectrons: low-$E_{\mathrm{T}}^{\mathrm{miss}}$

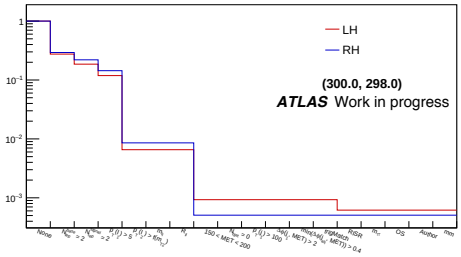

(d) Smuons: low-$E_{\mathrm{T}}^{\mathrm{miss}}$

Figure B.38: Cutflows for the $\left(m(\tilde{\ell}), m(\tilde{\chi}_1^0)\right) = (300, 298)$ signal point.

Appendix C

Cross-Section Upper Limits

Using the CL_s prescription, hypothesis tests are performed using the exclusive SRs to set upper limits on the production cross-section at 95% CL for the electroweakino and slepton processes considered in this search. The expected and observed upper limits are derived for each simulated signal point in the grid. Appendix C.1 shows the cross-section upper limits for electroweakino production, while Appendix C.2 shows the cross-section upper limits for slepton production.

C.1 Electroweakinos

Exclusion fits to the exclusive SRs targeting electroweakino production with a floating signal normalization parameter are used to derive upper limits on the production cross-sections at 95% CL. Figure C.1 shows the upper limits on the cross-section for wino production within each simplified wino/bino scenario considered. Figure C.2 shows the cross-section upper limits for higgsino production in the simplified model.

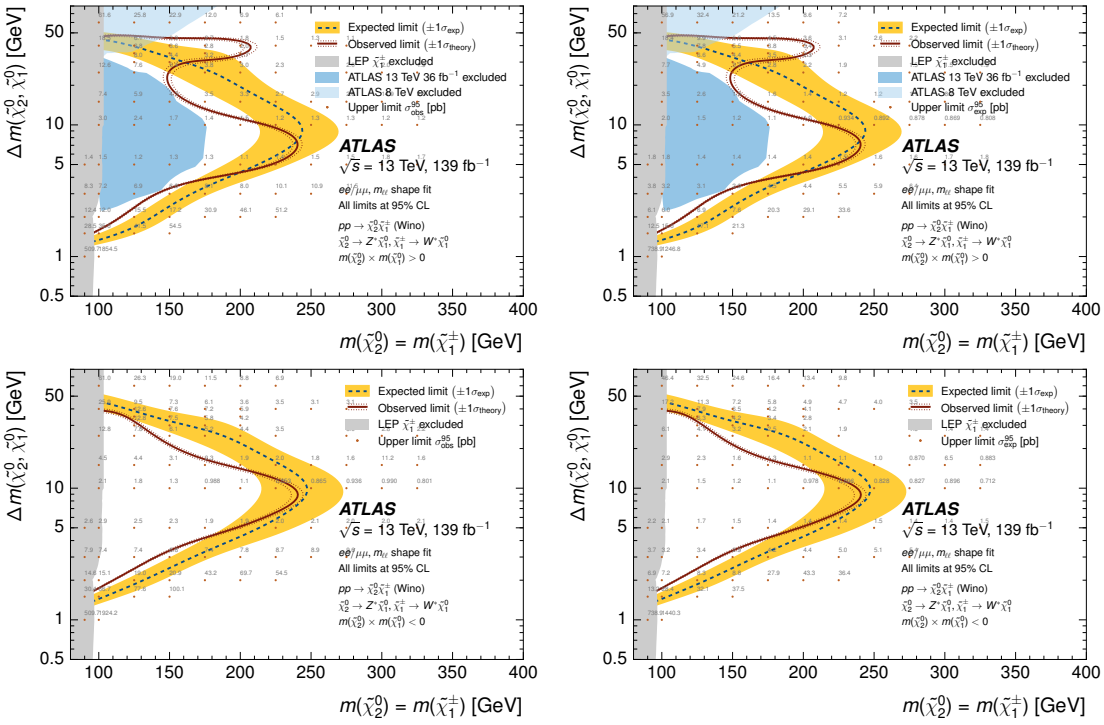

Figure C.1: The observed (left) and expected (right) upper limits on the production cross-section for the wino/bino scenarios. The top row assumes $m(\tilde{\chi}_1^0) \times m(\tilde{\chi}_2^0) > 0$, while the bottom row assumes $m(\tilde{\chi}_1^0) \times m(\tilde{\chi}_2^0) < 0$.

C.2 Sleptons

Exclusion fits to the exclusive SRs targeting slepton production with a floating signal normalization parameter are used to derive upper limits on the production cross-sections at 95% CL. Figures C.3–C.5 show the upper limits on the cross-section for slepton production assuming each mass-degeneracy scenario considered by this analysis.

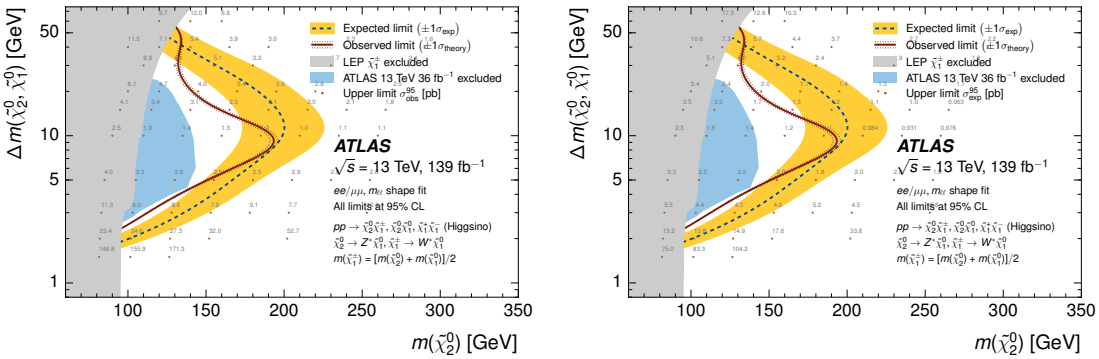

Figure C.2: The observed (left) and expected (right) upper limits on the production cross-section for higgsinos.

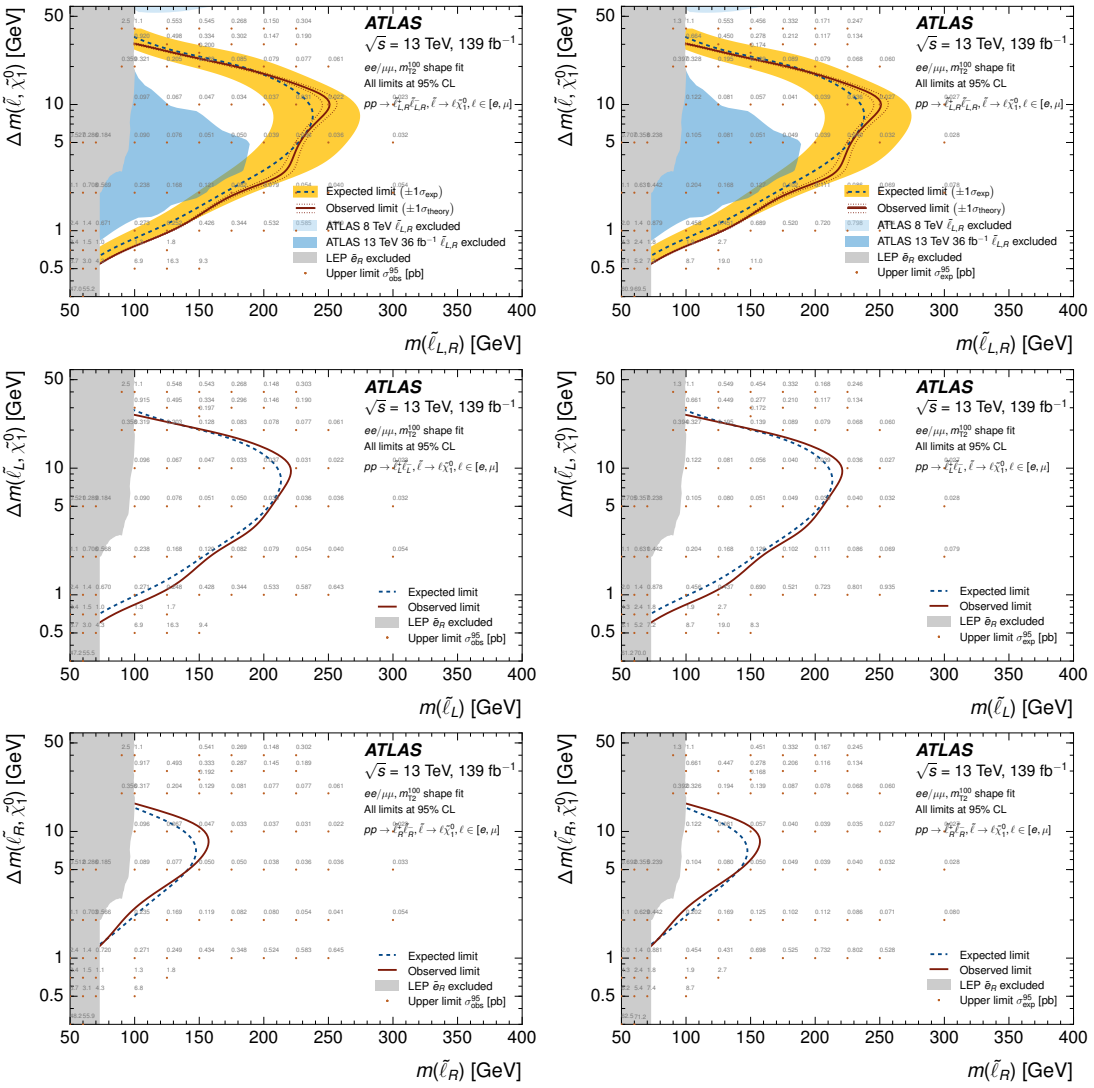

Figure C.3: The observed (left) and expected (right) upper limits on the production cross-section for sleptons (top), left-handed sleptons (middle) and right-handed sleptons (bottom).

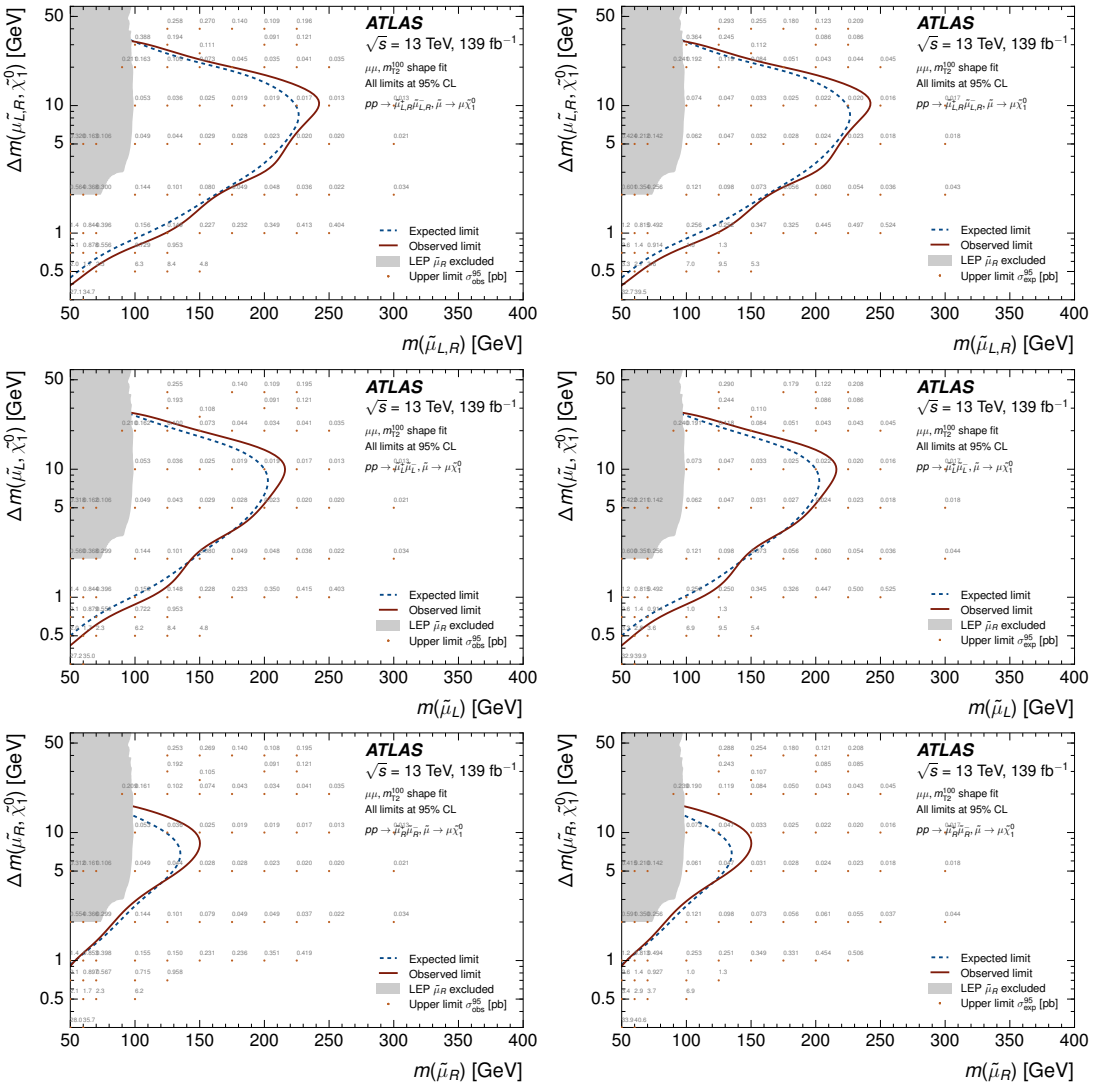

Figure C.4: The observed (left) and expected (right) upper limits on the production cross-section for smuons (top), left-handed smuons (middle) and right-handed smuons (bottom).

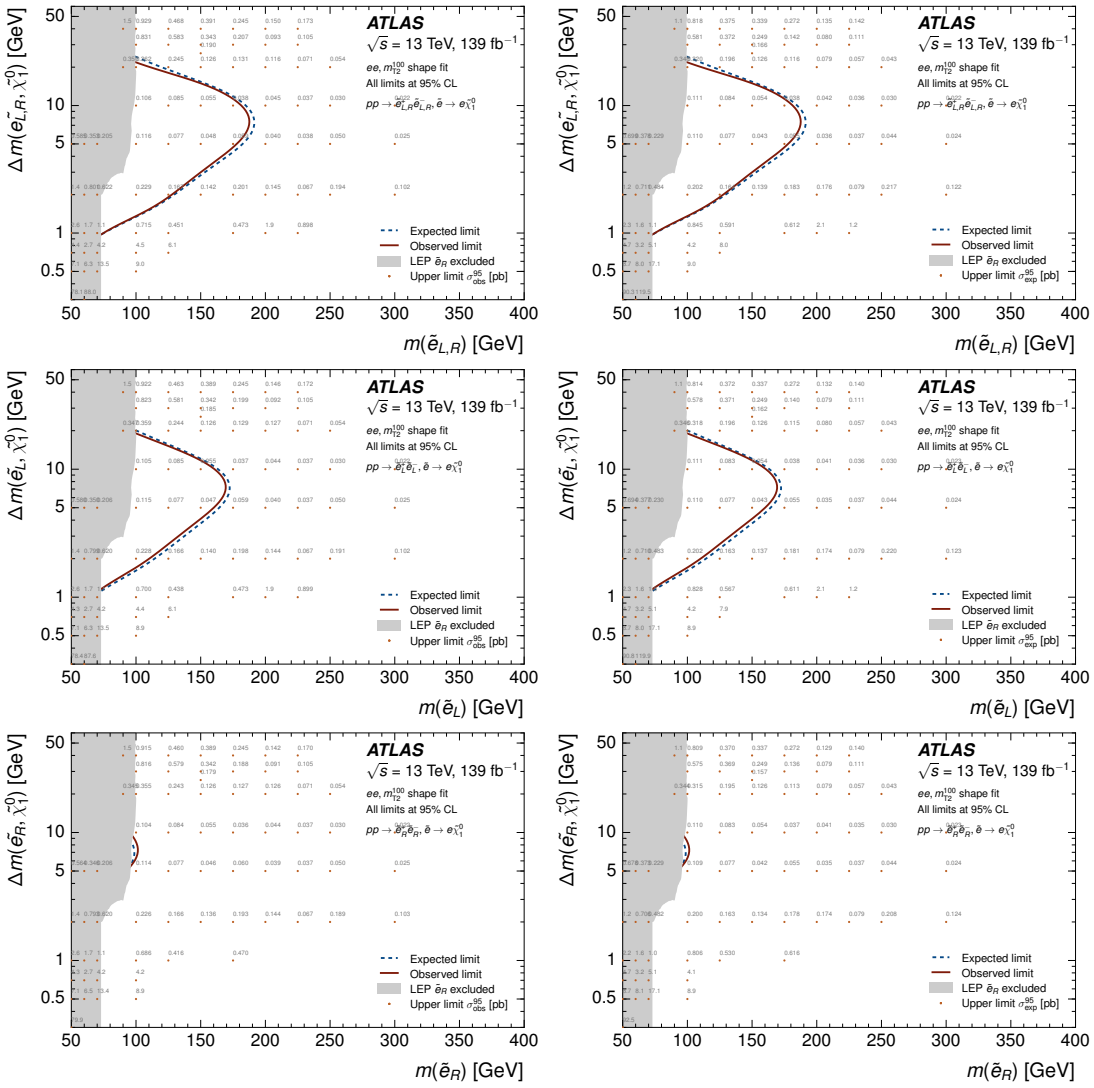

Figure C.5: The observed (left) and expected (right) upper limits on the production cross-section for selectrons (top), left-handed selectrons (middle) and right-handed selectrons (bottom).

Bibliography

[1] ATLAS Collaboration, *Observation of a new particle in the search for the Standard Model Higgs boson with the ATLAS detector at the LHC*, Phys. Lett. B **716** (2012) 1, arXiv:1207.7214 [hep-ex].

[2] CMS Collaboration, *Observation of a new boson at a mass of 125 GeV with the CMS experiment at the LHC*, Phys. Lett. B **716** (2012) 30, arXiv:1207.7235 [hep-ex].

[3] C. Burgard, *Example: Standard model of physics*, http://www.texample.net/tikz/examples/model-physics/.

[4] ATLAS Collaboration, *Standard Model Summary Plots Spring 2019*, ATL-PHYS-PUB-2019-010, 2019, https://cds.cern.ch/record/2668559.

[5] V.C. Rubin and W.K. Ford, Jr., *Rotation of the Andromeda Nebula from a Spectroscopic Survey of Emission Regions*, Astrophysical Journal **159** (1970) 379.

[6] F. Zwicky, *Die Rotverschiebung von extragalaktischen Nebeln*, Helv. Phys. Acta **6** (1933) 110–127, [Gen. Rel. Grav. 41, 207 (2009)].

[7] L. Aaron et al., *Chandra Observations of A2029: The Dark Matter Profile Down to below 0.01rvirin an Unusually Relaxed Cluster*, The Astrophysical Journal **586** (2003) 135–142.

[8] Planck Collaboration, *Planck2015 results*, Astronomy and Astrophysics **594** (2016) A13.

[9] E. Komatsu et al., *Seven-Year Wilkinson Microwave Anisotropy Probe (WMAP) Observations: Cosmological Interpretation*, The Astrophysical Journal Supplement Series **192** (2011) A13.

[10] M. Papucci, J. T. Ruderman, and A. Weiler, *Natural SUSY endures*, JHEP **09** (2012) 035, arXiv:1110.6926 [hep-ph].

[11] S. P. Martin, *A Supersymmetry Primer*, Advanced Series on Directions in High Energy Physics (1998) 1Ð98, arXiv:hep-ph/9709356 [hep-ph].

[12] Muon g-2 Collaboration, *Final report of the E821 muon anomalous magnetic moment measurement at BNL*, Phys. Rev. D **73** (2006) 072003, arXiv:hep-ex/0602035 [hep-ex].

[13] Muon g-2 Collaboration, *The Muon g - 2 experiment at Fermilab*, EPJ Web Conf. **212** (2019) 05003, arXiv:1905.00497 [hep-ex].

[14] Muon g-2 Collaboration, *Muon(g-2) Technical Design Report*, arXiv:1501.06858 [physics.ins-det].

[15] Y. A. Golfand and E. P. Likhtman, *Extension of the Algebra of Poincare Group Generators and Violation of p Invariance*, JETP Lett. **13** (1971) 323, [Pisma Zh. Eksp. Teor. Fiz. **13** (1971) 452].

[16] D. V. Volkov and V. P. Akulov, *Is the Neutrino a Goldstone Particle?*, Phys. Lett. B **46** (1973) 109.

[17] J. Wess and B. Zumino, *Supergauge transformations in four dimensions*, Nucl. Phys. B **70** (1974) 39.

[18] J. Wess and B. Zumino, *Supergauge invariant extension of quantum electrodynamics*, Nucl. Phys. B **78** (1974) 1.

[19] S. Ferrara and B. Zumino, *Supergauge invariant Yang-Mills theories*, Nucl. Phys. B **79** (1974) 413.

[20] A. Salam and J. A. Strathdee, *Supersymmetry and non-Abelian gauges*, Phys. Lett. B **51** (1974) 353.

[21] S. Dimopoulos, S. Raby, and F. Wilczek, *Supersymmetry and the scale of unification*, Phys. Rev. D **24** (1981) 1681–1683.

[22] K. Abe et al., *Search for proton decay via $p \to e^+\pi^0$ and $p \to \mu^+\pi^0$ in 0.31 megaton·years exposure of the Super-Kamiokande water Cherenkov detector*, Physical Review D **95** (2017).

[23] R. Barbieri and G. F. Giudice, *Upper bounds on supersymmetric particle masses*, Nucl. Phys. B **306** (1988) 63.

[24] B. de Carlos and J. A. Casas, *One loop analysis of the electroweak breaking in supersymmetric models and the fine tuning problem*, Phys. Lett. B **309** (1993) 320, arXiv:hep-ph/9303291.

[25] K. Griest and D. Seckel, *Three exceptions in the calculation of relic abundances*, Phys. Rev. D **43** (1991) 3191–3203.

[26] J. Edsjo and P. Gondolo, *Neutralino relic density including coannihilations*, Phys. Rev. D **56** (1997) 1879–1894, arXiv:hep-ph/9704361.

[27] B. C. Allanach et al., *SUSY Les Houches Accord 2*, Comput. Phys. Commun. **180** (2009) 8–25, arXiv:0801.0045 [hep-ph].

[28] B. Fuks, M. Klasen, S. Schmiemann, and M. Sunder, *Realistic simplified gaugino-higgsino models in the MSSM*, Eur. Phys. J. C **78** (2018) 209, arXiv:1710.09941 [hep-ph].

[29] A. S. Belyaev, S. F. King, and P. B. Schaefers, *Muon g-2 and dark matter suggest nonuniversal gaugino masses:* $\mathbf{SU(5)} \times \mathbf{A_4}$ *case study at the LHC*, Phys. Rev. D **97** (2018) 115002, arXiv:1801.00514 [hep-ph].

[30] L. Evans and P. Bryant, *LHC Machine*, JINST **3** (2008) S08001.

[31] ALICE Collaboration, *The ALICE experiment at the CERN LHC*, Journal of Instrumentation **3** (2008) S08002–S08002.

[32] ATLAS Collaboration, *The ATLAS Experiment at the CERN Large Hadron Collider*, JINST **3** (2008) S08003.

[33] CMS Collaboration, *The CMS experiment at the CERN LHC*, Journal of Instrumentation **3** (2008) S08004–S08004.

[34] LHCb Collaboration, *The LHCb Detector at the LHC*, Journal of Instrumentation **3** (2008) S08005–S08005.

[35] E. Mobs, *The CERN accelerator complex. Complexe des accŐlŐrateurs du CERN*, https://cds.cern.ch/record/2197559, General Photo.

[36] ATLAS Collaboration, *LuminosityPublicResultsRun2*, https://twiki.cern.ch/twiki/bin/view/AtlasPublic/LuminosityPublicResultsRun2.

[37] ATLAS Collaboration, *Event Displays from Run 2 physics analyses*, https://twiki.cern.ch/twiki/bin/view/AtlasPublic/EventDisplayRun2Physics.

[38] ATLAS Collaboration, *Performance of the ATLAS track reconstruction algorithms in dense environments in LHC Run 2*, Eur. Phys. J. C **77** (2017) 673, arXiv:1704.07983 [hep-ex].

[39] ATLAS Collaboration, *Study of the material of the ATLAS inner detector for Run 2 of the LHC*, JINST **12** (2017) P12009, arXiv:1707.02826 [hep-ex].

[40] ATLAS Collaboration, *ATLAS pixel detector electronics and sensors*, JINST **3** (2008) P07007.

[41] ATLAS Collaboration, *ATLAS Insertable B-Layer Technical Design Report*, Atlas-tdr-19, 2010, https://cds.cern.ch/record/1291633.

[42] ATLAS Collaboration, *Operation and performance of the ATLAS semiconductor tracker*, JINST **9** (2014) P08009, arXiv:1404.7473 [hep-ex].

[43] ATLAS Collaboration, *Performance of the ATLAS Transition Radiation Tracker in Run 1 of the LHC: tracker properties*, JINST **12** (2017) P05002, arXiv:1702.06473 [hep-ex].

[44] ATLAS Collaboration, *ATLAS liquid-argon calorimeter: Technical Design Report*, Atlas-tdr-2, 1996, https://cds.cern.ch/record/331061.

[45] ATLAS Collaboration, *ATLAS tile calorimeter: Technical Design Report*, Atlas-tdr-3, 1996, https://cds.cern.ch/record/331062.

[46] ATLAS Collaboration, *ATLAS muon spectrometer: Technical Design Report*, Atlas-tdr-10, 1997, https://cds.cern.ch/record/331068.

[47] H. Herde, *Muon reconstruction performance in ATLAS at Run-II*, PoS **EPS-HEP2015** (2015) 285.

[48] ATLAS Collaboration, *Performance of the ATLAS trigger system in 2015*, Eur. Phys. J. C **77** (2017) 317, arXiv:1611.09661 [hep-ex].

[49] ATLAS Collaboration, *2015 start-up trigger menu and initial performance assessment of the ATLAS trigger using Run-2 data*, ATL-DAQ-PUB-2016-001, 2016, https://cds.cern.ch/record/2136007.

[50] ATLAS Collaboration, *Trigger Menu in 2016*, ATL-DAQ-PUB-2017-001, 2017, https://cds.cern.ch/record/2242069.

[51] ATLAS Collaboration, *Trigger Menu in 2017*, ATL-DAQ-PUB-2018-002, 2018, https://cds.cern.ch/record/2625986.

[52] ATLAS Collaboration, *Trigger Menu in 2018*, ATL-DAQ-PUB-2019-001, 2019, https://cds.cern.ch/record/2693402.

[53] ATLAS Collaboration, *Trigger Operation Public Results*, https://twiki.cern.ch/twiki/bin/view/AtlasPublic/TriggerOperationPublicResults.

[54] J. Liu, *Discovery strategies for dark matter and Higgsinos at the LHC*, Jul, 2019. https://cds.cern.ch/record/2683899.

[55] ATLAS Collaboration, *Luminosity determination in pp collisions at $\sqrt{s} = 13$ TeV using the ATLAS detector at the LHC*, ATLAS-CONF-2019-021, 2019, https://cds.cern.ch/record/2677054.

[56] G. Avoni et al., *The new LUCID-2 detector for luminosity measurement and monitoring in ATLAS*, JINST **13** (2018) P07017.

[57] M. Cacciari, G. P. Salam, and G. Soyez, *FastJet user manual*, Eur. Phys. J. C **72** (2012) 1896, arXiv:1111.6097 [hep-ph].

[58] ATLAS Collaboration, *Topological cell clustering in the ATLAS calorimeters and its performance in LHC Run 1*, Eur. Phys. J. C **77** (2017) 490, arXiv:1603.02934 [hep-ex].

[59] ATLAS Collaboration, *The Pythia 8 A3 tune description of ATLAS minimum bias and inelastic measurements incorporating the Donnachie–Landshoff diffractive model*, ATL-PHYS-PUB-2016-017, 2016, https://cds.cern.ch/record/2206965.

[60] A. D. Martin, W. Stirling, R. S. Thorne, and G. Watt, *Parton distributions for the LHC*, Eur. Phys. J. C **63** (2009) 189, arXiv:0901.0002 [hep-ph].

[61] W. Lukas, *Fast Simulation for ATLAS: Atlfast-II and ISF*, Journal of Physics: Conference Series **396** (2012) 022031.

[62] L. Lönnblad and S. Prestel, *Matching tree-level matrix elements with interleaved showers*, JHEP **03** (2012) 19, arXiv:1109.4829.

[63] C. Borschensky, M. Krämer, A. Kulesza, M. Mangano, S. Padhi, T. Plehn, and X. Portell, *Squark and gluino production cross sections in pp collisions at $\sqrt{s} = 13, 14, 33$ and 100 TeV*, Eur. Phys. J. C **74** (2014) 3174, arXiv:1407.5066 [hep-ph].

[64] P. Artoisenet, R. Frederix, O. Mattelaer, and R. Rietkerk, *Automatic spin-entangled decays of heavy resonances in Monte Carlo simulations*, JHEP **03** (2013) 015, arXiv:1212.3460 [hep-ph].

[65] B. Fuks, M. Klasen, D. R. Lamprea, and M. Rothering, *Gaugino production in proton-proton collisions at a center-of-mass energy of 8 TeV*, JHEP **10** (2012) 081, arXiv:1207.2159 [hep-ph].

[66] B. Fuks, M. Klasen, D. R. Lamprea, and M. Rothering, *Precision predictions for electroweak superpartner production at hadron colliders with Resummino*, Eur. Phys. J. C **73** (2013) 2480, arXiv:1304.0790 [hep-ph].

[67] B. Fuks, M. Klasen, D. R. Lamprea, and M. Rothering, *Revisiting slepton pair production at the Large Hadron Collider*, JHEP **01** (2014) 168, arXiv:1310.2621 [hep-ph].

[68] A. Djouadi, M. M. Muhlleitner, and M. Spira, *Decays of supersymmetric particles: The Program SUSY-HIT (SUspect-SdecaY-Hdecay-InTerface)*, Acta Phys. Polon. B **38** (2007) 635–644, arXiv:hep-ph/0609292 [hep-ph].

[69] U. De Sanctis, T. Lari, S. Montesano, and C. Troncon, *Perspectives for the detection and measurement of supersymmetry in the focus point region of mSUGRA models with the ATLAS detector at LHC*, Eur. Phys. J. C **52** (2007) 743–758, arXiv:0704.2515 [hep-ex].

[70] ATLAS Collaboration, *The ATLAS Simulation Infrastructure*, Eur. Phys. J. C **70** (2010) 823, arXiv:1005.4568 [physics.ins-det].

[71] GEANT4 Collaboration, S. Agostinelli et al., *GEANT4 - a simulation toolkit*, Nucl. Instrum. Meth. A **506** (2003) 250.

[72] NNPDF Collaboration, R. D. Ball et al., *Parton distributions for the LHC Run II*, JHEP **04** (2015) 040, arXiv:1410.8849 [hep-ph].

[73] C. Anastasiou, L. J. Dixon, K. Melnikov, and F. Petriello, *High precision QCD at hadron colliders: Electroweak gauge boson rapidity distributions at NNLO*, Phys. Rev. D **69** (2004) 094008, arXiv:hep-ph/0312266.

[74] J. Pumplin et al., *New generation of parton distributions with uncertainties from global QCD analysis*, JHEP **07** (2002) 012, arXiv:hep-ph/0201195.

[75] LHC Higgs Cross Section Working Group Collaboration, D. de Florian et al., *Handbook of LHC Higgs Cross Sections: 4. Deciphering the Nature of the Higgs Sector*, CERN-2017-002-M (2016), arXiv:1610.07922 [hep-ph].

[76] R. D. Ball et al., *Parton distributions with LHC data*, Nucl. Phys. B **867** (2013) 244, arXiv:1207.1303 [hep-ph].

[77] M. Cacciari, M. Czakon, M. Mangano, A. Mitov, and P. Nason, *Top-pair production at hadron colliders with next-to-next-to-leading logarithmic soft-gluon resummation*, Phys. Lett. B **710** (2012) 612–622, arXiv:1111.5869 [hep-ph].

[78] M. Czakon and A. Mitov, *NNLO corrections to top-pair production at hadron colliders: the all-fermionic scattering channels*, JHEP **12** (2012) 054, arXiv:1207.0236 [hep-ph].

[79] M. Czakon and A. Mitov, *NNLO corrections to top pair production at hadron colliders: the quark-gluon reaction*, JHEP **01** (2013) 080, arXiv:1210.6832 [hep-ph].

[80] M. Czakon, P. Fiedler, and A. Mitov, *Total Top-Quark Pair-Production Cross Section at Hadron Colliders Through $O(\alpha_S^4)$*, Phys. Rev. Lett. **110** (2013) 252004, arXiv:1303.6254 [hep-ph].

[81] M. Czakon and A. Mitov, *Top++: A program for the calculation of the top-pair cross-section at hadron colliders*, Comput. Phys. Commun. **185** (2014) 2930, arXiv:1112.5675 [hep-ph].

[82] N. Kidonakis, *NNLL resummation for s-channel single top quark production*, Phys. Rev. D **81** (2010) 054028, arXiv:1001.5034 [hep-ph].

[83] N. Kidonakis, *Next-to-next-to-leading-order collinear and soft gluon corrections for t-channel single top quark production*, Phys. Rev. D **83** (2011) 091503, arXiv:1103.2792 [hep-ph].

[84] R. Frederix, E. Re, and P. Torrielli, *Single-top t-channel hadroproduction in the four-flavour scheme with POWHEG and aMC@NLO*, JHEP **09** (2012) 130, arXiv:1207.5391 [hep-ph].

[85] N. Kidonakis, *Two-loop soft anomalous dimensions for single top quark associated production with a W- or H-*, Phys. Rev. D **82** (2010) 054018, arXiv:1005.4451 [hep-ph].

[86] J. Alwall et al., *The automated computation of tree-level and next-to-leading order differential cross sections, and their matching to parton shower simulations*, JHEP **07** (2014) 079, arXiv:1405.0301 [hep-ph].

[87] S. Höche, F. Krauss, M. Schönherr, and F. Siegert, *QCD matrix elements + parton showers: The NLO case*, JHEP **04** (2013) 027, arXiv:1207.5030 [hep-ph].

[88] S. Frixione, P. Nason, and G. Ridolfi, *A positive-weight next-to-leading-order Monte Carlo for heavy flavour hadroproduction*, JHEP **09** (2007) 126, arXiv:0707.3088 [hep-ph].

[89] P. Nason, *A new method for combining NLO QCD with shower Monte Carlo algorithms*, JHEP **11** (2004) 040, arXiv:hep-ph/0409146.

[90] S. Frixione, P. Nason, and C. Oleari, *Matching NLO QCD computations with Parton Shower simulations: the POWHEG method*, JHEP **11** (2007) 070, arXiv:0709.2092 [hep-ph].

[91] S. Alioli, P. Nason, C. Oleari, and E. Re, *A general framework for implementing NLO calculations in shower Monte Carlo programs: the POWHEG BOX*, JHEP **06** (2010) 043, arXiv:1002.2581 [hep-ph].

[92] E. Re, *Single-top Wt-channel production matched with parton showers using the POWHEG method*, Eur. Phys. J. C **71** (2011) 1547, arXiv:1009.2450 [hep-ph].

[93] J. Pequenao and P. Schaffner, *How ATLAS detects particles: diagram of particle paths in the detector*, https://cds.cern.ch/record/1505342.

[94] R. Frühwirth, *Application of Kalman filtering to track and vertex fitting*, Nuclear Instruments and Methods in Physics Research Section A: Accelerators, Spectrometers, Detectors and Associated Equipment **262** (1987) 444 – 450.

[95] S. Boutle et al., *Primary vertex reconstruction at the ATLAS experiment*, Journal of Physics: Conference Series **898** (2017) 042056.

[96] ATLAS Collaboration, *Vertex Reconstruction Performance of the ATLAS Detector at* $\sqrt{s} = 13$ *TeV*, ATL-PHYS-PUB-2015-026, 2015, https://cds.cern.ch/record/2037717.

[97] ATLAS Collaboration, *Electron reconstruction and identification in the ATLAS experiment using the 2015 and 2016 LHC proton–proton collision data at* $\sqrt{s} = 13$ *TeV*, Eur. Phys. J. C **79** (2019) 639, arXiv:1902.04655 [hep-ex].

[98] ATLAS Collaboration, *Electron and photon energy calibration with the ATLAS detector using 2015–2016 LHC proton–proton collision data*, JINST **14** (2019) P03017, arXiv:1812.03848 [hep-ex].

[99] ATLAS Collaboration, *Electron and photon performance measurements with the ATLAS detector using the 2015-2017 LHC proton–proton collision data*, arXiv:1908.00005 [hep-ex].

[100] ATLAS Collaboration, *Muon reconstruction performance of the ATLAS detector in proton–proton collision data at* $\sqrt{s} = 13$ *TeV*, Eur. Phys. J. C **76** (2016) 292, arXiv:1603.05598 [hep-ex].

[101] ATLAS Collaboration, *Identification of very-low transverse momentum muons in the ATLAS experiment*, ATL-PHYS-PUB-2020-002, 2020, https://cds.cern.ch/record/2710574.

[102] S. Catani et al., *Longitudinally-invariant k_t-clustering algorithms for hadron-hadron collisions*, Nuclear Physics B **406** (1993) 187 – 224.

[103] Y. Dokshitzer, G. Leder, S. Moretti, and B. Webber, *Better jet clustering algorithms*, Journal of High Energy Physics **1997** (1997) 001Ð001.

[104] M. Cacciari, G. P. Salam, and G. Soyez, *The anti-k_t jet clustering algorithm*, JHEP **04** (2008) 063, arXiv:0802.1189 [hep-ph].

[105] ATLAS Collaboration, *Jet energy scale measurements and their systematic uncertainties in proton–proton collisions at $\sqrt{s} = 13$ TeV with the ATLAS detector*, Phys. Rev. D **96** (2017) 072002, arXiv:1703.09665 [hep-ex].

[106] ATLAS Collaboration, *Performance of pile-up mitigation techniques for jets in pp collisions at $\sqrt{s} = 8$ TeV using the ATLAS detector*, Eur. Phys. J. C **76** (2016) 581, arXiv:1510.03823 [hep-ex].

[107] ATLAS Collaboration, *ATLAS b-jet identification performance and efficiency measurement with $t\bar{t}$ events in pp collisions at $\sqrt{s} = 13$ TeV*, arXiv:1907.05120 [hep-ex].

[108] R. D. Cousins, J. T. Linnemann, and J. Tucker, *Evaluation of three methods for calculating statistical significance when incorporating a systematic uncertainty into a test of the background-only hypothesis for a Poisson process*, Nucl. Instrum. Meth. A **595** (2008) 480–501, arXiv:physics/0702156 [physics.data-an].

[109] Z. Han, G. D. Kribs, A. Martin, and A. Menon, *Hunting quasidegenerate Higgsinos*, Phys. Rev. D **89** (2014) 075007, arXiv:1401.1235 [hep-ph].

[110] H. Baer, A. Mustafayev, and X. Tata, *Monojet plus soft dilepton signal from light higgsino pair production at LHC14*, Phys. Rev. D **90** (2014) 115007, arXiv:1409.7058 [hep-ph].

[111] A. Barr and J. Scoville, *A boost for the EW SUSY hunt: monojet-like search for compressed sleptons at LHC14 with 100 fb^{-1}*, JHEP **04** (2015) 147, arXiv:1501.02511 [hep-ph].

[112] P. Jackson and C. Rogan, *Recursive jigsaw reconstruction: HEP event analysis in the presence of kinematic and combinatoric ambiguities*, Phys. Rev. D **96** (2017) 112007, arXiv:1705.10733 [hep-ph].

[113] P. Jackson, C. Rogan, and M. Santoni, *Sparticles in motion: Analyzing compressed SUSY scenarios with a new method of event reconstruction*, Phys. Rev. D **95** (2017) 035031, arXiv:1607.08307 [hep-ph].

[114] C. G. Lester and D. J. Summers, *Measuring masses of semi-invisibly decaying particles pair produced at hadron colliders*, Phys. Lett. B **463** (1999) 99–103, arXiv:hep-ph/9906349.

[115] A. Barr, C. Lester, and P. Stephens, *A variable for measuring masses at hadron colliders when missing energy is expected; m_{T2}: the truth behind the glamour*, J. Phys. G **29** (2003) 2343–2363, arXiv:hep-ph/0304226.

[116] ATLAS Collaboration, *Search for electroweak production of supersymmetric states in scenarios with compressed mass spectra at $\sqrt{s} = 13$ TeV with the ATLAS detector*, Phys. Rev. D **97** (2018) 052010, arXiv:1712.08119 [hep-ex].

[117] J. P. Reichert, *Electron Identification, Electronics Upgrades, and Electroweak Supersymmetry at ATLAS*, Apr, 2019. https://cds.cern.ch/record/2672349.

[118] ATLAS Collaboration, *E_T^{miss} performance in the ATLAS detector using 2015–2016 LHC pp collisions*, ATLAS-CONF-2018-023, 2018, https://cds.cern.ch/record/2625233.

[119] J. Butterworth et al., *PDF4LHC recommendations for LHC Run II*, J. Phys. G **43** (2016) 023001, arXiv:1510.03865 [hep-ph].

[120] M. Baak, G. J. Besjes, D. Côté, A. Koutsman, J. Lorenz, and D. Short, *HistFitter software framework for statistical data analysis*, Eur. Phys. J. C **75** (2015) 153, arXiv:1410.1280 [hep-ex].

[121] G. Cowan, K. Cranmer, E. Gross, and O. Vitells, *Asymptotic formulae for likelihood-based tests of new physics*, Eur. Phys. J. C **71** (2011) 1554, arXiv:1007.1727 [physics.data-an].

[122] A. L. Read, *Presentation of search results: the CL_S technique*, J. Phys. G **28** (2002) 2693.

[123] J. de Favereau et al., *DELPHES 3: a modular framework for fast simulation of a generic collider experiment*, Journal of High Energy Physics **2014** (2014).

[124] ALEPH, DELPHI, L3, OPAL Experiments, *Combined LEP Chargino Results, up to 208 GeV for low DM*, LEPSUSYWG/02-04.1, 2002, http://lepsusy.web.cern.ch/lepsusy/www/inoslowdmsummer02/charginolowdm_pub.html.

[125] ATLAS Collaboration, *Search for direct production of charginos, neutralinos and sleptons in final states with two leptons and missing transverse momentum in pp collisions at $\sqrt{s} = 8$ TeV with the ATLAS detector*, JHEP **05** (2014) 071, arXiv:1403.5294 [hep-ex].

[126] ATLAS Collaboration, *Search for direct production of charginos and neutralinos in events with three leptons and missing transverse momentum in $\sqrt{s} = 8$ TeV pp collisions with the ATLAS detector*, JHEP **04** (2014) 169, arXiv:1402.7029 [hep-ex].

[127] ALEPH, DELPHI, L3, OPAL Experiments, *Combined LEP Selectron/Smuon/Stau Results, 183-208 GeV*, Lepsusywg/04-01.1, 2004, http://lepsusy.web.cern.ch/lepsusy/www/sleptons_summer04/slep_final.html.

[128] K. Cranmer and I. Yavin, *RECAST - extending the impact of existing analyses*, Journal of High Energy Physics **2011** (2011), arXiv:1010.2506 [hep-ex].

[129] D. Merkel, *Docker: Lightweight Linux Containers for Consistent Development and Deployment*, https://dl.acm.org/doi/10.5555/2600239.2600241.

[130] K. Cranmer and L. Heinrich, *Yadage and Packtivity – analysis preservation using parametrized workflows*, Journal of Physics: Conference Series **898** (2017) 102019.